

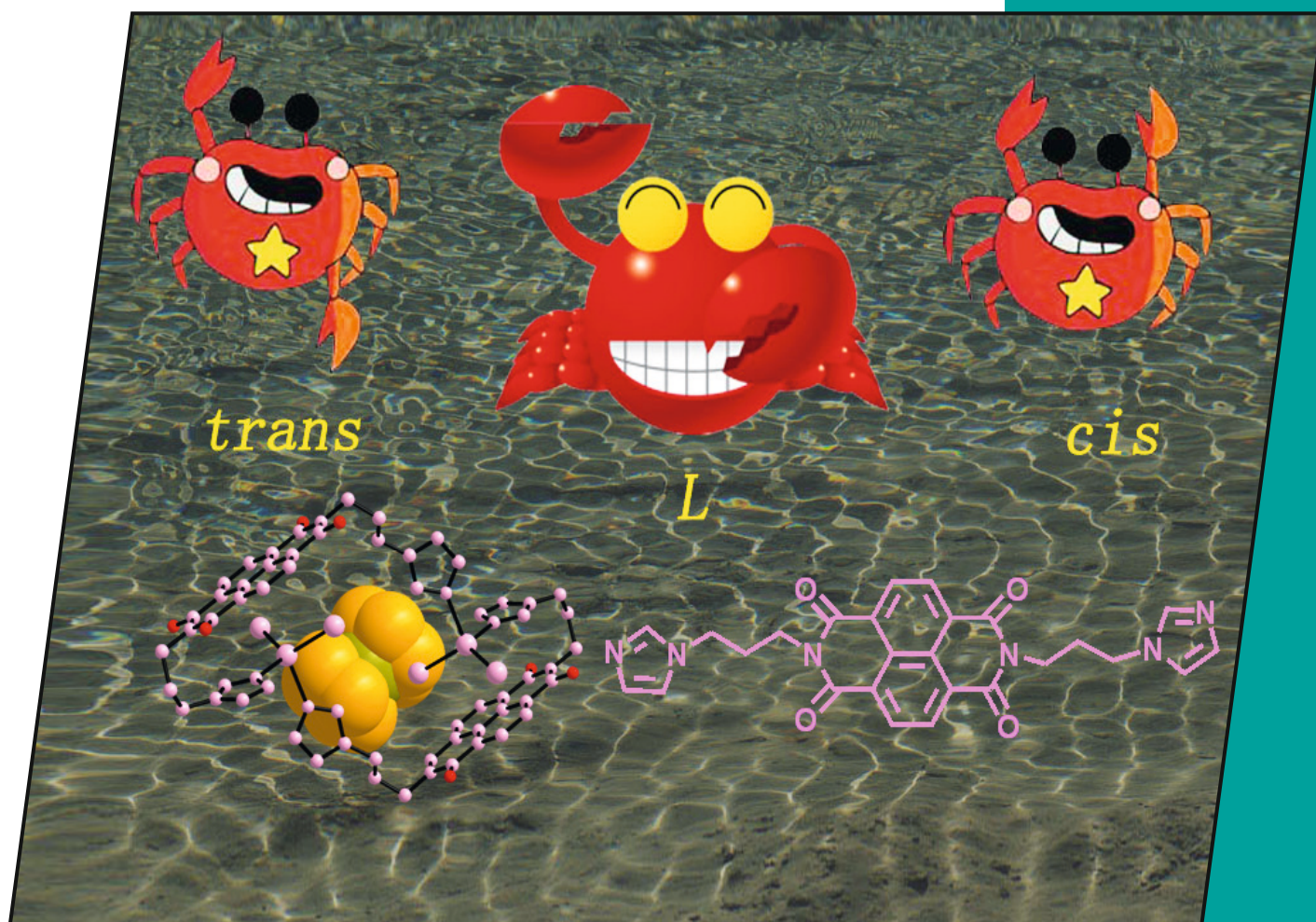


EurJIC

European Journal of
Inorganic Chemistry

8/2012

2nd March Issue



Cover Picture

Mei Pan, Cheng-Yong Su et al.

Structure and Properties of Imidazolyl-Substituted NDI and Its Complexes

 WILEY-VCH

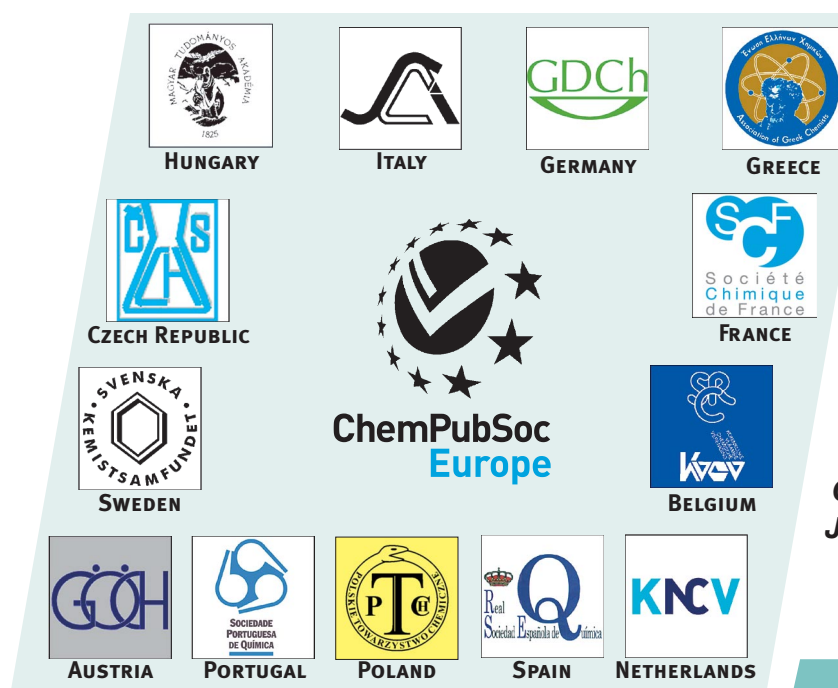
www.eurjic.org

EJICFK (8) 1149–1288 (2012) · ISSN 1434-1948 · No. 8/2012

A Journal of



ChemPubSoc
Europe

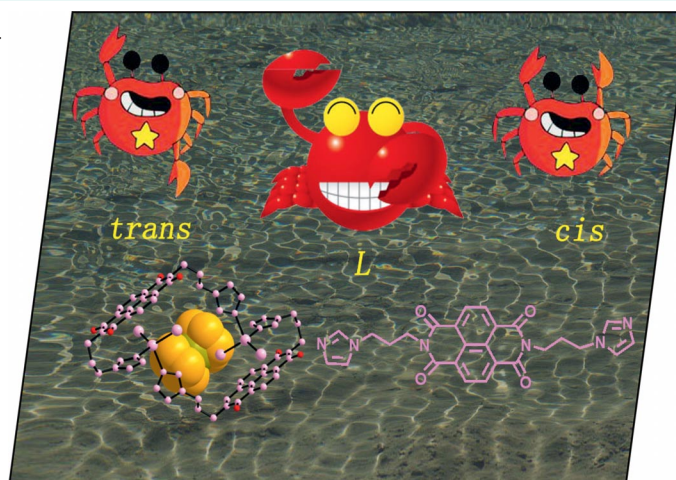


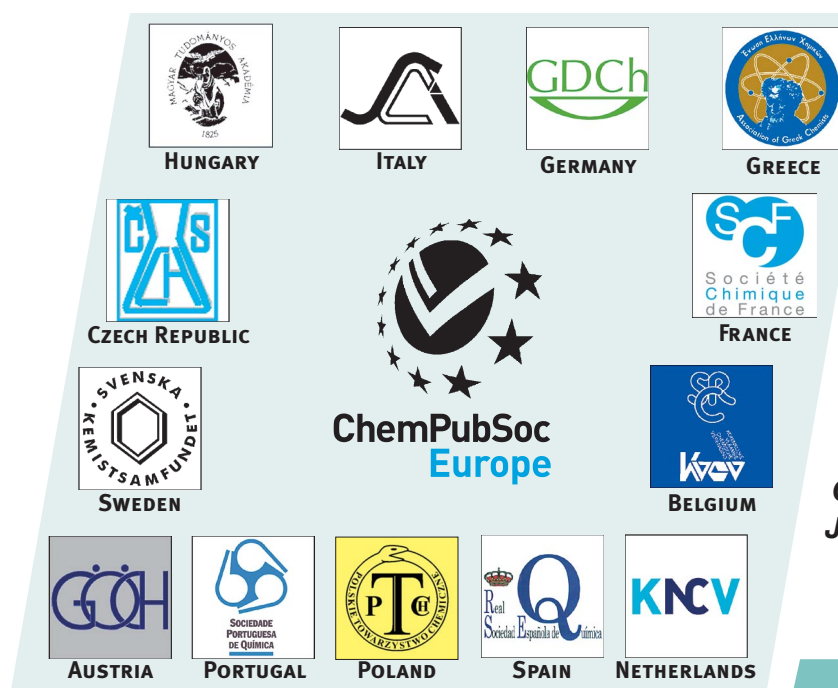
EurJIC is a journal of ChemPubSoc Europe, a union of 16 European chemical societies formed for the purpose of publishing high-quality science. All owners merged their national journals to form two leading chemistry journals, the *European Journal of Inorganic Chemistry* and the *European Journal of Organic Chemistry*.

Other ChemPubSoc Europe journals are *Chemistry – A European Journal*, *ChemBioChem*, *ChemPhysChem*, *ChemMedChem*, *ChemSusChem*, *ChemCatChem*, *ChemPlusChem* and *ChemistryOpen*.

COVER PICTURE

The cover picture shows that an “end-core-end”-type NDI-based ligand could take either *trans*, *L* or *cis* conformations, just like the two pincers of a crab can have different relative positions. Its coordination with Hg^{II} , Cd^{II} , Cu^{II} halides leads to the formation of M_2L_2 metallocycles, 1D zigzag chains or ML metallocycle structures. Details are discussed in the article by M. Pan, C.-Y. Su et al. on p. 1171ff.



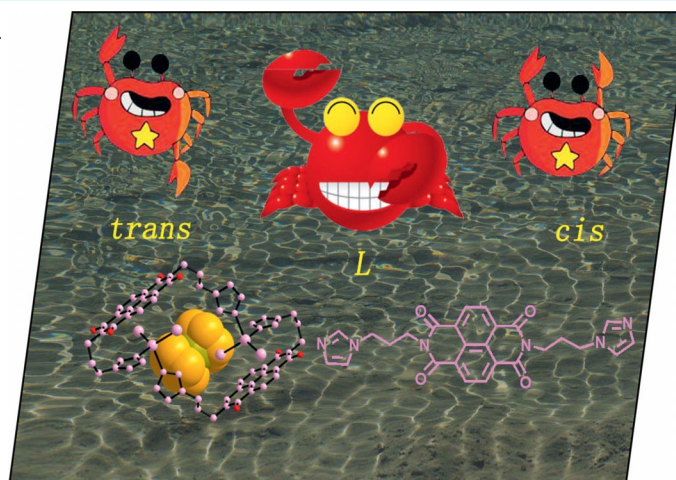


EurJIC is a journal of ChemPubSoc Europe, a union of 16 European chemical societies formed for the purpose of publishing high-quality science. All owners merged their national journals to form two leading chemistry journals, the *European Journal of Inorganic Chemistry* and the *European Journal of Organic Chemistry*.

Other ChemPubSoc Europe journals are *Chemistry – A European Journal*, *ChemBioChem*, *ChemPhysChem*, *ChemMedChem*, *ChemSusChem*, *ChemCatChem*, *ChemPlusChem* and *ChemistryOpen*.

COVER PICTURE

The cover picture shows that an “end-core-end”-type NDI-based ligand could take either *trans*, *L* or *cis* conformations, just like the two pincers of a crab can have different relative positions. Its coordination with Hg^{II} , Cd^{II} , Cu^{II} halides leads to the formation of M_2L_2 metallocycles, 1D zigzag chains or ML metallocycle structures. Details are discussed in the article by M. Pan, C.-Y. Su et al. on p. 1171ff.



SHORT COMMUNICATIONS

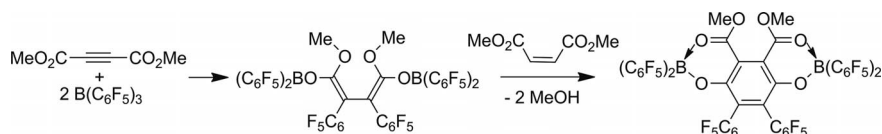
Boron Ester Enolates

H. Nakatsuka, R. Fröhlich, M. Kitamura,
G. Kehr, G. Erker* 1163–1166



Double Arylation of Acetylenedicarboxylate with $B(C_6F_5)_3$

Keywords: Boranes / Alkynes / Carboboration / Cycloaddition



Dimethyl acetylenedicarboxylate reacts with 2 mol-equiv. $B(C_6F_5)_3$ by C_6F_5 transfer to the central acetylenic $C\equiv C$ bond with formation of a tail-to-tail coupled bis(boron ester enolate) system. The central

hexasubstituted butadiene unit of this unique system reacts with dimethyl maleate in a Diels–Alder reaction to give a hydroquinone derivative.

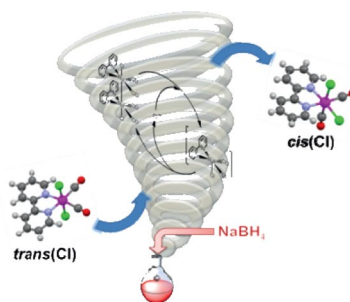
Isomerization Chain Reactions

Y. Kuramochi, Y. Ito,
H. Ishida* 1167–1170



Chain Reaction for Isomerization from *trans*(Cl) to *cis*(Cl)-Ru(bpy)(CO)₂Cl₂ (bpy = 2,2′-Bipyridine) Induced by $NaBH_4$

Keywords: Ruthenium / Isomerization / Reduction / Carbonyl ligands / N ligands



The novel chain reaction for isomerization from *trans*(Cl) to *cis*(Cl)-Ru(bpy)(CO)₂Cl₂, which is induced by a catalytic amount of $NaBH_4$ and proceeds smoothly even at room temperature, is reported. This chain isomerization is a rare reduction-triggered *trans*–*cis* isomerization, which is a promising methodology that produces the *cis*-ruthenium mono(bipyridine) derivatives under moderate conditions.

FULL PAPERS

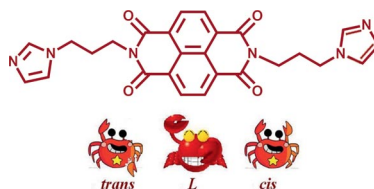
Self-Assembled Complexes

J.-J. Jiang, C. Yan, M. Pan,* Z. Wang,
H.-Y. Deng, J.-R. He, Q.-Y. Yang, L. Fu,
X.-F. Xu, C.-Y. Su* 1171–1179



Structural Conformation and Optical and Electrochemical Properties of Imidazolyl-Substituted Naphthalenediimide and Its Hg^{II} , Cd^{II} , and Cu^{II} Halide Complexes

Keywords: Coordination modes / Density functional calculations / Electrochemistry / Self-assembly



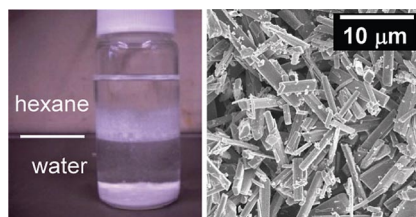
Self-assembly of an end–core–end naphthalenediimide-based ligand with Hg^{II} , Cd^{II} , and Cu^{II} halides leads to the formation of an M_2L_2 metallacycle, 1D zigzag chain, or ML metallacycle, which are directed by the geometric preference of the halide anions, metal centers, and conformational adaptation of the ligand.

Biphasic Sol–Gel Synthesis

M. Tanaka, S. Fujihara* 1180–1185

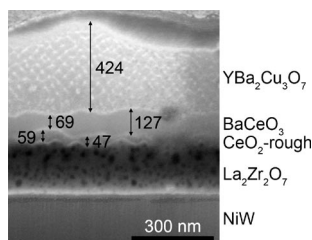
Room-Temperature Sol–Gel Synthesis of Sodium Hexaniobate in an Immiscible Hexane–Water System and Its Conversion into $NaNbO_3$

Keywords: Niobium / Alkoxides / Sol–gel processes / Crystal growth



Rod-like sodium hexaniobate particles were synthesized by a one-pot sol–gel method at room temperature by using an immiscible hexane–water system. They could be converted into $NaNbO_3$ by a heat treatment and a water dispersion treatment.

Smooth, well-textured CeO_2 buffer layers for coated conductors were synthesized by aqueous precursor formulations. The texture and morphology were characterized. Deposition of $\text{YBa}_2\text{Cu}_3\text{O}_7$ (YBCO) by metal–organic deposition with trifluoroacetate (TFA-MOD) and focussed ion beam analysis allowed the characterization of YBCO and the growth of secondary phases as a function of properties of the buffer layer.



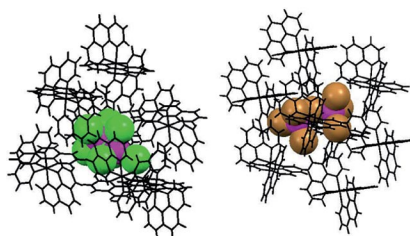
N. Van de Velde, T. Bruggeman, L. Stove, G. Pollefeyt, O. Brunkahl, I. Van Driessche* 1186–1194

Influence of Morphology and Texture of CeO_2 on $\text{YBa}_2\text{Cu}_3\text{O}_7$ (YBCO) Growth and BaCeO_3 Formation in Solution-Derived Synthesis

Keywords: Superconductors / Layered compounds / Cerium dioxide / Nanostructures / Surface morphology

Crystal Engineering

Two new discrete anionic species, $[\text{Cd}_2\text{Cl}_7]^{3-}$ and $[\text{Cd}_2\text{Br}_7]^{3-}$, have been isolated in the form of cobalt(III) complex salts. This successful isolation indicates the possibility of “caging” these ions with the help of a similarly sized and equally charged cation.



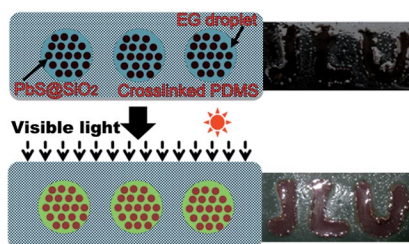
R. P. Sharma,* A. Singh, P. Venugopalan, G. Yanan, J. Yu, C. Angeli, V. Ferretti* 1195–1203

“Caging” Anions through Crystal Engineering to Avoid Polymerization: Structural, Conformational and Theoretical Investigations of New Halocadmate $[\text{Cd}_2\text{X}_7]^{3-}$ Anions (X = Cl/Br)

Keywords: Crystal engineering / Anions / Cadmium complexes / Density functional calculations / Conformation analysis

PbS Photonic Structures

Visible-light-responsive photonic structures have been prepared in alcohol solvents by using silica-modified PbS colloidal nanocrystal clusters as building blocks. Repulsive electrostatic and solvation forces contribute to the self-assembly of the $\text{PbS}@/\text{SiO}_2$ spheres. Solid polymer composite films with similar light-responsive optical properties have also been produced in polymer matrices.

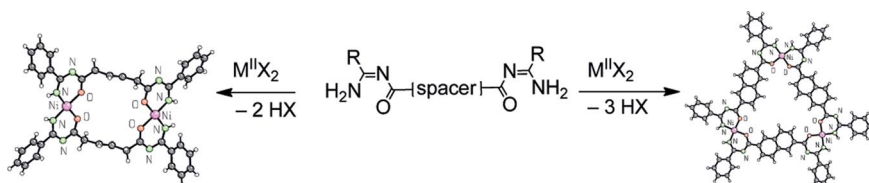


C. Li, T. Bai, T. Li, F. Li, W. Dong, Z. Shi,* S. Feng 1204–1209

A Facile Approach for Transferring PbS Colloidal Photonic Structures into Alkanol Solutions and Composite Solid Films

Keywords: Colloids / Nanostructures / Self-assembly / Photonic crystals / Lead

Metallomacrocycles



Bis(*N*-acylamidines) are potent bidentate ligands that form 2:2 and 3:3 metallomacrocycles with nickel(II) and copper(II) by self-assembly. The nature of the coordination compounds is directed by the shape

of the spacer. Bent spacers give 2:2 complexes, whereas linear spacers lead to 3:3 macrocycles. Both types form layers in the solid state, which intercalate solvent molecules (DMF, DMSO).

J. I. Clodt, R. Fröhlich, M. Eul, E.-U. Würthwein* 1210–1217

Metallomacrocyclic Complexes by Self-Assembly of Ni^{II} and Cu^{II} Ions and Chelating Bis(*N*-acylamidines)

Keywords: Supramolecular chemistry / N,O ligands / Metallomacrocycles / Nickel / Copper

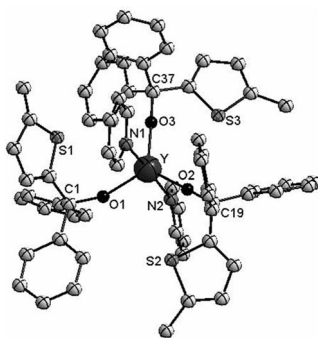
CONTENTS

Electroluminescent Materials

M. Veith,* C. Belot,
V. Huch 1218–1228

New Yttrium and Europium(+3) Alkoxides Bearing Thiophene Units: Syntheses, Crystal Structure Determinations and Physico-Chemical Properties

Keywords: Electroluminescent materials / Electrochemistry / Luminescence / Lanthanides / Yttrium / Europium



The reaction between a series of carbinols bearing thiophene and phenyl units and $\text{Ln}[\text{N}(\text{SiMe}_3)_2]_3$ ($\text{Ln} = \text{Y}, \text{Eu}$) in thf or a mixture of toluene and pyridine as solvent leads to the metal alkoxides: $\{\text{Y}[\text{OC}(\text{C}_{16}\text{H}_{13}\text{S})]_3(\text{thf})_2\} \cdot \text{toluene}$, $\{\text{Y}[\text{OC}(\text{C}_{16}\text{H}_{13}\text{S})]_3(\text{py})_2\} \cdot \text{toluene}$, $\{\text{Y}[\text{OC}(\text{C}_{17}\text{H}_{15}\text{S})]_3(\text{thf})_2\} \cdot \text{toluene}$, $\{\text{Y}[\text{OC}(\text{C}_{17}\text{H}_{15}\text{S})]_3(\text{py})_2\} \cdot \text{toluene}$, $\{\text{Y}[\text{OC}(\text{C}_{14}\text{H}_{11}\text{S}_2)]_3(\text{thf})_2\} \cdot 1/2 \text{ toluene}$, $\text{Y}[\text{OC}(\text{C}_{14}\text{H}_{11}\text{S}_2)]_3(\text{py})_2$, $\text{Y}[\text{OC}(\text{C}_{16}\text{H}_{13}\text{S})]_3(\text{py})_2$ and $\{\text{Eu}[\text{OC}(\text{C}_4\text{H}_3\text{S}_3)]_3(\text{thf})_3\} \cdot \text{thf}$. The molecular structures of the compounds are reported and discussed. The physico-chemical studies of yttrium and europium(3+) alkoxides are also presented.

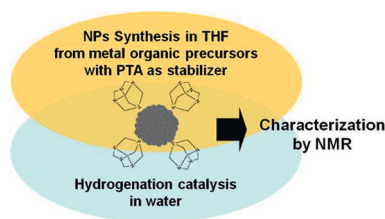
Stabilized Nanoparticles

P.-J. Debouttière, Y. Coppel,
A. Denicourt-Nowicki, A. Roucoux,
B. Chaudret, K. Philippot* 1229–1236



PTA-Stabilized Ruthenium and Platinum Nanoparticles: Characterization and Investigation in Aqueous Biphasic Hydrogenation Catalysis

Keywords: Ruthenium / Platinum / Nanoparticles / Heterogeneous catalysis / Hydrogenation / Sustainable chemistry



PTA-stabilized ruthenium and platinum nanoparticles prepared from organometallic precursors display interesting catalytic reactivity in aqueous biphasic hydrogenation catalysis under mild conditions. The coordination of PTA to the surfaces of the particles was investigated by NMR spectroscopy as it governs the characteristics of the particles as they disperse into water.

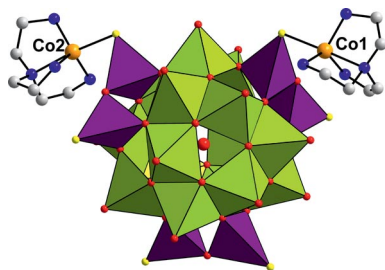
Polyoxovanadate Clusters

J. Wang, C. Näther, P. Kögerler,
W. Bensch* 1237–1242



$[\text{V}_{15}\text{Ge}_6\text{O}_{42}\text{S}_6(\text{H}_2\text{O})]^{12-}$, a Thiogermanatopolyoxovanadate Cluster Featuring the Spin Topology of the Molecular Magnet $[\text{V}_{15}\text{As}_6\text{O}_{42}(\text{H}_2\text{O})]^{6-}$

Keywords: Cluster compounds / Solvothermal synthesis / Solid-state structures / Polyoxovanadate / Magnetic properties



The new polyoxovanadate $[\{\text{Co}(\text{tren})\}_2\text{V}_{15}\text{Ge}_6\text{O}_{42}\text{S}_6(\text{H}_2\text{O})]^{8-}$ was directly synthesized from vanadate and elemental Ge and S. The cluster core $[\text{V}_{15}\text{Ge}_6\text{O}_{42}\text{S}_6(\text{H}_2\text{O})]^{12-}$ is the first V–Ge–O–S cluster and features the spin topology of the seminal molecular magnet $[\text{V}_{15}\text{As}_6\text{O}_{42}(\text{H}_2\text{O})]^{6-}$. The cluster anion is expanded by sulfur-bound, penta-coordinate Co^{2+} complexes.

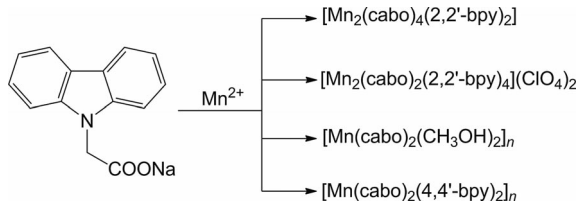
N-Carbazolylacetato Complexes

Y.-S. Ma,* X.-Y. Tang, F.-F. Xue,
B. Chen, Y.-L. Dai, R.-X. Yuan,*
S. Roy 1243–1249



Structural Diversity and Magnetic Properties of the Manganese(II)/Carbazol-9-ylacetato/ N,N' -Donor Reaction System

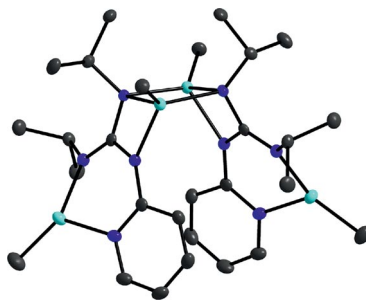
Keywords: Carboxylato ligands / Carbazol-9-ylacetic acid / Manganese / Magnetic properties / N ligands / O ligands



Four manganese-based carbazol-9-ylacetato (cabo) complexes with bipyridyl (bpy) as an ancillary ligand have been synthesized and their structures, and magnetic

properties have been characterized. Antiferromagnetic exchange interactions propagate among the Mn^{II} ions.

Bicyclic and acyclic guanidinate ligands stabilize several new oligonuclear zinc complexes.



C. Neuhäuser, M. Reinmuth, E. Kaifer, H.-J. Himmel* 1250–1260

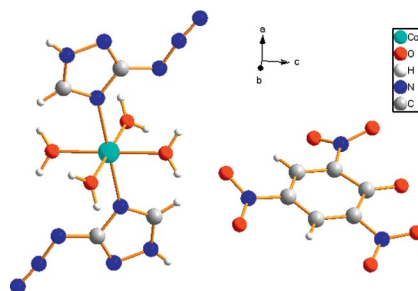
Synthesis of Oligomeric Zinc Complexes with Bicyclic and Acyclic Guanidinate Ligands



Keywords: Zinc / Oligomeric complexes / Alkyl complexes / N ligands / Hydrogen bonds / Guanidines

Energetic Compounds

The structure of $[\text{Co}(\text{AZT})_2(\text{H}_2\text{O})_4](\text{PA})_2$ (AZT = 3-azido-1,2,4-triazole, PA = picrate) shows that the Co^{II} ion is six-coordinate in a slightly distorted octahedral geometry. The energy of combustion and enthalpy of formation are 8.83 MJ kg^{-1} and $-3419.53 \text{ kJ mol}^{-1}$, respectively. Nonisothermal kinetic analysis indicated that the Arrhenius equation can be expressed as $\ln k = 15.23 - 153.3 \times 10^3/(RT)$.



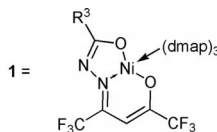
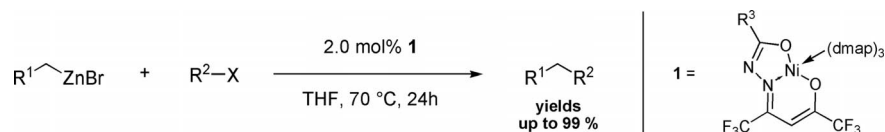
B.-D. Wu, J.-G. Zhang, T.-L. Zhang,* L. Yang, Z.-N. Zhou 1261–1268

Two Environmentally Friendly Energetic Compounds, $[\text{Mn}(\text{AZT})_4(\text{H}_2\text{O})_2](\text{PA})_2 \cdot 4\text{H}_2\text{O}$ and $[\text{Co}(\text{AZT})_2(\text{H}_2\text{O})_4](\text{PA})_2$, Based on 3-Azido-1,2,4-triazole (AZT) and Picrate (PA)



Keywords: N ligands / Picrate / Manganese / Cobalt / Decomposition / Sensitivity

Nickel Complexes



New nickel complexes modified by versatile 5-hydroxypyrazoline ligands have been synthesized and characterized. The catalytic

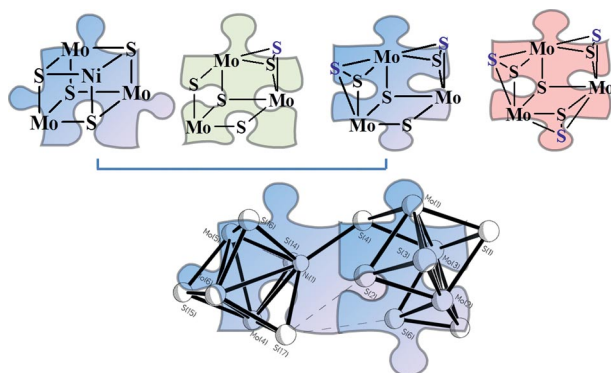
properties of the complexes have been investigated in nickel-catalyzed $\text{C}(\text{sp}^2)\text{---C}(\text{sp}^3)$ cross-coupling reactions.

C. Someya, S. Inoue, S. Krackl, E. Irran, S. Enthaler* 1269–1277

Application of Nickel Complexes Modified by Tridentate $\text{O},\text{N},\text{O}'$ -Ligands as Precatalysts in Nickel-Catalyzed $\text{C}(\text{sp}^2)\text{---C}(\text{sp}^3)$ Bond Formations

Keywords: Nickel / Tridentate ligands / Homogeneous catalysis / Cross-coupling

Aggregated Mo Cluster



A new cluster of formula $\{[\text{Mo}_3(\mu_3\text{-S})(\mu\text{-S})(\mu\text{-S}_2)_2(\text{dtp})_3(\mu\text{-OAc})][\text{Mo}_3\text{NiS}_4(\text{dtp})_3(\mu\text{-OAc})(\text{CH}_3\text{CN})]\}$ (**1**; dtp = diethyl dithiophosphate; OAc = acetate) comprising the

novel C_s -symmetrized $\text{Mo}_3(\mu_3\text{-S})(\mu\text{-S})(\mu\text{-S}_2)_2$ structural type covalently attached to a cubane-type Mo_3NiS_4 core has been isolated and fully characterized.

R. Hernandez-Molina,* J. Gonzalez-Platas, C. Vicent 1278–1284

Isolation of a New C_s -Symmetrized $\text{Mo}_3(\mu_3\text{-S})(\mu\text{-S})(\mu\text{-S}_2)_2$ Structural Type Through Complementary Association with a Cubane-Type Mo_3NiS_4 Cluster



Keywords: Cluster compounds / Nickel / Molybdenum / Chalcogens

CORRECTION

L. Siggelkow, V. Hlukhyy,
T. F. Fässler* 1285

Ca₂NiSn₂ – A Polymorphic Intermetallic Phase: Atomic and Electronic Structure as well as a Topological Description of the Phase Transition by a Sigmatropic-Type Rearrangement of Ni and Sn Atoms

Keywords: Tin / Intermetallic phases / ELF (Electron Localization Function) / Chemical bonding / Phase transitions

* Author to whom correspondence should be addressed.

 Supporting information on the WWW (see article for access details).

 This article is available online free of charge (Open Access).

If not otherwise indicated in the article, papers in issue 7 were published online on February 21, 2012

ICPC 2012

Rotterdam, The Netherlands

19th International Conference on Phosphorus Chemistry 8-12 July 2012 ROTTERDAM, The Netherlands

www.icpc2012.nl

Plenary speakers

- Guy Bertrand, University of California Riverside (US)
- Bernhard Breit, University of Freiburg (D)
- Neil Burford, Dalhousie University (CA)
- Frank H. Ebetino, Warner Chilcott (IE)
- Gabriel Filippelli, IUPUI Indianapolis (US)
- Stephen Hanessian, University of Montreal (CA)
- Piet Herdewijn, Catholic University Leuven (B)
- Klemens Massonne, BASF (D)
- Maurizio Peruzzini, ICCOM CNR, Florence (I)
- Paul Pringle, Bristol University (UK)
- Willem Schipper, Thermphos (NL)
- Doug Stephan, University of Toronto (CA)



Dear Colleagues,

We are delighted to invite you to the 19th International Congress on Phosphorus Chemistry taking place in the vibrant city of Rotterdam. Due to its great success, the ICPC is organized biannually from now on and intends to provide a valuable platform for scientific discussions as well as a stimulating meeting place encouraging a close partnership between all the delegates from academia and industry. The attendance of more than 400 delegates from more than 50 countries is expected. Developments and achievements in all fields of Phosphorus will be presented either in plenary presentations or as oral communications in different sections. We are thrilled to invite you to discover more about the congress on the website, which will be regularly updated with all congress news. Submit your abstracts and register your place using our on-line systems. We look forward to seeing you in Rotterdam in 2012.

Koop Lammertsma, *Chair of the Organizing Committee ICPC 2012*



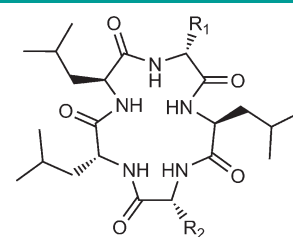


Natural Products

H. B. Bode,* D. Reimer, S. W. Fuchs, F. Kirchner, C. Dauth, C. Kegler, W. Lorenzen, A. O. Brachmann, P. Grün

Determination of the Absolute Configuration of Peptide Natural Products by Using Stable Isotope Labeling and Mass Spectrometry

Game over—structure solved: A combination of labeling experiments with mass spectrometry results in the reliable determination of the sum formula, the nature of the building blocks, and for peptide natural products also the determination of the absolute configuration as exemplified for the novel natural products GameXPeptide A–D (see scheme).



GameXPeptide A $R^1 = iPr, R^2 = Bn$
GameXPeptide B $R^1 = iBu, R^2 = Bn$
GameXPeptide C $R^1 = iPr, R^2 = iBu$
GameXPeptide D $R^1 = iBu, R^2 = iBu$
Chem. Eur. J.
 DOI: 10.1002/chem.201103479

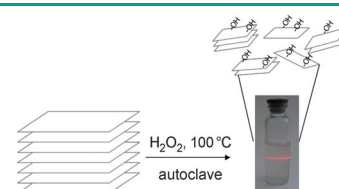


Nanomaterials

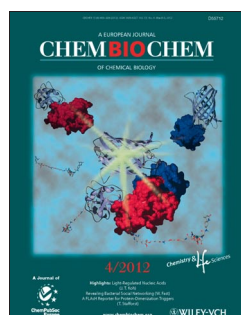
A. S. Nazarov, V. N. Demin,* E. D. Grayfer, A. I. Bulavchenko, A. T. Arymbaeva, H.-J. Shin, J.-Y. Choi, V. E. Fedorov*

Functionalization and Dispersion of Hexagonal Boron Nitride (h-BN) Nanosheets Treated with Inorganic Reagents

Divide and organize: Exfoliation and dispersion of hexagonal boron nitride (h-BN) was achieved through reaction with a range of inorganic reagents (see picture). The product exists in the form of stable colloids in water or *N,N*-dimethylformamide (DMF) as thin platelets of functionalized h-BN. Highlights of this method are high yields of soluble h-BN and increased concentrations of dispersions.



bulk h-BN
Chem. Asian J.
 DOI: 10.1002/asia.201100710

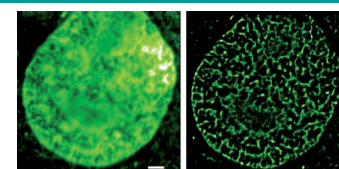


Super-Resolution Imaging

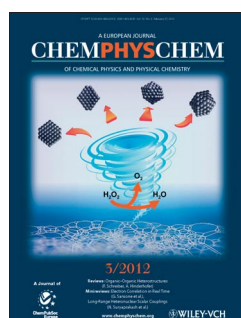
A. Benke, S. Manley*

Live-Cell dSTORM of Cellular DNA Based on Direct DNA Labeling

We have implemented the super-resolution method of direct stochastic optical reconstruction microscopy (dSTORM) to image nuclear and mitochondrial DNA in living cells. We also demonstrate time-lapse imaging, all using a dye that associates directly with cellular DNA: the commercially available dye Picogreen (see figure).



ChemBioChem
 DOI: 10.1002/cbic.201100679

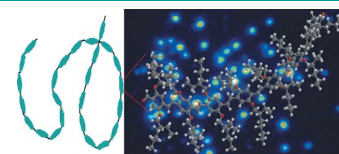


Conjugated Polymers

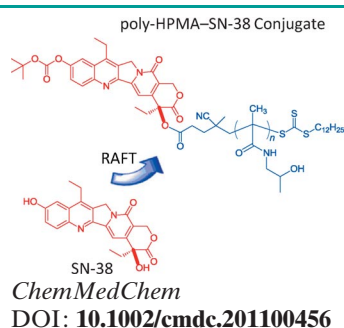
J. M. Lupton*

Chromophores in Conjugated Polymers—All Straight?

What shape is it? Single-molecule and ensemble time-resolved studies support the notion that the π -bond in large macromolecules, such as conjugated polymers, is remarkably persistent in space: even individual chromophores can be bent and twisted, so that caution is warranted when interpreting a wide range of polarization-based spectroscopies.



ChemPhysChem
 DOI: 10.1002/cphc.201100770

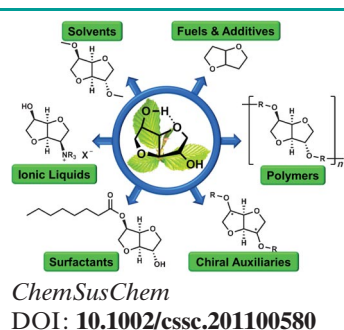
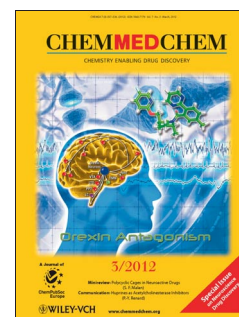


Drug Delivery

C. C. Williams, S. H. Thang, T. Hantke, U. Vogel, P. H. Seeberger, J. Tsanakisidis,* B. Lepenies*

RAFT-Derived Polymer–Drug Conjugates: Poly(hydroxypropyl methacrylamide) (HPMA)–7-Ethyl-10-hydroxycamptothecin (SN-38) Conjugates

A life RAFT! A series of well-defined polymer–drug conjugates have been prepared to increase the bioavailability of the known cytotoxic drug 7-ethyl-10-hydroxycamptothecin (SN-38). Reversible addition–fragmentation chain transfer (RAFT) polymerisation was used to covalently and site-specifically append an *N*-(2-hydroxypropyl)methacrylamide (HPMA) polymer to SN-38. The poly-HPMA–SN-38 conjugates displayed excellent aqueous solubility, cytotoxic activity, and specificity for cancer cells.

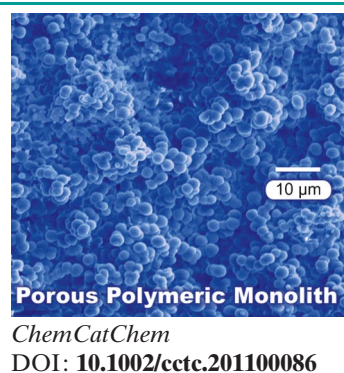


Renewable Chemicals

M. Rose, R. Palkovits*

Isosorbide as a Renewable Platform chemical for Versatile Applications—Quo Vadis?

Unwritten tales of isosorbide: Isosorbide is a versatile platform chemical that can be derived from cellulosic biomass as a sustainable resource. Numerous derivatives can be obtained by using various chemical, chemocatalytic, and biotechnological processes to enable the replacement of products in numerous applications that are currently based on fossil resources.

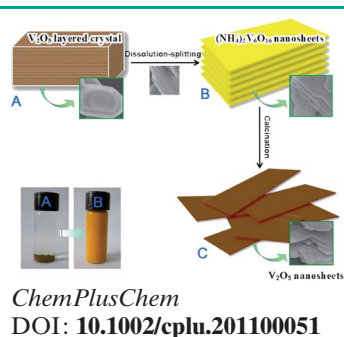
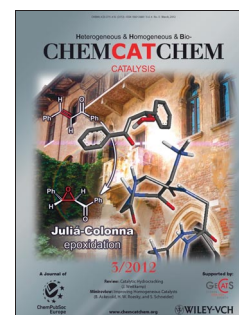


Immobilized Catalysts

E. B. Anderson, M. R. Buchmeiser*

Catalysts Immobilized on Organic Polymeric Monolithic Supports: From Molecular Heterogeneous Catalysis to Biocatalysis

Affixation with the monolith: This review elucidates advances in supported catalysis for metathesis, Heck, Suzuki, Sonogashira–Hagihara, and biocatalytic reactions. Syntheses and post-functionalizations of organic polymeric monoliths to affix functional catalysts are described. The function of these porous structures in both heterogeneous catalysis and biocatalysis under continuous flow conditions is illustrated.

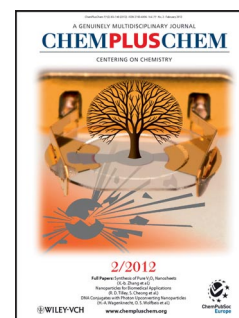


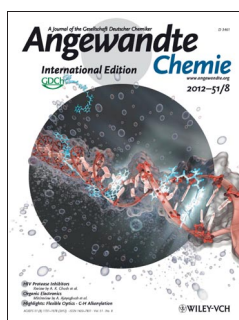
Lithium Ion Batteries

Z.-l. Wang, D. Xu, L.-m. Wang, X.-b. Zhang*

Facile and Low-Cost Synthesis of Large-Area Pure V₂O₅ Nanosheets for High-Capacity and High-Rate Lithium Storage over a Wide Temperature Range

Layer upon layer: Pure V₂O₅ nanosheets (see figure; C) have been successfully synthesized by a novel and facile dissolution–splitting method using low-cost raw materials (A). The as-prepared product exhibits enhanced lithium storage properties including good cycling and rate performance, 144 mAh g^{−1} at 10 C and 95 mAh g^{−1} at 20 C, as well as high reversible capacity, 290 mAh g^{−1}.





Water Splitting

J. Chen,* P. Wagner, L. Tong, G. G. Wallace, D. L. Officer, G. F. Swiegers*

A Porphyrin-Doped Polymer Catalyzes Selective, Light-Assisted Water Oxidation in Seawater

A flexible polymer for selective seawater splitting: Incorporation of a monomeric Mn-porphyrin that is normally catalytically inactive, into a flexible poly(terthiophene) film yields a remarkable light-assisted water oxidation catalyst with an apparent overpotential for water oxidation of a mere 0.09 V. The catalyst generates exclusively O₂ and no Cl₂ in seawater at 0.9 V versus Ag/AgCl.

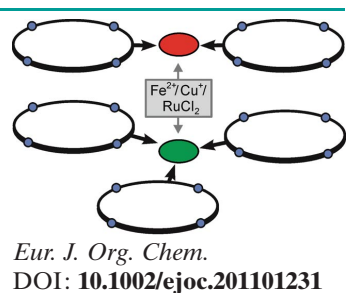


Supramolecular Chemistry

E. V. Dzyuba, B. Baytekin, D. Sattler, C. A. Schalley*

Phenanthroline- and Terpyridine-Substituted Tetralactam Macrocycles: A Facile Route to Rigid Di- and Trivalent Receptors and Interlocked Molecules

Hunter/Vögtle-type tetralactam macrocycles are equipped with metal coordination sites through Suzuki cross-coupling. The same bromo-substituted macrocycle can be used irrespective of the individual binding site, which provides versatile access to different complexes. The complexes represent multivalent hosts that are potentially useful for the formation of multiply interlocked molecules.



Synthesis of Pesto

Klaus Roth

Pesto – Mediterranean Biochemistry (Part 2)

In this last part we take a look at the synthesis of the perfect pesto. Close your eyes, inhale deeply the monoterpenes, and give isoprene units the opportunity to dance before your mind's eye. Surely there's no finer way to appreciate chemistry!



ChemViews magazine
DOI: 10.1002/chemv.201200002

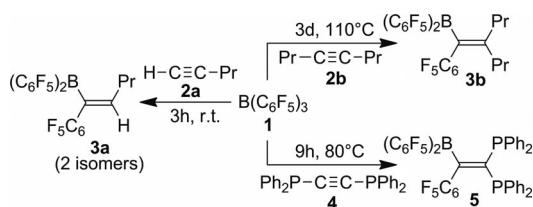
Double Arylation of Acetylenedicarboxylate with $B(C_6F_5)_3$ Hiroshi Nakatsuka,^[a,b] Roland Fröhlich,^{[a],‡} Masato Kitamura,^[b] Gerald Kehr,^[a] and Gerhard Erker*^[a]**Keywords:** Boranes / Alkynes / Carboboration / Cycloaddition

Dimethyl acetylenedicarboxylate reacts with 2 mol-equiv. $B(C_6F_5)_3$ by C_6F_5 transfer to the central acetylenic $C\equiv C$ bond with formation of a tail-to-tail coupled bis(boron ester enol-

ate) system. The central hexasubstituted butadiene unit of this unique system reacts with dimethyl maleate in a Diels–Alder reaction to give a hydroquinone derivative.

Introduction

The strong boron Lewis acid $B(C_6F_5)_3$ (**1**) reacts with a variety of acetylene substrates by 1,1-carboboration.^[1] A typical example is the reaction with 1-pentyne (**2a**) that proceeds rapidly at room temperature to give the alkenyl borane **3a** in high yield (see Scheme 1).^[2] Even the internal alkyne 4-octyne (**2b**) reacts with $B(C_6F_5)_3$ analogously, albeit at elevated temperature. The reaction can be viewed to be a novel method for carbon–carbon bond activation.^[3] Under rather forcing conditions (110 °C, 3 d), we obtained the 1,1-carboboration product **3b** in good yield.^[4] Phosphanyl-substituted alkynes react similarly. At 80 °C, the strong P–C bond of substrate **4** was cleaved upon treatment with $B(C_6F_5)_3$ to yield the respective 1,1-carboboration product **5** with formation of a new B–C and C–C bond and with a concomitant 1,2-shift of a phosphanyl group along the central former acetylenic C–C moiety.^[5]



Scheme 1.

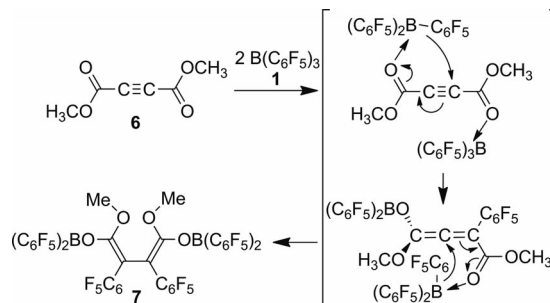
We have now tried to extend this interesting and useful $RB(C_6F_5)_2$ variant of the 1,1-carboboration reaction to organic acetylenes that bear reactive organic functional

groups. One example substrate is dimethyl acetylenedicarboxylate (**6**), which reacted readily with $B(C_6F_5)_3$ (**1**) but gave a markedly different type of product. Its formation, characterization and a typical subsequent reaction of the unusual product **7** is described in this account.

Results and Discussion

The reaction between $B(C_6F_5)_3$ (**1**) and dimethyl acetylenedicarboxylate (**6**) was carried in cyclopentane solution at room temperature in a 2:1 ratio. After storing the reaction mixture for 3 d at room temperature, the obtained yellow crystals that had formed during this time were isolated (53% yield). They were suitable for characterization by X-ray diffraction.

The X-ray crystal-structure analysis of compound **7** reveals that a C_6F_5 group had been symmetrically transferred from each of the $B(C_6F_5)_3$ molecules employed to the central acetylene moiety of substrate **6**. The pair of the remaining $-B(C_6F_5)_2$ units was found to be bonded to the carbonyl oxygen atoms of the former acetylenedicarboxylate substrate. Thus, we have not carried out a 1,1-carboboration reaction, but instead a pair of conjugate C_6F_5 -addition reactions had occurred (see Scheme 2) to yield a unique tail-to-tail connected conjugated bis(boron ester enolate).



Scheme 2.

[a] Organisch-Chemisches Institut, Universität Münster, Corrensstraße 40, 48149 Münster, Germany
Fax: +49-251-8336503

E-mail: erker@uni-muenster.de

[b] Department of Chemistry and Research Center for Materials Science, Nagoya University, Chikusa, Nagoya 464-8602, Japan

‡ X-ray structure analyses

Supporting information for this article is available on the WWW under <http://dx.doi.org/10.1002/ejic.201101413>.

In the crystal the molecule **7** was found in a close to C_2 -symmetric conformation. The central hexasubstituted butadiene unit features characteristically alternating carbon–carbon bond lengths of 1.337(3) (C2A–C3A), 1.479(3) (C3A–C3B), and 1.340(3) Å (C3B–C2B). The conjugated diene moiety was found in a *cisoid gauche* type conformation [C2A–C3A–C3B–C2B 42.3(3)°]. Consequently, the pair of C_6F_5 groups at C3A and C3B is facing each other. The $-O-B(C_6F_5)_2$ units are both *cis*-oriented to the carbon-bonded C_6F_5 groups. They exhibit bonding angles at oxygen C2A–O1A–B1A 122.8(2), C2B–O1B–B1B 125.6(2)° and of bond lengths C2A–O1A 1.385(2), B1A–O1A 1.354(3), C2B–O1B 1.383(2), B1B–O1B 1.353(3) Å. The pair of OCH_3 substituents of the ester enolate moieties points to the inner positions at the *cisoid* butadiene framework (see Figure 1).

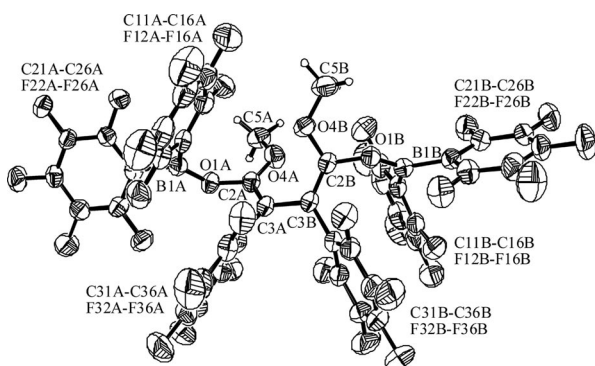


Figure 1. Molecular structure of product **7**.

The product **7** features a ^{11}B NMR resonance ($\delta = 44$ ppm, $\nu_{1/2} \approx 1400$ Hz) typical for a tricoordinate boron centre.^[6] We monitored two sets of ^{19}F NMR data in a 2:1 ratio for the $-B(C_6F_5)_2$ units and $-C_6F_5$ substituents. The former is characterized by a rather large $\Delta\delta^{19}F(m,p)$ separation of 14.9 ppm. The former carbonyl carbon atom of the ester enolates shows a ^{13}C NMR signal at $\delta = 154.8$ ppm, the internal enolate carbon resonance is found at $\delta = 83.9$ ppm.

Scheme 2 offers a tentative mechanistic interpretation of how compound **7** was formed. We assume that each ester carbonyl group of substrate **6** is activated by forming an adduct with the $B(C_6F_5)_3$ Lewis acid.^[7] Each of the thus “self-activated” α,β -unsaturated ynone sections can then undergo an intramolecular nucleophilic addition by C_6F_5 transfer from boron to carbon. We assume a stepwise process proceeding through the respective allenic boron enolate intermediate (Scheme 2).^[8] A consequence of this pathway is that any geometrical isomer of the resulting individual ester enolate moieties may be formed since each nucleophilic C_6F_5 attack takes place at a $C(sp)$ carbon centre. Apparently, the formation of the specific geometric isomer **7** featuring both the $-O-B(C_6F_5)_2$ units in the “outside” *syn* positions at the central conjugated butadiene unit is favoured in this reaction. The unique tail-to-tail connection of the pair of boron ester enolate moieties in **7** makes this butadiene derivative very special. Nevertheless, the system

may serve as an active electron-rich diene component in a Diels–Alder reaction. The [4+2]cycloaddition took place upon treatment with the electron-poor dienophile dimethyl maleate at elevated temperature in $[D_6]$ benzene (120 °C, 65 h). We isolated yellow crystals of product **9** suitable for characterization by X-ray diffraction (see Figure 2).

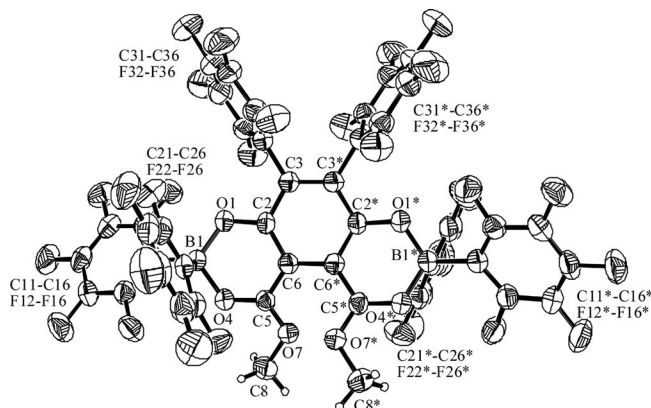
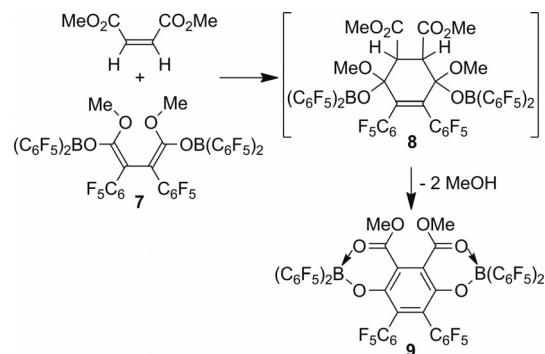


Figure 2. Molecular structure of cycloaddition product **9**.

The X-ray crystal-structure analysis of product **9** shows that a O-borylated tetrasubstituted hydroquinone was obtained from the reaction of **7** with dimethyl maleate. It features a central arene ring [C2–C6 1.392(4), C2–C3 1.427(4), C3–C3* 1.369(5), C6–C6* 1.428(5) Å]. The C_2 -symmetric structure contains a pair of C_6F_5 groups at C3/C3* and methyl ester substituents at the distal C6/C6* vector. The central hydroquinone moiety is O-borylated [C2–O1 1.325(3), O1–B1 1.471(4) Å], and the $-B(C_6F_5)_2$ function is chelated by both the hydroquinone and the adjacent ester oxygen atoms [O4–B1 1.548(4) Å, angle O1–B1–O4 105.8(2)°, O4–C5 1.267(3) Å, C5–O7 1.287(3) Å].

So far, product **9** was only characterized by X-ray diffraction since NMR spectroscopic data could not be collected as a result of the low solubility of **9**. However, its formation shows that the unusually composed tail-to-tail bis(ester enolate) **7** can apparently undergo Diels–Alder reactions: the alleged primary [4+2]cycloaddition product **8** (see Scheme 3) apparently loses 2 equiv. methanol under the harsh reaction conditions to form the favoured aromatic reaction product.



Scheme 3.

Conclusions

The easy formation of **7** and its ability to undergo a [4+2]cycloaddition reaction leads us to hope that such novel type of highly functionalized diene systems will develop an interesting application, complementing the ubiquitous electron-rich enol-type conjugated dienes in their use as interesting synthetic building blocks.^[9,10]

Experimental Section

Preparation of Compound 7: A solution of dimethyl acetylenedicarboxylate (57.0 mg, 0.4 mmol) in cyclopentane (3 mL) was added to a solution of B(C₆F₅)₃ (410 mg, 0.8 mmol) in cyclopentane (3 mL). The solution was kept in the glove box at room temperature for 3 d. The obtained yellow crystals were collected, washed with cyclopentane (2 × 0.5 mL) and dried under vacuum (53%, 247 mg). The obtained crystals were suitable for an X-ray crystal-structure analysis. The yield of product **7** was increased by additional fractional crystallization at −35 °C (68%, 70.6 mg). M.p. 147 °C. C₄₂H₆B₂F₃₀O₄ (1166.07): calcd. C 43.26, H 0.52; found C 42.83, H not detected. HRMS (C₄₂H₆B₂F₃₀O₄): calcd. 1165.99732; found 1165.99197. ¹H NMR (600 MHz, C₆D₆, 298 K): δ = 3.35 (s, 1 H, OMe) ppm. ¹³C{¹H} NMR (151 MHz, C₆D₆, 298 K): δ = 154.8 (=C–O), 148.6 (dm, ¹J_{FC} ≈ 249 Hz, BC₆F₅), 145.7 (dm, ¹J_{FC} ≈ 250 Hz, C₆F₅), 144.4 (dm, ¹J_{FC} ≈ 260 Hz, BC₆F₅), 141.5 (dm, ¹J_{FC} ≈ 256 Hz, C₆F₅), 138.2 (dm, ¹J_{FC} ≈ 254 Hz, C₆F₅), 137.7 (dm, ¹J_{FC} ≈ 256 Hz, BC₆F₅), 110.8 (br., *i*-C₆F₅), 107.1 (br., *i*-BC₆F₅), 83.9 (–C=), 56.2 (CH₃) ppm. ¹⁹F NMR (564 MHz, C₆D₆, 298 K): δ = −131.8 (br., 4 F, *o*), −145.3 (br., 2 F, *p*), −160.2 (m, 4 F, *m*), [Δδ¹⁹F(*m,p*) = 14.9] (BC₆F₅), −139.3 (m, 2 F, *o*), −153.2 (t, ³J_{FF} = 20.5 Hz, 1 F, *p*), −162.3 (m, 2 F, *m*), [Δδ¹⁹F(*m,p*) = 9.1] (C₆F₅) ppm. ¹¹B{¹H} NMR (96 MHz, C₆D₆, 298 K): δ = 44 (ν_{1/2} ≈ 1400 Hz) ppm.

Crystal Data of 7: C₄₂H₆B₂F₃₀O₄, *M* = 1166.09, triclinic, *P* $\bar{1}$ (No. 2), *a* = 10.7615(3), *b* = 10.8751(7), *c* = 19.1314(9) Å, *α* = 96.772(3), *β* = 100.899(3), *γ* = 97.915(3)°, *V* = 2153.68(18) Å³, *D*_c = 1.798 g cm^{−3}, *μ* = 1.859 mm^{−1}, *F*(000) = 1140, *Z* = 2, *λ* = 1.54178 Å, *T* = 223(2) K, 24131 reflections collected (*±h*, *±k*, *±l*), [(*sin θ*)/*λ*] = 0.60 Å^{−1}, 7407 independent (*R*_{int} = 0.042) and 6282 observed reflections [*I* ≥ 2σ(*I*)], 705 refined parameters, *R* = 0.045, *wR*² = 0.115, GoF = 1.032.

Preparation of Compound 9: A solution of dimethyl maleate (24.8 mg, 172 μmol) in toluene (1.0 mL) was added to a solution of the dienolate **7** (200.0 mg, 172 μmol) in toluene (1.0 mL). The reaction mixture was transferred to a 20-mL Schlenk tube and heated at reflux for 24 h. After it was cooled to room temperature, the supernatant was removed and the obtained yellow crystals were washed with toluene (3 × 0.5 mL). The yellow crystals were dried in vacuo (7.9%, 16.9 mg, 13.6 μmol). M.p. >300 °C. C₄₆H₆B₂F₃₀O₆ (1246.13): calcd. C 44.34, H 0.49; found C 43.96, H 0.81. IR (KBr): 1649, 1590, 1523, 1482, 1405, 1395, 1293, 1121, 1100, 987, 786, 738, 693 cm^{−1}.

NMR Scale: Dimethyl maleate (3.60 mg, 25 μmol) in C₆D₆ (0.5 mL) was mixed with dienolate **7** (29.2 mg, 25 μmol) in C₆D₆ (0.5 mL). The reaction mixture was transferred to an NMR tube, which was sealed under vacuum. The NMR tube was then placed in an autoclave and heating at 120 °C for 65 h. After the NMR tube was cooled to room temperature, yellow crystals suitable for an X-ray crystal-structure analysis were obtained. NMR characterization was not possible because of the low solubility of **9**.

Crystal Data of 9: C₄₆H₆B₂F₃₀O₆, *M* = 1246.13, monoclinic, *C*2/*c* (No. 15), *a* = 13.3931(5), *b* = 18.3589(10), *c* = 19.2265(6) Å, *β* = 110.298(5)°, *V* = 4433.9(3) Å³, *D*_c = 1.867 g cm^{−3}, *μ* = 1.893 mm^{−1}, *F*(000) = 2440, *Z* = 4, *λ* = 1.54178 Å, *T* = 223(2) K, 9816 reflections collected (*±h*, *±k*, *±l*), [(*sin θ*)/*λ*] = 0.60 Å^{−1}, 3521 independent (*R*_{int} = 0.040) and 2920 observed reflections [*I* ≥ 2σ(*I*)], 380 refined parameters, *R* = 0.048, *wR*² = 0.140, GoF = 1.048.

CCDC-859180 (for **7**), and -859181 (for **9**) contain the supplementary crystallographic data for this paper. These data can be obtained free of charge from The Cambridge Crystallographic Data Centre via www.ccdc.cam.ac.uk/data_request/cif.

Supporting Information (see footnote on the first page of this article): Details of the X-ray structure analysis and NMR spectra details are presented.

Acknowledgments

Financial support from the Deutsche Forschungsgemeinschaft and the Japan Society for the Promotion of Science (JSPS) are gratefully acknowledged.

- [1] G. Kehr, G. Erker, *Chem. Commun.* **2012**, 48, 1839–1850.
- [2] a) C. Chen, F. Eweiner, B. Wibbeling, R. Fröhlich, S. Senda, Y. Ohki, K. Tatsumi, S. Grimme, G. Kehr, G. Erker, *Chem. Asian J.* **2010**, 5, 2199–2208; b) C. Chen, T. Voss, R. Fröhlich, G. Kehr, G. Erker, *Org. Lett.* **2011**, 13, 62–65.
- [3] Selected examples: a) R. H. Crabtree, *Chem. Rev.* **1985**, 85, 245–269; b) M. Murakami, Y. Ito, *Topics in Organometallic Chemistry* (Ed.: S. Murai), Springer Verlag, New York **1999**, vol. 3, pp. 97–129; c) B. Rybtchinski, D. Milstein, *Angew. Chem.* **1999**, 111, 918–932; *Angew. Chem. Int. Ed.* **1999**, 38, 870–883; d) M. E. van der Boom, D. Milstein, *Chem. Rev.* **2003**, 103, 1759–1792; e) C.-H. Jun, *Chem. Soc. Rev.* **2004**, 33, 610–618; f) Y. J. Park, J. W. Park, C.-H. Jun, *Acc. Chem. Res.* **2008**, 41, 222–234; g) T. Li, J. J. García, W. Brennessel, W. D. Jones, *Organometallics* **2010**, 29, 2430–2445; h) Y. Nakao, A. Yada, T. Hiyama, *J. Am. Chem. Soc.* **2010**, 132, 10024–10026.
- [4] C. Chen, G. Kehr, R. Fröhlich, G. Erker, *J. Am. Chem. Soc.* **2010**, 132, 13594–13595.
- [5] a) O. Ekkert, R. Fröhlich, G. Kehr, G. Erker, *J. Am. Chem. Soc.* **2011**, 133, 4610–4616; b) O. Ekkert, G. Kehr, R. Fröhlich, G. Erker, *Chem. Commun.* **2011**, 47, 10482–10484.
- [6] B. Wrackmeyer, *Annu. Rep. NMR Spectrosc.* **1985**, 16, 73–186.
- [7] a) D. J. Parks, W. E. Piers, *J. Am. Chem. Soc.* **1996**, 118, 9440–9441; b) D. J. Parks, W. E. Piers, M. Parvez, R. Atencio, M. J. Zaworotko, *Organometallics* **1998**, 17, 1369–1377; c) D. Vagades, R. Fröhlich, G. Erker, *Angew. Chem.* **1999**, 111, 3561–3565; *Angew. Chem. Int. Ed.* **1999**, 38, 3362–3365; d) S. Mitu, M. C. Baird, *Organometallics* **2006**, 25, 4888–4896; e) S. Mitu, M. C. Baird, *Can. J. Chem.* **2006**, 84, 225–232; See also: f) H. Jacobsen, H. Berke, S. Döring, G. Kehr, G. Erker, R. Fröhlich, O. Meyer, *Organometallics* **1999**, 18, 1724–1735; g) F. Focante, P. Mercandelli, A. Sironi, L. Resconi, *Coord. Chem. Rev.* **2006**, 250, 170–188.
- [8] See also: a) A. Suzuki, A. Arase, H. Matsumoto, M. Itoh, H. C. Brown, M. M. Rogić, M. W. Rathke, *J. Am. Chem. Soc.* **1967**, 89, 5708–5709; b) H. C. Brown, M. M. Rogić, M. W. Rathke, G. W. Kabalka, *J. Am. Chem. Soc.* **1967**, 89, 5709–5710; c) G. W. Kabalka, H. C. Brown, A. Suzuki, S. Honma, A. Arase, M. Itoh, *J. Am. Chem. Soc.* **1970**, 92, 710–712; d) A. Suzuki, S. Nozawa, M. Itoh, H. C. Brown, G. W. Kabalka, G. W. Holland, *J. Am. Chem. Soc.* **1970**, 92, 3503–3505; e) H. C. Brown, M. M. Midland, *Angew. Chem.* **1972**, 84, 702–710; *Angew. Chem. Int. Ed. Engl.* **1972**, 11, 692–700; f) T. Mukaiyama, K. Inomata, M. Muraki, *J. Am. Chem. Soc.* **1973**, 95, 967–968; g) R. Köster, H.-J. Zimmermann, W. Fenzl, *Justus Liebigs Ann.*

- Chem.* **1976**, 1116–1134; h) K. Nozaki, K. Oshima, K. Utimoto, *Bull. Chem. Soc. Jpn.* **1991**, *64*, 403–409; i) A. K. Dash, R. F. Jordan, *Organometallics* **2002**, *21*, 777–779; j) B.-H. Xu, G. Kehr, R. Fröhlich, B. Wibbeling, B. Schirmer, S. Grimme, G. Erker, *Angew. Chem.* **2011**, *123*, 7321–7324; *Angew. Chem. Int. Ed.* **2011**, *50*, 7183–7186.
- [9] Selected examples: a) S. Danishefsky, T. Kitahara, *J. Am. Chem. Soc.* **1974**, *96*, 7807–7808; b) S. Danishefsky, T. Kitahara, C. F. Yan, J. Morris, *J. Am. Chem. Soc.* **1979**, *101*, 6996–7000; c) S. Danishefsky, C.-F. Yan, R. K. Singh, R. B. Gam-mill, P. M. McCurry Jr., N. Fritsch, J. Clardy, *J. Am. Chem. Soc.* **1979**, *101*, 7001–7008; d) S. Danishefsky, T. Harayama, R. K. Singh, *J. Am. Chem. Soc.* **1979**, *101*, 7008–7012; e) S. Danishefsky, M. Hiram, N. Fritsch, J. Clardy, *J. Am. Chem. Soc.* **1979**, *101*, 7013–7018; f) S. Danishefsky, F. J. Walker, *J. Am. Chem. Soc.* **1979**, *101*, 7018–7020; g) S. Danishefsky, M. Hiram, K. Gombatz, T. Harayama, E. Berman, P. F. Schuda, *J. Am. Chem. Soc.* **1979**, *101*, 7020–7031; See also: h) S. Kobayashi, S. Komiyama, H. Ishitani, *Angew. Chem.* **1998**, *110*, 1026–1028; *Angew. Chem. Int. Ed.* **1998**, *37*, 979–981; i) P. Langer, T. Eckardt, *Angew. Chem.* **2000**, *112*, 4503–4506; *Angew. Chem. Int. Ed.* **2000**, *39*, 4343–4346.
- [10] See also: a) M. Welker, *Tetrahedron* **2008**, *64*, 11529–11539; b) L. Wang, C. S. Day, M. W. Wright, M. E. Welker, *Beilstein J. Org. Chem.* **2009**, *5*, article no. 45c) A. M. Sarotti, P. L. Pisano, S. C. Pellegrinet, *Org. Biomol. Chem.* **2010**, *8*, 5069–5073; d) J. N. Payette, M. Akakura, H. Yamamoto, *Chem. Asian J.* **2011**, *6*, 380–384.

Received: December 19, 2011

Published Online: February 14, 2012

Chain Reaction for Isomerization from *trans*(Cl) to *cis*(Cl)-Ru(bpy)(CO)₂Cl₂ (bpy = 2,2'-Bipyridine) Induced by NaBH₄

Yusuke Kuramochi,^[a] Yasuhiro Ito,^[a] and Hitoshi Ishida*^[a,b]

Keywords: Ruthenium / Isomerization / Reduction / Carbonyl ligands / N ligands

trans(Cl)-Ru(bpy)(CO)₂Cl₂ (**1**; bpy = 2,2'-bipyridine) was found to efficiently isomerize to *cis*(Cl)-**1** in DMSO by addition of a catalytic amount of NaBH₄, even at room temperature. The isomerization reaction is air sensitive, but does not

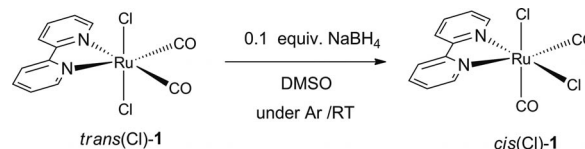
require photoirradiation. Addition of the Cl[−] ion remarkably accelerates the reaction. A plausible chain reaction mechanism mediated by the reduced ruthenium dimer and monomer of **1** is proposed for the *trans*–*cis* isomerization.

Introduction

The ruthenium mono(bipyridine) dicarbonyl dichloride complex Ru(bpy)(CO)₂Cl₂ (**1**) has been widely studied from the viewpoint of its photochemical decarbonylation,^[1] the catalytic activities for epoxidation of olefins,^[2] the water–gas shift reaction,^[3] and the photochemical^[4]/electrochemical reduction of CO₂.^[5] The complex has also been utilized as a synthetic precursor for ruthenium tris-heteroleptic polypyridyl complexes,^[6] which are, for instance, used in DNA biosensors.^[7] The ruthenium complex **1** has, in principle, three possible isomers, *cis*(CO),*trans*(Cl) [*trans*(Cl)-**1**], *cis*(CO),*cis*(Cl) [*cis*(Cl)-**1**], and *trans*(CO),*cis*(Cl) forms. Only *cis*(Cl)-**1** has enantiomers (Δ and Λ). The *trans*(CO),*cis*(Cl) complex is thermodynamically unfavorable and has not been isolated.^[8] Complex **1** has been synthesized mostly by reaction of bpy with the so-called “red carbonyl solution”^[4a,5b–5e,5g,5h,9] or [Ru(CO)₃Cl₂]₂.^[1,8,10] The latter of which is commercially available. Although these synthetic procedures afford a mixture of *trans*(Cl)-**1** and *cis*(Cl)-**1**, a ruthenium precursor of [Ru(CO)₂Cl₂]_n, which was prepared by heating RuCl₃ at reflux in formic acid, selectively produces *trans*(Cl)-**1** in the reaction with bpy in methanol.^[4b,5a,5f,6,11] Although numerous works on ruthenium complex **1** have been reported, to the best of our knowledge, there is no report on *trans*–*cis* isomerization.^[12]

The compound *trans*(Cl)-**1** is stable and remains unchanged in common organic solvents such as acetonitrile, methanol, DMF, and DMSO at room temperature for at

least several days. However, we sometimes experienced unexpected isomerization from *trans*(Cl)- to *cis*(Cl)-**1**. For example, *trans*(Cl)-**1** in [D₆]DMSO in a NMR tube was stored in a dark place at room temperature, and a few days later (on the next day in the earliest case), the ¹H NMR spectrum dramatically changed to that for *cis*(Cl)-**1**. The isomerization had a long induction period, and, if once started, it rapidly proceeded, but, unfortunately, it was not reproducible. We noticed that the isomerization frequently occurred when the crude sample of *trans*(Cl)-**1**, which was prepared from the ruthenium polymer precursor [Ru(CO)₂Cl₂]_n, was used. We further observed that there would be a higher probability for isomerization in deaerated solution. These results implied some reducing impurities triggered the isomerization. We finally discovered that the isomerization efficiently proceeded by addition of a catalytic amount of NaBH₄ without any induction period (Scheme 1). Herein, we report the novel isomerization from *trans*(Cl)-**1** to *cis*(Cl)-**1** with a discussion of the plausible reaction mechanism.



Scheme 1. Isomerization from *trans*(Cl) to *cis*(Cl) isomer.

Results and Discussion

The compound *trans*(Cl)-**1** was prepared by using the ruthenium precursor [Ru(CO)₂Cl₂]_n^[6b,11] and was purified by recrystallization from methanol. For the pure sample, the isomerization in solution was confirmed not to occur at least for one week. On the addition of a small amount of NaBH₄ to a [D₆]DMSO solution of *trans*(Cl)-**1**, the point

[a] Department of Chemistry, Graduate School of Science, Kitasato University, 1-15-1 Kitasato, Minami-ku, Sagami-hara, Kanagawa 252-0373, Japan
Fax: +81-42-778-9925
E-mail: ishida@sci.kitasato-u.ac.jp

[b] Precursory Research for Embryonic Science (PRESTO), Japan Science and Technology Agency (JST) 4-1-8 Honcho, Kawaguchi, Saitama 332-0012, Japan

Supporting information for this article is available on the WWW under <http://dx.doi.org/10.1002/ejic.201200090>.

of contact with NaBH_4 immediately turned to black, and then the color of the solution changed to pale red. The ^1H NMR spectral changes show that a set of eight signals for *cis*(Cl)-**1** newly appear and the original set of four signals for *trans*(Cl)-**1** diminish in size (Figure 1). The isomerization also proceeds in $[\text{D}_6]\text{MeCN}$, but the reaction is slightly slower than in $[\text{D}_6]\text{DMSO}$. The product was confirmed to be *cis*(Cl)-**1** by the ^{13}C NMR spectrum of an authentic sample, which was prepared according to the literature^[1a] and characterized by X-ray crystallographic analysis (see the Supporting Information).

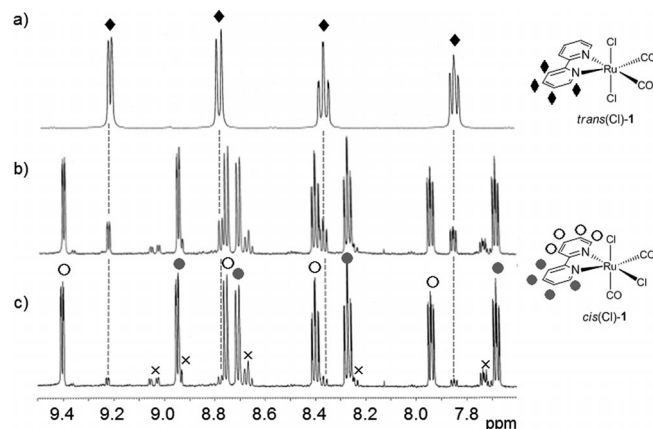


Figure 1. ^1H NMR spectral changes in a $[\text{D}_6]\text{DMSO}$ solution of *trans*(Cl)-**1** (6.9 mM) under Ar atmosphere at room temperature: (a) before, (b) 10 min, and (c) 3 h after the addition of NaBH_4 (0.88 mM). \times : unidentified peaks.

The reaction progress in $[\text{D}_6]\text{DMSO}$ was also monitored with high-performance liquid chromatography (HPLC). As shown in Figure 2, *cis*(Cl)-**1** (retention time: 4.4 min) newly appears, while the peak for *trans*(Cl)-**1** (6.0 min) decreases soon after NaBH_4 was added. Some small peaks were also observed around 2–4 min and 10 min; the former might be for by-products and the latter for reduced ruthenium oligomers (or polymers), which are known to be generated during electrochemical reduction.^[5b–5h,13] The plots of each peak area vs. time are shown in Figure 3. Both the reaction rates for decreasing *trans*(Cl)-**1** and increasing *cis*(Cl)-**1** are zero-order with respect to the concentration of *trans*(Cl)-**1**, and the reaction suddenly stopped at the point at which 5% of *trans*(Cl)-**1** remained. The isomerization rate is drastically enhanced by adding tetrabutylammonium chloride ($n\text{Bu}_4\text{NCl}$), whereas *trans*(Cl)-**1** does not change without NaBH_4 even in the presence of $n\text{Bu}_4\text{NCl}$ [25 equiv. vs. *trans*(Cl)-**1**]. The reaction rate was also found to be dependent on the concentration of NaBH_4 (see Figure S5 in the Supporting Information) but independent of the initial *trans*(Cl)-**1** concentration.

Although there are many reports on oxidation-triggered *cis*–*trans* isomerization of ruthenium complexes,^[14] there are only a few reports on one that is triggered by reduction.^[15] In many cases, the *cis*-ruthenium complex isomerizes into the *trans* form, and the reverse isomerization (from *trans* to *cis*) is rare. The isomerization is based on electron-transfer catalysis, where in most cases *cis*- Ru^{II} is

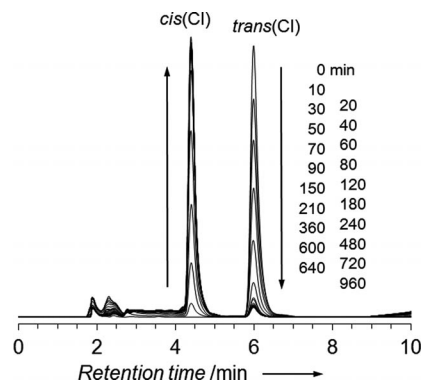


Figure 2. HPLC time traces for a $[\text{D}_6]\text{DMSO}$ solution of *trans*(Cl)-**1** (3.0 mM) after the addition of NaBH_4 (0.33 mM); eluent: $\text{MeCN}/\text{H}_2\text{O}$ (30:70) containing 0.1% TFA, monitored at 254 nm. The reaction was carried out under Ar atmosphere at room temperature.

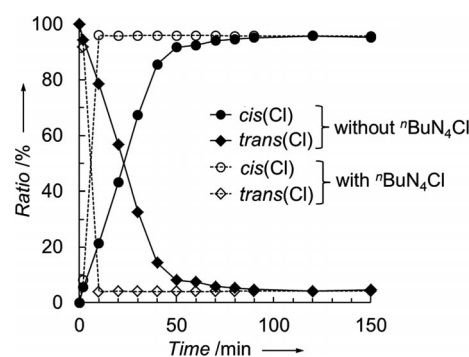
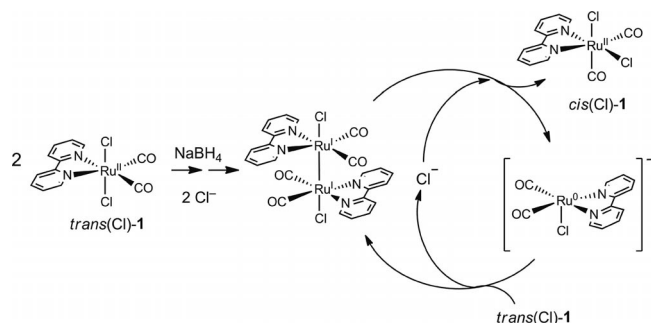


Figure 3. HPLC peak ratios of *cis*(Cl)/[*cis*(Cl)+*trans*(Cl)] and *trans*(Cl)/[*cis*(Cl)+*trans*(Cl)] vs. time in the isomerization of *trans*(Cl)-**1** (3.0 mM) with NaBH_4 (0.33 mM) without and with $n\text{Bu}_4\text{NCl}$ (0.15 M) in Ar-saturated $[\text{D}_6]\text{DMSO}$ at room temperature.

oxidized to *cis*- Ru^{III} , which readily isomerizes to *trans*- Ru^{III} , followed by re-oxidation of *cis*- Ru^{II} with *trans*- Ru^{III} (see Figure S6 in the Supporting Information).^[16] For such a catalytic system, the 18-electron configuration is stable in the *cis* form, while the oxidized 17-electron state favors the *trans* form. However, for the *trans*–*cis* isomerization of ruthenium complex **1**, this is not the case, because the reduction potential of the *trans*(Cl)-**1** is close to that of *cis*(Cl)-isomer.^[5h] The numerous studies on the electrochemical reduction of *trans*(Cl)-**1** exhibit that the ruthenium polymers $[\text{Ru}^0(\text{bpy})(\text{CO})_2]_n$ are initially produced via the five-coordinate two-electron reduced species, $[\text{Ru}(\text{bpy})(\text{CO})_2\text{Cl}]^-$. Actually, the addition of a large amount of NaBH_4 to the solution of *trans*(Cl)-**1** results in a dark black ruthenium species, which suggests the production of the ruthenium polymers, consistent with the literature.^[5b–5h,13] Although it is reported that the Ru^{I} dimer $[\text{Ru}^{\text{I}}(\text{bpy})(\text{CO})_2(\text{MeCN})_2]_2^{2+}$ is oxidized to yield *cis*(CO)- and *cis*(MeCN)- $[\text{Ru}^{\text{II}}(\text{bpy})(\text{CO})_2(\text{MeCN})_2]^{2+}$,^[17] there is no report that indicates that a catalytic amount of the ruthenium reduced species induces the *trans*–*cis* isomerization.

A plausible mechanism that is consistent with the reports so far and the results obtained in this work are summarized in Scheme 2. During the isomerization, the ^1H NMR spec-

tra of the solution always show sharp and distinct signals, which indicates that no paramagnetic species (e.g. monomeric Ru^I complex) is generated. In the first step, *trans*(Cl)-**1** is reduced by NaBH₄ to probably afford the diamagnetic Ru^I dimer.^[18] Although it is reported that the ruthenium(I) dimer is more electrochemically reducible than the corresponding precursor monomer,^[19] further reduction would be suppressed because the amount of NaBH₄ is very small under the experimental conditions. In the course of the generation of the dimer, the chloride ions are released. The chloride ion again would attack the dimer to yield *cis*(Cl)-**1**. Since theoretical calculations exhibit that the total energy difference between *trans*(Cl) and *cis*(Cl)-**1** is very small,^[8] *cis*(Cl)-**1** would kinetically be produced; the chloride ion attacks the ruthenium dimer from the outside so as to avoid steric hindrance to selectively yield *cis*(Cl)-**1**. From the result that addition of chloride ions drastically enhances the reaction rate, this chloride ion attacking step would be rate determining. The resulting Ru⁰ species would promptly react with *trans*(Cl)-**1** to reproduce the ruthenium dimer.



Scheme 2. A proposed mechanism for the isomerization.

We further investigated the reason as to why the *trans*–*cis* isomerization occurs for crude *trans*(Cl)-**1** even in the absence of NaBH₄. As we noticed that the sample that was prepared from the ruthenium precursor [Ru(CO)₂Cl₂]_n frequently isomerized to the *cis* form, we recorded the infrared spectrum of the starting material. It showed an absorption at 1561 cm^{−1}, which suggests that crude *trans*(Cl)-**1** contains the formate or hydroxy carbonyl derivative as an impurity.^[20] We suppose that the formate or hydroxy carbonyl species give hydride complexes, which induce the *trans*–*cis* isomerization.

Conclusions

We found a novel chain reaction for the isomerization from *trans*(Cl)- to *cis*(Cl)-Ru(bpy)(CO)₂Cl₂, which was induced by a catalytic amount of NaBH₄ and proceeded smoothly even at room temperature. This chain isomerization might be categorized as electron-transfer catalysis; however, this is not the case, but rather it is a rare reduction-triggered *trans*–*cis* isomerization. This reaction could lead to a promising methodology for the production of *cis*-ruthenium mono(bipyridine) derivatives under moderate conditions. The syntheses of novel ruthenium complexes for CO₂ reduction catalysts are underway.

Experimental Section

Isomerization: In a NMR tube or a 1.5-mL vial were placed *trans*(Cl)-**1** (1.4–10 mg, 3.6 × 10^{−4}–2.6 × 10^{−3} mol) and deuterium solvent ([D₆]DMSO or [D₃]MeCN; 0.5–1.2 mL), and the mixture was then degassed by bubbling with Ar. A solution (10–50 μL) of NaBH₄ (2.5 mg, 6.5 × 10^{−5} mol) dissolved in water (1–5 mL) was added to start the reaction. The reaction progress was monitored by ¹H NMR spectroscopy or HPLC analysis. *cis*(Cl)-**1**: ¹H NMR (600 MHz, [D₆]DMSO): δ = 9.40 (dd, *J* = 5.4, 1.2 Hz, 1 H), 8.95 (dd, *J* = 5.4, 1.2 Hz, 1 H), 8.76 (d, *J* = 7.8 Hz, 1 H), 8.71 (d, *J* = 7.8 Hz, 1 H), 8.40 (td, *J* = 7.8, 1.2 Hz, 1 H), 8.27 (td, *J* = 7.8, 1.2 Hz, 1 H), 7.94 (ddd, *J* = 7.8, 5.4, 1.2 Hz, 1 H), 7.68 (ddd, *J* = 7.8, 5.4, 1.2 Hz, 1 H) ppm. ¹³C NMR (150 MHz, [D₆]DMSO): δ = 196.1 (C=O), 191.2 (C=O), 156.7, 156.0, 155.6, 149.6, 141.2, 140.3, 128.3, 127.5, 124.8, 124.4 ppm. HPLC [MeCN/H₂O (30:70) containing 0.1% TFA]: 4.4 min.

Supporting Information (see footnote on the first page of this article): Synthesis, NMR spectra, and X-ray crystallographic data of authentic *cis*(Cl)-**1** and HPLC time traces containing 0.15 M *n*Bu₄NCl are presented.

Acknowledgments

We thank Prof. Dr. Mao Minoura (Kitasato University) for help with X-ray crystallographic analysis. This work was supported by the PRESTO Program of JST and a Grant-in-Aid for Scientific Research (C) from the Ministry of Education, Culture, Sports, Science and Technology (21550163).

- [1] a) E. Eskelinen, M. Haukka, T. Venäläinen, T. A. Pakkanen, M. Wasberg, S. Chardon-Noblat, A. Deronzier, *Organometallics* **2000**, *19*, 163–169; b) A. Gabriësson, S. Zalis, P. Matousek, M. Towrie, A. Vlcek Jr., *Inorg. Chem.* **2004**, *43*, 7380–7388; c) N. A. Bokach, M. Haukka, P. Hirva, D. S. M. F. C. Guedes, V. Y. Kukushkin, A. J. L. Pombeiro, *J. Organomet. Chem.* **2006**, *691*, 2368–2377.
- [2] P. Aguirre, R. Sariego, S. A. Moya, *J. Coord. Chem.* **2001**, *54*, 401–413.
- [3] M. Haukka, T. Venäläinen, M. Kallinen, T. A. Pakkanen, *J. Mol. Catal. A* **1998**, *136*, 127–134.
- [4] a) J.-M. Lehn, R. Ziessel, *J. Organomet. Chem.* **1990**, *382*, 157–173; b) S. Sato, T. Arai, T. Morikawa, K. Uemura, T. M. Suzuki, H. Tanaka, T. Kajino, *J. Am. Chem. Soc.* **2011**, *133*, 15240–15243.
- [5] a) H. Ishida, K. Fujiki, T. Ohba, K. Ohkubo, K. Tanaka, T. Terada, T. Tanaka, *J. Chem. Soc., Dalton Trans.* **1990**, 2155–2160; b) M. N. Collomb-Dunand-Sauthier, A. Deronzier, R. Ziessel, *J. Electroanal. Chem.* **1993**, *350*, 43–55; c) M.-N. Collomb-Dunand-Sauthier, A. Deronzier, R. Ziessel, *J. Organomet. Chem.* **1993**, *444*, 191–198; d) M. N. Collomb-Dunand-Sauthier, A. Deronzier, R. Ziessel, *J. Chem. Soc., Chem. Commun.* **1994**, 189–191; e) M.-N. Collomb-Dunand-Sauthier, A. Deronzier, R. Ziessel, *Inorg. Chem.* **1994**, *33*, 2961–2967; f) S. Chardon-Noblat, A. Deronzier, R. Ziessel, D. Zsoldos, *Inorg. Chem.* **1997**, *36*, 5384–5389; g) S. Chardon-Noblat, A. Deronzier, R. Ziessel, D. Zsoldos, *J. Electroanal. Chem.* **1998**, *444*, 253–260; h) S. Chardon-Noblat, C. P. Da, A. Deronzier, M. Haukka, T. A. Pakkanen, R. Ziessel, *J. Electroanal. Chem.* **2000**, *490*, 62–69.
- [6] a) G. F. Strouse, P. A. Anderson, J. R. Schoonover, T. J. Meyer, F. R. Keene, *Inorg. Chem.* **1992**, *31*, 3004–3006; b) P. A. Anderson, G. B. Deacon, K. H. Haarmann, F. R. Keene, T. J. Meyer, D. A. Reitsma, B. W. Skelton, G. F. Strouse, N. C. Thomas, J. A. Treadway, A. H. White, *Inorg. Chem.* **1995**, *34*, 6145–6157.

- [7] a) M. E. Nunez, D. B. Hall, J. K. Barton, *Chem. Biol.* **1999**, *6*, 85–97; b) M. Pascaly, J. Yoo, J. K. Barton, *J. Am. Chem. Soc.* **2002**, *124*, 9083–9092.
- [8] M. Haukka, P. Hirva, S. Luukkanen, M. Kallinen, M. Ahlgrén, T. A. Pakkanen, *Inorg. Chem.* **1999**, *38*, 3182–3189.
- [9] a) J. V. Kingston, J. W. S. Jamieson, G. Wilkinson, *J. Inorg. Nucl. Chem.* **1967**, *29*, 133–138; b) J. M. Kelly, C. M. O'Connell, J. G. Vos, *Inorg. Chim. Acta* **1982**, *64*, L75–L76.
- [10] a) M. Haukka, J. Kiviaho, M. Ahlgren, T. A. Pakkanen, *Organometallics* **1995**, *14*, 825–833; b) M. Haukka, T. Venäläinen, M. Ahlgren, T. A. Pakkanen, *Inorg. Chem.* **1995**, *34*, 2931–2936; c) P. Homanen, M. Haukka, T. A. Pakkanen, J. Pursiainen, R. H. Laitinen, *Organometallics* **1996**, *15*, 4081–4084; d) P. Homanen, M. Haukka, M. Ahlgren, T. A. Pakkanen, *Inorg. Chem.* **1997**, *36*, 3794–3797; e) T.-J. J. Kinnunen, M. Haukka, M. Nousiainen, A. Patrikka, T. A. Pakkanen, *J. Chem. Soc., Dalton Trans.* **2001**, 2649–2654; f) N. Masciocchi, A. Sironi, S. Chardon-Noblat, A. Deronzier, *Organometallics* **2002**, *21*, 4009–4012.
- [11] D. S. C. Black, G. B. Deacon, N. C. Thomas, *Aust. J. Chem.* **1982**, *35*, 2445–2453.
- [12] Photochemical isomerization of ruthenium-bipyridyl complexes accompanied by ligand exchange has been reported (e.g. ref.^[1c]).
- [13] a) S. Myllynen, M. Wasberg, M. Haukka, *J. Electroanal. Chem.* **2006**, *586*, 217–224; b) S. Myllynen, M. Wasberg, *J. Electroanal. Chem.* **2008**, *623*, 93–101.
- [14] a) B. P. Sullivan, T. J. Meyer, *Inorg. Chem.* **1982**, *21*, 1037–1040; b) N. Bag, G. K. Lahiri, A. Chakravorty, *J. Chem. Soc., Dalton Trans.* **1990**, 1557–1561; c) L. Ballester, O. Esteban, A. Gutierrez, M. F. Perpignan, C. Ruiz-Valero, E. Gutierrez-Puebla, M. J. Gonzalez, *Polyhedron* **1992**, *11*, 3173–3182; d) V. E. Barton, J. F. Bickley, L. A. Cain, E. Leary, J. Ledger, S. J. Higgins, F. Mouffouk, *Inorg. Chim. Acta* **2004**, *357*, 4488–4495.
- [15] a) D. H. Tom, W. Kollvitz, I. Kleinwaechter, *Inorg. Chem.* **1984**, *23*, 2685–2691; b) S. Fukui, Y. Shimamura, Y. Sunamoto, T. Abe, T. Hirano, T. Oi, H. Nagao, *Polyhedron* **2007**, *26*, 4645–4652.
- [16] A. J. L. Pombeiro, d. S. M. F. C. Guedes, M. A. N. D. A. Lemos, *Coord. Chem. Rev.* **2001**, *219–221*, 53–80.
- [17] a) S. Chardon-Noblat, G. H. Cripps, A. Deronzier, J. S. Field, S. Gouws, R. J. Haines, F. Southway, *Organometallics* **2001**, *20*, 1668–1675; b) C. Cripps, A. Pellissier, S. Chardon-Noblat, A. Deronzier, R. J. Haines, *J. Organomet. Chem.* **2004**, *689*, 484–488.
- [18] G. Gerbaud, J.-M. Mouesca, S. Hediger, S. Chardon-Noblat, F. Lafalet, A. Deronzier, M. Bardet, *Phys. Chem. Chem. Phys.* **2010**, *12*, 15428–15435.
- [19] S. Chardon-Noblat, A. Deronzier, D. Zsoldos, R. Ziessel, M. Haukka, T. A. Pakkanen, T. Venäläinen, *J. Chem. Soc., Dalton Trans.* **1996**, 2581–2583.
- [20] M. Majumdar, A. Sinha, T. Ghatak, S. K. Patra, N. Sathukhan, S. M. W. Rahaman, J. K. Bera, *Chem. Eur. J.* **2010**, *16*, 2574–2585.

Received: January 28, 2012

Published Online: February 14, 2012

Structural Conformation and Optical and Electrochemical Properties of Imidazolyl-Substituted Naphthalenediimide and Its Hg^{II}, Cd^{II}, and Cu^{II} Halide Complexes

Jia-Jian Jiang,^[a] Cheng Yan,^[a] Mei Pan,^{*[a]} Zi Wang,^[a] Hai-Ying Deng,^[a] Jian-Rong He,^[a] Qing-Yuan Yang,^[a] Lei Fu,^[a] Xian-Fang Xu,^[a] and Cheng-Yong Su^{*[a,b]}

Keywords: Coordination modes / Density functional calculations / Electrochemistry / Self-assembly

A new end–core–end naphthalenediimide-based ligand *N,N'*-bis(3-imidazol-1-yl-propyl)naphthalene diimide (3-imntd) was synthesized. Single crystals of the free ligand and its Hg^{II}, Cd^{II}, and Cu^{II} halide complexes were obtained. All the compounds were fully characterized by elemental analysis, IR spectroscopy, single-crystal XRD, and DFT studies. The XRD and DFT calculations revealed three different kinds

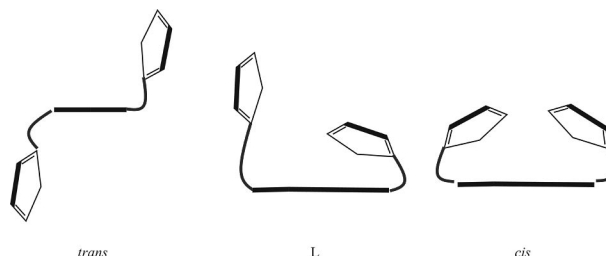
of conformations for 3-imntd (*cis*, *trans*, and *L*). The variation in the ligand conformation and the resulting final structures of the coordination assemblies, M₂L₂ metallacycle, 1D zigzag chain, or ML metallacycle, seem to be induced by the different geometric characters of the coordination tetrahedra around the metal centers. The optical and electrochemical properties of the compounds were also investigated.

Introduction

Naphthalenediimides (NDIs) are neutral, aromatic compounds with a large conjugated plane, which show simultaneous chemical stability and reactivity to accept electrons upon photonic or electronic excitation.^[1] Therefore, they are widely used in electronically and optically induced electron transfer systems, and can be integrated into field-effect transistors,^[2] artificial biological mimics,^[3] solar energy converters,^[4] and supramolecular devices and machines.^[5] In recent years, there has been a steady increase in the study of NDI ligands and their coordination complexes. Most of these ligands are designed with an end–core–end conformation, in which there are two main sites able to be functionalized: through the diimide nitrogen atoms or core substitution (substitution on the naphthalene ring). The focus of modification of the naphthalene is mainly to produce compounds with exceptional optical or electronic characters. For example, the introduction of halides or long alkyl chains will give rise to typical white–blue fluorescence. The modification of the diimide nitrogen atoms largely introduces various coordination moieties, such as pyridine, bipyridine, multipyridine, carboxylic/sulfonic/phosphonic groups, acetylene, porphyrin, metallacycles, or other com-

plicated organic groups.^[6–10] Coordination complexes of various dimensions have been assembled from these NDI-based ligands and are finding potential applications in fields such as artificial models for photoinduced electron transfer, biological or luminescent sensors for DNA, and gas adsorption frameworks.^[11–13]

We have focused on the fabrication of end–core–end NDI ligands that comprise pyridyl groups and their assembly of coordination complexes with different transition metals.^[6a,6b] In this work, imidazolyl (Im) arms were connected to the diimide nitrogen atoms to give a flexible ligand: *N,N'*-bis(3-imidazol-1-yl-propyl)naphthalenediimide (3-imntd, Scheme 1). The self-assembly of this ligand with Hg^{II}, Cd^{II}, and Cu^{II} halides gave five coordination complexes, [Hg₂(3-imntd)₂I₄]·CHCl₃ (**1**), [Hg₂(3-imntd)₂I₄]·FeCp₂ (**2**), [{Hg(3-imntd)Cl₂}·CHCl₃]_n (**3**), [Cd₂(3-imntd)₂I₄]·2H₂O (**4**), and [Cu(3-imntd)Cl₂] (**5**). Complexes **1**, **2**, and **4** form discrete M₂L₂ metallacycles, **3** shows a polymeric 1D chain structure, and **5** comprises ML metallacycles. The structural diversity seems to be correlated with the degree of distortion of the coordination tetrahedron around the



Scheme 1. Different conformations of 3-imntd.

[a] KLGHEI of Environment and Energy Chemistry, MOE Laboratory of Bioinorganic and Synthetic Chemistry, School of Chemistry and Chemical Engineering, Sun Yat-sen University, Guangzhou 510275, China
E-mail: panm@mail.sysu.edu.cn

[b] State Key Laboratory of Applied Organic Chemistry, Lanzhou University, Lanzhou 730000, China

Supporting information for this article is available on the WWW under <http://dx.doi.org/10.1002/ejic.201101181>.

metal centers, which causes the ligand to have different conformations and the complexes to have varied optical and electronic properties.

Results and Discussion

Conformation Modes of 3-imntd

The 3-imntd ligand features two rotatable imidazole groups linked by flexible propyl junctures on both sides of the NDI central core. Therefore, 3-imntd can present various conformation modes, which depend on how the two imidazole groups are orientated. Scheme 1 illustrates the three conformations observed in this work. In general, the free ligand adopts a *trans* conformation, in which the two imidazole groups point in opposite directions. The two arms are nearly perpendicular to the central NDI unit. Complexes **1–4** adopt the *L* conformation, in which the two propyl chains point upwards, but one extends further to cause the imidazole group to lie perpendicular to the NDI unit, and the other bends inwards to lie almost parallel to the NDI unit. In comparison, **5** adopts a *cis* conformation, in which the two propyl chains simultaneously point in the same direction and bend inwards to give an “embracing” configuration, in which the two imidazole groups are both nearly parallel to the NDI core.

Description of Crystal Structures

The 3-imntd ligand crystallizes in monoclinic symmetry with the $P2_1/n$ space group. As seen from Figure 1a, the free ligand adopts the *trans* conformation, in which the two arms bend in opposite directions relative to the central naphthalene ring. In the crystal packing along the *a* direction, alternative lines were formed with an opposite head-to-tail arrangement (Figure 1b). It is interesting that the inorganic part of the crystal was solved as monomethyl sulfate, which could be an in situ product of the reaction of *p*-toluenesulfonate under the hydrothermal conditions.

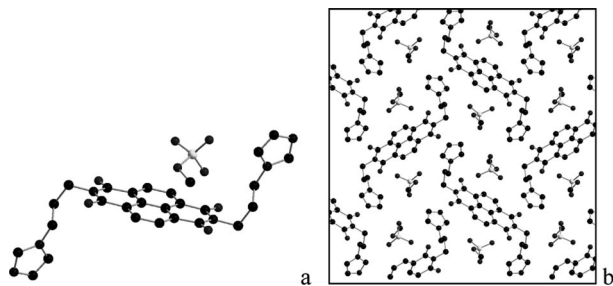


Figure 1. (a) The crystal structure of 3-imntd. (b) Packing along the *a* axis (H atoms are omitted for clarity).

Single-crystal XRD revealed that the structures of **1** and **2** are basically the same as both comprise M_2L_2 type discrete metallacycles. Each Hg^{II} metal center is coordinated to two N atoms from two different 3-imntd ligands and two terminal I^- ions. Therefore, a distorted $\{N_2I_2\}$ coordination

tetrahedron is formed around each metal center (Figure 2a). In each M_2L_2 molecular ring, the distance between the two Hg^{II} metal centers is 7.58 Å, and the two naphthalene planes from two 3-imntd ligands are almost parallel (dihedral angle of 1.70°). For each 3-imntd ligand, the conformations of the two imidazole ends are totally different, with one nearly parallel to the naphthalene plane (dihedral angle of 20°) and another nearly perpendicular (dihedral angle of 80°).

As shown in Figure 2b and c, the neighboring metallacycles are connected by intermolecular π – π interactions, which are formed between the parallel naphthalene rings with a distance of 3.32 Å. In addition, C–H \cdots O hydrogen bonds (C \cdots O 3.10 Å) are present between the imido O atoms and the H atoms of the propyl group, which link the metallacycles in another direction. The H bonds join the metallacycles in one direction to give infinite 1D chains, which are further connected by π – π interactions to give 2D layers that extend in the *bc* plane (Figure 2d). The solvated H_2O molecules are located between the metallacycles. There are weak interactions between the OH groups of H_2O and the O atoms of the ligands (O \cdots O 3.23 Å), which also serve as bridges to interconnect the metallacycles. Therefore, the rings are packed very closely, which leaves a potential solvent accessible area of 2.3% (estimated by PLATON).^[14]

The coordination units and packing modes in **2** (Figure 3) are basically the same as those in **1**, except that ferrocene is located between the metallacycles instead of solvent molecules. However, the packing effects of $FeCp_2$ result in additional stabilization of the M_2L_2 metallacycles and their packing in the crystal lattice, which will be discussed later.

When the anions were changed from I^- to Cl^- , a 1D zigzag chain structure was obtained in **3**. The Hg^{II} center is coordinated to two N atoms from two different 3-imntd ligands and two terminal Cl^- ions to form a distorted $\{N_2Cl_2\}$ coordination tetrahedron (Figure 4a). Different to the metallacycles in **1** and **2**, anion– π interactions were formed between the Cl^- anions and the naphthalene rings (Cl $\cdots\pi$ 3.27 Å). Therefore, the two arms of the 3-imntd ligand bend outwards to form a 1D chain. The dihedral angles of the two imidazole rings to the basal naphthalene plane in each ligand are 15 and 74°. The nearest Hg–Hg distance in the chain is 7.21 Å, and the dihedral angle of the two naphthalene planes in neighboring ligands is 10°.

Furthermore, the chains are connected by π – π interactions and C–H \cdots O bonds (C \cdots O 3.34–3.41 Å) into a 2D net. The nets are further linked by C–H \cdots O bonds in another direction into a 3D structure (C \cdots O 3.43 Å, Figure 4b). Solvent molecules are stacked between the chains (Figure 4c) and the potential solvent accessible area is 20% (estimated by PLATON).

Although the metal center in **4** is Cd^{II} , the coordination units and packing modes are almost the same as those in **1**. Each Cd^{II} is coordinated to two imidazole N atoms from two different 3-imntd ligands and two terminal I^- ions to form a $\{N_2I_2\}$ coordination tetrahedron, and a M_2L_2 metallacycle is formed by two ligands and two Cd^{II} centers (Figure 5a). In each metallacycle, the Cd–Cd distance is

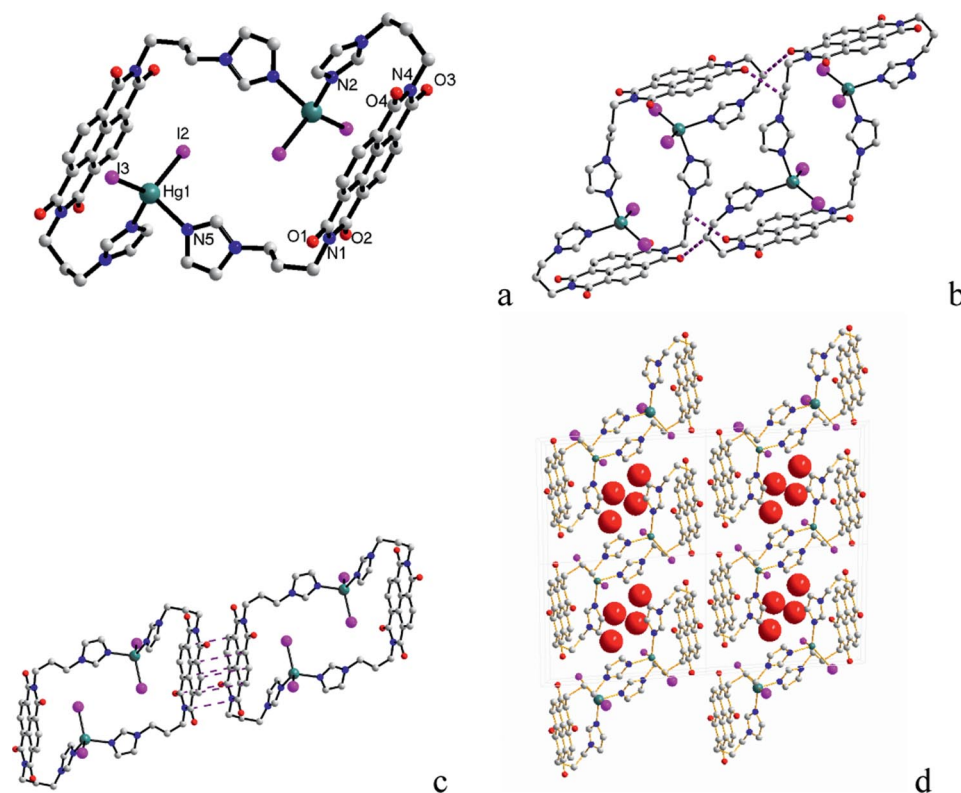


Figure 2. (a) The M_2L_2 metallacycle in **1**, which shows the coordination geometry of the Hg^{II} ion and atom labeling scheme. (b) The H bonds formed between the adjacent metallacycles. (c) The π - π interactions formed between the adjacent metallacycles. (d) The packing of metallacycles along the a axis, which shows the solvents (H atoms are omitted for clarity).

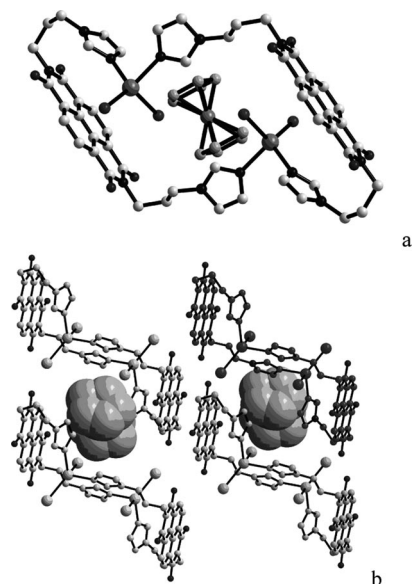


Figure 3. (a) The M_2L_2 metallacycle in **2**, which shows the coordination geometry of the Hg^{II} ion and the presence of $FeCp_2$. (b) The packing of metallacycles along the a axis, which shows the ferrocene (H atoms are omitted for clarity).

7.59 Å and the two naphthalene planes are almost parallel (dihedral angle of 2.0°). For each ligand, the dihedral angles of the ends of the two imidazoles to the naphthalene core are 17.4 and 79.7°.

Two kinds of hydrogen bonds are formed between the metallacycles (Figure 5b and c): (i) between the naphthalene N atoms and methylene groups on the ligand ($N\cdots C$ 3.58 Å) and (ii) between the formyl O atoms and methylene groups on the ligand ($O\cdots C$ 3.03–3.39 Å). There are also π - π interactions between adjacent rings (π - π 3.32 Å, Figure 5d). Similar to **1**, the metallacycles extend into 2D layers in the bc plane. Solvated H_2O molecules are located between the metallacycles, and the potential solvent accessible area is 3.5% (estimated by PLATON).

With Cu^{II} , a different ML metallacycle was obtained in **5** (the Cu^+ ions in the $CuCl$ starting material were oxidized during self-assembly). The Cu^{II} ion is coordinated to two imidazole N atoms from the same 3-imntd ligand and two terminal Cl^- ions. The $\{N_2Cl_2\}$ coordination geometry in this situation is between square planar and tetrahedral. Due to the demand of the large N-Cu-N angle, the two imidazole arms bend inwards to be nearly parallel, and their dihedral angles to the naphthalene core plane are 13.9 and 13.1° (Figure 6a).

Three different types of H bonds exist between the neighboring metallacycles in **5** (Figure S1a–c): (i) between coordinated Cl^- anions and methylene groups on the ligand ($Cl\cdots C$ 3.67 Å), (ii) between formyl O atoms and naphthalene rings on the ligand ($O\cdots C$ 3.21 Å), and (iii) between formyl O atoms and methylene groups on the ligand ($O\cdots C$ 3.24–3.35 Å). There are also π - π interactions between adja-

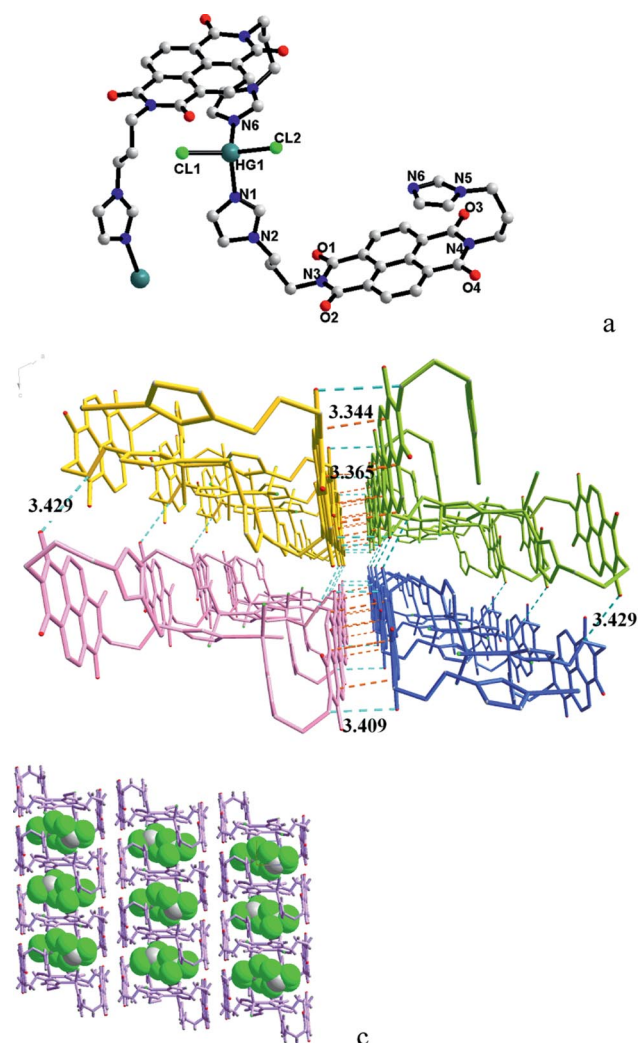


Figure 4. (a) The 1D chain in **3**, which shows the coordination geometry of the Hg^{II} ion and the anion- π interaction between Cl[−] and the naphthalene ring. (b) The H bonds and π - π interactions formed between the adjacent chains. (c) The packing of chains along the *b* axis, which shows the solvents (H atoms are omitted for clarity).

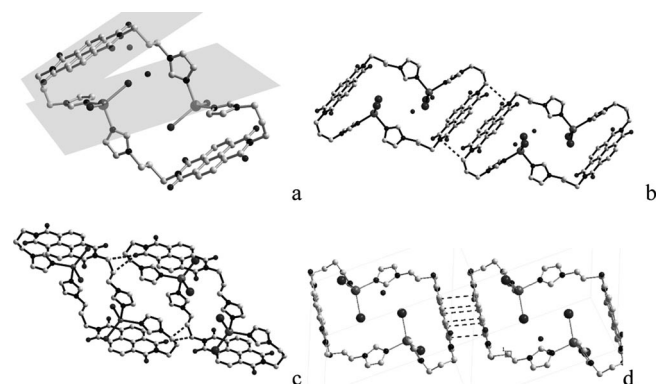


Figure 5. (a) The M_2L_2 metallacycle in **4**, which shows the coordination geometry of Cd^{II} ion and the dihedral angle between the end of one imidazole and the naphthalene core. (b–d) Three different types of H bonds and π - π interactions formed between the adjacent metallacycles (H atoms are omitted for clarity).

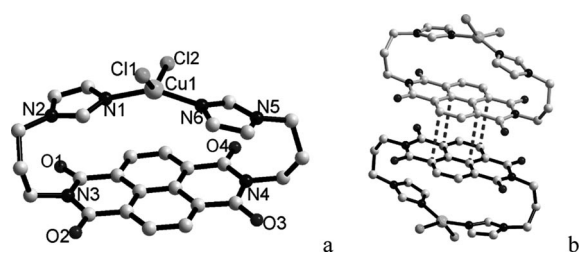
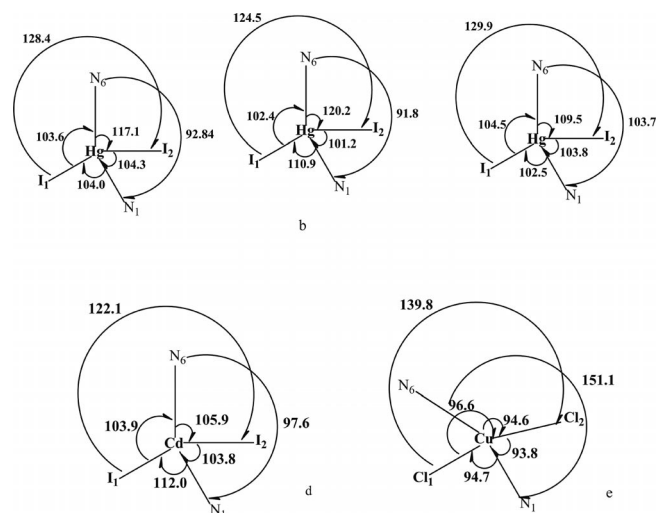


Figure 6. (a) The ML metallacycle in **5**, which shows the coordination geometry of the Cu^{II} ion and the atom labeling scheme. (b) π - π interactions between the adjacent metallacycles.

cent rings (π - π 3.35 Å, Figure 6b). Altogether, the metallacycles are packed in a 2D plane along the *a* direction (Figure S1d).

Synergistic Anion and Metal Effects on the Coordination Conformation of the Complexes

In general, the coordination of organic ligands with transition metals (particularly those with d^{10} configuration) with the aid of halide anions usually affords tetrahedral coordination geometries, which has the minimal electron repulsion and lowest energy.^[6b,15] In our five complexes, all the metal centers are coordinated to two imidazole N atoms and two halide anions to form distorted tetrahedra, but their detailed conformations show some differences. In **1** and **2**, the $\{N_2I_2\}$ coordination tetrahedron around the Hg^{II} center is more distorted than the $\{N_2Cl_2\}$ tetrahedron in **3**, deduced by comparison of the angles around the metal center where 109.5° is ideal for a tetrahedron (Scheme 2). The large distortion to nearly 90° of the N-Hg-N angle is more suitable for the strain requirement to form the M_2L_2 metallacycle, in which the imidazole arms of the two ligands are bent inwards to form a closed circle. In comparison, the more regular tetrahedral geometry in **3** with Cl[−] anions cannot meet this requirement. The imidazole arms of two adjacent ligands bend in different directions, and a 1D chain is



Scheme 2. Coordination geometries of the metal centers in **1–5**.

formed instead of a metallacycle. Herein, the differences in electronegativity of I and Cl may be the reason for the different coordination geometries under similar preparation conditions. Furthermore, when we used HgBr_2 under the same conditions, single crystals were hard to cultivate. This may be due to the fact that the electronegativity of Br is between that of I and Cl, and its preferred coordination geometry is not so definite. Therefore, more uncertainty could arise during crystal growth. To date, we have been unable to obtain single crystals with Br^- anions with high enough quality to be tested by XRD.

In **4**, the similar d^{10} configuration of Cd^{II} and presence of I^- anions resulted in a structure that resembles that of **1** and **2** and gave rise to a distorted tetrahedral geometry and M_2L_2 metallacycle. Although Cu^{II} -containing **5** also forms a $\{\text{N}_2\text{Cl}_2\}$ tetrahedron, the d^9 configuration of the Cu^{2+} ion tends to form square planar geometries. That is, it requires the N–Cu–N and N–Cu–Cl angles to be close to 180 and 90°, respectively. Due to the spatial congestion, the bending of two imidazole rings from two different 3-imntd ligands to be nearly coplanar may be difficult, and two arms from the same ligand are more able to achieve this geometry. Therefore, an ML type metallacycle is formed.

It should also be noted that the difference in electronegativity of Cl and I also results in different intermolecular interactions. As stated above, in **3**, strong $\text{Cl}\cdots\pi$ interactions are formed between coordinated Cl^- anions and the naphthalene ring, although no $\text{I}\cdots\pi$ interactions are formed in **1**, **2**, and **4**. The introduction of FeCp_2 in **2** does not cause much difference in the coordination structure compared with that of **1**, the packing effects of FeCp_2 result in an additional stabilization to the M_2L_2 metallacycles and their packing. In the similar metallacycle structures of **1** and **4** without FeCp_2 , disorder is very pronounced on the atoms from one arm of the ligand, whereas **2** has no disorder.

UV/Vis and Luminescence Spectroscopy

The UV/Vis absorption spectra of 3-imntd, **2**, and **3** were determined in dimethyl sulfoxide (DMSO)/ CH_3OH (1:50, 10^{-5} mol/L, Figure 7). We can see that the complexes show similar absorption bands to the ligand, which are centered at 378, 358, and 340 nm and can be assigned to the π – π^* transition of the ligand, in accordance with the time-dependent (TD)-DFT calculations discussed below. At the same concentration, we can see that the molar extinction coefficients of the free ligand and **3** are basically the same, whereas that of **2** is nearly double, which is in accordance with the different M/L ratio in the coordination complexes.

The luminescence spectra of 3-imntd and **1–5** are shown in Figure 8. In solution, two peaks can be observed for 3-imntd and **2–4**, one with short wavelength (SW, centered at 410 nm) and one with long wavelength (LW, centered at 590 nm). As the peak positions of 3-imntd and **1–5** are similar, we can conclude that the emissions are all ligand centered. However, interestingly, the relative intensities of the SW and LW emissions are different between the com-

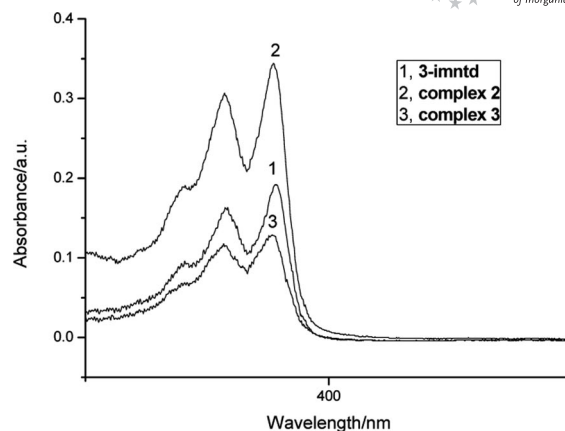


Figure 7. UV/Vis absorption spectra of 3-imntd, **2**, and **3**.

pounds. The LW emission of the ligand is much stronger than the SW one, whereas this tendency is less pronounced in **4**. In **2**, the intensities of these two emissions are almost identical, and in **3**, the SW emission is stronger than the LW one.

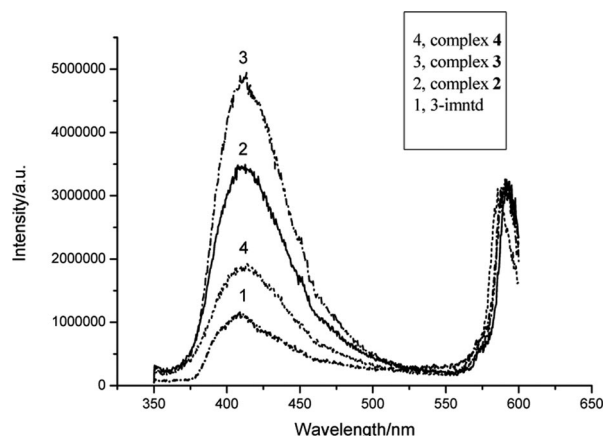


Figure 8. Luminescence spectra of 3-imntd and **1–5** in DMSO/methanol (v:v = 1:100, 10^{-5} mol/L) solution excited at 309 nm.

To illustrate the phenomenon of double fluorescence emission, we assigned the LW emission to the transition between imidazole (electron donating group, D) to NDI (electron withdrawing group, A) with perpendicular orientation, and the SW emission to the transition between the two groups with nearly parallel orientation.^[16] When 3-imntd adopts a *trans* conformation with the two imidazoles perpendicular to the NDI central core, the LW emission is much stronger than the SW one. In **2–4**, the ligands adopt an *L* conformation with one imidazole perpendicular to NDI and the other parallel to NDI, and the two emissions had similar intensities.

Electrochemistry

The cyclic voltammograms (CVs) of 3-imntd, **2**, and **3** in *N,N*-dimethylformamide (DMF) are shown in Figure 9. With a scan rate of 0.1 V/s, as the potential goes from 1.2 to -0.67 V (vs. SCE), 3-imntd shows a $1e^-$ reduction peak.

This is associated with the process in which the NDI accepts one electron to become NDI*. During the negative scan, an oxidation peak centered at -0.35 V was observed. $E_{1/2}$ is calculated to be -0.51 V and ΔE_p between the reduction and oxidation peaks is more than 0.3 V, which indicates that the redox process is quasireversible (for a reversible process, the gap between the two peaks should be about 0.06 V).^[17] Compared with 3-imntd, a positive shift is observed for the reduction and oxidation peaks in the CV curve of **2** (to -0.36 and 0.08 V, respectively; $E_{1/2} = -0.14$ V, $\Delta E_p = 0.44$ V). This may be due to the fact that the coordination of Hg^{II} to the imidazole group alters the electron delocalization on the π conjugation system. Furthermore, due to the existence of FeCp_2 in the lattice, another oxidation peak was observed in **2** centered at 0.51 V. Importantly, the introduction of FeCp_2 brings an increase in the intensity of the reduction and oxidation peaks (Figure 9). Therefore, we can deduce that the introduction of FeCp_2 into the coordination complex makes **2** more responsive to the changes in potential than 3-imntd and **3** (which shows redox process similar to 3-imntd but the peaks are less obvious), which may be helpful to fabricate materials with n-type conducting behavior.

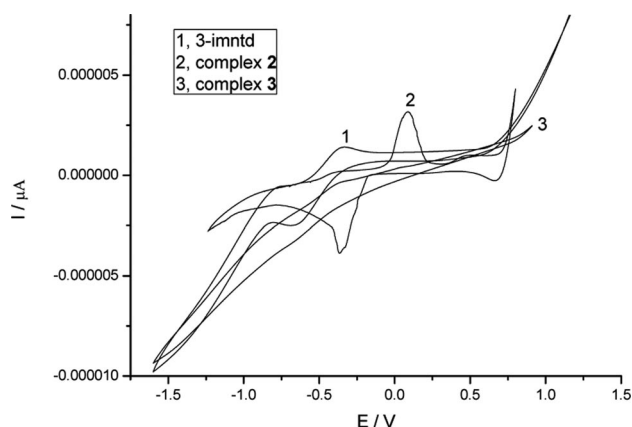


Figure 9. CVs of 3-imntd, **2**, and **3**.

DFT Study of the Molecular Geometries and Frontier Orbitals in 3-imntd and 1–5

The geometries of 3-imntd with different conformations and **1–5** were optimized by DFT calculations using the B3LYP method. The 6-31G* basis set was used for C, H, N, and O and LANL2DZ for the metal cations and halide anions.

As three different conformations, *cis*, *trans*, and L, were observed for 3-imntd in the crystals of the pure ligand and the five complexes, their geometries were optimized in both gas and solution phase, and their energies are summarized in Table 1. We can see that in H_2O solvent, which is more analogous to the real state in crystal, the *trans* conformation has the lowest energy. This is in accordance with experimental data for the pure ligand. In comparison, the energies of the L and *cis* states are only 8.93 or 23.10 kJ/mol

higher than the lowest *trans* state, which are favorable energy gaps for the conformation of the ligand to convert easily from one to another upon coordination. Furthermore, both the highest occupied molecular orbital (HOMO) and lowest unoccupied molecular orbital (LUMO) of the *trans* and L conformations have similar energy levels, whereas the gap between the HOMO and LUMO of the *cis* conformation is relatively small.

Table 1. Relative energies of the optimized geometries and frontier orbitals for three different conformations of 3-imntd (in kJ/mol).^[a]

Conformations	<i>cis</i>	<i>trans</i>	L
Energies			
in the gas phase	0	+4.20	+4.46
in H_2O solvent	+23.10	0	+8.93
Orbitals			
HOMO	-0.221	-0.226	-0.225
LUMO	-0.118	-0.120	-0.121

[a] Both in the gas phase and H_2O solvent, the lowest energy among the three conformations was taken as zero, and the other two were calculated for the relative value.

The calculated absorption maxima from TD-DFT calculations of the ligand in methanol solvent correlate to their UV absorption spectra. From the excited state assignment (Table 2 and Figure S2), the peak at 386 nm mainly refers to the transition of the σ electrons to the π^* orbitals on the naphthalene ring, the peak at 356 nm is the π – π^* transition state, and the peak at 343 nm is dominated by the transition of σ electrons on the imidazole rings to the π^* orbitals of naphthalene ring.

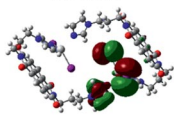
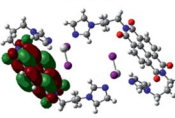
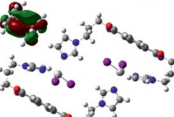
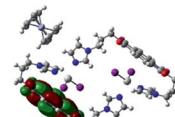
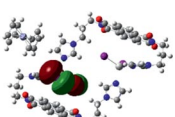
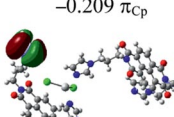
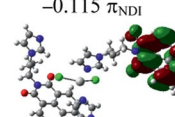
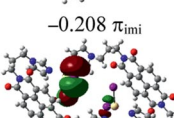
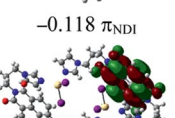
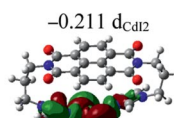
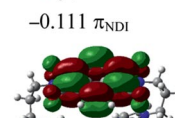
Table 2. Comparison of calculated TD-DFT data for optimized geometries of 3-imntd in methanol and observed UV absorption maxima.

Entry	Excited state	$\lambda_{\text{max,calcd}}$	Oscillator strength (f_{calcd})	$\lambda_{\text{max,exp}}$
1	117–127	386 nm	0.0019	378 nm
2	118–127	356 nm	0.0198	358 nm
3	121–127	343 nm	0.0081	340 nm

Table 3 lists the HOMO–LUMO gaps and the molecular orbitals for **1–5** (Table 3). In general, most of the HOMO or HOMO-1 orbital contributions of the five complexes correspond to the π system from the imidazole arms of the ligands, and the d orbitals of the metal center also contribute to those of **1**, **4**, and **5**. The LUMOs for all of the complexes are dominated by the large conjugated π system of the naphthalene core. Although **3** has a different chain-like structure compared to the M_2L_2 ring in **1**, **2**, and **4**, the energies of their frontier orbitals and the gaps between the HOMO and LUMO are quite close, therefore, their optical

and electronic properties are also similar. In comparison, both the HOMO and LUMO orbitals of **5** reside at lower energies, which is in accordance with its different ML macrocyclic structure.

Table 3. Calculated HOMO–LUMO gaps and MO nature of **1–5**.

	HOMO	LUMO	HOMO-1
1	 −0.213 $\pi_{\text{imi-dHgl2}}$	 −0.114 π_{NDI}	
2	 −0.209 π_{Cp}	 −0.115 π_{NDI}	 −0.211 d_{Hgl2}
3	 −0.208 π_{imi}	 −0.118 π_{NDI}	
4	 −0.211 d_{CdI2}	 −0.111 π_{NDI}	
5	 −0.236 $\pi_{\text{imi dCuCl2}}$	 −0.127 π_{NDI}	

Conclusions

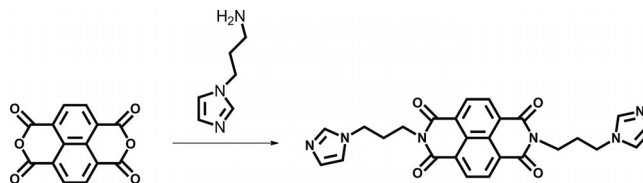
A new NDI-type ligand and its Hg^{II}, Cd^{II}, and Cu^{II} halide complexes have been synthesized and fully characterized. The single-crystal XRD analyses of the ligand and complexes reveal three different kinds of conformations for 3-imntd, which include *cis*, *trans*, and L. According to the theoretical calculations, the *trans* conformation has the lowest energy in the solution state, and therefore, this conformation was observed in the crystal structure of the free ligand. In the complexes, due to the synergistic effects of the preferred coordination geometries of the halide anions and metal centers, variations in the extent of the distortion of the coordination tetrahedron around the metal centers were observed. Accordingly, the ligand takes either L or *cis* conformation to adapt to the varied coordination geometry. As a result, M₂L₂ metallacycles, 1D zigzag chains, and ML metallacycles were observed in **1–5**. The optical and electronic properties of the ligand and complexes were also compared. The compounds might show potential applications in chemical or electrochemical luminescent sensors. Related work is underway in our laboratory.

Experimental Section

Materials and Method: All chemicals were of reagent grade obtained from commercial sources and used without further purification. ¹H NMR spectra were measured with a Varian/Mercury-Plus 300 instrument. IR spectra were measured with a Nicolet/Nexus-670 FTIR spectrometer as KBr pellets in the range 4000–400 cm^{−1}. The powder (P)XRD data were recorded with a Bruker D8 ADVANCE X-ray powder diffractometer (Cu-K_α, 1.5418 Å). The C, H, and N elemental analyses were performed with a Perkin–Elmer 240 elemental analyzer. Thermogravimetric analysis (TGA) was performed in air and under 1 atm of pressure at a heating rate of 10 °C/min with a NETZSCH TG209 analyzer.

Syntheses and Characterization of the Ligand and Complexes

N,N'-Bis(3-imidazol-1-ylpropyl)naphthalenediimide (3-imntd): The ligand was synthesized as shown in Scheme 3. A mixture of naphthalene dianhydride (1.0 g, 5 mmol) and 3-(aminopropyl)imidazole (1.2 g, 10 mmol) in DMF (20 mL) was heated to reflux with stirring for 24 h. On cooling, the black solution was filtered, and the black crude solid was collected and washed with acetone. A brown product was obtained by extraction with CHCl₃. Yield: 32%. ¹H NMR (300 MHz, [D₆]DMSO, 25 °C): δ = 2.09–2.18 (m, 4 H), 4.08 (t, *J* = 6.4 Hz, 4 H), 4.09 (t, *J* = 7.0 Hz, 4 H), 6.86 (s, 2 H), 7.20 (s, 2 H), 7.64 (s, 2 H), 8.66 (s, 4 H) ppm. IR (KBr): $\tilde{\nu}$ = 3432 (s), 1703 (s), 1657 (s), 1580 (m), 1343 (m), 1269 (w), 1245 (m), 1169 (m), 1079 (w), 770 (m), 667 (w) cm^{−1}. During a hydrothermal experiment of the ligand with nickel(II) *p*-toluenesulfonate (110 °C, CHCl₃ and methanol), crystals of pure 3-imntd were obtained. C₂₈H₃₀N₆O₂S₂ (706.70): calcd. N 11.88, C 47.54, H 4.24; found N 11.79, C 47.50, H 4.18.



Scheme 3. Synthesis of 3-imntd.

[Hg₂(3-imntd)₂I₄]·2H₂O (1): A buffer layer of CH₃OH (2 mL) was carefully layered over a solution of 3-imntd (12 mg, 0.025 mmol) in CHCl₃ (10 mL). A solution of HgI₂ (12 mg, 0.025 mmol) in CH₃OH (2 mL) was layered over the buffer layer. The solution was left to stand for two weeks at room temperature, and reddish orange crystals were obtained in 30% yield. IR (KBr): $\tilde{\nu}$ = 121 (w), 2935 (w), 1702 (s), 1667 (s), 1587 (m), 1516 (m), 1432 (m), 1332 (s), 1243 (m), 1079 (w), 701 (w), 651 (w) cm^{−1}.

[Hg₂(3-imntd)₂I₄]·FeCp₂ (2): A buffer layer of CH₃OH (2 mL) was carefully layered over a solution of 3-imntd (6 mg, 0.0125 mmol) and ferrocene (116 mg, 0.625 mmol) in CHCl₃ (10 mL). A solution of HgI₂ (12 mg, 0.025 mmol) in CH₃OH (2 mL) was layered over the buffer layer. The solution was left to stand for two weeks at room temperature, and black crystals were obtained in 30% yield. IR (KBr): $\tilde{\nu}$ = 122 (w), 2931 (w), 1707 (s), 1667 (s), 1577 (m), 1510 (m), 1452 (m), 1332 (s), 1246 (m), 1083 (w), 761 (w), 653 (w) cm^{−1}. C₆₂H₅₄FeHg₂I₄N₁₂O₈ (2059.83): calcd. N 8.16, C 36.14, H 2.62; found N 8.204, C 34.27, H 2.705.

[{Hg(3-imntd)Cl₂}·CHCl₃]_n (3): A buffer layer of acetone (2 mL) was carefully layered over a solution of 3-imntd (6 mg, 0.0125 mmol) in CHCl₃ (10 mL). A solution of HgCl₂ (7 mg, 0.025 mmol) in acetone (2 mL) was layered over the buffer layer.

The solution was left to stand for one week at room temperature, and black crystals were obtained in 30% yield. IR (KBr): $\tilde{\nu}$ = 118 (w), 1707 (m), 1667 (s), 1577 (m), 1516 (w), 1450 (m), 1373 (w), 1333 (s), 1246 (s), 1091 (w), 763 (m) cm^{-1} . $\text{C}_{27}\text{H}_{23}\text{Cl}_5\text{HgN}_6\text{O}_4$ (873.37): calcd. N 9.61, C 37.09, H 2.63; found N 9.58, C 37.30, H 2.78.

[Cd₂(3-imntd)₂I₄·2H₂O (4): A buffer layer of ethanol (2 mL) was carefully layered over a solution of 3-imntd (6 mg, 0.0125 mmol) in CHCl_3 (10 mL). A solution of CdI_2 (5 mg, 0.0125 mmol) in ethanol (2 mL) was layered over the buffer layer. The solution was left to stand for two weeks at room temperature, and yellow crystals were obtained in 30% yield. IR (KBr): $\tilde{\nu}$ = 093 (w), 1707 (s), 1667 (s), 1577 (m), 1513 (w), 1452 (m), 1379 (w), 1336 (s), 1246 (s), 1101 (s), 1059 (w), 767 (s) cm^{-1} . $[\text{Cd}_2(3\text{-imntd})_2\text{I}_4]\cdot 2\text{H}_2\text{O}\cdot\text{CHCl}_3$ ($\text{C}_{53}\text{H}_{49}\text{Cd}_2\text{Cl}_3\text{I}_4\text{N}_{12}\text{O}_{10}$) (1761.39): calcd. N 9.07, C 34.35, H 2.65; found N 9.03, C 34.89, H 2.75.

[Cu(3-imntd)Cl₂] (5): The mixture of 3-imntd (24 mg, 0.05 mmol) and CuCl (0.012 g, 0.1 mmol) in CHCl_3 (5.5 mL) and CH_3OH (3 mL) was sealed in a 15 mL Teflon-lined reaction vessel and heated at 110 °C for 4 d, then cooled to room temperature. The dark green crystals were collected by filtration, washed with water and ethanol, and dried in air. Yield: 80%. IR (KBr): $\tilde{\nu}$ = 3438 (s), 3122 (w), 1708 (s), 1668 (s), 1577 (m), 1515 (w), 1454 (m), 1375 (w), 1338 (s), 1248 (s), 1091 (w), 767 (s) cm^{-1} . $\text{C}_{26}\text{H}_{22}\text{Cl}_2\text{CuN}_6\text{O}_4$ (616.95): calcd. N 13.62, C 50.61, H 3.57; found N 13.43, C 50.74, H 3.65.

X-ray Crystallography: The intensity data of 3-imntd and **1–5** were collected with an Oxford Gemini S Ultra CCD diffractometer or a Bruker Smart 1000 CCD diffractometer with graphite monochromated Mo- K_α radiation (λ = 0.71073 Å) at 150, 173, or 293 K. Absorption corrections were applied using the program SCALE3 ABSPACK.^[18] The structures were solved by direct methods and refined using the full-matrix least-squares method against I^2 using SHELXTL software.^[19] The coordinates of the non-hydrogen atoms were refined anisotropically. All hydrogen atoms were introduced in calculated positions and refined with fixed geometry with respect to their carrier atoms. Crystallographic data and other pertinent information for 3-imntd and **1–5** are summarized in Table S1. Selected bond lengths and angles are listed in Table S2. The phase purities of the complexes were proved by PXRD (Figure S3).

CCDC-850312 (for 3-imntd), -850313 (for **1**), -850314 (for **2**), -850315 (for **3**), -850316 (for **4**), and -850317 (for **5**) contain the supplementary crystallographic data for this paper. These data can be obtained free of charge from The Cambridge Crystallographic Data Centre via www.ccdc.cam.ac.uk/data_request/cif.

Electrochemistry: All experiments employed a standard three-electrode cell; the reference electrode was a saturated calomel electrode (SCE), the auxiliary electrode a platinum wire, and the working electrode a platinum carbon electrode with a diameter of 1 mm (CV and electrochemiluminescence experiments in DMF). The supporting electrolyte was 0.1 M tetrabutylammonium bromide.

DFT Calculations: All calculations were performed with the Gaussian 03 software package^[20] using the default convergence criteria. Models created from fragments of the crystal structures were used as starting points. Geometry optimizations were conducted in both gas phase and water using self-consistent B3LYP density functional methods. In terms of disk space, computer time, and the size of the molecules studied here, the standard 6-31G* basis set was used for the light atoms C, H, N, and O and LANL2DZ for metal ions.^[20] For the TD-DFT calculation, three lowest excited singlet states were calculated.

Supporting Information (see footnote on the first page of this article): PXRD, crystallographic details, more crystal structural graphs, and results from theoretical calculations.

Acknowledgments

This work was supported by the National Basic Research Program of China (973 Program, 2012CB821700), the National Natural Science Foundation of China (NSF of China) (Grants U0934003, 20903120, 20821001, 21173272), the Research Fund for the Doctoral Program (RFDP) of Higher Education of China (No. 20090171120042), the Fundamental Research Funds for the Central Universities (FDYT) (No. 09lgpy15 and LYM09004).

- [1] a) H. E. Katz, A. J. Lovinger, C. Kloc, T. Siegrist, W. Li, Y. Y. Lin, A. Dodabalapur, *Nature* **2000**, *404*, 478–481; b) S. V. Bho-sale, C. H. Jani, S. J. Langford, *Chem. Soc. Rev.* **2008**, *37*, 331–342.
- [2] a) M. A. Rodrigues, G. J. F. Demets, M. J. Politi, *J. Mater. Chem.* **2002**, *12*, 1250–1255; b) B. A. Jones, A. Facchetti, T. J. Marks, M. R. Wasielewski, *Chem. Mater.* **2007**, *19*, 2703–2705.
- [3] S. J. Langford, M. J. Latter, C. P. Woodward, *Photochem. Photobiol.* **2006**, *82*, 1530–1540.
- [4] D. Gosztola, M. P. Niemczyk, M. R. Wasielewski, *J. Am. Chem. Soc.* **1998**, *120*, 5118–5119.
- [5] T. Iijima, S. A. Vignon, H. R. Tseng, T. Jarrosson, J. K. M. Sanders, F. Marchioni, M. Venturi, E. Apostoli, V. Balzani, J. F. Stoddart, *Chem. Eur. J.* **2004**, *10*, 6375–6392.
- [6] a) M. Pan, X. M. Lin, G. B. Li, C. Y. Su, *Coord. Chem. Rev.* **2011**, *255*, 1921–1936; b) H. Y. Deng, J. R. He, M. Pan, L. Li, C. Y. Su, *CrystEngComm* **2009**, *11*, 909–917; c) G. B. Li, J. M. Liu, Z. Q. Yu, W. Wang, C. Y. Su, *Inorg. Chem.* **2009**, *48*, 8659–8661; d) K. P. Ghiggino, J. A. Hutchison, S. J. Langford, M. J. Latter, M. A. P. Lee, M. Takezaki, *Aust. J. Chem.* **2006**, *59*, 179–185; e) Z. Gao, N. Tansil, *Anal. Chim. Acta* **2009**, *636*, 77–82; f) H. N. Lee, Z. Xu, S. K. Kim, K. M. K. Swamy, Y. Kim, S. J. Kim, J. Yoon, *J. Am. Chem. Soc.* **2007**, *129*, 3828–3829.
- [7] a) O. Johansson, M. Borgström, R. Lomoth, M. Palmblad, J. Bergquist, L. Hammarström, L. Sun, B. Åkermark, *Inorg. Chem.* **2003**, *42*, 2908–2918; b) O. Johansson, H. Wolpher, M. Borgström, L. Hammarström, J. Bergquist, L. C. Sun, B. Åkermark, *Chem. Commun.* **2004**, 194–195; c) S. Ulrich, A. Petitjean, J. M. Lehn, *Eur. J. Inorg. Chem.* **2010**, 1913–1928.
- [8] a) K. A. Lee, V. Lozan, S. J. Langford, B. Kersting, *Dalton Trans.* **2009**, 7481–7485; b) J. F. Penneau, B. J. Stallman, P. H. Kasai, L. L. Miller, *Chem. Mater.* **1991**, *3*, 791–796; c) E. M. Bauer, C. Bellitto, C. J. G. Garcias, G. Righini, *J. Solid State Chem.* **2008**, *181*, 1213–1219; d) M. A. Rodrigues, M. P. Bemquerer, N. D. S. Mohallem, M. J. Politi, *Langmuir* **2006**, *22*, 8939–8944; e) M. A. Rodrigues, M. P. Bemquerer, M. J. Politi, M. S. Baptista, *J. Photochem. Photobiol. A: Chem.* **2006**, *180*, 218–221; f) M. S. Khoshbin, M. V. Ovchinnikov, K. S. Sallaita, C. A. Mirkin, C. L. Stern, L. N. Zakharov, A. L. Rheingold, *Chem. Asian J.* **2006**, *1*, 686–692.
- [9] a) S. Suzuki, R. Sugimura, M. Kozaki, K. Keyaki, K. Nozaki, N. Ikeda, K. Akiyama, K. Okada, *J. Am. Chem. Soc.* **2009**, *131*, 10374–10375; b) C. Liao, J. E. Yarnell, K. D. Glusac, K. S. Schanze, *J. Phys. Chem. B* **2010**, *114*, 14763–14771; c) K. Ohtsuka, K. Komizo, S. Takenaka, *J. Organomet. Chem.* **2010**, *695*, 1281–1286.
- [10] a) A. Osuka, R. P. Zhang, K. Maruyama, T. Ohno, K. Nozaki, *Bull. Chem. Soc. Jpn.* **1993**, *66*, 3773–3782; b) A. Osuka, R. Yoneshima, H. Shiratori, T. Okada, S. Taniguchi, N. Mataga, *Chem. Commun.* **1998**, 1567–1568; c) M. J. Gunter, Z. Merican, *Supramol. Chem.* **2005**, *17*, 521–528.
- [11] a) S. Wallin, C. Monnereau, E. Blart, J. R. Gankou, F. Odobel, L. Hammarström, *J. Phys. Chem. A* **2010**, *114*, 1709–1721; b) M. Borgström, N. Shaikh, O. Johansson, M. F. Anderlund, S.

- Styring, B. Åkermark, A. Magnuson, L. Hammarström, *J. Am. Chem. Soc.* **2005**, *127*, 17504–17515.
- [12] a) Z. Q. Gao, N. Tansil, *Anal. Chim. Acta* **2009**, *636*, 77–82; b) M. Licchelli, A. O. Biroli, A. Poggi, *Org. Lett.* **2006**, *8*, 915–918; c) X. Lu, W. Zhu, Y. Xie, X. Li, Y. Gao, F. Li, H. Tian, *Chem. Eur. J.* **2010**, *16*, 8355–8364; d) L. Shen, X. Lu, H. Tian, W. Zhu, *Macromolecules* **2011**, *44*, 5612–5618.
- [13] a) B. Q. Ma, K. L. Mulfort, J. T. Hupp, *Inorg. Chem.* **2005**, *44*, 4912–4914; b) K. L. Mulfort, J. T. Hupp, *J. Am. Chem. Soc.* **2007**, *129*, 9604–9605.
- [14] PLATON, A. L. Spek, *J. Appl. Crystallogr.* **2003**, *36*, 7–13.
- [15] a) K. Skorda, T. C. Stamatatos, A. P. Vafiadis, A. T. Lithoxidou, A. Terzis, S. P. Perlepes, J. Mrozinski, C. P. Raptopoulou, J. C. Plakatouras, E. G. Bakalbassis, *Inorg. Chim. Acta* **2005**, *358*, 565–582; b) M. Hatano, T. Asai, K. Ishihara, *Chem. Lett.* **2006**, *35*, 172–173.
- [16] a) G. J. Hu, L. F. Lv, L. Li, Q. Zhang, X. L. Li, Y. P. Tian, J. Y. Wu, B. K. Jin, H. P. Zhou, J. X. Yang, S. Y. Zhang, *Dyes Pigm.* **2011**, *89*, 105–110; b) B. A. Jones, M. J. Ahrens, M. H. Yoon, A. Facchetti, T. J. Marks, M. R. Wasielewski, *Angew. Chem.* **2004**, *116*, 6523; *Angew. Chem. Int. Ed.* **2004**, *43*, 6363–6366.
- [17] J. A. Zhang, M. Pan, R. Yang, Z. G. She, W. Kaim, Z. J. Fan, C. Y. Su, *Polyhedron* **2010**, *29*, 581–591.
- [18] G. M. Sheldrick, *SADABS: Program for Scaling and Correction of Area Detector Data*, University of Göttingen, Göttingen, Germany, **1996**.
- [19] *SHELXTL*, version 5.10, Bruker Analytical X-ray Systems, Madison, WI, **1998**.
- [20] M. J. Frisch, G. W. Trucks, H. B. Schlegel, G. E. Scuseria, M. A. Robb, J. R. Cheeseman, J. A. Montgomery Jr., Vreven, T. K. N. Kudin, J. C. Burant, J. M. Millam, S. S. Iyengar, J. Tomasi, V. Barone, B. Mennucci, M. Cossi, G. Scalmani, N. Rega, G. A. Petersson, H. Nakatsuji, M. Hada, M. Ehara, K. Toyota, R. Fukuda, J. Hasegawa, M. Ishida, T. Nakajima, Y. Honda, O. Kitao, H. Nakai, M. Klene, X. Li, J. E. Knox, H. P. Hratchian, J. B. Cross, C. Adamo, J. Jaramillo, R. Gomperts, R. E. Stratmann, O. Yazyev, A. J. Austin, R. Cammi, C. Pomelli, J. W. Ochterski, P. Y. Ayala, K. Morokuma, G. A. Voth, P. J. Salvador, J. Dannenberg, V. G. Zakrzewski, S. Dapprich, A. D. Daniels, M. C. Strain, O. Farkas, D. K. Malick, A. D. Rabuck, K. Raghavachari, J. B. Foresman, J. V. Ortiz, Q. Cui, A. G. Baboul, S. Clifford, J. Cioslowski, B. B. Stefanov, G. Liu, A. Liashenko, P. Piskorz, I. Komaromi, R. L. Martin, D. J. Fox, T. Keith, M. A. Al-Laham, C. Y. Peng, A. Nanayakkara, M. Challacombe, P. M. W. Gill, B. Johnson, W. Chen, M. W. Wong, C. Gonzalez, J. A. Pople, *Gaussian 03*, Revision D.01, Gaussian, Inc., Wallingford CT **2004**.

Received: October 26, 2011

Published Online: January 26, 2012

Room-Temperature Sol–Gel Synthesis of Sodium Hexaniobate in an Immiscible Hexane–Water System and Its Conversion into NaNbO_3

Masahiro Tanaka^[a] and Shinobu Fujihara^{*[a]}

Keywords: Niobium / Alkoxides / Sol–gel processes / Crystal growth

Sodium hexaniobate ($\text{Na}_7[\text{HNb}_6\text{O}_{19}] \cdot 15\text{H}_2\text{O}$) was synthesized by a one-pot sol–gel method at room temperature by using an immiscible, biphasic solution. An organic solution was prepared by dissolving niobium pentaethoxide $[\text{Nb}(\text{OC}_2\text{H}_5)_5]$ in ethanol, which was then added to hexane. This solution was brought into contact with an aqueous NaOH solution to form a reaction system consisting of two separate phases. A white precipitate was formed within 12 h at the bottom of the aqueous solution. It exhibited well-defined rod-like morphology on a micrometer scale. A compar-

ative study was performed on the basis of a single-phase solution by mixing $\text{Nb}(\text{OC}_2\text{H}_5)_5$ in ethanol and the aqueous NaOH solution. The results indicated that the product formed by way of the single-phase solution was rather different in morphology from that obtained in the biphasic system. In both cases, $\text{Na}_7[\text{HNb}_6\text{O}_{19}] \cdot 15\text{H}_2\text{O}$ could be converted to NaNbO_3 by heating at 600 °C. Mechanisms underlying the formation of $\text{Na}_7[\text{HNb}_6\text{O}_{19}] \cdot 15\text{H}_2\text{O}$ and its conversion to NaNbO_3 are discussed on the basis of the experimental results.

Introduction

Complex metal oxides having perovskite or related structures have been extensively studied to develop new functional materials such as lead-free piezoelectrics,^[1,2] thermoelectrics,^[3,4] or photocatalysts.^[5,6] Antiferroelectric sodium niobate (NaNbO_3) with a pseudoperovskite structure is widely recognized as the starting compound for synthesizing various types of functional solid solutions with other perovskite-type metal oxides.^[7,8] Synthetic pathways to NaNbO_3 have been explored to control its composition and microstructure precisely by means of a low-temperature solution process such as a hydrothermal method or a sol–gel process.^[9–13] Generally, the direct synthesis of NaNbO_3 from chemical solutions leads to the formation of nanometer-scale particles or wires of lower crystallinity. Recently, Yamazoe et al. reported an interesting method to obtain micrometer-scale needle-like NaNbO_3 .^[14] The synthesis starts with the reaction of Nb_2O_5 with molten NaOH at 450 °C. Needle-like single crystals of sodium hexaniobate ($\text{Na}_7[\text{HNb}_6\text{O}_{19}] \cdot 15\text{H}_2\text{O}$) were formed as an intermediate compound, which was converted to NaNbO_3 by heat treatment. This result indicates that sodium hexaniobate can be a key material in preparing large NaNbO_3 particles through a low-temperature process.

It was reported that $\text{Na}_7[\text{HNb}_6\text{O}_{19}] \cdot 15\text{H}_2\text{O}$ could be obtained by the reaction of niobium pentaethoxide $[\text{Nb}(\text{OC}_2\text{H}_5)_5]$ and NaOH in aqueous medium under hydrother-

mal conditions at 190 °C for 1 h.^[15] However, the fact that metal alkoxides are highly reactive with water makes it difficult to control hydrolysis, nucleation, and crystal growth in solutions at low temperatures. It is still a challenging undertaking to obtain particles with controlled morphology in a sol–gel process by using metal alkoxides. In this work, we offer a novel way to synthesize $\text{Na}_7[\text{HNb}_6\text{O}_{19}] \cdot 15\text{H}_2\text{O}$ by starting from $\text{Nb}(\text{OC}_2\text{H}_5)_5$ and NaOH and using a liquid–liquid biphasic system. $\text{Nb}(\text{OC}_2\text{H}_5)_5$ is dissolved first in ethanol and subsequently in hexane to prepare an organic solution. Separately, NaOH is dissolved in deionized water to prepare an aqueous solution. These solutions are immiscible, and a liquid–liquid biphasic system is formed by injecting the organic solution gently into the aqueous solution with a syringe. The interface between the solution phases affords a reaction space where metal alkoxides and water molecules meet with each other. The environment of the interface is probably different from that of the bulk of the solutions.^[16] Particular chemical reactions are then expectedly promoted, resulting in the formation of compounds with characteristic morphologies and compositions. From a variety of raw materials, which cannot be employed in a single-phase solution but can be dissolved in separate phases, organic–inorganic hybrid materials are also synthesized in one step by the principle of the distribution equilibrium of solutes between two liquid phases.^[17,18] This paper focuses on a comparison between a single-phase and a biphasic solution system as reaction media for synthesizing $\text{Na}_7[\text{HNb}_6\text{O}_{19}] \cdot 15\text{H}_2\text{O}$ through a sol–gel process. It is shown that a biphasic hexane–water system is suitable for obtaining rod-like $\text{Na}_7[\text{HNb}_6\text{O}_{19}] \cdot 15\text{H}_2\text{O}$ particles of higher uniformity at room temperature. The conversion from $\text{Na}_7[\text{HNb}_6\text{O}_{19}] \cdot 15\text{H}_2\text{O}$ to NaNbO_3 is also investigated.

[a] Department of Applied Chemistry, Keio University, 3-14-1 Hiyoshi, Kohoku-ku, Yokohama 223-8522, Japan
Fax: +81-45-566-1551
E-mail: shinobu@apcl.Keio.ac.jp

Results and Discussion

We attempted first to synthesize $\text{Na}_7[\text{HfNb}_6\text{O}_{19}]\cdot 15\text{H}_2\text{O}$ from a single-phase solution. $\text{Nb}(\text{OC}_2\text{H}_5)_5$ was dissolved in ethanol. The resultant solution was added dropwise to an aqueous NaOH solution. A white precipitate was immediately (within 1 min) obtained at the bottom of the container at room temperature. Figure 1a shows a field-emission scanning electron microscopy (FESEM) image of the as-prepared solid product from the single-phase solution, which indicates particles more than 10 μm in size without any specific morphology. This means that hydrolysis and solid formation reactions were not controlled well. An X-ray diffraction (XRD) analysis revealed that the product is crystalline, and it was identified as an orthorhombic $\text{Na}_7[\text{HfNb}_6\text{O}_{19}]\cdot 15\text{H}_2\text{O}$ phase (ICDD No. 77-0059) with two characteristic intense peaks at $2\theta = 10.1$ and 11.3° , as shown in Figure 2a. These results indicate that $\text{Na}_7[\text{HfNb}_6\text{O}_{19}]\cdot 15\text{H}_2\text{O}$ can be formed through a sol–gel process conducted at room temperature. A sample of the $\text{Na}_7[\text{HfNb}_6\text{O}_{19}]\cdot 15\text{H}_2\text{O}$ particles was examined after heat treatment to check their conversion to NaNbO_3 . Figure 1b and c show FESEM images of samples after heat treatment in air for 1 h at 150 and 600 $^\circ\text{C}$, respectively. Large particles maintain their shape after heating at 150 and 600 $^\circ\text{C}$. Additionally, small particles less than one micrometer in size appear to be scattered on the large particles. According to the XRD analysis, the sample heated at 150 $^\circ\text{C}$ was identified as anhydrous $\text{Na}_7[\text{HfNb}_6\text{O}_{19}]$, by referring to the pattern reported in the literature,^[9] as shown in Figure 2b. Considerably broadened peaks of the $\text{Na}_7[\text{HfNb}_6\text{O}_{19}]$ phase suggest that a dehydration from $\text{Na}_7[\text{HfNb}_6\text{O}_{19}]\cdot 15\text{H}_2\text{O}$ to $\text{Na}_7[\text{HfNb}_6\text{O}_{19}]$ would fragment the large, single-crystalline particles into small crystallites. By heating at 600 $^\circ\text{C}$, $\text{Na}_7[\text{HfNb}_6\text{O}_{19}]\cdot 15\text{H}_2\text{O}$ is converted completely to NaNbO_3 (ICDD No. 33-1270), as indicated by its characteristic XRD pattern (Figure 2c). Thus, large NaNbO_3 particles more than 10 μm in size are obtained through a sol–gel process in association with a solid-state transformation from $\text{Na}_7[\text{HfNb}_6\text{O}_{19}]\cdot 15\text{H}_2\text{O}$.

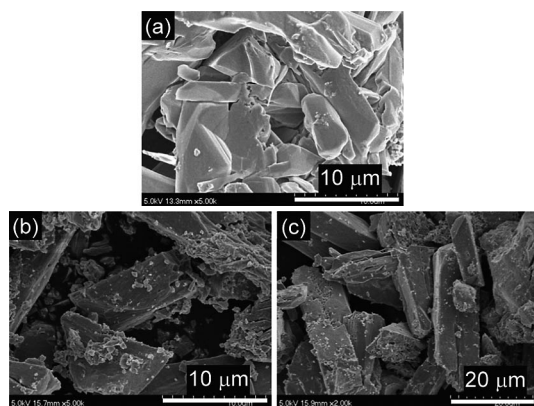


Figure 1. FESEM images of (a) the product of reaction in the single-phase solution and the samples obtained by heating this product at (b) 150 and (c) 600 $^\circ\text{C}$.

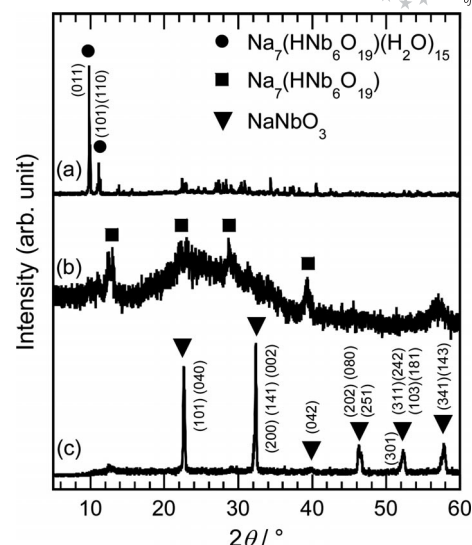


Figure 2. XRD patterns of (a) the product of reaction in the single-phase solution and the samples obtained by heating this product at (b) 150 and (c) 600 $^\circ\text{C}$. All peaks can be indexed with $\text{Na}_7[\text{HfNb}_6\text{O}_{19}]\cdot 15\text{H}_2\text{O}$ in (a).

In the single-phase solution, the $\text{Nb}(\text{OC}_2\text{H}_5)_5$ /ethanol droplets were directly added to the NaOH aqueous phase, which led to intensive hydrolysis, a rapid increase of the amount of niobate species, and subsequently a high degree of supersaturation. This synthetic condition made the $\text{Na}_7[\text{HfNb}_6\text{O}_{19}]\cdot 15\text{H}_2\text{O}$ particles grow in a large scale without any specific morphology. We then employed an immiscible liquid–liquid system to control a series of reactions to form $\text{Na}_7[\text{HfNb}_6\text{O}_{19}]\cdot 15\text{H}_2\text{O}$. $\text{Nb}(\text{OC}_2\text{H}_5)_5$ was dissolved in ethanol, and this solution was added to hexane. The resultant organic solution was injected into an aqueous NaOH solution to obtain a liquid–liquid biphasic system at room temperature. Changes in the appearance of the solutions with time of reaction are shown in Figure 3. Soon after a distinct liquid–liquid interface appeared (0 min), the solutions turned turbid in the region near the interface. This indicates that hydrolysis and polycondensation reactions are promoted in the region where $\text{Nb}(\text{OC}_2\text{H}_5)_5$ and H_2O molecules can meet with each other. A white precipitate started to form in the aqueous solution, and simultaneously the whole organic solution turned cloudy after 1 min. The amount of precipitate increased with time (10 to 20 min) both at the bottom and at the interface. After keeping the solutions unstirred for 12 h, the organic solution became transparent again and the precipitation at the interface almost stopped. Figure 4a shows a FESEM image of a sample of the precipitate. Well-defined morphology is observed with rod-like particles 1–2 μm in width and 5–10 μm in length. The difference in morphology is remarkable from the sample obtained by the single-phase solution method (Figure 1a). An XRD pattern of the product from the hexane–water system is shown in Figure 5a. This product can also be identified as $\text{Na}_7[\text{HfNb}_6\text{O}_{19}]\cdot 15\text{H}_2\text{O}$. This comparison shows that the growth of $\text{Na}_7[\text{HfNb}_6\text{O}_{19}]\cdot 15\text{H}_2\text{O}$ crystals differs greatly between the single-phase and the biphasic solution system.

FULL PAPER

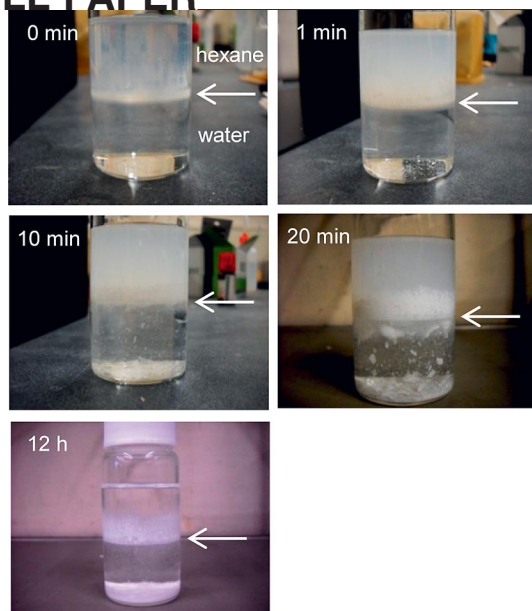


Figure 3. The appearance of the immiscible hexane–water system with the progress of the reaction time from 0 min to 12 h. The arrow indicates the interface.

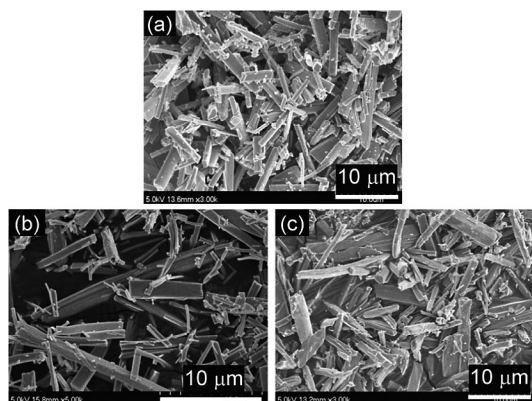
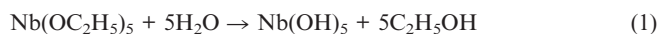


Figure 4. FESEM images of (a) the product of reaction in the biphasic solution and the samples obtained by heating this product at (b) 150 and (c) 600 °C.

The formation reaction of $\text{Na}_7[\text{HNb}_6\text{O}_{19}]\cdot 15\text{H}_2\text{O}$ starts from the generation of the Lindqvist ion, $[\text{H}_x\text{Nb}_6\text{O}_{19}]^{(8-x)-}$, through the hydrolysis of $\text{Nb}(\text{OC}_2\text{H}_5)_5$. At room temperature, liquid $\text{Nb}(\text{OC}_2\text{H}_5)_5$ exists predominantly as a six-coordinate dimer.^[19] It reacts readily with water as shown in Equation (1).



Further ololation/oxolation processes between $\text{Nb}(\text{OH})_5$ molecules with elimination of water lead to the formation of isopolyniobate ions such as $[\text{Nb}_6\text{O}_{19}]^{8-}$, $[\text{Nb}_{10}\text{O}_{28}]^{6-}$, $[\text{Nb}_{12}\text{O}_{37}]^{4-}$, or $[\text{Nb}_{24}\text{O}_{65}]^{10-}$.^[20] The hexaniobate ion is the most dominant and smallest, and it is an ideal source for aqueous synthesis of niobate materials.^[20,21] The single-phase, basic aqueous solution is readily supersaturated with Na^+ and $[\text{Nb}_6\text{O}_{19}]^{8-}$, leading to the rapid nucleation and

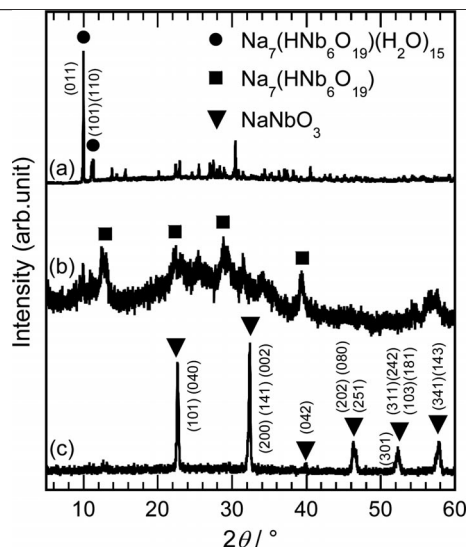


Figure 5. XRD patterns of (a) the product of reaction in the biphasic solution and the samples obtained by heating this product at (b) 150 and (c) 600 °C. All peaks can be indexed with $\text{Na}_7[\text{HNb}_6\text{O}_{19}]\cdot 15\text{H}_2\text{O}$ in (a).

growth of $\text{Na}_7[\text{HNb}_6\text{O}_{19}]\cdot 15\text{H}_2\text{O}$ without any specific morphology. On the other hand, the biphasic solution can slow down the reaction rate because of the limited reaction space. The degree of supersaturation is also lowered, and the nucleation and crystal growth are better controlled. The framework of $\text{Na}_7[\text{HNb}_6\text{O}_{19}]\cdot 15\text{H}_2\text{O}$ is composed of $[\text{Nb}_6\text{O}_{19}]^{8-}$ units and tends to grow along the $\langle 101 \rangle$ direction.^[14,21] The rod-like particles are then formed in the vicinity of the hexane–water interface. They are dispersed into the bulk of the aqueous solution where the hexaniobate ions are absent, limiting the further growth of crystals. Nonetheless, unreacted $\text{Nb}(\text{OC}_2\text{H}_5)_5$ is continuously hydrolyzed by water molecules delivered from the aqueous solution under the presence of the Na^+ ions, and the formation of $\text{Na}_7[\text{HNb}_6\text{O}_{19}]\cdot 15\text{H}_2\text{O}$ does not stop until the reactants are consumed completely. As a result, the particles with the well-defined morphology precipitate at the bottom of the container at room temperature.

The rod-like $\text{Na}_7[\text{HNb}_6\text{O}_{19}]\cdot 15\text{H}_2\text{O}$ particles from the biphasic solution are also converted to $\text{Na}_7[\text{HNb}_6\text{O}_{19}]$ and NaNbO_3 by heating at 150 and 600 °C, respectively, as shown in Figure 5b and 5c. The FESEM observation reveals that the morphology is maintained after heating at 150 and 600 °C (Figure 4b and 4c). The thermal conversion of $\text{Na}_7[\text{HNb}_6\text{O}_{19}]\cdot 15\text{H}_2\text{O}$ was examined by thermogravimetry - differential thermal analysis (TG-DTA) and the result is shown in Figure 6. A first weight loss is observed at temperatures between 70 and 120 °C in the TG curve, accompanied by a sharp endothermic peak at 110 °C in the DTA curve. This thermal behavior corresponds to the dehydration of $\text{Na}_7[\text{HNb}_6\text{O}_{19}]\cdot 15\text{H}_2\text{O}$, shown in Equation (2).



The theoretical weight loss is calculated to be 20.9%, which matches well the observed loss in Figure 6. The fur-

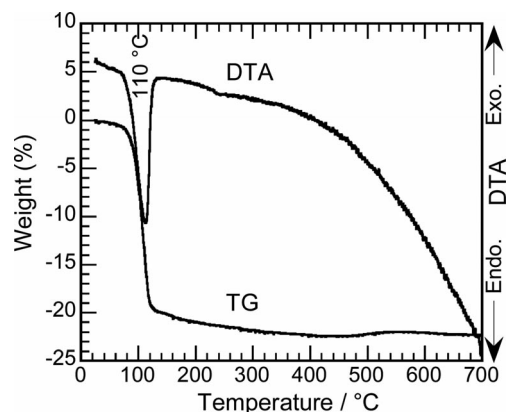


Figure 6. TG-DTA curves of the $\text{Na}_7[\text{HNb}_6\text{O}_{19}]\cdot 15\text{H}_2\text{O}$ sample obtained from the biphasic hexane–water system.

ther conversion from $\text{Na}_7[\text{HNb}_6\text{O}_{19}]\cdot 15\text{H}_2\text{O}$ is not clearly observed in the TG-DTA curves. However, a close look at the TG curve tells that there is some slight increase in weight at around 500 °C. The reason will be discussed later.

Figure 7 compares Fourier transform infrared (FTIR) spectra of the $\text{Na}_7[\text{HNb}_6\text{O}_{19}]\cdot 15\text{H}_2\text{O}$ sample from the biphasic solution and the NaNbO_3 sample obtained by heating at 600 °C. Broad absorption bands, centered at 3400 cm^{-1} , appearing in the spectra of both samples are assigned to the O–H stretching vibration. This absorption dramatically decreases in intensity but does not disappear completely after heating at 600 °C, suggesting that the NaNbO_3 particles contain some hydroxy groups. An absorption peak at 1650 cm^{-1} observed for the $\text{Na}_7[\text{HNb}_6\text{O}_{19}]\cdot 15\text{H}_2\text{O}$ sample is due to the H–O–H deformation vibration of the water of hydration. Another peak appears at 1400 cm^{-1} in the NaNbO_3 sample, which may come from the antisymmetric stretching mode of CO_3^{2-} , as will be discussed later. The $\text{Na}_7[\text{HNb}_6\text{O}_{19}]\cdot 15\text{H}_2\text{O}$ sample exhibits another series of absorption bands at lower wavenumbers: 875, 850, 778, 664, 525, and 420 cm^{-1} . As shown in the inset

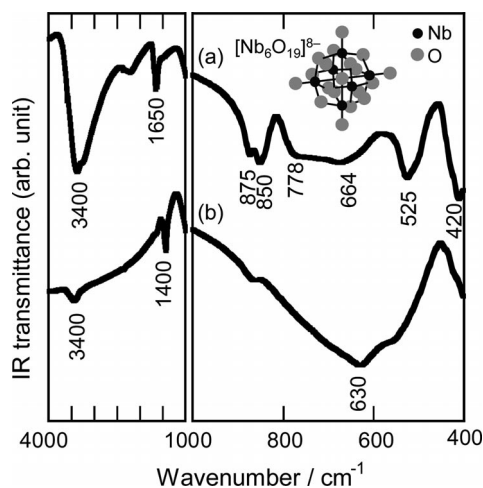


Figure 7. FTIR spectra of (a) the $\text{Na}_7[\text{HNb}_6\text{O}_{19}]\cdot 15\text{H}_2\text{O}$ sample obtained from the biphasic hexane–water system and (b) the NaNbO_3 sample heated at 600 °C.

of Figure 7, the Lindqvist ion is composed of edge-sharing NbO_6 octahedra with different types of Nb–O bonding. There are six terminal oxygen atoms (O_t), twelve bridging oxygen atoms (O_b), and one central oxygen atom (O_c).^[22] While the bands at the higher wavenumbers of 875 and 850 cm^{-1} correspond to the Nb– O_t vibration, those at the lower wavenumbers of 778, 664, 525, and 420 cm^{-1} are assigned to the Nb– O_b –Nb vibration.^[10,23] The absorption band at 630 cm^{-1} observed in the NaNbO_3 sample is ascribed to the Nb–O vibration of corner-sharing NbO_6 octahedra in the perovskite structure.^[24]

In the transformation from the dehydrated $\text{Na}_7[\text{HNb}_6\text{O}_{19}]$ to NaNbO_3 , some important information was obtained from the TG-DTA and FTIR measurements. Nominally, the reaction would proceed as shown in Equation (3).



There would be no weight change due to this reaction. Actually, however, we observed some weight increase at around 500 °C in the TG curve and a change in the absorption peak due to CO_3^{2-} in the FTIR spectrum of the heated NaNbO_3 sample. These results suggested the occurrence of an alternative reaction, shown in Equation (4).



This reaction is accompanied by an increase in weight arising from the formation of another solid phase (Na_2CO_3). Reactions 3 and 4 seem to proceed competitively in air with a low partial pressure of CO_2 . This can explain the coexistence of the peaks due to OH^- and CO_3^{2-} in the FTIR spectrum of the heated NaNbO_3 sample. The presence of the basic species (NaOH and/or Na_2CO_3) was further examined by dispersing the heated NaNbO_3 sample (0.0273 g) in deionized water (10 mL). We then observed a change in pH from 6.14 to 10.84, indicating that the basic species was dissolved in water. The inorganic residue was collected, and its weight was measured to be 0.0212 g, which supports the above explanation. Figure 8 shows FESEM images of the sample after the water dispersion treatment. Obviously the rod-like particles undergo micronization due to the dissolution of their basic contaminants in water, although their overall shape is not changed. Therefore, it is concluded that the sol–gel-derived $\text{Na}_7[\text{HNb}_6\text{O}_{19}]\cdot 15\text{H}_2\text{O}$ rods should be converted into the NaNbO_3 rods by the procedures involving both the heat treatment and the water dispersion treatment.

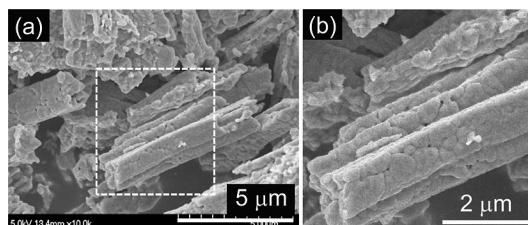


Figure 8. FESEM images of the NaNbO_3 sample after the water treatment: (a) low and (b) high magnification.

FULL PAPER

Finally, the phase evolution and morphology of NaNbO_3 by a conventional solid-state reaction were compared with those of the sol–gel-derived NaNbO_3 . Figure 9a shows XRD patterns of products obtained by heating a mixture of Na_2CO_3 and Nb_2O_5 at 600 or 1200 °C for 5 h in air. At 600 °C, $\text{Na}_2\text{Nb}_4\text{O}_{11}$ (ICDD No. 72-1694) is formed as a byproduct, indicating that the reaction is not completed at this temperature.^[25] In contrast, the product is a single-phase NaNbO_3 when the reaction temperature is increased to 1200 °C. The morphology of this NaNbO_3 sample is shown in Figure 9b. Oval-shaped particles 1–5 μm in size are observed with well-developed necking between the particles. These results are largely different from those described in this article for the sol–gel-derived NaNbO_3 rods. In terms of applications, the rod-like NaNbO_3 particles might not be suitable for the fabrication of dense bulk materials by usual ceramic processing methods. Instead, the anisotropic particles have recently found use in a sophisticated processing technology such as a templated grain growth method for synthesizing textured ceramics.^[26,27]

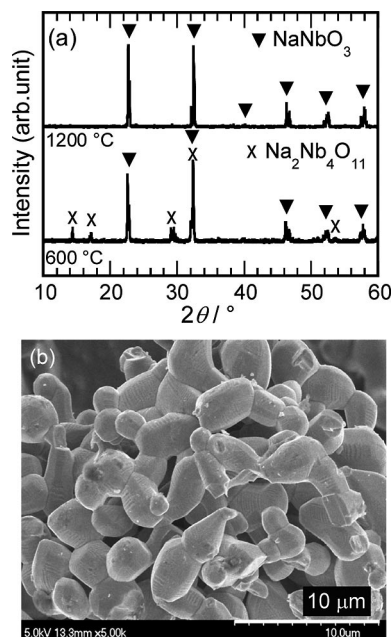


Figure 9. (a) XRD patterns of products obtained by the solid-state reaction of Na_2CO_3 and Nb_2O_5 at 600 or 1200 °C for 6 h in air; (b) FESEM image of the product heated at 1200 °C.

Conclusions

Rod-like $\text{Na}_7[\text{HNb}_6\text{O}_{19}]\cdot 15\text{H}_2\text{O}$ particles on the micrometer scale were synthesized by the sol–gel method based on the biphasic solution system at room temperature. They were converted to NaNbO_3 by heating at 600 °C without destroying the morphology. A comparison with the synthesis from the single-phase solution revealed that the biphasic system was advantageous in that the hydrolysis of $\text{Nb}(\text{OC}_2\text{H}_5)_5$ was controlled well by the limited reaction

space. It is believed that the biphasic sol–gel synthesis is a unique method that can be applied to a variety of metal alkoxides.

Experimental Section

Sample Preparation: In the method using the single-phase solution, $\text{Nb}(\text{OC}_2\text{H}_5)_5$ (0.1 mL, 99.9%; Wako Pure Chemical Industries Co., Ltd., Japan) was dissolved in ethanol (0.9 mL, 99%; Amakasu Chemical Industries Co., Ltd., Japan). The resultant solution was added dropwise to an aqueous NaOH solution (10 mL, 0.1 M). A white precipitate was formed within 1 min at the bottom of the container at room temperature; it was collected by filtration under reduced pressure and then dried at 60 °C for 6 h. The dried samples were heated at 150 or 600 °C for 1 h in air.

In the method using the biphasic solution, $\text{Nb}(\text{OC}_2\text{H}_5)_5$ (0.1 mL) was dissolved in ethanol (0.9 mL). The resultant solution was added to anhydrous hexane (9 mL, 96.0%; Wako). The final hexane solution was injected into an aqueous NaOH solution (10 mL, 0.1 M) with a syringe, making sure that the aqueous phase was only minimally disturbed. Soon after a distinct liquid–liquid interface appeared, both the solutions near the interface turned turbid. The white precipitate fell from the interface region to the bottom of the container after 12 h. It was collected by filtration under reduced pressure, dried at 60 °C for 6 h, and heated at 150 or 600 °C for 1 h in air.

For the solid-state reaction, Na_2CO_3 (99.8%, Wako) and Nb_2O_5 (99.9%, Mitsui Mining & Smelting Co., Ltd., Japan) powders ($\text{Na}/\text{Nb} = 1:1$) were mixed in a mortar with the addition of acetone. The mixture was dried at 100 °C and then heated at 600 or 1200 °C for 5 h in air, followed by furnace cooling.

Characterization: Crystalline phases of the samples were identified with an X-ray diffractometer (Bruker AXS D8 ADVANCE) by using $\text{Cu-K}\alpha$ radiation. The morphology of the samples was observed with a FESEM (Hitachi S-4700 or FEI Sirion) instrument. The chemical species in the samples were examined by FTIR spectroscopy (Bruker ALPHA) by using samples prepared with KBr. The thermal decomposition behavior of the samples was examined by TG-DTA (Mac Science 2020S) with a heating rate of 3 °C min^{-1} in flowing air.

Acknowledgments

This work was supported by a Grant-in-Aid for Challenging Exploratory Research from the Japan Society for the Promotion of Science (21655078). We also thank The Murata Science Foundation for financial support.

- [1] M. Matsubara, T. Yamaguchi, W. Sakamoto, K. Kikuta, T. Yogo, S. Hirano, *J. Am. Ceram. Soc.* **2005**, *88*, 1190–1196.
- [2] T. Takenaka, H. Nagata, *J. Eur. Ceram. Soc.* **2005**, *25*, 2693–2700.
- [3] D. Flahaut, T. Miura, R. Funahashi, N. Nabeshima, K. Lee, H. Ohta, K. Koumoto, *J. Appl. Phys.* **2006**, *100*, 084911.
- [4] L. Bocher, M. H. Aguirre, D. Logvinovich, A. Shkabko, R. Robert, M. Trottman, A. Weidenkaff, *Inorg. Chem.* **2008**, *47*, 8077–8085.
- [5] D. Chen, J. H. Ye, *Chem. Mater.* **2007**, *19*, 4585–4591.
- [6] H. G. Kim, P. H. Borse, J. S. Jang, C. W. Ahn, E. D. Jeong, J. S. Lee, *Adv. Mater.* **2011**, *23*, 2088–2092.
- [7] R. M. Glaister, *J. Am. Ceram. Soc.* **1960**, *43*, 348–353.

- [8] I. P. Raevski, S. A. Prosandeev, *J. Phys. Chem. Solids* **2002**, *63*, 1939–1950.
- [9] H. Zhu, Z. Zheng, X. Gao, Y. Huang, Z. Yan, J. Zou, H. Yin, Q. Zou, S. H. Kable, J. Zhao, Y. Xi, W. N. Martens, R. L. Frost, *J. Am. Chem. Soc.* **2006**, *128*, 2373–2384.
- [10] H. Tong, J. Ye, *Eur. J. Inorg. Chem.* **2010**, 1473–1480.
- [11] W. Liu, H. Wang, K. Li, *J. Sol–Gel Sci. Technol.* **2010**, *55*, 229–234.
- [12] D. Q. Zhang, Z. C. Qin, X. Y. Yang, H. B. Zhu, M. S. Cao, *J. Sol–Gel Sci. Technol.* **2011**, *57*, 31–35.
- [13] Y. D. Hou, L. Hou, J. L. Zhao, M. K. Zhu, H. Yan, *J. Electroceram.* **2011**, *26*, 37–43.
- [14] S. Yamazoe, T. Kawawaki, T. Imai, T. Wada, *J. Ceram. Soc. Jpn.* **2010**, *118*, 741–744.
- [15] T. M. Alam, M. Nyman, B. R. Cherry, J. M. Segall, L. E. Lybarger, *J. Am. Chem. Soc.* **2004**, *126*, 5610–5620.
- [16] F. Scholz, U. Hasse, *Electrochem. Commun.* **2005**, *7*, 541–546.
- [17] S. Inoue, S. Fujihara, *Langmuir* **2010**, *26*, 15938–15944.
- [18] S. Inoue, S. Fujihara, *Inorg. Chem.* **2011**, *50*, 3605–3612.
- [19] D. Saulys, V. Joshkin, M. Khoudiakov, T. F. Kuech, A. B. Ellis, S. R. Oktyabrsky, L. McCaughan, *J. Cryst. Growth* **2000**, *217*, 287–301.
- [20] C. Alquier, M. T. Vandenborre, M. Henry, *J. Non-Cryst. Solids* **1986**, *79*, 383–395.
- [21] M. Nyman, T. M. Anderson, P. P. Provencio, *Cryst. Growth Des.* **2009**, *9*, 1036–1040.
- [22] G. K. L. Goh, F. F. Lange, S. M. Haile, C. G. Levi, *J. Mater. Res.* **2003**, *18*, 338–345.
- [23] R. P. Bontchev, M. Nyman, *Angew. Chem.* **2006**, *118*, 6822; *Angew. Chem. Int. Ed.* **2006**, *45*, 6670–6672.
- [24] Lj. Radonjić, M. Todorović, J. Miladinović, *Mater. Chem. Phys.* **2004**, *88*, 427–432.
- [25] B. Malic, D. Jenko, J. Holc, M. Hrovat, M. Kosec, *J. Am. Ceram. Soc.* **2008**, *91*, 1916–1922.
- [26] T. Kimura, *J. Ceram. Soc. Jpn.* **2006**, *114*, 15–25.
- [27] M. H. Cao, W. Q. Wang, F. Li, H. Hao, Z. Y. Yu, H. X. Liu, *Ferroelectrics* **2010**, *404*, 39–44.

Received: November 28, 2011

Published Online: February 6, 2012

Influence of Morphology and Texture of CeO₂ on YBa₂Cu₃O₇ (YBCO) Growth and BaCeO₃ Formation in Solution-Derived Synthesis

Nigel Van de Velde,^[a] Tom Bruggeman,^[a] Lander Stove,^[b] Glenn Pollefeyt,^[a] Oliver Brunkahl,^[c] and Isabel Van Driessche*^[a]

Keywords: Superconductors / Layered compounds / Cerium dioxide / Nanostructures / Surface morphology

When working with chemical solution deposition techniques, one of the main issues for optimal performance of CeO₂ buffer layers in coated conductors is the insufficient chemical stability of the CeO₂ layer during YBa₂Cu₃O₇ (YBCO) thermal processing. This work focusses on the morphology and nanostructure in thin CeO₂ films prepared by means of a novel aqueous synthesis route and incorporated into a Ni–W/La₂Zr₂O₇/CeO₂/YBa₂Cu₃O₇-coated conductor. Optimization of precursor chemistry and thermal processing led to a reduction in barium cerate formation. In a new precursor design, iminodiacetic acid was used as a stabilizing ligand, which resulted in an improved morphology of the buffer layer. A shelf life of more than 6 months was established by using a metal-to-ligand ratio of 1 to 5. During thermal pro-

cessing, a combination of a slow calcination ramp with a high sintering ramp, short sintering dwell time and a low oxygen partial pressure during the synthesis resulted in a root mean square roughness below 3 nm for AFM analysis, a [111] to [002] ratio of 1 to 90 in X-ray diffraction and well-defined patterns in reflection high-energy electron diffraction (RHEED) analysis of the CeO₂ surface. Trifluoroacetate-YBCO was deposited on top of the CeO₂ buffer layer. Cross-section analysis with a focussed ion beam allowed us to correlate the morphology and nanostructure of the CeO₂ buffer layer with the formation of BaCeO₃ and the appearance of voids and secondary phases throughout the YBa₂Cu₃O₇ layer.

Introduction

Applications for high-temperature superconductors have recently become more numerous. Yet there are still many chemical and technological drawbacks to overcome to be able to integrate most of these possible applications into economically viable conditions. Upscaling towards continuous production and maintaining good superconducting characteristics are the main interests in this research field. Therefore, a great deal of attention has been given to the development of coated conductors that uses a low-cost deposition technique [i.e., chemical solution deposition (CSD) for buffer layers and superconducting coatings on flexible metallic tapes].^[1–3] This route towards the synthesis of ceramic materials gives an improved control of material characteristics by adjusting the chemistry of the system. As it is a nonvacuum technique and does not require ultrapure precursor targets or substantial facility investments, it contributes to the economic applicability of these innovative

materials. In this perspective and in comparison to other well-known deposition techniques such as pulsed laser deposition (PLD^[4]) and metal–organic chemical vapour deposition (MOCVD^[5]), CSD routes are very convenient for production on a large scale. CSD routes for YBa₂Cu₃O₇ (YBCO) with the use of trifluoroacetates as metal precursors in an organic solvent are well studied.^[6,7] Although this route leads to good electrical and magnetic properties, the release of aggressive, fluorine-containing gases and the need for a long heat treatment because of an exothermic combustion makes the approach unfavourable for the production of long-length coated conductors.^[8] Therefore, effort is being made to develop new precursors that are more environmentally benign and that result in a shortened production process. Promising results by using nonfluorine YBCO precursor solutions in a polymer-assisted deposition method (PAD) or by using trimethyl acetates as metal salts have been published.^[9–13] The deposition of both buffer layers and YBCO starting from aqueous precursors by using dip coating was described by us previously.^[1,14–17] In this approach, metal salts are dissolved in water in the presence of appropriate complexing agents, thus leading to the formation of metal–chelate complexes, which is necessary to control hydrolysis of the metal salts.^[18]

To minimize chemical interactions and optimize crystal growth of the superconducting YBCO layer, an efficient buffer layer architecture of sufficient thickness is required

[a] Department of Inorganic and Physical Chemistry (SCRiPTS), Ghent University, Krijgslaan 281 (S3), 9000 Ghent, Belgium
Fax: +32-9-2644983
E-mail: isabel.vandriessche@ugent.be

[b] Department of Applied Engineering Sciences, College University Ghent, Valentin Vaerwyckweg 1, 9000 Ghent, Belgium

[c] Zenenergy Power GmbH, Heisenbergstrasse 16, 53359 Rheinbach, Germany

in between the metal tape and the superconducting layer. The requirement of a good buffer layer architecture is three-fold. First, a biaxial lattice alignment of YBCO is needed for high critical current transport. This requires the buffer layers to be biaxially textured as well and to exhibit only a minor lattice mismatch with both the preceding and subsequent layer. A second demand is directly attributed to the use of Ni-based tapes as a substrate. In oxidative conditions, which are required for YBCO processing, Ni_xO_y phases will grow and diffuse towards the surface, which will influence the growth of biaxially textured YBCO and degrade its superconducting characteristics. The use of an oxygen barrier is therefore required. A third requirement can be found in the necessity of forming stoichiometric YBa₂Cu₃O_{7-δ}. Therefore, there should be no chemical interaction between the buffer layer structure and the superconducting layer, which would introduce secondary phases and disrupt the stoichiometry of the superconducting material.

Based on their good lattice mismatch, low oxygen diffusion and relatively easy synthesis chemistry, CeO₂ ($a = 5.411 \text{ \AA}$) and La₂Zr₂O₇ ($a = 10.804 \text{ \AA}$) serve as a good combination for a buffer-layer architecture.^[19] As the thickness of the CeO₂ buffer layer is limited to approximately 70 nm before cracks are formed,^[16] which is insufficient to avoid Ni_xO_y diffusion into the YBCO layer, La₂Zr₂O₇ is used as a thick (150–300 nm) extra buffer layer. This phase, on the other hand, has the tendency to form nanovoids throughout the layer thickness.^[20] A dense top layer in the form of CeO₂ remains necessary to allow good *c* axis YBCO growth. One of the main difficulties in using this buffer layer combination is the insufficient chemical stability of the CeO₂ layer during the YBCO thermal process when working with chemical solution deposition techniques. Formation of an intermediate BaCeO₃ phase is almost always observed, thus leading to significant reduction in current density values for the superconducting layer.^[21–23] This can be avoided by minimizing the surface roughness and optimizing the nanostructure of the CeO₂ buffer layer. This results in a lower active surface in which the CeO₂ and the YBCO precursors are brought together in high concentrations during the YBCO thermal synthesis process.

This publication focusses on these morphology issues and on the texture of CeO₂ buffer layers, which can be positively influenced by the sol chemistry and by the thermal synthesis process. Aqueous precursor designs were used for CSD of the CeO₂ layers. The choice of the organic ligands for the stabilization of Ce³⁺ metal ions up to high concentration will have an effect on the decomposition behaviour of the system and the resulting nanostructure. A variation in the material properties of the pure CeO₂ route will indicate the importance of an optimized nanostructure on the formation and growth of the YBCO layer.

Results and Discussion

An inappropriate film morphology (i.e., high surface roughness and the presence of artefacts in the nanostructure

of the film) will result in unwanted intermediate phases during the YBCO process. To improve the morphology, the following criteria must be considered: a high concentration of volatile decomposition products (e.g., CO_x and NO_x, which mainly originate from the organic ligand) results in a less dense structure; exothermicity during the thermal process should be limited; and the thermal expansion coefficients should match with the underlying layer. As the latter is a material constant of the oxide material, we focus on the first criteria. In literature there is a range of known ligands that improve the stability of the Ce³⁺ metal ions up to high concentrations.^[24] Well-studied ones are, for example, citric acid, ethylenediaminetetraacetic acid and nitrilotriacetic acid.^[15,16,25] All of them are rather bulky ligands, thereby resulting in quite exothermic decomposition reactions throughout the formation of CeO₂. Therefore, in this work we chose to use iminodiacetic acid (IDA) ($\log K_1 = 6.18$ and $\log K_2 = 10.71$) as a smaller ligand.^[24] Morphological properties of the CeO₂ coating synthesized by this precursor route are also compared with the ones obtained using citric acid as a stabilizing agent. Both homogeneous gels and stable sols with an extended shelf life of over 6 months were obtained at a Ce³⁺-to-IDA ratio of 1 to 5 and pH values starting from 8.5.

Thermal analysis of both systems was performed on gels dried at 200 °C. The weight loss before 200 °C can be related to a small amount of absorbed and structural water in the samples. The first exothermic decomposition reaction occurs at 290 °C and is the result of the decomposition of the NO₃[−] groups from the metal precursor. The exothermic peak is equal in intensity, yet slightly broader for the citrate gel system than the IDA system. Starting from 350 °C, the decomposition of carbon-containing groups was observed. For the citrate gel system, this step occurs slightly slower than for the IDA system, respectively ranging from 350 up to 500 °C and from 350 up to 450 °C. The total area underneath the differential thermal analysis (DTA) curve is similar for both systems, thus revealing similar total exothermicity. The decomposition process of nitrates in the presence of citric acid is regarded to be a very exothermic reaction, which was expected to be less pronounced for the IDA system. However, this is not reflected in the measurements. There is only a marginal difference in total mass loss. If we compare the molecular weight of iminodiacetic acid (C₄H₇NO₄) to citric acid (C₆H₈O₇·H₂O), 133.1 and 192.1 g mol^{−1}, respectively, we can see that this difference in possible mass loss is compensated by the respective metal-to-ligand ratios of 1 to 5 and 1 to 3. As the total mass loss and the formation of volatile decomposition products is therefore quite similar for both systems, we cannot expect improvements in surface morphology based on these factors.

There are, however, several other parameters that could effect the final morphology. The hardness of the gel, which plays a key role during the removal of the solvent in the sol-to-gel transition, is significantly lower for the iminodiacetate route. Besides this, Figure 1 shows that oxide formation happens earlier for the IDA-based system. The combi-

nation of a more viscous gel and more time for relaxation of the oxide material before sintering is likely to have a positive effect on surface morphology of the IDA-based system. The thermal process to convert the wet Ce^{3+} -containing dipcoated layer into a crystalline CeO_2 coating can be basically divided into three main steps (i.e., drying, calcination and sintering). Each of these steps will show an influence on both the texture and the morphology of the thin film. From thermal analysis in Figure 1, we can see that the drying process basically continues up to 250 °C, at which point the first decomposition reaction takes place.

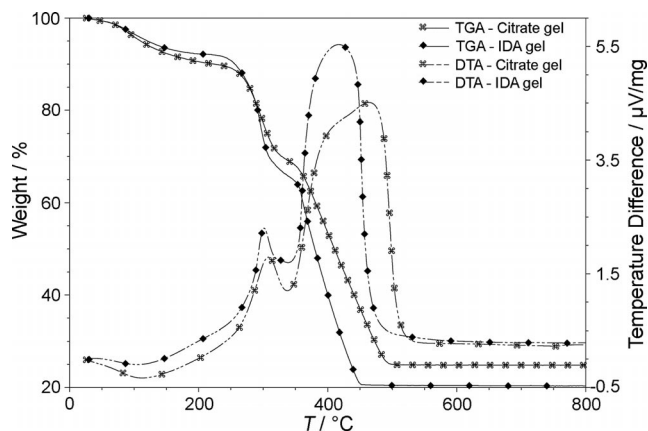


Figure 1. Study of the thermal decomposition of the Ce^{3+} citrate gel versus the Ce^{3+} iminodiacetate gel.

During the drying step, the metal complexes approach each other and in some cases we can even observe crosslinking and formation of a Ce–O network by Raman analysis. In the Raman spectrum of Figure 2 (c), the Ce–O stretching vibration can be found at 460–470 cm^{-1} for pure CeO_2 treated at 900 °C. At 1047 cm^{-1} , the symmetric stretching vibration for the NO_3^- groups can be seen, which should not change during the sol-to-gel transition and serves as a reference. In Figure 2 (a), the Ce–O stretching vibration is already present in the IDA-based precursor sol and increases throughout the drying phase (a Raman scan taken at 60 °C is shown in Figure 2, b). A similar behaviour was not detected for the citrate gel system.

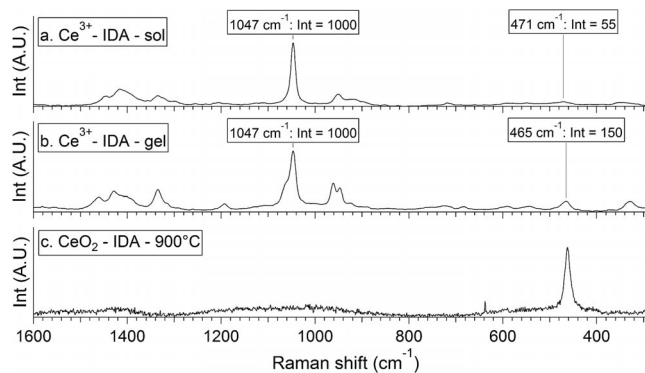


Figure 2. Ce–O bond formation during the sol-to-gel transition for the IDA-based system.

Further influence of drying was studied by X-ray diffraction, performed on fully sintered CeO_2 thin films synthesized by the IDA process. Here, a significant influence was seen by using either the standard hot-air furnace or by using an infrared lamp.

The calcination and sintering step comprised, respectively, a temperature increase of 2 °C min^{-1} up to 900 °C for 60 min and a temperature increase of 10 °C min^{-1} up to 1050 °C for 30 min. In Figure 3, we can see that a variation in drying temperature for air-furnace-assisted drying hardly has any influence on the final texture. An insignificant increase in *c*-axis orientation with a [111]-to-[002] ratio equal to 1 to 16 and 1 to 17 is seen for drying at 90 and 170 °C, respectively. The effect of an increased drying temperature is more pronounced for IR-assisted drying (Figure 3). Dried samples at 90 and 170 °C give respective ratios of 1 to 7 and 1 to 21. We can thus conclude that IR drying at relatively high temperatures is optimal in terms of final texture and [002] growth. In Figure 4, we can see that the [111]-to-[002] ratio even improves for drying temperatures of 190 °C and higher. A ratio of 1 to 40 or better can be achieved from 190 °C onwards; it stays quite stable for a further increase. The absolute intensities of the [002] reflection remains constant.

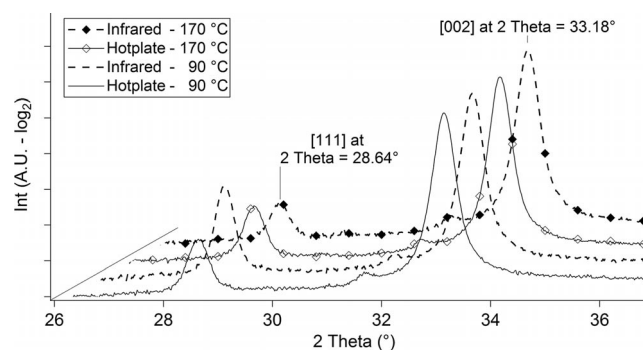


Figure 3. Effect of the drying method on the biaxial orientation of the CeO_2 coating.

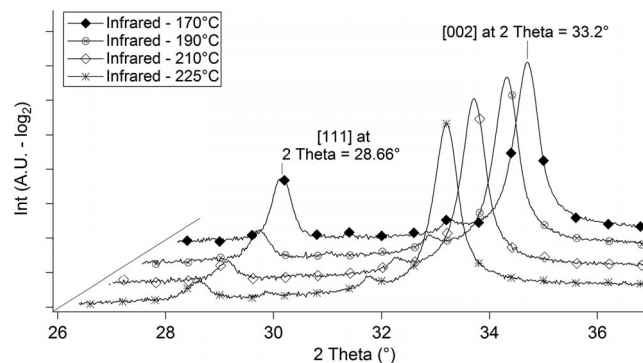


Figure 4. Effect of IR-drying temperature on the biaxial orientation of the CeO_2 coating.

Reflection high-energy electron diffraction (RHEED) analysis allows us to characterize texture very close to the surface, which is a key factor in attaining biaxial texturation throughout the layer structure. Measurements along the

[110] direction of the CeO₂ show a slightly sharper RHEED pattern for the infrared-dried samples.

Raman measurements during the drying process in Figure 2 indicate network formation at low temperatures for the iminodiacetate system. The assumption that this network formation during the early stages of the process will have an effect on the nucleation behaviour was confirmed by X-ray diffraction and RHEED analysis in Figures 4, 5 and 6, in which clear improvements in the texture of the fully calcined and sintered CeO₂ material were obtained as a function of the drying process.

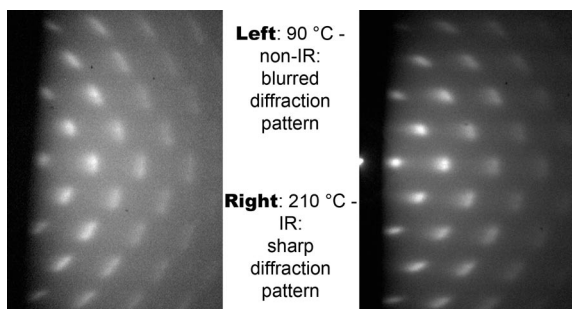


Figure 5. Effect of drying method on the RHEED pattern of the CeO₂ coating.

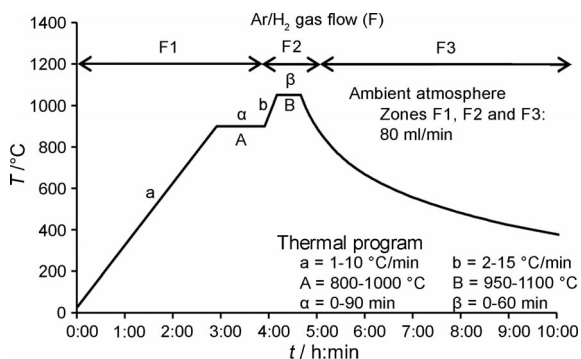


Figure 6. Thermal synthesis process for the conversion from gel to oxide coating.

After the drying stage, the samples were treated in a tube furnace under an Ar/(5%) H₂ atmosphere in which they underwent further thermal processing as presented in Figure 6. Temperature ramps, levels and dwell times are the parameters of interest when optimizing the texture and surface morphology.

As seen in a three-dimensional AFM representation of the film surface in Figure 7, the effect of the calcination ramp on the morphology is substantial. Calcination ramps of 2, 5 and 10 °Cmin⁻¹ up to 900 °C yield RMS values of 2.6, 6.6 and 4.5 nm, respectively. Synthesis parameters *a*, *b*, *B* and *β* were respectively fixed at 60 min, 10 °Cmin⁻¹, 1050 °C and 30 min. As can be seen, intermediate calcination ramps (5 °Cmin⁻¹) seem to be detrimental in terms of surface roughness. The slowest calcination ramp results in a controlled decomposition process and enough time to release internal thermomechanical stresses before the oxide starts the sintering stage. The detailed study that describes

thermal expansion behaviour and bulk moduli calculations will be discussed in further publications. Besides this, a faster calcination leads to a less homogeneous nucleation during this stage and a decrease in orientation of the crystalline phase. As crystals and grains with different orientation will exhibit different energy states, the solid material will try to minimize the total surface of the interface, thereby leading to a change in surface morphology on a larger scale.^[26]

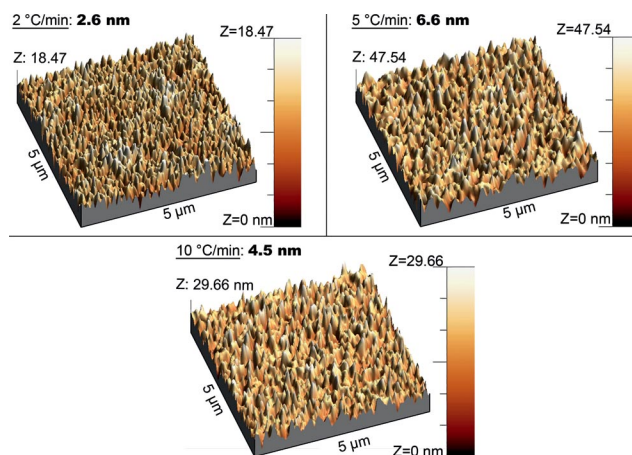


Figure 7. Effect of a varying calcination ramp on the surface roughness of the CeO₂ coating.

However, the fact that an intermediate calcination ramp yielded a worse surface roughness than a high calcination ramp shows that other parameters influence the final properties as well. As the calcination ramp directly influences the moment at which, for example, nucleation takes place, we can see that the available time for stabilization of the atmosphere after opening the furnace and inserting the sample is changed. During the calcination step, the transition from Ce^{III} to Ce^{IV} uses oxygen as well. The total stabilization time after this transition and before crystallization will vary as a function of the calcination ramp. Synthesis conditions such as the ambient atmosphere and the oxygen partial pressure inside the tube will correspondingly vary as a function of the calcination ramp. In previous work, it was shown that atmospheric conditions and in turn the oxygen partial pressure during the synthesis of CeO₂ buffer layers have a serious impact on the film characteristics.^[16] It is likely that the oxygen partial pressure inside the tube furnace affects the surface morphology as well. Changing the calcination level to 600 °C instead of 900 °C results in a faster total synthesis process. The RMS roughness increases from 2.6 nm up to 3.7 nm. As the complete decomposition process in the first case is already finished, the increase in surface roughness is probably related to higher thermomechanical stresses during the subsequent faster sintering ramp. Calcination dwell times longer than 60 min also result in an increase in surface roughness [e.g., up to a 50% increase for a dwell time of 120 min (Figure 8)].

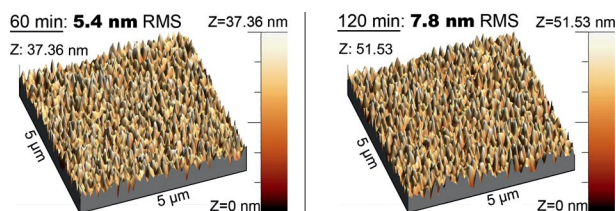


Figure 8. Influence of calcination dwell times on the surface roughness of the CeO₂ coating.

According to X-ray diffraction in Figure 9, the texture of the CeO₂ layer follows the same trend as the surface morphology for variable calcination ramps. The [111] to [002] ratio can be as low as 1 to 90 for slow calcination ramps.

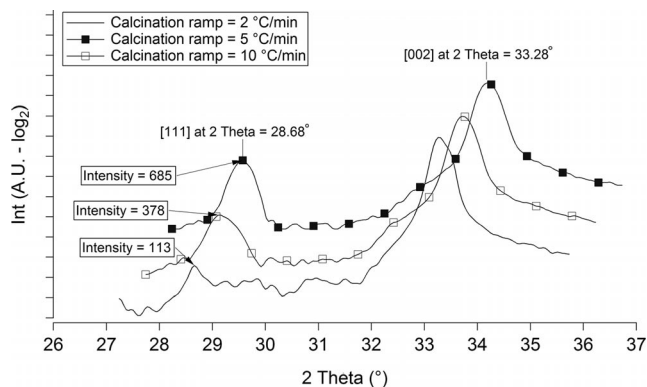


Figure 9. Influence of calcination ramps on the biaxial orientation of the CeO₂ coating.

If we overlook the calcination step, we can summarize that fast decomposition reactions result in a rough surface morphology and a relatively high fraction of [111] crystal growth. A calcination ramp of 2 °C min⁻¹ between drying at 210 and 900 °C yields optimal results in terms of surface morphology and crystal growth.

Similar observations as seen during calcination are observed during the sintering process at higher temperatures. A sintering ramp of 3, 10 and 14 °C min⁻¹, respectively, between 900 and 1050 °C results in root mean square (RMS) roughness values of 5.2, 2.6 and 3.2 nm. The AFM images in Figure 10 show that the grains grow together and higher peaks are being formed for the slow sintering ramps.

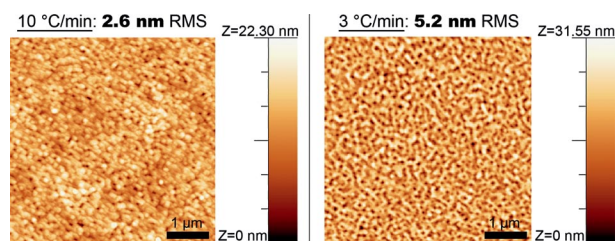


Figure 10. Influence of the sintering ramp on the surface roughness of the CeO₂ coating.

Here, the effect on the orientation was minimal; the [111] to [002] ratios are 1 to 90 or lower for all examined sintering ramps (Figure 11), whereas the full width at half-maximum

(FWHM) fluctuates around 0.2°. The increasing intensity, which is related to increased crystallinity, is maximal for the higher sintering ramps.

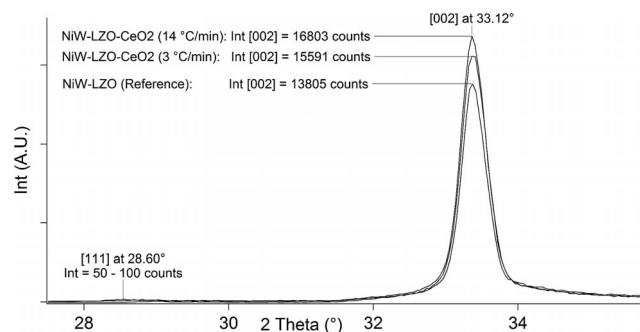


Figure 11. Influence of sintering ramp on the biaxial orientation of the CeO₂ coating.

In previous work, it was shown that the effect of the sintering level on the texture was only minor at temperatures that exceeded 1000 °C.^[16] With regards to the surface morphology, there is, however, a bigger influence because the grains will start growing quicker at higher temperatures. For sintering levels of 1010, 1050 and 1090 °C, the RMS roughness values are 3.2, 2.6 and 5.0 nm, respectively. It is remarkable to see that this severe change in surface morphology above 1050 °C is not reflected in the texture of the thin film, as it did for the calcination step. This can be explained by the fact that the nucleation temperature for the crystallization is already reached during the calcination. The temperatures during sintering are therefore less crucial for texture and mainly effect the growth of the grains themselves. Similar observations about the surface morphology were carried out for the sintering dwell times at 1050 °C. Increasing the synthesis time at this temperature again results in a deteriorating surface morphology. In addition to this, the texture deteriorated as well, with an increase in [111]-to-[002] ratios from 1 to 90 up to 1 to 30.

If we overlook the sintering step, we can conclude that the characteristics of the layer are deteriorated whenever the total sintering step (i.e., the time where the temperature was situated above 900 °C) lasted too long. A good compromise for the sintering process can be found for a temperature ramp, level and dwell time of 10 °C min⁻¹, 1050 °C and 30 min, respectively.

The in-plane texture was analyzed by pole figure ϕ scans of the [002] reflection of NiW–La₂Zr₂O₇ and NiW–La₂Zr₂O₇–CeO₂ (Figure 12). The analyzed NiW–La₂Zr₂O₇–CeO₂ sample was synthesized by the proposed synthesis process for drying, calcinations and sintering. The comparison between FWHM values for both the analyzed CeO₂ sample and the as-provided NiW–La₂Zr₂O₇ substrate indicated that good in-plane texture had been achieved.

We can see that there is a difference in FWHM between rolling direction and transverse direction. In the rolling direction of the NiW substrate, we observe a FWHM between 5.5 and 6° for CeO₂, whereas it increases to more than 7.5° for the transverse direction. A similar behaviour can be observed for the as-provided NiW–La₂Zr₂O₇ tape, which indi-

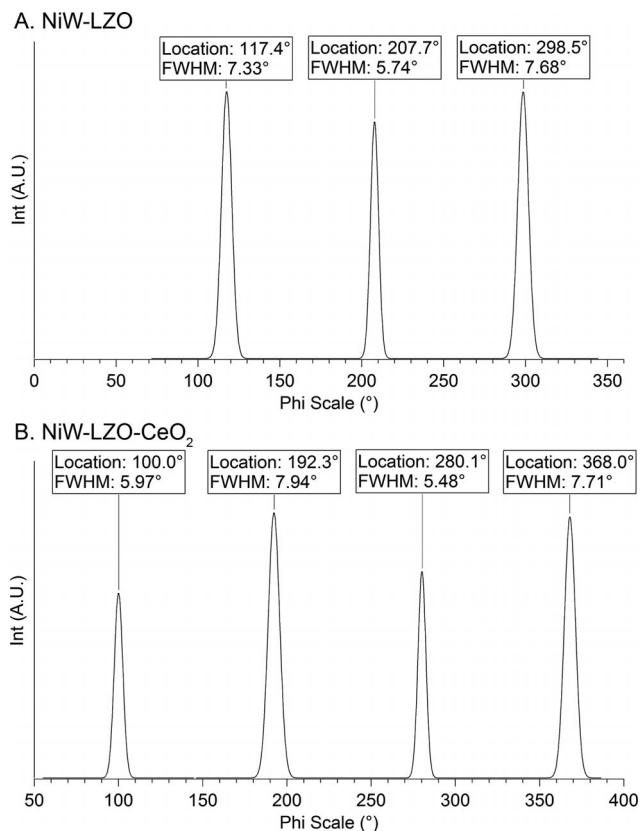


Figure 12. Pole figure ϕ scans indicating good in-plane alignment for (A) NiW–La₂Zr₂O₇ and (B) NiW–La₂Zr₂O₇–CeO₂.

icates that in-plane alignment is not deteriorating throughout the buffer stack.

In Table 1, an overview of the optimized synthesis parameters for the IDA system is given.

Table 1. Summary of the process variables and their effect on surface roughness and texture of the CeO₂ coating (+: positive influence; -: negative influence; 0: negligible influence).

Synthesis process parameter	Effect on surface morphology	Effect on texture
Calcination ramp: 2 °Cmin ⁻¹	+	+
Calcination ramp: 5 °Cmin ⁻¹	–	–
Calcination ramp: 10 °Cmin ⁻¹	–	–
Calcination level: 600 °C	–	0
Calcination level: 900 °C	+	0
Calcination dwell time: 0 min	+	0
Calcination dwell time: 60 min	+	0
Calcination dwell time: 120 min	–	0
Sintering ramp: 3 °Cmin ⁻¹	–	–
Sintering ramp: 10 °Cmin ⁻¹	+	+
Sintering ramp: 14 °Cmin ⁻¹	+	+
Sintering level: 1010 °C	+	0
Sintering level: 1050 °C	+	0
Sintering level: 1090 °C	–	0
Sintering dwell time: 0 min	+	0
Sintering dwell time: 60 min	+	0
Sintering dwell time: 180 min	–	–

As surface roughness is a direct effect of the tendency towards a minimal total surface energy, it is interesting to note in Table 1 that morphology and texture are never influ-

enced in opposite directions for a certain parameter. This seems quite logical because different orientations exhibit a different surface energy. These local variations, which are caused by a deteriorating texture, will result in displacements at the surface and in the formation of a higher surface roughness.^[27]

The optimization of the complete synthesis process results in the following proposed thermal process: an IR-assisted drying stage at 210 °C, a calcination ramp of 2 °Cmin⁻¹, a calcination level of 900 °C, a calcination dwell time of 60 min, a sintering ramp of 10 °Cmin⁻¹, a sintering level of 1050 °C and a sintering dwell time of 30 min. The applied Ar/(5%) H₂ flow was kept constant at 80 mLmin⁻¹, which resulted in an appropriate oxygen partial pressure in our tube furnace setup.

By applying this optimized synthesis process to the citrate gel system, we only achieved a surface roughness of 5.5 nm RMS. The difference with the IDA system, for which we reached RMS roughness values under 3 nm, are attributed to the slight differences in decomposition behaviour during the calcination step and to the softer nature of the gel phase. As the difference in surface roughness between the citrate gel system and the iminodiacetate gel system is related to the different precursor chemistry, this means that the surface roughness varies mainly during the calcination step. Therefore we expect to see an analogy between calcination effects on surface roughness and on texture. Electron backscatter diffraction (EBSD) comparisons (Table 2) between 50 nm-thick CeO₂ coatings synthesized starting from both systems confirm this relationship.

Table 2. Comparison of surface roughness and texture for CeO₂ coatings synthesized by the citrate gel and the iminodiacetate (IDA) gel route.

Synthesis route	Citrate gel system	IDA system
Surface roughness (nm RMS)	5.5	2.6
% indexed	70.7	93.8
<5° misorientation [%]	82	76
<10° misorientation [%]	99	99.9

Two striking differences can be noticed: the number of untextured or immeasurable spots in the grains is far bigger for the citrate-gel-based system, thereby resulting in a lower percentage of indexed points. This can be caused by the influence of the higher surface roughness of the citric acid-based CeO₂ on the measurement. On the other hand, the degree of out-of-plane misorientation (< 5°) is slightly better for the textured points of the citric acid-based system. Both systems result in a minimal fraction of grains that are misoriented by more than 10°.

Applications of these buffer layers in superconductivity require either the citrate gel system to improve its surface morphology or the IDA-based system to improve the degree of misorientation. This degree of misorientation is largely dependent on the lattice mismatch with the substrate ($a = 5.411$ Å for CeO₂ and $a = 10.804$ Å for La₂Zr₂O₇). This mismatch can be influenced by use of metal substitution.^[27,28] CSD methods allow for easy control of this metal

substitution on an atomic scale. A further optimization of the surface morphology, on the other hand, will prove to be significantly harder, as the thermal synthesis process has already been fine-tuned. Focussing on the IDA system will therefore result in the preferred synthesis route for aqueous CeO_2 buffer layers.

Trifluoroacetate (TFA)-YBCO was deposited on top of $\text{NiW-La}_2\text{Zr}_2\text{O}_7\text{-CeO}_2$.^[29] Cross sections of the coated conductor were made by using a focussed ion beam (FIB). Study of the formation of artefacts, such as BaCeO_3 formation, was performed and linked to the morphological and structural properties of the samples, as discussed before. According to Goswami et al., BaCeO_3 is formed after the YBCO synthesis on top of CeO_2 and should have no detrimental effect on the epitaxial growth of the YBCO.^[22] Nevertheless, the formation of BaCeO_3 will result in an excess amount of yttrium and copper and into the formation of Y and Cu oxide phases. These sites are likely to cause internal stresses in the superconducting material, which is expected to result in a decrease in superconductivity. These internal stresses (e.g., caused by growing interstitial phases or lattice mismatch between subsequent layers) need to be counter-balanced once they get too high for the system to withstand. As a result, interfacial defects such as lattice distortions, lattice plane tilting, dislocations, stacking faults or grain boundary effects must occur during the film growth processes to relax these induced stresses.^[30] As perfect *c*-axis alignment is essential for the superconducting behaviour of the YBCO material, unwanted phase growth and its correlating induced stresses need to be minimized.

In Figure 13, the cross section and surface for a coated conductor, which consist of a NiW metal substrate, a $\text{La}_2\text{Zr}_2\text{O}_7$ and CeO_2 buffer-layer architecture and a YBCO superconducting layer, is shown. For Figure 13 (A–C),

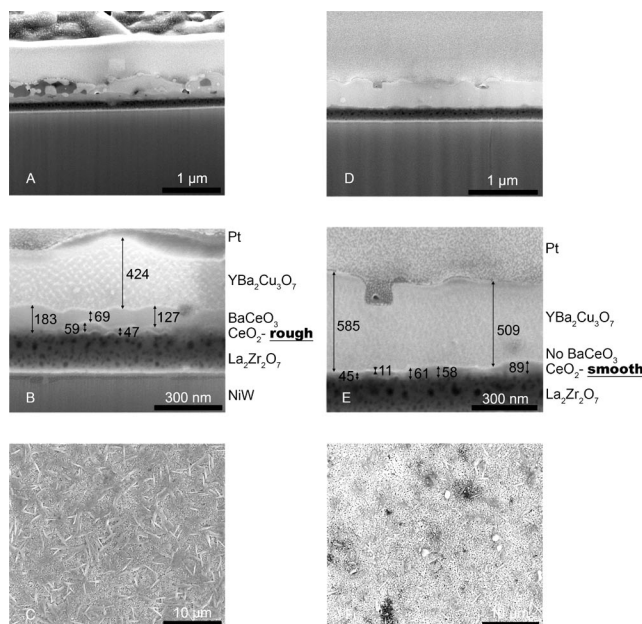


Figure 13. FIB analysis of a $\text{NiW-La}_2\text{Zr}_2\text{O}_7\text{-CeO}_2\text{-YBCO}$ -coated conductor.

CeO_2 has a higher surface roughness (6 nm RMS) than for Figure 13 (see parts D–F; 3 nm RMS). Synthesizing YBCO on the rougher buffer layer results in the formation of a 150 nm-thick BaCeO_3 layer, which can clearly be seen in part B of Figure 13. A considerable part of the deposited CeO_2 was consumed during this formation. Depositing YBCO on the smooth buffer layer does not show any detectable BaCeO_3 formation, whereas the CeO_2 thickness after YBCO deposition fluctuates around the expected 50–60 nm (Figure 13, E). In Figure 13A and D, we see the effects of this BaCeO_3 formation on a larger scale. The YBCO seems very homogeneous and dense when it was deposited on smooth CeO_2 . As long as there is no BaCeO_3 formation observed, there is hardly any sign of unwanted intermediate phases.

YBCO deposition on top of rough CeO_2 results in voids, secondary phases and *a* axis YBCO growth. The YBCO top surface in Figure 13 (C and F) demonstrates a clear difference in quality as well.

Conclusion

CeO_2 thin films were prepared by starting from an iminodiacetic acid-based aqueous sol by dip coating. Texture and morphology were examined as a function of the synthesis process parameters. A long calcination step followed by relatively fast sintering resulted in optimal characteristics for 50 nm-thick pure CeO_2 coatings. Surface roughness values of lower than 3 nm RMS were established, whereas good RHEED and EBSD patterns show the positive influence of the processing conditions employed on the texture. The importance of a smooth buffer-layer surface on the quality of a coated conductor and the $\text{YBa}_2\text{Cu}_3\text{O}_7$ superconducting layer was demonstrated by cross sections and FIB analysis. The formation of BaCeO_3 was directly related to the roughness of the CeO_2 buffer layer and secondary phases and voids were formed in between the YBCO layer as a consequence.

Experimental Section

General: The citrate gel route was covered in detail in previously published work.^[14,16,31] $\text{Ce}(\text{NO}_3)_3$ (Sigma–Aldrich, Ce^{III} nitrate hexahydrate) was used in a 0.45 M concentration in a 1:3 ratio with citric acid (Carl Roth, citric acid monohydrate, >99.5%). The pH was set at 6.1 using ammonia (Carl Roth, ammonia, 25%). The final viscosity of the sols was 3 cP.

Sols prepared for the iminodiacetic acid gel route were made as follows: Iminodiacetic acid (IDA) (1 M, Alfa Aesar, iminodiacetic acid 98+%) was dissolved in deionized water at pH 8. $\text{Ce}(\text{NO}_3)_3$ was added in a 1-to-5 metal-to-ligand ratio, whereas the pH was controlled at pH 8.5 by adding ammonia. The precursor sol was finally concentrated by thermal evaporation at 70 °C up to a concentration of approximately 0.35 M and a final viscosity of 2 cP.

Gels were prepared by subjecting the stock precursor sol (7 mL) for several hours at 60 °C to initiate the condensation reactions towards a gel structure. A set of tests was conducted with different pH values and metal-to-ligand ratios to obtain homogeneous and

stable gels, which are prone to result in buffer layers of optimal quality.

A commonly chosen metal substrate for coated conductors is the biaxially textured NiW (Ni 5%) tape, fabricated by the rolling assisted biaxially textured substrates (RABiTS) process as explained elsewhere.^[32] As the CeO₂ coating is not sufficient to avoid Ni_xO_y diffusion during the YBCO process by itself, an extra buffer layer (i.e., La₂Zr₂O₇) was required in the total structure. Therefore all experiments were conducted on NiW tape (EVICO) buffered with a 250 nm-thick CSD La₂Zr₂O₇ coating provided by Zenergy Power GmbH. Cleaning of the tapes was performed by subjecting the tape to 400 °C for 30 s. An optional cleaning step involved wiping the tape with a fibre-free cloth drenched in a mild solvent (e.g., 2-propanol).

Thin film depositions were performed by dip coating by means of a computer-controlled dip-coating unit (KSV Instruments) in a clean room facility. Prior to the thermal treatment, the sol–gel transition proceeded in a conventional dry furnace at 60 °C over 1 h or by infrared radiation (Heraeus carbon infrared emitter, 2 µm) at temperatures up to 210 °C. The high temperature synthesis was performed in a quartz tube furnace with controlled Ar/(5%) H₂ atmosphere (Carbolite Furnaces; length: 1 m; inner tube diameter: 6 cm). The Ar/(5%) H₂ was kept at a flow of 80 mL min⁻¹ for all experiments. All CeO₂ coatings were approximately 50 nm thick, as measured by spectroscopic ellipsometry and confirmed by FIB cross sections.

Characterization of the texture and phase composition was performed by means of X-ray diffraction (Thermo Scientific ARL X'TRA, Cu anode, $K_{\alpha 1}$: 1.5406 Å), EBSD measurements (JEOL JSM 6400F, EBSD Camera HKL Nordlys) and RHEED analysis (Staib Instruments RHEED system). A 30 keV electron beam was used under an incident angle of about 1 to 2° parallel to the transverse direction of the metal tape. This corresponds to the [110] orientations of CeO₂.

Structural characterization was carried out with a FESEM microscope (FEI Quanta 200F), whereas spectroscopic ellipsometry (JA Woollam Alpha-SE) allowed us to determine the thickness of the thin films. Film cross sections were performed and analyzed with an FEI Nova 600 Nanolab Dual-beam FIB. Thermal analysis (Netzsch STA 449 F3 Jupiter) of the starting products was performed to determine the exact water content and purity of the precursors as well as to follow the decomposition process from precursor sol to solid oxide material. When studying the decomposition process, all samples were dried at 200 °C prior to the analysis. This results in more detailed measurements and better reproducibility due to limited foaming of the precursor materials.

Roughness analysis of the thin films was carried out by atomic force microscopy (Molecular Imaging PicoPlus) operating in tapping mode with Budgetsensors Tap 300 tips and WSxM software analysis.^[33]

Acknowledgments

We would like to thank IFW Dresden, Ruben Hühne (Institute for Metallic Materials) for RHEED analysis of the CeO₂ buffer layers and Ghent University, COMOC (P. Van Der Voort) for X-ray diffraction. Zenergy Power GmbH is thanked for funding and scientific support and the Agency for Innovation by Science and Technology (IWT) for funding one of the authors (G. P.) by a Ph.D. grant. This work was also funded by the European Union under the project EFFECTS (FP7-NMP-2007-SMALL-1, grant number

205854) and by the Belgian State Federal Science Policy Office under the Interuniversity Attraction Poles Programme (INANO-MAT), grant number IAP/VI-17.

- [1] B. Schoofs, V. Cloet, P. Vermeir, J. Schaubroeck, S. Hoste, I. Van Driessche, *Supercond. Sci. Technol.* **2006**, *19*, 1178–1184.
- [2] I. Van Driessche, S. Cattoir, S. Hoste, *Appl. Supercond.* **1994**, *2*, 101–110.
- [3] I. Van Driessche, G. Penneman, E. Bruneel, S. Hoste, *Pure Appl. Chem.* **2002**, *74*, 2101–2109.
- [4] K. Develos-Bagarinao, H. Yamasaki, Y. Nakagawa, *Supercond. Sci. Technol.* **2006**, *19*, 873–882.
- [5] O. Stadel, J. Schmidt, M. Liekefett, G. Wahl, O. Y. Gorbenco, A. R. Kaul, *IEEE Trans. Appl. Supercond.* **2003**, *13*, 2528–2531.
- [6] X. Obradors, T. Puig, A. Pomar, F. Sandiumenge, N. Mestres, M. Coll, A. Cavallaro, N. Roma, J. Gazquez, J. C. Gonzalez, O. Castano, J. Gutierrez, A. Palau, K. Zalamova, S. Morlens, A. Hassini, M. Gibert, S. Ricart, J. M. Moreto, S. Pinol, D. Isfort, J. Bock, *Supercond. Sci. Technol.* **2006**, *19*, S13–S26.
- [7] M. S. Bhuiyan, M. Paranthaman, K. Salama, *Supercond. Sci. Technol.* **2006**, *19*, R1–R21.
- [8] Y. Xu, A. Goyal, K. Leonard, P. Martin, *Phys. C* **2005**, *421*, 67–72.
- [9] S. Donglu, Y. Zhang, Y. Xin, L. Jie, W. Lumin, L. Aihua, H. K. Liu, Y. Haibo, H. Zhenghe, L. Laifeng, X. Yongli, *Phys. C* **2006**, *436*, 62–67.
- [10] L. Lei, G. Zhao, J. Zhao, H. Xu, *IEEE Trans. Appl. Supercond.* **2010**, *20*, 2286–2293.
- [11] T. Manabe, M. Sohma, I. Yamaguchi, W. Kondo, K. Tsukada, S. Mizuta, T. Kumagai, *Phys. C* **2004**, *412*, 896–899.
- [12] Y. R. Patta, D. E. Wesolowski, M. J. Cima, *Phys. C* **2009**, *469*, 129–134.
- [13] D. E. Wesolowski, Y. R. Patta, M. J. Cima, *Phys. C* **2009**, *469*, 766–773.
- [14] G. Penneman, I. Van Driessche, E. Bruneel, S. Hoste, *Key Eng. Mater.* **2004**, *264–268*, 501–504.
- [15] T. T. Thuy, P. Lommens, V. Narayanan, N. Van de Velde, K. De Busscher, G. G. Herman, V. Cloet, I. Van Driessche, *J. Solid State Chem.* **2010**, *183*, 2154–2160.
- [16] N. Van de Velde, D. Van de Vyver, O. Brunkahl, S. Hoste, E. Bruneel, I. Van Driessche, *Eur. J. Inorg. Chem.* **2010**, *2*, 233–241.
- [17] P. Vermeir, I. Cardinael, M. Baecker, J. Schaubroeck, E. Schacht, S. Hoste, I. Van Driessche, *Supercond. Sci. Technol.* **2009**, *22*, article ID 075009.
- [18] I. Van Driessche, G. Penneman, C. De Meyer, I. Stambolova, E. Bruneel, S. Hoste, *Key Eng. Mater.* **2002**, *206*, 479–482.
- [19] S. Engel, K. Knoth, R. Huhne, L. Schultz, B. Holzapfel, *Supercond. Sci. Technol.* **2005**, *18*, 1385–1390.
- [20] L. Molina, H. Tan, E. Biermans, K. J. Batenburg, J. Verbeeck, S. Bals, G. Van Tendeloo, *Supercond. Sci. Technol.* **2011**, *24*, article ID 065019.
- [21] K. C. Chung, Y. K. Kim, X. L. Wang, S. X. Dou, *Kor. J. Met. Mater.* **2009**, *47*, 681–685.
- [22] R. Goswami, R. L. Holtz, G. Spanos, *IEEE Trans. Appl. Supercond.* **2007**, *17*, 3294–3297.
- [23] K. D. Develos, H. Yamasaki, A. Sawa, Y. Nakagawa, *Phys. C* **2001**, *361*, 121–129.
- [24] A. E. Martell, R. M. Smith, *Critical Stability Constants.*, vol. 1–6, **1977**, Plenum Press.
- [25] G. Chen, S. Sun, X. Song, Z. Yin, H. Yu, C. Fan, W. Zhao, *J. Mater. Sci.* **2007**, *42*, 6977–6981.
- [26] W. D. Callister, *Materials Science and Engineering: An Introduction*, Wiley, New York, **1999**.
- [27] M. Coll, J. Gazquez, F. Sandiumenge, T. Puig, X. Obradors, J. P. Espinos, R. Huhne, *Nanotechnology* **2008**, *19*, article ID 395601.

- [28] E. Gilioli, M. Baldini, M. Bindi, F. Bissi, F. Pattini, S. Rampino, S. Ginocchio, A. Gauzzi, M. Rocca, S. Zannella, *Phys. C* **2007**, *463*, 609–614.
- [29] M. Falter, W. Hassler, B. Schlobach, B. Holzapfel, *Phys. C* **2002**, *372*, 46–49.
- [30] C. H. Hsueh, M. Paranthaman, *J. Mater. Sci.* **2008**, *43*, 6223–6232.
- [31] I. Van Driessche, G. Penneman, J. S. Abell, E. Bruneel, S. Hoste, *Mater. Sci. Forum* **2003**, *426-4*, 3517–3522.
- [32] T. G. Truchan, F. H. Rountree, M. T. Lanagan, S. M. McClellan, D. J. Miller, K. C. Goretta, M. Tomsic, R. Foley, *IEEE Trans. Appl. Supercond.* **2000**, *10*, 1130–1133.
- [33] I. Horcas, R. Fernandez, J. M. Gomez-Rodriguez, J. Colchero, J. Gomez-Herrero, A. M. Baro, *Rev. Sci. Instrum.* **2007**, *78*, article ID 013705.

Received: September 7, 2011

Published Online: February 3, 2012

“Caging” Anions through Crystal Engineering to Avoid Polymerization: Structural, Conformational and Theoretical Investigations of New Halocadmate $[\text{Cd}_2\text{X}_7]^{3-}$ Anions (X = Cl/Br)

Raj P. Sharma,^{*,[a]} Ajnesh Singh,^[a] Paloth Venugopalan,^[a] Guo Yanan,^[b] Jihong Yu,^[b] Celestino Angeli,^[c] and Valeria Ferretti^{*,[c,d]}

Keywords: Crystal engineering / Anions / Cadmium complexes / Density functional calculations / Conformation analysis

Two new discrete anionic species, $[\text{Cd}_2\text{Cl}_7]^{3-}$ and $[\text{Cd}_2\text{Br}_7]^{3-}$, have been isolated in the form of cobalt(III) complex salts, $[\text{Co}(\text{phen})_3][\text{Cd}_2\text{Cl}_7] \cdot 3\text{H}_2\text{O}$ (**1**) and $[\text{Co}(\text{phen})_3][\text{Cd}_2\text{Br}_7] \cdot 2\text{H}_2\text{O}$ (**2**). The complex salts have been characterized by spectroscopic techniques and other investigations like TGA, solubility product measurements, conductance measurements, luminiscent study, DFT calculations and single crystal structure determinations. The new discrete $[\text{Cd}_2\text{X}_7]^{3-}$ anions

reside in cavities that are formed by complex cations and are stabilized by different noncovalent interactions (hydrogen bonding, π - π stacking, C-H $\cdots\pi$ and anion $\cdots\pi$). With the help of DFT calculations, an in depth investigation has been conducted into what happens to the conformation of these anions in crystal, solution and gas phase, and the nature of the Cd-halogen bond has been elucidated.

Introduction

Halocadmates(II) have been receiving considerable attention due to their structural diversity, polymorphic behaviour, electronic configuration and lattice location, which are key issues in semiconductor physics, supramolecular and bioinorganic studies.^[1] Cadmium(II) halides are known with cadmium to halide ratios from 1:3 to 1:6 and they crystallize in a wide variety of polymeric anionic structures, $[\text{Cd}_n\text{X}_m]^{(2n-m)-}$. Halocadmates of the type $[\text{Cd}_2\text{X}_7]^{3-}$ are rarely reported in the literature and, in all such reports, the $[\text{Cd}_2\text{X}_7]^{3-}$ units are never discrete but consist of polymeric $[\text{CdX}_3]_n^{n-}$ and $[\text{CdX}_4]^{2-}$ anions. In general, they have the propensity to form polymeric structures in the solid state. In this context, it becomes significant to probe the viability of isolating these anions as a discrete entities and the conducive stereoelectronic conditions for such an isolation. If the cations are endowed with proper functional groups that can effectively interact with one another to generate a “cage” and if the molecular topologies of the anions are such that a proper fitting is achieved, it may be possible to

trap them in these cages. In such a situation, the isolation of anions as “discrete entities” can be viable even though they have a strong propensity to polymerize. In a nutshell, the anions get trapped into pockets that are generated by cations, which thereby block the chance of polymerization.

Recently, the role of topology and the hydrogen bonding capabilities of a large counterion, $[\text{Co}(\text{NH}_3)_6]^{3+}$, have been shown in the isolation of new anionic species such as $[\text{Hg}_2(\text{SCN})_7]^{3-}$ and $[\text{HgBr}_5]^{3-}$ by our group^[2] and the isolation of $[\text{Cu}_4(\text{OH})(\text{CO}_3)_8]^{9-}$ by Robson and coworkers.^[3] These studies indicate that the compatibility in size and topology of counteranions is important in the lattice stabilization along with complementarity in the second sphere interactions. Tying up these concepts, we hypothesized that, in all probability, the $[\text{Cd}_2\text{X}_7]^{3-}$ anion would resemble a “boomerang” in spatial topology (similar to a dichromate anion), which has an overall wedge shape, and that the tips of the boomerang would be “sticky” as three halogen atoms that are present there can act as effective hydrogen-bond acceptors. The next step is to find a counterion in which the wedge-shaped species can fit well with a lattice stabilizing effect. In addition, the counterion should “cage” these $[\text{Cd}_2\text{X}_7]^{3-}$ anions from one another so that their polymerization tendency is fully curbed. The $[\text{Co}(\text{phen})_3]^{3+}$ cation became a judicious choice as it has three grooved faces (for shape complementarity), it is large in size (size complementarity) and it has a three unit positive charge (for coulombic attraction). In addition, the periphery of the ion is endowed with a large number of C-H groups (24) that can have multiple C-H $\cdots\text{X}$ hydrogen bonds within the cage, which would be lattice stabilizing. The above mentioned considerations

[a] Department of Chemistry, Panjab University, Chandigarh 160014, India
E-mail: rpsharmapu@yahoo.co.in

[b] State Key Lab of Inorganic Synthesis and Preparative Chemistry, College of Chemistry, Jilin University, Changchun 130012, PR China

[c] Dipartimento di Chimica, University of Ferrara, Via L. Borsari 46, 44121, Ferrara, Italy

[d] Centro di Strutturistica Diffraattometrica, University of Ferrara, Via L. Borsari 46, 44121 Ferrara, Italy
E-mail: frt@unife.it

Supporting information for this article is available on the WWW under <http://dx.doi.org/10.1002/ejic.201101144>.

should favour the isolation of new anionic species and thus this paper reports the successful syntheses and characterization of the complexes $[\text{Co}(\text{phen})_3][\text{Cd}_2\text{Cl}_7]\cdot 3\text{H}_2\text{O}$ (**1**) and $[\text{Co}(\text{phen})_3][\text{Cd}_2\text{Br}_7]\cdot 2\text{H}_2\text{O}$ (**2**) that contain two new discrete anions $[\text{Cd}_2\text{X}_7]^{3-}$, where $\text{X} = \text{Cl}/\text{Br}$. In the solid state, as evidenced by X-ray diffraction studies and quantum mechanical calculations, the new “boomerang-shaped” $[\text{Cd}_2\text{Cl}_7]^{3-}$ and $[\text{Cd}_2\text{Br}_7]^{3-}$ anions are flexible objects that exhibit conformations that do not correspond to an intramolecular energy minimum, a phenomenon that is observed from time to time and that is usually attributed to crystal-packing effects. Diphenyl may be the best known case, which is reported to be nonplanar in the gas phase, in solution and in the molten state,^[4] but assumes a planar conformation in the crystalline state. With the help of DFT calculations, an in depth investigation of what happens in crystal, solution and gas phase for these new anions is presented in this paper.

Results and Discussion

Synthesis and Characterization

Both $[\text{Co}(\text{phen})_3][\text{Cd}_2\text{Cl}_7]\cdot 3\text{H}_2\text{O}$ (**1**) and $[\text{Co}(\text{phen})_3][\text{Cd}_2\text{Br}_7]\cdot 2\text{H}_2\text{O}$ (**2**) have been prepared from an aqueous solution of $[\text{Co}(\text{phen})_3]\text{Cl}_3$, CdCl_2 and KCl/KBr in the molar ratio 1:1:2/4 (Experimental Section). They have been fully characterized by spectroscopic techniques, TGA, solubility product measurements, conductance measurements, luminescent studies, DFT calculations and single crystal structure determination.

Solubility of ionic salts in water differs to a great extent and, on the basis of the solubility criterion, the salts are classified into three categories: soluble, sparingly soluble and insoluble. The solubility products were measured as 4.5×10^{-7} and 9.4×10^{-11} for **1** and **2**, respectively, compared to that of 2.7×10^{-3} for $[\text{Co}(\text{phen})_3]\text{Cl}_3$, which indicated that the affinity of the cationic complex $[\text{Co}(\text{phen})_3]^{3+}$ is greater for the $[\text{Cd}_2\text{X}_7]^{3-}$ anions than for the chloride ion. The nearly 10^4 and 10^8 decrease in the solubility product for **1** and **2** points towards this affinity, which may be the driving force behind the formation of these complexes, hydration also influences the solubility product, especially in the case of different sized ions.

The ^1H and ^{13}C NMR spectroscopic chemical shift values are in good agreement with literature values.^[5] The FTIR spectra of the complex salts showed the characteristic bands for coordinated ligands to the metal ion and the presence of lattice water molecules.^[6] The IR bands in the 3583 to 3419, 3053 to 3055, 1650 to 1400 and 843 to 846 cm^{-1} regions were assigned to $\nu(\text{O}-\text{H})$, $\nu(\text{C}-\text{H})$, $\nu(\text{C}=\text{C}/\text{C}=\text{N})$, and $\delta(\text{C}-\text{H})$ vibrations, respectively. The shift in the IR band of the $\nu(\text{O}-\text{H})$ vibrations from the expected value of around 3600 cm^{-1} to 3550 to 3400 cm^{-1} was indicative of intermolecular hydrogen bonding in the complex salts. The UV/Vis spectra of **1** and **2** in H_2O were mainly dominated by the presence of bands around 460 and 342 nm, which were assigned to d-d transitions typical for low spin Co^{III} octahedral complexes. Peaks in the UV region were also

observed around 280 and 220 nm, which were assigned to $\pi-\pi$ transitions of aromatic moieties (1,10-phenanthroline) coordinated to the cobalt(III) centre.

The luminescent properties of complex salts **1** and **2** were investigated in the solid state at room temperature (25 °C) (Figure S1, Supporting Information). The emission spectra of complex salts **1** and **2** both exhibit a strong peak at 455 nm when excited at a wavelength of 352 nm, which is due to a Co^{III} polypyridyl emission from a LMCT excited state.

Conductance measurements for **1** and **2** were carried out at 25 °C in an aqueous medium and a graph was plotted between Λ (molar conductance) and $C^{1/2}$ (square root of concentration). When the concentration was extrapolated to zero, it gave the Λ_0 value of 596 and 553 $\text{Scm}^2\text{mol}^{-1}$ for **1** and **2**, respectively, which are closer to those observed for similar complexes that have a 3+/3- charge, for example, 561 $\text{Scm}^2\text{mol}^{-1}$ for $[\text{Co}(\text{NH}_3)_6][\text{HgBr}_5]$ and 531 $\text{Scm}^2\text{mol}^{-1}$ for $[\text{Co}(\text{NH}_3)_6][\text{HgBr}_4\text{Cl}]$.^[7] Although **1** and **2** consist of only two ions, that is, 1:1 electrolytes, and should have a Λ_0 value^[8] between 135 and 150 $\text{Scm}^2\text{mol}^{-1}$, high Λ_0 values were obtained at infinite dilution. This can be explained on the basis of three unit positive/negative charges on the respective ions. The contribution of each ion towards the molar conductance at infinite dilution is $1/3[\text{Co}(\text{phen})_3]^{3+} = 56.26 \text{ Scm}^2\text{mol}^{-1}$, $1/3[\text{Cd}_2\text{Cl}_7]^{3-} = 142.4 \text{ Scm}^2\text{mol}^{-1}$ and $1/3[\text{Cd}_2\text{Br}_7]^{3-} = 128.1 \text{ Scm}^2\text{mol}^{-1}$. These values were calculated according to the Kohlrausch's law (using Λ_0 of $[\text{Co}(\text{phen})_3]\text{Cl}_3 = 398 \text{ Scm}^2\text{mol}^{-1}$ and Λ_0 of $\text{Cl}^- = 76.4 \text{ Scm}^2\text{mol}^{-1}$) and were taken as 1/3 because of the three unit positive/negative charge, which gave a Λ_0 value of 184 and 198 $\text{Scm}^2\text{mol}^{-1}$ for **1** and **2**, respectively, which are closer to the range of 1:1 electrolytes.^[9]

The thermal stability of complexes **1** and **2** or the robustness of the crystal lattices was examined through TGA (Figure S2, Supporting Information) and the results indicated that the first weight loss of 4.97 and 2.74% occurs from 70 to 200 °C, which is due to the loss of lattice water molecules and is consistent with the calculated value of 4.79 and 2.54% for **1** and **2**, respectively. The loss of lattice water molecules from 70 °C indicated that they are not involved in significant interactions. After the loss of lattice water molecules, both of the complexes are stable up to 400 °C. Further heating to 1000 °C led to decomposition of **1** and **2** and the final inorganic residue was obtained. The final pyrolysis product was Co_2O_3 contaminated with the unknown phase that contained cobalt and cadmium at an unidentified stoichiometry.

The electrochemical behaviours of the complexes were studied in aqueous medium by CV method. The electrochemical properties of $[\text{Co}(\text{phen})_3]^{3+}$ systems have been studied in the past^[10] and the cyclic voltammogram of the complex was reported to have an E_{pc} and E_{pa} of 0.143 and 0.215 V versus Ag/AgCl , respectively. Complexes **1** and **2** showed a similar CV response at a glassy carbon electrode in a 0.1 M KCl aqueous solution with a scan rate of 100 mVs^{-1} . CV of the $[\text{Co}(\text{phen})_3]\text{Cl}_3$, **1** and **2** salts showed similar behaviours. The complex cation $[\text{Co}(\text{phen})_3]^{3+}$ undergoes a one electron reduction process from the 3+ to 2+

oxidation state with a peak potential (E_{pc}) of 0.141, 0.124 and 0.121 V versus Ag/AgCl. The cyclic voltammograms that were obtained for the complexes are shown in the Supporting Information (Figure S3). On the reverse scan, $[\text{Co}(\text{phen})_3]^{2+}$ is reoxidized at an E_{pa} of 0.220, 0.209 and 0.207 V, respectively. The peak potential separation (ΔE) was 79, 85 and 86 mV, which indicated that this is, most likely, the quasireversible one electron couple. No electroactivity was seen for the Cd^{2+} species in the potential range

studied (0.9 to -0.9 V). When I_{pa} was plotted with the square root of the scan rate, a straight line was obtained, which further indicated the reversible couple.

Description of Crystal Structures and DFT Calculations

X-ray structure determinations revealed the ionic nature of the complexes. The ORTEPIII^[11] diagrams of **1** and **2** are shown in Figures 1 and 2, respectively. The asymmetric

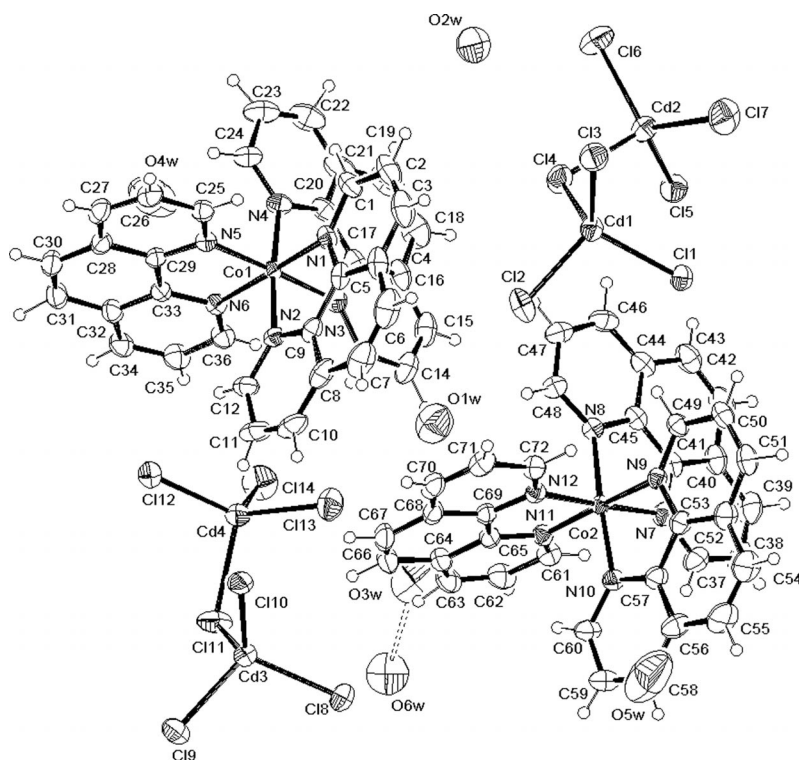


Figure 1. ORTEPIII diagram of complex salt **1**. Ellipsoids are drawn at 40% probability.

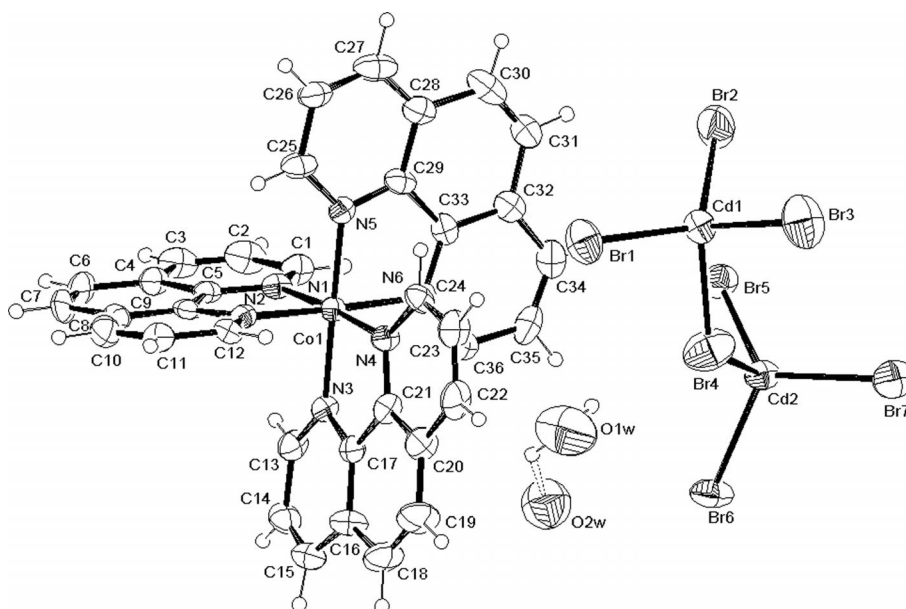


Figure 2. ORTEPIII diagram of complex salt **2**. Ellipsoids are drawn at 40% probability.

unit of **1** consists of two crystallographically independent $[\text{Co}(\text{phen})_3]^{3+}$ complex cations, two $[\text{Cd}_2\text{Cl}_7]^{3-}$ anions and six water molecules, while the complex salt **2** consists of one $[\text{Co}(\text{phen})_3]^{3+}$ cation, one $[\text{Cd}_2\text{Br}_7]^{3-}$ anion and two cocrystallized water molecules. The $[\text{Cd}_2\text{X}_7]^{3-}$ anions, found in both of the structures, represent the first structurally characterized examples of isolated heptahalocadmiate(II) anions in metallorganic chemistry. In both cases the cobalt atom is coordinated to three chelating, bidentate 1,10-phenanthroline ligands, which results in a slightly distorted octahedral geometry around the Co^{III} centre, the maximum deviation of *cis* N–Co–N angle is 6.0° and 5.5° for **1** and **2**, respectively, from the ideal value of 90° . The Co–N bond lengths and N–Co–N bond angles (Table 1) are comparable with those reported for similar complex salts,^[12] irrespective of the nature of the anionic species. In discrete $[\text{Cd}_2\text{Cl}_7]^{3-}$ and $[\text{Cd}_2\text{Br}_7]^{3-}$ anions, one halide atom from each of the tetrahedrally coordinated Cd^{II} atoms is shared, which results in the formation of two tetrahedra that are joined through a common corner. The two crystallographically independent anions in complex **1** have slightly different structural parameters, as shown in Table 1. The $\text{Cd}\cdots\text{Cd}$ distances and $\text{Cd}-\text{Cl}_b-\text{Cd}$ bond angles (subscript b denotes bridge) are $4.2225(4) \text{ \AA}$, $111.58(4)^\circ$ and $3.9983(5) \text{ \AA}$, $103.92(4)^\circ$ in the two molecules, respectively.

In complex salt **2**, the $\text{Cd}\cdots\text{Cd}$ distance and $\text{Cd}-\text{Br}_b-\text{Cd}$ bond angle measure $4.668(1) \text{ \AA}$ and $126.59(9)^\circ$, respectively; the slight increase in $\text{Cd}\cdots\text{Cd}$ contact as compared to that of compound **1** is attributed to the large size of the Br atom attached to cadmium. A comparison of structural parameters of complexes that contain different cadmium(II) halides is reported in Table 2. It is observed that as the number of halides increases or as the geometry changes (tetrahedral to octahedral) there is a corresponding increase in $\text{Cd}-\text{X}$ bond lengths. It is also noteworthy that in halocadmiate anions and in polymeric structures the $\text{Cd}-\text{X}-\text{Cd}$ angle ($\text{X} = \text{Cl}$ or Br) can be as small as $86(2)^\circ$ (last column of Table 2). Moreover, Table 2 data reveals that halocadmiate fragments are present in polymeric structures. The tendency to form a polymeric structure is present in analogous complexes with Hg as the central atom, although there are few structures with isolated $\text{Hg}_2\text{X}_7^{3-}$ ($\text{X} = \text{halogen}$, six structures).^[13] Besides these compounds, only two other struc-

Table 1. Selected bond lengths [\AA] and angles [$^\circ$].

Complex salt 1			
Co1–N1	1.949(3)	Co2–N7	1.951(2)
Co1–N2	1.939(3)	Co2–N8	1.946(3)
Co1–N3	1.948(2)	Co2–N9	1.950(3)
Co1–N4	1.946(3)	Co2–N10	1.950(3)
Co1–N5	1.941(2)	Co2–N11	1.936(3)
Co1–N6	1.945(3)	Co2–N12	1.932(2)
Cd1–Cl1	2.443(1)	Cd3–Cl8	2.456(1)
Cd1–Cl2	2.463(1)	Cd3–Cl9	2.459(1)
Cd1–Cl4	2.549(1)	Cd3–Cl10	2.419(1)
Cd1–Cl3	2.426(1)	Cd3–Cl11	2.540(1)
Cd2–Cl4	2.557(1)	Cd4–Cl11	2.536(1)
Cd2–Cl5	2.437(1)	Cd4–Cl12	2.452(1)
Cd2–Cl6	2.451(1)	Cd4–Cl13	2.459(1)
Cd2–Cl7	2.423(1)	Cd4–Cl14	2.434(1)
N1–Co1–N2	84.2(1)	N7–Co2–N8	84.2(1)
N1–Co1–N3	90.3(1)	N7–Co2–N9	88.3(1)
N1–Co1–N4	92.4(1)	N7–Co2–N10	93.7(1)
N1–Co1–N5	93.1(1)	N7–Co2–N11	93.1(1)
N2–Co1–N3	91.3(1)	N8–Co2–N9	92.6(1)
N2–Co1–N5	89.6(1)	N8–Co2–N11	90.6(1)
N2–Co1–N6	93.7(1)	N8–Co2–N12	92.8(1)
N3–Co1–N4	84.4(1)	N9–Co2–N10	84.0(1)
N3–Co1–N6	92.2(1)	N9–Co2–N12	94.2(1)
N4–Co1–N5	94.8(1)	N10–Co2–N11	92.8(1)
N4–Co1–N6	89.8(1)	N10–Co2–N12	89.5(1)
N5–Co1–N6	84.5(1)	N11–Co2–N12	84.6(1)
Complex Salt 2			
Co1–N1	1.932(8)	Co1–N4	1.935(7)
Co1–N2	1.946(7)	Co1–N5	1.924(8)
Co1–N3	1.923(7)	Co1–N6	1.943(7)
Cd1–Br1	2.529(2)	Cd2–Br4	2.628(2)
Cd1–Br2	2.548(2)	Cd2–Br5	2.559(2)
Cd1–Br3	2.518(2)	Cd2–Br6	2.600(16)
Cd1–Br4	2.620(2)	Cd2–Br7	2.550(2)
N1–Co1–N2	85.2(3)	N2–Co1–N5	93.1(3)
N1–Co1–N3	92.1(3)	N3–Co1–N4	84.5(3)
N1–Co1–N5	89.6(3)	N3–Co1–N6	95.8(3)
N1–Co1–N6	94.6(3)	N4–Co1–N5	93.8(3)
N2–Co1–N3	86.5(3)	N4–Co1–N6	88.0(3)
N2–Co1–N4	92.4(3)	N5–Co1–N6	84.6(3)

tures, of formula $[\text{Co}_2\text{Cl}_7]^{3-}$, have been found in the Cambridge Crystallographic Database (CSD) that contain isolated halodimetallate anions.^[14]

It is pertinent to understand the packing conditions required to hinder the polymer formation. A well known em-

Table 2. A comparison of structural parameters of complex salts containing different cadmium(II) halides [\AA , $^\circ$]. In the first column, the number of the structures retrieved from the Cambridge Structural Database is reported. (t: terminal atom; b: bridging atom).

Number of structures ^[a]	Chemical formula of halocadmiate anion	Cd–X	X–Cd–X	Cd–X–Cd
44	$[\text{CdCl}_4]^{2-}$ (tetrahedron)	2.46 ^[3]	109 ^[4]	
1	$[\text{CdCl}_5]^{3-}$ (trigonal bipyramidal)	2.58 ^[9]	120 ^[4] (base), 172.19(2)	
3	$[\text{CdCl}_6]^{4-}$ (octahedron)	2.64 ^[7]	90 ^[2]	
1 (this work)	$[\text{Cd}_2\text{Cl}_7]^{3-}$	2.440(1) t, 2.553(1) b	111.93(1)	111.58(4)
3	$[\text{Cd}_2\text{Cl}_8]^{4-}$	2.54 ^[9] t, 2.66 ^[9] b		97 ^[1]
28	$[\text{Cd}_n\text{Cl}_m]$ polymeric structures			89.4 ^[2]
56	$[\text{CdBr}_4]^{2-}$ (tetrahedron)	2.58 ^[4]	108.9 ^[5]	
1	$[\text{CdBr}_6]^{4-}$ (octahedron)	2.78 ^[2]	90 ^[2]	
1 (this work)	$[\text{Cd}_2\text{Br}_7]^{3-}$	2.55 ^[3] t, 2.624 ^[6] b	112.70(1)	126.59(9)
3	$[\text{Cd}_2\text{Br}_6]^{2-}$	2.67 ^[1] b, 2.53 ^[1] t		86 ^[2]
14	$[\text{Cd}_n\text{Br}_m]$ polymeric structures			86.4 ^[4]

[a] The list of the CSD ref codes is available in the Supporting Information (see Table S1).

irical rule states that solid metal complexes are stabilized by large counterions, preferably ions of the same but opposite charge, as found in the present structures. In both of the structures, each anion is surrounded at a maximum distance of 4 Å by eight Co^{III} complexes that form a cage that prevents any close contact with the other anions and thus inhibits the formation of polymeric chains (Figures 3 and 4 for **1** and **2**, respectively). Besides the electrostatic forces of attraction, the intermolecular interactions that hold the cations and anions together in both crystal structures are of the type $\text{C}-\text{H}\cdots\text{Cl}/\text{Br}$, $\pi-\pi$ stacking, $\text{C}-\text{H}\cdots\pi$ and anion $\cdots\pi$ interactions^[15] (Figures S4 and S5, Supporting Information). In addition, the cocrystallized water molecules contribute to the packing robustness that is involved in $\text{O}-\text{H}\cdots\text{O}$ as well as $\text{C}-\text{H}\cdots\text{O}$ hydrogen bonds. The structural parameters of all of the intermolecular interactions are re-

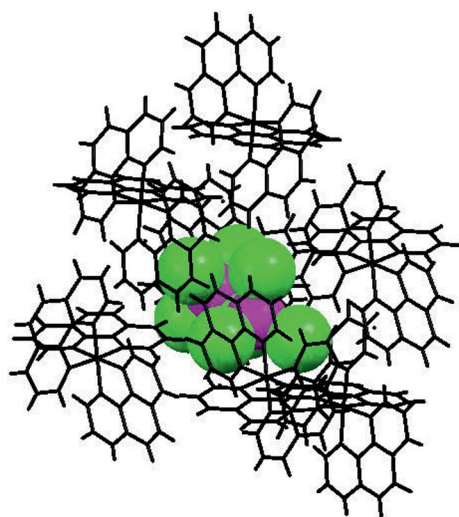


Figure 3. $[\text{Cd}_2\text{Cl}_7]^{3-}$ anion trapped in the cage-like cavity formed by complex cations.

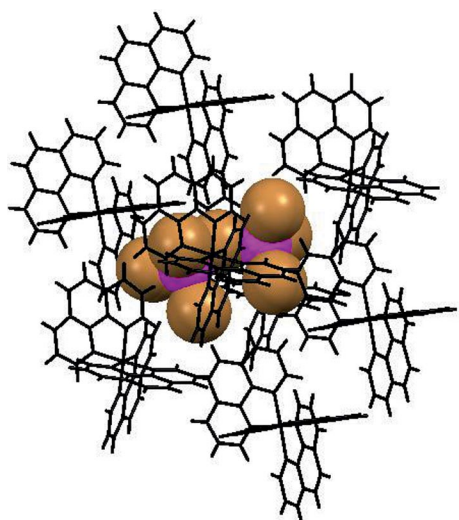


Figure 4. $[\text{Cd}_2\text{Br}_7]^{3-}$ anion trapped in the cage-like cavity formed by complex cations.

ported in Table 3. Analysis of the packing modes of the analogous Hg structures that were found in the CSD revealed that the “molecular cage” around the anions is always present, even if the size of the cationic species is not comparable to the anion; as an example, the crystal envi-

Table 3. Hydrogen bonding parameters [Å, °]. The $\text{C}-\text{H}\cdots\text{O}/\text{X}$ interactions where the $\text{H}\cdots\text{X}$ distance is less than the sum of van der Waal's radii [Å] and the $\text{C}-\text{H}\cdots\text{X}$ angle is greater than 120° were considered to be significant.

D \cdots H \cdots A	D \cdots H	D \cdots A	H \cdots A	\angle D-H \cdots A
Complex salt 1				
C1-H3 \cdots Cl8 ⁱ	1.20(5)	3.571(4)	2.70(5)	128(3)
C2-H46 \cdots O2w	0.93	3.523(7)	2.62	164
C6-H28 \cdots Cl2	0.95(6)	3.494(5)	2.70(6)	141(4)
C11-H2 \cdots Cl10	0.83(6)	3.569(4)	2.79(6)	157(5)
C12-H1 \cdots Cl12	0.95(4)	3.439(4)	2.65(4)	140(3)
C13-H38 \cdots Cl3	1.12(6)	3.639(4)	2.87(5)	125(3)
C13-H38 \cdots O1w	1.12(6)	3.345(7)	2.64(5)	120(3)
C15-H47 \cdots Cl1 ⁱⁱ	0.91(4)	3.623(3)	2.76(4)	159(4)
C22-H35 \cdots O6w ⁱ	1.02(6)	3.55(1)	2.55(6)	169(4)
C23-H5 \cdots Cl1 ⁱ	0.99(4)	3.677(4)	2.85(5)	141(4)
C24-H18 \cdots Cl9 ⁱ	1.05(3)	3.548(3)	2.77(3)	131(3)
C27-H48 \cdots O2w ⁱⁱⁱ	0.81(3)	3.519(5)	2.72(3)	169(3)
C30-H29 \cdots O5w ^{iv}	0.95(4)	3.391(6)	2.67(4)	133(3)
C31-H17 \cdots Cl3 ^v	1.13(5)	3.627(3)	2.83(3)	127(3)
C34-H8 \cdots Cl1 ^v	0.97(4)	3.639(4)	2.78(4)	148(3)
C38-H43 \cdots O3w ^{vi}	0.77(4)	3.350(7)	2.63(5)	158(4)
C39-H34 \cdots Cl8 ^{vi}	1.01(4)	3.485(3)	2.68(4)	136(4)
C46-H20 \cdots Cl5	0.96(4)	3.825(4)	2.95(4)	152(3)
C47-H19 \cdots Cl4	0.93(4)	3.624(4)	2.95(5)	130(4)
C49-H11 \cdots Cl1	1.02(4)	3.452(4)	2.70(5)	130(3)
C54-H23 \cdots Cl9 ^{vii}	0.94(5)	3.627(5)	2.77(5)	152(4)
C61-H30 \cdots Cl6 ⁱⁱ	0.85(3)	3.490(3)	2.93(3)	125(3)
C63-H33 \cdots Cl8	0.99(5)	3.705(5)	2.84(5)	146(3)
C66-H14 \cdots Cl10	0.99(5)	3.502(4)	2.61(4)	149(3)
C71-H26 \cdots Cl1 ^{viii}	0.95(4)	3.575(4)	2.92(4)	127(3)
C72-H25 \cdots Cl2 ^{viii}	1.00(4)	3.370(4)	2.74(4)	121(3)
Short contacts				
O2w \cdots O6w		3.05(15)		
O2w \cdots O5w(1 - x, -y, 1 - z)		2.854(9)		
Cl10 \cdots Cg		3.36	(Cg = centroid of the N8, C44-48 ring)	
Equivalent positions: (i) x - 1, y, z; (ii) 1 - x, 1 - y, 1 - z; (iii) -x, -y, -z; (iv) x - 1, y, z - 1; (v) x, y, z - 1; (vi) 2 - x, 1 - y, 1 - z; (vii) x, y, z + 1; (viii) 1 - x, -y, 1 - z				
Complex salt 2				
O1w-H2w \cdots O2wa	0.99	2.50(10)	1.66	140
O1w-H1w \cdots Br4	0.87(4)	3.49(4)	2.668(2)	157(2)
Cl1-H1 \cdots O2wa ⁱ	0.93	3.25(9)	2.58	130
C7-H5 \cdots Br2 ⁱⁱ	0.93	3.78(1)	3.03	139
C7-H5 \cdots Br5 ⁱⁱ	0.93	3.61(1)	3.02	122
C13-H9 \cdots Br1 ⁱⁱⁱ	0.93	3.79(1)	3.02	141
C18-H12 \cdots Br5 ^{iv}	0.93	3.70(1)	2.96	137
C23-H15 \cdots Br7 ^v	0.93	3.47(1)	2.82	128
C27-H19 \cdots Br7 ^{vi}	0.93	3.58(1)	2.93	128
C31-H21 \cdots Br2	0.93	3.60(1)	2.91	132
Short contact:				
Cl10 \cdots Cg		3.20	(Cg = centroid of the N2, C8-12 ring)	
Equivalent positions: (i) 1 - x, y - 1/2, 1 - z; (ii) x + 1, y, z + 1; (iii) x + 1, y, z; (iv) 1 - x, y + 1/2, 1 - z; (v) x, y, z + 1; (vi) -x, y - 1/2, 1 - z				

ronment found in KULPIR^[13b] is reported in Figure 5, where each $[\text{Hg}_2\text{I}_7]^{3-}$ is surrounded by as many as 16 guanidinium molecules.

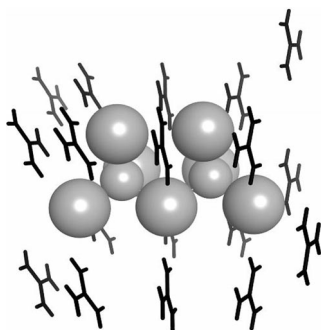


Figure 5. $[\text{Hg}_2\text{I}_7]^{3-}$ anion surrounded by 16 guanidinium molecules.

An interesting observation regarding the conformation of the $[\text{M}_2\text{X}_7]^{3-}$ molecule with respect to the M–X–M bond angles (reported in Table 4) is its great variation from 98.5 to 180°. In an attempt to investigate the effects of the crystal packing with regard to molecular conformation, DFT calculations on the $[\text{Cd}_2\text{X}_7]^{3-}$ ions (X = Br or Cl) were performed both in vacuo and in a simulated solvent environment (water). The results were similar for both of the anions; in vacuo, the molecules assume a near linear geometry around the bridging atom with a Cd–X–Cd angle of 165.15 and 169.11° in $[\text{Cd}_2\text{Cl}_7]^{3-}$ and $[\text{Cd}_2\text{Br}_7]^{3-}$, respectively. However, when the calculations were carried out in a simulated aqueous environment, the calculated conformations become comparable to those found in the crystals, as shown in Figure 6 where the optimized geometry of $[\text{Cd}_2\text{Cl}_7]^{3-}$ is reported together with the bond lengths and angles obtained for $[\text{Cd}_2\text{Br}_7]^{3-}$ (bottom values). By using the same level of theory, geometry optimization calculations were repeated on the $\text{Hg}_2\text{Cl}_7^{3-}$ anion and similar results were obtained: in vacuo the Hg–Cl–Hg angle is close to 180° (174.6°), while in an aqueous environment the angle becomes 102.9°.

Table 4. M–X–M angle in halodicadmte and halodimercurate anions (M = metal, X = halogen).

CSD code	Type	M–X–M angle [°]	Solvent
GODDUY	Hg–I–Hg	180.00(2)	water
GODFAG	Hg–I–Hg	129.10(6)	methanol + water
KULPIR	Hg–I–Hg	108.28(4)	methanol
LITSOW	Hg–I–Hg	98.5(1)	water
POTGAG	Hg–Cl–Hg	162.1(3)	water
TIGHIA	Hg–Cl–Hg	112.2(2)	water
Compound 1	Cd–Cl–Cd	111.58(4)	water
		103.92(4)	
Compound 2	Cd–Br–Cd	126.59(9)	water

At first sight, it seems that in a polar environment the “angular” geometry is preferred to the “linear” one mainly for two reasons: (i) there is a gain in solvation energy due to the exposure of the central chloride to the solvent and (ii) the volume of the cavity, which is formed to accommodate the solute molecule, is smaller. However, this hypothe-

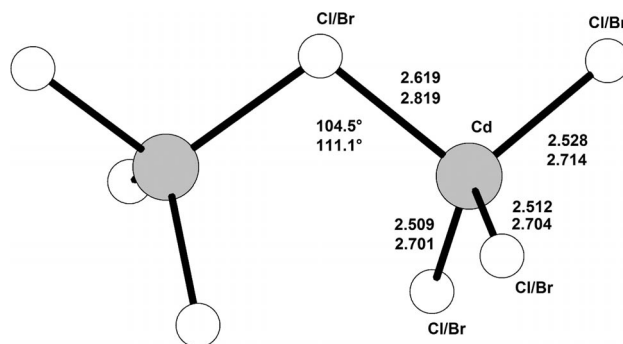


Figure 6. DFT geometries of $[\text{Cd}_2\text{Cl}_7]^{3-}$ with the calculated bond lengths [Å] and angles [°]. The bottom values refer to the optimized geometry of $[\text{Cd}_2\text{Br}_7]^{3-}$.

sis is not able to explain the variety of angular values found in the crystals as reported in Table 3. In order to explore the possible role of the solvent, two calculation series were performed on $[\text{Cd}_2\text{Cl}_7]^{3-}$: (i) geometry optimization in simulated solvents of different dielectric constants and (ii) constrained optimization in vacuo and in a simulated aqueous environment where the central Cl–Cd–Cl angle was kept at a chosen value and varied from 105 to 180° with steps of about 10°. The results are summarized in Table 5 and Figure 7, which shows the plot of ΔE versus Cd–Cl–Cd angle, where ΔE is the energy difference between the actual geometry and the most stable one. The values of the Cd–Cl–Cd angles (°), DFT calculated energy (*Ha*) and ΔE values are reported in Table S2 (Supporting Information).

Table 5. Calculated Cd–Cl–Cd angles [°].

Solvent	Dielectric constant	Angle
Vacuum	–	165.1
<i>n</i> -Hexane	1.89	144.2
Ethyl ether	4.33	115.2
Methylene chloride	9.08	112.0
Acetone	20.70	109.2
Methanol	32.63	111.3
Water	78.53	104.5

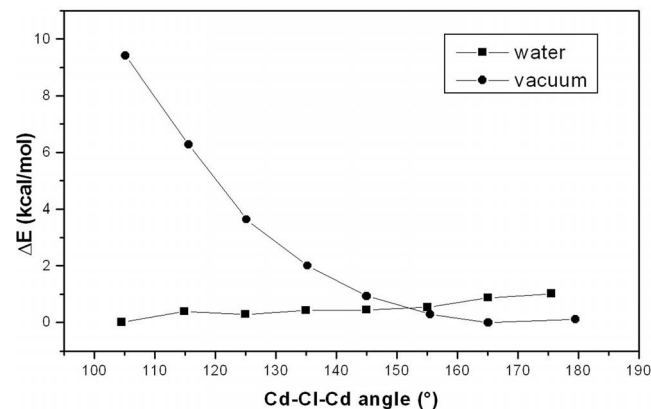


Figure 7. ΔE [kcalmol^{−1}] vs. Cd–Cl–Cd angle [°]. ΔE is the energy difference between the actual geometry and the most stable one. Values obtained in vacuo (circles) and in simulated water (squares) are reported.

It is evident from Table 4 data that the nature of the solvent does not strongly affect the halocadmate conformation, possibly with the exception of *n*-hexane that exhibits a very low dielectric constant. Moreover, from Figure 7 it is clearly visible that the molecule in vacuo is definitely more stable in the “linear” conformation but in water it experiences a very flat potential energy surface, which means that practically all conformations are allowed.

In order to better understand the nature of the electronic structure, an analysis based on localized orbitals was performed on the $[\text{Cd}_2\text{Cl}_7]^{3-}$ molecule in the “bent” and “linear” conformations, focusing on the lone pairs of the chloride atoms and on the electron pairs involved in the Cd–Cl bonds, that is, on the 21 highest occupied molecular orbitals. The localized orbitals obtained for the linear and bent geometries are given in Table 6, together with their overlap with the pure atomic *p* orbitals of chlorine. In both of the conformations, an overlap that is close to one is observed, which clearly indicates the small contribution of the cadmium atomic orbitals to the bond formation, that is, the electrostatic nature of the Cl–Cd interaction. The modification of the nuclear geometry from linear to angular affects mainly the bridging chlorine orbitals: two *p* nonequivalent orbitals of the linear molecule, one bonding and one non-bonding [first and third entries in Table 6 (a), respectively], mix together to give two equivalent bonding orbitals [first and second entries of Table 6 (b)] while the last *p* orbital [second entry of Table 6 (a) and third entry of Table 6 (b)] remains substantially unchanged.

Based on the above evidence, final conclusions were drawn as follows. Although the equilibrium geometry of the

new $[\text{Cd}_2\text{X}_7]^{3-}$ anions is well established in the gas phase, in “solution” it is not possible to identify a preferred conformation, even though a bent geometry is slightly more stable than a linear one mainly due to the increase in solvation energy when the central chloride becomes accessible to the solvent. Analysis of the localized orbitals indicates that the Cd–Cl bond has an ionic character and, therefore, it is not forced to assume a given direction. A closer inspection of the packing architecture of the structures that contain analogous $[\text{Hg}_2\text{X}_7]^{3-}$ anions (Table 4) shows that in all cases the intermolecular interactions, of the type $\text{C/O} \cdots \text{H} \cdots \text{X}$, involve only the external halogens, irrespective of the conformation of the anion. Crystallization can be envisioned therefore, as a process in which the newborn crystal nucleus acquires the right conformation to obtain the closest molecular packing that becomes the only feature that affects the final conformation.



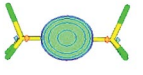

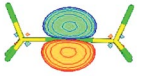
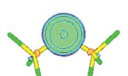
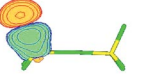
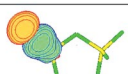
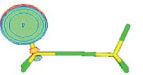

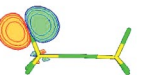
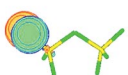
Conclusions

The successful isolation of $[\text{Cd}_2\text{X}_7]^{3-}$ anions indicate that it is possible to “cage” these ions, with the help of a similarly sized and equally charged $[\text{Co}(\text{phen})_3]^{3+}$ cation, to form discrete entities. The size and charge complementarity provides the requisite impetus to reduce the lattice enthalpy considerably through the interplay of a large number of second sphere interactions, such as $\text{C} \cdots \text{H} \cdots \text{O/X}$ and $\text{C} \cdots \text{H} \cdots \pi$. Consequently, the cation attains the capability to prevent polymerization of molecules that have an intrinsic tendency to associate themselves like $[\text{Cd}_2\text{X}_7]^{3-}$ anions. This study provides a viable strategy to avoid polymerization of anions through the judicious selection of cations and thus may have implications in future investigations that are concerned with the search, stability and isolation of new anions in inorganic chemistry.

Experimental Section

Materials and Physical Measurements: Analytical grade reagents were used without any further purification. $[\text{Co}(\text{phen})_3]\text{Cl}_3$ was prepared by the reaction between $[\text{Co}(\text{NH}_3)_5\text{Cl}]\text{Cl}_2$ and 1,10-phenanthroline monohydrate according to the method described in the literature.^[16] Elemental analyses (C, H and N) were performed with an automatic Perkin–Elmer 2400CHN elemental analyzer. Cobalt, Cadmium and halides were determined by reported methods of estimation.^[17] UV/Vis spectra were recorded with a HITACHI 330 spectrophotometer in aqueous solution. The luminescent properties were measured with a RF-5310(PC) spectrofluorophotometer. The slit width for both the excitation and emission measurements was 5 nm. Infrared spectra of the complex salts were recorded with a PERKIN ELMER spectrum RX FTIR system instrument with KBr pellets. The ^1H and ^{13}C NMR spectra were recorded in D_2O and $[\text{D}_6]\text{dmsO}$ at 25 °C with a JEOL AL 300 MHz FT NMR spectrometer. The chemical shift values are expressed as δ value (ppm) down field from tetramethylsilane as an internal standard. The thermogravimetric analysis (TGA) was conducted with a SDT Q600 instrument. The specimens (26.9350 and 24.6060 mg) were contained in an alumina pan. TGA was carried out from 25 to 1000 °C at a constant heating rate of 10 °C min^{−1}. Electrochemical

Table 6. Localized orbitals for the (a) linear and (b) bent geometries in the $[\text{Cd}_2\text{Cl}_7]^{3-}$ molecule and their overlap with the Cl atomic *p* orbitals. Only three representative orbitals are reported for the six external atoms.

(a) linear		(b) bent	
Localized Orbital	Overlap	Localized Orbital	Overlap
	0.973		0.979
	0.996		0.983
	0.996		0.996
	0.975		0.974–0.976
	0.966		0.966
	0.966		0.966

measurements were conducted with a potentiostat (μ AUTOLAB type III) with a glass encased 3 mm diameter glassy carbon electrode (Metrohm), Pt wire and Ag/AgCl (0.1 M KCl) as the working, auxiliary and reference electrodes, respectively.

[Co(phen)₃]Cd₂Cl₇·3H₂O (1): A solution of CdCl₂ (0.129 g, 0.7 nmol) and KCl (0.105 g, 1.4 mmol) in water (10 mL) were added to a solution of [Co(phen)₃]Cl₃ (0.5 g, 0.7 mmol) in water (10 mL). When the resulting solution was allowed to evaporate slowly at room temperature, yellow coloured rectangular crystals were obtained after one week; yield 50%, m.p. > 230 °C. ¹H NMR (300 MHz, D₂O, 298 K): δ = 9.13 (d, 2 H, phen-H-2,9), 8.54 (s, 2 H, phen-H-5,6), 7.95 (t, 2 H, phen-H-3,8), 7.65 (d, 2 H, phen-H-4,7) ppm. ¹³C NMR (75 MHz, D₂O): δ = 151.16 (C-2), 143.25 (C-10a), 139.66 (C-4), 129.59 (C-4a,6a), 126.89 (C-5), 126.42 (C-3) ppm. FTIR (KBr pellet): $\tilde{\nu}$ = 3400 (w, br.), 3055 (w), 1604 (s), 1581 (m), 1518 (s), 1427 (s), 839 (s), 710 (s), 523 (w), 463 (w) cm⁻¹. UV/Vis (H₂O): λ_{max} = 459, 342, 280, 218 nm. C₃₆H₃₀N₆O₃Cd₂Cl₇ (1126.5): calcd. C 38.34, H 2.84, N 7.46, Cd 19.96, Cl 22.06; found C 38.27, H 2.79, N 7.41, Cd 19.40, Cl 21.80. K_{sp} = 4.5×10^{-7} .

[Co(phen)₃]Cd₂Br₇·2H₂O (2): A solution of [Co(phen)₃]Cl₃ (0.5 g, 0.7 mmol) in water (10 mL) was prepared. In another beaker, CdCl₂ (0.129 g, 0.7 nmol) and KBr (0.337 g, 2.8 mmol) were dissolved in water (10 mL). When both of the solutions were mixed, a yellow coloured precipitated product was obtained. This precipitated product was recrystallized from hot water, which resulted in yellow coloured single crystals; yield 52%, m.p. > 230 °C. ¹H NMR (300 MHz, [D₆]dmsO, 298 K): δ = 8.92 (d, 2 H, phen-H-2,9), 8.33 (s, 2 H, phen-H-5,6), 7.77 (t, 2 H, phen-H-3,8), 7.52 (d, 2 H, phen-H-4,7) ppm. ¹³C NMR (75 MHz, [D₆]dmsO): δ = 150.81 (C-2), 144.58 (C-10a), 141.02 (C-4), 130.99 (C-4a,6a), 127.47 (C-5), 127.01 (C-3) ppm. FTIR (KBr pellet): $\tilde{\nu}$ = 3419 (w, br.), 3053 (w), 1623, 1582 (m), 1518 (s), 1427 (s), 843 (s), 712 (s), 523 (w), 463 (w) cm⁻¹. UV/Vis (H₂O): λ_{max} = 459, 342, 280, 219 nm. C₃₆H₂₈N₆O₂Cd₂Br₇ (1419.74): calcd. C 30.42, H 1.97, N 5.91, Br 39.39, Cd 15.83; found C 30.34, H 1.90, N 5.86, Br 38.80, Cd 15.30. K_{sp} = 9.4×10^{-11} .

X-ray Crystallography: The crystallographic data for compounds **1** and **2** were collected with a Nonius Kappa CCD diffractometer at room temperature by using graphite-monochromated Mo-K α radiation (λ = 0.71073 Å) with a ϕ scan followed by ω scan to fill the sphere. All of the intensities were corrected for Lorentz, polarization and absorption effects.^[18] The structure was solved by direct methods with the SIR97 program^[19] and refined on F^2 by full-matrix least-squares methods with anisotropic non-H atoms, with the exception of the O6w atom in **1** and the O2w atom in **2** that are disordered over two equivalent positions. In compound **1** all of the H atoms, except those linked to the water molecules, were found in the difference Fourier map and refined isotropically. In compound **2**, the hydrogen atoms of the 1,10-phenanthroline moieties were given calculated positions; the hydrogen atoms bound to O1w were found in the difference Fourier map and refined isotropically with restraints on the bond lengths. All other calculations were accomplished with SHELX97,^[20] WingX^[21] and PARST.^[22]

CCDC-718659 (for **1**) and -718660 (for **2**) contain the supplementary crystallographic data for this paper. These data can be obtained free of charge from The Cambridge Crystallographic Data Centre via www.ccdc.cam.ac.uk/data_request/cif.

Crystal Data for 2(CoC₃₆H₂₄N₆)·2(Cd₂Cl₇)·6(H₂O) (Compound 1): M_r = 2253.08 g mol⁻¹, triclinic, space group $P\bar{1}$; a = 15.3543(2) Å, b = 16.0841(2) Å, c = 18.3036(2) Å; α = 105.6500(5)°, β = 101.1800(5)°, γ = 103.6960(5)°; V = 4065.23(9) Å³; Z = 2; 19581

independent reflections (R_{int} = 0.042), R_1 = 0.038, wR_2 = 0.105. R_1 was calculated for observed data and wR_2 for all data.

Crystal Data for 2(CoC₃₆H₂₄N₆)·2(Cd₂Br₇)·2(H₂O) (Compound 2): M_r = 1419.74 g mol⁻¹, monoclinic, space group $P2_1$; a = 10.4435(3) Å, b = 16.0990(4) Å, c = 12.4226(4) Å; β = 94.1160 (11)°; V = 2083.19(10) Å³; Z = 2; 8318 independent reflections (R_{int} = 0.052), R_1 = 0.061, wR_2 = 0.175. R_1 was calculated for observed data and wR_2 for all data.

Quantum Mechanical Calculations: The “in vacuo” fully optimized geometries of the [M₂X₇]³⁻ anions (M = Cd, Hg; X = halogen) were obtained by density functional theory (DFT) calculations that were carried out at the GGA-PW91/DNP level of theory^[23] with the DMol³ module of the Material Studio system of programs.^[24] Afterwards, the calculations were repeated and included a continuum solvation model (CSM)^[25] in which the solute molecule forms a cavity within a dielectric continuum of permittivity ϵ that represents the solvent. The calculated electronic structure of the [Cd₂-Cl₇]³⁻ molecule was analyzed in terms of localized orbitals. The canonical (delocalized) Self Consistent Fied (SCF) orbitals computed with the Atomic Natural Orbital (ANO) basis set^[26] were localized following an a priori strategy.^[27] This approach allows the electronic wavefunctions to be described in terms close to the Lewis’ view^[28] and has been used to unravel the nature of complex wavefunctions.^[29]

Supporting Information (see footnote on the first page of this article): Figures depicting luminescent spectra, TGA curves, cyclic voltammograms and crystal packing along with tables representing CSD reference codes and details of DFT calculations.

Acknowledgments

The authors gratefully acknowledge the financial support of Council of Scientific and Industrial Research (CSIR), New Delhi (grant number 09/135/0594/2010/EMR-1).

- [1] a) R. Mokhlisse, M. Couzi, N. B. Chanh, Y. Haget, C. Hauw, A. Meresse, *J. Phys. Chem. Solids* **1985**, *46*, 187–195; b) N. B. Chanh, C. Hauw, A. Meresse, M. Rey-Lafon, L. Ricard, *J. Phys. Chem. Solids* **1985**, *46*, 1413–1420; c) M. Bensekrane, A. Goltzene, B. Meyer, C. Schwab, D. Elwell, R. S. Feigelson, *J. Phys. Chem. Solids* **1985**, *46*, 481–486; d) J. Luo, M. Hong, R. Wang, R. Cao, Q. Shi, J. Weng, *Eur. J. Inorg. Chem.* **2003**, 1778–1784; e) J. M. Perez, V. Cerrillo, A. I. Matesanz, J. M. Millan, P. Navarro, C. Alonso, P. Souza, *ChemBioChem* **2001**, *2*, 119–123; f) Y. A. Shihadeh, A. Benito, J. M. Lloris, R. Martinez-Manez, T. Pardo, J. Soto, M. D. Marcos, *J. Chem. Soc., Dalton Trans.* **2000**, 1199–1205.
- [2] a) R. Bala, R. P. Sharma, R. Sharma, B. M. Kariuki, *Inorg. Chem. Commun.* **2006**, *9*, 852–855; b) R. P. Sharma, R. Sharma, A. Kumar, P. Venugopalan, P. Brando, V. Felix, *Inorg. Chem. Commun.* **2009**, *12*, 945–947.
- [3] B. F. Abrahams, M. G. Haywood, R. Robson, *Chem. Commun.* **2004**, 938–939.
- [4] a) O. Bastiansen, *Acta Chem. Scand.* **1949**, *3*, 408–414; b) R. M. Barrett, D. Steele, *J. Mol. Struct.* **1972**, *11*, 105–125; c) H. Suzuki, *Bull. Chem. Soc. Jpn.* **1959**, *32*, 1340–1350; d) A. Bree, C. Y. Pang, L. Rabenack, *Spectrochim. Acta* **1971**, *27A*, 1293–1288; e) E. D. Schmid, B. Brosa, *J. Chem. Phys.* **1972**, *56*, 6267–6268.
- [5] a) J. D. Miller, R. H. Prince, *J. Chem. Soc.* **1965**, 3185–3194; b) N. C. Thomas, K. Pringle, G. B. Deacon, *J. Chem. Educ.* **1989**, *68*, 516–517; c) H. O. Kalinowski, S. Berger, S. Braun, *¹³C Spectroscopy*, John Wiley & Sons, New York, **1986**.

- [6] K. Nakamoto, *Infrared and Raman Spectra of Inorganic and Coordination Compounds*, 5th ed., John Wiley & Sons, New York, **1997**.
- [7] R. P. Sharma, A. Singh, A. Saini, P. Venugopalan, V. Ferretti, *Inorg. Chem. Commun.* **2011**, *14*, 1–4.
- [8] a) W. J. Geary, *Coord. Chem. Rev.* **1971**, *7*, 81–122; b) G. S. Girolami, T. B. Rauchfuss, R. J. Angelici, *Synthesis and techniques in Inorganic Chemistry: A laboratory manual*, University Science Books, **1999**, pp. 272.
- [9] A. L. Horvath, *Handbook of Aqueous electrolytes solutions: Physical properties, estimation and correlation methods*; John Wiley and Sons, New York, **1985**.
- [10] a) R. P. Sharma, A. Singh, P. Venugopalan, R. Dansby-Sparks, Z.-L. Xue, S. Rossetti, V. Ferretti, *J. Coord. Chem.* **2010**, *63*, 3016–3027; b) M. T. Carter, A. J. Brad, *J. Am. Chem. Soc.* **1987**, *109*, 7528–7530; c) K. M. Davies, A. Hussam, B. R. Rector, I. M. Owen, P. King, *Inorg. Chem.* **1994**, *33*, 1741–1747; d) B. Jin, X. Ji, T. Nakamura, *Electrochim. Acta* **2004**, *50*, 1049–1055.
- [11] M. N. Burnett, C. K. Johnson, *ORTEP III: Oak Ridge Thermal Ellipsoids Plot Program for Crystal Structure Illustrations*, Report ORNL-6895, Oak Ridge National Laboratory, Tennessee, **1996**.
- [12] a) E. C. Niederhoffer, A. E. Martell, P. Rudolf, A. Clearfield, *Cryst. Struct. Commun.* **1982**, *11*, 1951–1957; b) M. Hanauer, A. Neshat, T. P. Bigioni, *Acta Crystallogr., Sect. C* **2008**, *64*, m111–113; c) A. Singh, R. P. Sharma, P. Brandão V. Felix, P. Venugopalan, *J. Mol. Struct.* **2008**, *891*, 396–403.
- [13] a) GODDUY, GODFAG: N.-H. Hu, Y.-S. Liu, K. Aoki, *Acta Crystallogr., Sect. C: Cryst. Struct. Commun.* **1999**, *55*, 304–308; b) KULPIR: H. Terao, Y. Kai, T. M. Gesing, H. Ishihara, Y. Furukawa, B. T. Gowda, *J. Mol. Struct.* **2009**, *932*, 61–66; c) LITSOW: I. F. Burshtein, A. L. Poznyak, *Kristallografiya* **1999**, *44*, 1059–1063; d) POTGAG: M. J. Cox, E. R. T. Tiekink, *Z. Kristallogr.* **1998**, *213*, 528–533; e) TIGHIA: A. Derwahl, F. Wasgestian, D. A. House, W. T. Robinson, *Coord. Chem. Rev.* **2001**, *211*, 45–67.
- [14] a) L. R. MacGillivray, J. L. Atwood, *Chem. Commun.* **1996**, 735–736; b) C. S. Campos-Fernandez, B. W. Smucker, R. Clerac, K. R. Dunbar, *Isr. J. Chem.* **2001**, *41*, 207–218.
- [15] a) Y. S. Rosokha, S. V. Lindeman, S. V. Rosokha, J. K. Kochi, *Angew. Chem.* **2004**, *116*, 4750; *Angew. Chem. Int. Ed.* **2004**, *43*, 4650–4652; b) S. Demeshko, S. Dechert, F. Meyer, *J. Am. Chem. Soc.* **2004**, *126*, 4508–4509.
- [16] P. Pfeiffer, B. Werdemann, *Z. Anorg. Allg. Chem.* **1950**, *293*, 31–38.
- [17] K. Grzedzicki, A. Bujewski, *Chem. Anal.* **1990**, *35*, 557–560.
- [18] R. H. Blessing, *Acta Crystallogr., Sect. A* **1995**, *51*, 33–38.
- [19] A. Altomare, M. C. Burla, M. Camalli, G. Casciarano, C. Giacovazzo, A. Guagliardi, A. A. G. Moliterni, G. Polidori, R. Spagna, *J. Appl. Crystallogr.* **1999**, *32*, 115–119.
- [20] G. M. Sheldrick, *SHELXL-97: Program for Crystal Structure Refinement*, University of Göttingen, Germany, **1997**.
- [21] L. J. Farrugia, *J. Appl. Crystallogr.* **1999**, *32*, 837–838.
- [22] M. Nardelli, *J. Appl. Crystallogr.* **1995**, *28*, 659.
- [23] a) M. Dolg, W. Liu, S. Kalvoda, *Int. J. Quantum Chem.* **2000**, *76*, 359; b) J. P. Perdew, Y. Wang, *Phys. Rev. B* **1992**, *45*, 13244–13249.
- [24] *Material Studio*, version 4.4, Accelrys Software Inc., **2008**.
- [25] J. Tomasi, M. Persico, *Chem. Rev.* **1994**, *94*, 2027–2094.
- [26] B. O. Roos, R. Lindh, P.-A. Malmqvist, V. Veryazov, P.-O. Widmark, *J. Phys. Chem. A* **2004**, *108*, 2851–2858.
- [27] C. Angeli, G. Del Re, M. Persico, *Chem. Phys. Lett.* **1995**, *233*, 102–110.
- [28] J.-P. Malrieu, N. Guihery, C. J. Calzado, C. Angeli, *J. Comput. Chem.* **2007**, *28*, 35–50.
- [29] C. Angeli, *J. Comput. Chem.* **2009**, *30*, 1319–1333.

Received: October 18, 2011

Published Online: February 8, 2012

A Facile Approach for Transferring PbS Colloidal Photonic Structures into Alkanol Solutions and Composite Solid Films

Chunguang Li,^[a] Tianyu Bai,^[a] Tao Li,^[a] Feifei Li,^[a] Wenjun Dong,^[b] Zhan Shi,^{*[a]} and Shouhua Feng^[a]

Keywords: Colloids / Nanostructures / Self-assembly / Photonic crystals / Lead

Visible-light-responsive photonic structures have been prepared in alcohol solvents by using silica-modified PbS colloidal nanocrystal clusters (CNCs) as building blocks. Further modification of the PbS CNCs with a coating of silica allowed the dispersion of the particles into nonaqueous solutions. Repulsive electrostatic and solvation forces contribute to the self-assembly of the PbS@SiO₂ spheres. The core-shell par-

ticles have optical properties similar to those of CNCs, and they can also be assembled into close-packing films through simple drop-casting on silicon substrates. Embedding droplets of such a PbS@SiO₂ colloidal solution in a polymer matrix produced solid composite materials with visible-light-responsive optical properties with potential applications as sensors and optical switches.

Introduction

Functional photonic band-gap materials and devices have been intensively pursued because of their significant applications in optical switches, sensors, and color displays. These photonic structures can be successfully fabricated by assembling monodisperse colloidal particles with narrow size distribution into periodically ordered structures.^[1–12] The refractive indices of these colloidal particles differ from that of the surrounding medium, and the resulting photonic structures diffract UV, visible, or near-IR light, depending on their lattice constant. Considerable effort has been devoted to the development of tunable photonic crystals, the properties of which can be controlled by any chemical or physical means. These external means (i.e., temperature, electrical or magnetic field, light, pH value, and ionic strength of the system) can effectively cause changes in the refractive indices of the colloids or the surrounding matrix, the lattice constants, and the symmetry of the colloidal arrays.^[13–26]

Recently we developed a simple modification of the traditional polyol process for the synthesis of polyacrylate-capped PbS colloidal nanocrystal clusters (CNCs) with tunable sizes from around 155 to around 240 nm and relatively narrow size distributions.^[27] Polyacrylate capping on the surfaces of PbS CNCs confers upon the particles not only

a high degree of water dispersibility but also a high number of surface charges. The high density of charge on the colloid surface produces sufficient repulsive electrostatic interactions that three-dimensional photonic crystals can be constructed in aqueous solutions. These short-range periodic structures of PbS CNCs with regular interparticle spacing in the order of hundreds of nanometers strongly diffract visible light under external irradiation. This novel photonic crystal system is optically responsive. Because different particle sizes lead to different interparticle spacing, one can conveniently tune the diffraction wavelength by controlling the dimensions of the CNCs. Owing to the high refractive index of PbS (ca. 3.921), strong diffraction is observed at a relatively low volume fraction of particles (ca. 0.5%). This novel optical property of PbS nanoparticles has never been reported in the literature before. Herein, we report the development of optically responsive PbS colloidal photonic structures that can be operated in alkanol solution by modification of the particle surface with a layer of silica. Interestingly, upon application of external visible light irradiation, the modified particles in alkanol solution can also assemble into periodic structures and diffract light. Moreover, we can embed PbS@SiO₂ colloids in a polymer matrix to produce a solid composite film with similar light-responsive optical properties.

Results and Discussion

The PbS CNCs were successfully synthesized by a polyol-mediated reaction.^[27] The particle size could be tuned from around 155 to around 240 nm by simply changing the molar ratio of thiourea/Pb(Ac)₂ while keeping all other parameters fixed (Figure 1a–c). We used polyacrylic acid (PAA)

[a] State Key Laboratory of Inorganic Synthesis and Preparative Chemistry, College of Chemistry, Jilin University
Qianjin Street 2699, Changchun, Jilin 130012, P. R. China
Fax: +86-431-85168624
E-mail: zshi@mail.jlu.edu.cn

[b] Center for Optoelectronics Materials and Devices, Department of Physics, Zhejiang Sci-Tech University,
Hangzhou 310018, P. R. China

Supporting information for this article is available on the WWW under <http://dx.doi.org/10.1002/ejic.201101183>.

as capping agent to confer on the particles excellent water dispersibility. The FTIR spectrum clearly shows that almost all the stretching modes of the coordinated and uncoordinated carboxylate groups of the polymer chains are present on the surfaces of the PbS CNCs (Figure S1). In fact, the PbS CNCs are composed of small primary crystals with sizes of 6–8 nm. The primary nanocrystals are slightly larger with a smaller molar ratio of Pb/S, which leads to the production of larger of CNCs. Therefore, the CNCs still show visible and near-infrared absorption although their particle size far exceeds the excitation Bohr radius owing to the secondary structures.

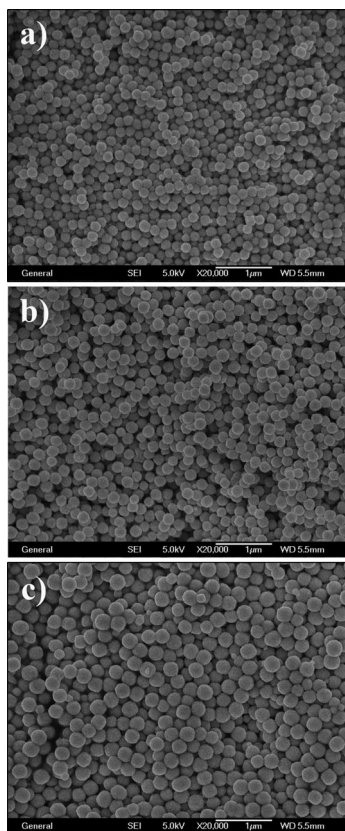


Figure 1. SEM images of PbS CNCs with different particle sizes: (a) 155, (b) 180 and (c) 240 nm.

Unlike the previously reported polyacrylate-capped PbS CNCs, which are only dispersible in water, by coating a layer of silica onto the surfaces of the particle allows them to disperse into alkanols such as ethanol and ethylene glycol (EG). Interestingly, the modified particles can also assemble into similar periodic structures and diffract light in particular directions in alkanol solutions. The differences between the self-assembled ordered structures of PbS CNCs in water and PbS@SiO₂ particles in alkanols are a result of their surface chemistry. In aqueous solution, the stability of colloidal particles with plenty of charges should be considered to arise from both van der Waals attractions and electrostatic repulsion resulting from the overlap of electric double layers of two adjacent particles according to the Derjaguin–Landau–Verwey–Overbeek (DLVO) theory.^[28]

The polyacrylate molecule chains wrap loosely around the particle surface, keeping the nearby particles relatively distant from each other. For the dispersion of core–shell particles into alkanols, the electrostatic repulsion of the silica surface is reduced compared with the repulsion of the polymer chains, but the particles can also assemble into ordered structures, because another repulsive force may dominate the interparticle repulsions at small separation. It is widely accepted by research groups that a wetting film of solvent formed on the silica surface by hydrogen bonding enables the silica particles to disperse into ethanol. Neighboring particles are strongly separated when the film layers of two adjacent particles overlap,^[29–33] and CNCs with silica shells and wetting solvent films retain similar photonic properties. The thickness of the solvation layer is related to the ability of the solvent to form hydrogen bonds. For strong hydrogen-bonding solvents (such as ethanol, EG, and methanol), relatively thick solvation layers lead to strong diffraction peaks at slightly longer wavelengths under external light irradiation. However, longer-chain and branched alkanols^[34] are weak hydrogen-bonding solvents, and thus the solvation layers are much thinner and the diffraction peaks tend to be weaker at shorter wavelengths.

Surface coating of the silica layer was achieved by the classic Stöber method in which tetraethoxysilane (TEOS) was hydrolyzed in a mixture of ethanol, NH₃·H₂O, and an aqueous solution of PbS CNCs.^[35] The thickness of the silica shell could be precisely controlled by changing the reaction parameters, for example, the amount of NH₃·H₂O, TEOS, or CNCs. As shown in Figure 2a–g, the thickness of the silica shell could be varied from around 5 to around 30 nm while keeping a core size of around 185 nm. To avoid the homogeneous nucleation of small silica particles, TEOS was slowly and continuously added to the reaction mixture during the synthesis process. We also calculated the dependence of the size of the PbS@SiO₂ core–shell structures on the amount of added TEOS (Figure 2h). Furthermore, Figure 3a–c shows TEM images that confirm that three different sizes of PbS CNCs can be modified with the desired thickness of silica shell also by controlling the reaction parameters. The carboxylate groups of polymer chains in polyacrylate-capped CNCs would be protonated in polar organic solvents other than water. The CNCs can be dispersed in a mixture of ethanol and NH₃·H₂O, because the high pH value of NH₃·H₂O prevents the protonation of particles, and thus there are many uncoordinated carboxylate groups on the particle surface. However, the protonation of the carboxylate groups in the polymer chains would still occur without strong alkaline surroundings. Thus, the modification of the PbS CNCs with a silica layer is a simple and effective way of transferring particles into nonaqueous solutions. More importantly, in contrast to the aqueous CNC system, the PbS@SiO₂ colloids are able to remain dispersed in ethanol for a longer period of time and still display photonic response after storage for several months owing to the lower ionic strength of the alkanol solutions and nonelectrostatic contribution to interparticle repulsion. The size of CNCs is limited by the synthetic procedure, and sil-

ica coating on the one hand allows an increase in the particle size to a desired dimension for potential applications and on the other hand makes the colloids compatible with many alkanol solutions. The silanol surface could also be easily modified and enables several other functional groups to be linked to the particle surface for special purposes.

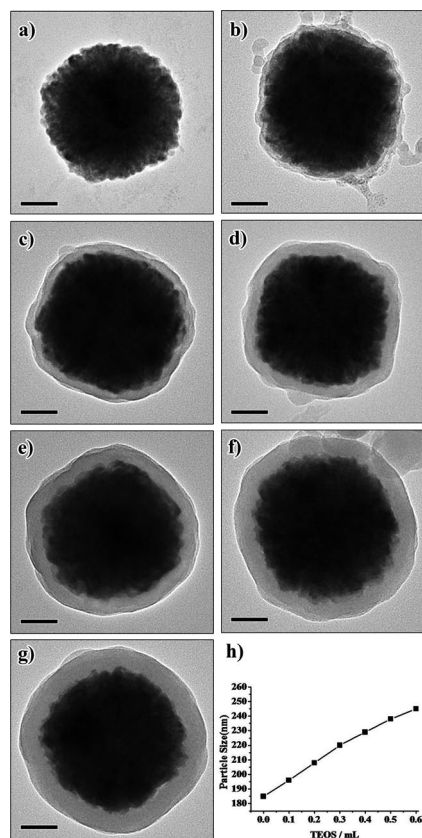


Figure 2. Representative TEM images of the PbS@SiO₂ particles with a similar core size of around 185 nm and shell thicknesses of (a) 0, (b) 5, (c) 12, (d) 17, (e) 22, (f) 27, and (g) 30 nm. (h) Dependence of the particle size of PbS@SiO₂ core-shell structures to the added volume of TEOS. All scale bars are 50 nm.

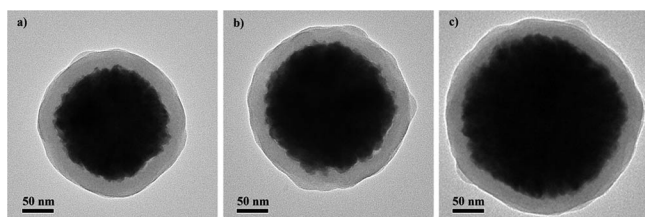


Figure 3. TEM images of the PbS@SiO₂ particles with a similar shell thicknesses of around 22 nm and core sizes of (a) 155, (b) 185, and (c) 240 nm.

After silica coating, we demonstrated the photonic response of PbS@SiO₂ colloids in ethanol. According to our previous report, PbS CNCs with a size of around 185 nm (Figure 4a) have excellent dispersibility in water, and the solution color is dark blue (Figure 4c, left). The CNCs show a clear red color under external visible light (Figure 4d, left). After coating with a layer of silica, the

PbS@SiO₂ colloids are well dispersed in ethanol (Figure 4c, right) and still show a red color under visible light (Figure 4d, right). This result indicates that the visible-light-responsive nature of PbS CNCs can be extended to alkanol solutions by simply coating the particle surface with a silica layer. Note also that the color of the solution hardly changes after silica coating because electrostatic forces still remain effective at larger separations, and the solvation force may dominate the interparticle repulsions at small separations, making it possible for a similar interparticle space with an increased thickness of silica shell in a fixed range. The absorption spectra of CNCs with a size of around 185 nm before and after silica coating are shown in Figure 5a. The absorption spectrum of the PbS@SiO₂ colloids corresponding to the sample in Figure 2g is quite similar to that of the PbS CNCs cores, and the absorption spectra of PbS cluster cores with different thicknesses of silica shells (corresponding to Figure 2b–g) are also similar, which demonstrates that the size of the primary nanocrystal determines the optical absorption of the CNCs. The absorption spectra of yellow-green (core size ca. 155 nm), red (core size ca. 185 nm), and dark-green (core size ca. 240 nm) PbS@SiO₂ colloids are shown in Figure 5b. These spectra imply that silica coating of the particle surface has almost no effect on the absorption properties of CNCs.

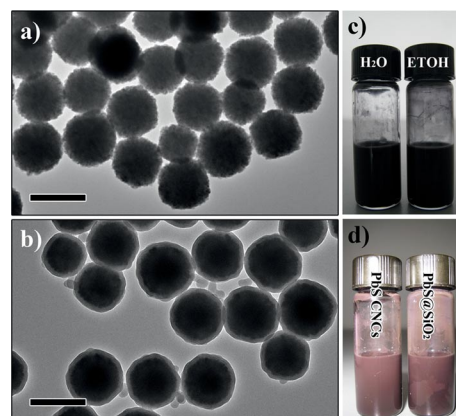


Figure 4. TEM images of PbS CNCs (a) before and (b) after coating silica shell. (c) Photograph of PbS CNCs dispersed in water (left) and PbS@SiO₂ in ethanol (right) without light illumination. (d) Photograph of the corresponding colloids of (c) formed in response to light illumination. All scale bars are 200 nm.

Because of their high uniformity, narrow size distribution, and regular shape, PbS colloidal spheres should assemble into close-packing films. Unfortunately, these CNCs can barely close-pack due to the poor volatility of water (Figure 6a), and they are only stable in aqueous solution. The SEM images in Figure 6b show that as a result of silica modification, two-dimensional close-packing of PbS@SiO₂ colloids occurs easily at a relatively high cover level simply by drop-casting the colloidal solution into ethanol on silicon substrates. Through the simple preparation of a large-area film by low-cost techniques (such as drop-casting and spin-coating), it is envisioned that these PbS@SiO₂ colloids will be useful for the fabrication of various functional de-

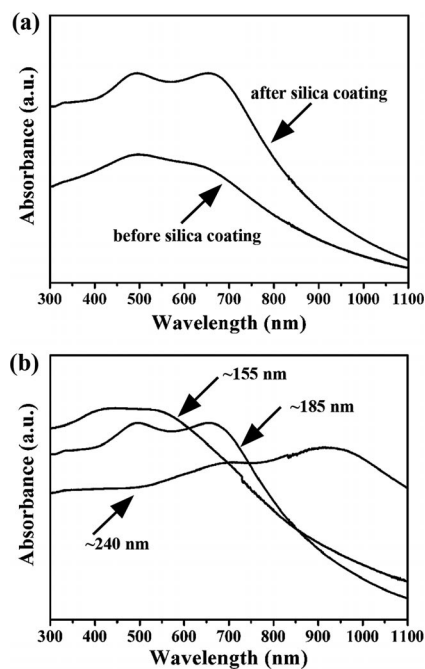


Figure 5. Absorption spectra of (a) PbS CNCs (ca. 185 nm) before and after silica coating, and (b) PbS@SiO₂ colloids with different core sizes (ca. 155, 185, and 240 nm).

vices such as chemical sensors, solar absorbers, and photonic and optical switching devices.

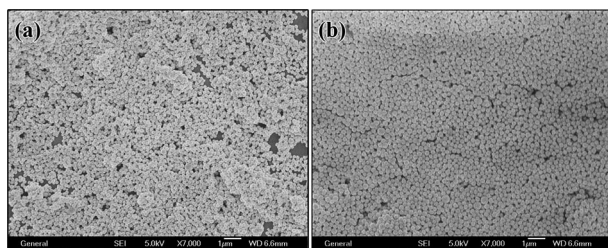


Figure 6. SEM images of PbS CNCs (a) before and (b) after modifying with silica layer on silicon substrates.

The successful assembly of PbS CNCs into ordered structures in ethanol inspired us to produce further solid composite materials with visible-light-responsive optical properties by embedding alkanol solutions of PbS@SiO₂ colloids in a poly(dimethylsiloxane) (PDMS) matrix. The fabrication of solid composite materials is briefly illustrated in Figure 7a. The PbS@SiO₂ colloids were redispersed in EG solution after being separated from ethanol, because EG solutions form very stable emulsion-like droplets in the liquid prepolymer of PDMS.^[36] The prepolymer containing the liquid droplets of the colloid dispersion was then solidified to form a composite film through polymerization. As the PbS@SiO₂ colloids are still able to assemble into ordered structures, each droplet behaves like a small photonic crystal that can diffract light. The SEM image of a PbS@SiO₂/PDMS film cross-section also proves the existence of EG droplets (Figure S2). The PbS@SiO₂ colloids in droplets of around 2 µm can self-assemble into short-range ordered structures so that the solid film is still op-

tically responsive. Figure 7b demonstrates a stable and flexible composite film with visible-light-responsive optical properties. It was prepared first by separating the PbS@SiO₂ colloids from ethanol solution and then redispersing them into EG solution. The EG solution containing the PbS@SiO₂ colloids was added to the liquid PDMS prepolymer and curing agent under fast stirring, and then thermal curing of the mixture at about 60 °C for 2 h produced a very dark-brown silicone film, which shows a dark-blue color when light passes through the film and displays a red color when placed under external visible-light irradiation. After curing, the composite film is very stable and flexible. It can be stretched or folded casually while still retaining light-responsive characteristics (Figure 7b). We also fabricated a patterned PDMS film that includes PbS@SiO₂ colloids of two different core sizes for the background and letters, as schematically outlined in Figure 7c. The particle sizes of the PbS@SiO₂ colloids used as the background and letters were 185/17 nm and 240/17 nm (core diameter/silica shell thickness), respectively. Without irradiation with external light, there is nearly no contrast between the background and letters across the whole solid film except for the rough edges of the letters. When the direction of irradiation with sunlight was not blocked, however, red letters contrasting against a dark-green background was clearly observed (Figure 7d).

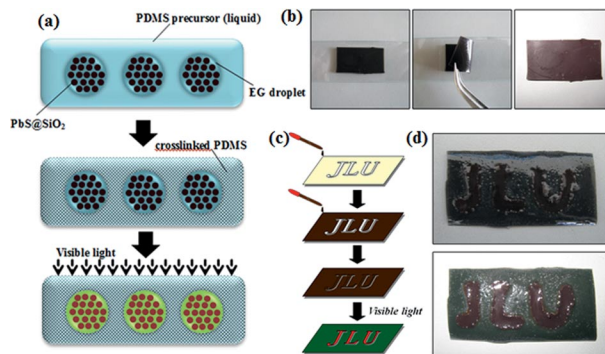


Figure 7. (a) Schematic illustration showing the fabrication procedure for a visible-light-responsive PDMS composite embedded with EG droplets containing PbS@SiO₂ particles. (b) Visible-light-induced color change of a PDMS film. (c) Schematic illustration of the two-step procedure for fabricating a patterned composite PDMS film. (d) Digital photos of a patterned PDMS film that displays letters upon the application of an external visible light.

The absorption and reflectance spectra of the PbS@SiO₂/PDMS film prepared with particles with a core size of around 240 nm are shown in Figure 8. The absorption edge of the solid film (Figure 8a) is similar to that of the PbS CNCs and PbS@SiO₂ colloids. The absorption peak at about 820 nm indicates that the composite film also exhibits near-infrared absorption. The reflectance spectrum shows a strong reflectance peak at 820 nm, and this is confirmed by the absorption spectra (Figure 8b). These observations demonstrate that both the colloids and the composite films have the potential to form novel colloidal crystals and to be used for optical device manufacturing.

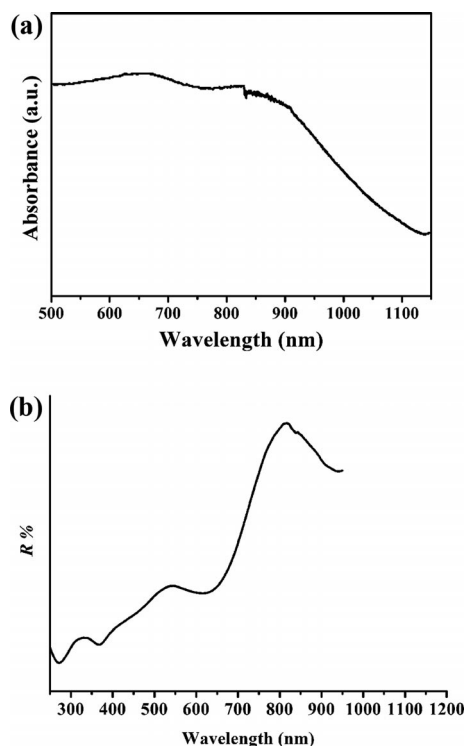


Figure 8. (a) Absorption and (b) reflectance spectra of a PbS@SiO₂/PDMS film.

Conclusions

Visible-light-responsive photonic structures in alkanol solutions have been fabricated by assembling silica-coated PbS CNCs under light irradiation. After coating a silica shell onto the particle surface, the PbS@SiO₂ colloids are able to disperse into a variety of alkanol solutions as well as ethanol. Desired particle sizes are easily obtained by tuning the hydrolysis with TEOS, and the PbS@SiO₂ colloids in ethanol display fast and reversible photonic response even after several months. A wetting film of solvent formed through hydrogen bonds contributes to interparticle repulsions at small separations in alkanol solutions. These uniform PbS@SiO₂ particles easily form two-dimensional close-packing films simply by drop-casting, which indicates that they have potential in applications such as chemical and photonic devices. The assembly of PbS CNCs into ordered structures in ethanol inspired us to produce solid composite films with visible-light-responsive optical properties. Note that the visible-light-responsive characteristics of PbS CNCs can be extended to alkanol solutions by coating the particle surface with a layer of silica. The silica surface renders the colloids compatible with other polar organic solutions, and the silanol surface also provides many anchors for linking other functional groups. The successful fabrication of visible-light-responsive polymer composite films reveals the great potential of these optically active materials in applications such as color sensors and optical switches.

Experimental Section

Synthesis of the PbS@SiO₂ Colloids: The PbS CNCs were synthesized by means of the high-temperature polyol-mediated reaction reported previously.^[27] Briefly, thiourea reacted with Pb(Ac)₂ at around 220 °C in diethylene glycol solution with polyacrylic acid as a capping agent. The size of the CNCs could be easily tuned by simply changing the molar ratio of thiourea to Pb(Ac)₂ while keeping all the other parameters fixed. PbS@SiO₂ core-shell particles were prepared by a modified Stöber process. Typically, an aqueous solution (3 mL) of PbS CNCs (ca. 95 mg) was mixed with ethanol (20 mL) and NH₃·H₂O (1 mL) at room temperature whilst stirring. TEOS (0.1 mL) was injected into the mixture every 20 min until the total volume reached 0.6 mL. After obtaining the silica shell with the desired thickness, the spheres were collected by centrifugation, washed with ethanol several times, and finally redispersed in ethanol (3 mL).

Synthesis of the PbS@SiO₂/PDMS Composite Film: PbS@SiO₂ core-shell particles were separated from the above ethanol solution (1.5 mL) and redispersed in EG (250 μL) by sonication. Then this EG solution was mixed with silicone elastomer prepolymer (4 g, Sylgard 184) and curing agent (0.75 g) under stirring and cross-linked in a small beaker at about 60 °C for 2 h.

The patterned PDMS composite film was prepared by introducing different colored PbS@SiO₂ particles. First, the as-prepared template of letters was placed on the glass slide, and PDMS precursor 1 (containing 150 nm of PbS core with 30 nm of silica shell) was added to fill the area around the template. After heating for around 2 h, the template was removed, and PDMS precursor 2 (containing 185 nm of PbS core with 30 nm of silica shell) was added to fill the area left by the template. After further heating, the film was finally cured.

SEM images were obtained with a JEOL JSM 6700F instrument. TEM and HRTEM images were recorded with a FEI Tecnai G2 S-Twin instrument with a field emission gun operating at 200 kV. All samples for TEM observation were prepared by dropping aqueous suspensions of uniformly dispersed nanoparticles onto carbon-coated copper grids. The IR spectra were acquired with a Bruker IFS 66v/S FTIR spectrometer. The absorption and reflectance spectra of the PbS CNCs and composite films at normal incidence were obtained with a Shimadzu UV-3600 spectrophotometer.

Supporting Information (see footnote on the first page of this article): FTIR spectra of PAA-capped PbS CNCs and SEM image of the PDMS composite film.

Acknowledgments

This work was supported by the National Natural Science Foundation of China (No. 20671040, 20971054 and 90922034), and the Specialized Research Fund for the Doctoral Program of Higher Education.

- [1] J. H. Holtz, S. A. Asher, *Nature* **1997**, *389*, 829–832.
- [2] A. van Blaaderen, *MRS Bull.* **1998**, *23*, 39–43.
- [3] O. D. Velev, A. M. Lenhoff, E. W. Kaler, *Science* **2000**, *287*, 2240–2243.
- [4] A. Blanco, E. Chomski, S. Grabtchak, M. Ibisate, S. John, S. W. Leonard, C. Lopez, F. Meseguer, H. Miguez, J. P. Mondia, G. A. Ozin, O. Toader, H. M. Van Driel, *Nature* **2000**, *405*, 437–440.
- [5] P. Jiang, G. N. Ostojic, R. Narat, D. M. Mittleman, V. L. Colvin, *Adv. Mater.* **2001**, *13*, 389–393.

- [6] P. V. Braun, S. A. Rinne, F. Garcia-Santamaria, *Adv. Mater.* **2006**, *18*, 2665–2678.
- [7] K. Matsubara, M. Watanabe, Y. Takeoka, *Angew. Chem.* **2007**, *119*, 1718; *Angew. Chem. Int. Ed.* **2007**, *46*, 1688–1692.
- [8] S. Colodrero, M. Ocana, H. Miguez, *Langmuir* **2008**, *24*, 4430–4434.
- [9] Y. J. Zhao, X. W. Zhao, J. Hu, M. Xu, W. J. Zhao, L. G. Sun, C. Zhu, H. Xu, Z. Z. Gu, *Adv. Mater.* **2009**, *21*, 569–572.
- [10] D. Xu, K. P. Chen, K. Ohlinger, Y. Lin, *Nanotechnology* **2011**, *22*, 035303.
- [11] Y. Liu, H. Dai, X. Sun, *J. Mater. Chem.* **2011**, *21*, 2982–2986.
- [12] J. F. Galisteo-López, M. Ibisate, R. Sapienza, L. S. Froufe-Pérez, Á. Blanco, C. López, *Adv. Mater.* **2011**, *23*, 30–69.
- [13] S. W. Leonard, J. P. Mondia, H. M. van Driel, O. Toader, S. John, K. Busch, A. Birner, U. Gsele, V. Lehmann, *Phys. Rev. B* **2000**, *61*, R2389–R2392.
- [14] Z. Z. Gu, A. Fujishima, O. Sato, *J. Am. Chem. Soc.* **2000**, *122*, 12387–12388.
- [15] K. Sumioka, H. Kayashima, T. Tsutsui, *Adv. Mater.* **2002**, *14*, 1284–1286.
- [16] M. Kamenjicki Maurer, I. K. Lednev, S. A. Asher, *Adv. Funct. Mater.* **2005**, *15*, 1401–1406.
- [17] U. Jeong, Y. Xia, *Angew. Chem.* **2005**, *117*, 3159; *Angew. Chem. Int. Ed.* **2005**, *44*, 3099–3103.
- [18] A. B. Pevtsov, D. A. Kurdyukov, V. G. Golubev, A. V. Akimov, A. A. Meluchev, A. V. Sel'kin, A. A. Kaplyanskii, D. R. Yakovlev, M. Bayer, *Phys. Rev. B* **2007**, *75*, 153101.
- [19] F. Fleischhaker, A. C. Arsenault, V. Kitaev, F. C. Peiris, G. von Freymann, I. Manners, R. Zentel, G. A. Ozin, *J. Am. Chem. Soc.* **2005**, *127*, 9318–9319.
- [20] E. T. Tian, J. X. Wang, Y. M. Zheng, Y. L. Song, L. Jiang, D. B. Zhu, *J. Mater. Chem.* **2008**, *18*, 1116–1122.
- [21] H. Kim, J. Ge, J. Kim, S.-E. Choi, H. Lee, H. Lee, W. Park, Y. Yin, S. Kwon, *Nat. Photonics* **2009**, *3*, 534–540.
- [22] M. Honda, T. Seki, Y. Takeoka, *Adv. Mater.* **2009**, *21*, 1801–1804.
- [23] J. H. Kang, J. H. Moon, S. K. Lee, S. G. Park, S. G. Jang, S. Yang, S. M. Yang, *Adv. Mater.* **2008**, *20*, 3061–3065.
- [24] D. P. Puzzo, A. C. Arsenault, I. Manners, G. A. Ozin, *Angew. Chem.* **2009**, *121*, 961; *Angew. Chem. Int. Ed.* **2009**, *48*, 943–947.
- [25] G. S. Wiederhecker, L. Chen, A. Gondarenko, M. Lipson, *Nature* **2009**, *462*, 633–636.
- [26] J. Ge, Y. Yin, *Angew. Chem. Int. Ed.* **2011**, *50*, 1492–1522.
- [27] C. Li, Y. Zhao, F. Li, Z. Shi, S. Feng, *Chem. Mater.* **2010**, *22*, 1901–1907.
- [28] Y. Xia, B. Gates, Y. Yin, Y. Lu, *Adv. Mater.* **2000**, *12*, 693–713.
- [29] A. Arsenault, F. Fleischhaker, G. von Freymann, V. Kitaev, H. Miguez, A. Mihi, N. Te'treault, E. Vekris, I. Manners, S. Aitchison, D. Perovic, G. A. Ozin, *Adv. Mater.* **2006**, *18*, 2779–2785.
- [30] Y. Liang, N. Hilal, P. Langston, V. Starov, *Adv. Colloid Interface Sci.* **2007**, *134–135*, 151–166.
- [31] S. R. Raghavan, H. J. Walls, S. A. Khan, *Langmuir* **2000**, *16*, 7920–7930.
- [32] J. Ren, S. Song, A. Lopez-Valdivieso, J. Shen, S. Lu, *J. Colloid Interface Sci.* **2001**, *238*, 279–284.
- [33] S. Song, C. Peng, *J. Dispersion Sci. Technol.* **2005**, *26*, 197–201.
- [34] M. Korn, E. Killmann, J. Eisenlauer, *J. Colloid Interface Sci.* **1980**, *76*, 7–18.
- [35] Y. Yin, Y. Lu, Y. Sun, Y. Xia, *Nano Lett.* **2002**, *2*, 427–430.
- [36] J. Ge, Y. Yin, *Adv. Mater.* **2008**, *20*, 3485–3491.

Received: October 26, 2011

Published Online: February 3, 2012

Metallomacrocyclic Complexes by Self-Assembly of Ni^{II} and Cu^{II} Ions and Chelating Bis(*N*-acylamidines)^[†]

Juliana Isabel Clodt,^[a] Roland Fröhlich,^[a] and Matthias Eul,^{[b][‡]} and Ernst-Ulrich Würthwein*^[a]

Keywords: Supramolecular chemistry / N,O ligands / Metallomacrocycles / Nickel / Copper

Bis(*N*-acylamidines) **1**, which contain various rigid or flexible spacer units with different spatial orientations, are potent bis(bidentate) ligands for the coordination of metal ions. Treatment of **1** with Ni^{II} or Cu^{II} salts gave two 2:2 (**3**) and four 3:3 (**4**) metallomacrocycles by self-assembly. The structures of the hitherto unknown products were determined by the geometry of the ligands that incorporate either linear or

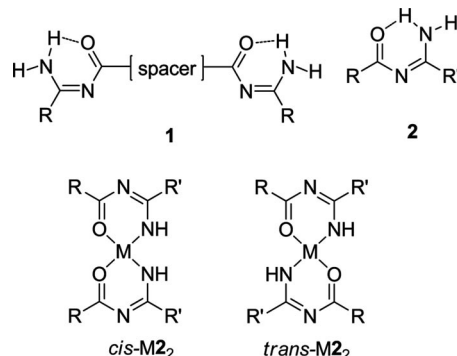
bent spacers between the two binding sites. Complex **3b** is especially interesting due to its two vinyl subunits orientated perpendicular to the plane of the molecule. Complexes **3** and **4** crystallize in planar layers with intercalated solvent molecules (*N,N*-dimethylformamide, dimethyl sulfoxide). The molecular structures of five coordination compounds in the solid state have been elucidated by X-ray diffraction.

Introduction

The synthesis of metallomacrocycles by the self-assembly of suitable ligands and metal ions is an important field of current interest in supramolecular coordination chemistry, not only from a structural point of view, but also with respect to molecular containers, catalysis, recognition, and magnetochemistry.^[1–3] A large number of literature examples are based on pyridyl or bipyridyl units, which assemble architectures such as triangles, squares, rectangles, polyhedra, and cages.^[4–6] Various synthetic approaches to design supramolecular architectures have been discussed by Holliday and Mirkin.^[5] The symmetry interaction approach,^[7] a method to design metallomacrocycles based on chelating ligands with two or more binding sites, has been widely used by Saalfrank,^[8–10] Lehn,^[11,12] and Raymond^[13] to assemble a variety of macrocyclic systems based on main-group and transition-metal coordination compounds.

We have used this approach to generate new macrocyclic complexes from bis(*N*-acylamidines) **1** as chelating ligands. *N*-Acylamidines **2** are interesting nitrogen-rich monodentate or bidentate ligands for metal-ion coordination.^[14–20] Compared to β -imino ketones^[21] and β -diimines,^[22] the nitrogen atom in the central 3-position alters the electronic structures at the binding sites considerably. Furthermore, conjugation over all five atoms is observed

even in the neutral form, and an additional coordination site is offered at the central nitrogen atom. The synthesis of 2:1 *N*-acylamidine/metal complexes was described by Ley and Werner in 1913 as a reaction of the ligands with metal(II) acetates.^[23] This reaction yielded neutral 2:1 metal complexes with anionic ligands, the structures of which were proven to be *trans* complexes by Oehme and Pracejus in 1969.^[24] The first platinum(II) complex of a chelating *N*-acylamidine has been recently reported.^[25] We have previously described several types of metal complexes formed from primary *N*-acylamidines and copper(II) or palladium(II) salts.^[14–16] In general, 2:1 metal complexes of **2** have been found to have *trans* or *cis* arrangements (Scheme 1).



Scheme 1. Bis(*N*-acylamidines) **1**, *N*-acylamidines **2**, and 2:1 metal complexes of primary **2** with *cis* and *trans* arrangements of the ligands.

To the best of our knowledge, no examples of 2:2 or 3:3 metallomacrocycles or higher-order assemblies of **1** as ligands have been reported. The coordination geometry of these ligands is expected to be similar to that of bis(β -diketones) or bis(*N*-acylthioureas), which have been synthesized

[†] Unsaturated Hetero Chains, XXI. Part XX: Ref.^[8]

[‡] Magnetic Measurements

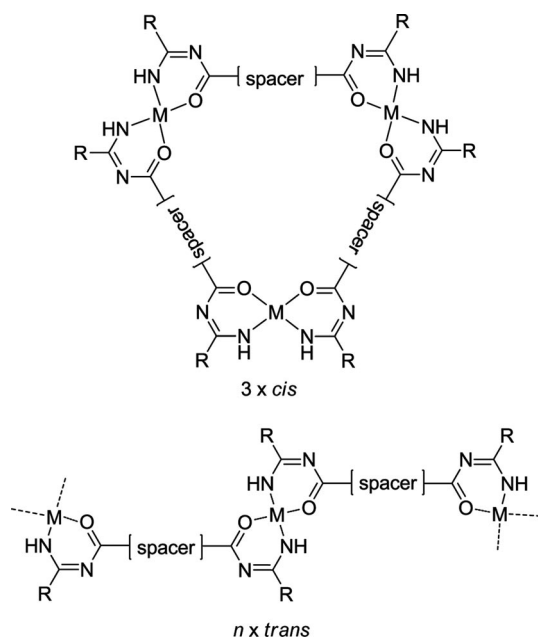
[a] Organisch-Chemisches Institut, Westfälische Wilhelms-Universität, Corrensstraße 40, 48149 Münster, Germany
Fax: +49-251-83-39772
E-mail: wurthwe@uni-muenster.de

[b] Institut für Anorganische und Analytische Chemie, Westfälische Wilhelms-Universität, Corrensstraße 38/30, 48149 Münster, Germany

and studied with respect to their coordination behavior by Reedijk et al.,^[26] Köhler et al.,^[27] Koch et al.,^[28,29] and Ugur et al.^[30] In this context, we were interested to learn, which types of assemblies were formed by metal complexation of such bis(bidentate) bis(*N*-acylamidines) with bulky, flexible, or rigid spacers of designed geometries. Such ligands have recently been synthesized in our laboratory for the first time.^[31,32]

Results and Discussion

The possibilities for the chelate binding of bis(*N*-acylamidines) **1** in a square-planar coordination environment to give *syn* and *anti* isomers with respect to the spatial orientation of the spacer groups are illustrated in Scheme 2. For *syn* isomers metallomacrocycles, for instance triangles, are expected, whereas *anti* isomers would lead to polymeric chains. Furthermore, the macrocyclic structures will be different if the ligand is not linear but bent, if the coordination

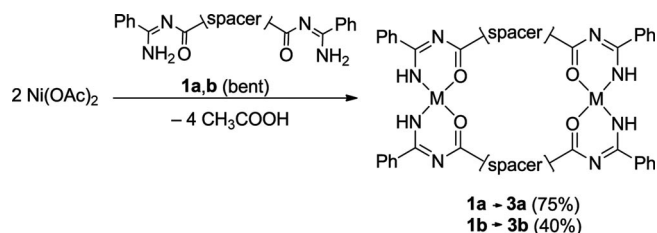


Scheme 2. Superstructures arising from *syn* and *anti* arrangements of the coordination sites for bis(*N*-acylamidine)metal complexes.

sphere is tetrahedral or octahedral, and if the linker has special steric properties. All these possibilities complicate the prediction of the structures of such metal complexes.

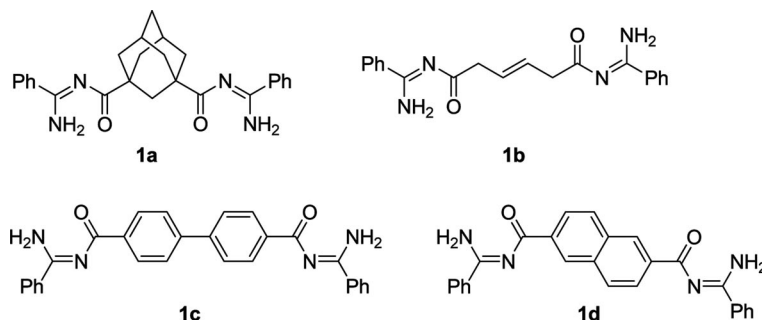
In this work, the coordination behavior of four different primary bis(*N*-acylamidines) **1** towards nickel(II) and copper(II) salts was examined (Scheme 3). The four ligands mainly differ with respect to their coordination geometry: **1a** bears the sterically fixed, bent 1,3-adamantanediyl spacer with a tetrahedral (109.5°) spatial orientation, which allows bis(coordination) in a parallel orientation. Ligand **1b** combines two flexible methylene units with a rigid (*E*)-configured olefinic subunit within the 2-butenediyl spacer. Here, one may expect various types of bis(coordination). Ligand **1c** has a linear biphenyl spacer, which may be subject to internal rotation, and **1d** contains a linear, inflexible 2,5-naphthlenediyl spacer. Ligands **1c** and **1d** allow bis(coordination) in a trigonal-planar (120°) orientation.

Ligands **1a** and **1b** were easily prepared from bis(*N*-acylbenzotriazoles) and *N*-phenylbenzamidines.^[31] Ligands **1c** and **1d** were synthesized by using diacyl dichlorides and benzamidines as precursors.^[32] The metal complexes (**3** and **4**) of these four ligands were generated by reaction of copper or nickel salts with *cis* coordination within the individual complexes and *syn* orientation with respect to the two binding sites. In general, **1a** and **1b**, with angled spacers, assemble 2:2 metallomacrocycles **3a** and **3b** (Scheme 4), whereas **1c** and **1d**, with linear spacers, led to triangular 3:3 metallomacrocycles **4a–d** (Scheme 5).



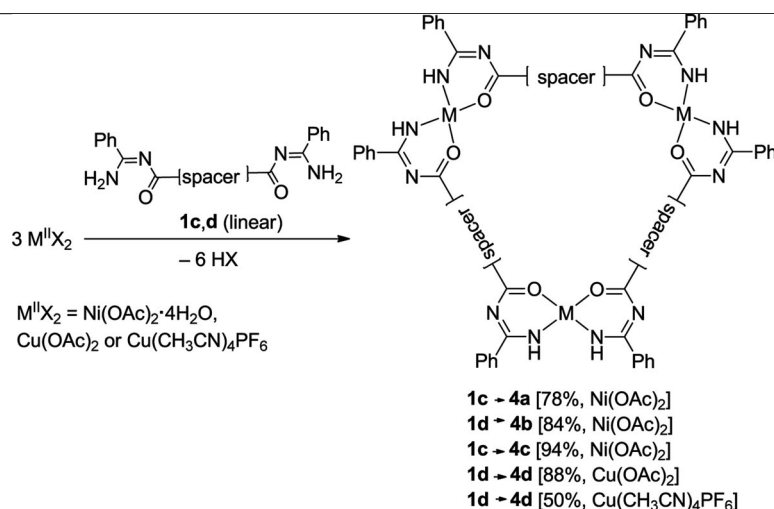
Scheme 4. Self-assembly of 2:2 metallomacrocycles **3a** and **3b** from bent **1a** and **1b** and nickel(II) salts.

In detail, 2:2 metallomacrocycles **3a** and **3b** were synthesized from metal acetates and **1a** and **1b** in *N,N*-dimethylformamide (DMF) at 40 °C in moderate to good yields (Scheme 4). Both compounds were crystalline solids, and their molecular structures were obtained by X-ray analysis.



Scheme 3. Bis(*N*-acylamidines) **1a–d**.

FULL PAPER

Scheme 5. Self-assembly of 3:3 metallamacrocycles **4a–d** from linear **1c** and **1d** and nickel(II) and copper(II) salts.

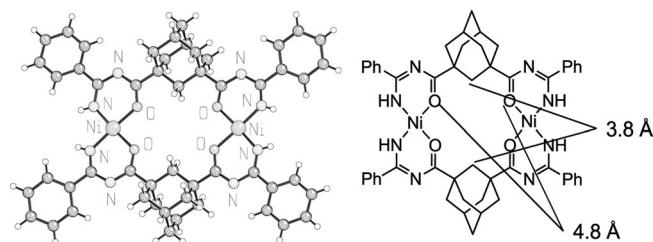
In order to generate 3:3 metallomacrocycles **4a–d**, 1 equiv. of **1c** or **1d** was treated with 1 equiv. of nickel(II) acetate, copper(II) acetate, or [Cu^I(CH₃CN)₄]PF₆ in DMF at 40 °C. In the case of the copper(I) salt, during the reaction copper(I) was oxidized to copper(II), most probably by air, which was not excluded. Four 3:3 metallomacrocycles **4a–d** were obtained in good yields (Scheme 5). Metallomacrocyclic **4d** was synthesized by two different ways, either by using copper(I) hexafluorophosphate or copper(II) acetate. The latter method gave the product in a higher yield.

These metallomacrocycles are only poorly soluble in polar and nonpolar solvents; thus, ¹H and ¹³C NMR spectra could not be obtained.

Description of the Structures

The crystal structures of **3a**, **3b**, **4a**, **4b**, and **4d** were determined by single-crystal X-ray diffraction. In order to generate crystals suitable for X-ray analysis, it was important to cool DMF or dimethyl sulfoxide (DMSO) solutions of the complexes very slowly to room temperature at a rate of around 10 °C/h without stirring. The crystallization process started at ca. 80 °C. Other crystallization methods are described in the Experimental Section. Many of the crystals contained intercalated solvent molecules (DMF, DMSO), which could not be removed even by prolonged evaporation in vacuo.

Complex **3a** crystallized in the triclinic space group *P* $\bar{1}$ with one metallomacrocyclic in the unit cell together with four molecules of DMSO (Figure 1, Table 1). The two nickel atoms are coordinated by two ligands to form square-planar *cis*-N,O chelates from the deprotonated *N*-acylamidine moieties. Small deviations from ideal square-planar geometry are observed with the Ni^{II} ion 0.009 Å above the plane. The size of the cavity formed is given by the distance between the two face-to-face adamantane units (3.8 Å) and the distance between two oxygen atoms of the same ligand (4.8 Å, Figure 1, right).

Figure 1. Molecular structure **3a** (left) and internal distances (right).Table 1. Selected (average) geometrical parameters for **3a**.

Distances [Å]		Angles [°]		Torsional angles [°]	
HN–C	1.303(4)	N–C–N	125.4(3)	N–C–N–C	2.9(6)
HN–C–N	1.353(4)	C–N–C	120.5(3)	C–N–C–O	3.9(6)
HN–C–N–C	1.326(4)	N–C–O	127.9(3)	N–C–O–Ni	2.5(5)
C–O	1.273(3)	C–O–Ni	126.7(2)	C–O–Ni–N	4.2(3)
O–Ni	1.848(2)	O–Ni–N	91.6(1)/176.4(1)	O–Ni–N–C	6.5(3)
Ni–N	1.833(3)	Ni–N–C	127.5(2)	Ni–N–C–N	4.9(6)

Selected bond lengths, bond angles, and torsion angles for **3a** (average of the two six-membered chelate rings), which are also typical for the other Ni^{II} complexes, are listed in Table 1. The O–Ni and N–Ni bond lengths are 1.848(2) and 1.833(3) Å, respectively, which are slightly shorter than those of nickel complexes of neutral *N*-acylamidines as expected. These bond lengths are comparable with 2:2 nickel macrocycles of bis(*N*-acylthioureas) and bis(*N*-acylisoureas).^[33] The data reveal the expected electron delocalization within the chelate ring. The shortest Ni–Ni distance is 6.44 Å.

The crystal packing of **3a** (Figure 2) is characterized by a layered structure wherein intercalated DMSO and the metallomacrocyclics are stacked on top of each other. Every second DMSO molecule is connected to two amino protons of the metal complex by hydrogen bonding (2.24 and 2.32 Å). The other solvent molecules are located in a layer

between two metallomacrocycles (Figure 2, bottom). There is little interaction of the DMSO molecules with the Ni^{II} ions as indicated by the Ni...S distance of 3.75 Å.

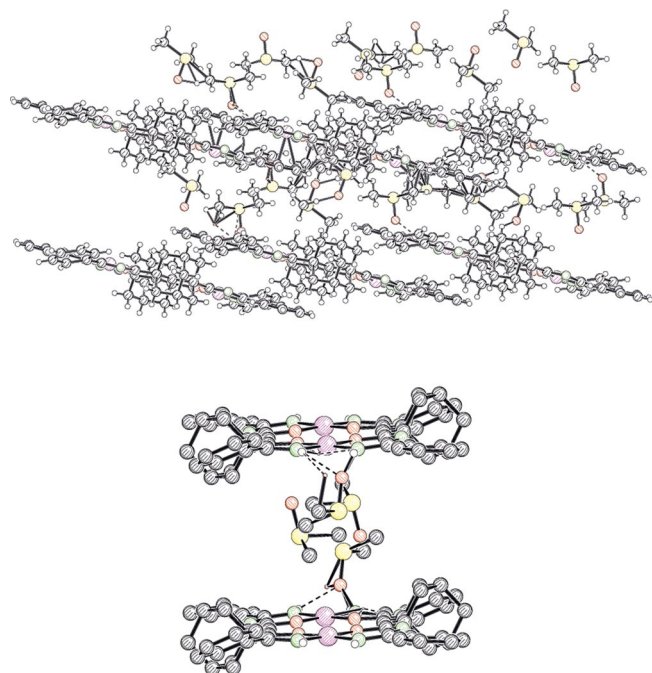


Figure 2. Crystal packing of **3a** (top) and hydrogen bonding between the layers with the intercalating DMSO molecules (bottom). Most hydrogen atoms are omitted for clarity.

Complex **3b** crystallized from the slow diffusion of diethyl ether into a solution of DMF. It crystallized in the monoclinic space group $P2_1/n$ with two metallomacrocycles in every unit cell together with four DMF molecules (Figure 3). Like **3a**, the two four-coordinate nickel ions are bridged by two deprotonated bis(*N*-acylamidines), which results in approximately square-planar bidentate *cis* coordination with the Ni^{II} ion approximately 0.004 Å above the plane. Interestingly, with respect to the geometry of the 2-butene-1,4-diyl spacer unit, the two olefin groups of the two ligands are orientated exactly parallel to each other (Figure 3, left) with the π orbitals arranged perpendicular to the plane of the macrocycle, which suggests an additional possibility for coordination inside the metallomacrocyclic, e.g. for late-transition metal ions. Thus, **1b** unexpectedly shows the same complexation behavior as **1a**, which has a bent adamantane-1,3-diyl spacer, with the ability to position the coordination sites in a parallel fashion. The distances between the opposing olefinic carbon atoms is 6.6 Å and that of the two oxygen atoms is 5.7 Å.

The crystal lattice of **3b** is characterized by separate layers of the macrocycles, which are interconnected by DMF molecules (Figure 4, bottom). Thus, the oxygen atoms of the DMF molecules are hydrogen-bonded to two *cis*-NH groups of the chelates (NH...O 2.17 and 2.22 Å) and to the oxygen atoms of the chelate of the next layer by the DMF CH group [O...CH(DMF) 2.42 Å]. The crystal packing (Figure 4, bottom) shows two different layers of metallomacrocycles stacked on top of each other with the shortest

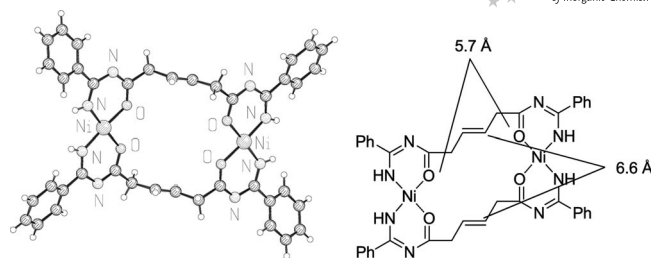


Figure 3. Molecular structure of **3b** (left) and internal distances (right).

Ni–Ni distance of 3.60 Å. The second layer completely covers the cavity between two layers of the same arrangement. Therefore, no channels were observed in the crystal structure. The structural parameters for the six-membered chelate rings are similar to those of **3b**.

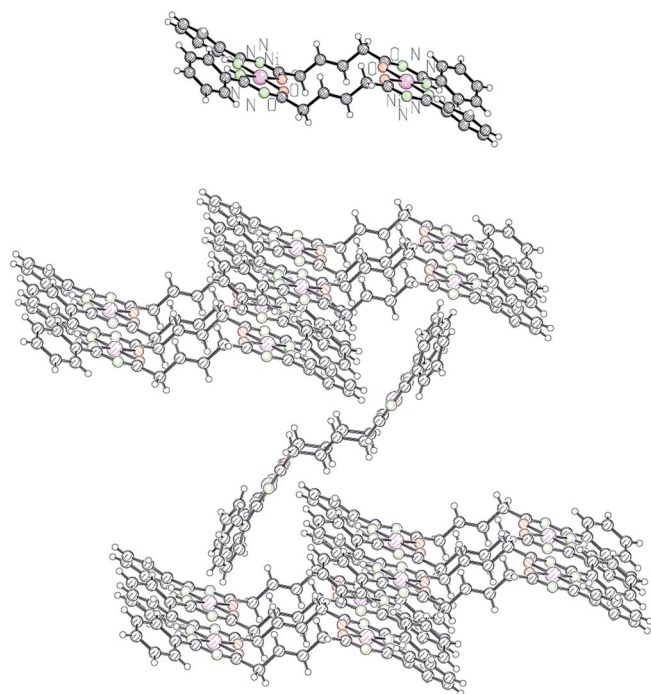
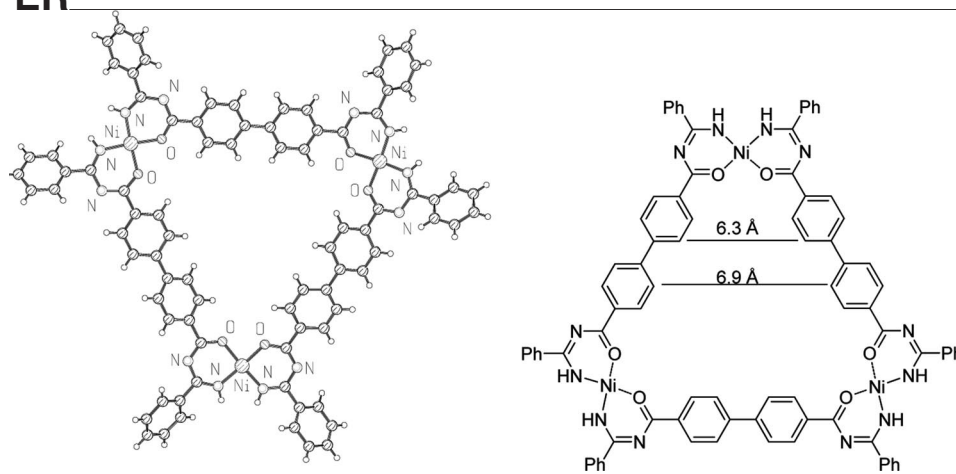


Figure 4. Another view of the molecular structure of **3b** (top) and crystal packing (bottom). Solvent molecules are omitted for clarity.

Complex **4a** (Figure 5) crystallizes in the triclinic space group $P\bar{1}$ with four metallomacrocycles in the unit cell together with 32 DMSO molecules. The three nickel ions are connected to three anionic *N*-acylamidine ligands in a square-planar *cis*-N,O chelate coordination. A minor deviation from ideal square-planar geometry is observed as the chelate rings are slightly twisted. The size of the internal cavity of the metallomacrocyclic measured between the aromatic protons of the spacer unit is 6.3 and 6.9 Å (Figure 5, right). The biphenyl spacer units are almost coplanar with the coordination sphere of the nickel atoms but display a torsion angle within the biphenyl system of about 30°. The planar macrocycles crystallize to form layers with an approximate distance of 3.6–3.8 Å. The bond lengths and

FULL PAPER

Figure 5. Molecular structure of **4a** (left) and internal distances (right).

angles resemble those of 2:2 nickel macrocycles of bis(*N*-acylamidines) and are comparable to 3:3 nickel macrocycles of bis(*N*-acylthioureas) with phenyl spacer units.^[27]

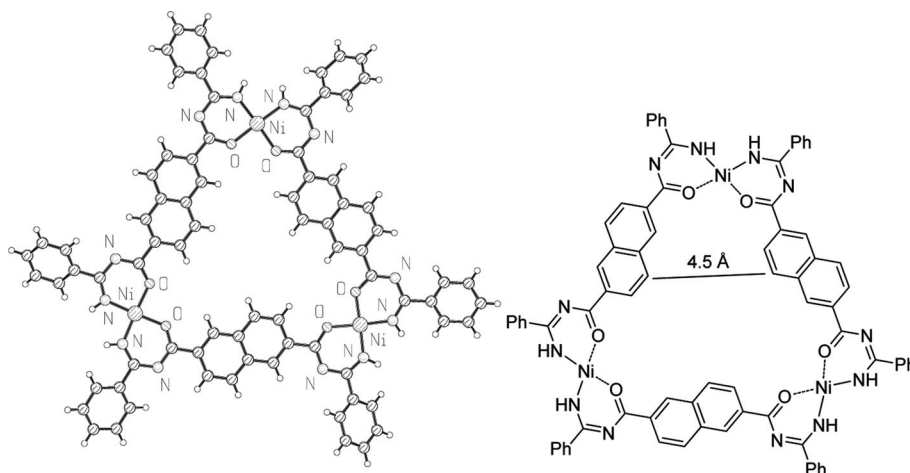
Complex **4b** crystallized in the trigonal space group $R\bar{3}$ with six metallomacrocycles per unit cell together with 18 DMSO molecules (Figure 6). The structural properties of this C_3 -symmetrical complex are similar to those of **4a**. Square-planar coordination spheres of the nickel atoms were found. The average N–Ni–O angle is $91.2(1)^\circ$, which leads to a small deviation from ideal square-planar geometry with the nickel atom approximately 0.019 \AA above the plane. This is also indicated by the torsion angles within the chelate ring system, which are between $1.6(8)$ and $8.2(8)^\circ$ and show substantial deviations from the ideal planar chelate ring system compared to **4a**, where all of the torsion angles are less than $5(6)^\circ$. The shortest distance between the aromatic protons of the two different ligands in the inside of the metallomacrocycle is 4.5 \AA (Figure 6, right).

The naphthalene units are coplanar with the nickel coordination spheres, whereas the phenyl substituents of the *N*-acylamidines are tilted [$-21.1(6)$ and $-40.9(6)^\circ$]. Three of the DMSO molecules are connected to the macrocycle by

hydrogen bonds to each two of the NH groups of the chelates (NH \cdots O 2.16 and 2.44 \AA). Similar to **4a**, **4b** crystallizes to form layers with distances of approximately 3.8 \AA .

The magnetic properties of **4b** in the solid state were measured in the temperature range of $3\text{--}300 \text{ K}$. The compound is essentially diamagnetic, which indicates that there is no significant interaction of the interlayer DMSO molecules with the nickel(II) ions. On the basis of these measurements, the nickel(II) ions can be described as square-planar.^[34]

Crystals of **4d** suitable for X-ray analysis were obtained from $[\text{Cu}(\text{CH}_3\text{CN})_4]\text{PF}_6$ and **1d** but not from Cu^{II} salts. The reactants were stirred in DMF in the presence of air so that the copper(I) salt was oxidized. The slightly yellow solution slowly turned blue on formation of copper(II). Slow diffusion of diethyl ether into the solution led to red crystals of **4d**. Complex **4d** crystallized in the triclinic space group $P\bar{1}$ with two metallomacrocycles in the unit cell together with a minimum of six molecules of DMF. Due to the presence of these solvent molecules, the structure could not be refined with high precision ($R_1 = 0.1011$, Figure 7). The three copper atoms are interconnected by three deproton-

Figure 6. Molecular structure of **4b** (left) and internal distances (right).

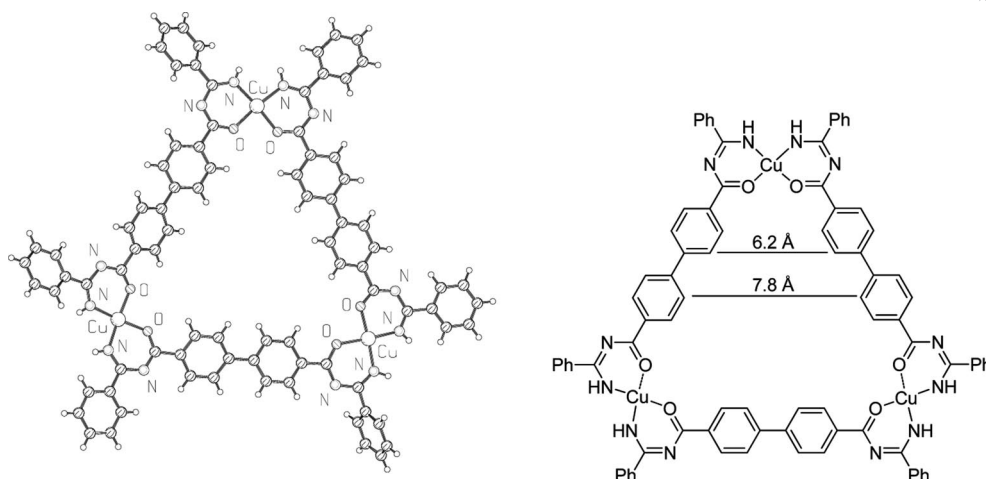


Figure 7. Molecular structure of **4d** (left) and internal distances (right).

ated *N*-acylamidine ligands in a square-planar *cis*-N,O coordination. Again, we observed small deviations from the ideal square-planar geometry, as the Cu^{II} ion is located 0.047 Å below the plane of the complex.

The internal distances of the metallomacrocyclic are 6.2 and 7.8 Å, measured between the aromatic protons of the spacer unit (Figure 7, right). The biphenyl spacer units are almost coplanar with the coordination sphere of the copper atoms but are tilted by about 25° within the biphenyl system. The average O–Cu and N–Cu bond lengths are 1.918(3) and 1.919(3) Å, respectively, which are slightly longer than those of **4a** as expected. The bond lengths of the *N*-acylamidine moieties reveal the expected electron delocalization within the chelate rings.

Conclusions

We have demonstrated that the bis(bidentate) bis(*N*-acylamidines) **1**, which incorporate various spacer units, are well suited for the preparation of supramolecular architectures by self-assembly. We obtained two 2:2 metallomacrocycles (**3a** and **3b**) from the bent **1a** and **1b**. The structure of **3b** is surprising, as – in spite of the (*E*) configuration of the alkenyl moieties – the two π bonds are located perpendicular to the molecular plane, which creates a cavity with internal π-donor properties. Furthermore, four 3:3 metallomacrocycles **4a–d** were obtained, which are characterized by planar structures and often crystallized in layers with intercalated solvent molecules (DMF, DMSO). Further work directed towards the synthesis of 3D coordination compounds based on *N*-acylamidine ligands is underway.

Experimental Section

Materials and Methods: IR spectra were recorded with a Varian 3100 FTIR spectrometer by using a Specac Golden Gate Single Reflection ATR sampling system. MALDI MS data were recorded with Lazarus IIIIDE (Organic Institut, Münster) or Reflex IV (Bruker Daltonics, Bremen) instruments by using an N₂ laser,

337 nm, 3 ns. CHN elemental analysis was performed with a Elementar Vario El III apparatus.

General Procedure (GP) for the Synthesis of **3a and **4a–d**:** A solution of metal acetate (0.1 mmol) in DMF (2 mL) was stirred at 40 °C until the metal salt had dissolved. The ligand (0.1 mmol) dissolved in DMF (2 mL) at 40 °C was added dropwise over 10 min, and the mixture was stirred at 40 °C for 30 min. The metal complex precipitated immediately or on cooling to room temperature. The solid was collected by filtration and washed with a small amount of DMF. The products were purified as stated below.

***cis*-[Ni{(1a-2H)-N,O}]₂ (**3a**):** Adamantane-1,3-dicarboxylic acid bis(1-amino-1-phenylmethylideneamide) (**1a**, 42.8 mg (0.100 mmol)) and Ni(OAc)₂·4H₂O (24.7 mg, 0.100 mmol) were treated according to the GP. Recrystallization from DMSO gave orange crystals. Yield: 36.2 mg (0.037 mmol, 75%). M.p. >300 °C. IR (ATR): $\tilde{\nu}$ = 3069 (vw), 2932 (w), 2903 (m), 2853 (w), 1591 (m), 1545 (s), 1479 (m), 1452 (s), 1429 (m), 1414 (m), 1377 (s), 1350 (m), 1325 (m), 1308 (s), 1258 (m), 1240 (m), 1140 (w), 1103 (w), 1030 (w), 1003 (w), 957 (w), 918 (w), 793 (w), 758 (w), 704 (s), 685 (vs) cm⁻¹. MS (MALDI, matrix DCTB {*trans*-2-[3-(4-*tert*-butylphenyl)-2-methyl-2-propenylidene]malononitrile}): m/z = 969–976 [C₅₂H₅₂N₈Ni₂O₄ + H]⁺. C₅₂H₅₂N₈Ni₂O₄ (970.4): calcd. C 64.36, H 5.40, N 11.55; found C 64.11, H 5.38, N 11.52.

X-ray Crystal Structure Analysis of **3a:**^[35] C₅₂H₅₂N₈Ni₂O₄·4C₂H₆OS, M = 1282.95, orange crystal, 0.40 × 0.15 × 0.07 mm, a = 10.4056(4), b = 12.3064(7), c = 13.0618(4) Å, α = 64.856(3), β = 83.375(3), γ = 86.827(2)°, V = 1503.99(11) Å³, $\rho_{\text{calcd.}}$ = 1.416 g cm⁻³, μ = 0.826 mm⁻¹, empirical absorption correction (0.734 ≤ T ≤ 0.944), Z = 1, triclinic, space group $P\bar{1}$ (No. 2), λ = 0.71073 Å, T = 223(2) K, ω and ϕ scans, 17245 reflections collected ($\pm h$, $\pm k$, $\pm l$), $[(\sin\theta)/\lambda]$ = 0.66 Å⁻¹, 7092 independent (R_{int} = 0.064) and 4484 observed reflections [$I \geq 2\sigma(I)$], 380 refined parameters, R = 0.061, wR^2 = 0.177, max. (min.) residual electron density 0.72 (–1.07) e Å⁻³, hydrogen atoms at N1 found from difference fourier calculations, others calculated and refined as riding atoms.

***cis*-[Ni{(1b-2H)-N,O}]₂ (**3b**):** A solution of Ni(OAc)₂·4H₂O (24.7 mg, 0.100 mmol) in DMF (2 mL) was stirred at 40 °C until the metal salt had dissolved. (*E*)-Hex-3-enedioic acid bis(1-amino-1-phenylmethylideneamide) (**1b**, 34.8 mg, 0.100 mmol) dissolved in DMF (2 mL) at 40 °C was added dropwise to the metal salt solution over 10 min, and the mixture was stirred for 30 min. Slow diffusion of diethyl ether (5 mL) into the DMF solution led to red

FULL PAPER

crystals of **3b** within a week. The crystals were collected by filtration and dried under vacuum. Yield: 16.6 mg (0.020 mmol, 40%). M.p. 140 °C (decomposition). IR (ATR): $\tilde{\nu}$ = 3217 (w), 2930 (vw), 1653 (m), 1553 (s), 1408 (vs), 1342 (m), 1256 (w), 1101 (w), 1049 (w), 1028 (w), 926 (w), 824 (w), 779 (m), 754 (w), 737 (w), 675 (s), 665 (s), 615 (s) cm^{-1} . MS (MALDI): m/z = 809.1 [$\text{C}_{40}\text{H}_{36}\text{N}_8\text{Ni}_2\text{O}_4 + \text{H}$] $^+$.

X-ray Crystal Structure Analysis of 3b:^[35] $\text{C}_{40}\text{H}_{36}\text{N}_8\text{Ni}_2\text{O}_4 \cdot 2\text{C}_3\text{H}_7\text{NO}$, M = 956.38, orange crystal, $0.35 \times 0.25 \times 0.03$ mm, a = 10.5711(2), b = 16.8185(3), c = 15.5769(2) Å, β = 90.504(1)°, V = 2769.31(8) Å³, $\rho_{\text{calcd.}}$ = 1.147 g cm^{-3} , μ = 0.729 mm^{-1} , empirical absorption correction (0.785 $\leq T \leq$ 0.979), Z = 2, monoclinic, space group $P2_1/n$ (No. 14), λ = 0.71073 Å, T = 223(2) K, ω and ϕ scans, 20639 reflections collected ($\pm h$, $\pm k$, $\pm l$), $[(\sin\theta)/\lambda]$ = 0.66 Å⁻¹, 6462 independent (R_{int} = 0.046) and 5410 observed reflections [$I \geq 2\sigma(I)$], 297 refined parameters, R = 0.059, wR^2 = 0.183, max. (min.) residual electron density 0.57 (−0.52) e Å^{-3} ; other solvents (probably diethyl ether) could not be refined in a chemically meaningful way, therefore, the SQUEEZE routine was used, hydrogen atoms at N1 and N12 were found from difference fourier calculations, others were calculated and refined as riding atoms.

cis-[Ni{(1c-2H)-N,O}]₃ (4a): Biphenyl-4,4'-dicarboxylic acid bis(1-amino-1-phenylmethyldeneamide) (**1c**, 44.6 mg, 0.100 mmol) and $\text{Ni}(\text{OAc})_2 \cdot 4\text{H}_2\text{O}$ (24.7 mg, 0.100 mmol) were treated according to the GP. In order to obtain crystals, the solid was recrystallized from DMSO to give orange crystals. Yield: 45.5 mg (0.028 mmol, 84%). M.p. > 300 °C. IR (ATR): $\tilde{\nu}$ = 3304 (w), 3061 (w), 1607 (vw), 1589 (w), 1566 (m), 1533 (m), 1495 (w), 1452 (m), 1423 (s), 1404 (m), 1369 (vs), 1302 (m), 1271 (m), 1246 (m), 1180 (m), 1157 (m), 1057 (w), 1028 (m), 1003 (m), 847 (m), 810 (m), 795 (m), 756 (s), 704 (vs), 644 (m), 629 (m) cm^{-1} . MS (MALDI): m/z = 1509.3 [$\text{C}_{84}\text{H}_{60}\text{N}_{12}\text{Ni}_3\text{O}_6 + \text{H}$] $^+$. $\text{C}_{84}\text{H}_{60}\text{N}_{12}\text{Ni}_3\text{O}_6 + 1.5$ DMSO (1626.7): calcd. C 64.23, H 4.28, N 10.33; found C 64.25, H 4.21, N 10.54.

X-ray Crystal Structure Analysis of 4a:^[35] $\text{C}_{84}\text{H}_{60}\text{N}_{12}\text{Ni}_3\text{O}_6 \cdot 8\text{C}_2\text{H}_6\text{OS}$, M = 2134.59, orange crystal, $0.40 \times 0.30 \times 0.05$ mm, a = 15.5954(2), b = 22.4297(3), c = 30.5163(5) Å, α = 91.203(1), β = 93.253(1), γ = 102.921(2)°, V = 10381.3(3) Å³, $\rho_{\text{calcd.}}$ = 1.366 g cm^{-3} , μ = 0.766 mm^{-1} , empirical absorption correction (0.749 $\leq T \leq$ 0.963), Z = 4, triclinic, space group $P\bar{1}$ (No. 2), λ = 0.71073 Å, T = 223(2) K, ω and ϕ scans, 58596 reflections collected ($\pm h$, $\pm k$, $\pm l$), $[(\sin\theta)/\lambda]$ = 0.59 Å⁻¹, 35585 independent (R_{int} = 0.069) and 24804 observed reflections [$I \geq 2\sigma(I)$], 2499 refined parameters, R = 0.123, wR^2 = 0.330, max. (min.) residual electron density 3.61 (−2.46) e Å^{-3} ; hydrogen atoms were calculated and refined as riding atoms, solvent molecules were refined with geometrical and thermal restraints, weakly diffracting crystals of poor quality.

cis-[Ni{(1d-2H)-N,O}]₃ (4b): Naphthalene-2,6-dicarboxylic acid bis(1-amino-1-phenylmethyldeneamide) (**1d**, 42.0 mg, 0.100 mmol) and $\text{Ni}(\text{OAc})_2 \cdot 4\text{H}_2\text{O}$ (24.7 mg, 0.100 mmol) were treated according to the GP. In order to obtain crystals suitable for X-ray analysis, the solid was recrystallized from DMSO to give orange crystals. Yield: 37.0 mg (0.026 mmol, 78%). M.p. > 300 °C. IR (ATR): $\tilde{\nu}$ = 3059 (vw), 3026 (vw), 1601 (vw), 1587 (w), 1537 (s), 1456 (m), 1425 (m), 1391 (s), 1354 (s), 1261 (m), 1242 (m), 1200 (m), 1184 (m), 1146 (w), 1117 (m), 1051 (w), 1028 (w), 1001 (w), 966 (w), 918 (m), 822 (w), 770 (s), 691 (vs) cm^{-1} . MS (MALDI, matrix DCTB): m/z = 1429–1431 [$\text{C}_{78}\text{H}_{54}\text{N}_{12}\text{Ni}_3\text{O}_6 + \text{H}$] $^+$. $\text{C}_{78}\text{H}_{54}\text{N}_{12}\text{Ni}_3\text{O}_6$ (1431.4): calcd. C 65.45, H 3.80, N 11.74; found C 64.93, H 3.89, N 11.67.

X-ray Crystal Structure Analysis of 4b:^[35] $\text{C}_{78}\text{H}_{54}\text{N}_{12}\text{Ni}_3\text{O}_6 \cdot 3\text{C}_2\text{H}_6\text{OS}$, M = 1665.85, orange crystal, $0.15 \times 0.12 \times 0.03$ mm, a = 26.2897(4), c = 19.8066(4) Å, V = 11855.3(3) Å³, $\rho_{\text{calcd.}}$ = 1.400 g cm^{-3} , μ = 0.853 mm^{-1} , empirical absorption correction

(0.883 $\leq T \leq$ 0.975), Z = 6, trigonal, space group $R\bar{3}$ (No. 148), λ = 0.71073 Å, T = 223(2) K, ω and ϕ scans, 18683 reflections collected ($\pm h$, $\pm k$, $\pm l$), $[(\sin\theta)/\lambda]$ = 0.66 Å⁻¹, 6280 independent (R_{int} = 0.050) and 4664 observed reflections [$I \geq 2\sigma(I)$], 342 refined parameters, R = 0.0601, wR^2 = 0.136, max. (min.) residual electron density 0.94 (−0.37) e Å^{-3} ; hydrogen atoms at N1 and N18 were found from difference fourier calculations, others were calculated and refined as riding atoms.

cis-[Cu{(1d-2H)-N,O}]₃ (4c): Naphthalene-2,6-dicarboxylic acid bis(1-amino-1-phenylmethyldeneamide) (**1d**, 42.0 mg, 0.100 mmol) and $\text{Cu}(\text{OAc})_2$ (18.1 mg, 0.100 mmol) were treated according to the GP. The precipitate was collected by filtration and washed with DMF (2 mL), toluene (2 mL), and pentane (2 mL) to give a brown solid. Yield: 45.3 mg (0.031 mmol, 94%). M.p. > 300 °C. IR (ATR): $\tilde{\nu}$ = 3325 (w), 3267 (w), 3065 (vw), 2922 (vw), 2884 (vw), 1665 (m), 1589 (w), 1543 (s), 1470 (m), 1454 (s), 1422 (s), 1383 (s), 1350 (vs), 1256 (m), 1234 (m), 1198 (m), 1188 (m), 1115 (m), 1092 (m), 1055 (m), 1028 (m), 1001 (w), 924 (m), 827 (m), 797 (m), 762 (vs), 689 (s), 660 (m) cm^{-1} . MS (MALDI, matrix DCTB): m/z = 1443–1450 [$\text{C}_{78}\text{H}_{54}\text{N}_{12}\text{Cu}_3\text{O}_6 + \text{H}$] $^+$. $\text{C}_{78}\text{H}_{54}\text{N}_{12}\text{Cu}_3\text{O}_6$ (1446.0): calcd. C 64.79, H 3.76, N 11.62; found C 64.38, H 3.76, N 11.58.

cis-[Cu{(1c-2H)-N,O}]₃ (4d). **Method 1:** Ligand **1c** (44.6 mg, 0.100 mmol) and $\text{Cu}(\text{OAc})_2$ (18.1 mg, 0.100 mmol) were treated according to the GP. The precipitate was collected by filtration and washed with DMF (2 mL), toluene (2 mL), and pentane (2 mL). Yield: 45.1 mg (0.029 mmol, 88%). **Method 2:** Ligand **1c** (44.6 mg, 0.100 mmol) was dissolved in DMF (1 mL) and added dropwise to a solution of $[\text{Cu}(\text{CH}_3\text{CN})_4]\text{PF}_6$ (37.2 mg, 0.100 mmol) in DMF (1 mL). On stirring for 15 min, the solution slowly turned blue due to the formation of copper(II). Slow diffusion of diethyl ether into the solution led to red crystals of **4d** within a week. The crystals were collected by filtration and dried under vacuum. Yield: 26.0 mg (0.017 mmol, 50%). M.p. > 300 °C. IR (ATR): $\tilde{\nu}$ = 3314 (vw), 3063 (vw), 2926 (vw), 2870 (vw), 1661 (m), 1589 (m), 1568 (m), 1535 (s), 1495 (m), 1454 (s), 1425 (s), 1406 (m), 1366 (vs), 1256 (m), 1231 (m), 1180 (m), 1155 (m), 1096 (m), 1028 (w), 1003 (m), 934 (w), 851 (m), 795 (m), 754 (s), 745 (m), 708 (s), 660 (m) cm^{-1} . MS (MALDI, matrix DCTB): m/z = 1546–1550 [$\text{C}_{84}\text{H}_{60}\text{N}_{12}\text{Cu}_3\text{O}_6 + \text{Na}$] $^+$. $\text{C}_{84}\text{H}_{60}\text{Cu}_3\text{N}_{12}\text{O}_6 + 0.5$ DMF (1557.8): calcd. C 65.80, H 4.10, N 11.22; found C 65.64, H 4.04, N 10.97.

X-ray Crystal Structure Analysis of 4d:^[35] $\text{C}_{84}\text{H}_{60}\text{Cu}_3\text{N}_{12}\text{O}_6 \cdot 3\text{C}_3\text{H}_7\text{NO}$, M = 1743.35, red crystal, $0.40 \times 0.35 \times 0.10$ mm, a = 13.3524(2), b = 13.4896(3), c = 25.5935(6) Å, α = 79.232(1), β = 76.486(1), γ = 79.531(1)°, V = 4357.08(16) Å³, $\rho_{\text{calcd.}}$ = 1.329 g cm^{-3} , μ = 0.792 mm^{-1} , empirical absorption correction (0.742 $\leq T \leq$ 0.925), Z = 2, triclinic, space group $P\bar{1}$ (No. 2), λ = 0.71073 Å, T = 223(2) K, ω and ϕ scans, 58467 reflections collected ($\pm h$, $\pm k$, $\pm l$), $[(\sin\theta)/\lambda]$ = 0.66 Å⁻¹, 20282 independent (R_{int} = 0.071) and 14756 observed reflections [$I \geq 2\sigma(I)$], 1118 refined parameters, R = 0.075, wR^2 = 0.210, max. (min.) residual electron density 1.14 (−0.89) e Å^{-3} ; other solvents could not be identified in a chemically meaningful way, therefore the SQUEEZE routine was used, hydrogen atoms at N1 were found from difference fourier calculations, others were calculated and refined as riding atoms, some phenyl groups show disorder (refined for C12E–C17E).

Acknowledgments

We are grateful to cand. chem. Thomas Bucher for experimental help and Dr. Christof Wigbers for preliminary experiments in this field. We thank Prof. Dr. R. W. Saalfrank, Erlangen, for helpful discussions. This work was supported by the International Re-

search Training Group 1444 Münster–Amsterdam (DFG) and the Fonds der Chemischen Industrie (Frankfurt).

- [1] E. Zangrando, M. Casanova, E. Alessio, *Chem. Rev.* **2008**, *108*, 4979–5013 and references cited therein.
- [2] J. M. Lehn, *Science* **2002**, *295*, 2400–2403.
- [3] G. F. Swiegers, T. J. Malefetse, *Coord. Chem. Rev.* **2002**, *225*, 91–121.
- [4] M. Fujita, K. Ogura, *Coord. Chem. Rev.* **1996**, *148*, 249–264; M. Fujita, *Chem. Soc. Rev.* **1998**, *27*, 417–425.
- [5] B. J. Holliday, C. A. Mirkin, *Angew. Chem.* **2001**, *113*, 2076–2097.
- [6] J. M. Lehn, *Supramolecular Chemistry*, VCH, Weinheim, New York, Basel, Cambridge, Tokyo, **1995**.
- [7] S. Leininger, B. Olenyuk, P. J. Stang, *Chem. Rev.* **2000**, *100*, 853–908.
- [8] R. W. Saalfrank, I. Bernt, E. Uller, F. Hampel, *Angew. Chem.* **1997**, *109*, 2596; *Angew. Chem. Int. Ed. Engl.* **1997**, *36*, 2482–2485.
- [9] R. W. Saalfrank, R. Burak, S. Reihs, N. Low, F. Hampel, H. D. Stachel, J. Lentmaier, K. Peters, E. M. Peters, H. G. von Schnering, *Angew. Chem.* **1995**, *107*, 1085; *Angew. Chem. Int. Ed. Engl.* **1995**, *34*, 993–995.
- [10] R. W. Saalfrank, H. Maid, A. Scheurer, *Angew. Chem.* **2008**, *120*, 8924–8956; *Angew. Chem. Int. Ed.* **2008**, *47*, 8794–8824.
- [11] P. N. W. Baxter, J. M. Lehn, G. Baum, D. Fenske, *Chem. Eur. J.* **1999**, *5*, 102–112.
- [12] P. N. W. Baxter, J. M. Lehn, B. O. Kneisel, G. Baum, D. Fenske, *Chem. Eur. J.* **1999**, *5*, 113–120.
- [13] D. L. Caulder, K. N. Raymond, *Acc. Chem. Res.* **1999**, *32*, 975–982.
- [14] J. K. Eberhardt, R. Fröhlich, E.-U. Würthwein, *J. Org. Chem.* **2003**, *68*, 6690–6694.
- [15] J. K. Eberhardt, R. Fröhlich, S. Venne-Dunker, E.-U. Würthwein, *Eur. J. Inorg. Chem.* **2000**, 1739–1743.
- [16] J. K. Eberhardt, T. Glaser, R.-D. Hoffmann, R. Fröhlich, E.-U. Würthwein, *Eur. J. Inorg. Chem.* **2005**, 1175–1181.
- [17] C. Wigbers, J. Prigge, Z. Mu, R. Fröhlich, L. Chi, E.-U. Würthwein, *Eur. J. Org. Chem.* **2011**, 861–877.
- [18] J. C. J. Bart, J. W. Bassi, M. Calcaterra, M. Pieroni, *Inorg. Chim. Acta* **1978**, *28*, 201–210.
- [19] M. J. Carney, P. J. Walsh, F. J. Hollander, R. G. Bergman, *Organometallics* **1992**, *11*, 761–777.
- [20] K. Hiraki, Y. Kinoshita, J. Kinoshita-Kawashima, H. Kawano, *J. Chem. Soc., Dalton Trans.* **1996**, 291–298.
- [21] I.-M. Lee in *Focus on Organometallic Chemistry Research* (Ed.: M. A. Casto), Nova Science Publishers, Inc. New York, Chapt. 5, p. 133, **2005**.
- [22] L. Bourget-Merk, M. F. Lappert, J. R. Severn, *Chem. Rev.* **2002**, *102*, 3031–3066.
- [23] H. Ley, F. Werner, *Ber. Dtsch. Chem. Ges.* **1913**, *46*, 4040–4049.
- [24] G. Oehme, H. Pracejus, *Z. Chem.* **1969**, *9*, 140–141.
- [25] T. B. Anisimova, N. A. Bokach, K. V. Luzyanin, M. Haukka, V. Yu. Kukushkin, *Dalton Trans.* **2010**, *39*, 10790–10998.
- [26] G. Aromi, P. Gamez, J. Reedijk, *Coord. Chem. Rev.* **2008**, *252*, 964–989.
- [27] R. Köhler, R. Kirmse, R. Richter, J. Siehler, E. Hoyer, *Z. Anorg. Allg. Chem.* **1986**, *537*, 133–144.
- [28] K. R. Koch, S. A. Bourne, A. Coetzee, J. Miller, *J. Chem. Soc., Dalton Trans.* **1999**, 3157–3161.
- [29] O. Hallale, S. R. Bourne, K. R. Koch, *CrystEngComm* **2005**, *7*, 161–166.
- [30] D. Ugur, H. Arslan, N. Külcü, *Russ. J. Coord. Chem.* **2006**, *32*, 669–675.
- [31] J. I. Clodt, V. D. Hack, R. Fröhlich, E.-U. Würthwein, *Synthese* **2010**, 1485–1492.
- [32] J. I. Clodt, C. Wigbers, R. Reiermann, R. Fröhlich, E.-U. Würthwein, *Eur. J. Org. Chem.* **2011**, 3197–3298.
- [33] U. Schröder, L. Beyer, R. Richter, J. Angulo-Cornejo, M. Castillo-Montoya, M. Lino-Pacheco, *Inorg. Chim. Acta* **2003**, *353*, 59–67.
- [34] Above 270 K, the thermal variation of the molar susceptibility exceeds the value of the product $\chi_M T = 0.375 \text{ emu K mol}^{-1}$. With regard to the number of three nickel(II) atoms per molecule, we interpret this observation by the presence of a small amount of a paramagnetic impurity.
- [35] Data sets were collected with Nonius KappaCCD diffractometers, equipped with a rotating anode generator. Programs used: data collection COLLECT (Nonius B. V., **1998**), data reduction Denzo-SMN (Z. Otwinowski, W. Minor, *Methods Enzymol.* **1997**, *276*, 307–326), absorption correction SORTAV (R. H. Blessing, *Acta Crystallogr., Sect. A* **1995**, *51*, 33–37; R. H. Blessing, *J. Appl. Crystallogr.* **1997**, *30*, 421–426) and Denzo (Z. Otwinowski, D. Borek, W. Majewski, W. Minor, *Acta Crystallogr., Sect. A* **2003**, *59*, 228–234), structure solution SHELXS-97 (G. M. Sheldrick, *Acta Crystallogr., Sect. A* **1990**, *46*, 467–473), structure refinement SHELXL-97 (G. M. Sheldrick, *Acta Crystallogr., Sect. A* **2008**, *64*, 112–122), graphics SCHAKAL (E. Keller, University of Freiburg, **1997**). CCDC-854332 (for **3a**), -854333 (for **3b**), -854334 (for **4a**), -854335 (for **4b**), and -854336 (for **4d**) contain the supplementary crystallographic data for this paper. These data can be obtained free of charge from The Cambridge Crystallographic Data Centre via www.ccdc.cam.ac.uk/data_request/cif.

Received: December 2, 2011

Published Online: February 8, 2012

New Yttrium and Europium(+3) Alkoxides Bearing Thiophene Units: Syntheses, Crystal Structure Determinations and Physico-Chemical Properties

Michael Veith,^{*,[a,b]} Céline Belot,^[a,b,c] and Volker Huch^[a]

Keywords: Electroluminescent materials / Electrochemistry / Luminescence / Lanthanides / Yttrium / Europium

The synthesis, structural characterization, electrochemistry and luminescence properties of a series of new yttrium and europium(+3) alkoxides bearing thiophene moieties are presented. The yttrium compounds were obtained by the reaction between $Y[N(SiMe_3)_2]_3$ and the tertiary alcohols $HO-C(C_{16}H_{13}S)$ (**2**), $HO-C(C_{17}H_{15}S)$ (**3**), $HO-C(C_{14}H_{11}S_2)$ (**4**) and $HO-C(C_{16}H_{13}S)$ (**5**) in thf or in a mixture of toluene and pyridine. The X-ray crystal diffraction measurements show a five-coordinated yttrium atom in distorted trigonal-bipyramidal geometry. The metal centres are surrounded by three methoxido ligands in equatorial positions and two tetrahydrofuran [for $Y[OC(C_{16}H_{13}S)]_3(thf)_2 \cdot toluene$ (**8**), $Y[OC(C_{17}H_{15}S)]_3(thf)_2 \cdot toluene$ (**10**) and $Y[OC(C_{14}H_{11}S_2)]_3(thf)_2 \cdot 1/2 toluene$ (**12**)] or two pyridine [for $Y[OC(C_{16}H_{13}S)]_3(py)_2 \cdot toluene$ (**9**) and $Y[OC(C_{17}H_{15}S)]_3(py)_2 \cdot toluene$ (**11**)] molecules in axial positions. The compounds $Y[OC(C_{14}H_{11}S_2)]_3(py)_2$ (**13**) and $Y[OC(C_{16}H_{13}S)]_3(py)_2$ (**14**) were identified by NMR spectroscopy. In addition, a novel europium(+3) alkoxide $[Eu[OC(C_4H_3S)_3]_3(thf)_3] \cdot thf$ (**15**) was synthesized by the reaction between $Eu[N(SiMe_3)_2]_3$ and the

tertiary alcohol $HO-C(C_4H_3S)_3$ (**1**) in thf. The molecular structure of this compound reveals an approximately octahedral coordination sphere around the europium(+3) metal centre with three methoxido ligands and three facially arranged tetrahydrofuran molecules. The cyclic voltammograms of the yttrium alkoxides indicate that the electrochemical properties are essentially dominated by the organic ligands. The electrochemical properties of $[Eu[OC(C_4H_3S)_3]_3(thf)_3] \cdot thf$ (**15**) are dominated by the oxidation of the thienyl moieties and in addition a reduction wave due to the reduction of Eu^{3+} to Eu^{2+} is visible. In comparison to the carbinols, the oxidation peak potentials of the thienyl units for the yttrium and europium(+3) alkoxides are marginally shifted towards higher values. The emission spectra of the carbinols and their derived yttrium compounds display broad bands attributed to the $\pi^* \rightarrow \pi$ transitions of the aromatic ligands. Luminescence studies performed on compound **15** reveal the typical f–f transitions of the Eu^{3+} ions and suggest that an energy transfer from the ligand to the metal atom operates.

Introduction

During the last decade, the reactivity of rare earth metals towards organic ligands has been investigated due to attractive luminescence properties of the synthesized molecules and their applications in electronic materials and biological systems.^[1]

However, the compounds of Sc, Y, La, Gd and Lu belong to the group of ligand-emission systems. Indeed, Sc, Y and La in their trivalent state do not possess f electrons in outer shells and the high energy levels of their d electrons inhibit the emission occurring from the metal electronic states. Nevertheless, this group of metal derivatives has attracted special attention as they are used for the production of electroluminescent materials.^[2–3] Among several categories of ligands, acetylacetonate,^[4] cyclopentadienyl,^[5] aryl-

siloxide,^[6] alkoxide and aryloxide,^[7] were used to form this type of metal compound. Alkoxide derivatives of yttrium, scandium, and the lanthanides are currently of interest due to their potential applications as precursors for ceramics and electronic materials.^[8] Nevertheless, although alkoxide complexes of yttrium have been known for many years, only a few examples of yttrium alkoxides bearing thiophene moieties have been reported.^[9] The interest stems from the fact that thiophene derivatives are quite attractive as organic ligands because of their electron-rich system and their electroactive character.

Among the rare earths possessing f electrons, an attractive ion is europium, especially in the +3 oxidation state. Indeed, for example, a good sensitization of the ion can lead to an energy transfer from the ligand to the metal centre due to the narrow f–f transitions and luminescence studies may be used to obtain information about the symmetry and the geometry around the europium ion.^[10–12] Several researchers have shown that Eu^{3+} can be successfully incorporated into thiophene-based polymers yielding thin films with $Eu(+3)$ -based emission.^[13] Moreover, although europium is more stable in the oxidation state +3 as the other lanthanides, this ion can also adopt the +2 oxidation

[a] Institute for Inorganic Chemistry, Saarland University, Postfach 151150, 66041 Saarbrücken, Germany

[b] INM – Leibniz Institute for New Materials, Campus D2 2, 66123 Saarbrücken, Germany
Fax: +49-681-9300-223
E-mail: michael.veith@inm-gmbh.de

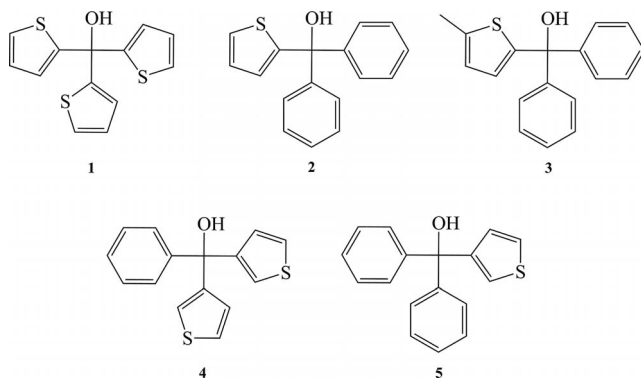
[c] Institut UTINAM UMR CNRS 6213 – Université de Franche-Comté, 16, Route de Gray, 25030 Besançon, France

state.^[14] Therefore, electrochemical and/or electropolymerization studies of europium(+3) compounds in addition to our other investigations of lanthanide compounds seemed attractive to us.

In previous papers, we presented the synthesis and X-ray crystal structure analyses of some rare earth alkoxides (Y^{3+} , Nd^{3+} , Sm^{3+} and Tb^{3+}) bearing thiophene moieties.^[9,15–17] Moreover, for the lanthanide compounds, their electrochemical and luminescence properties were also investigated.^[17–18] The studies revealed that the redox properties are dominated solely by the organic ligand (the oxidation values of the metal derivatives are marginally increased in comparison with the carbinols) and the luminescence properties are due to an energy transfer from the ligand to the metal centre and are tunable dependent on the nature of the ligand.^[17,18] To further study the possible influence of the ligand on the metal electronic states of metal alkoxides, new yttrium and europium(3+) alkoxides have been synthesized and their electrochemical and photoluminescence properties have been measured.

Results and Discussions

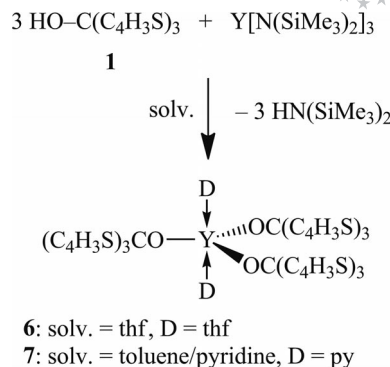
The strategy we have employed in our recent studies consists in the preparation of suitable tertiary alcohols with phenyl and/or thienyl substituents (Scheme 1) which can be attached to rare earth metal centres through a covalent M–O–R bond, leading to coordination compounds with singular redox and luminescence properties.^[9,17–18]



Scheme 1. Overview of carbinols **1–5** used as starting materials.

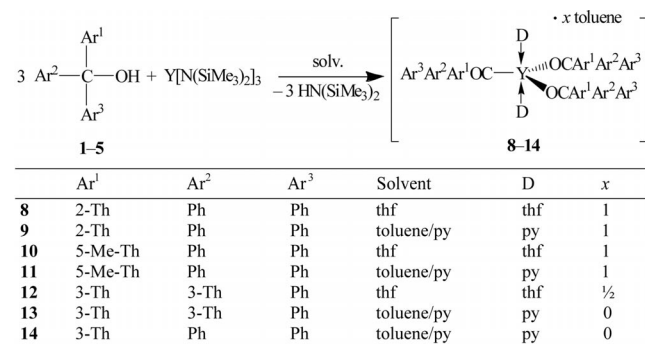
Yttrium Alkoxides

$\text{Y}[\text{OC}(\text{C}_4\text{H}_3\text{S})_3]_3(\text{thf})_2$ (**6**) and $\{\text{Y}[\text{OC}(\text{C}_4\text{H}_3\text{S})_3]_3(\text{py})_2\}$ (**7**) were synthesized by following the procedure described previously reacting one equivalent of silyl amide $\{\text{Y}[\text{N}(\text{SiMe}_3)_2]_3\}$ and three equivalents of tris(2-thienyl)-methanol (**1**) in a tetrahydrofuran solution or in a toluene/pyridine solvent mixture in the ratio 9:1, respectively (Scheme 2).^[9]



Scheme 2. Synthesis of the yttrium alkoxides **6** and **7**.^[9]

Here, we present new derivatives of yttrium, which, compared to **6** and **7**, have less thienyl and more phenyl substituents and/or the linked position of the thienyl units are different and/or the heterocycles are functionalized by a methyl group (Scheme 1). $\{\text{Y}[\text{OC}(\text{C}_{16}\text{H}_{13}\text{S})_3]_3(\text{thf})_2\} \cdot \text{toluene}$ (**8**), $\{\text{Y}[\text{OC}(\text{C}_{17}\text{H}_{15}\text{S})_3]_3(\text{thf})_2\} \cdot \text{toluene}$ (**10**) and $\{\text{Y}[\text{OC}(\text{C}_{14}\text{H}_{11}\text{S}_2)_3]_3(\text{thf})_2\} \cdot 1/2 \text{ toluene}$ (**12**) were synthesized by reacting three equivalents of the carbinols and one equivalent of the yttrium silyl amide in tetrahydrofuran at room temperature for two days (Scheme 3). The solvents were evaporated and the solids were redissolved in toluene to obtain colourless single crystals (yields: 55, 11 and 40%, respectively). The pyridine adducts $\{\text{Y}[\text{OC}(\text{C}_{16}\text{H}_{13}\text{S})_3]_3(\text{py})_2\} \cdot \text{toluene}$ (**9**) and $\{\text{Y}[\text{OC}(\text{C}_{17}\text{H}_{15}\text{S})_3]_3(\text{thf})_2\} \cdot \text{toluene}$ (**11**) were prepared in an analogous manner using a toluene/pyridine solvent mixture in the ratio 9:1 (Scheme 3). Colourless air-sensitive single crystals of **9** and **11** were obtained from toluene in yields of 42 and 61 %, respectively. A procedure similar to that was applied with **4** and **5** as organic ligands in a toluene/pyridine mixture (9:1) (Scheme 3). Unfortunately, we failed to grow single crystals, although white solids were precipitated by concentration of the solutions. In agreement with their ^1H NMR spectra, we suppose that $\text{Y}[\text{N}(\text{SiMe}_3)_2]_3$ and the carbinols **4** and **5** react in the same manner and postulate tentatively a trigonal-bipyramidal structure for the isolated solids with composition $\text{Y}[\text{OC}(\text{C}_{14}\text{H}_{11}\text{S}_2)_3]_3(\text{py})_2$ (**13**) and $\text{Y}[\text{OC}(\text{C}_{16}\text{H}_{13}\text{S})_3]_3(\text{py})_2$ (**14**)



Scheme 3. Synthesis of the yttrium alkoxides **8–14** (Th = thienyl, Me = methyl; Ph = phenyl).

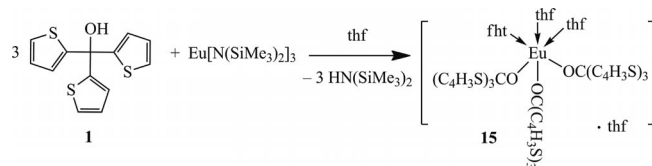
FULL PAPER

(yields: 70 and 75%, respectively). Note that the reaction of **5** with yttrium silyl amide in thf does not lead to the isolation of the desired compound.

The ^1H NMR spectra of the yttrium alkoxides **8–14** recorded in CDCl_3 (see Exp. Section) show the typical aromatic signals of thienyl and/or phenyl groups and singlets for the methyl units (for **10** and **11**). In addition, the signals of the solvent molecules ligated to the metal centre (or not) are also observed. Note that, as **6**, the ^1H NMR spectra of **9**, **11**, **13** and **14** display broad signals. The broadening of the signals could be due to a dynamic phenomenon in which the organic ligands are involved.

Europium(+3) Alkoxide (**15**)

$\{\text{Eu}[\text{OC}(\text{C}_4\text{H}_3\text{S})_3](\text{thf})_3\} \cdot \text{thf}$ (**15**) was synthesized by reacting one equivalent of europium(III) silyl amide $\{\text{Eu}[\text{N}(\text{SiMe}_3)_2]_3\}$ and three equivalents of the carbinol tris(2-thienyl)methanol **1** in tetrahydrofuran as solvent (Scheme 4). Pale red crystals of **15** were obtained in a concentrated tetrahydrofuran solution placed at 5°C . The yield after crystallization was 17%.^[9,15–17]



Scheme 4. Synthesis of $\{\text{Eu}[\text{OC}(\text{C}_4\text{H}_3\text{S})_3](\text{thf})_3\} \cdot \text{thf}$ (**15**).

The ^1H NMR spectrum recorded in CDCl_3 exhibits only broad peaks. This is because of the paramagnetic character of the europium metal centres. The broadening is similar to previous ^1H NMR spectra recorded for neodymium or samarium alkoxides bearing thiophene moieties.^[9,17–18] The spectrum shows two signals at δ 7.3 and 6.9 ppm assigned to the protons of the thienyl ligands, and three further broad resonances at δ 3.9, 3.3 and 1.9 ppm. These latter signals reveal the presence of methylenic protons of tetrahydrofuran entities, either coordinated or not coordinated at the metal centre. The ^1H NMR spectrum is in agreement with dissolution of **15** in tetrahydrofuran without degradation.

X-ray Structure Determinations

Yttrium Alkoxides

According to the X-ray diffraction studies presented in our previous paper,^[9] the coordination spheres around the yttrium metal centres are distorted trigonal-bipyramidal for $\text{Y}[\text{OC}(\text{C}_4\text{H}_3\text{S})_3](\text{thf})_2$ (**6**) and $\{\text{Y}[\text{OC}(\text{C}_4\text{H}_3\text{S})_3](\text{py})_2\}$ (**7**). Single crystal X-ray structure determinations of **8–12**, which crystallize at 5°C from toluene as colourless crystals, were performed. Unfortunately, because of the poor quality of the crystals translated by the high R-values, no dis-

cussion or comparison of the bond lengths and angle values is possible for compounds **8**, **9** and **10**. The X-ray diffraction data for these compounds have been deposited at the Cambridge Crystallographic Data Centre (see Exp. Section). Moreover, for **12** the differentiation between the thienyl and phenyl groups is difficult. This may be attributed to the fact that the crystallization process has taken place with a disordered arrangement of the thienyl and phenyl groups.

The structure determinations of **8–12** confirm the formation of mononuclear compounds with a five-coordinated yttrium atom in distorted trigonal-bipyramidal geometry. The metal centres are surrounded by three methoxido ligands in equatorial positions and two tetrahydrofuran (for **8**, **10** and **12**) or pyridine (for **9** and **11**) molecules in axial positions (Figure 1). Because of packing effects, toluene molecules are included in the crystal lattice. Selected bond lengths and angles for **11** and **12** are assembled in Table 1. These X-ray crystal structure determinations confirm the clear difference to the corresponding lanthanide compounds which have a distorted octahedral environment around the metal centres with facial arrangement of the methoxido ligands.^[9,15–17]

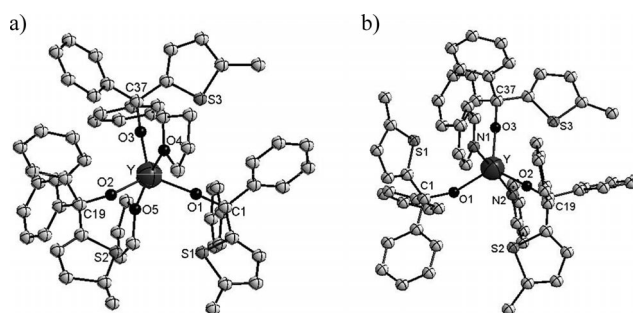


Figure 1. a) Molecular structure of $\{\text{Y}[\text{OC}(\text{C}_{17}\text{H}_{15}\text{S})_3](\text{thf})_2\} \cdot \text{toluene}$ (**10**); b) Molecular structure of $\{\text{Y}[\text{OC}(\text{C}_{17}\text{H}_{15}\text{S})_3](\text{py})_2\} \cdot \text{toluene}$ (**11**). For the two molecular structures, hydrogen atoms and lattice toluene molecules are omitted for clarity.

For $\{\text{Y}[\text{OC}(\text{C}_{17}\text{H}_{15}\text{S})_3](\text{py})_2\} \cdot \text{toluene}$ (**11**) (Figure 1), the yttrium–oxygen distances in $\text{Y}–\text{OC}(\text{C}_{17}\text{H}_{15}\text{S})$ have a mean value of $2.083(3) \text{ \AA}$ and correspond to those observed in similar yttrium alkoxides.^[9] The $\text{Y}–\text{N}$ bond lengths to the coordinated pyridine molecules ($2.474(4)$ and $2.509(4) \text{ \AA}$) are similar to the ones found for **7** ($2.493(3)$ and $2.520(3) \text{ \AA}$).^[9] The $\text{O}–\text{Y}–\text{O}$ angles involving pairs of $–\text{OC}(\text{C}_{16}\text{H}_{13}\text{S})$ ligands are in the range of $117.7(1)$ to $122.1(1)^\circ$, and the $(\text{C}_{16}\text{H}_{13}\text{S})\text{CO}–\text{Y}–\text{N}$ angles vary from $88.1(1)$ to $90.7(1)^\circ$. In comparison with **7**^[9] the angles are somewhat more affected by variation, presumably due to the presence of methyl groups which increase the steric hindrance exerted by the organic ligands.

For $\{\text{Y}[\text{OC}(\text{C}_{14}\text{H}_{11}\text{S}_2)_3](\text{thf})_2\} \cdot 1/2 \text{ toluene}$ (**12**) (Table 1), the $\text{Y}–\text{O}$ bond lengths of the phenylbis(3-thienyl)-methoxido ligands ($2.070(3)$ to $2.112(3) \text{ \AA}$) are in good agreement with the distances found for related tris(2,6-di-

Table 1. Selected bond lengths [\AA] and angles [$^\circ$] for $\{\text{Y}[\text{OC}(\text{C}_{17}\text{H}_{15}\text{S})]_3(\text{py})_2\} \cdot \text{toluene}$ (**11**) and $\{\text{Y}[\text{OC}(\text{C}_{14}\text{H}_{11}\text{S}_2)]_3 \cdot (\text{thf})_2\} \cdot 1/2 \text{ toluene}$ (**12**).

11		12	
Y–O(1)	2.086(3)	Y–O(1)	2.083(3)
Y–O(2)	2.080(3)	Y–O(2)	2.112(3)
Y–O(3)	2.083(3)	Y–O(3)	2.070(3)
Y–N(1)	2.492(4)	Y–O(4)	2.414(3)
Y–N(2)	2.515(4)	Y–O(5)	2.364(3)
O(1)–C(1)	1.399(5)	O(1)–C(1)	1.398(6)
O(2)–C(19)	1.384(5)	O(2)–C(16)	1.414(6)
O(3)–C(37)	1.403(5)	O(3)–C(31)	1.406(5)
O(2)–Y–O(1)	120.2(1)	O(1)–Y–O(2)	123.1(1)
O(3)–Y–O(1)	117.7(1)	O(3)–Y–O(1)	119.0(1)
O(2)–Y–O(3)	122.1(1)	O(3)–Y–O(2)	117.6(1)
O(1)–Y–N(2)	88.1(1)	O(1)–Y–O(5)	89.3(1)
O(1)–Y–N(1)	90.7(1)	O(1)–Y–O(4)	85.1(1)
O(2)–Y–N(1)	88.2(1)	O(2)–Y–O(4)	88.9(1)
O(3)–Y–N(2)	92.1(1)	O(3)–Y–O(5)	96.5(1)
N(1)–Y–N(2)	174.4(1)	O(5)–Y–O(4)	172.6(1)
C(1)–O(1)–Y	160.3(3)	C(1)–O(1)–Y	172.7(3)
C(19)–O(2)–Y	173.0(3)	C(16)–O(2)–Y	158.3(3)
C(37)–O(3)–Y	177.5(3)	C(31)–O(3)–Y	173.1(3)

methylphenoxido)yttrium complexes^[7c,19] and yttrium thienyl-substituted methoxides.^[9] The Y–O(thf) distances (2.364(3) \AA and 2.414(3) \AA) correspond to those obtained for **6**^[9] and for yttrium *tert*-butoxide complexes.^[7c,7f] The three methoxide oxygen atoms around the yttrium centre are coplanar (with the sum of angles $\Sigma \text{O–Y–O} = 359.7(1)^\circ$) and the O(thf)–Y–O(thf) angle of $172.6(1)^\circ$ is not far from a linear O–Y–O arrangement.

Europium(+3) Alkoxide (**15**)

Compound **15** crystallizes in the rhombohedral system, space group $R\bar{3}$. The molecular structure reveals a mononuclear compound with an approximately octahedral geometry around the europium metal centre. It is surrounded by three tris(2-thienyl)methoxido ligands and by three tetrahydrofuran molecules in a facial arrangement (Figure 2). This facial coordination geometry around the metal centre is similar to previously published neodymium, samarium and terbium(+3) alkoxide containing thiophene moieties.^[9,15–18] A solvent molecule is also present in the crystal lattice with no interaction with the molecule. The molecule is situated on the threefold axis in the crystal. Selected bond lengths and angles are assembled in Table 2.

The Eu–OC(C₄H₃S)₃ and Eu–O(thf) bond lengths (2.142(2) and 2.564(2) \AA , respectively) are longer than those observed for $\{\text{Tb}[\text{OC}(\text{C}_4\text{H}_3\text{S})_3]_3(\text{thf})_3\} \cdot \text{thf}$ (2.129(2) and 2.543(2) \AA , respectively)^[15] and shorter than the value obtained for $\{\text{Nd}[\text{OC}(\text{C}_4\text{H}_3\text{S})_3]_3(\text{thf})_3\} \cdot \text{thf}$ (2.186(1) and 2.620(2) \AA , respectively).^[9] The (C₄H₃S)₃OC–Eu–OC(C₄H₃S)₃, O(thf)–Eu–OC(C₄H₃S)₃ and O(thf)–Eu–O(thf) angle values are very similar to those found for $\{\text{Nd}[\text{OC}(\text{C}_4\text{H}_3\text{S})_3]_3(\text{thf})_3\} \cdot \text{thf}$ and $\{\text{Tb}[\text{OC}(\text{C}_4\text{H}_3\text{S})_3]_3 \cdot (\text{thf})_3\} \cdot \text{thf}$.^[9,15]

Generally speaking, the distances between the lanthanide ion and the oxygen atom of the alcoholate group are all longer than the corresponding yttrium–oxygen distance re-

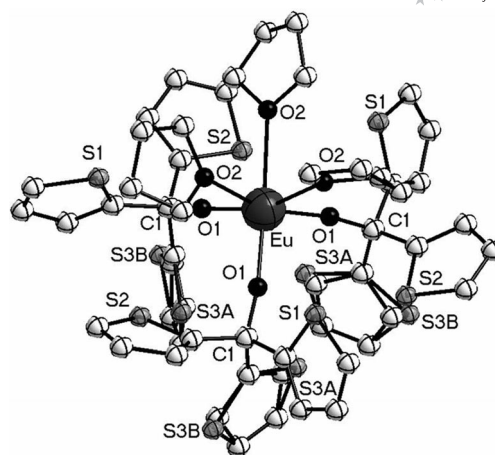


Figure 2. Molecular structure of $\{\text{Eu}[\text{OC}(\text{C}_4\text{H}_3\text{S})_3]_3(\text{thf})_3\} \cdot \text{thf}$ (**15**). Tetrahydrofuran lattice molecule and hydrogen atoms are omitted for clarity. The sulfur atom S(3) is found in two split-positions [S(3A) and S(3B)].

Table 2. Selected bond lengths [\AA] and angles [$^\circ$] for $\{\text{Eu}[\text{OC}(\text{C}_4\text{H}_3\text{S})_3]_3(\text{thf})_3\} \cdot \text{thf}$ (**15**).

Eu–O(1)	2.142(2)
Eu–O(2)	2.564(2)
O(1)–Eu–O(1)	100.9(1)
O(2)–Eu–O(1)	89.9(1)
O(2)–Eu–O(2)	73.8(1)
C(1)–O(1)–Eu	100.8(1)

flecting the presence of f-electrons within the lanthanides. Within the series of lanthanide ions the increasing Ln–O distance ($\text{Tb}^{3+} < \text{Eu}^{3+} < \text{Nd}^{3+}$) reflects the atomic radius which is affected by the number of f-electrons and the contraction of the electron shell by the number of protons in the nucleus [$r(\text{Tb}^{3+}) = 92.3$, $r(\text{Eu}^{3+}) = 94.7$, $r(\text{Nd}^{3+}) = 98.3 \text{ pm}$].^[20]

Electrochemical Studies

Recently, electrochemical studies of thiophene and derivatives containing transition metals have emerged as an interesting method of forming a polymeric film on the surface of electrodes or semi-conducting surfaces.^[21–24] They are also performed to depict the delocalization of electrons between the metal centre and the organic ligands or from the organic ligand to the metal centre.^[22–23,25] However, these studies have been carried out to a lesser degree on metals of group 3.^[17–18] Lanthanide ions are more stable in the oxidation state +3, nevertheless samarium and europium can additionally form ions in the oxidation state +2. The value of the $\text{Ln}^{3+}/\text{Ln}^{2+}$ potential depends on the environment around the metal.^[20,26,27]

Therefore, we present here the electrochemical studies of some yttrium and europium(+3) alkoxides containing thiophene units.

FULL PAPER

Yttrium Alkoxides

The values of the peak potentials for the organic ligands **1–5** and its derived yttrium alkoxides **6–14** are given in Table 3. The peak potentials previously published by us for the corresponding neodymium alkoxide are also included in Table 3 for comparison.^[16–17]

Table 3. Values of standard potentials of the free carbinols, the yttrium compounds **1–14** and corresponding neodymium compounds in dichloromethane (vs. Ag/AgClO₄) deduced from cyclic voltammetric measurements: E_{pa} : oxidation of the thienyl units forming the cation radical; E_{pc} : reduction of the carbocation; n.r.w.: no reduction wave visible.

	E_{pa}	E_{pc}
HO–C(C ₄ H ₃ S) ₃ (1)	1.48	–0.20
Y[OC(C ₄ H ₃ S) ₃](thf) ₂ (6)	1.49	n.r.w.
Y[OC(C ₄ H ₃ S) ₃](py) ₂ (7)	1.59	n.r.w.
{Nd[OC(C ₄ H ₃ S) ₃](thf) ₃ }·thf	1.53	n.r.w.
HO–C(C ₁₆ H ₁₃ S) (2)	1.64	–0.22
{Y[OC(C ₁₆ H ₁₃ S) ₃](thf) ₂ }·toluene (8)	1.69	–0.10
{Y[OC(C ₁₆ H ₁₃ S) ₃](py) ₂ }·toluene (9)	1.69	–0.21
{Nd[OC(C ₁₆ H ₁₃ S) ₃](thf) ₃ }·thf	1.66	–0.10
HO–C(C ₁₇ H ₁₅ S) (3)	1.39	–0.31
{Y[OC(C ₁₇ H ₁₅ S) ₃](thf) ₂ }·toluene (10)	1.41	–0.32
{Y[OC(C ₁₇ H ₁₅ S) ₃](py) ₂ }·toluene (11)	1.55	n.r.w.
HO–C(C ₁₄ H ₁₁ S ₂) (4)	1.59	–0.11
{Y[OC(C ₁₄ H ₁₁ S ₂) ₃](thf) ₂ }·1/2 toluene (12)	1.76	–0.28
Y[OC(C ₁₄ H ₁₁ S ₂) ₃](py) ₂ (13)	1.71	n.r.w.
{Nd[OC(C ₁₄ H ₁₁ S ₂) ₃](thf) ₃ }·thf	1.69	n.r.w.
HO–C(C ₁₆ H ₁₃ S) (5)	1.61	–0.06
Y[OC(C ₁₆ H ₁₃ S) ₃](py) ₂ (14)	1.81	n.r.w.
{Nd[OC(C ₁₆ H ₁₃ S) ₃](thf) ₃ }·thf	1.81	n.r.w.

As described in our previous papers,^[17–18] the cyclic voltammograms of the carbinols **1–5**, at 100 mV s^{–1} in dichloromethane, show an irreversible oxidation wave assigned to the oxidation of the thienyl units forming the radical cat-

ions.^[17–18,28] A reduction wave is also observed and corresponds to the reduction of the carbocation generated during the process.^[17–18] No polymeric films are obtained during the cycling in accordance with our previous results.

The oxidation of the yttrium alkoxides **6–14** leads to an irreversible peak assigned to the oxidation of the thienyl units (Figure 3). A reduction wave due to the reduction of the carbocation is also observed for **8–10** and **12**. Note that for **6**, **7**, **11**, **13** and **14**, the life time of this species is not long enough to be reduced during the experiment at this scan rate. No oxidation or reduction waves due to the metal centre have been observed.

In comparison with **2**, **8** and **9** the oxidation peak potentials measured for **3**, **10** and **11** are shifted towards lower values due to the introduction of an electron donor (methyl group) which facilitates the oxidation process manifested by a decrease of potentials. These variations are similar to our previous results obtained with sodium and potassium alkoxides.^[18]

The oxidation values of the metal derivatives are marginally increased by 0.01–0.20 V in comparison with their corresponding carbinols (Table 3 and Figure 3). There are two factors that may contribute to this shift: the inductive effect of the metal and the change of the internuclear conjugation within the structure of the metal alkoxides.^[22b] Therefore, we can conclude that a weak electronic transfer inside the molecule exists. In our case, as obtained for neodymium alkoxides containing thienyl substituents,^[17] the electron backbone ligands have a donor effect on the yttrium leading to a more difficult oxidation process of thienyl units. By cycling of potentials, no formation of polymeric films is observed in agreement with the corresponding carbinols.

These results resemble those obtained for the neodymium alkoxides bearing thiophene ligands (Table 3).^[17] We can conclude that yttrium and neodymium alkoxides^[17] have the

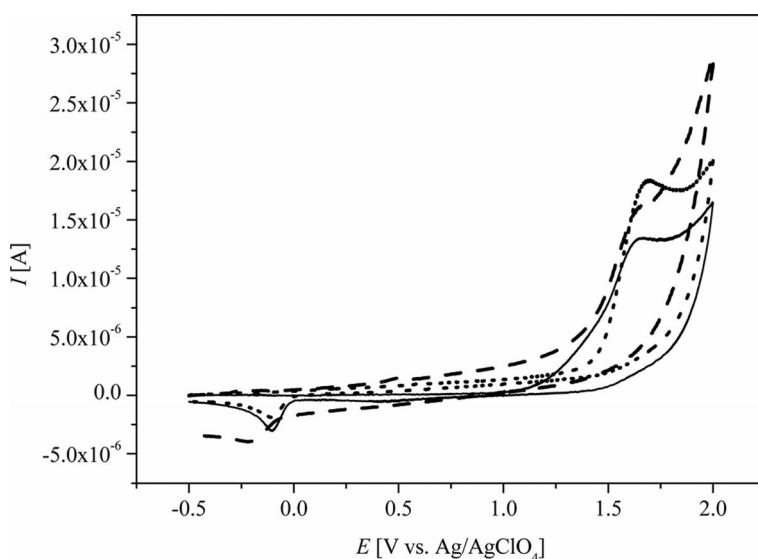


Figure 3. Cyclic voltammograms recorded on a platinum electrode (diameter 1 mm) in a dichloromethane solution containing HO–C(C₁₆H₁₃S) (**4**) (dashed line), {Y[OC(C₁₆H₁₃S)₃](thf)₂}·toluene (**8**) (solid line) and {Y[OC(C₁₆H₁₃S)₃](py)₂}·toluene (**9**) (10^{–3} M) and [NBu₄][PF₆] (0.1 M), vs. Ag/AgClO₄, scan rate 100 mV s^{–1}.

same redox behaviour: no redox activities due to the metal centre have been observed and the metal has an electron acceptor effect (contrary to the erbium alkoxides bearing thiophene moieties).^[17]

Europium(+3) Alkoxide (**15**)

The voltammogram of $\{\text{Eu}[\text{OC}(\text{C}_4\text{H}_3\text{S})_3]_3(\text{thf})_3\} \cdot \text{thf}$ (**15**) obtained in dichloromethane is shown in Figure 4.

It exhibits an irreversible wave at 1.64 V attributed to the oxidation of the thienyl units. This oxidation value is increased by 0.16 V in comparison with the corresponding carbinol **1** and by 0.05–0.15 V with the corresponding yttrium (**7** and **8**) and neodymium alkoxides.^[17] A more

pronounced electronic transfer inside the molecule in comparison to the other metal alkoxide is found which is characterized by a donor effect on the europium(+3).

Moreover when potentials are cycled from 0 to –1.5 V a reduction wave at –1.05 V is detected (Figure 5). This cathodic reduction peak is ascribed to the reduction of Eu^{3+} to Eu^{2+} .^[20,26–27] This is the first time we have detected a reduction of a rare earth ion by cyclic voltammetry in our series of carbinolates.^[17–18] This also indicates that our ligands with their steric shielding and their high electronic donor effect do not completely wrap up the metal ion. The relatively weak intensity of this peak compared to the oxidation peak of the thienyl moieties necessitates a magnification of the plot. Nevertheless, no oxidation of Eu^{2+} to Eu^{3+}

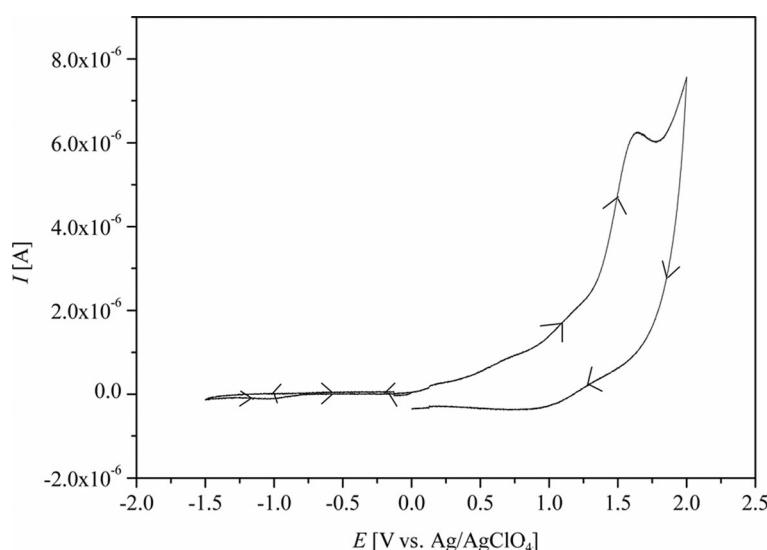


Figure 4. Cyclic voltammograms recorded on a platinum electrode (diameter 1 mm) in a dichloromethane solution containing $\{\text{Eu}[\text{OC}(\text{C}_4\text{H}_3\text{S})_3]_3(\text{thf})_3\} \cdot \text{thf}$ (**15**) between 0 → –1.5 → 2 and 0 V.

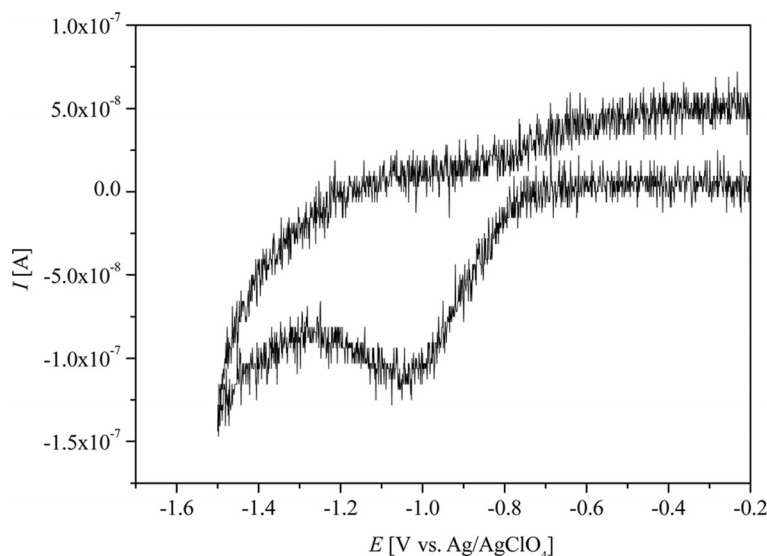


Figure 5. Magnification (region –1.5 to –0.2 V) of the cyclic voltammograms recorded on a platinum electrode (diameter 1 mm) in a dichloromethane solution containing $\{\text{Eu}[\text{OC}(\text{C}_4\text{H}_3\text{S})_3]_3(\text{thf})_3\} \cdot \text{thf}$ (**15**).

FULL PAPER

was observed. The absence of the europium oxidation peak suggests that the reaction $\text{Eu}^{3+} \rightarrow \text{Eu}^{2+}$ is irreversible. Contrary to $\{\text{Sm}[\text{OC}(\text{C}_4\text{H}_3\text{S})_3]_3(\text{thf})_3\} \cdot \text{thf}^{[18]}$ in which no reduction of the Sm^{3+} is obtained, here the organic ligands do not inhibit the reduction process of the metal centre: the potentials of $\text{Sm}^{3+}/\text{Sm}^{2+}$ and $\text{Eu}^{3+}/\text{Eu}^{2+}$ are approximately 1–1.2 V different, the latter being more positive,^[20,26–27] explaining the observation in the europium case.

Luminescence Studies

In the last decade, trivalent lanthanide compounds containing antenna ligands have been developed for their luminescent properties.^[29] Indeed, these properties lead to some attractive applications in electronic materials and in biological systems.^[30] Recently, the use of thiophene derivatives as antenna ligands has emerged due to their electron-rich system.^[14,17–18,31–32] Contrary to the other rare earth ions, compounds of metals such as Sc, Y, La, Gd and Lu belong to the group of ligand-emission compounds (emission does not occur from the metal electronic states) because of the high energy of metal-centred excited states. In this manuscript, we present our luminescence studies of the carbinols and the yttrium alkoxides to gain some insight into the ligand absorption and emission. In addition, we add the luminescence investigations of the europium(+3) alkoxide **15** in which the trivalent lanthanide is part of the metal emission group.

Yttrium Alkoxides

All luminescence spectra were recorded in the solid state to limit the dissociation of the compounds during the measurements. Nevertheless, the investigations of $\{\text{Y}[\text{OC}(\text{C}_{16}\text{H}_{13}\text{S})_3]_3(\text{thf})_2\} \cdot \text{toluene}$ (**8**) and $\{\text{Y}[\text{OC}(\text{C}_{16}\text{H}_{13}\text{S})_3]_3(\text{thf})_2\} \cdot \text{toluene}$ (**9**) cannot be performed due to a photodegradation during the experiments, indicated by a colour change of the compounds. The solid-state emission maxima of the tertiary alcohols **1**, **3–5** and their derived yttrium alkoxides **6**, **7** and **10–14** are given in Table 4.

Table 4. Solid-state emission maxima λ_{em} [nm] of the carbinols and the corresponding yttrium alkoxides upon a λ_{ex} [nm] excitation.

	λ_{ex} [nm]	λ_{em} [nm]
$\text{HO}-\text{C}(\text{C}_4\text{H}_3\text{S})_3$ (1)	280	430
$\text{Y}[\text{OC}(\text{C}_4\text{H}_3\text{S})_3]_3(\text{thf})_2$ (6)	250	394
$\text{Y}[\text{OC}(\text{C}_4\text{H}_3\text{S})_3]_3(\text{py})_2$ (7)	250	338, 392
$\text{HO}-\text{C}(\text{C}_{17}\text{H}_{15}\text{S})$ (3)	360	527
$\{\text{Y}[\text{OC}(\text{C}_{17}\text{H}_{15}\text{S})_3]_3(\text{thf})_2\} \cdot \text{toluene}$ (10)	260	399
$\{\text{Y}[\text{OC}(\text{C}_{17}\text{H}_{15}\text{S})_3]_3(\text{py})_2\} \cdot \text{toluene}$ (11)	260	398
$\text{HO}-\text{C}(\text{C}_{14}\text{H}_{11}\text{S}_2)$ (4)	260	400
$\{\text{Y}[\text{OC}(\text{C}_{14}\text{H}_{11}\text{S}_2)_3]_3(\text{thf})_2\} \cdot 1/2 \text{ toluene}$ (12)	260	398
$\text{Y}[\text{OC}(\text{C}_{14}\text{H}_{11}\text{S}_2)_3]_3(\text{py})_2$ (13)	260	399
$\text{HO}-\text{C}(\text{C}_{16}\text{H}_{13}\text{S})$ (5)	260	398
$\text{Y}[\text{OC}(\text{C}_{16}\text{H}_{13}\text{S})_3]_3(\text{py})_2$ (14)	260	399

In agreement with our previous papers,^[17–18] the luminescence spectra of the carbinols show broad emission bands assigned to the $\pi^* \rightarrow \pi$ transitions of the aromatic groups.

The emission spectra of the yttrium alkoxides are very similar and consist of broad, nearly Gaussian-shaped bands that are ascribed to the $\pi^* \rightarrow \pi$ transitions of the aromatic ligands.

Nearly identical maxima or slight blue shifts of the emission maxima for the yttrium alkoxides **6–7**, **12–13** and **14** compared to the thiophenic alcohols **1**, **4** and **5**, respectively are observed. Nevertheless, for the yttrium alkoxides **10** and **11** their emission bands are more blue-shifted by 127 and 128 nm compared to the carbinol **3** (Figure 6). These more important shifts may be due to the electronic or steric effect caused by the presence of a methyl group on the thiophene units leading to a more significant distortion of these units when bounded to the yttrium metal.^[22b] Similar shifts due to distortion can be observed in alkali metal alcoholates bearing thiophene moieties.^[18]

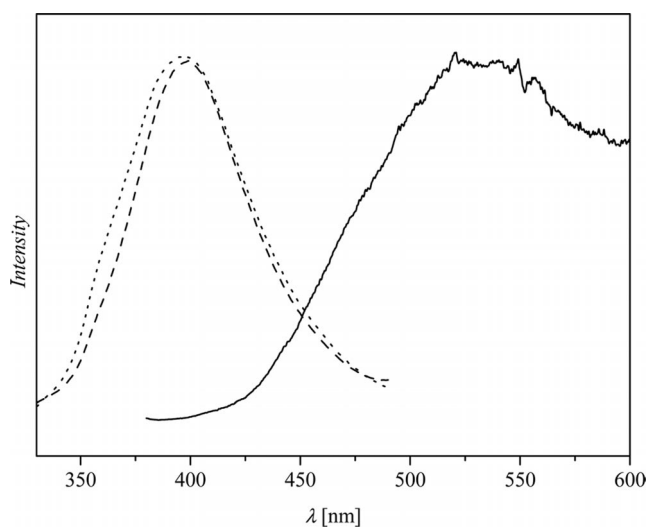


Figure 6. Room temperature solid-state emission spectra. Solid line: **3** (λ_{ex} = 360 nm), dash line: **10** (λ_{ex} = 260 nm), dot line **11** (λ_{ex} = 260 nm).

By comparison with **6**, it can be shown that **7** also has an emission band at 338 nm which can be assigned to the pyridine rings. Nevertheless, this pyridine band is not detectable in the emission spectra of the other pyridine adducts **11**, **13** and **14**, which may be due to the broadness of the ligand emission band. In agreement with previous work, no yttrium emissions were observed^[2,33] contrary to the lanthanide alkoxides containing thiophene ligands.^[17–18]

Europium(+3) Alkoxide (**15**)

The solid-state excitation and emission spectra of $\{\text{Eu}[\text{OC}(\text{C}_4\text{H}_3\text{S})_3]_3(\text{thf})_3\} \cdot \text{thf}$ (**15**) are shown in Figures 7 and 8, respectively.

The excitation spectrum was obtained by monitoring the characteristic emission of Eu^{+3} at 612 nm. The spectrum displays a broad band ranging from 320–400 nm assigned to the absorption of the organic ligands and inside it some

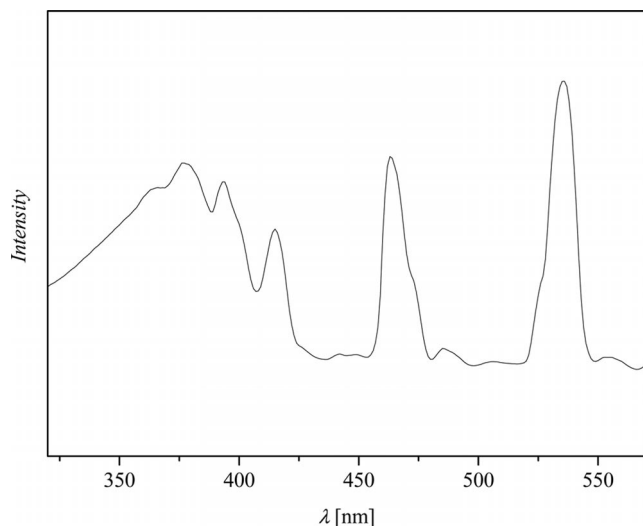


Figure 7. Solid-state excitation spectrum of $\{\text{Eu}[\text{OC}(\text{C}_4\text{H}_3\text{S})_3]_3 \cdot \text{thf}\}$ (**15**), $\lambda_{\text{em}} = 612$ nm.

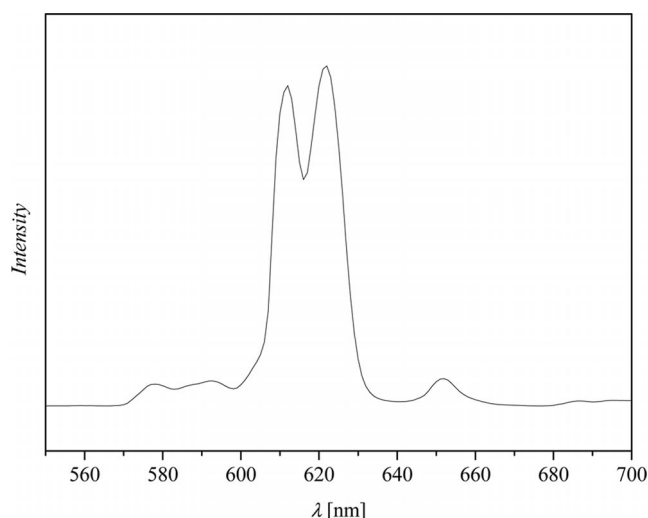


Figure 8. Solid-state emission spectrum of $\{\text{Eu}[\text{OC}(\text{C}_4\text{H}_3\text{S})_3]_3 \cdot \text{thf}\}$ (**15**), $\lambda_{\text{ex}} = 360$ nm.

sharp bands are visible due to the Eu^{3+} f–f transitions: $^1\text{F}_1 \rightarrow ^5\text{L}_7$ (377 nm) and $^7\text{F}_0 \rightarrow ^5\text{L}_6$ (393 nm).^[34–35] The other sharp bands at 414, 436 and 535 nm are attributed to the Eu^{3+} centred $^7\text{F}_1 \rightarrow ^5\text{L}_3$, $^7\text{F}_0 \rightarrow ^5\text{D}_2$ and $^7\text{F}_0 \rightarrow ^5\text{D}_1$ transition.^[34–36] The presence of the ligand absorption suggests the existence of an energy transfer from the ligand to the europium metal centre.

The emission spectrum upon an excitation on the organic ligand at 360 nm consists of six bands corresponding to the f–f transitions $^5\text{D}_0 \rightarrow ^7\text{F}_0$ (electronic dipole transition, 578 nm), $^5\text{D}_0 \rightarrow ^7\text{F}_1$ (magnetic dipole transition, 592 nm), $^5\text{D}_0 \rightarrow ^7\text{F}_2$ (electronic dipole transition, 612 and 622 nm), $^5\text{D}_0 \rightarrow ^7\text{F}_3$ (electronic dipole transition, 652 nm) and $^5\text{D}_0 \rightarrow ^7\text{F}_4$ (electronic dipole transition, 686 nm).^[34,37] The

presence of the Eu^{3+} f–f transitions and the absence of the ligand-based emission upon an excitation on the organic ligands suggest that the sensitization of the emissive metal centre is produced by an energy transfer mediated by the organic ligand.

The large intensity ratios of $^5\text{D}_0 \rightarrow ^7\text{F}_2 / ^5\text{D}_0 \rightarrow ^7\text{F}_1$ show the low symmetry of the Eu^{3+} ion sites in **15** (C_3 vs. O_h).^[1b,35] The emissions at 612 and 622 nm from the hypersensitive $^5\text{D}_0 \rightarrow ^7\text{F}_2$ electronic dipole transition dominate the emission spectrum and indicate that the europium ion does not lie in an inversion centre.^[11] The hypersensitive $^5\text{D}_0 \rightarrow ^7\text{F}_2$ transition is split into two peaks which should be the result of a crystal field effect.

Conclusions and Perspectives

A series of novel yttrium and europium(+3) alkoxides containing thienyl substituents was prepared and their crystal structures investigated by X-ray diffraction. We showed that the geometry around the yttrium atom is trigonal-bipyramidal: the metal centres are surrounded by three methoxido ligands in equatorial positions and two solvent molecules in axial positions. This is clearly different from the europium(+3) alkoxide **15** and the corresponding lanthanide compounds which have a distorted octahedral environment around the metal centres with facial arrangement of the methoxide ligands. The smaller M^{3+} radius of yttrium compared to the lanthanides is primarily responsible for the different geometries found.

The physico-chemical investigations of the yttrium methoxides containing thienyl substituents have shown that the electrochemical properties are above all dominated by the organic ligands. The oxidation values of the thienyl units are marginally increased in comparison with their corresponding carbinols: therefore, from an electrochemical point of view, the electronic transfers from metal to ligands or from ligands to metal do exist but are weak. These results are similar to those obtained for neodymium alkoxides bearing thiophene ligands.^[10] The electrochemical investigations of the europium alkoxide **15** show an oxidation wave due to the thienyl moieties and a more pronounced shift of the wave maximum compared to the other lanthanide alkoxides. Moreover, an irreversible reduction wave due to the reduction of Eu^{3+} to Eu^{2+} is visible.

The emission spectra of the carbinols and their derived yttrium compounds depict broad bands attributed to the $\pi^* \rightarrow \pi$ transitions of the aromatic ligands due to the high energy of the yttrium-centred excited state. Note that for **7** emission bands due to the pyridine rings acting as donor are also observed. The emission bands of the yttrium alkoxides **10** and **11** are more blue-shifted compared to the carbinol **3**. This can be correlated to the electronic and/or steric effect caused by the presence of a methyl group on the thiophene units leading to a more significant distortion of these units when bounded to the yttrium metal. The luminescence spectra of the europium(+3) alkoxide exhibit an energy transfer from the ligand to the lanthanide centre.

FULL PAPER

Experimental Section

General: All reactions were performed under nitrogen in a Schlenk apparatus. The solvents (tetrahydrofuran, diethyl ether, toluene and benzene) were distilled from sodium and kept under nitrogen. Dichloromethane was distilled from CaCl_2 and kept under nitrogen. Pyridine was distilled from KOH and kept under nitrogen. $\text{Y}[\text{N}(\text{SiMe}_3)_2]_3$,^[38] $\text{Eu}[\text{N}(\text{SiMe}_3)_2]_3$,^[24] tris(2-thienyl)methanol (**1**),^[39] diphenyl(2-thienyl)methanol (**2**),^[39] diphenyl(5-methyl-2-thienyl)methanol (**3**),^[18] phenylbis(3-thienyl)methanol (**4**),^[39] diphenyl(3-thienyl)methanol (**5**)^[39] were prepared according to the literature. The ^1H NMR spectra were recorded with a Bruker ACF-NMR (200 MHz) or a Bruker Avance 400 spectrometer (400 MHz, ^1H , ^2H -COSY). The UV/Vis spectra were recorded with a Lambda 35 Perkin–Elmer spectrometer. Analytical data were measured with a LECO CHN-900 instrument.

Cyclic voltammetry experiments were performed at room temperature on an Autolab PGSTAT 20 Potentiostat Galvanostat (Ecochemie) equipped with a three-electrode assembly with 0.1 M $[\text{NBu}_4][\text{PF}_6]$ (TBAF) as supporting electrolyte and CH_2Cl_2 as solvent. The working electrode was a platinum disk of 1 mm diameter. It was polished consecutively with polishing alumina and diamond suspension between the runs. The reference electrode was Ag/AgClO_4 (0.1 M in CH_3CN). A platinum disk was used as an auxiliary electrode. The solvent was freshly distilled and the solutions were prepared under nitrogen and purged with N_2 before the first scan. The scan rates employed were 100 mV s^{-1} . The concentration of the monomeric substrates was approximately 10^{-3} M or $2 \times 10^{-3} \text{ M}$. Under these conditions, the $E_{1/2}$ of $\text{Cp}_2\text{Fe}^{+/0}$ was found to be 0.16 V (CH_2Cl_2) vs. an Ag/AgClO_4 reference.

The solid-state emission and excitation spectra were recorded at room temperature with a Jobin–Yvon Fluorolog-3 spectrometer equipped with a 1000-W Xenon lamp, two double-grating monochromators for emission and excitation, respectively, and a photo-

multiplier with a photon counting system. The emission spectra were corrected for photomultiplier sensitivity, the excitation spectra for lamp intensity and both for the transmission of the monochromators.

Crystallographic Details: The data was collected with a X8 ApexII CCD diffractometer with $\text{Mo-K}\alpha$ radiation ($\lambda = 0.71073 \text{ \AA}$). All structures were solved by direct methods and refined by full-matrix least square methods on F^2 with SHELX-97.^[40] The plots of the molecular structures were made with Diamond.^[41] No sign of deterioration during storage under nitrogen was observed. The high R values are related to the imperfect crystals which are characterized by high-temperature factors of motion or disorder of the organic ligands. Crystallographic data for the structure determinations are listed in Table 5 and relevant bond lengths and angles are given in Tables 1 and 2.

CCDC-847212 (for **8**), -847213 (for **9**), -847214 (for **10**), -847215 (for **11**), -847216 (for **12**) and 858945 (for **15**) contain the supplementary crystallographic data for this paper. These data can be obtained free of charge from The Cambridge Crystallographic Data Centre via www.ccdc.cam.ac.uk/data_request/cif.

General Procedure for Preparation of Yttrium Alkoxides **8, **10** and **12**:** One equivalent of $\text{Y}[\text{N}(\text{SiMe}_3)_2]_3$ (0.844 g, 1.5 mmol; 0.668 g, 1.17 mmol; 0.703 g, 1.2 mmol; respectively) in thf (20 mL) was added to the solutions of three equivalents of the carbinols (1.18 g, 4.4 mmol of **2**; 0.986 g, 3.5 mmol of **3**; 1.008 g, 3.7 mmol of **4**) in thf (20 mL). The mixtures were stirred at room temperature for two days. The solvents were evaporated and white solids were obtained. The products were subsequently recrystallized as colourless crystals from toluene at 5°C .

{Y[OC(C₁₆H₁₃S)]₃(thf)₂}-toluene (8**):** The isolated yield was 55% (0.906 g). ^1H NMR (400.13 MHz, CDCl_3): δ = 7.3 (m, 33 H, 5-H, ϕ -H), 6.9 (m, 3 H, 4-H), 6.7 (dd, $^3J_{\text{H4,H3,5}} = 2.92 \text{ Hz}$, 3 H, 3-H), 3.7 (thf), 1.8 (thf), 7.1 (toluene), 2.3 (toluene) ppm. UV/Vis (190–

Table 5. X-ray crystallographic and refinement data for **11**, **12** and **15**.

Compounds	11	12	15
Empirical formula	$\text{C}_{71}\text{H}_{63}\text{N}_2\text{O}_3\text{S}_3\text{Y}$	$\text{C}_{56.5}\text{H}_{53}\text{O}_5\text{S}_6\text{Y}$	$\text{C}_{55}\text{H}_{59}\text{O}_7\text{S}_9\text{Eu}$
Formula weight	1177.32	1093.26	1272.52
Temperature [K]	150(2)	213(2)	122(2)
Crystal system	triclinic	monoclinic	rhombohedral
Space group	$P\bar{1}$	$P2_1/n$	$R\bar{3}$
a [Å]	12.627(1)	13.598(3)	13.928(1)
b [Å]	14.478(2)	16.935(3)	13.928(1)
c [Å]	18.270(2)	23.892(5)	24.621(2)
α [°]	97.84(1)	90	90
β [°]	95.21(1)	102.22(3)	90
γ [°]	113.65(1)	90	120
Volume [Å ³]	2991.5(5)	5377(1)	4136.4(2)
Z	2	4	3
$\rho_{\text{calcd.}}$ [mg m ⁻³]	1.307	1.350	1.533
μ [mm ⁻¹]	1.129	1.364	1.529
$F(000)$	1228	2268	1956
Crystal size [mm ³]	$0.77 \times 0.28 \times 0.27$	$0.40 \times 0.35 \times 0.23$	$0.26 \times 0.21 \times 0.16$
Theta range for data collection [°]	1.14 to 27.93	2.39 to 28.19	1.88 to 29.26
Reflexion collected	50050	55056	18656
Independent reflections	13931 [$R(\text{int}) = 0.0363$]	12833 [$R(\text{int}) = 0.1099$]	5024 [$R(\text{int}) = 0.0426$]
Completeness to theta [%]	97.2 (27.93°)	97.1 (28.19°)	100.0 (29.26°)
Absorption correction	multiscan	multiscan	semi-empirical
Data/restraints/parameters	13931/0/682	12833/0/578	5024/36/245
Goodness-of-fit on F^2	2.086	1.138	1.034
Final R indices [$I > 2\sigma(I)$]	$R_1 = 0.0779$, $wR_2 = 0.2188$	$R_1 = 0.0737$, $wR_2 = 0.1701$	$R_1 = 0.0296$, $wR_2 = 0.0635$
Largest diff. peak and hole [e Å ⁻³]	1.607 and -1.728	1.086 and -0.771	0.625 and -0.588

1100 nm, CH_2Cl_2 , 10^{-5} M): $\lambda = 236$ nm ($\epsilon = 267 \times 10^3 \text{ M}^{-1} \text{ cm}^{-1}$). $\text{C}_{66}\text{H}_{63}\text{O}_5\text{S}_3\text{Y}$ ($1121.25 \text{ g mol}^{-1}$): calcd. C 70.63, H 5.61; found C 72.74, H 5.89. Crystal data: monoclinic, space group $P2_1/c$, $a = 14.678(2) \text{ \AA}$, $b = 13.760(2) \text{ \AA}$, $c = 27.649(3) \text{ \AA}$, $\beta = 94.50(1)^\circ$, $V = 5567(1) \text{ \AA}^3$, $Z = 4$.

$\{\text{Y}[\text{OC}(\text{C}_{17}\text{H}_{15}\text{S})]_3(\text{thf})_2\} \cdot \text{toluene}$ (10): The isolated yield was 11% (0.144 g). ^1H NMR (400.13 MHz, CDCl_3): $\delta = 7.4$ (m, 12 H, ϕ -H), 7.3 (m, 18 H, ϕ -H), 6.6 (m, 3 H, 4-H), 6.4 (m, 3 H, 3-H), 2.7 (s, 9 H, -CH₃), 3.7 (thf), 1.8 (thf), 7.1 (toluene), 2.3 (toluene) ppm. UV/Vis (190–1100 nm, CH_2Cl_2 , 10^{-5} M): $\lambda = 241$ nm ($\epsilon = 138 \times 10^2 \text{ M}^{-1} \text{ cm}^{-1}$). $\text{C}_{69}\text{H}_{69}\text{O}_5\text{S}_3\text{Y}$ ($1163.33 \text{ g mol}^{-1}$): calcd. C 71.17, H 5.93; found C 72.41, H 6.19. Crystal data: monoclinic, space group $P2_1/c$, $a = 18.687(4) \text{ \AA}$, $b = 14.686(3) \text{ \AA}$, $c = 28.052(6) \text{ \AA}$, $\beta = 93.56(3)^\circ$, $V = 7684(3) \text{ \AA}^3$, $Z = 4$.

$\{\text{Y}[\text{OC}(\text{C}_{14}\text{H}_{11}\text{S}_2)]_3(\text{thf})_2\} \cdot 1/2 \text{ toluene}$ (12): The isolated yield was 40% (0.521 g). ^1H NMR (400.13 MHz, CDCl_3): $\delta = 7.3$ (m, 6 H, ϕ -H), 7.1 (m, 15 H, ϕ -H, 5-H), 6.9 (m, 8 H, 4-H), 6.8 (m, 8 H, 2-H), 3.4 (thf), 1.5 (thf) ppm. UV/Vis (190–1100 nm, CH_2Cl_2 , 10^{-5} M): $\lambda = 236$ nm ($\epsilon = 510 \times 10^2 \text{ M}^{-1} \text{ cm}^{-1}$). $\text{C}_{56.5}\text{H}_{53}\text{O}_5\text{S}_6\text{Y}$ ($1093.26 \text{ g mol}^{-1}$): calcd. C 62.01, H 4.84; found C 64.01, H 4.87.

General Procedure for Preparation of Yttrium Alkoxides 9 and 11: One equivalent of $\text{Y}[\text{N}(\text{SiMe}_3)_2]_3$ (0.939 g, 1.6 mmol; 0.581 g, 1.0 mmol; respectively) in toluene (25 mL) and pyridine (5 mL) was added to a solution of three equivalents of the carbinols (1.31 g, 4.9 mmol of **2**; 0.857 g, 3.0 mmol of **3**) in toluene (25 mL). The mixtures were stirred at room temperature for two days. The solvents were evaporated and white solids were obtained. The products were subsequently recrystallized as colourless crystals from toluene at 5 °C.

$\{\text{Y}[\text{OC}(\text{C}_{16}\text{H}_{13}\text{S})]_3(\text{py})_2\} \cdot \text{toluene}$ (9): The isolated yield was 42% (0.766 g). ^1H NMR (400.13 MHz, CDCl_3): $\delta = 7.2$ (m, 33 H, 5-H, ϕ -H), 6.8 (br. s, 3 H, 4-H), 6.6 (br. s, 3 H, 3-H), 8.4 (py), 6.9 (py), 6.6 (py), 7.1 (toluene), 2.3 (toluene) ppm. UV/Vis (190–1100 nm, CH_2Cl_2 , 10^{-5} M): $\lambda = 235$ nm ($\epsilon = 153.5 \times 10^3 \text{ M}^{-1} \text{ cm}^{-1}$). $\text{C}_{68}\text{H}_{57}\text{N}_2\text{O}_3\text{S}_3\text{Y}$ ($1135.25 \text{ g mol}^{-1}$): calcd. C 71.87, H 5.02, N 2.46; found C 68.30, H 4.22, N 2.50.

$\{\text{Y}[\text{OC}(\text{C}_{17}\text{H}_{15}\text{S})]_3(\text{thf})_2\} \cdot \text{toluene}$ (11): The isolated yield was 61% (0.707 g). ^1H NMR (400.13 MHz, CDCl_3): $\delta = 7.6$ (br. s, 12 H, ϕ -H), 7.2 (br. s, 18 H, ϕ -H), 6.5 (m, 3 H, 4-H), 6.4 (m, 3 H, 3-H), 2.9 (s, 9 H, -CH₃), 8.4 (py), 6.9 (py), 7.1 (toluene), 2.4 (py) ppm. UV/Vis (190–1100 nm, CH_2Cl_2 , 10^{-5} M): $\lambda = 244$ nm ($\epsilon = 637 \times 10^2 \text{ M}^{-1} \text{ cm}^{-1}$). $\text{C}_{71}\text{H}_{63}\text{N}_2\text{O}_3\text{S}_3\text{Y}$ ($1177.32 \text{ g mol}^{-1}$): calcd. C 72.36, H 5.35, N 2.37; found C 71.37, H 4.83, N 2.45.

General Procedure for Preparation of Yttrium Alkoxides 13 and 14: One equivalent of $\text{Y}[\text{N}(\text{SiMe}_3)_2]_3$ (0.666 g, 1.1 mmol) in toluene (20 mL) and pyridine (4 mL) was added to a solution of three equivalents of the carbinols (0.955 g, 3.5 mmol of **4**; 0.935 g, 3.5 mmol of **5**) in toluene (20 mL). The mixtures were stirred at room temperature for two days. The solvents were slowly evaporated and white solids precipitated which were filtered.

$\text{Y}[\text{OC}(\text{C}_{14}\text{H}_{11}\text{S}_2)]_3(\text{py})_2$ (13): The isolated yield was 70% (0.813 g). ^1H NMR (400.13 MHz, CDCl_3): $\delta = 7.2$ (br. s, 21 H, 5-H, ϕ -H), 6.9 (br. s, 12 H, 4-H, 2-H), 8.4 (py), 7.6 (py) ppm. UV/Vis (190–1100 nm, CH_2Cl_2 , 10^{-5} M): $\lambda = 245$ nm ($\epsilon = 934 \times 10^3 \text{ M}^{-1} \text{ cm}^{-1}$). $\text{C}_{55}\text{H}_{43}\text{N}_2\text{O}_3\text{S}_6\text{Y}$ (1060 g mol^{-1}): calcd. C 62.26, H 4.06, N 2.64; found C 63.51, H 4.15, N 3.16.

$\text{Y}[\text{OC}(\text{C}_{16}\text{H}_{13}\text{S})]_3(\text{py})_2$ (14): The isolated yield was 75% (0.860 g). ^1H NMR (400.13 MHz, CDCl_3): $\delta = 7.2$ (br. s, 33 H, 5-H, ϕ -H), 6.9 (br. s, 6 H, 4-H, 2-H), 8.4 (py), 7.6 (py), 7.2 (py) ppm. UV/Vis (190–1100 nm, CH_2Cl_2 , 10^{-4} M): $\lambda = 244$ nm ($\epsilon =$

$110.5 \times 10^2 \text{ M}^{-1} \text{ cm}^{-1}$). $\text{C}_{61}\text{H}_{49}\text{N}_2\text{O}_3\text{S}_3\text{Y}$ (1042 g mol^{-1}): calcd. C 70.25, H 4.70, N 2.69; found C 70.88, H 5.19, N 3.60 (the considerable difference in the contents of nitrogen calculated and found may be due in part to the high sensitivity of the compounds to air).

$\text{Eu}[\text{OC}(\text{C}_4\text{H}_3\text{S})_3]_3(\text{thf})_3$ (15): To a solution of three equivalents of tris[2-thienyl]methanol (0.746 g, 2.68 mmol) in thf (25 mL) was added one equivalent of $\text{Eu}[\text{N}(\text{SiMe}_3)_2]_3$ (0.556 g, 0.89 mmol) in thf (25 mL). The mixture was stirred at room temperature for two days. The solution was concentrated, and pale red crystals were obtained at 5 °C a few days later. The isolated yield was 17% (0.197 g). ^1H NMR (400.13 MHz, CDCl_3): $\delta = 7.3$ (br., 9 H, 5-H), 6.9 (br. s, 18 H, 3-H, 4-H), 3.9 (br. s, 6 H, thf), 3.3 (br. s, 2 H, thf), 1.9 (br. s, 8 H, thf) ppm. No elemental analysis could be obtained due to the high sensibility of **15** to water.

Acknowledgments

We gratefully acknowledge the financial support provided by the Deutsche Forschungsgemeinschaft (DFG) in the framework of SPPI166 (Lanthanoidspezifische Funktionalitäten in Molekül und Material), by the Saarland University and the Fonds der Chemischen Industrie. We thank Dr. Michael Zimmer for the ^1H NMR spectra and Dr. Laurent Guyard, Dr. Fabrice Guyon, Prof. Michael Knorr and Dr. Abderrahim Khatyr for valuable help in the registry of the electrochemical and luminescence spectra.

- a) I. A. Hemmilä, *Application of Fluorescence in Immunoassays*, Wiley, New York, **1991**; b) J.-C. G. Bünzli, G. R. Choppin (Eds.), *Lanthanide Probes in Life, Chemical and Earth Science—Theory and Practice*, Elsevier, Amsterdam, **1989**; c) R. Reyes, E. N. Hering, M. Cremona, C. F. B. Silva, H. F. Brito, C. A. Achete, *Thin Solid Films* **2002**, 420–421, 23–29.
- M. A. Katkova, V. A. Ilchev, A. N. Konav, M. N. Bochkarev, A. G. Vitukhnovsky, M. A. Parshin, L. Pandey, M. Van der Auweraer, *J. Appl. Phys.* **2008**, 104, 053706.
- H. Hin, M. Shi, M. Guan, C. H. Huang, K. Ibrahim, F. Q. Liu, *New J. Chem.* **2003**, 27, 1485–1489.
- E. H. Barash, P. S. Coan, E. B. Lobkovsky, W. E. Streib, K. G. Caulton, *Inorg. Chem.* **1993**, 32, 497–501.
- a) P. L. Arnold, S. A. Mungur, A. J. Blake, C. Wilson, *Angew. Chem.* **2003**, 115, 6163; *Angew. Chem. Int. Ed.* **2003**, 42, 5981–5984; b) A. K. Dash, A. Razavi, A. Mortreux, C. W. Lehmann, J.-F. Carpentier, *Organometallics* **2002**, 21, 3238–3249.
- a) P. Shao, D. J. Berg, G. W. Bushnell, *Inorg. Chem.* **1994**, 33, 6334–6339; b) P. S. Gradef, J. K. Yunlu, T. J. Deming, J. M. Olofson, R. J. Doedens, W. J. Evans, *Inorg. Chem.* **1990**, 29, 420–424.
- a) M. J. McGeary, P. S. Coan, K. Folting, W. E. Streib, K. G. Caulton, *Inorg. Chem.* **1989**, 28, 3284–3285; b) W. J. Evans, J. M. Olofson, J. W. Ziller, *J. Am. Chem. Soc.* **1990**, 112, 2308–2314; c) W. J. Evans, J. M. Olofson, J. W. Ziller, *Inorg. Chem.* **1989**, 28, 4309–4311; d) P. B. Hitchcock, M. F. Lappert, R. G. Smith, *Inorg. Chim. Acta* **1987**, 139, 183–184; e) P. B. Hitchcock, M. F. Lappert, A. Singh, *J. Chem. Soc., Chem. Commun.* **1983**, 1499–1501; f) W. J. Evans, M. S. Sollberger, T. P. Hanusa, *J. Am. Chem. Soc.* **1988**, 110, 1841–1850; g) W. J. Evans, M. S. Sollberger, *Inorg. Chem.* **1988**, 27, 4417–4423; h) D. C. Bradley, H. Ci-Iudzynska, M. E. Hammond, M. B. Hursthouse, M. Motevall, W. Ruowen, *Polyhedron* **1992**, 1, 337–379.
- D. C. Bradley, *Chem. Rev.* **1989**, 89, 1317–1322.
- M. Veith, C. Belot, L. Guyard, V. Huch, M. Knorr, M. Zimmer, *Eur. J. Inorg. Chem.* **2008**, 2397–2406.
- J.-C. G. Bünzli, G. R. Choppin (Eds.), *Lanthanide Probes in Life, Chemical and Earth Science – Theory and Practice*, Elsevier, Amsterdam, **1989**, ch. 7.

FULL PAPER

- [11] S. Cotton, in: *Lanthanide and Actinide Chemistry, Inorganic Chemistry: A Wiley Textbook Series*, Wiley, Chichester, **2006**, chapter 5.
- [12] G. Vicentini, L. B. Zinner, J. Zukerman-Schpector, K. Zinner, *Coord. Chem. Rev.* **2000**, *196*, 353–382.
- [13] a) J. Kim, S. K. Tripathy, J. Kumar, K. G. Chittibabu, *Mater. Sci. Eng. C* **1999**, *11*–18; b) D. Wang, J. Zhang, Q. Lin, L. Fu, H. Zhang, B. Yang, *J. Mater. Chem.* **2003**, *13*, 2279–2284; c) J. Kim, H.-C. Wang, J. Kumar, S. K. Tripathy, K. G. Chittibabu, M. J. Cazeca, W. Kim, *Chem. Mater.* **1999**, *11*, 2250–2256; d) H. Chen, R. D. Archer, *Macromolecules* **1996**, *29*, 1957–1964; e) Y. Okamoto, Y. Ueba, N. F. Dzhanibekov, E. Banks, *Macromolecules* **1981**, *14*, 17–22; f) Y. Ueba, E. Banks, Y. Okamoto, *J. Appl. Polym. Sci.* **1980**, *25*, 2007–2017.
- [14] S. Viswanathan, A. de Bettencourt-Dias, *Inorg. Chem.* **2006**, *45*, 10138–10146.
- [15] M. Veith, C. Belot, V. Huch, *Acta Crystallogr., Sect. E* **2011**, *67*, m1712.
- [16] M. Veith, C. Belot, V. Huch, *Inorg. Chem. Commun.*, in press, DOI: 10.1016/j.inoche.2012.01.027.
- [17] M. Veith, C. Belot, V. Huch, H.-L. Cui, L. Guyard, M. Knorr, C. Wickleder, *Eur. J. Inorg. Chem.* **2010**, 879–889.
- [18] M. Veith, C. Belot, V. Huch, L. Guyard, M. Knorr, A. Khatyr, C. Wickleder, *Z. Anorg. Allg. Chem.* **2010**, *636*, 2262–2275.
- [19] W. J. Evans, M. A. Ansari, J. W. Ziller, S. I. Khan, *J. Organomet. Chem.* **1998**, *553*, 141–148.
- [20] S. Cotton, in: *Lanthanide and Actinide Chemistry, Inorganic Chemistry: A Wiley Textbook Series*, Wiley, Chichester, **2006**, chapter 1.
- [21] a) X. Wang, G. Shi, Y. Liang, *Electrochem. Commun.* **1999**, *1*, 536–539; b) G. Zotti, A. Berlin, G. Schiavon, S. Zecchin, *Synth. Met.* **1999**, *101*, 622–623; c) S. Abaci, A. Yildiz, *J. Electroanal. Chem.* **2004**, 161–168; d) K. Palaniappan, J. W. Murphy, N. Khanam, J. Horvath, H. Alshareef, M. Quevedo-Lopez, M. C. Biewer, S. Y. Park, M. J. Kim, B. E. Gnade, M. C. Stefan, *Macromolecules* **2009**, *42*, 3845–3848; e) A. Benedetto, M. Balog, H. Rayah, F. Le Derf, P. Viel, S. Palacin, M. Sallé, *Electrochim. Acta* **2008**, *53*, 3779–3788; f) A. Cithaner, A. M. Önal, *J. Electroanal. Chem.* **2007**, *601*, 68–76; g) A. Arnanz, M.-L. Marcos, S. Delgado, J. González-Velasco, C. Moreno, *J. Organomet. Chem.* **2008**, *693*, 3457–3470; h) L. Guyard, M. Nguyen Dinh An, P. Audebert, *Adv. Mater.* **2001**, *13*, 133–136; i) M. Beley, D. Delabouglise, G. Houppy, J. Husson, J.-P. Petit, *Inorg. Chim. Acta* **2005**, *358*, 3075–3083.
- [22] a) O. Clot, M. O. Wolf, B. O. Patrick, *J. Am. Chem. Soc.* **2001**, *123*, 9963–9973; b) O. Clot, Y. Akahori, C. Moorlag, D. B. Leznoff, M. O. Wolf, B. O. Patrick, M. Ishii, *Inorg. Chem.* **2003**, *42*, 2704–2713.
- [23] a) V. G. Albano, M. Bandini, C. Moorlag, F. Piccinelli, A. Pietrangelo, S. Tommasi, A. Umani-Ronchi, M. O. Wolf, *Organometallics* **2007**, *26*, 4373–4375; b) J. Hjelm, R. W. Handel, A. Hagfeldt, E. C. Constable, C. E. Housecroft, R. J. Forster, *Electrochem. Commun.* **2004**, *6*, 193–200; c) J. Hjelm, R. W. Handel, A. Hagfeldt, E. C. Constable, C. E. Housecroft, R. J. Forster, *Inorg. Chem.* **2005**, *44*, 1073–1081.
- [24] T. L. Stoot, M. O. Wolf, *Coord. Chem. Rev.* **2003**, *246*, 89–101.
- [25] a) K. R. J. Thomas, J. T. Lin, *Organometallics* **1999**, *18*, 5285–5291; b) M. O. Wolf, M. S. Wrighton, *Chem. Mater.* **1994**, *6*, 1526–1533; c) W.-Y. Wong, *Comments Inorg. Chem.* **2005**, *26*, 39–74.
- [26] A. M. Bond, G. B. Deacon, R. H. Newnham, *Organometallics* **1986**, *5*, 2312–2316.
- [27] A. I. Bhatt, I. May, V. A. Volkovich, D. Collison, M. Helliwell, I. B. Polovov, R. G. Lewin, *Inorg. Chem.* **2005**, *44*, 4934–4940.
- [28] M. Turbiez, P. Frère, M. Allain, N. Gallego-Planas, J. Roncali, *Macromolecules* **2005**, *38*, 6806–6812.
- [29] a) G. E. Buono-Core, H. Li, B. Marcinak, *Coord. Chem. Rev.* **1990**, *99*, 55–87; b) J. Kido, Y. Okamoto, *Chem. Rev.* **2002**, *102*, 2357–2368; c) S. Quici, M. Cavazzini, G. Marzanni, G. Accorsi, N. Armaroli, B. Ventura, F. Barigelletti, *Inorg. Chem.* **2005**, *44*, 529–537.
- [30] a) M. P. Oude Wolbers, F. C. J. M. van Veggel, B. H. M. Snelink-Ruel, J. W. Hofstra, F. A. J. Geurts, D. N. Reinhoudt, *J. Chem. Soc. Perkin Trans. 2* **1998**, 2141–2150; b) R. Reisfeld, C. K. Jorgensen, *Laser and Excited States of Rare Earths*, Springer, Berlin, **1977**; c) V.-M. Mikkala, M. Helenius, I. K. Hemmilä, J. Kankare, H. Takalo, *Helv. Chim. Acta* **1993**, *76*, 1361–1378; d) G. A. Kumar, R. E. Riman, L. A. Diaz Torrez, O. B. Garcia, S. Banerjee, A. Kornienko, J. Brennan, *Chem. Mater.* **2005**, *17*, 5130–5135; e) G. A. Kumar, R. E. Riman, L. A. Diaz Torrez, S. Banerjee, M. D. Romanelli, T. J. Emge, J. Brennan, *Chem. Mater.* **2007**, *19*, 2937–2946.
- [31] a) X.-Y. Chen, X. Yang, B. J. Holliday, *Polym. Prepr. Am. Chem. Soc. Div. Polym. Chem.* **2007**, *48*, 595; b) D. Wang, D. Cui, W. Miao, S. Li, B. Huang, *Dalton Trans.* **2007**, 4576–4591; c) J. Lloret, F. Estevan, P. Lahuerta, P. Hirva, J. Pérez-Prieto, M. Sanaü, *Organometallics* **2006**, *25*, 3156–3165; d) S. Destri, M. Pasini, W. Porzio, F. Rizzo, G. Dellepiane, M. Ottonelli, G. Musso, F. Meinardi, L. Veltri, *J. Lumin.* **2007**, *127*, 601–610; e) W. S. Hwang, D. L. Wang, M. Y. Chiang, *J. Organomet. Chem.* **2000**, *613*, 231–235; f) Y. F. Tzeng, C. Y. Wu, W. S. Hwang, C. H. Hung, *J. Organomet. Chem.* **2003**, *687*, 16–26; g) Y.-F. Yuan, T. Cardinaels, K. Lunstroot, K. Van Hecke, L. Van Meervelt, C. Görrler-Walrand, K. Binnemans, P. Nockemann, *Inorg. Chem.* **2007**, *46*, 5302–5309; h) R. Sultan, K. Gadamssetti, S. Swavey, *Inorg. Chim. Acta* **2006**, *359*, 1233–1238; i) E. E. S. Teotonio, M. C. F. C. Felinto, H. F. Brito, O. L. Malta, A. C. Trindade, R. Najjar, W. Strek, *Inorg. Chim. Acta* **2004**, *357*, 451–460.
- [32] a) A. de Bettencourt-Dias, Department of Chemistry, *Syracuse University*, Syracuse, NY, USA. Abstract of Papers, 232nd ACS National Meeting, San Francisco, CA, United States, Sept. 10–14, **2006**, INOR–102; b) A. de Bettencourt-Dias, S. Viswanathan, A. Rollet, *J. Am. Chem. Soc.* **2007**, *129*, 15436–15437.
- [33] L. Shen, J. Yang, Y.-S. Ma, X.-Y. Tang, G.-W. Yang, Q.-Y. Li, F. Zhou, Z.-F. Miao, X.-W. Fei, J.-W. Huang, *J. Coord. Chem.* **2011**, *64*, 431–439.
- [34] V. Zolin, L. Puntus, V. Kudryashova, V. Tsaryuk, J. Legendziewicz, P. Gawryszewska, R. Szostak, *J. Alloys Compd.* **2002**, *341*, 376–380.
- [35] M.-C. Yin, L.-J. Yuan, C.-C. Ai, C. W. Wang, E.-T. Yuan, J.-T. Sun, *Polyhedron* **2004**, *23*, 529–536.
- [36] S. V. Eliseeva, M. Ryazanov, F. Gumy, S. I. Troyanov, L. S. Lepnev, J.-C. Bünzli, N. P. Kuzmina, *Eur. J. Inorg. Chem.* **2006**, 4809–4820.
- [37] C. R. De Silva, J. R. Maeyer, R. Wang, G. S. Nichol, Z. Zheng, *Inorg. Chim. Acta* **2007**, *360*, 3543–3552.
- [38] R. Rapalaviciute, Ph. D. Dissertation, Saarland University, Saarbrücken, **2004**.
- [39] B. Abarca, G. Asencio, R. Ballesteros, T. Varea, *J. Org. Chem.* **1991**, *56*, 3224–3229.
- [40] G. M. Sheldrick, *SHELX-97, Program for refinement of crystal structures*, University of Göttingen, Germany, **1997**.
- [41] *Diamond*, Crystal and molecular structure visualization software, CRYSTAL IMPACT, Postfach 1251, 53002 Bonn, Germany (www.crystalimpact.com/diamond/).

Received: October 10, 2011

Published Online: February 8, 2012

PTA-Stabilized Ruthenium and Platinum Nanoparticles: Characterization and Investigation in Aqueous Biphasic Hydrogenation Catalysis

Pierre-Jean Debouttière,^[a,b] Yannick Coppel,^[a,b] Audrey Denicourt-Nowicki,^[c,d]
Alain Roucoux,^[c,d] Bruno Chaudret,^[a,b] and Karine Philippot^{*[a,b]}

Keywords: Ruthenium / Platinum / Nanoparticles / Heterogeneous catalysis / Hydrogenation / Sustainable chemistry

Very small ruthenium and platinum nanoparticles have been prepared from organometallic complexes by using 1,3,5-triaza-7-phosphaadamantane (PTA) as stabilizer, which allowed their easy dispersion into water. These nanoparticles were fully characterized by different techniques. In particular, the coordination of PTA to the surfaces of the particles was studied by NMR spectroscopy. The potential of these

nanoparticles as catalysts was investigated in aqueous biphasic catalysis; olefins and arene derivatives were hydrogenated under mild conditions of temperature and pressure with interesting conversions and selectivities despite the change of environment they underwent after their dissolution in water.

Introduction

On the path towards more sustainable chemistry, the development of active and recyclable catalysts for industrial applications is still an ongoing field of research.^[1] On one hand, heterogeneous catalysts, although easily recoverable, present some drawbacks, such as the drastic reaction conditions and the mass transport problems. On the other hand, in the field of homogeneous catalysis, the separation of expensive transition-metal catalysts from substrates and products remains a key issue for industrial applications.^[2] This has led to the development of several concepts for low-cost catalyst recovery, including the use of multiphase reaction systems like liquid/liquid biphasic systems.^[3] In many cases the catalyst is soluble in water whereas the substrates and products are only soluble in the organic phase, hence providing a feasible separation process.

In this context, metallic nanoparticles (NPs) finely dispersed in water, which are on the border between mononuclear metal complexes and heterogeneous bulk catalysts, have proved to be sustainable alternatives to conventional catalysts.^[4] Their main advantages in catalytic applications are linked to their high metal surface area and consequently

their high number of potential active sites, which could greatly improve their specific catalytic activity as well as their potential recycling.^[5] That is why the synthesis of metal nanoparticles for application in catalysis has been the subject of tremendous interest during the past few decades. Owing to environmental and economic concerns,^[6] the transfer of metal nanoparticles into water remains of high importance. Several methods are known for the synthesis of metallic nanospecies, but for the preparation of water-soluble metal NPs, the reduction of metal salts is the most common approach.^[7]

For our part, we have developed a reproducible methodology for the synthesis of metal NPs from organometallic complexes^[8] and their efficient stabilization by ligands;^[9,10] this has allowed metal NPs to be obtained with tunable surface properties. The mild conditions of temperature and gas pressure applied to the decomposition of the precursor permit stable metal NPs to be obtained that display average sizes of less than 5 nm with narrow size distributions and well-controlled surface states, three key parameters for catalytic applications. In a recent communication,^[11] we extended our strategy to the use of 1,3,5-triaza-7-phosphaadamantane (PTA) as stabilizing ligand, an organic- and water-soluble aminophosphane derivative well known for the formation of water-soluble complexes.^[12] This ligand allowed a facile dispersion of our nanoparticles into water, giving rise to stable aqueous colloidal solutions. We now report the full characterization of these ruthenium and platinum nanoparticles and their use in the catalytic hydrogenation of model substrates. In particular, solution and solid-state NMR and DOSY experiments were performed to demonstrate the coordination of the ligand to the particle surface. The performance of these Ru and Pt nanocatalysts

[a] CNRS, LCC (Laboratoire de Chimie de Coordination),
205 Route de Narbonne, 31077 Toulouse, France
Fax: +33-5-61553003
E-mail: karine.philippot@lcc-toulouse.fr

[b] Université de Toulouse, UPS, INPT, LCC,
31077 Toulouse, France

[c] Ecole Nationale Supérieure de Chimie de Rennes, CNRS,
UMR 6226,
Avenue du Général Leclerc, CS 50837, 35708 Rennes Cedex 7,
France

[d] Université Européenne de Bretagne

Supporting information for this article is available on the
WWW under <http://dx.doi.org/10.1002/ejic.201101159>.

was evaluated in the hydrogenation of olefins and arenes in pure biphasic liquid/liquid (neat water/substrate) conditions.

Results and Discussion

Synthesis and Characterization of Ruthenium and Platinum Nanoparticles

To the best of our knowledge, most examples of water-soluble Ru nanoparticles (RuNPs) and Pt nanoparticles (PtNPs) reported in the literature were directly obtained by the reduction of metal salts in aqueous media.^[13] In addition, a few papers report a phase transfer from an organic solvent to water as a result of the use of a phase-transfer agent such as the thiol derivatives^[14] thioglycolic acid^[15] or tris(4-phosphonatophenyl)phosphane.^[16] The application of our organometallic strategy using PTA as ligand allowed us to obtain nanoparticles that are well controlled in size and surface state and that are soluble in THF and water without the need for the subsequent addition of a phase-transfer agent.

RuNPs were obtained by the decomposition of a THF solution of the organometallic precursor [Ru(cod)(cot)] (cod = 1,5-cyclooctadiene; cot = 1,3,5-cyclooctatriene) in the presence of 1,3,5-triaza-7-phosphaadamantane (PTA) under hydrogen gas (3 bar). The first syntheses were carried out at room temperature in the presence of a [PTA]/[Ru] molar ratio of 0.2, which is usually enough to obtain stable RuNPs following our method. Agglomerates with a regular size of around 20 nm were obtained, as observed by TEM (Figure 1, a). These agglomerates were formed of individual nanoparticles, but their mean size was difficult to determine and thus this was estimated to be 2 nm. The presence of these agglomerates was attributed to a lack of a ligand to achieve a good stabilization of the nanoparticles. An increase in the [PTA]/[Ru] ratio to 0.8 gave individual RuNPs of almost 4 nm in size that are not agglomerated on the TEM grid (Figure 1, b) but neither are they well controlled in size. Maintaining the same [PTA]/[Ru] ratio of 0.8 but increasing the temperature to 70 °C led to reproducible nanoparticle syntheses (Scheme 1). Note that at this temperature, PTA is more soluble in THF, which may explain the better results.

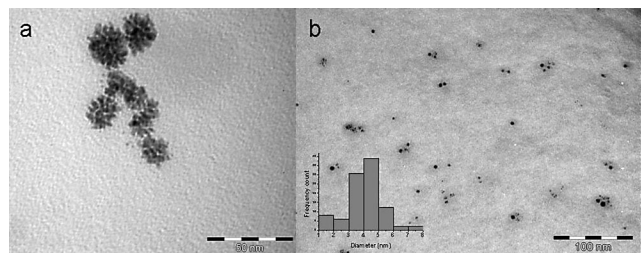
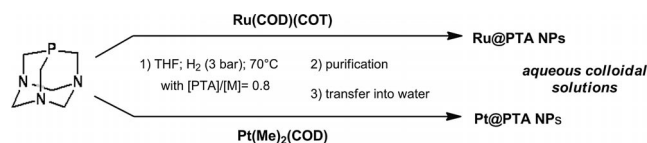


Figure 1. TEM micrographs of agglomerates (a) and 4-nm nanoparticles (b) obtained by the decomposition of [Ru(cod)(cot)] at room temperature with [PTA]/[Ru] = 0.2 and 0.8, respectively.



Scheme 1. Preparation of aqueous colloidal solutions of ruthenium and platinum nanoparticles stabilized by PTA.

Under these optimized conditions, we observed well-dispersed and very small RuNPs with a mean size of 1.3 ± 0.2 nm by TEM analysis (Figure 2, a,b). They were purified by precipitation with pentane and further dissolved in water without any change in either their dispersion or their mean diameter (1.4 ± 0.2 nm), as observed by TEM (Figure 2, c). Wide-angle X-ray scattering (WAXS) showed the usual hexagonal close-packed (hcp) structure of bulk ruthenium. Elementary analysis of the purified solid indicates a molar ratio [PTA]/[Ru] of 0.75, which is in good agreement with the theoretical ratio of 0.8 used for the synthesis of the particles.

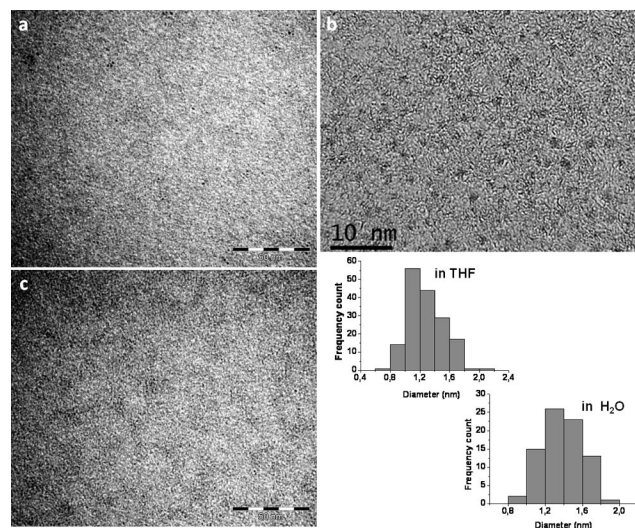


Figure 2. TEM (a) and HRTEM (b) micrographs in THF and TEM micrograph in H₂O (c) of PTA-stabilized ruthenium nanoparticles obtained under the optimized conditions and (d) corresponding size distributions.

Platinum nanoparticles were prepared in the same way by hydrogenation of the complex [Pt(Me)₂(cod)] in the presence of 0.2 or 0.8 mol-equiv. of PTA relative to platinum at 70 °C (Scheme 1). With a [PTA]/[Pt] ratio of 0.2, small PtNPs of around 1.5 nm were formed. In the case of [PTA]/[Pt] = 0.8, smaller PtNPs with a mean size of 0.9 ± 0.1 nm were observed by TEM/HRTEM (Figure 3, a,b); these PtNPs displayed the face-centred cubic (fcc) crystalline structure of bulk platinum (WAXS). Elementary analysis of the purified solid indicated a [PTA]/[Pt] molar ratio of 0.85, which is in good agreement with the theoretical ratio of 0.8 used for the synthesis of the particles. The formation of smaller PtNPs when a higher quantity of PTA was used in the reaction medium may result from better control during the nucleation step. However, in comparison with Ru nanoparticles, the Pt nanoparticles are slightly smaller. As for

ruthenium, the PtNPs were purified by precipitation with pentane and could be dispersed into water without any significant change in size ($d_m = 1.1 \pm 0.2$ nm, Figure 3, c). Note that the redispersion of PtNPs into water appeared easier than for RuNPs for which a residual solid was sometimes noticed.

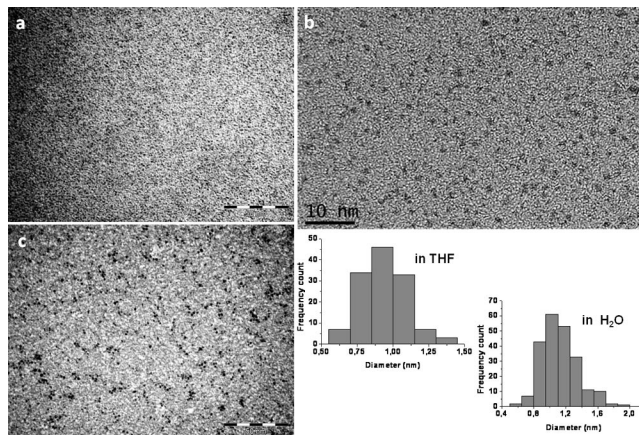


Figure 3. TEM (a) and HRTEM (b) micrographs in THF and TEM micrograph in H₂O (c) of the PTA-stabilized platinum nanoparticles obtained under optimized conditions and (d) corresponding size distributions.

According to previous results showing a better control of nanoparticle size with phosphanes than with amines,^[9,10a] the coordination of PTA to the surfaces of the particles was expected to be through the phosphorus atom, which was confirmed by NMR investigations. First, the ³¹P NMR spectra of the RuNPs and PtNPs recorded in D₂O solution under air (see Figure S1 of the Supporting Information) reveal no free PTA in solution (expected signal at $\delta \approx -98$ ppm) but a signal at $\delta = -2.9$ ppm corresponding to free PTA oxide, as described in the literature.^[17] The ¹³C NMR spectrum of Ru@PTA corroborates the presence of free PTA oxide with sharp peaks observed at $\delta = 69.9$ and 52.8 ppm (Figure 4). The formation of PTA oxide has been further studied in depth (see below). In addition to carbon signals from free PTA oxide, a broad peak is present at $\delta = 70.6$ ppm (and at 71.0 ppm for PtNPs; see Figure S2 in the Supporting Information), which has been attributed to the NCH₂N carbon atoms of PTA coordinated to the surfaces of the particles. Such signal broadening and chemical shift result from the proximity of the metal, the nanoparticles inducing a shielding effect.^[18] The other carbon signals of coordinated PTA (PCH₂N), expected in the range $\delta = 45$ – 50 ppm, are not observed. Such behaviour is well known for ligands with low mobility when coordinated to the surfaces of metal nanoparticles^[19] and proves the strong coordination of PTA to the surfaces of the nanoparticles by the phosphorus atom.

The ¹H NMR spectra (Figure 5, a; see also Figure S3 in the Supporting Information for assignments) also indicate the enlargement of the signal ($\delta \approx 4.5$ – 4.6 ppm) corresponding to the N(CH₂)N protons of PTA ligands coordinated to the surfaces of the particles, whereas the peaks from the

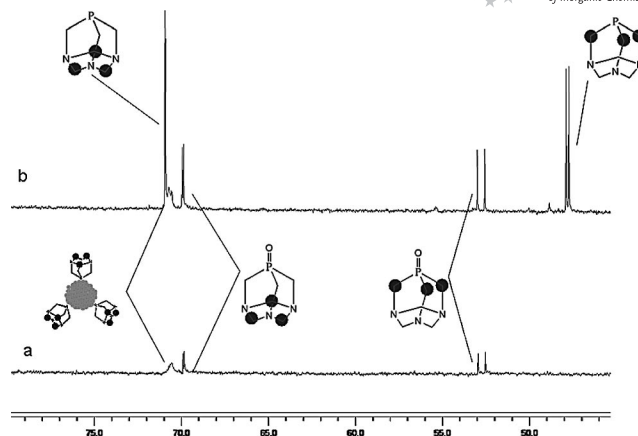


Figure 4. ¹³C{¹H} NMR (295 K, D₂O) spectra of Ru@PTA nanoparticles before (a) and after (b) addition of excess PTA.

PCH₂N protons are not visible due to their close proximity to the surfaces of the particles, which renders them impossible to observe. It also confirms the absence of free PTA and the presence of PTA oxide.

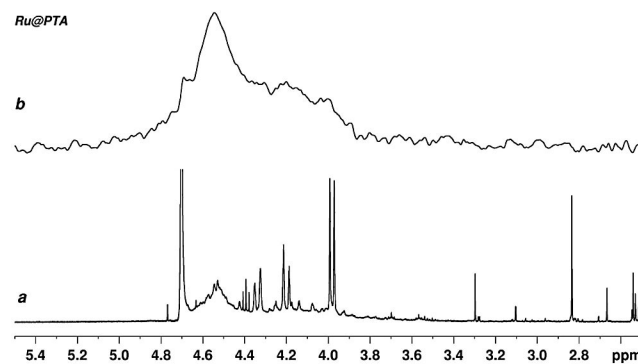


Figure 5. ¹H NMR (a) and diffusion-filtered ¹H NMR (b) (295 K, D₂O) spectra of Ru@PTA NPs.

DOSY ¹H NMR experiments were also carried out on Ru@PTA NPs dispersed in D₂O under argon. This technique can be used as a diffusion-filtered ¹H NMR experiment to eliminate the contribution of free and small molecules with fast diffusion thereby leaving visible only the signals corresponding to larger species with low diffusion coefficients, such as ligands coordinated to the surfaces of nanoparticles. The diffusion-filtered ¹H NMR spectrum of Ru@PTA nanoparticles (Figure 5, b) reveals two broad signals at $\delta = 4.55$ and 4.2 ppm, which correspond, respectively, to the N(CH₂)N and PCH₂N protons of PTA ligands coordinated to the surfaces of the particles. After addition of a small quantity of free PTA to the NMR tube (see Figure S4 in the Supporting Information), no exchange on the NMR timescale (from ms to s) was observed between the free and coordinated ligand, which indicates a strong interaction of PTA with the surfaces of the nanoparticles. Determination of the diffusion coefficients (D) revealed a value for Ru@PTA nanoparticles 2.3 times lower than for free PTA ($2.5 \pm 0.2 \times 10^{-10}$ against $5.7 \pm 0.2 \times 10^{-10}$ m²s⁻¹). This

also indicates a hydrodynamic radius 2.3 times higher, estimated to be 1.7 ± 0.2 nm. This value is in good accord with the mean size determined by TEM taking into account a ligand layer around the nanoparticles.

The strength of the interaction of PTA with the surfaces of the NPs was studied by a ligand-exchange reaction with dodecanethiol (DDT). Indeed, as sulfur derivatives are well known for their strong affinity to noble metal surfaces, we believed that DDT could displace PTA ligands in the case of weak affinity. Ru@PTA NPs were dispersed in a THF solution containing a large excess of DDT. Contrary to what we had previously observed for phenylpropylpyridine-stabilized RuNPs,^[20] no signals corresponding to free PTA were observed by ^1H and ^{31}P NMR after 24 h of reaction with DDT, which indicates that PTA was not released into solution (see Figure S5 in the Supporting Information). This is in agreement with a previous observation with tris-(4-phosphonatophenyl)phosphane-stabilized PtNPs, with which no displacement of the stabilizing phosphane was observed after the addition of excess 2-mercaptoethanol.^[16] PTA thus appears to be strongly coordinated to the surfaces of the particles.

To complete this study, a DOSY ^1H NMR experiment was carried out. In addition to the absence of PTA release, peaks at $\delta = 2.5$, 1.6, 1.3 and 0.9 ppm corresponding to DDT molecules linked to the surfaces of RuNPs are detected in the diffusion-filtered ^1H NMR spectrum (Figure 6). These signals show the same diffusion coefficient as the strongly bonded PTA in the DOSY spectrum (see Figure S6 in the Supporting Information). This observation indicates that even if no PTA ligands are displaced from the surfaces of the RuNPs, sufficient space is available for coordination of DDT molecules. This hypothesis was reinforced by the increased solubility of the RuNPs in THF after DDT addition. Based on the integration of the peaks of PTA at $\delta = 4.6$ ppm (NCH_2N) and DDT at $\delta = 1.6$ and 1.3 ppm in the diffusion-filtered ^1H NMR spectrum, a molecular ratio $[\text{PTA}]/[\text{DDT}]$ of 1.6 could be estimated (relaxation factors were not taken into account). These results demonstrate the

strong interaction of PTA with the RuNPs, even greater than that of the thiol molecules.

PTA-stabilized ruthenium nanoparticles were also characterized in the solid state by cross-polarization magic-angle spinning (CP-MAS) NMR spectroscopy. In the $^{31}\text{P}\{^1\text{H}\}$ MAS NMR spectrum, the Ru@PTA NPs exhibit a broad band containing several peaks in the range -50 to 20 ppm (Figure 7, a). These chemical shifts are in the same range as those reported for Ru-PTA complexes.^[10a] It has also been reported that phosphane-stabilized PdNPs display a chemical shift close to that of the corresponding complex.^[21] Thus, the observed chemical shifts can be attributed to PTA coordinated to the surfaces of the nanoparticles. The absence of peaks at around $\delta = -98$ ppm confirmed the absence of free PTA. The observed signals correspond to PTA molecules coordinated to the surfaces of the NPs through phosphorus atoms rather than through nitrogen atoms.^[10a] The multiplicities of the peaks detected for PTA-RuNPs do not have to be linked to different coordinated ligands but more to the heterogeneity of the signal at the nanoparticle surface. When the ruthenium nanoparticles were exposed to air, we observed first a quick burning and second the appearance of sharp peaks at around 0.5 and -10 ppm in the $^{31}\text{P}\{^1\text{H}\}$ MAS NMR spectra (Figure 7, b). These peaks have been attributed to PTA oxide, as already observed in liquid NMR, despite a slight shift probably due to the close proximity to the RuNPs. The quantity of PTA oxide was estimated to be around 10% by comparison of the peak areas. Burning in air is usually characteristic of a high reactivity of the particles mainly due to their small size as well as clean surface state. The formation of a small quantity of PTA oxide does not reveal a lack of stability but more an interesting surface reactivity of the particles. The $^{13}\text{C}\{^1\text{H}\}$ CP-MAS NMR spectrum of Ru@PTA NPs shows two broad signals at $\delta = 73$ and 60 ppm (see Figure S7 in the Supporting Information), in agreement with the coordination of phosphanyl groups to the surfaces of the particles. Indeed, the PCH_2N carbon is more deshielded than the NCH_2N carbon when coordinated to the nanoparticle compared to free PTA (δ_{C} in D_2O : 70.9 and 47.8 ppm for NCH_2N and PCH_2N , respectively).

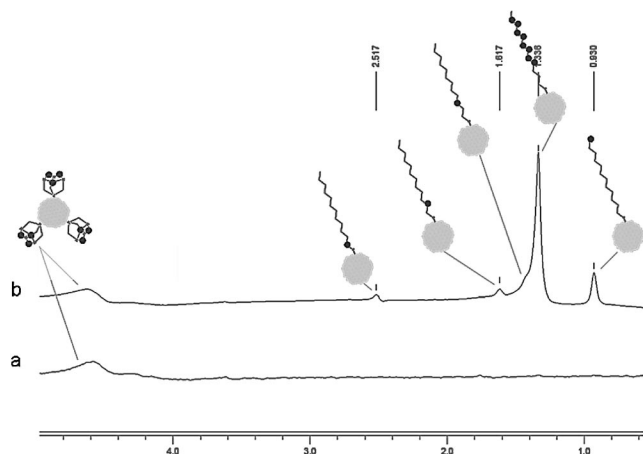


Figure 6. Diffusion-filtered ^1H NMR (Avance 500; 500 MHz; room temperature, $[\text{D}_8]\text{THF}$) spectra of RuNPs in THF before (a) and after (b) the addition of dodecanethiol.

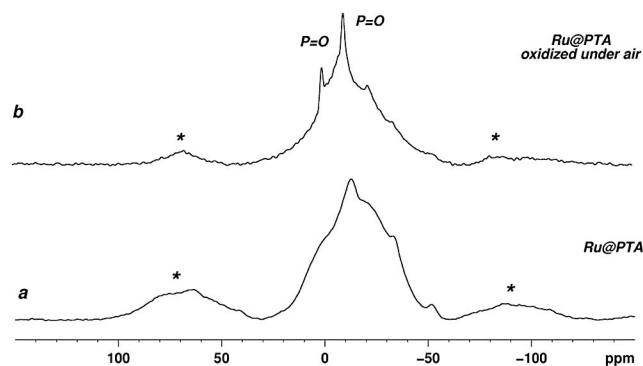


Figure 7. $^{31}\text{P}\{^1\text{H}\}$ MAS NMR spectra of Ru@PTA NPs (295 K; $\nu_r = 12$ kHz) before (a) and after (b) exposure to air. *: spinning sidebands.

Finally, in addition to signals corresponding to PTA ligands, the $\{^1\text{H}\}$ MAS NMR spectrum (Figure 8) of Ru@PTA NPs revealed a weak signal at $\delta = -14$ ppm, a value typical of hydrides. No difference in chemical shift was observed after variation of the rotation speed from 12 to 14.5 kHz, thus excluding confusion with a rotation band. As the presence of hydrides on the surfaces of various ruthenium nanoparticles has already been demonstrated through indirect methods,^[11] we attributed this peak to surface hydrides. As a confirmation, this signal disappeared after oxidation of the ruthenium surface in air. Note that hydrides at nanoparticle surfaces are observed here by direct ^1H NMR investigation for the first time.

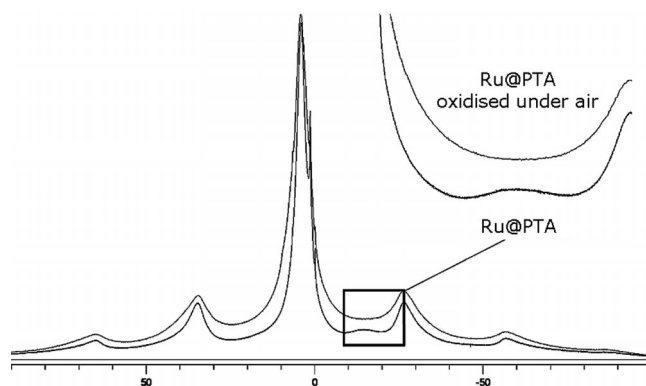


Figure 8. ^1H MAS NMR spectra of Ru@PTA NPs before (bottom) and after (top) oxidation under air (295 K; $\nu_r = 12$ kHz).

As PTA oxide was detected during the characterization of the nanoparticles, we tried to clarify its origin. First, ^{31}P and ^1H NMR spectra were recorded for solutions of pure PTA in $[\text{D}_8]\text{THF}$ and D_2O without any metal. Only traces of PTA oxide were observed and most importantly, no evolution was noticed with time even after long exposure to air, which indicates that the formation of PTA oxide needs the presence of metal. Secondly, ^1H and ^{31}P NMR characterization of solutions of RuNPs in THF and D_2O prepared under argon showed weak PTA oxide signals with no evolution after 1 day (see Figure S8 in the Supporting Information), which indicates that the RuNPs do not efficiently produce PTA oxide in the absence of air. Thirdly, fresh aqueous ruthenium solutions under air were studied by ^1H NMR over 24 h (see Figure S9 in the Supporting Information). An increase in the PTA oxide signals (at $\delta = 4.4$, 4.3 and 4.1 ppm) was observed in comparison with added free PTA used as standard [$\delta = 4.5$ (NCH_2N) and 4.0 ppm (PCH_2N)], which shows that in the presence of air, RuNPs catalyse the oxidation of PTA into PTA oxide. Finally, when free PTA was added to an aqueous solution of RuNPs under argon we observed after a few hours a weak increase in the intensity of the PTA oxide peak (see Figure S10 in the Supporting Information) with no evolution after 1 day. Exposure of this solution to air led to a slight increase in the intensities of the PTA(O) peak and other minor peaks without any evolution after 3 days. These observations are consistent with those previously reported for rhodium-PTA^[17] and -TPPTS complexes^[22] or rhodium clusters sta-

bilized by phosphanylphosphonic acid^[23] and allowed us to conclude that the oxidation of PTA takes place only when excess PTA and air are present. However, the formation of PTA oxide is limited as no evolution with time was observed.

In summary, the PTA ligand has allowed us to perform reproducible syntheses of RuNPs and PtNPs of very small size that are soluble in both organic and aqueous media by applying our simple organometallic approach. Complementary NMR studies attest to the strong coordination of PTA through the phosphorus atom to the surfaces of the particles and it is even impossible to displace PTA by the addition of excess thiol. This coordination is thus the key step in controlling the characteristics of the nanoparticles. Nevertheless, and as already reported by other groups, a small quantity of PTA oxide was formed under air. It appears that this oxidation occurred only when free PTA was added to the NMR tube.

Stability Study and Investigation for Catalysis

Before performing catalytic experiments with PTA-stabilized nanoparticles, we investigated the stability of the aqueous colloidal solutions over time. When the ruthenium and platinum water colloidal solutions were studied with time inside closed flasks under air, the platinum colloidal solutions were clearly more stable than the corresponding ruthenium solutions for which the formation of a precipitate was detected after a few (2–3) days. However, the stability of the platinum and ruthenium aqueous colloidal solutions could be increased by storing them under argon or under air after the addition of extra PTA (1 mol-equiv./introduced metal). Under these conditions, the resulting colloidal solutions remained completely stable for several months (up to 18 to date). A higher stability in the presence of excess PTA has already been observed by Darensbourg et al. and was explained by the formation of less PTA(O).^[17a]

The aqueous colloidal Ru@PTA and Pt@PTA suspensions were then investigated in the biphasic liquid/liquid hydrogenation of model olefins and aromatic substrates, a reaction frequently performed with metal nanoparticles,^[24] to probe their surface states as well as their stabilities under catalytic conditions. The catalytic experiments were performed without taking any particular precaution. The results are presented in Table 1. First, octene was fully converted into the corresponding alkane with Pt@PTA in 2 h at room temperature under atmospheric hydrogen pressure (entry 1) with an activity of 50 mol product (mol metal) $^{-1}$ h $^{-1}$. No destabilization of the suspension with formation of aggregates was observed. Under the same mild conditions, the more lipophilic dodecene was also reduced by Ru@PTA in 5 h but with a weaker activity of 20 mol product (mol metal) $^{-1}$ h $^{-1}$ (entry 7). An increase in hydrogen pressure was not detrimental to the stability of the suspension, as shown in the hydrogenation of octene with Ru@PTA NPs under 10 bar H_2 (entry 8).

Table 1. Hydrogenation of olefins and aromatic derivatives with Ru@PTA and Pt@PTA aqueous colloidal solutions.^[a]

Entry	Catalyst	Substrate	P_{H_2} [bar]	Time [h]	Conversion [%] ^[f]
1	Pt@PTA ^[b]	octene	1	2	100
2	Pt@PTA ^[b]	octene	1	2	68 ^[g]
3	Pt@PTA ^[c]	toluene	10	2	8
4	Pt@PTA ^[c]	toluene	10	16	100
5	Pt@PTA ^[c]	<i>m</i> -methylanisole	10	2	15
6	Pt@PTA ^[c]	<i>m</i> -methylanisole	10	16	100
7	Ru@PTA ^[d]	dodecene	1	5	100 ^[h]
8	Ru@PTA ^[d]	octene	10	1	100
9	Ru@PTA ^[e]	toluene	10	16	100
10	Ru@PTA ^[e]	<i>m</i> -methylanisole	10	16	60

[a] Reaction conditions: [substrate]/[metal] = 100, $T = 20^\circ\text{C}$ stirred at 1500mm^{-1} . [b] 0.0119 mmol Pt and 1.19 mmol substrate. [c] 0.0122 mmol Pt and 1.22 mmol substrate. [d] 0.0159 mmol Ru and 1.59 mmol substrate. [e] 0.020 mmol Ru and 2 mmol substrate. [f] Substrate conversion determined by gas chromatography. [g] Recycling of the aqueous suspension of entry 1. [h] Determined by ^1H and ^{13}C NMR spectroscopy.

In a second set of experiments, we studied the performances of suspensions of Ru@PTA and Pt@PTA in the hydrogenation of various aromatic derivatives such as toluene and *m*-methylanisole. As previously described with surfactant-stabilized ruthenium nanoparticles,^[25] the catalytic reactions were performed under hydrogen pressure. Complete hydrogenation of toluene to cyclohexane was observed overnight (16 h) with Ru@PTA whereas 60% of *m*-methoxymethylcyclohexane was formed from *m*-methylanisole (entries 9 and 10, respectively). In comparison, total reduction was demonstrated with Pt@PTA after 16 h (entries 4 and 6) even though very low conversions were observed after 2 h with 8 and 15% yields of the cyclohexyl derivatives, respectively (entries 3 and 5). Note that in the hydrogenation of *m*-methylanisole, no byproduct such as the corresponding cyclic 3-methyl ketone (e.g., 3-methylcyclohexanone) was detected as is sometimes observed in water during the hydrogenation of oxygenated arenes.^[26]

Finally, we investigated the stability and reusability of the aqueous suspensions of Pt⁰ in the hydrogenation of octene under mild conditions (20°C , 1 bar H_2). After 2 h (entry 1), the aqueous phase containing Pt@PTA was separated from the organic phase and reused in a second run. For the same reaction time, a decrease in catalytic activity was observed with a conversion of 68%.

Thus, the aqueous colloidal suspensions of PTA-stabilized Ru and Pt nanoparticles display interesting catalytic activity in the hydrogenation of simple olefins and aromatic compounds under mild conditions. However, the preliminary results from the reuse of the Pt@PTA nanocatalyst show a decrease in conversion. This can be explained by leaching of the metal or to a lack of stability of the particles under the conditions of catalysis.

Conclusions

Water-soluble ruthenium and platinum nanoparticles have been easily prepared from metal–organic complexes by

using 1,3,5-triaza-7-phosphaadamantane (PTA) as stabilizer. Note that these nanoparticles display low size dispersity and very small mean diameters of 1.4 and 1.1 nm for ruthenium and platinum, respectively, making them interesting systems for application in catalysis. In addition to controlling their size, the coordination of PTA ligands to the surfaces of the particles is the driving force for their dissolution in water as it does not necessitate the use of an extra phase-transfer agent. This coordination has been evidenced by solution and solid-state ^1H , ^{13}C and ^{31}P NMR studies. DOSY experiments also provided information on the behaviour of this ligand at the surfaces of the particles. No exchange was noticed on the NMR timescale. However, PTA was not released after the addition of excess dodecanethiol, which shows the strong interaction of PTA at the nanoparticle surface. In addition, the formation of small quantities of PTA oxide was observed in the presence of excess PTA and air. Finally, aqueous colloidal solutions of the nanoparticles were used as catalysts in the hydrogenation of simple olefins and arenes. These nanocatalysts appeared to be efficient under mild conditions. The results demonstrate that these nanocatalysts are active despite the change of environment they undergo after their dissolution in water. However, preliminary recycling tests showed that greater stability and/or better recovery is necessary to increase their potential as catalysts.

Experimental Section

Reagents and General Procedures: All operations relating to nanoparticle synthesis were carried out in Schlenk or Fischer–Porter glassware or in a glove-box under argon. The organometallic complexes used as precursors, $[\text{Ru}(\text{cod})(\text{cot})]$ and $[\text{Pt}(\text{Me})_2(\text{cod})]$, were purchased from Nanomeps-Toulouse. 1,3,5-Triaza-7-phosphaadamantane (PTA) used as stabilizing ligand was synthesized following a published procedure^[27] by reaction of tris(hydroxymethyl)phosphane $\text{P}(\text{CH}_2\text{OH})_3$ {which was previously obtained by in situ reaction of tetrakis(hydroxymethyl)phosphonium chloride $[\text{P}(\text{CH}_2\text{OH})_4]\text{Cl}$ (Aldrich) and sodium hydroxide} with formaldehyde and hexamethylenetetramine (also from Aldrich). Solvents were dried and distilled before use: THF over sodium benzophenone and pentane over calcium hydride. All the reagents and solvents were degassed before use by three freeze–pump–thaw cycles. Water was distilled twice before use by a conventional method. All the organic compounds, such as octene, dodecene, toluene, *m*-methylanisole, investigated as model substrates were purchased from Acros Organics or Sigma–Aldrich–Fluka and used without further purification.

Samples for TEM analyses were prepared by slow evaporation of a drop of the crude colloidal solution deposited onto holey carbon-covered copper grids under argon (in a glove-box) for THF solutions and under air for aqueous solutions. The TEM and HRTEM analyses were performed at the “Service Commun de Microscopie Electronique de l’Université Paul Sabatier” (UPS-TEMSCAN). TEM images were obtained by using a JEOL 1011 electron microscope operating at 100 kV with resolution point of 4.5 Å. HRTEM was carried out with a JEOL JEM 2010 electron microscope operating at 200 kV with a resolution point of 2.5 Å. The size distributions were determined by manual analysis of enlarged micrographs with Imagetool software to obtain a statistical size distribution and a mean diameter.

NMR analyses were performed at the NMR facility of LCC. All ^1H and ^{13}C chemical shifts were measured relative to TMS. ^{31}P chemical shifts are referenced to external 85% H_3PO_4 .

1D and 2D ^1H , ^{31}P and ^{13}C NMR spectra in the liquid state were recorded with a Bruker Avance 500 spectrometer equipped with a 5 mm triple resonance inverse Z-gradient probe (TBI ^1H , ^{31}P , BB).

All diffusion measurements were made by using the stimulated echo pulse sequence. The recycle delay was adjusted to 3 s. The strength of the gradient was calibrated by measuring the self-diffusion of the residual HDO signal in a 100% D_2O sample at 298 K ($1.90 \times 10^{-9} \text{ m}^2 \text{ s}^{-1}$). For 2D diffusion ordered spectroscopy (DOSY), after Fourier transformation and baseline correction the diffusion dimension was processed with the Bruker Topspin software package DOSY.

Solid-state NMR experiments were recorded with a Bruker Avance 400 spectrometer equipped with a 4 mm probe. The rotor for solid-state NMR was loaded with metal nanoparticle powders inside a glove-box under argon and the powder was extracted from the rotor during 1 h before reloading. Samples were spun at 12 kHz at the magic angle by using ZrO_2 rotors. For ^1H MAS and ^{31}P MAS single pulse experiments, a small flip angle ($\approx 30^\circ$) was used with recycle delays of 5 and 20 s, respectively. ^{13}C -CP/MAS spectra were recorded with a recycle delay of 5 s and contact times of 1 ms. All the ^{13}C and ^{31}P NMR spectra were recorded under high-power proton decoupling conditions.

All gas chromatography analyses were performed by using a Carlo-Erba GC 6000 instrument with an FID detector equipped with a Factor Four column (30 m, 0.25 mm i.d.). The parameters used were as follows: initial temperature, 40 $^\circ\text{C}$; initial time, 10 min; ramp, 10 $^\circ\text{C min}^{-1}$; final temperature, 80 $^\circ\text{C}$; final time, 30 min; injector temperature, 220 $^\circ\text{C}$; detector temperature, 250 $^\circ\text{C}$.

Synthesis of Ruthenium Nanoparticles (Ru@PTA): [Ru(cod)(cot)] (100 mg, 0.317 mmol) was introduced into a Fisher–Porter bottle and left under vacuum for 0.5 h. THF (100 mL) degassed by three freeze–pump–thaw cycles was added. The resulting yellow solution was cooled to 193 K and a solution of THF (100 mL) containing PTA (40 mg, 0.254 mmol, [PTA]/[Ru] = 0.8) was introduced into the reactor. The Fisher–Porter bottle was heated to 343 K and then pressurized with hydrogen gas (3 bar). After 12 h, a homogeneous brown colloidal solution was obtained. The volume of the solution was reduced to approximately 10 mL by solvent evaporation before its transfer into a solution of deoxygenated pentane (100 mL). A brown precipitate formed, which was filtered and dried under vacuum to give the nanoparticles as a dark brown powder (yield of the isolated sample: 50–60%).

Synthesis of Platinum Nanoparticles (Pt@PTA): [PtMe₂(cod)] (150 mg, 0.45 mmol) was introduced into a Fisher–Porter bottle and left under vacuum for 0.5 h. THF (100 mL) degassed by three freeze–pump cycles was added. A solution of THF (100 mL) containing PTA (60 mg, 0.38 mmol, [PTA]/[Pt] = 0.8) was then introduced into the reactor. The Fisher–Porter bottle was heated to 343 K and then pressurized with hydrogen gas (3 bar). After 12 h, a homogeneous brown solution was obtained. The volume of the solution was then reduced to approximately 10 mL before its transfer into a solution of deoxygenated pentane (100 mL). A dark-brown precipitate formed, which was filtered and dried in vacuo to give the nanoparticles as a dark-brown powder (yield of the isolated sample: 50–60%).

Hydrogenation Catalysis at Atmospheric Hydrogen Pressure: A 25 mL round-bottomed flask, charged with the previously prepared aqueous suspensions of Ru@PTA or Pt@PTA and a magnetic stir-

rer, was connected with a gas burette (500 mL) to a flask to balance the pressure. The flask was closed by a septum and the system was filled with hydrogen and purged three times. The appropriate amount of substrate (up to 2×10^{-3} mol, molar ratio Substrate/Metal = 100) was injected through the septum. The reaction mixture was magnetically stirred at room temperature under 1 bar of H_2 . The reaction was monitored by the volume of hydrogen consumed. The reaction progress was monitored by gas chromatographic analysis.

Hydrogenation Catalysis Under Hydrogen Pressure: A stainless steel autoclave was charged with an aqueous suspension of Ru@PTA or Pt@PTA nanoparticles and a magnetic stirrer. The appropriate substrate (2×10^{-3} mol, 100 equiv.) was added to the autoclave and hydrogen gas was admitted to the system at constant pressure (up to 10 bar). The reaction progress was monitored by gas chromatographic analysis.

Supporting Information (see footnote on the first page of this article): Complementary NMR spectra.

Acknowledgments

The authors thank V. Collière (LCC-CNRS and UPS-TEMSCAN) for HRTEM analysis and P. Lecante (CEMES-CNRS) for WAXS analysis. The authors are also grateful to the Centre National de la Recherche Scientifique (CNRS) and the EU (project Artizymes STREP-FP6-2003-NEST-B3-0151471) for financial support.

- a) I. P. Beletskaya, L. M. Kustov, *Russ. Chem. Rev.* **2010**, 79, 441; b) Y. Uozumi, *Synlett* **2010**, 1988.
- D. J. Cole Hamilton, *Science* **2003**, 299–302, 1702.
- M. J. Muldoon, *Dalton Trans.* **2010**, 39, 337.
- a) V. Polshettiwar, R. S. Varma, *Green Chem.* **2010**, 12, 743; b) N. Yan, C. X. Xiao, Y. Kou, *Coord. Chem. Rev.* **2010**, 254, 1179.
- a) D. Astruc, F. Lu, J. R. Aranzas, *Angew. Chem.* **2005**, 117, 8062; *Angew. Chem. Int. Ed.* **2005**, 44, 7852; b) L. D. Pachón, G. Rothenberg, *Appl. Organomet. Chem.* **2008**, 22, 288; c) A. Roucoux, in: *Topics in Organometallic Chemistry: Surface and Interfacial Organometallic Chemistry and Catalysis* (Eds.: B. Chaudret, C. Copéret), Springer, Heidelberg, Germany, **2005**, vol. 16, p. 261; d) A. Roucoux, A. Nowicki, K. Philippot, in: *Nanoparticles and Catalysis* (Ed.: D. Astruc), Wiley-VCH, Weinheim, Germany, **2008**, p. 349.
- Y. Zhu, C. N. Lee, R. A. Kemp, N. S. Hosmane, J. A. Maguire, *Chem. Asian J.* **2008**, 3, 650.
- B. L. Cushing, V. L. Kolesnichenko, C. J. O'Connor, *Chem. Rev.* **2004**, 104, 3893.
- K. Philippot, B. Chaudret, in: *Comprehensive Organometallic Chemistry III* (Eds.: R. H. Crabtree, M. P. Mingos), Elsevier, Amsterdam, The Netherlands, **2007**, chapter 12–03, pp. 71–99.
- a) E. Ramirez, S. Jansat, K. Philippot, P. Lecante, M. Gómez, A. Masdeu-Bultó, B. Chaudret, *J. Organomet. Chem.* **2004**, 689, 4601; b) J. García-Antón, M. R. Axet, S. Jansat, K. Philippot, B. Chaudret, T. Pery, G. Buntkowsky, H.-H. Limbach, *Angew. Chem.* **2008**, 120, 2104; *Angew. Chem. Int. Ed.* **2008**, 47, 2074.
- a) C. Pan, K. Pelzer, K. Philippot, B. Chaudret, F. Dassenoy, P. Lecante, M.-J. Casanove, *J. Am. Chem. Soc.* **2001**, 123, 7584; b) K. Philippot, B. Chaudret, *C.R. Chim.* **2003**, 6, 1019; c) E. Ramirez, L. Eradès, P. Lecante, K. Philippot, B. Chaudret, *Adv. Funct. Mater.* **2007**, 17, 2219.
- P.-J. Debouttière, V. Martinez, K. Philippot, B. Chaudret, *Dalton Trans.* **2009**, 10172.
- a) A. D. Philips, L. Gonsalvi, A. Romerosa, F. Vizza, M. Peruzzini, *Coord. Chem. Rev.* **2004**, 248, 955; b) M. Zablocka, A.

- Hameau, A.-M. Caminade, J.-P. Majoral, *Adv. Synth. Catal.* **2010**, 352, 2341.
- [13] a) E. Guyonnet-Bilé, A. Denicourt-Nowicki, R. Sassine, F. Launay, A. Roucoux, *Dalton Trans.* **2011**, 40, 6524; b) C. Hubert, A. Denicourt-Nowicki, A. Roucoux, D. Landy, B. Leger, G. Crowyn, E. Monflier, *Chem. Commun.* **2009**, 10, 1228.
- [14] S. E. Eklund, D. E. Cliffler, *Langmuir* **2004**, 20, 6012; T. Tsukatani, H. Fujihara, *Langmuir* **2005**, 21, 12093.
- [15] S. Giuffrida, G. Ventimiglia, F. L. Callari, S. Sortino, *Eur. J. Inorg. Chem.* **2006**, 4022.
- [16] C. N. Kostelansky, J. J. Pietron, M.-S. Chen, W. J. Dressick, K. E. Swider-Lyons, D. E. Ramaker, R. M. Stroud, C. A. Klug, B. S. Zelakiewicz, T. L. Schull, *J. Phys. Chem.* **2006**, 110, 21487.
- [17] a) D. J. Darensbourg, N. White Stafford, F. Joo, J. R. Reibenspies, *J. Organomet. Chem.* **1995**, 488, 99; b) P. Smolenski, C. Dinoi, M. Fatima, C. Guedes da Silva, A. J. L. Pombeiro, *J. Organomet. Chem.* **2008**, 693, 2338.
- [18] F. Dassenoy, K. Philippot, T. Ould Ely, C. Amiens, P. Lecante, E. Snoeck, A. Mosset, M.-J. Casanove, B. Chaudret, *New J. Chem.* **1998**, 22, 703.
- [19] a) R. H. Terrill, T. A. Postlethwaite, C.-H. Chen, C.-D. Poon, A. Terzis, A. Chen, J. E. Hutchison, M. R. Clark, G. Wignall, J. D. Londono, R. Superfine, M. Falvo, C. S. Johnson, Jr., E. T. Samulski, R. W. Murray, *J. Am. Chem. Soc.* **1995**, 117, 12537; b) A. Badia, W. Gao, S. Singh, L. Demers, L. Cuccia, L. Reven, *Langmuir* **1996**, 12, 1262.
- [20] I. Favier, S. Massou, E. Teuma, K. Philippot, B. Chaudret, M. Gomez, *Chem. Commun.* **2008**, 3296.
- [21] S. U. Seong, Y. Jang, K. Y. Yoon, E. Kang, T. Hyeon, *Nano Lett.* **2004**, 4, 1147.
- [22] a) C. Larpent, R. Dabard, H. Patin, *Inorg. Chem.* **1987**, 26, 2922; b) C. Larpent, R. Dabard, H. Patin, *New J. Chem.* **1988**, 12, 907.
- [23] J. Glöckler, S. Klütze, W. Meyer-Zaika, A. Reller, F. J. García-García, H.-H. Strehblow, P. Keller, E. Rentschler, W. Kläui, *Angew. Chem.* **2007**, 119, 1183; *Angew. Chem. Int. Ed.* **2007**, 46, 1164.
- [24] a) D. Marquardt, C. Vollmer, R. Thomann, P. Steurer, R. Mülhaupt, E. Redel, C. Janiak, *Carbon* **2011**, 49, 1326–1332, and references cited therein; b) A. Roucoux, K. Philippot, *Homogeneous Hydrogenation: Colloids - Hydrogenation with noble metal nanoparticles*, in: *The Handbook of Homogeneous Hydrogenation* (Eds.: J. G. de Vries, C. J. Elsevier), Wiley-VCH, Weinheim, Germany, **2007**, p. 217.
- [25] A. Nowicki, V. Le Boulaire, A. Roucoux, *Adv. Synth. Catal.* **2007**, 349, 2326.
- [26] a) C. Hubert, A. Denicourt-Nowicki, J. P. Guégan, A. Roucoux, *Dalton Trans.* **2009**, 36, 7356; b) C. Hubert, E. G. Bilé, A. Denicourt-Nowicki, A. Roucoux, *Appl. Catal. A* **2011**, 394, 215.
- [27] D. J. Daigle M. Y. Darensbourg, *Inorg. Synth.* **1998**, 32, 40.

Received: October 21, 2011

Published Online: February 6, 2012

$[V_{15}Ge_6O_{42}S_6(H_2O)]^{12-}$, a Thiogermanatopolyoxovanadate Cluster Featuring the Spin Topology of the Molecular Magnet $[V_{15}As_6O_{42}(H_2O)]^{6-}$

Jing Wang,^[a] Christian Näther,^[a] Paul Kögerler,^[b] and Wolfgang Bensch^{*[a]}

Keywords: Cluster compounds / Solvothermal synthesis / Solid-state structures / Polyoxovanadate / Magnetic properties

The new compound $[Co(tren)(trenH_2)]_2\{[Co(tren)]_2-V_{15}Ge_6O_{42}S_6(H_2O)] \cdot 9H_2O$ (**1**, tren = tris(2-aminoethyl)amine) has been obtained under solvothermal conditions and features the unique thiogermanatopolyoxovanadate anion $[V_{15}^{IV}Ge_6^{IV}O_{42}S_6(H_2O)]^{12-}$ as the main structural motif. Compound **1** crystallizes in the monoclinic space group $P2_1/c$ with $a = 15.4711(2)$, $b = 26.4031(4)$, $c = 26.7213(4)$ Å, $V = 10874.2(3)$ Å³, and $Z = 4$. The $[V_{15}Ge_6O_{42}S_6(H_2O)]^{12-}$ cluster anion displays the spin topology reported for the molecular magnets $[V_{15}^{IV}As_6^{III}O_{42}(H_2O)]^{6-}$ and $[V_{15}^{IV}Sb_6^{III}O_{42}]^{6-}$ and

therefore represents a new member of the $\{V_{15}E_6\}$ family, which has allowed us to study the magnetic exchange interactions between the vanadyl (d^1) groups of the geometrically frustrated central V_3 triangle, which is sandwiched between strongly antiferromagnetically coupled V_6 hexagons. The cluster shell is expanded by two $\{Co(tren)\}^{2+}$ -based complexes through Co–S bonds, which reduce the high negative charge of the anion. The Co^{2+} ions in the $[Co(tren)(trenH_2)]^{4+}$ counteranions are coordinated to one tetradentate tren and a monodentate, doubly protonated tren ligand.

Introduction

Polyoxometalates (POMs) are a class of spherical metal–oxygen clusters composed of corner- and/or edge-sharing $\{MO_x\}$ polyhedra ($M = Mo, W, V, Nb$; $x = 4–7$). Due to their unique topological and electronic versatility, POM-based systems have been studied in different areas such as magnetism, catalysis, and medicine.^[1,2] Many properties of these materials are promising for a large range of potential applications. Polyoxovanadates (POVs) are an important member of the POM family and have been studied intensively. A large number of new POMs have been isolated and characterized,^[3,4] but the number of possible structures based on $\{VO_x\}$ polyhedra appears to be limited. In order to extend the structural class of POVs with new physical properties, additional elements have been incorporated in the spherical vanadium–oxygen clusters to modify, for example, the $\{V_{18}O_{42}\}$ archetype by the substitution of V with As, Sb, Ge, or Si. From these new approaches, different new clusters with the general formula $[V_{18-x}M_{2x}O_{42+y}]$ [$M = As$ or Sb , with $x = 2–4$, $y = 0$; or $M = Ge$, with $y = 2x = 6$ or 8 , or $x = 2$, $y = (OH)_4$], such as $[V_{16}As_4O_{42}]^{8-}$,^[5] $[V_{15}As_6O_{42}]^{6-}$,^[6,7] $[V_{14}As_8O_{42}]^{4-}$,^[7,8] $[V_{16}Sb_4O_{42}]^{8-}$,^[9,10] $[V_{15}Sb_6O_{42}]^{6-}$,^[11] $[V_{14}Sb_8O_{42}]^{4-}$,^[9] $[V_{15}Ge_6O_{48}]^{12-}$,^[12] $[V_{14}Ge_8O_{50}]^{12-}$,^[13,14] $[V_{16}Ge_4O_{42}(OH)_4]^{8-}$,^[12,13] $[(V_{16}O_{40})-$

$(Si_{4.5}V_{1.5}O_{10})]^{10.5-}$,^[15] and $[H_4V_{14}O_{44}(SiO)_8]^{12-}$,^[16] have been discovered.

The heteropolyoxovanadates mentioned above have been further modified by various methods to form new materials with interesting features and properties. For example, organic amines can be directly connected to the cluster anion to lead to charge-neutral compounds that exhibit increased solubility in nonpolar solvents.^[17] The addition of an amine-coordinated 3d transition metal complex can result in either discrete species, again with a decreased negative charge, or network structures, in which the complexes are interlinked by the transition metal–amine complexes to higher hierarchical structures.^[18–20] Additionally, the V centers of the cluster can be directly replaced by transition metals.^[21]

Reports of Ge-substituted POVs are scarce,^[12–14] and they suggest that V–Ge–O cluster chemistry may present a similarly vast structural diversity as V–As–O- and V–Sb–O-based cluster anions. Examples of Ge-containing POVs are $[V_{16}Ge_4O_{42}(OH)_4]^{8-}$, $[V_{15}Ge_6O_{48}]^{12-}$, and $[V_{12}Cd_2Ge_8O_{40}(OH)_8]^{4-}$, which can be further modified by transition-metal-complex linkers to result in various network structures.^[22] One particularly interesting feature of Ge-substituted POV clusters is the possibility to substitute oxygen atoms by sulfur atoms as in $[V_{14}Ge_8O_{42}S_8]^{12-}$,^[23] a reaction not observed for Sb- or As-containing POVs. Furthermore, the oxygen/sulfur sites of the GeO_3S tetrahedra characteristic for such thiogermanate POV structures can be used as donor sites for further connection to transition-metal complexes, which adds to the arsenal of potential modifications of the structural and physical properties of the clusters.

[a] University of Kiel, Institute of Inorganic Chemistry, Max-Eyth-Str. 2, 24118 Kiel, Germany
Fax: +49-431-8801520
E-mail: wbensch@ac.uni-kiel.de

[b] RWTH Aachen, Institut für Anorganische Chemie, Landoltweg 1, 52074 Aachen, Germany

Supporting information for this article is available on the WWW under <http://dx.doi.org/10.1002/ejic.201101187>.

Compared with V–As–O and V–Sb–O clusters, the V–Ge–O clusters exhibit high negative charges, such as $[\text{V}_{14}\text{Ge}_8\text{O}_{50}]^{12-}$ and $[\text{V}_{14}\text{Ge}_8\text{O}_{42}\text{S}_8]^{12-}$ as well as the new $[\text{V}_{15}\text{Ge}_6\text{O}_{42}\text{S}_6]^{12-}$ cluster presented here. The advantage of this high negative charge together with the possibility to use the Ge–S connection mode is that they can generate new structures with connection modes that have not been reported for the $\{\text{V}_{18}\text{O}_{42}\}$ archetype.

In our ongoing work, we were able to isolate $[\text{Co}(\text{tren})(\text{trenH}_2)]_2[\{\text{Co}(\text{tren})\}_2\text{V}_{15}\text{Ge}_6\text{O}_{42}\text{S}_6(\text{H}_2\text{O})]\cdot 9\text{H}_2\text{O}$ (**1**), which presents a hitherto unobserved modification of the cluster core $\{\text{V}_{15}\}$. In addition, the central cluster is extended by $[\text{Co}(\text{tren})]^{2+}$ complexes attached by Co–S bonds. We report the hydrothermal synthesis, which starts from vanadate(V) and elemental Ge, Co, and S, the crystal structure, and physical properties of **1**.

Results and Discussion

Compound **1** crystallizes in the monoclinic space group $P2_1/c$ with four formula units per unit cell and was obtained as dark red-brown blocks. The structure consists of a $[\{\text{Co}(\text{tren})\}_2\text{V}_{15}\text{Ge}_6\text{O}_{42}\text{S}_6(\text{H}_2\text{O})]^{8-}$ heteropolyanion (Figure 1), two $[\text{Co}(\text{tren})(\text{trenH}_2)]^{4+}$ counteranions, and nine water solvent molecules. Selected crystal data and details of the structure determination of **1** are summarized in Table 2.

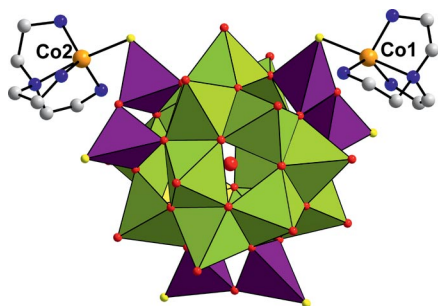


Figure 1. Polyhedral representation of the $[\{\text{Co}(\text{tren})\}_2\text{V}_{15}\text{Ge}_6\text{O}_{42}\text{S}_6(\text{H}_2\text{O})]^{8-}$ heteropolyanion in **1**. $\{\text{VO}_5\}$ polyhedra are shown in green and $\{\text{GeO}_3\text{S}\}$ in purple.

The central cluster fragment $[\text{V}_{15}\text{Ge}_6\text{O}_{42}\text{S}_6(\text{H}_2\text{O})]^{12-}$ is related to the spherical $\{\text{V}_{18}\text{O}_{42}\}$ archetype and is formed by six slightly distorted GeO_3S tetrahedra and 15 VO_5 square pyramids with a water molecule located in the central cavity of the cluster. All Ge–O [1.752(5)–1.791(5) Å], V–O_{term} [1.599(5)–1.624(5) Å], and V–(μ-O) [1.912(5)–2.013(5) Å] bond lengths are in the range common to other germanatopolyoxovanadates.^[13,22,23] The Ge–S bond lengths [2.088(2)–2.135(2) Å] match well with the values reported for the first mixed Ge–V-based polyoxothioanion.^[23] The oxidation states of the V and Ge atoms in **1** were calculated by the bond valence sum (BVS) method.^[24] The resulting average values of 4.1 for V, 4.1 for Ge, and 1.5 for S justify the assignment of the valence states as V^{4+} , Ge^{4+} , and S^{2-} . The presence of only V^{4+} in the cluster is in line with the IR spectrum where only one V–O stretching mode was observed at 972 cm^{-1} with no splitting into a $\text{V}^{\text{IV}}=\text{O}$

and a $\text{V}^{\text{V}}=\text{O}$ mode (the latter at slightly higher wavenumbers), as omnipresent in mixed-valent polyoxovanadate(IV/V) compounds [cf. e.g. $\text{K}_7[\text{As}^{\text{V}}\text{V}_{12}^{\text{IV}}\text{O}_{40}]\cdot 12\text{H}_2\text{O}$ and $[\{\text{Cu}(\text{H}_2\text{O})(\text{C}_5\text{H}_{14}\text{N}_2)_2\}_2\{\text{V}_{16}\text{O}_{38}(\text{Cl})\}]\cdot 4(\text{C}_5\text{H}_{16}\text{N}_2)_2$].^[18,25]

In the $[\text{V}_{15}\text{Ge}_6\text{O}_{42}\text{S}_6(\text{H}_2\text{O})]^{12-}$ cluster in **1**, three VO_5 pyramidal units of the $\{\text{V}_{18}\text{O}_{42}\}$ cluster archetype are replaced by three $\text{Ge}_2\text{O}_5\text{S}_2$ units. The dumbbell-shaped $\text{Ge}_2\text{O}_5\text{S}_2$ moiety shares corners with two neighboring VO_5 pyramids. The V_8O_{24} ring found in the $\{\text{V}_{18}\text{O}_{42}\}$ cluster is formally broken up by the insertion of the $\text{Ge}_2\text{O}_5\text{S}_2$ unit to define a new $\text{V}_7\text{Ge}_2\text{O}_{24}\text{S}_2$ ring (Figure 2). The three $\text{V}_7\text{Ge}_2\text{O}_{24}\text{S}_2$ rings are perpendicular to each other and combine to give the spherical $[\text{V}_{15}\text{Ge}_6\text{O}_{42}\text{S}_6]^{12-}$ cluster anion. Alternatively, the structure can be constructed by linking the three $\text{Ge}_2\text{O}_5\text{S}_2$ units by three VO_5 pyramids, which results in a $\text{V}_3\text{Ge}_6\text{O}_{24}\text{S}_6$ ring (Figure 3). The $\text{V}_3\text{Ge}_6\text{O}_{24}\text{S}_6$ ring is capped by six VO_5 pyramids above and below the horizontal ring plane to form the final cluster anion. This structural feature is reminiscent of the well-known molecular magnets $[\text{V}_{15}\text{As}_6\text{O}_{42}(\text{H}_2\text{O})]^{6-}$ and $[\text{V}_{15}\text{Sb}_6\text{O}_{42}]^{6-}$ with spherical shells composed of edge-sharing VO_5 square pyramids that contain V_2O_2 and V_3O_3 pores typical for reduced POVs. The three M_2O_5 ($\text{M} = \text{As}, \text{Sb}$) groups are centered around the

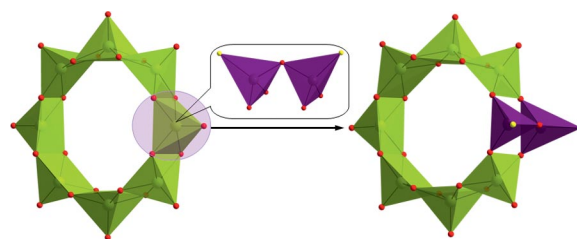


Figure 2. The $\text{V}_7\text{Ge}_2\text{O}_{24}\text{S}_2$ ring in the $[\text{V}_{15}\text{Ge}_6\text{O}_{42}\text{S}_6(\text{H}_2\text{O})]^{12-}$ cluster derived by substitution of a VO_5 pyramid. VO_5 polyhedra are shown in green, the $\text{Ge}_2\text{O}_5\text{S}_2$ unit in purple, O in red, and S in yellow.

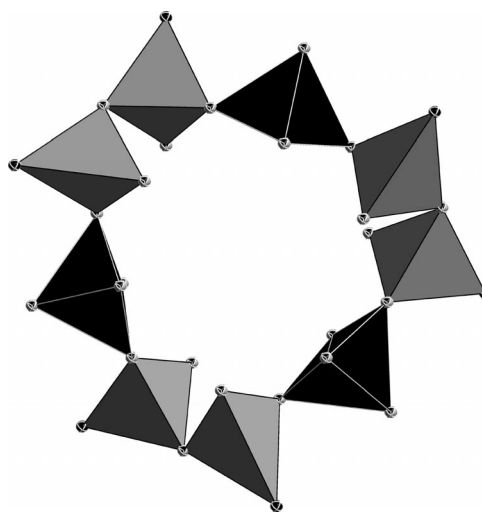


Figure 3. Polyhedral representation of the $\text{V}_3\text{Ge}_6\text{O}_{24}\text{S}_6$ ring constructed by the interconnection of the $\text{Ge}_2\text{O}_5\text{S}_2$ moieties (in gray) with the central three VO_5 pyramids (in black).

equatorial plane of the cluster and are condensed to two outer V₆ hexagons and central V position so that each of the 15 VO₅ moieties share common vertices with an MO₃ group. The [V₁₅Ge₆O₄₂S₆(H₂O)]¹²⁻ cluster represents another magnetic reference system, which only differs in the exchange groups (Ge₂O₅S₂ vs. As₂O₅/Sb₂O₅) that are crucial for superexchange interactions within the central V₃ triangle.

In **1**, the high negative charge of the [V₁₅Ge₆O₄₂S₆(H₂O)]¹²⁻ cluster is reduced by coordination of two [Co(tren)]²⁺ complexes (Co1, Co2). Each [Co(tren)]²⁺ group is joined to the central [V₁₅Ge₆O₄₂S₆(H₂O)]¹²⁻ cluster by a terminal S atom, which results in the formation of a distorted trigonal-bipyramidal environment around the Co²⁺ ions. In the [Co(tren)S] complexes (Figure 4a), the Co–S bond lengths [2.390(3)–2.442(2) Å] are slightly longer than reported values,^[25,26] and the Co–N bonds, which range between 2.021(8) and 2.304(12) Å, are in accordance with literature data.^[26,27]

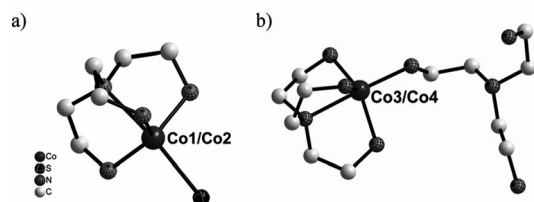


Figure 4. View of the different Co complexes in **1**. (a) [Co(tren)S]; (b) [Co(tren)(trenH₂)]⁴⁺.

The two [Co(tren)(trenH₂)]⁴⁺ complexes (Co3, Co4) act as counteranions and placeholders (Figure 4b). In these complexes, the Co²⁺ ion is coordinated by five N atoms of two different tren ligands to form a slightly distorted trigonal bipyramid. One of the tren ligands binds in a tetradentate mode, whereas the second ligand is doubly protonated and bound to Co²⁺ by only one N atom. The Co–N bond lengths [2.058(8)–2.251(7) Å] are in agreement with the values reported for other Co(tren) complexes.^[26,27] Different coordination modes for tren have been reported in the literature: a tridentate coordination mode was reported for [Mn(Se₆(tren))] where the free ethylamine groups bind to neighboring complexes to form chains,^[28] and a similar binding mode was observed in the structures of [{Ni₂(tren)₃}{Mo₂O₂S₆}₂·2.75H₂O]_n^[29] and [Mn₂(tren)₃][Mo₂O₂S₆]₂·1.3H₂O.^[30] tren also acts as a tridentate ligand in [Ni(tren)₂](BF₄)₂,^[31] [Ni(tren)₂]Cl₂, and [Ni(tren)₂]-WS₄.^[32] In the structure of [Mn(tren)₂]Cl₂, one tren molecule is tetradentate, and three tren molecules coordinate in a monodentate fashion.^[28] There are also examples in the literature where protonated tren molecules act as charge-compensating counterions despite the presence of transition-metal cations.^[33,34]

Figure 5 displays the arrangement of the [{Co(tren)}₂V₁₅Ge₆O₄₂S₆(H₂O)]⁸⁻ clusters in the (100) plane. An extended hydrogen-bonding network between N–H and O atoms generates a 3D framework (Table 1). By neglecting the H₂O molecules, four [{Co(tren)}₂-

V₁₅Ge₆O₄₂S₆(H₂O)]⁸⁻ clusters with their Co1 and Co2 complexes are joined by the H-bonding interactions (indicated by the shaded area in Figure 5) to yield a repeating unit in the (100) plane. The H-bonding pattern generates two differently oriented channels (A and B) along the [100] direction with a diameter of ca. 14.8 × 3.4 Å.

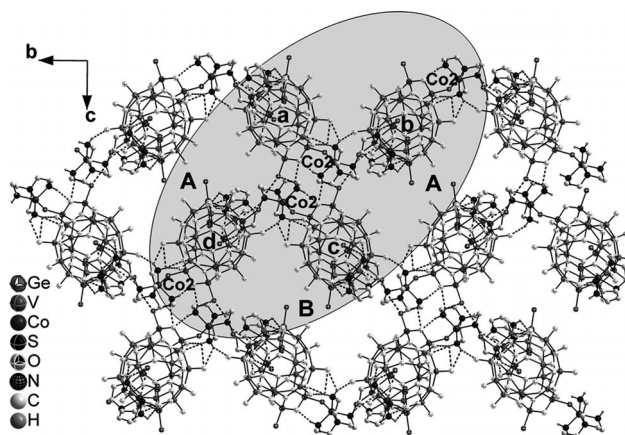


Figure 5. View of the arrangement of the [{Co(tren)}₂-V₁₅Ge₆O₄₂S₆(H₂O)]⁸⁻ clusters and hydrogen bonds (dashed lines) in the (100) plane. The four clusters around the Co²⁺-centered complexes are indicated by a–d, and the two types of channels by A and B.

Table 1. Geometric parameters of the hydrogen bonds in **1** (D = donor atom).

D–H	<i>d</i> (H···A) [Å]	∠D–H–A [°]	<i>d</i> (D···A) [Å]	Site
N12–H1	2.699	163.14	3.569	O45
N12–H2	2.409	148.61	3.211	O35
N12–H2	2.914	136.91	3.624	S6
N13–H3	2.228	129.05	2.880	O32
N13–H3	2.939	126.23	3.546	O11
N13–H4	2.356	156.25	3.202	O49
N14–H5	2.752	147.59	3.546	S6
N14–H6	2.243	141.48	3.000	O34
N22–H7	2.706	137.55	3.425	S3
N22–H8	2.495	156.90	3.341	O8
N22–H8	3.004	136.58	3.709	O18
N23–H9	2.130	157.81	2.984	O18
N23–H9	2.552	125.63	3.163	O30
N23–H10	2.278	139.74	3.020	O25
N23–H10	2.446	141.40	3.197	O28
N24–H11	1.995	162.46	2.866	O6
N24–H12	2.485	143.72	3.255	O6
N24–H12	2.799	142.363	3.554	S4

Figure 6 shows the relative positions of the cluster anions (green spheres) and the two crystallographically independent cationic Co3/4 complexes. The Co4 complexes are located in the (100) plane (Figure 6a) and alternate with anionic cluster layers (blue plane) along the [100] direction to form a Co4···V–Ge–O–S cluster···Co4 sequence (Figure 6b). The Co3 complexes are perpendicular to the *bc* plane (Figure 6b) and embedded in the channels.

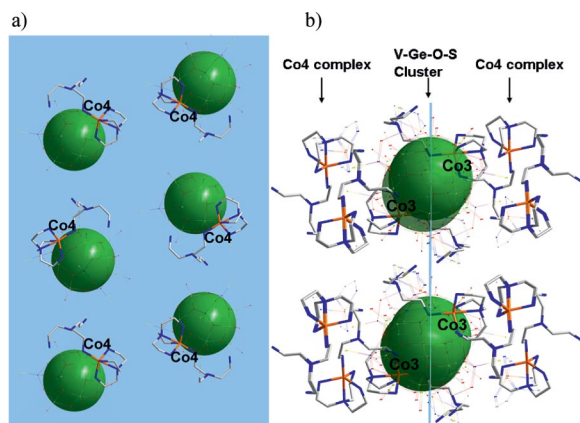


Figure 6. (a) Arrangement of the anions and Co4-centered complexes in the (100) plane with the anionic clusters shown as large green spheres and the cationic complexes wire models; the (100) plane is represented by the blue plane; (b) arrangement in the (010) plane; the (100) plane is represented by the blue line that intersects the spheres.

The main structural differences to the other Ge–V polyoxothioanion $[\text{V}_{14}\text{Ge}_8\text{O}_{42}\text{S}_8]^{12-}$ are the expansion by the Co^{2+} complexes and the topology of the V^{4+} (d^1) centers. In the $[\text{V}_{14}\text{Ge}_8\text{O}_{42}\text{S}_8]^{12-}$ cluster shell, a central V_8O_{24} ring remains intact and is capped by three VO_5 pyramids on both sides of the ring.

Magnetic Properties

The archetypal $\{\text{V}_{15}\text{E}_6\}$ ($\text{E} = \text{As}, \text{Sb}, \text{Ge}$) spin cluster is characterized by all antiferromagnetic, strongly diverging coupling strengths: the $S = 1/2$ centers of the two outer V^{IV}_6 rings, formed from edge-sharing $\text{O}=\text{VO}_4$ square pyramids, are strongly coupled, whereas the central three vanadyl groups (Figure 3), which define an equilateral triangle sandwiched between the two V_6 rings, show weak superexchange by the $\{\text{E}_2\}$ exchange pathways. This gives rise to a geometrically frustrated system that can be effectively represented by a “three-spin” model.^[35] Important in this context is that, based on the very similar magnetic susceptibility features of the known $\{\text{V}_{15}\text{As}_6\}$ and $\{\text{V}_{15}\text{Sb}_6\}$ clusters, we can assume that the corresponding $\{\text{V}_{15}\text{Ge}_6\}$ fragment in **1** will result in a comparable contribution (Figure 7, bottom line).

Based on this approximation, the low-field magnetic susceptibility of **1** indicates weak coupling between the $\{\text{V}_{15}\text{Ge}_6\}$ core cluster and the two adjoined Co^{II} complexes linked to the $\{\text{Ge}_2\text{O}_5\text{S}_2\}$ groups, which define the primary exchange pathways for the central three $S = 1/2$ vanadyl groups and result in net antiferromagnetic exchange interactions (Figure 7). A comparison of the experimental $\chi_{\text{mol}}T$ data with the sum of the contributions of four Co^{II} centers {the two $[\text{Co}(\text{tren})(\text{trenH}_2)]^{4+}$ counteranions and the $[\text{Co}(\text{tren})]^{2+}$ groups} and the $\chi_{\text{m}}T$ data previously established for $\{\text{V}_{15}\text{E}_6\}$ -type clusters ($\text{E} = \text{As}, \text{Sb}$) reveals two important aspects: (1) the intracluster $\text{V}\cdots\text{V}$ exchange interactions within the $\{\text{V}_{15}\text{Ge}_6\}$ core structure apparently do not differ

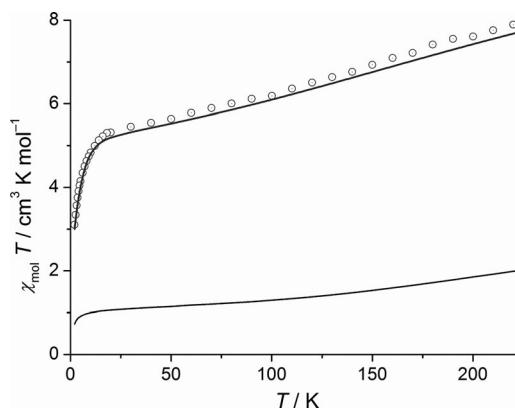


Figure 7. Temperature dependence of $\chi_{\text{mol}}T$ of **1** at an external static field of 0.1 Tesla (open circles). Top line: best fit to the model description (see text) of four trigonal-bipyramidally coordinated Co^{II} centers and the contribution of a $\{\text{V}_{15}\text{E}_6\}$ core cluster (bottom line, corresponding data taken from ref.^[11]), augmented by a molecular-field correction.

significantly from those in the other $\{\text{V}_{15}\text{E}_6\}$ cluster structures, and (2) antiferromagnetic coupling of the adjoined Co^{II} centers through $\text{Co}-\text{S}=\text{Ge}-\text{V}$ bridges can be accounted for by a (purely phenomenological) molecular field approach ($\chi^{-1} = \chi'^{-1} - \lambda$), where χ' represents the sum of the contributions from the Co^{2+} centers and the $\{\text{V}_{15}\text{E}_6\}$ core, which is weak but significant, to yield $\lambda = -0.22 \text{ mol cm}^{-3}$, which can be related to a Weiss temperature of $\theta = -2.3 \text{ K}$ in the high-temperature expansion limit of a Curie–Weiss model. The four Co^{II} centers, which are in slightly distorted trigonal-bipyramidal ligand-field environments in **1**, are characterized by a nondegenerate 4A_2 ground state, and the Co^{II} ions can therefore be approximated as $S = 3/2$ spin-only sites and were modeled as uniform, C_{3v} -symmetric complexes, in contrast to octahedral Co^{II} complexes (4T_1). By using CONDON 2.0,^[35] a least-squares fit yielded the ligand-field parameters $B^2_0 = -24780 \text{ cm}^{-1}$, $B^4_0 = -21550 \text{ cm}^{-1}$, and $B^4_2 = -26400 \text{ cm}^{-1}$ (Wyborne notation, see ref.^[36] for the definition of the Hamiltonian). The ligand-field parameters are in line with the results from a point charge electrostatic model calculation and translate to an effective isotropic g factor of 1.9 for the individual Co^{II} centers in their C_{3v} -symmetric CoO_5 environments. We will pursue the isolation of the discrete $[\text{V}_{15}\text{Ge}_6\text{O}_{42}\text{S}_6(\text{H}_2\text{O})]^{12-}$ cluster core without additional spin centers in order to focus on the coupling properties of the $\{\text{Ge}_2\text{O}_5\text{S}_2\}$ building blocks compared to the analogous $\{\text{As}_2\}$ and $\{\text{Sb}_2\}$ substructures in known $\{\text{V}_{15}\text{E}_6\}$ polyanions.

Thermoanalytical Measurements

The thermogravimetric and differential thermal analysis (TG-DTA) and MS curves for **1** are shown in Figure 8. The first weight loss of about 5% in the range of 23–140 °C corresponds to the loss of ten crystal water molecules ($\Delta m_{\text{calcd.}} = 5.4\%$), which can be seen in the MS. The following weight loss ($\Delta m = 20\%$) between 140 and 600 °C, with

no pronounced endothermic event, is due to the decomposition of about 4.7 tren molecules. Even at 600 °C, the decomposition is not complete.

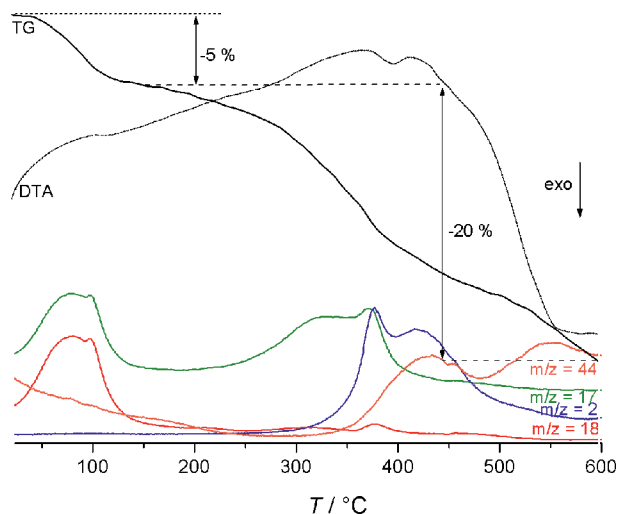


Figure 8. TG-DTA-MS curves of **1**. Intensities of the signals are in standardized units, $m/z = 2$: H₂; $m/z = 17$: OH; $m/z = 18$: H₂O or NH₄⁺; $m/z = 44$: fragment of the tren molecule (percentage numbers: relative mass loss).

Conclusions

The cluster anion [V₁₅Ge₆O₄₂S₆(H₂O)]¹²⁻ is a new member of the {V₁₈O₄₂} family and is the second example of a thiogermanatopolyoxovanadate cluster shell. The cluster shell features {Ge₂O₅S₂} units that are further expanded by Co(tren) complexes, attached by the sulfide groups, which reduce the high negative charge of the cluster core. The formal replacement of three {VO₅} pyramids in the {V₁₈O₄₂} archetype cluster by three {Ge₂O₅S₂} moieties yields a spin topology very similar to that of [V₁₅As₆O₄₂(H₂O)]⁶⁻ and [V₁₅Sb₆O₄₂]⁶⁻, yet the {Ge₂O₅S₂} building blocks apparently differ significantly in their magnetic exchange properties compared to the corresponding Sb- and As-based groups. Two additional Co²⁺-centered complexes, attached to terminal sulfide sites, act as charge-balancing cations. We plan to further explore the integration of thiogermanate-based building blocks into archetypal POV structures, with the prospect of recreating existing polyoxovanadate spin topologies with different exchange coupling strengths.

Experimental Section

Synthesis of [Co(tren)(trenH₂)]₂[{Co(tren)}₂V₁₅Ge₆O₄₂S₆(H₂O)]·9H₂O (1**):** Ge (74 mg, 1 mmol), NH₄VO₃ (201 mg, 1.7 mmol), Co (59 mg, 1 mmol), and S (97 mg, 3 mmol) were added to an aqueous solution of tren (50% in water, 10 mL). The mixture was heated in a PTFE-lined steel autoclave at 140 °C for 7 d and cooled to room temperature. Dark red-brown blocks (Figure 9) were collected, washed with distilled water, and dried in a desiccator. The yield based on vanadium was 60%. C₃₆H₁₃₂Co₄Ge₆N₂₄O₅₂S₆V₁₅ (3361.37): calcd. C 12.9, H 4.0, N 10.0, S 5.7; found

C 12.7, H 4.0, N 10.2, S 5.8. IR (KBr): $\tilde{\nu} = 3424$ (s), 3215 (s), 2953 (w), 2866 (w), 1632 (m), 1473 (w), 1317 (w), 1124 (w), 1083 (w), 972 (s), 778 (s), 683 (m), 639 (m), 546 (wm), 478 (m) cm⁻¹.

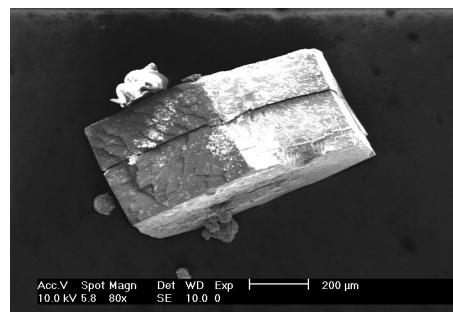


Figure 9. Scanning electron microscope image of a crystal of **1**.

Magnetic Measurements: Magnetic susceptibility data for **1** were measured as a function of field (0.1–5.0 Tesla) and temperature (2.0–290 K) by using a Quantum Design MPMS-5XL SQUID magnetometer. For simulations with CONDON 2.0, the following standard Racah and spin-orbit constants were employed: $B = 825$ cm⁻¹, $C = 3300$ cm⁻¹, $\zeta = 533$ cm⁻¹. Field-dependent magnetization data at $T = 2.0$ K show characteristic saturation effects (Figure S1).

Crystal Structure Determination: The single-crystal diffraction data were collected with a STOE Imaging Plate Diffraction System (IPDS-1) with Mo- K_{α} radiation ($\lambda = 0.71073$ Å, Table 2). The intensities were corrected for Lorentz and polarization effects. The structure was solved with SHELXS 97^[37] and refined against F^2 with SHELXL 97.^[37] All non-H atoms were refined anisotropically except for some of the C and N atoms of the tren ligands and the O atoms of the water molecules. All C–H and N–H hydrogen atoms were positioned in idealized geometries and were refined by using a split model. It was assumed that the four noncoordinating N atoms were protonated. The water H atoms could not be located in difference Fourier maps and thus were not considered. After structure refinement, some residual electron density was found in cavities of the structure, which could not be assigned unambiguously. Therefore, the data were corrected for disordered solvent by using the SQUEEZE option in Platon.^[38] The number of electrons collected during the SQUEEZE procedure matches well with six water molecules. The potential free solvent area calculated by Pla-

Table 2. Details of the data collection and selected refinement results for **1**.

	1
Empirical formula	C ₃₆ H ₁₃₂ Co ₄ Ge ₆ N ₂₄ O ₅₂ S ₆ V ₁₅
Formula mass [g mol ⁻¹]	3361.37
Crystal system	monoclinic
Space group	$P2_1/c$
a [Å]	15.4711(2)
b [Å]	26.4031(4)
c [Å]	26.7213(4)
β [°]	94.970(1)
V [Å ³]	10874.2(3)
Z	4
$F(000)$	6532
Reflections collected	144023
Independent reflections	20558
GooF on F^2	1.186
R_1 [$I > 2\sigma(I)$]	0.0710
wR_2	0.1521

ton amounts to 682.7 \AA^3 , which is about 6.3% of the unit cell volume. For the O atom in the cluster core, a large anisotropic displacement parameter was observed. This cannot be traced back to the correction with SQUEEZE, because refinement without this option led to comparable values of the components of the anisotropic displacement parameters. It is more likely that this large value is due to a mixture of static and dynamic disorder, and one can also envisage that this crystallographic position is not fully occupied. However, several other compounds in which water molecules are included in such clusters are known, and a similar behavior is frequently observed. CCDC-850100 contains the supplementary crystallographic data for this paper. These data can be obtained free of charge from The Cambridge Crystallographic Data Centre via www.ccdc.cam.ac.uk/data_request/cif.

Supporting Information (see footnote on the first page of this article): Field-dependent magnetization data of **1** at $T = 2.0 \text{ K}$.

Acknowledgments

Financial support by the State of Schleswig-Holstein is gratefully acknowledged.

- [1] M. T. Pope, A. Müller, *Angew. Chem.* **1991**, *103*, 56; *Angew. Chem. Int. Ed. Engl.* **1991**, *30*, 34–48.
- [2] X. H. Wang, J. F. Liu, M. T. Pope, *Dalton Trans.* **2003**, 957–960.
- [3] H. T. Evans Jr., *Inorg. Chem.* **1966**, *5*, 967–977.
- [4] A. Müller, R. Sessoli, E. Krickemeyer, H. Bögge, J. Meyer, D. Gatteschi, L. Pardi, J. Westphal, K. Hovemeier, R. Rohlfing, J. Döring, F. Hellweg, C. Beugholt, M. Schmidtman, *Inorg. Chem.* **1997**, *36*, 5239–5250.
- [5] S.-T. Zheng, J. Zhang, B. Li, G.-Y. Yang, *Dalton Trans.* **2008**, 5584–5587.
- [6] A. Müller, J. Döring, *Angew. Chem.* **1988**, *100*, 1787; *Angew. Chem. Int. Ed. Engl.* **1988**, *27*, 1719–1721.
- [7] A. Müller, J. Döring, *Z. Anorg. Allg. Chem.* **1991**, *595*, 251–274.
- [8] G. H. Huan, M. A. Greaney, A. J. Jacobson, *J. Chem. Soc., Chem. Commun.* **1991**, 260–261.
- [9] R. Kiebach, C. Näther, W. Bensch, *Solid State Sci.* **2006**, *8*, 964–970.
- [10] A. Wutkowski, C. Näther, P. Kögerler, W. Bensch, *Inorg. Chem.* **2008**, *47*, 1916–1918.
- [11] R. Kiebach, C. Näther, P. Kögerler, W. Bensch, *Dalton Trans.* **2007**, 3221–3223.
- [12] J. Zhou, J. Zhang, W.-H. Fang, G.-Y. Yang, *Chem. Eur. J.* **2010**, *16*, 13253–13261.
- [13] T. Whitfield, X. Wang, A. J. Jacobson, *Inorg. Chem.* **2003**, *42*, 3728–3733.
- [14] J. Wang, C. Näther, P. Kögerler, W. Bensch, *Inorg. Chim. Acta* **2010**, *363*, 4399–4404.
- [15] X.-Q. Wang, L.-M. Liu, G. Zhang, A. J. Jacobson, *Chem. Commun.* **2001**, 2472–2473.
- [16] A. Tripathi, T. Hughbanks, A. Clearfield, *J. Am. Chem. Soc.* **2003**, *125*, 10528–10529.
- [17] E. Antonova, P. Kögerler, C. Näther, W. Bensch, *Angew. Chem.* **2011**, *123*, 790–793.
- [18] A. Wutkowski, C. Näther, M. Speldrich, P. Kögerler, W. Bensch, *Z. Anorg. Allg. Chem.* **2009**, *635*, 1094–1099.
- [19] X.-B. Cui, J.-Q. Xu, Y. Li, Y.-H. Sun, G.-J. Yang, *Eur. J. Inorg. Chem.* **2004**, 1051–1055.
- [20] M. I. Khan, E. Yohannes, R. J. Doedens, *Inorg. Chem.* **2003**, *42*, 3125–3129.
- [21] S.-T. Zheng, M.-H. Wang, G.-Y. Yang, *Inorg. Chem.* **2007**, *46*, 9503–9508.
- [22] J. Zhou, J. Zhang, W.-H. Fang, G.-Y. Yang, *Chem. Eur. J.* **2010**, *16*, 13253–13261.
- [23] D. Pitzschke, J. Wang, D. Hoffmann, R. Pöttgen, W. Bensch, *Angew. Chem.* **2006**, *118*, 1327–1331; *Angew. Chem. Int. Ed.* **2006**, *45*, 1305–1308.
- [24] a) I. D. Brown, K. K. Wu, *Acta Crystallogr., Sect. B* **1976**, *32*, 1957–1959; b) I. D. Brown, D. Altermatt, *Acta Crystallogr., Sect. B* **1985**, *41*, 244–247.
- [25] A. Müller, J. Döring, M. I. Khan, V. Wittneben, *Angew. Chem.* **1991**, *103*, 203–205.
- [26] M. Behrens, S. Scherb, C. Näther, W. Bensch, *Z. Anorg. Allg. Chem.* **2003**, *629*, 1367–1373.
- [27] R. Stähler, W. Bensch, *Eur. J. Inorg. Chem.* **2001**, 3073–3078.
- [28] A. Kromm, W. S. Sheldrick, *Z. Anorg. Allg. Chem.* **2007**, *633*, 529–532.
- [29] J. Ellermeier, W. Bensch, *Z. Naturforsch. B* **2001**, *56*, 611–619.
- [30] J. Ellermeier, W. Bensch, *Transition Met. Chem.* **2002**, *27*, 763–768.
- [31] G. J. Colpas, M. Kumar, R. O. Day, M. J. Maroney, *Inorg. Chem.* **1990**, *29*, 4779–4788.
- [32] J. Ellermeier, R. Stähler, W. Bensch, *Acta Crystallogr., Sect. C* **2002**, *58*, m70–m73.
- [33] M. Behrens, M.-E. Ordolff, C. Näther, W. Bensch, K.-D. Becker, C. Guillot-Deudon, A. Lafond, J. A. Cody, *Inorg. Chem.* **2010**, *49*, 8305–8309.
- [34] C. Näther, S. Scherb, W. Bensch, *Acta Crystallogr., Sect. E* **2003**, *59*, m280–m282.
- [35] P. Kögerler, B. Tsukerblat, A. Müller, *Dalton Trans.* **2010**, 39, 21–36.
- [36] M. Speldrich, H. Schilder, H. Lueken, P. Kögerler, *Isr. J. Chem.* **2011**, *51*, 215–227.
- [37] G. M. Sheldrick, *Acta Crystallogr., Sect. A* **2008**, *64*, 112–122.
- [38] A. L. Spek, *Acta Crystallogr., Sect. A* **1990**, *46*, C34.

Received: October 26, 2011

Published Online: February 3, 2012

Structural Diversity and Magnetic Properties of the Manganese(II)/Carbazol-9-ylacetate/*N,N'*-Donor Reaction System

Yun-Sheng Ma,^{*,[a]} Xiao-Yan Tang,^[a] Feng-Feng Xue,^[a] Bin Chen,^[a] Yao-Liang Dai,^[a] Rong-Xin Yuan,^{*,[a]} and Soumyajit Roy^[a,b]

Keywords: Carboxylato ligands / Carbazol-9-ylacetic acid / Manganese / Magnetic properties / N ligands / O ligands

Four manganese-based carbazol-9-ylacetato complexes $[\text{Mn}_2(\text{cabo})_4(2,2'\text{-bpy})_2]$ (**1**), $[\text{Mn}_2(\text{cabo})_2(2,2'\text{-bpy})_4](\text{ClO}_4)_2$ (**2**), $[\text{Mn}(\text{cabo})_2(\text{CH}_3\text{OH})_2]_n$ (**3**), and $[\text{Mn}(\text{cabo})_2(4,4'\text{-bpy})_2]_n$ (**4**) (cabo^- = carbazol-9-ylacetate, $2,2'\text{-bpy}$ = $2,2'$ -bipyridine, $4,4'\text{-bpy}$ = $4,4'$ -bipyridine) have been synthesized and characterized. The crystal structure of **1** consists of a symmetrical dimeric Mn^{II} carboxylato paddle-wheel unit, whereas dinu-

clear **2** consists of a dimeric unit with two Mn^{II} ions bridged by two carboxylato ligands. Compounds **3** and **4** present comparable 1D structures with Mn^{II} ions bridged by carboxylato ligands. Magnetic-property studies show that antiferromagnetic exchange interactions propagate among the Mn^{II} ions in **1**, **2**, and **3**.

Introduction

(Carboxylato)manganese complexes have received considerable attention for their importance in bioinorganic chemistry in the oxygen-evolving complex of photosystem II and for the design of magnetic materials.^[1,2] Formic acid (HCOOH), a small ligand with a miniscule steric effect, forms $[\text{Mn}_3(\text{HCOO})_6]$, which possesses a flexible diamondoid or adamantoid framework with porous channels. The complex exhibits properties such as guest inclusion and long-range magnetic ordering.^[3] Acetic acid (CH_3COOH) has been used to construct $[\text{Mn}_{12}\text{O}_{12}(\text{CH}_3\text{COO})_{16}(\text{H}_2\text{O})_4]$, which is the first and most studied single-molecular magnet (SMM) model.^[4] Over the past decade, many types of $\{\text{Mn}_{12}\}$ clusters with different carboxylato ligands (RCOO^-) have been synthesized, and their magnetic properties have been found to be slightly dependent on the alkyl group.^[5] By changing the reaction conditions, a polynuclear $\{\text{Mn}_{84}\}$ cluster was constructed with acetato as the ligand, which shows SMM behavior.^[6] 2,2-Dimethylpropanoic acid $[(\text{CH}_3)_3\text{CCOOH}]$, which has a sterically hindering group on the carboxylate group, has been used to construct an Mn^{II} pivalate polymer $[\text{Mn}(\text{OOCMe}_3)_2(\text{EtOH})]_n$. This complex shows antiferromagnetic properties and reactivity.^[7] Other than carboxylates, ferrocenecarboxylate, which bears an or-

ganometallic functional group, has also been used to construct manganese complexes. The use of ancillary ligands led to variation in the overall complex structure. For instance, the use of 1,10-phenanthroline (phen) as an ancillary ligand led to the formation of a triply carboxylato-bridged dimanganese complex, whereas the use of $2,2'$ -bipyridine ($2,2'\text{-bpy}$) as an ancillary ligand and variation of the stoichiometric ratio of the reactants led to a linear trinuclear complex and a butterfly-like tetranuclear complex.^[8] In the absence of ancillary ligands, the reaction of Mn^{II} with ferrocenecarboxylate gave a 1D polymer, whereas a 2D polymer was obtained in the presence of $4,4'$ -bipyridine ($4,4'\text{-bpy}$) as a bridging ancillary ligand.^[9] All of these complexes show antiferromagnetic properties.

Carbazol-9-ylacetic acid, which has a bulky group, has been used to synthesize 3d-metal complexes with photoluminescent and magnetic properties.^[10] Examples of such complexes are still limited in number and include dinuclear $[\text{Cu}_2(\text{cabo})_4(\text{dmf})_2]$,^[10a] $[\text{Cu}_2(\text{cabo})_3(\text{phen})_2]\text{ClO}_4$,^[10a] and $[\text{Ag}_2(\text{dppm})_2(\text{cabo})_2]$,^[10b] mononuclear $[\text{Cu}(\text{cabo})_2(\text{phen})]$,^[10a] $[\text{Cu}(\text{cabo})(\text{PPh}_3)_2]$,^[10a] $[\text{Zn}(\text{cabo})(\text{phen})_2]\text{ClO}_4$,^[10c] $[\text{Cd}(\text{cabo})(\text{phen})_2]\text{ClO}_4$,^[10c] and $[\text{Ag}(\text{cabo})(\text{PPh}_3)_2]$,^[10d] as well as 1D polymers $[\text{Co}_2(\text{cabo})_2(\text{NO}_3)_2(4,4'\text{-bpy})_2]_n$,^[10e] $[\text{Zn}(\text{cabo})_2(\text{EtOH})_2(4,4'\text{-bpy})]_n$,^[10f] and $[\text{Zn}_2(\text{cabo})_2(\text{NO}_3)_2(4,4'\text{-bpy})_2]_n$.^[10g] cabo^- = carbazol-9-ylacetate, dmf = N,N -dimethylformamide, dppm = 1,1-bis(diphenylphosphanyl)methane]. In these complexes, the cabo^- ligand exhibits four coordinating modes: bridging bidentate, chelating bidentate, bridging monoatomic, and monodentate.

We present the syntheses, structures, and magnetic properties of three new manganese carbazol-9-ylacetates with N,N' -donors as ancillary ligands. For comparison, $[\text{Mn}(\text{cabo})_2(\text{CH}_3\text{OH})_2]_n$ (**3**) with carbazol-9-ylacetic acid alone was also synthesized and characterized.

[a] School of Chemistry and Materials Engineering, Jiangsu Key Laboratory of Advanced Functional Materials, Changshu Institute of Technology, Changshu, Jiangsu 215500, P. R. China
Fax: +86-512-52251842
E-mail: myschem@hotmail.com

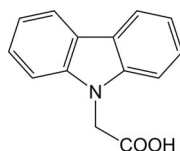
[b] Eco-friendly Applied Materials Laboratory, Indian Institute of Science Education & Research, Kolkata, India

Supporting information for this article is available on the WWW under <http://dx.doi.org/10.1002/ejic.201101206>.

Results and Discussion

Syntheses

The reaction of Mn^{II} with carbazol-9-ylacetate and 2,2'-bpy in a ratio of 1:2:1 in CH_3OH at room temperature resulted in a dinuclear Mn^{II} complex $[\text{Mn}_2(\text{cabo})_4(2,2'\text{-bpy})_2]$ (**1**). When the ratio was changed to 1:1:2, a dinuclear complex $[\text{Mn}_2(\text{cabo})_2(2,2'\text{-bpy})_4](\text{ClO}_4)_2$ (**2**) formed. Clearly, the reaction stoichiometry plays a key role in the formation of the final product. The reaction of Mn^{II} with carbazol-9-ylacetate gave polymeric **3** in the absence of ancillary ligands, whereas in the presence of potentially bridging 4,4'-bpy, $[\text{Mn}(\text{cabo})_2(4,4'\text{-bpy})_2]_n$ (**4**) was formed. The potentially bridging ancillary ligand 4,4'-bpy did not bridge two Mn^{II} ions, which seems to be due to the steric hindrance of the carbazol-9-yl groups (Scheme 1).



Scheme 1. Carbazol-9-ylacetic acid.

Description of the Crystal Structures

Compound **1** crystallized in a low-symmetry monoclinic space group $P2_1/c$. The asymmetric unit consists of one Mn^{II} ion, two carbazol-9-yl ligands, and one 2,2'-bpy ligand. The Mn ion adopts a distorted octahedral coordination environment. Four of the six coordination sites are filled with oxygen atoms [O(1), O(2A), O(3), O(4A)] from four carbazol-9-ylacetato ligands. The two remaining sites are occupied by nitrogen atoms [N(3) and N(4)] from one 2,2'-bpy ligand (Figure 1). The Mn(1)–O bond lengths fall in the range 2.154(2)–2.252(2) Å, which is in agreement with those reported for $[\text{Mn}_2(\text{FcCO}_2)_3(\text{phen})_2]\text{ClO}_4$.^[8] The Mn(1)–N distances are 2.307(3) and 2.325(3) Å (Table 1). An interesting feature is the formation of the $[\text{Mn}_2(\text{cabo})_4]$ dimer as shown in Figure 1. The Mn^{II} ions are connected by four *syn-syn* μ_2 -carbazol-9-ylacetato ligands with an $\text{Mn}\cdots\text{Mn}$ separation of 3.540(1) Å, with each carbazolyl group pointing away from its neighbor. The short intradimer $\text{Mn}\cdots\text{Mn}$ separation is comparable to that reported for a dinuclear Mn^{II} complex bridged by four organic carboxylato ligands,^[11] which suggests a nonbonding interaction between the two Mn^{II} ions. These bonds are longer than those of the analogous copper(II) complexes, where the usual M–M and M–O distances are ca. 2.7 and 2.1 Å, respectively. This is expected from the larger ionic size and lack of ligand-field stabilization in high-spin Mn^{II} .^[10a] A π – π stacking interaction was found between the molecules approximately in the [001] direction. The centroid–centroid distance between the phenyl rings of the 2,2'-bpy ligands is 3.68 Å (Figure 2).^[12]

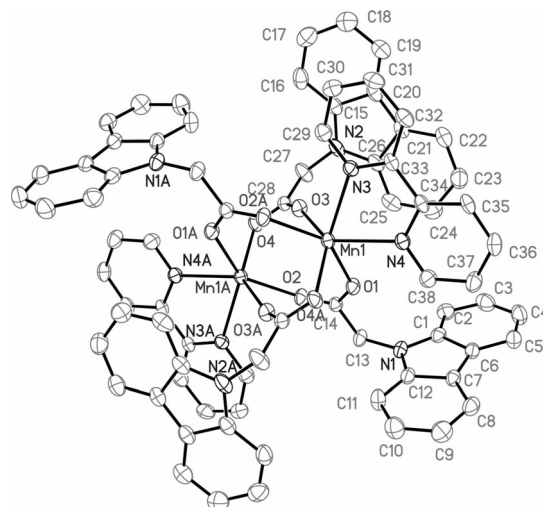


Figure 1. ORTEP drawing of **1** (30% probability ellipsoids). Hydrogen atoms are omitted for clarity.

Table 1. Selected bond lengths [Å] and angles [°] for **1**.^[a]

Mn1–O1	2.182(2)	Mn1–O3	2.155(2)
Mn1–N4	2.307(2)	Mn1–O2A	2.252(2)
Mn1–N3	2.325(3)	Mn1–O4A	2.220(2)
O1–Mn1–N4	82.67(9)	O1–Mn1–O3	86.96(9)
O1–Mn1–O4A	88.02(9)	O1–Mn1–O2A	143.32(9)
O2A–Mn1–O3	81.93(9)	O3–Mn1–N3	84.88(9)
N3–Mn1–N4	69.10(9)	O2A–Mn1–N3	80.25(9)
O4A–Mn1–N3	125.01(9)	O2A–Mn1–N4	130.07(9)
O1–Mn1–N3	133.52(9)	O2A–Mn1–O4A	78.99(9)
O3–Mn1–N4	130.82(10)	O4A–Mn1–N4	87.30(9)
O3–Mn1–O4A	140.34(9)		

[a] Symmetry code: A: $-x, 1-y, -z$.

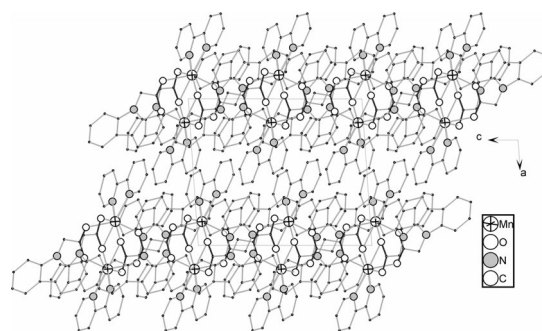


Figure 2. Crystal packing diagram of **1** viewed along the *b* axis. Hydrogen atoms are omitted for clarity.

The asymmetric unit of **2** consists of one Mn^{II} ion, one carbazol-9-ylacetato ligand, two 2,2'-bpy ligands, and one ClO_4^- anion. The Mn atom adopts a distorted octahedral coordination environment. Two of the six coordination sites are filled by carbazol-9-ylacetate oxygen atoms [O(1), O(2A)] from two equivalent cabo^- ligands (Figure 3). The remaining four sites are occupied by the nitrogen atoms [N(1), N(2), N(3) and N(4)] from two 2,2'-bpy ligands. The Mn(1)–O bond lengths are 2.087(4) and 2.100(4) Å, which are in agreement with those of $[\text{Mn}_2(2\text{-ClC}_6\text{H}_4\text{COO})_2(\text{bpy})_4](\text{ClO}_4)_2$.^[13] The Mn(1)–N distances fall in the range of

2.238(4)–2.305(5) Å (Table 2). The Mn^{II} ions are connected by two *syn-anti* μ_2 -carbazol-9-ylacetato ligands with an Mn \cdots Mn separation of 4.642(2) Å. All of the structural parameters are analogous to those of other dinuclear Mn^{II} compounds with doubly μ_2 -acetato bridging ligands in a *syn-anti* mode with 2,2'-bpy as capping ligands.^[14] A π - π stacking interaction was also found between the phenyl rings of the 2,2'-bpy ligands. The centroid-centroid distance between the phenyl rings is 3.91 Å (Figure 4).^[12]

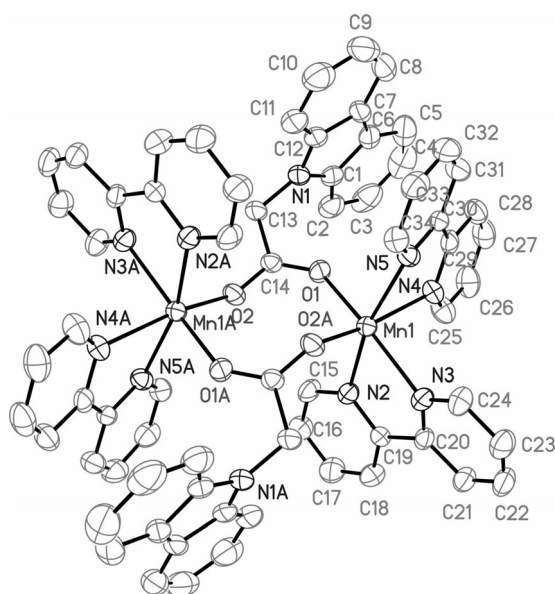


Figure 3. ORTEP drawing of **2** (30% probability ellipsoids). Hydrogen atoms are omitted for clarity.

Table 2. Selected bond lengths [Å] and angles [°] for **2**.^[a]

Mn1–O1	2.100(4)	Mn1–N2	2.258(4)
Mn1–N4	2.305(5)	Mn1–N5	2.238(4)
Mn1–N3	2.259(4)	Mn1–O2A	2.087(4)
O1–Mn1–N2	93.24(14)	O1–Mn1–N3	163.14(15)
O1–Mn1–N5	90.33(14)	O1–Mn1–O2A	100.60(14)
N2–Mn1–N4	93.49(16)	N2–Mn1–N5	164.36(15)
N3–Mn1–N4	90.17(16)	N3–Mn1–N5	101.55(15)
N4–Mn1–N5	71.92(16)	O2A–Mn1–N4	164.29(15)
O1–Mn1–N4	82.13(15)	O2A–Mn1–N3	90.88(15)
N2–Mn1–N3	72.19(15)	O2A–Mn1–N5	92.52(15)
O2A–Mn1–N2	101.76(15)		

[a] Symmetry code: A: 1 – x, 1 – y, 2 – z.

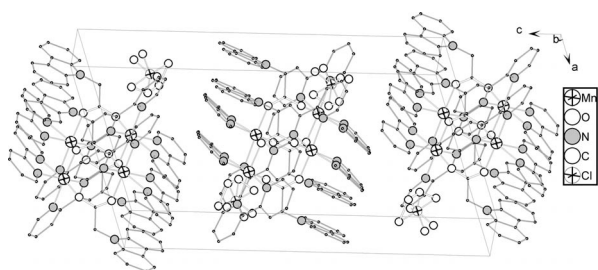


Figure 4. Crystal packing diagram of **2** viewed along the *b* axis. Hydrogen atoms are omitted for clarity.

The asymmetric unit of **3** consists of half an Mn^{II} ion, one carbazol-9-ylacetato ligand, and one CH₃OH molecule. The Mn ion is located at an inversion center and has a distorted octahedral coordination environment with the six positions occupied by O(1), O(1A), O(2B), and O(2C) from four equivalent carbazol-9-ylacetato ligands and O(3) and (O3A) from two CH₃OH molecules (Figure S1). The Mn–O bond lengths are in the range 2.139(2)–2.212(2) Å (Table 3), which are comparable to those in related [Mn(OOCCMe₃)₂-(EtOH)]_n. The Mn^{II} ions are connected by two *syn-anti* carbazol-9-ylacetato ligands with an Mn \cdots Mn separation of 4.686(1) Å, which is analogous to the Mn \cdots Mn separation in **2**. A 1D infinite chain with repeating [Mn(cabo)₂-(CH₃OH)₂] units is formed along the *b* axis (Figure 5). These chains are packed together through van der Waals forces into a 3D network (Figure S2).

Table 3. Selected bond lengths [Å] and angles [°] for **3**.^[a]

Mn1–O1	2.198(2)	Mn1–O3	2.212(3)
Mn1–O2B	2.139(2)		
O1–Mn1–O3	95.38(9)	O1–Mn1–O2B	89.04(9)
O1–Mn1–O2C	90.97(9)	O2B–Mn1–O3	87.20(9)

[a] Symmetry codes: A: 2 – x, –y, 2 – z; B: x, –1 + y, z; C: 2 – x, 1 – y, 2 – z.

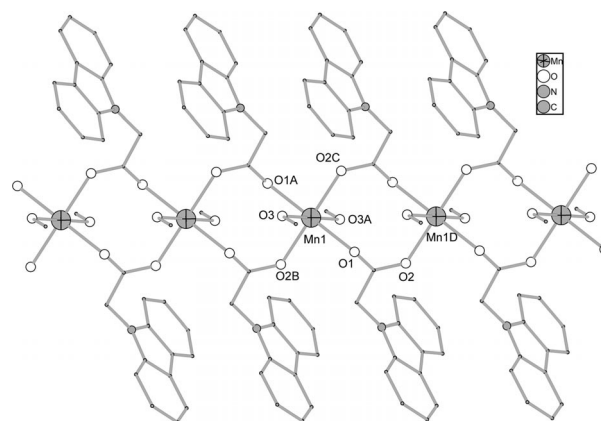


Figure 5. 1D structure of **3**. Hydrogen atoms are omitted for clarity.

The asymmetric unit of **4** consists of half an Mn^{II} ion, one cabo[–] ligand, and one 4,4'-bpy molecule. The Mn ion is located at an inversion center and has a distorted octahedral coordination environment with the six positions occupied by O(1B), O(1C), O(2), and O(2A) from four equivalent carbazol-9-ylacetato ligands and N(2) and N(2A) from two 4,4'-bpy ligands (Figure S3). The Mn–O bond lengths are 2.168(4) and 2.201(4) Å (Table 4), which are comparable to those in **3**. Compound **4** has a 1D polymeric conformation analogous to that of **3**, in which CH₃OH is replaced by 4,4'-bpy (Figure 6). The Mn \cdots Mn separation is 5.123(1) Å, which is longer than that in **2** and **3**. This longer Mn \cdots Mn separation may be due to the steric hindrance of 4,4'-bpy and cabo[–]. The 4,4'-bpy ligand does not bridge two Mn^{II} ions but acts as a monodentate ligand to coordinate one Mn^{II} ion. This may be attributed to the steric hindrance of the

carbazol-9-yl groups. The 1D polymeric chains are packed together through van der Waals forces into a 3D network (Figure S4).

Table 4. Selected bond lengths [Å] and angles [°] for **4**.^[a]

Mn1–O2	2.196(3)	Mn1–N2	2.322(4)
Mn1–O1C	2.163(3)	Mn1–O2A	2.196(3)
Mn1–O1B	2.163(3)	Mn1–N2A	2.322(4)
O2–Mn1–N2	87.05(14)	O1B–Mn1–O2	92.01(12)
O1C–Mn1–N2	89.13(14)		

[a] Symmetry codes: A: 2 – x, 1 – y, 1 – z; B: 1 + x, y, z; C: 1 – x, 1 – y, 1 – z.

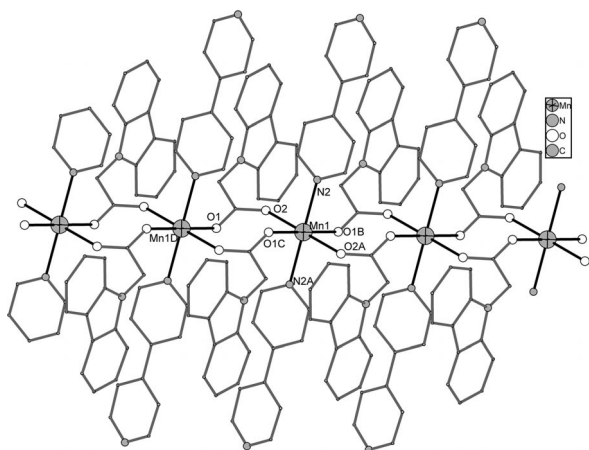


Figure 6. 1D structure of **4**. Hydrogen atoms are omitted for clarity.

Magnetic Properties

The temperature-dependent molar magnetic susceptibilities (χ_M) of **1–3** were measured at 1000 Oe in the temperature (T) range 1.8–300 K. The χ_M and $\chi_M T$ vs. T plots for **1** are shown in Figure 7. The room-temperature magnetic moment per Mn ($5.89 \mu_B$) is close to the spin-only value expected for an Mn^{II} ion ($S = 5/2$). Upon cooling, $\chi_M T$ decreases smoothly from $8.685 \text{ cm}^3 \text{ K mol}^{-1}$ at 300 K to a minimum of $0.391 \text{ cm}^3 \text{ K mol}^{-1}$ at 1.8 K, which suggests a dominant antiferromagnetic interaction.

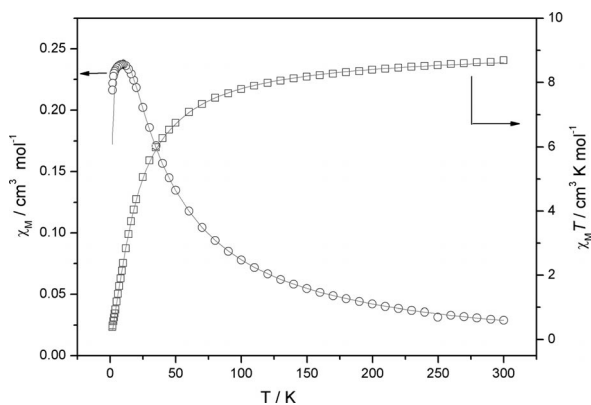


Figure 7. Plot of χ_M and $\chi_M T$ vs. T for **1**. Solid lines show the best fit of the data according to the proposed model.

By assuming isotropic exchange, the exchange Hamiltonian of **1** is $H = -JS_1S_2$, where $S = 5/2$, and the susceptibility per mol of the dimer is given by:^[15]

$$\chi_M = \frac{2Ng^2\beta^2}{kT} \frac{\exp(2J/kT) + 5\exp(6J/kT) + 14\exp(12J/kT) + 30\exp(20J/kT) + 55\exp(30J/kT)}{1 + 3\exp(2J/kT) + 5\exp(6J/kT) + 7\exp(12J/kT) + 9\exp(20J/kT) + 11\exp(30J/kT)}$$

$$\chi_M = \frac{\chi_M}{1 - (zj'/Ng^2\beta^2)\chi_M}$$

where J is the coupling constant, and N , g , β , and k have their usual meanings, zj' accounts for the interdimer Mn²⁺ unit exchange interactions. The best fitting parameters obtained for **1** are $g = 2.03$, $J = -1.21 \text{ cm}^{-1}$, and $zj' = -0.28 \text{ cm}^{-1}$ (solid lines in Figure 7). The J value of -1.21 cm^{-1} falls in the normal range for an Mn^{II} dimer constructed by four carboxylato bridges.^[9]

The χ_M and $\chi_M T$ vs. T plots for **2** are shown in Figure 8. The room-temperature magnetic moment per Mn ($5.84 \mu_B$) is close to the spin-only value expected for an Mn^{II} ion ($S = 5/2$). Upon cooling, $\chi_M T$ decreases smoothly from $8.521 \text{ cm}^3 \text{ K mol}^{-1}$ at 300 K to a minimum of $0.626 \text{ cm}^3 \text{ K mol}^{-1}$ at 1.8 K, which suggests a dominant antiferromagnetic exchange interaction. The data were fitted by using the dimer mode to give $g = 2.00$, $J = -0.83 \text{ cm}^{-1}$, and $zj' = 0.076 \text{ cm}^{-1}$. The J value of -0.83 cm^{-1} is smaller than that of **1**. This is consistent with the fact that a *syn-syn* carboxylato bridge transfers stronger antiferromagnetic coupling than a *syn-anti* bridge. In addition, this may be explained by the number of bridging ligands: two in **2** and four in **1**.

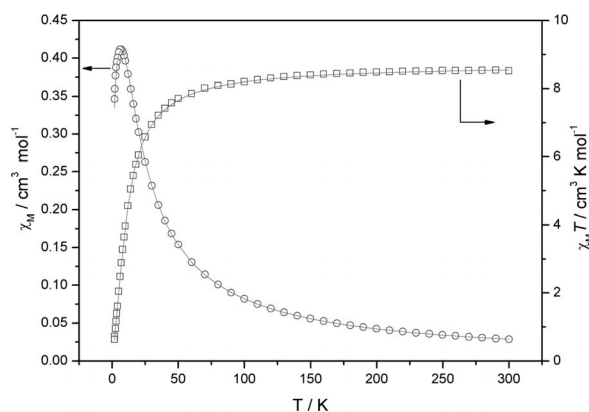


Figure 8. Plot of χ_M and $\chi_M T$ vs. T for **2**. Solid lines show the best fit of the data according to the proposed model.

The χ_M and $\chi_M T$ vs. T plots for **3** are shown in Figure 9. The room-temperature magnetic moment per Mn ($5.92 \mu_B$) is close to the spin-only value expected for an Mn^{II} ion ($S = 5/2$). Upon cooling, $\chi_M T$ decreases smoothly from $4.386 \text{ cm}^3 \text{ K mol}^{-1}$ at 300 K to a minimum of $0.290 \text{ cm}^3 \text{ K mol}^{-1}$ at 1.8 K, which suggests a dominant antiferromagnetic interaction. According to the structure of **3**, the magnetic exchange between the Mn^{II} ions is propagated through the O–C–O units within the chains. Therefore, the susceptibility data of the chain were analyzed by Fisher's expression for a uniform chain, with $S = 5/2$:

$$\chi = \frac{Ng^2\beta^2 S(S+1)}{3kT} \frac{1+u}{1-u}$$

$$\text{where } u = \coth\left[\frac{JS(S+1)}{kT}\right] - \left[\frac{kT}{JS(S+1)}\right]$$

finally:

$$\chi = \frac{1.09375 \times g^2 (1 + \cosh(12.60875 \times J/T) / \sin(12.60875 \times J/T) - (T/J/12.60875))}{(1 - \cosh(12.60875 \times J/T) / \sin(12.60875 \times J/T) + (T/J/12.60875)) \times T}$$

$$\chi_M = \frac{\chi}{1 - (zJ'/Ng^2\beta^2)\chi}$$

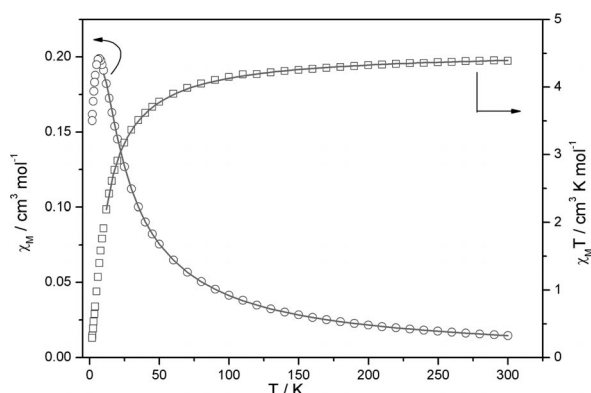


Figure 9. Plot of χ_M and $\chi_M T$ vs. T for **3**. Solid lines show the best fit of the data according to the proposed model.

A good fit, shown as solid lines in Figure 9, was obtained above 10 K with $g = 2.04$, $J = -0.41 \text{ cm}^{-1}$, and $zJ' = -0.33 \text{ cm}^{-1}$. The J value is close to that of the analogous compound $[\text{Mn}(\text{O}_2\text{CCMe}_3)_2(\text{EtOH})]_n$ ($J = -0.44 \text{ cm}^{-1}$).^[7]

Conclusions

In this study, four (carboxylato)manganese complexes, which bear carbazol-9-ylacetato ligands, were isolated from the reactions of cabo^- with $\text{Mn}(\text{ClO}_4)_2 \cdot 6\text{H}_2\text{O}$ in the presence of 2,2'-bpy and 4,4'-bpy in methanol. Compounds **1** and **2** have dimeric cores that consist of four and two carbazol-9-ylacetato ligands, respectively. Four carboxylato-bridged dimeric manganese cores are rare and have been observed in $[\text{Mn}_2(\text{Ph}_2\text{CHCOO})_4(\text{L})_2]$,^[13] $[\text{Mn}_2(\text{Me}_3\text{CCOO})_4(\text{L})_2]$,^[7] and $[\text{Mn}_3(\text{FcCOO})_6(\text{CH}_3\text{OH})_4]$,^[9] which has a sterically hindering group on the carboxylato group. Compounds **3** and **4** have similar 1D structures, which are bridged by carbazol-9-ylacetato ligands. The most salient feature of **4** is the monodentate coordination mode of 4,4'-bpy. Magnetic measurements of **1–3** revealed that all of these compounds mediate a weak antiferromagnetic coupling between the Mn^{II} ions bridged by cabo^- ligands. Further work is in progress to study new (carboxylato)manganese compounds with bulky fluorene groups.

Experimental Section

Materials and Methods: All the starting materials were of reagent grade and were used as purchased. Carbazol-9-ylacetic acid

(Hcabo, Scheme 1) was prepared according to a literature method.^[10c] Elemental analyses were performed with a PE 240C elemental analyzer. IR spectra were recorded with a Nicolet 380 spectrometer from pressed KBr pellets. The magnetic studies were performed with microcrystalline samples. Magnetic susceptibilities were measured with a Quantum Design MPMS SQUID-XL7 magnetometer. Diamagnetic corrections were made for both the sample holder and the compound estimated from Pascal's constants.^[15]

Syntheses

[Mn₂(cabo)₄(2,2'-bpy)₂] (1): To a CH_3OH solution (5 mL) of $\text{Mn}(\text{ClO}_4)_2 \cdot 6\text{H}_2\text{O}$ (0.362 g, 1 mmol) was added a CH_3OH solution (5 mL) of 2,2'-bpy (0.156 g, 1 mmol) and Nacabo (0.512 g, 2 mmol). The resulting mixture was stirred for 5 h and filtered. Colorless block-shaped crystals of **1** formed after slow concentration of the reaction solution at room temperature over a week. Yield: 40% based on $\text{Mn}(\text{ClO}_4)_2 \cdot 6\text{H}_2\text{O}$. $\text{C}_{76}\text{H}_{56}\text{Mn}_2\text{N}_8\text{O}_8$ (1319.17): calcd. C 69.20, H 4.28, N 8.49; found C 69.53, H 4.55, N 8.20. IR (KBr): $\tilde{\nu} = 3049.6$ (w), 1632.8 (vs), 1600.1 (vs), 1484.7 (m), 1447.6 (s), 1403.2 (s), 1315.6 (s), 1206.3 (m), 1153.3 (m), 1093.2 (s), 751.8 (vs), 723.3 (s), 631.4 (m) cm^{-1} . The two very strong bands centered at 1600 and 1403 cm^{-1} , attributed to the $\nu_{\text{as}}(\text{COO})$ and $\nu_{\text{s}}(\text{COO})$ of cabo^- with $\Delta = 197 \text{ cm}^{-1}$, confirm coordination to Mn^{II} by bidentate bridging carboxylato ligands.^[16]

[Mn₂(cabo)₂(2,2'-bpy)₄(ClO₄)₂] (2): To a CH_3OH solution (5 mL) of $\text{Mn}(\text{ClO}_4)_2 \cdot 6\text{H}_2\text{O}$ (0.362 g, 1 mmol) was added a CH_3OH solution (5 mL) of 2,2'-bpy (0.312 g, 2 mmol) and Nacabo (0.256 g, 1 mmol). The solution was stirred for 5 h and filtered. Yellow block-shaped crystals of **2** formed after slow concentration of the reaction solution at room temperature over a week. Yield: 35% based on $\text{Mn}(\text{ClO}_4)_2 \cdot 6\text{H}_2\text{O}$. $\text{C}_{68}\text{H}_{52}\text{Cl}_2\text{Mn}_2\text{N}_{10}\text{O}_{12}$ (1381.98): calcd. C 59.10, H 3.79, N 10.14; found C 58.81, H 3.44, N 9.87. IR (KBr): $\tilde{\nu} = 3065.5$ (w), 1626.8 (vs), 1597.7 (vs), 1481.7 (m), 1438.2 (s), 1404.2 (s), 131.6 (s), 1089.1 (vs), 1010.3 (m), 755.8 (vs), 622.9 (s) cm^{-1} . The two very strong bands centered at 1598 and 1404 cm^{-1} , attributed to the $\nu_{\text{as}}(\text{COO})$ and $\nu_{\text{s}}(\text{COO})$ of cabo^- with $\Delta = 194 \text{ cm}^{-1}$, confirm coordination to Mn^{II} by bidentate bridging carboxylato ligands.

[Mn(cabo)₂(CH₃OH)₂]_n (3): To a CH_3OH solution (5 mL) of $\text{Mn}(\text{ClO}_4)_2 \cdot 6\text{H}_2\text{O}$ (0.362 g, 1 mmol) was added a CH_3OH solution (5 mL) of Nacabo (0.512 g, 2 mmol). The solution was stirred for 5 h and filtered. Colorless block-shaped crystals of **3** formed after slow concentration of the reaction solution at room temperature over a week. Yield: 56% based on $\text{Mn}(\text{ClO}_4)_2 \cdot 6\text{H}_2\text{O}$. $\text{C}_{30}\text{H}_{28}\text{MnN}_2\text{O}_6$ (567.48): calcd. C 63.49, H 4.97, N 4.94; found C 63.19, H 4.55, N 4.58. IR (KBr): $\tilde{\nu} = 3444.5$ (br. s), 3065.5 (w), 1571.8 (vs), 1485.4 (m), 1458.5 (s), 1396.6 (s), 1358.0 (s), 1300.19 (s), 748.9 (s), 714.1 (s), 630.1 (m) cm^{-1} . The two very strong bands centered at 1572 and 1397 cm^{-1} , attributed to the $\nu_{\text{as}}(\text{COO})$ and $\nu_{\text{s}}(\text{COO})$ of cabo^- with $\Delta = 175 \text{ cm}^{-1}$, confirm coordination to Mn^{II} by bidentate bridging carboxylato ligands.

[Mn(cabo)₂(4,4'-bpy)₂]_n (4): To a CH_3OH solution (5 mL) of $\text{Mn}(\text{ClO}_4)_2 \cdot 6\text{H}_2\text{O}$ (0.362 g, 1 mmol) was added a CH_3OH solution (5 mL) of 4,4'-bpy (0.312 g, 2 mmol) and Nacabo (0.512 g, 2 mmol). The solution was stirred for 5 h and filtered. Colorless block crystals of **4** formed after slow concentration of the reaction solution at room temperature over a week. Yield: 61% based on $\text{Mn}(\text{ClO}_4)_2 \cdot 6\text{H}_2\text{O}$. $\text{C}_{48}\text{H}_{36}\text{MnN}_6\text{O}_4$ (815.77): calcd. C 70.67, H 4.45, N 10.30; found C 70.35, H 4.22, N 10.55. IR (KBr): $\tilde{\nu} = 3048.8$ (w), 1574.2 (vs), 1486.6 (m), 1447.4 (s), 1430.0 (m), 1397.5 (s), 1357.1 (m), 1301.4 (s), 1208.9 (m), 1152.4 (w), 1023.1 (w), 749.3 (vs), 719.3 (s), 631.5 (m) cm^{-1} . The two very strong bands centered at 1574 and 1398 cm^{-1} , attributed to the $\nu_{\text{as}}(\text{COO})$ and $\nu_{\text{s}}(\text{COO})$ of

Table 5. Crystal data and structure refinements for **1–4**.

	1	2	3	4
Empirical formula	C ₇₆ H ₅₆ Mn ₂ N ₈ O ₈	C ₆₈ H ₅₂ Mn ₂ N ₁₀ O ₄ ·2ClO ₄	C ₃₀ H ₂₈ MnN ₂ O ₆	C ₄₈ H ₃₆ MnN ₆ O ₄
<i>M</i>	1319.17	1381.98	567.48	815.77
Crystal system	monoclinic	monoclinic	monoclinic	triclinic
Space group	<i>P</i> 2 ₁ / <i>c</i>	<i>P</i> 2 ₁ / <i>c</i>	<i>P</i> 2 ₁ / <i>c</i>	<i>P</i> 1̄
<i>a</i> [Å]	10.737(2)	12.562(3)	12.305(3)	5.1225(10)
<i>b</i> [Å]	22.459(5)	10.979(2)	4.6863(9)	10.774(2)
<i>c</i> [Å]	12.690(3)	23.876(8)	23.278(5)	18.128(4)
<i>α</i> [°]	90	90	90	85.23(3)
<i>β</i> [°]	93.93(3)	107.08(3)	96.11(3)	82.34(3)
<i>γ</i> [°]	90	90	90	81.47(3)
<i>V</i>	3052.9(11)	3147.7(15)	1334.7(5)	978.5(4)
<i>Z</i>	2	2	2	1
$\rho_{\text{calcd.}}$ [g cm ^{−3}]	1.435	1.458	1.412	1.384
μ [mm ^{−1}]	0.483	0.559	0.542	0.393
<i>F</i> (000)	1364	1420	590	423
<i>R</i> _{int}	0.079	0.109	0.0942	0.1084
GoF on <i>F</i> ²	1.04	1.12	1.01	1.067
<i>R</i> ₁ , <i>wR</i> ₂ [<i>I</i> > σ (<i>I</i>)] ^[a]	0.073, 0.1223	0.0745, 0.1525	0.0608, 0.1039	0.0868, 0.1399
<i>R</i> ₁ , <i>wR</i> ₂ (all data)	0.1264, 0.1417	0.1297, 0.1753	0.1094, 0.1177	0.1784, 0.1718
($\Delta\rho$) _{max} , ($\Delta\rho$) _{min} [e Å ^{−3}]	0.272, −0.441	0.385, −0.491	0.220, −0.248	0.405, −0.456

[a] $R_1 = \Sigma||F_o| - |F_c||/\Sigma|F_o|$; $wR_2 = \{\Sigma w(F_o^2 - F_c^2)^2/\Sigma w(F_o^2)\}^{1/2}$.

cabo[−] with $\Delta = 176 \text{ cm}^{-1}$, confirm coordination to Mn^{II} by bidentate bridging carboxylato ligands.

X-ray Crystallographic Analysis: Single crystals with dimensions $0.30 \times 0.20 \times 0.20 \text{ mm}$ for **1**, $0.38 \times 0.24 \times 0.22 \text{ mm}$ for **2**, $0.25 \times 0.22 \times 0.20 \text{ mm}$ for **3**, and $0.30 \times 0.20 \times 0.16 \text{ mm}$ for **4** were selected for indexing and intensity data collection with a Rigaku SCX mini CCD diffractometer by using graphite-monochromated Mo- K_{α} radiation ($\lambda = 0.71073 \text{ Å}$) at room temperature. A hemisphere of data was collected in the θ range $3.01\text{--}27.48^\circ$ for **1**, $3.26\text{--}25.00^\circ$ for **2**, $3.33\text{--}26.00^\circ$ for **3**, and $3.07\text{--}25.00^\circ$ for **4** by using a narrow-frame method with scan widths of 0.03° in ω and an exposure time of 10 s/frame^{−1}. The numbers of observed and unique reflections are 28117 and 6973 ($R_{\text{int}} = 0.079$) for **1**, 24609 and 5519 ($R_{\text{int}} = 0.1093$) for **2**, 11359 and 2610 ($R_{\text{int}} = 0.0942$) for **3**, and 8056 and 3424 ($R_{\text{int}} = 0.1084$) for **4**. Cell parameters were refined by using the program CrystalClear^[17] on all observed reflections. The collected data were reduced by using the program CrystalClear, and an absorption correction (multiscan) was applied. The reflection data were also corrected for Lorentz and polarization effects. The structures were solved by direct methods and refined on F^2 by full-matrix least squares using SHELXTL.^[18] All the non-hydrogen atoms were located from the Fourier maps and were refined anisotropically. All H atoms were refined isotropically with the isotropic vibration parameters related to the non-H atom to which they are bonded. Crystallographic and refinement details of **1–4** are listed in Table 5. Selected bond lengths and angles are given in Tables 1, 2, 3, and 4 for **1–4**, respectively. CCDC-833313 (for **1**), -833310 (for **2**), -833311 (for **3**), and -833312 (for **4**) contain the supplementary crystallographic data for this paper. These data can be obtained free of charge from The Cambridge Crystallographic Data Centre via www.ccdc.cam.ac.uk/data_request/cif.

Supporting Information (see footnote on the first page of this article): Coordination environment and crystal packing diagrams for **3** and **4**.

Acknowledgments

This work was supported by the National Natural Science Foundation of China (NSFC) (No. 21001018), the National Science Foun-

dation (NSF) of Jiangsu Province (No. 08KJB 150001, 11KJB 150001), the State Key Laboratory of Coordination Chemistry of Nanjing University, and the Qinglan Project of Jiangsu Province.

- a) Y. Umena, K. Kawakami, J.-R. Shen, N. Kamiya, *Nature* **2011**, 473, 55–60; b) G. Aromi, S. M. J. Aubin, M. A. Bolcar, G. Christou, H. J. Eppley, K. Folting, D. N. Hendrickson, J. C. Huffman, R. C. Squire, H.-L. Tsai, S. Wang, M. W. Wemple, *Polyhedron* **1998**, 17, 3005–3020.
- a) T. C. Stamatatos, D. Foguet-Albiol, S. C. Lee, C. C. Stoumpos, C. P. Raptopoulou, A. Terzis, W. Wernsdorfer, S. O. Hill, S. P. Perlepes, G. Christou, *J. Am. Chem. Soc.* **2007**, 129, 9484–9499; b) M. N. Collomb, A. Deronzier, *Eur. J. Inorg. Chem.* **2009**, 2025–2030.
- a) Z. Wang, B. Zhang, H. Fujiwara, H. Kobayashi, M. Kurmoo, *Chem. Commun.* **2004**, 416–417; b) B. Zhang, Z. Wang, M. Kurmoo, S. Gao, K. Inoue, H. Kobayashi, *Adv. Funct. Mater.* **2007**, 17, 577–584; c) K. Li, D. H. Olson, J. Y. Lee, W. Bi, K. Wu, T. Yuen, Q. Xu, J. Li, *Adv. Funct. Mater.* **2008**, 18, 2205–2214; d) H. Kim, D. G. Samsonenko, M. Yoon, J. W. Yoon, Y. K. Kwang, J.-S. Chang, K. Kim, *Chem. Commun.* **2008**, 4697–4699.
- a) T. Lis, *Acta Crystallogr., Sect. B* **1980**, 36, 2042–2046; b) R. Sessoli, H.-L. Tsai, A. R. Schake, S. Wang, J. B. Vincent, K. Folting, D. Gatteschi, G. Christou, D. N. Hendrickson, *J. Am. Chem. Soc.* **1993**, 115, 1804–1816; c) R. Sessoli, D. Gatteschi, A. Caneschi, M. A. Novak, *Nature* **1993**, 365, 141–143.
- a) R. Bagai, G. Christou, *Chem. Soc. Rev.* **2009**, 38, 1011–1026; b) G. Aromi, E. K. Brechin, *Struct. Bonding (Berlin)* **2006**, 122, 1–67.
- a) A. J. Tasiopoulos, A. Vinslava, W. Wernsdorfer, K. A. Aboud, G. Christou, *Angew. Chem.* **2004**, 116, 2169–2173; *Angew. Chem. Int. Ed.* **2004**, 43, 2117–2121; b) G. E. Kostakis, A. M. Rko, A. K. Powell, *Chem. Soc. Rev.* **2010**, 39, 2238–2271.
- M. A. Kiskin, I. G. Fomina, G. G. Aleksandrov, A. A. Sidorov, V. M. Novotortsev, Y. V. Rakitin, Z. V. Dobrokhotova, V. N. Ikorskii, Y. G. Shvedenkov, I. L. Eremenko, I. I. Moiseev, *Inorg. Chem. Commun.* **2005**, 8, 89–93.
- Z.-L. Chen, Y.-S. Ma, F.-P. Liang, Z.-H. Zhou, *J. Organomet. Chem.* **2008**, 693, 646–654.
- Z.-L. Chen, Y.-S. Ma, F.-P. Liang, Z.-H. Zhou, *Eur. J. Inorg. Chem.* **2007**, 2040–2045.

- [10] a) Y.-P. Tian, X.-J. Zhang, J.-Y. Wu, H.-K. Fun, M.-H. Jiang, Z.-Q. Xu, A. Usman, S. Chantrapromma, L. K. Thompson, *New J. Chem.* **2002**, 26, 1468–1473; b) B. Ruan, Y. Tian, H. Zhou, J. Wu, Z. Liu, C. Zhu, J. Yang, H. Zhu, *J. Organomet. Chem.* **2009**, 694, 2883–2887; c) X.-J. Zhang, Y.-P. Tian, S.-L. Li, M.-H. Jiang, A. Usman, S. Chantrapromma, H.-K. Fun, *Polyhedron* **2003**, 22, 397–402; d) J.-Y. Wu, Y.-L. Pan, X.-J. Zhang, T. Sun, Y.-P. Tian, J.-X. Yang, Z.-N. Chen, *Inorg. Chim. Acta* **2007**, 360, 2083–2091; e) J.-Y. Wu, Y.-L. Pan, X.-J. Zhang, M.-L. Zhang, Y.-P. Tian, H.-K. Fun, *Chin. J. Inorg. Chem.* **2003**, 19, 1347–1350; f) X.-J. Zhang, J.-Y. Wu, M.-L. Zhang, Y.-P. Tian, M.-H. Jiang, A. Usman, S. Chantrapromma, H.-K. Fun, *Transition Met. Chem.* **2003**, 28, 707–711.
- [11] M. Nakashima, H. Maruo, T. Hata, T. Tokii, *Chem. Lett.* **1999**, 28, 1277–1278.
- [12] C. Janiak, *J. Chem. Soc., Dalton Trans.* **2000**, 3885–3896.
- [13] V. Gomez, M. Corbella, *J. Chem. Crystallogr.* **2011**, 41, 843–846.
- [14] H. Chen, X.-F. Zhang, D.-G. Huang, C.-N. Chen, Q.-T. Liu, *Chin. J. Struct. Chem.* **2006**, 25, 103–107.
- [15] O. Kahn, *Molecular Magnetism*, VCH Publishers, Inc., New York, **1993**.
- [16] K. Nakamoto, *Infrared and Raman Spectra of Inorganic and Coordination Compounds*, John Wiley and Sons, New York, **1986**, p. 233.
- [17] *CrystalClear*, Rigaku Corporation, Tokyo, Japan, **2005**.
- [18] G. M. Sheldrick, *Acta Crystallogr., Sect. A: Found. Crystallogr.* **2008**, 64, 112.

Received: October 30, 2011

Published Online: February 8, 2012

Synthesis of Oligomeric Zinc Complexes with Bicyclic and Acyclic Guanidinate Ligands

Christiane Neuhäuser,^[a] Matthias Reinmuth,^[a] Elisabeth Kaifer,^[a] and
Hans-Jörg Himmel^{*[a]}

Dedicated to Prof. Dr. mult. Alois Haas on the occasion of his 80th birthday

Keywords: Zinc / Oligomeric complexes / Alkyl complexes / N ligands / Hydrogen bonds / Guanidines

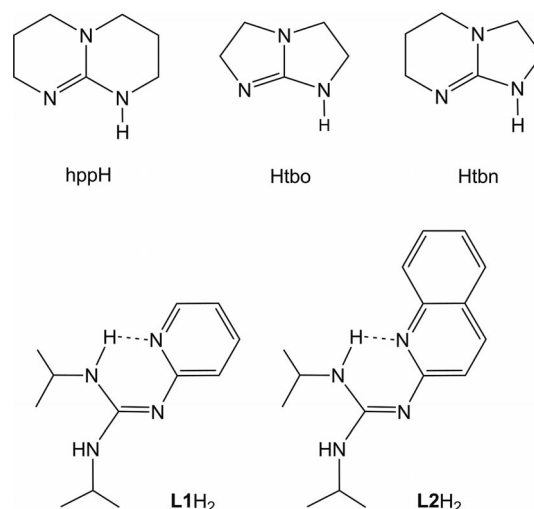
Zinc dichloride and dimethylzinc were treated with several acyclic and bicyclic guanidines. Three different bicyclic guanidines and their potassium guanidinate salts were treated with ZnCl_2 . The reaction with the neutral guanidines afforded mononuclear complexes, stabilized by intramolecular hydrogen bonding. The reaction with the potassium guanidinate salts led to trinuclear complexes, which were extremely water sensitive. The reaction in the presence of added water furnished a tetranuclear complex with a central OZn_4 unit in good yield, to which six guanidinate ligands were bound.

The reaction of dimethylzinc with 2-[*N,N'*-diisopropylguanidino]pyridine and 2-[*N,N'*-diisopropylguanidino]quinoline afforded di- and tetranuclear Zn methyl complexes with mono- and dianionic guanidinate ligands. Dinuclear complexes of the monoanionic guanidinate ligands were formed at room temperature. At higher temperatures (75 °C), complete deprotonation of the guanidino groups and formation of tetranuclear Zn alkyl complexes was observed, which feature low-coordinate zinc sites.

Introduction

Guanidines and guanidates are widely applied as ligands in transition metal complexes or substituents in main-group element compounds.^[1–6] A number of zinc complexes with guanidine or guanidinate ligands have been synthesized and applied as catalysts for the polymerization of lactide^[7–13] and epoxidation of olefins.^[14] Bicyclic, monoanionic guanidinate ligands, formed by the deprotonation of neutral guanidines, such as hppH (1,3,4,6,7,8-hexahydro-2*H*-pyrimido[1,2-*a*]pyrimidine), Htbn (1,5,7-triazabicyclo[4.3.0]non-6-ene) and Htbo (1,4,6-triazabicyclo[3.3.0]oct-4-ene) (Scheme 1), were applied to the synthesis of dinuclear transition metal complexes with multiple bonding between the metals,^[15–17] catalytically active complexes or dinuclear main group element compounds of special reactivity.^[18–25] Due to their flexible bonding modes and preference for bridging positions, the use of bicyclic guanidates generally leads to di- or oligonuclear complexes. For example, the reaction between hppH or Htbo and ZnMe_2 in toluene afforded the trinuclear complexes $[\text{Zn}_3(\mu\text{-hpp})_4\text{Me}_2]$ and $[\text{Zn}_3(\mu\text{-tbo})_4\text{Me}_2]$.^[26,27] Several zinc complexes of acy-

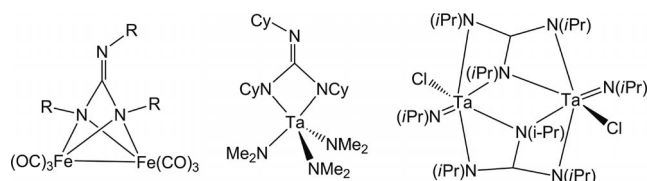
lic monoanionic guanidates are also known. With particular relevance to this work, the room temperature reaction between 2-[*N,N'*-diisopropylguanidino]pyridine (**L1H₂**, Scheme 1) and ZnMe_2 yielded the dinuclear Zn alkyl complex $[(\text{L1H})\text{ZnMe}]_2$.^[28] Acyclic dianionic guanidates of the general formula $[\text{C}(\text{NR})(\text{NR}')(\text{NR}'')]^{2-}$ are isoelectronic with $[\text{CO}_3]^{2-}$. To date, only a few examples of transition metal complexes that feature dianionic guanidinate ligands are known. The first authenticated examples, dinu-



Scheme 1.

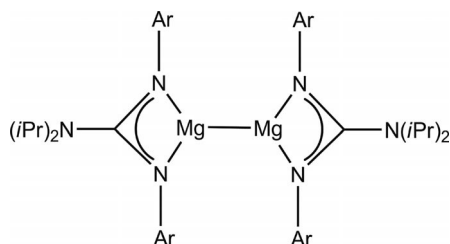
[a] Anorganisch-Chemisches Institut, Ruprecht-Karls-Universität Heidelberg, Im Neuenheimer Feld 270, 69120 Heidelberg, Germany
Fax: +49-6221-545707
E-mail: hans-jorg.himmel@aci.uni-heidelberg.de
Supporting information for this article is available on the WWW under <http://dx.doi.org/10.1002/ejic.201101223>.

clear Fe^{II} complexes of the formula $[\{\text{(OC)}_3\text{Fe}\}_2\{\mu\text{-(RN)}_3\text{-C}\}]$ ($\text{R} = \text{Cy}, i\text{Pr}$, Scheme 2), were the unexpected products of the reaction between $\text{Fe}(\text{CO})_5$ and carbodiimides.^[29] Two of the three nitrogen atoms of the guanidinate dianions establish bonds to both metal centres, whereas the third nitrogen atom is not directly coordinated. Richeson et al. have reported the synthesis of several complexes of early transition metals (particularly Ta^{V} and Nb^{V}). Structurally authenticated examples (Scheme 2) include mononuclear $[(\text{Me}_3\text{N})_3\text{Ta}\{\text{(CyN)}_3\text{C}\}]$ ^[30] and dinuclear $[(i\text{PrN})_3\text{Ta}(\text{Cl})\{\mu\text{-(}i\text{PrN)}_3\text{C}\}]_2$.^[31]



Scheme 2.

In addition to their advantageous properties for catalytic applications, guanidinate substituents have been shown to stabilize low-valent main group elements. The most prominent example is $[(\text{Priso})\text{Mg}]_2$ (Scheme 3) with the bulky monoanionic guanidinate Priso ligand $[(\text{Ar})\text{NC}(\text{NR}'_2)\text{-N}(\text{Ar})]$ ($\text{Ar} = 2,6\text{-diisopropylphenyl}$).^[32] Zn^{I} complexes of the form LZnZnL are also known where $\text{L} = \text{Cp}^*$ ^[33] or β -diketiminato^[34] and not guanidinate. All reduction and salt-elimination experiments starting with LZnX ($\text{L} = \text{bulky guanidinate}$, $\text{X} = \text{halide}$) led to the deposition of elemental zinc.^[35]



Scheme 3.

Herein we report the synthesis of several new oligomeric zinc complexes with mono- and dianionic guanidinate ligands. The new complexes might be interesting for catalytic applications, especially one species with low-coordinate zinc sites. In addition, they could be used as possible starting reagents for the synthesis of subvalent zinc clusters with direct Zn-Zn bonds.

Results and Discussion

Reactions with Neutral Bicyclic Guanidines

The three mononuclear complexes $[\text{ZnCl}_2(\text{hppH})_2]$, $[\text{ZnCl}_2(\text{Htbn})_2]$ and $[\text{ZnCl}_2(\text{Htbo})_2]$ were obtained as the products of reactions between ZnCl_2 and hppH , Htbn or Htbo and crystallized from CH_3CN . Their molecular structures are displayed in Figure 1. In the case of $[\text{ZnCl}_2\text{-(Htbn)}_2]$, only one of three possible tautomers crystallized,

but variable-temperature NMR experiments support an equilibrium in solution (see Supporting Information). All complexes are stabilized by intramolecular $\text{N-H}\cdots\text{Cl}$ hydrogen bonding.^[36] As an example, Figure 2 shows the ^1H NMR spectrum of $[\text{ZnCl}_2(\text{Htbo})_2]$ in solvents of different polarity. The signal due to the NH proton shifts significantly as a function of the solvent polarity. In apolar solvents (6.62 ppm in C_6D_6) intact $\text{NH}\cdots\text{Cl}$ hydrogen bonds are present. The signal shifts to lower fields with increasing solvent polarity, which indicates competition between inter- and intramolecular hydrogen bonding. The most stable hydrogen bonding seems to be present in $[\text{ZnCl}_2(\text{hppH})_2]$,

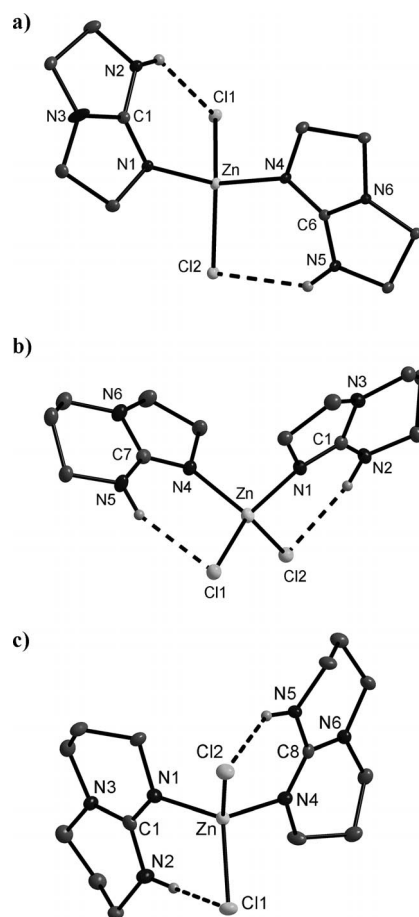


Figure 1. Molecular structures of a) $[\text{ZnCl}_2(\text{Htbo})_2]$, b) $[\text{ZnCl}_2(\text{Htbn})_2]$ and c) $[\text{ZnCl}_2(\text{hppH})_2]$. The hydrogen atoms bound to carbon are omitted. Thermal ellipsoids drawn at the 50% probability level. Selected bond lengths [pm] and angles $^\circ$: a) Zn-N1 199.45(3), Zn-N4 198.23(3), Zn-C11 227.95(3), Zn-Cl2 226.83(3), $\text{H2N}\cdots\text{Cl1}$ 256.57(3), $\text{H5N}\cdots\text{Cl2}$ 258.40(3), N1-C1 129.66(2), N2-C1 134.04(2), N3-C1 134.10(2), N4-C6 130.63(2), N5-C6 134.16(2), N6-C6 136.96(2), N1-Zn-N4 111.974(8), Cl1-Zn-Cl2 115.528(7) b) Zn-N1 198.94(5), Zn-N4 199.86(9), Zn-C11 227.24(7), Zn-Cl2 227.14(8), $\text{H2N}\cdots\text{Cl2}$ 244.47(5), $\text{H5N}\cdots\text{Cl1}$ 239.50(12), N1-C1 131.23(3), N2-C1 135.50(4), N3-C1 134.91(3), N4-C7 131.42(4), N5-C7 133.39(4), N6-C7 136.03(6), N1-Zn-N4 105.688(13), Cl1-Zn-Cl2 115.357(13) c) Zn-N1 200.70(4), Zn-N4 201.19(3), Zn-C11 227.95(4), Zn-Cl2 226.77(5), $\text{H2N}\cdots\text{Cl1}$ 253.08(6), $\text{H5N}\cdots\text{Cl2}$ 252.15(6), N1-C1 130.04(2), N2-C1 137.06(3), N3-C1 135.73(3), N4-C8 130.31(2), N5-C8 138.69(4), N6-C8 135.04(3), N1-Zn-N4 106.619(9), Cl1-Zn-Cl2 110.473(5).

with a peak at 7.65 ppm for the NH protons in C_6D_6 solution. Traces of water led immediately to guanidine protonation. We isolated small amounts of $[hphH_2][(hphH)ZnCl_3]$ and $[hphH_2][(THF)ZnCl_3]$, and parts of their crystal structures are shown in Figure 3. Hydrogen bonds connect the cationic and anionic parts.

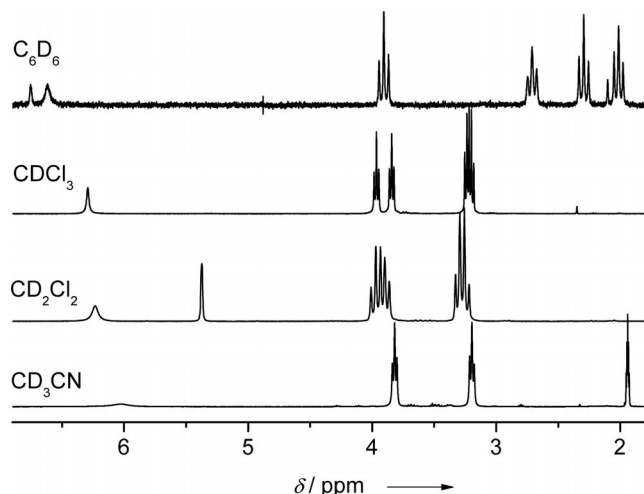


Figure 2. 1H NMR spectra of $[ZnCl_2(Htbo)_2]$ in solvents of different polarity (399.89 MHz).

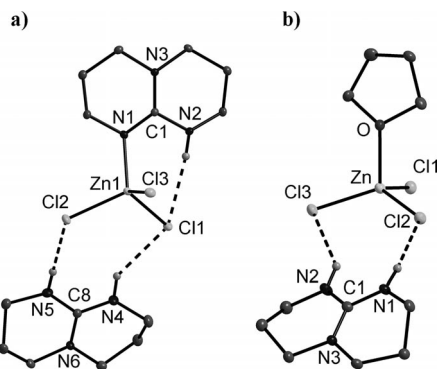
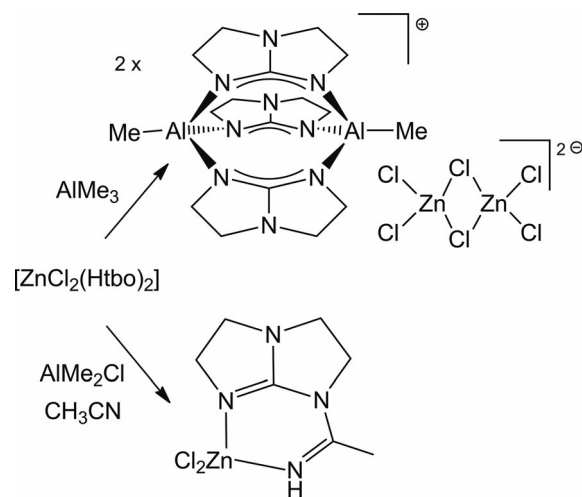


Figure 3. Parts of the crystal structures of a) $[hphH_2][(hphH)ZnCl_3]$ and b) $[hphH_2][(THF)ZnCl_3]$. The hydrogen atoms bound to carbon are omitted. Thermal ellipsoids drawn at the 50% probability level. Selected bond lengths [pm] and angles [°]: a) Zn–N1 199.46(6), Zn–C11 230.15(6), Zn–Cl2 227.91(7), Zn–Cl3 225.35(6), H2N–C11 245.40(8), H4N–C11 252.75(6), H5N–C12 235.64(7), N1–C1 132.77(5), N2–C1 137.00(3), N3–C1 133.99(4), N4–C8 131.34(4), N5–C8 133.73(3), N6–C8 132.62(4), Cl1–Zn–Cl2 106.004(23), Cl1–Zn–Cl3 111.953(22), Cl2–Zn–Cl3 111.775(14), Cl1–Zn–N1 111.085(26), Cl2–Zn–N1 108.817(15), Cl3–Zn–N1 107.217(25), b) Zn–O 204.74(6), Zn–C11 221.81(6), Zn–Cl2 226.24(9), Zn–Cl3 223.20(6), H1N–C12 235.19(5), H2N–C13 260.05(9), N1–C1 133.72(3), N2–C1 133.66(5), N3–C1 132.53(3), N4–C8 131.34(4), Cl1–Zn–Cl2 114.641(10), Cl1–Zn–Cl3 117.872(17), Cl2–Zn–Cl3 110.705(15), Cl1–Zn–O 103.206(22), Cl2–Zn–O 102.253(11), Cl3–Zn–O 106.190(18).

The reactivity of the three complexes was assessed in several experiments. The main intention was guanidine deprotonation followed by the introduction of a second metal to give heterobimetallic compounds. Although these experiments were for the most part unsuccessful, some remark-

able side products were isolated (Scheme 4). From the reaction of $[ZnCl_2(Htbo)_2]$ with $AlMe_3$, we obtained a small amount of a crystalline product, which was $[(MeAl)_2(\mu-tbo)_3]_2[(ZnCl_2)_2(\mu-Cl)_2]$. Part of the crystal structure of this salt is shown in Figure 4 (a). The guanidine was transferred completely from zinc to aluminium,^[37] and the resulting dicationic and dinuclear aluminium complex was stabilized by the weakly coordinating dianion $[Zn_2Cl_6]^{2-}$. In experiments with $AlMe_2Cl$ in place of $AlMe_3$, we obtained a very different product in CH_3CN solutions, namely, $[ZnCl_2\{tboC(CH_3)NH\}]$. Hence a CH_3CN solvent molecule inserted into the guanidine N–H bond (which presumably was activated by the aluminium compound) and led to a new chelating ligand system (Scheme 4 and Figure 4, b). In both cases only small amounts of product were isolated, and the NMR spectra of the reaction solutions indicated the presence of mixtures of different compounds.



Scheme 4.

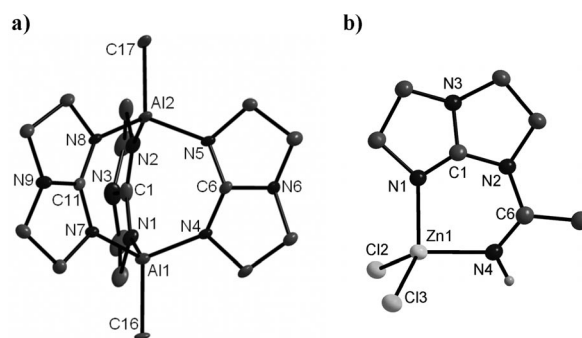


Figure 4. Structures of the isolated products of the reaction between $[ZnCl_2(Htbo)_2]$ and a) $AlMe_3$ and b) $AlMe_2Cl$. The hydrogen atoms bound to carbon are omitted. Thermal ellipsoids drawn at the 50% probability level. Selected bond lengths [pm] and angles [°]: a) Al1–N1 186.37(4), Al2–N2 187.73(3), Al1–C16 200.81(5), Al1...Al2 369.74(8), N1–C1 132.76(2), N2–C1 132.63(3), N3–C1 135.24(3), N1–Al1–N4 109.302(9), N1–Al1–C16 108.607(12), b) Zn–N1 199.64(4), Zn–N4 202.34(4), Zn–Cl2 225.93(5), Zn–Cl3 222.57(5), N1–C1 129.67(2), N2–C1 137.54(2), N3–C1 135.28(3), N2–C6 138.94(3), N4–C6 128.30(3), N1–Zn–N4 91.064(6), Cl3–Zn–Cl2 108.716(3).

Reactions with the Salts of Bicyclic Guanidines

As the experiments to deprotonate the bicyclic guanidines after coordination led to product mixtures, we first deprotonated the guanidines with KH and then reacted ZnCl_2 with the potassium guanidinate salts. In the case of Khpp, the NMR spectra indicated the formation of a product mixture, which was impossible to separate. The experiments with Ktbn and Ktbo were more promising. Crystalline products were obtained, which were identified as the trinuclear Zn complexes $[\text{Zn}_3\text{Cl}_2(\text{tbn})_4]$ and $[\text{Zn}_3\text{Cl}_2(\text{tbo})_4]$. Their structures are shown in Figures 5 and 6, respectively, and resemble that reported for $[\text{Zn}_3\text{Me}_2(\text{hpp})_4]$.^[26] Unfortunately the two complexes were extremely water sensitive. Furthermore, their solubility in standard organic solvents was low. Finally, it was difficult to remove traces of KCl from the compounds to isolate them in a clean form.

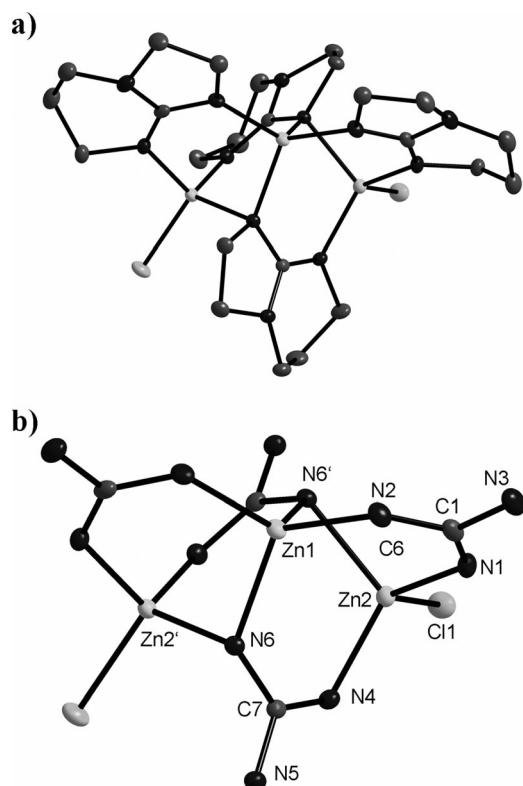


Figure 5. a) Molecular structure of $[\text{Zn}_3\text{Cl}_2(\text{tbn})_4]$ (hydrogen atoms omitted). b) Representation without the CH_2 groups of the guanidinate ligands. Thermal ellipsoids drawn at the 50% probability level. Selected bond lengths [pm] and angles [°]: Zn1-N2 196.72(4), Zn1-N6 206.36(3), Zn2-N1 197.60(3), Zn2-N4 197.88(4), Zn2-N6 209.54(4), Zn2-Cl1 225.66(3), N1-C1 132.09(2), N2-C1 133.71(4), N3-C1 137.78(2), N4-C7 130.70(3), N5-C7 135.61(3), N6-C7 138.04(2), Zn1-N6-Zn2 91.269(6).

Motivated by the water sensitivity, we deliberately added water to the reaction mixture and isolated the product of the reaction with water in a pure form. In this case, water did not lead to guanidine protonation but the formation of the tetranuclear complex $[\text{OZn}_4(\text{tbo})_6]$, which is highly soluble in organic solvents such as benzene. The complex was also prepared in 35% yield by the slow addition of toluene

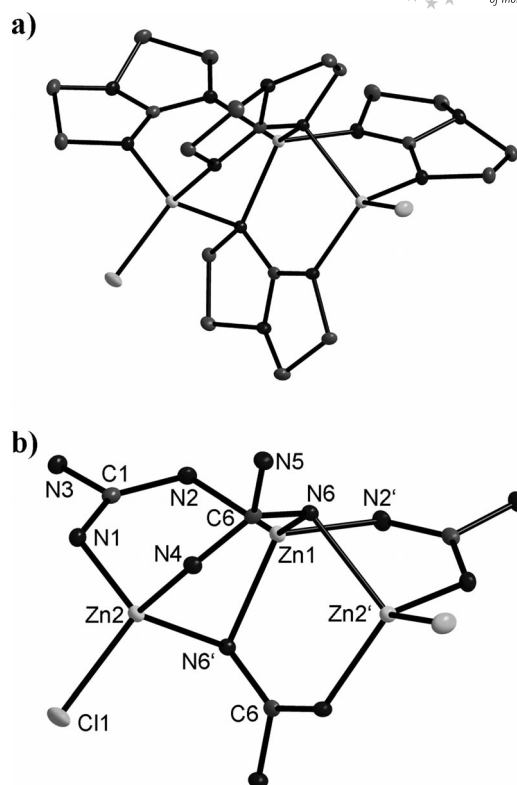
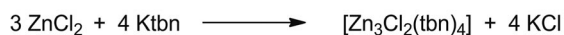


Figure 6. a) Molecular structure of $[\text{Zn}_3\text{Cl}_2(\text{tbo})_4]$ (hydrogen atoms omitted). b) Representation without the CH_2 groups of the guanidinate ligands. Thermal ellipsoids drawn at the 50% probability level. Selected bond lengths [pm] and angles [°]: Zn1-N2 195.21(4), Zn1-N6 207.38(3), Zn2-N1 197.94(3), Zn2-N4 197.80(4), Zn2-N6 213.93(4), Zn2-Cl1 222.92(3), N1-C1 132.26(2), N2-C1 132.21(3), N3-C1 138.45(3), N4-C6 130.91(2), N5-C6 136.44(3), N6-C6 136.20(2), Zn1-N6-Zn2 95.716(6).

saturated with H_2O to a mixture of ZnH_2 and Htbo (Scheme 5). $[\text{OZn}_4(\text{tbo})_6]$ was crystallized from CH_3CN or toluene at -21°C , and the structure is shown in Figure 7. The central tetrahedral OZn_4 unit is a structural element that is found in a number of other Zn complexes such as $[\text{OZn}_4(\text{O}_2\text{CNR}_2)_6]$,^[38] where R are alkyl or amino groups, and $[\text{OZn}_4(\text{OAc})_6]$.^[39] The similarity of the OZn_4 unit in such complexes and the building blocks in bulk ZnO has been analyzed in detail, and it has been shown that complexes of this kind can be applied as precursors for ZnO nanoparticles. Thermogravimetric (TG) measurements for $[\text{OZn}_4(\text{tbo})_6]$ show that decomposition proceeds slowly at around 300°C . Hence this compound is not an ideal precursor for ZnO nanoparticles.



Scheme 5.

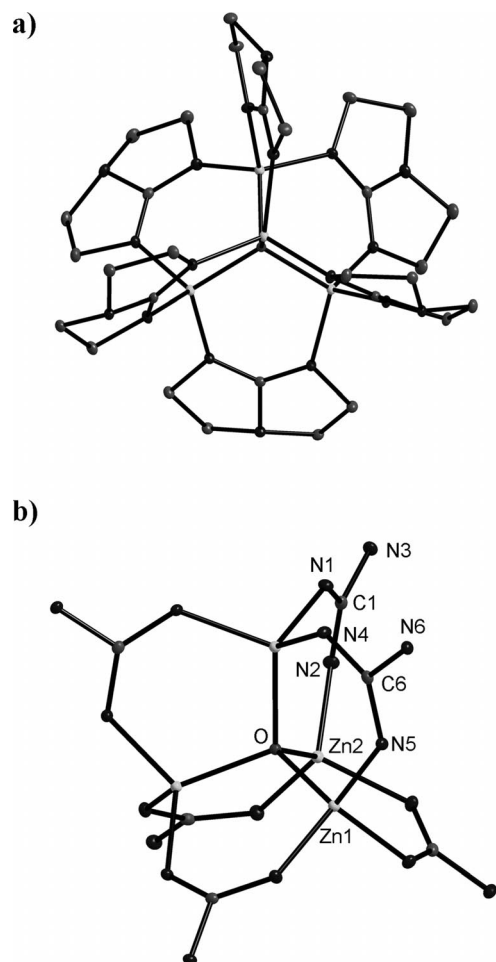


Figure 7. a) Molecular structure of $[\text{OZn}_4(\text{tbo})_6]$ (hydrogen atoms omitted). b) Representation without the CH_2 groups of the guanidinate ligands. Thermal ellipsoids drawn at the 50% probability level. Selected bond lengths [pm] and angles [°]: Zn1–O 200.59(2), Zn2–O 199.91(4), Zn1–N1 199.75(3), Zn2–N2 198.46(2), C1–N1 132.09(2), C1–N2 132.03(2), C1–N3 139.46(2), Zn1–O–Zn1 110.198(5), Zn1–O–Zn2 108.734(8), N2–Zn2–N5 108.873(5), N1–Zn1–N4 105.516(9).

Reactions with Acyclic Guanidines

Zinc complexes with dianionic guanidinate ligands were realized with 2- $[\text{N},\text{N}']$ -diisopropylguanidino]pyridine (**L1H₂**) and 2- $[\text{N},\text{N}']$ -diisopropylguanidino]quinoline (**L2H₂**), which could be doubly deprotonated (Scheme 1). The ligands were prepared by the reaction between N,N' -diisopropylcarbodiimide and 2-aminopyridine (for **L1H₂**)^[40,41] or 2-aminoquinoline (for **L2H₂**) with catalytic AlClMe_2 . In addition to the guanidino N atoms, these ligands bind to the Zn centre through the additional N atom in the aromatic ring. We grew crystals of **L2H₂** suitable for XRD analysis, and its molecular structure is shown in Figure 8. The structural parameters indicate hydrogen bonding between the quinoline nitrogen atom and one of the protons attached to nitrogen within the guanidino group [N1...HN4 estimated bond length 191.2(4) pm]. At 133.11(17) pm, the imino bond (N2–C10) is relatively long. The bond lengths from the cen-

tral carbon atom (C10) to the remaining two nitrogen atoms in **L2H₂** are relatively short [135.83(16) pm for N3–C10 and 134.78(15) pm for N4–C10].

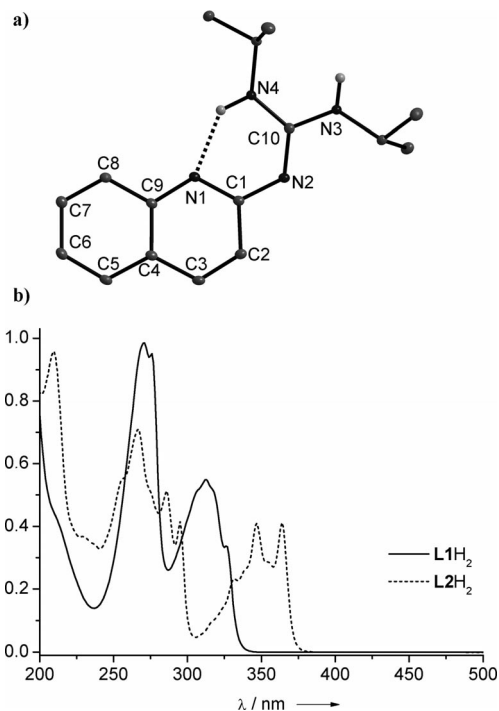
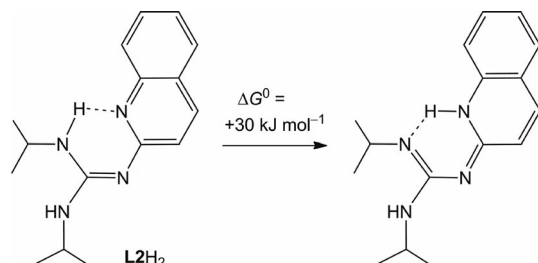


Figure 8. a) Molecular structure of **L2H₂**. Vibrational ellipsoids are drawn at the 50% probability level. All hydrogen atoms attached to C atoms are omitted for clarity. Selected bond lengths [pm] and angles [°]: N1–C1 134.01(16), N1–C9 137.40(16), N1...N4 265.8(4), N1...HN4 191.2(4), N2–C1 137.15(17), N2–C10 133.11(17), N3–C10 135.83(16), N4–C10 134.78(15), C1–C2 144.36(18), C2–C3 135.22(18), C3–C4 142.74(18), C4–C5 141.21(18), C4–C9 141.91(17), C5–C6 137.5(2), C6–C7 140.55(19), C7–C8 137.28(19), C8–C9 141.35(18), N1–C1–N2 124.36(11), C2–C1–N2 114.98(11), C1–N2–C10 122.32(10), N2–C10–N3 117.21(11), N2–C10–N4 125.08(11), N3–C10–N4 117.70(11). b) UV/Vis spectra of solutions of **L1H₂** and **L2H₂** in hexane.

The structure of **L2H₂** was compared by quantum chemical (B3LYP) calculations with that of its tautomer, in which the proton is attached to the quinoline N atom (Scheme 6). This tautomer is energetically disfavoured in the gas phase [ΔE , ΔH^0 and ΔG^0 values of 30, 28 and 30 kJ mol^{-1} , respectively, were calculated with B3LYP/6-31+G(d), and 28, 26 and 28 kJ mol^{-1} with B3LYP/def2-TZVP]. Table 1 compares the experimental data for **L2H₂** with those calculated. The corresponding tautomer in the case of **L1H₂** is also energetically disfavoured [gas-phase ΔE , ΔH^0 and ΔG^0 values of 41, 39 and 41 kJ mol^{-1} , respectively, were calculated with B3LYP/6-31+G(d), and 39, 36 and 38 kJ mol^{-1} with B3LYP/def2-TZVP]. Figure 9 shows the UV/Vis spectra of hexane solutions of **L1H₂** and **L2H₂**. For **L1H₂**, two intense absorptions are visible at $\lambda_{\text{max}} = 271/276$ and 327/312 nm, which show signs of vibrational fine structure. The spectrum of **L2H₂** in hexane is relatively complex, with absorption maxima at 210, 266/286/295 and 332/347/364 nm. The bands are broader in CH_3CN , which leads to a less clearly

resolved vibrational fine structure. Figure 9 (a) displays the emission spectrum alongside the absorption spectrum in CH_3CN . The fluorescence signal reaches its maximum at ca. 400 nm, which corresponds to a Stokes shift of approximately 40 nm.



Scheme 6.

Table 1. Comparison of selected experimental and calculated (B3LYP/def2-TZVP) bond lengths [pm] for L2H_2 . The calculated structural parameters of the tautomer (protonation at the quinoline N atom) are included.

	Experimental	Calculated L2H_2	tautomer
N1...H(N4)	191.2(4)	184.4	–
N4...H(N1)	–	–	177.1
N1–C1	134.0(2)	133.2	136.7
N2–C1	137.2(2)	136.6	131.0
N2–C10	133.1(2)	131.6	137.9
N3–C10	135.8(2)	136.7	137.5
N4–C10	134.8(2)	135.3	130.6
C1–C2	144.4(2)	143.7	144.4

The guanidine L2H_2 was first reacted at room temperature with Me_2Zn , which led to a single reaction product. The ^1H NMR spectrum indicated the presence of intact MeZn units with a signal at 0.32 ppm. Furthermore, a band at 3440 cm^{-1} in the IR spectrum signalled the presence of NH. Hence not all of the NH protons were removed in the course of the reaction. The product was crystallized as colourless cubic crystals from toluene at -20°C .

From the data, the complex was identified as dinuclear $[(\text{L2H})\text{ZnMe}]_2$ (Scheme 7 and Figure 10). Deprotonation and complex formation was accompanied by some significant structural changes within the ligand unit. The N2–C10 bond length, formerly a double bond, was elongated in $[(\text{L2H})\text{ZnMe}]_2$ to 137.8(3) pm. At the same time, the N3–C10 bond length decreased significantly from 135.83(16) pm in free L2H_2 to 131.5(3) pm in $[(\text{L2H})\text{ZnMe}]_2$. The N4–C10 bond length increased from 134.78(15) in L2H_2 to 136.6(3) in $[(\text{L2H})\text{ZnMe}]_2$. All these structural changes favour the Lewis structure shown in Scheme 7, in which the imino $\text{N}=\text{C}$ double bond has migrated with respect to free L2H_2 . As anticipated, the change in the electronic structure led to some changes in the absorption and emission spectra of $[(\text{L2H})\text{ZnMe}]_2$ (Figure 9, b). The absorption spectrum again features two bands with vibrational fine structure at 265/276/284/292 and 348/355/363 nm, and a new, sharp band appears at 381 nm. The emission signal undergoes a

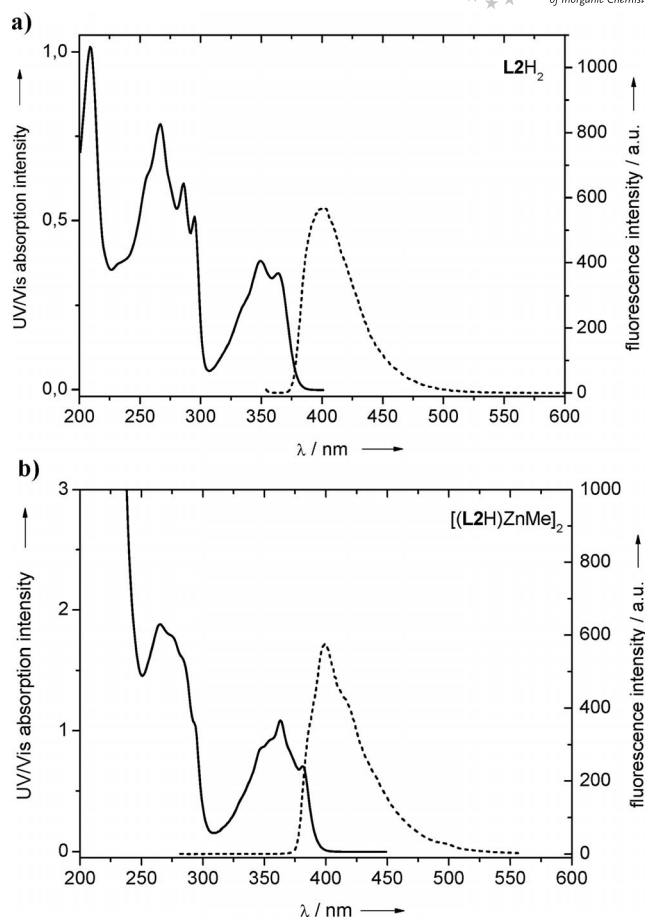
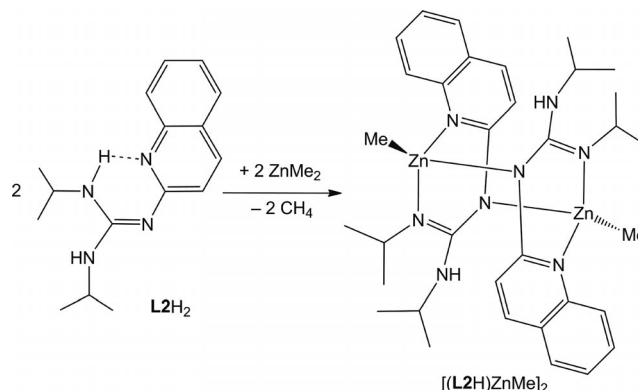


Figure 9. UV/Vis (solid lines) and fluorescence (dashed lines) spectra of a) L2H_2 and b) $[(\text{L2H})\text{ZnMe}]_2$ in CH_3CN . Fluorescence spectra excited with light at 349 nm (L2H_2) or 265 nm $[(\text{L2H})\text{ZnMe}]_2$.

small redshift, and its maximum is at 412 nm. Vibrational fine structure of this signal is visible (e.g. a shoulder at ca. 430 nm).



Scheme 7.

We tested the possibility of twofold deprotonation of the guanidine ligand at higher temperatures. NMR spectra indicated formation of two products in a stoichiometric ratio of 6:1 when the reaction between L1H_2 and Me_2Zn was carried out at 75°C . The minor product was known $[(\text{L1H})$

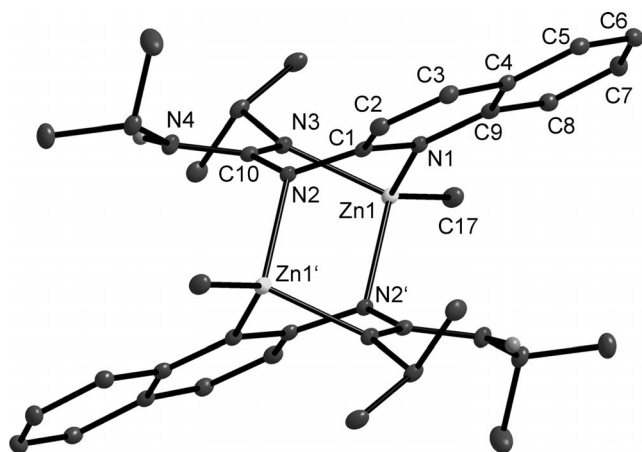
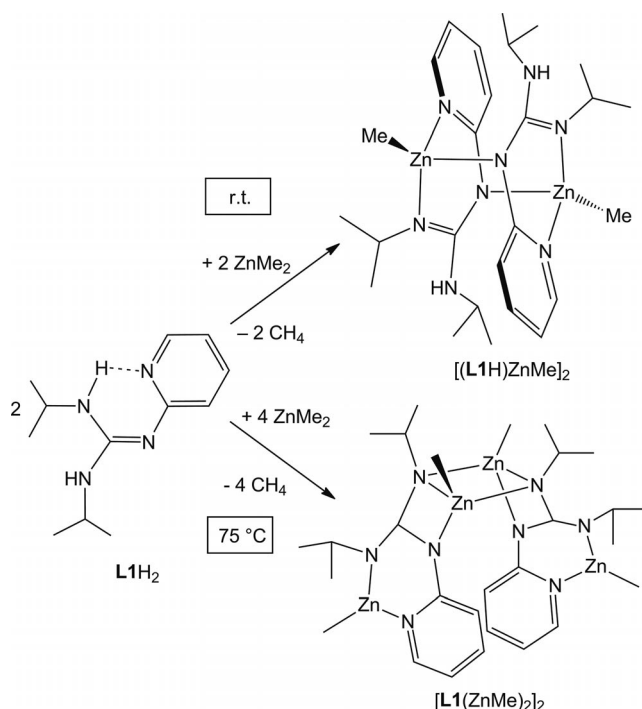


Figure 10. Molecular structure of $[(\text{L2H})\text{ZnMe}]_2$. Only one of two slightly different molecules in the crystal is shown. Vibrational ellipsoids are drawn at the 50% probability level. All hydrogen atoms attached to C atoms are omitted for clarity. Selected bond lengths [pm] and angles $^\circ$: Zn1–N1 208.77(19), Zn1–N2 214.43(19), Zn1–N3 202.8(2), Zn1–C17 199.5(2), Zn1...Zn1' 432.4(8), N1–C1 133.5(3), N1–C9 137.7(3), N2–C1 137.7(3), N2–C10 137.8(3), N3–C10 131.5(3), N4–C10 136.6(3), C1–C2 143.9(3), C2–C3 134.5(3), C3–C4 142.4(3), C4–C5 141.5(3), C4–C9 141.6(3), C5–C6 137.4(3), C6–C7 139.7(3), C7–C8 137.9(3), C8–C9 142.0(3), N2'–Zn1–N1 93.51(7), N1–Zn1–N3 87.07(8), N3–Zn1–C17 124.90(9), C1–N2–C10 121.01(18), N3–C10–N4 123.0(2).

ZnMe_2 . The second (main) product was identified as new tetranuclear $[\text{L1}(\text{ZnMe})_2]_2$ with guanidinate dianions as ligands (Scheme 8).



Scheme 8.

The complex was crystallized from a toluene solution, and Figure 11 illustrates its crystal structure. There are two remarkable structural features: Firstly, two of the zinc

atoms are only three coordinate and, secondly, all four nitrogen atoms of each ligand contribute directly to the bonding with the metal. The shape of the molecule is reminiscent of a gateway with a $\text{Zn}(\mu\text{-N})_2\text{Zn}$ unit as an architrave. A similar structure has been reported with a very different ligand (Scheme 9), and the complex was shown to exhibit a high catalytic activity in intramolecular hydroamination reactions of unactivated olefins at relatively low temperatures.^[42] $[\text{L1}(\text{ZnMe})_2]_2$ was extremely water sensitive, presumably because of the two three-coordinate Zn atoms. Initial experiments to probe the Lewis acidity of the low-coordinate Zn sites in $[\text{L1}(\text{ZnMe})_2]_2$ by their reaction with pyridine resulted in the decomposition of the tetranuclear complex. If tetrahydrofuran (THF) is used in place of toluene as the solvent during the reaction, the same products were obtained, which indicates that THF does not or only very loosely coordinates to the three-coordinate Zn^{II} . Finally, if CH_3CN was used as the reaction medium, the precipitation of an intense yellow solid was observed, which was insoluble in all common organic solvents and H_2O .

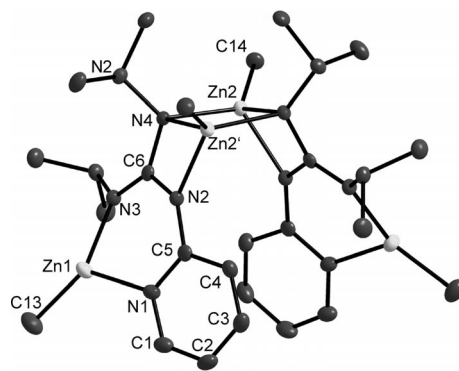
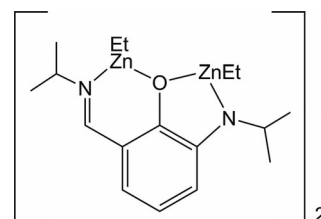


Figure 11. Molecular structure of $[\text{L1}(\text{ZnMe})_2]_2$. Vibrational ellipsoids are drawn at the 50% probability level. All hydrogen atoms attached to C atoms are omitted for clarity. Selected bond lengths [pm] and angles $^\circ$: Zn1–N1 202.2(2), Zn1–N3 195.9(2), Zn1–C13 195.7(3), Zn2–N2 206.7(2), Zn2–N4 218.3(2), Zn2–N4' 209.41(19), Zn2–C14 198.0(2), Zn2...Zn2' 288.20(10), N1–C1 135.4(3), N1–C5 135.3(3), N2–C5 136.8(3), N2–C6 137.0(3), N3–C6 132.8(3), N4–C6 139.6(3), N1–Zn1–N3 93.01(8), N1–Zn1–C13 122.68(11), N3–Zn1–C13 140.32(11), N4–Zn2–N4' 95.12(7), N2–Zn2–N4 63.31(8), N2–Zn2–N4' 108.77(8), N2–Zn2–C14 121.55(9), N4–Zn2–C14 128.69(9), N4'–Zn2–C14 123.37(9), C5–N1–Zn1 120.24(17), C5–N2–Zn2 134.74(16), C5–N2–C6 128.0(2), C6–N3–Zn1 120.91(16), N1–C5–N2 123.4(2), N2–C6–N3 124.3(2), N2–C6–N4 107.58(19), N3–C6–N4 128.1(2).



Scheme 9.

Conclusions

Several oligonuclear Zn complexes with bicyclic or acyclic guanidinate ligands were synthesized and characterized. In some cases the characterization was limited due to the extremely high reactivity of the complexes and problems with product mixtures. We successfully synthesized a tetranuclear Zn complex with highly reactive low-coordinate zinc sites, which might be of interest for catalytic applications. Initial experiments with Lewis bases resulted in decomposition. In addition, some of the compounds described here might be of use as starting points for the synthesis of low-valent zinc clusters with direct Zn–Zn bonds.

Experimental Section

General: All reactions were carried out under an inert atmosphere using standard Schlenk techniques. LiH_2 was synthesized as described previously.^[40,41] IR spectra were recorded with a BIORAD Excalibur FTS 3000 instrument. NMR spectra were recorded with BRUKER Avance II 400 or BRUKER Avance DPX AC200 spectrometers. Elemental analyses were carried out at the Microanalytical Laboratory of the University of Heidelberg. UV/Vis spectra were recorded with a Varian Cary 5000 spectrometer. Fluorescence measurements were measured with a Varian Cary Eclipse machine.

[ZnCl₂(hppH)₂]: To a CH_3CN solution of hppH (263 mg, 1.89 mmol) was added a 1 M solution of ZnCl_2 (0.63 mL, 0.63 mmol) in Et_2O dropwise, and the reaction mixture was stirred at r.t. for 24 h. The solvent was removed under vacuum, and the solid residue washed three times with toluene (10 mL) to remove traces of hppH. The crude product was dried under vacuum overnight. Recrystallization from CH_3CN at -21°C afforded colourless crystals of $[\text{ZnCl}_2(\text{hppH})_2]$; yield 0.222 g (0.54 mmol, 85%). $\text{C}_{14}\text{H}_{26}\text{Cl}_2\text{N}_6\text{Zn}$ (414.68): calcd. C 40.55, H 6.32, N 20.26; found C 40.21, H 6.16, N 20.09. ^1H NMR (399.89 MHz, C_6D_6 , 23°C): δ = 7.65 (s, 2 H, NH), 3.45 (t, 4 H, CH_2), 2.58 (t, 4 H, CH_2), 2.34 (t, 4 H, CH_2), 2.17 (t, 4 H, CH_2), 1.44 (quint, 4 H, CH_2), 1.02 (quint, 4 H, CH_2) ppm. ^1H NMR (399.89 MHz, CD_2Cl_2 , 23°C): δ = 6.66 (s, 2 H, NH), 3.07–3.33 (m, 16 H, CH_2), 1.90 (quint, 4 H, CH_2), 1.82 (quint, 4 H, CH_2) ppm. ^1H NMR (399.89 MHz, $[\text{D}_8]\text{-THF}$, 23°C): δ = 7.24 (s, 2 H, NH), 3.22 (t, 4 H, CH_2), 3.16 (m, 12 H, CH_2), 1.88 (quint, 4 H, CH_2), 1.79 (quint, 4 H, CH_2) ppm. ^1H NMR (399.89 MHz, CD_3CN , 23°C): δ = 6.64 (br. s, 2 H, NH), 3.34–3.15 (m, 16 H, CH_2), 1.91 (quint, 4 H, CH_2), 1.82 (quint, 4 H, CH_2) ppm. $^{13}\text{C}\{^1\text{H}\}$ NMR (100.55 MHz, C_6D_6 , 23°C): δ = 154.46 (CN_3), 47.51 (CH_2), 47.35 (CH_2), 38.46 (CH_2), 39.18 (CH_2), 22.70 (CH_2), 21.75 (CH_2) ppm. $^{13}\text{C}\{^1\text{H}\}$ NMR (100.55 MHz, CD_2Cl_2 , 23°C): δ = 154.60 (CN_3), 48.14 (CH_2), 47.25 (CH_2), 43.22 (CH_2), 39.18 (CH_2), 22.89 (CH_2), 22.41 (CH_2) ppm. $^{13}\text{C}\{^1\text{H}\}$ NMR (100.55 MHz, CD_3CN , 23°C): δ = 155.31 (CN_3), 48.27 (CH_2), 48.25 (CH_2), 43.60 (CH_2), 39.36 (CH_2), 23.14 (CH_2), 22.66 (CH_2) ppm. IR (KBr): $\tilde{\nu}$ = 3300 (m), 3205 (w), 3029 (w), 2968 (w), 2935 (w), 2855 (m), 2750 (w), 1612 (s), 1548 (s), 1439 (m), 1395 (w), 1367 (w), 1317 (s), 1196 (m), 1133 (w), 1112 (w), 1065 (m), 1025 (m), 941 (w), 893 (w), 801 (w), 733 (m), 718 (m), 578 (w), 527 (w) cm^{-1} . FAB⁺ MS: m/z = 415.1 [M]⁺, 377.2 [$\text{M} - \text{Cl}$]⁺, 341.2 [$\text{M} - \text{Cl}_2$]⁺, 315.2 [$\text{M} - \text{Cl} - \text{Zn}$]⁺, 279.3 [$\text{M} - \text{hppH}$]⁺, 140.1 [hppH_2]⁺. Crystal data for $\text{C}_{14}\text{H}_{26}\text{Cl}_2\text{N}_6\text{Zn}$: M_r = 414.68, a = 8.2350(16) Å, b = 14.067(3) Å, c = 15.589(3) Å, β = 97.32(3)°, V = 1791.1(6) Å³, Z = 4, $d_{\text{calcd.}}$ = 1.538 Mg m^{-3} , T = 200 K, θ_{range} 1.96 to 27.40°. Reflections mea-

sured 14524, independent 4052, R_{int} = 0.1265. Final R indices [$I > 2\sigma(I)$]: R_1 = 0.0592, wR_2 = 0.1053.

[ZnCl₂(Htbn)₂]: Htbn (291 mg, 2.32 mmol) was dissolved in CH_3CN (25 mL), a 1 M solution of ZnCl_2 (0.77 mL, 0.77 mmol) in Et_2O was added dropwise, and the reaction mixture was stirred at r.t. for 24 h. The solvent was removed under vacuum, and the solid residue was washed three times with toluene (10 mL) to remove traces of Htbn. The crude product was dried overnight under vacuum. Recrystallization from CH_3CN at -21°C yielded colourless crystals suitable for XRD analysis; yield 0.260 mg (0.67 mmol, 87%). $\text{C}_{12}\text{H}_{22}\text{N}_6\text{Cl}_2\text{Zn}$ (386.63): calcd. C 37.28, H 5.73, N 21.73; found C 36.85, H 5.69, N 21.20. ^1H NMR (399.89 MHz, CDCl_3 , 23°C): δ = 6.82 (s, 2 H, NH), 3.58 (t, 4 H, CH_2), 3.36 (t, 4 H, CH_2), 3.25 (t, 4 H, CH_2), 3.15 (t, 4 H, CH_2), 1.98 (quint, 4 H, CH_2) ppm. ^1H NMR (399.89 MHz, CD_3CN , 23°C): δ = 6.57 (s, 2 H, NH), 3.42 (m, 4 H, CH_2), 3.37 (m, 4 H, CH_2), 3.23 (m, 4 H, CH_2), 3.16 (m, 4 H, CH_2), 1.94 (quint, 4 H, CH_2) ppm. ^1H NMR (399.89 MHz, CDCl_3 , 23°C): δ = 6.44 (s, 2 H, NH), 3.41 (8 H, CH_2), 3.32 (4 H, CH_2), 3.18 (4 H, CH_2), 1.86 (4 H, CH_2) ppm. $^{13}\text{C}\{^1\text{H}\}$ NMR (100.55 MHz, CDCl_3 , 23°C): δ = 160.31 (CN_3), 50.02 (CH_2), 46.78 (CH_2), 43.22 (CH_2), 38.94 (CH_2), 21.29 (CH_2) ppm. $^{13}\text{C}\{^1\text{H}\}$ NMR (100.55 MHz, CD_3CN , 23°C): δ = 161.33 (CN_3), 50.57 (CH_2), 47.45 (CH_2), 43.80 (CH_2), 39.77 (CH_2), 22.02 (CH_2) ppm. IR (KBr): $\tilde{\nu}$ = 3308 (m), 2959 (w), 2938 (w), 2872 (m), 1622 (s), 1568 (s), 1527 (m), 1467 (w), 1433 (m), 1381 (w), 1327 (m), 1327 (m), 1279 (m), 1232 (w), 1203 (w), 1178 (w), 1099 (w), 1043 (m), 980 (w), 949 (w), 886 (w), 783 (w), 717 (m), 657 (w), 588 (w) cm^{-1} . FAB⁺ MS: m/z = 387.0 [M]⁺, 349.1 [$\text{M} - \text{Cl}$]⁺, 313.1 [$\text{M} - \text{Cl}_2$]⁺, 287.1 [$\text{M} - \text{Cl} - \text{Zn}$]⁺, 224.0 [$\text{M} - \text{Htbn}$]⁺, 126.0 [$\text{Htbn} + \text{H}$]⁺. Crystal data for $\text{C}_{12}\text{H}_{22}\text{N}_6\text{Cl}_2\text{Zn}$: M_r = 386.63, $0.20 \times 0.10 \times 0.10 \text{ mm}^3$, triclinic, space group $P\bar{1}$, a = 8.2780(17) Å, b = 8.9620(18) Å, c = 12.352(3) Å, α = 68.86(3)°, β = 88.91(3)°, γ = 73.52(3)°, V = 816.0(3) Å³, Z = 2, $d_{\text{calcd.}}$ = 1.574 Mg m^{-3} , T = 100 K, θ_{range} 2.51 to 27.56°. Reflections measured 6701, independent 3687, R_{int} = 0.0442. Final R indices [$I > 2\sigma(I)$]: R_1 = 0.0431, wR_2 = 0.0942.

[ZnCl₂(Htbo)₂]: Htbo (365 mg, 3.32 mmol) was dissolved in CH_3CN (ca. 40 mL), a 1 M solution of ZnCl_2 (1.1 mL, 1.1 mmol) in Et_2O was added dropwise, and the reaction mixture was stirred at r.t. for 24 h. The solvent was removed under vacuum, and the solid residue was washed three times with toluene (10 mL) to remove traces of Htbo. The crude product was dried overnight under vacuum. Recrystallization from CH_3CN at -21°C yielded colourless crystals suitable for XRD analysis; yield 0.355 g (0.99 mmol, 90%). $\text{C}_{10}\text{H}_{18}\text{N}_6\text{Cl}_2\text{Zn}$ (358.58): calcd. C 33.49, H 5.06, N 23.44; found C 34.49, H 5.61, N 23.40. ^1H NMR (399.89 MHz, CD_3CN , 23°C): δ = 6.03 (s, 2 H, NH), 3.82 (t, 8 H, CH_2), 3.20 (t, 8 H, CH_2) ppm. ^1H NMR (399.89 MHz, C_6D_6 , 23°C): δ = 6.62 (s, 2 H, NH), 3.91 (t, 4 H, CH_2), 2.71 (t, 4 H, CH_2), 2.29 (t, 4 H, CH_2), 2.01 (t, 4 H, CH_2) ppm. ^1H NMR (399.89 MHz, CD_2Cl_2 , 23°C): δ = 6.18 (s, 2 H, NH), 3.92 (t, 4 H, CH_2), 3.85 (t, 4 H, CH_2), 3.24 (t, 4 H, CH_2), 3.20 (t, 4 H, CH_2) ppm. ^1H NMR (399.89 MHz, CDCl_3 , 23°C): δ = 6.29 (s, 2 H, NH), 3.97 (t, 4 H, CH_2), 3.84 (t, 4 H, CH_2), 3.24 (t, 4 H, CH_2), 3.20 (t, 4 H, CH_2) ppm. $^{13}\text{C}\{^1\text{H}\}$ NMR (100.55 MHz, CD_3CN , 23°C): δ = 172.01 (CN_3), 54.91 (CH_2), 49.06 (CH_2), 47.72 (CH_2), 45.92 (CH_2) ppm. $^{13}\text{C}\{^1\text{H}\}$ NMR (100.55 MHz, CDCl_3 , 23°C): δ = 171.33 (CN_3), 55.71 (CH_2), 48.68 (CH_2), 47.79 (CH_2), 46.77 (CH_2) ppm. IR (KBr): $\tilde{\nu}$ = 3374 (m), 2964 (w), 2879 (w), 2847 (w), 1653 (s), 1551 (m), 1458 (w), 1298 (m), 1274 (m), 1244 (w), 1206 (m), 1162 (w), 1103 (w), 1048 (m), 1001 (w), 945 (w), 928 (w), 873 (w), 810 (w), 774 (w), 727 (w), 678 (w), 630 (w), 588 (w), 514 (m) cm^{-1} . FAB⁺ MS: m/z = 357.0 [M]⁺, 321.0 [$\text{M} - \text{Cl}$]⁺, 209.9 [$\text{M} - \text{Cl} - \text{Htbo}$]⁺, 112.0 [$\text{Htbo} + \text{H}$]⁺.

Crystal data for $\text{C}_{80}\text{H}_{144}\text{Cl}_{16}\text{N}_{48}\text{Zn}_8$: $M_r = 2868.59$, $0.40 \times 0.40 \times 0.35 \text{ mm}^3$, orthorhombic, space group $Pbca$, $a = 8.0690(16) \text{ \AA}$, $b = 14.770(3) \text{ \AA}$, $c = 24.131(5) \text{ \AA}$, $V = 2875.9(10) \text{ \AA}^3$, $Z = 1$, $d_{\text{calcd.}} = 1.656 \text{ Mg m}^{-3}$, $T = 100 \text{ K}$, $\theta_{\text{range}} 1.69$ to 30.04° . Reflections measured 8445, independent 4207, $R_{\text{int}} = 0.0204$. Final R indices [$I > 2\sigma(I)$]: $R_1 = 0.0376$, $wR_2 = 0.0786$.

[hppH₂][h(hppH)ZnCl₃]: The compound was isolated as product of hydrolysis of $[\text{ZnCl}_2(\text{hppH})_2]$. ^1H NMR (399.89 MHz, CD_3CN): $\delta = 1.79$ (quint, 2 H, CH_2), 1.87 (quint, 2 H, CH_2), 1.95 (quint, 4 H, CH_2 '), 3.15 (sh, 7 H, CH_2), 3.26 (m, 9 H, CH_2), 6.60 (s, 1 H, NH), 6.74 (s, 2 H, NH') ppm. $^{13}\text{C}\{^1\text{H}\}$ NMR (100.55 MHz, CD_3CN): $\delta = 20.30$ (CH_2), 21.811 (CH_2), 22.23 (CH_2), 37.91 (CH_2'), 38.41 (CH_2), 42.66 (CH_2), 46.58 (CH_2'), 47.38 (CH_2), 151.19 (CN_3), 153.88 (CN_3) ppm. IR: $\tilde{\nu} = 3628$ [m, $\nu(\text{NH})$ of hppH_2^+], 3547 [m, $\nu(\text{NH})$ of hppH_2^+], 3317 [m, $\nu(\text{NH})$ of $\text{hppH}\cdot\text{Cl}$], 2938 [m, $\nu(\text{CH})$], 2882 [m, $\nu(\text{CH})$], 1617 [s, $\nu(\text{C}=\text{N})$] cm^{-1} . FAB⁺ MS: $m/z = 140.2$ [hppH_2]⁺. FAB[−] MS: $m/z = 341.2$ [$\text{M}_2 - \text{Cl}$][−], 188.0 [$\text{M} - \text{Cl}$][−], 170.8 [ZnCl_3][−]. Crystal data for $\text{C}_{14}\text{H}_{27}\text{Cl}_3\text{N}_6\text{Zn}$: $M_r = 451.14$, $0.40 \times 0.30 \times 0.30 \text{ mm}^3$, triclinic, space group $P\bar{1}$, $a = 7.9500(16) \text{ \AA}$, $b = 8.1430(16) \text{ \AA}$, $c = 15.194(3) \text{ \AA}$, $\alpha = 89.50(3)^\circ$, $\beta = 80.56(3)^\circ$, $\gamma = 80.04(3)^\circ$, $V = 955.5(3) \text{ \AA}^3$, $Z = 2$, $d_{\text{calcd.}} = 1.568 \text{ Mg m}^{-3}$, $T = 200 \text{ K}$, $\theta_{\text{range}} 1.36$ to 27.53° . Reflections measured 8092, independent 4389, $R_{\text{int}} = 0.0392$. Final R indices [$I > 2\sigma(I)$]: $R_1 = 0.0614$, $wR_2 = 0.1711$.

[h(hppH₂)(THF)ZnCl₃]: The compound was isolated as product of hydrolysis of $[\text{ZnCl}_2(\text{hppH})_2]$ in THF. ^1H NMR (399.89 MHz, $[\text{D}_8]\text{-THF}$): $\delta = 1.77$ (quint, 4 H, CH_2'), 2.00 (quint, 4 H, CH_2'), 3.32 (t, 4 H, CH_2), 3.40 (t, 4 H, CH_2'), 3.63 (t, 4 H, CH_2'), 6.87 (s, 2 H, NH') ppm. $^{13}\text{C}\{^1\text{H}\}$ NMR (100.55 MHz, $[\text{D}_8]\text{THF}$): $\delta = 21.68$ (CH_2'), 26.46 (CH_2'), 39.26 (CH_2'), 47.88 (CH_2'), 68.58 (CH_2'), 152.037 (CN_3) ppm. Crystal data for $\text{C}_{11}\text{H}_{22}\text{Cl}_3\text{N}_3\text{OZn}$: $M_r = 384.04$, $0.30 \times 0.25 \times 0.15 \text{ mm}^3$, triclinic, space group $P\bar{1}$, $a = 7.6660(15) \text{ \AA}$, $b = 8.0430(16) \text{ \AA}$, $c = 14.177(3) \text{ \AA}$, $\alpha = 100.01(3)^\circ$, $\beta = 103.48(3)^\circ$, $\gamma = 99.51(3)^\circ$, $V = 817.5(3) \text{ \AA}^3$, $Z = 2$, $d_{\text{calcd.}} = 1.560 \text{ Mg m}^{-3}$, $T = 200 \text{ K}$, $\theta_{\text{range}} 1.51$ to 27.50° . Reflections measured 8241, independent 3648, $R_{\text{int}} = 0.0732$. Final R indices [$I > 2\sigma(I)$]: $R_1 = 0.0496$, $wR_2 = 0.1294$.

[(MeAl)₂(μ-tbo)₃]₂[Zn₂Cl₆]: A suspension of $[\text{ZnCl}_2(\text{Htbo})_2]$ (200 mg, 0.58 mmol) in toluene (50 mL) was cooled to -72°C before a 2 M solution of AlMe_3 (0.4 mL, 0.8 mmol) in toluene was added dropwise. The reaction mixture was stirred for 30 min and then gradually warmed to r.t. After 4 d, crystals of $[(\text{MeAl})_2(\mu\text{-tbo})_3]_2[\text{Zn}_2\text{Cl}_6]$ formed. Crystal data for $\text{C}_{34}\text{H}_{60}\text{Al}_4\text{Cl}_6\text{N}_{18}\text{Zn}_2$: $M_r = 1172.36$, $0.40 \times 0.35 \times 0.35 \text{ mm}^3$, monoclinic, space group $C2/c$, $a = 22.386(5) \text{ \AA}$, $b = 12.330(3) \text{ \AA}$, $c = 38.685(8) \text{ \AA}$, $\beta = 106.02(3)^\circ$, $V = 10263(4) \text{ \AA}^3$, $Z = 8$, $d_{\text{calcd.}} = 1.517 \text{ Mg m}^{-3}$, $T = 100 \text{ K}$, $\theta_{\text{range}} 1.90$ to 27.56° . Reflections measured 48510, independent 10550, $R_{\text{int}} = 0.0497$. Final R indices [$I > 2\sigma(I)$]: $R_1 = 0.0653$, $wR_2 = 0.1917$.

[ZnCl₂{tboC(CH₃)NH}]: A suspension of $\text{ZnCl}_2(\text{Htbo})_2$ (148 mg, 0.41 mmol) in CH_3CN (25 mL) was cooled to -72°C before AlMe_2Cl (0.6 mL, 0.54 mmol, 0.9 M in *n*-heptane) was added dropwise, and the reaction mixture was stirred at -72°C for 30 min. The reaction mixture was warmed to r.t. and stirred for 24 h. After 3 d, crystals of $[\text{ZnCl}_2\{\text{tboC}(\text{CH}_3)\text{NH}\}]$ were obtained. Crystal data for $\text{C}_7\text{H}_{12}\text{Cl}_2\text{N}_4\text{Zn}$: $M_r = 288.50$, $0.20 \times 0.10 \times 0.10 \text{ mm}^3$, monoclinic, space group $P2_1/n$, $a = 7.9720(16) \text{ \AA}$, $b = 8.4540(17) \text{ \AA}$, $c = 15.930(3) \text{ \AA}$, $\beta = 94.39(3)^\circ$, $V = 1070.4(4) \text{ \AA}^3$, $Z = 4$, $d_{\text{calcd.}} = 1.790 \text{ Mg m}^{-3}$, $T = 100 \text{ K}$, $\theta_{\text{range}} 2.56$ to 28.71° . Reflections measured 5481, independent 2774, $R_{\text{int}} = 0.0277$. Final R indices [$I > 2\sigma(I)$]: $R_1 = 0.0363$, $wR_2 = 0.0932$.

Ktbo and Ktbn: Toluene was added to a mixture of KH and the guanidine at -72°C . The suspension was gradually warmed to r.t. over 24 h. The solvent was removed, and the solid white residue used directly without further purification. Ktbo: ^1H NMR (200.13 MHz, C_6D_6 , 30°C): $\delta = 3.54$ (t, $J = 6.96 \text{ Hz}$, 4 H, CH_2), 2.45 (t, $J = 6.98 \text{ Hz}$, 4 H, CH_2) ppm. Ktbn: ^1H NMR (200.13 MHz, CD_3CN , 30°C): $\delta = 3.0\text{--}3.4$ (m, 8 H, CH_2), 1.82 (m, 2 H, CH_2) ppm.

[Zn₃Cl₂(tbo)₄]: Ktbo (313.4 mg, 2.1 mmol) and ZnCl_2 (214.7 mg, 1.6 mmol) were dissolved in toluene (50 mL) and stirred at r.t. for 24 h. KCl was removed by filtration. Crystals were grown from toluene solutions. Crystal data for $\text{C}_{20}\text{H}_{32}\text{Cl}_2\text{N}_{12}\text{Zn}_3$: $M_r = 707.59$, $0.45 \times 0.40 \times 0.40 \text{ mm}^3$, monoclinic, space group $C2/c$, $a = 16.925(3) \text{ \AA}$, $b = 9.880(2) \text{ \AA}$, $c = 16.390(3) \text{ \AA}$, $\beta = 90.65(3)^\circ$, $V = 2740.5(10) \text{ \AA}^3$, $Z = 4$, $d_{\text{calcd.}} = 1.715 \text{ Mg m}^{-3}$, $T = 100 \text{ K}$, $\theta_{\text{range}} 2.39$ to 33.15° . Reflections measured 9710, independent 5210, $R_{\text{int}} = 0.0239$. Final R indices [$I > 2\sigma(I)$]: $R_1 = 0.0289$, $wR_2 = 0.0677$.

[Zn₃Cl₂(tbn)₄]: Ktbn (386.9 mg, 2.37 mmol) and a 1 M solution of ZnCl_2 (1.77 mL, 1.77 mmol) in Et_2O were stirred at r.t. in toluene (50 mL) for 24 h. KCl was removed by filtration. Crystals were grown from toluene solutions. Crystal data for $\text{C}_{24}\text{H}_{40}\text{Cl}_2\text{N}_{12}\text{Zn}_3$: $M_r = 763.75$, $0.60 \times 0.60 \times 0.50 \text{ mm}^3$, monoclinic, space group $C2/c$, $a = 16.912(3) \text{ \AA}$, $b = 10.151(2) \text{ \AA}$, $c = 17.523(4) \text{ \AA}$, $\beta = 92.33(3)^\circ$, $V = 3005.8(10) \text{ \AA}^3$, $Z = 4$, $d_{\text{calcd.}} = 1.688 \text{ Mg m}^{-3}$, $T = 100 \text{ K}$, $\theta_{\text{range}} 2.33$ to 30.52° . Reflections measured 8903, independent 4575, $R_{\text{int}} = 0.0233$. Final R indices [$I > 2\sigma(I)$]: $R_1 = 0.0323$, $wR_2 = 0.0802$.

[OZn₄(tbo)₆]: Toluene (20 mL) was added to a mixture of ZnH_2 (126.8 mg, 1.88 mmol) and Htbo (316.2 mg, 2.84 mmol). After the dropwise addition of water-saturated toluene (5 mL), the reaction mixture was stirred at r.t. for 24 h. The solvent was removed under vacuum. Colourless crystals were obtained from CH_3CN or toluene solutions at -21°C ; yield 599.8 mg (0.64 mmol, 35%). $\text{C}_{30}\text{H}_{48}\text{N}_{18}\text{OZn}_4$ (938.34): calcd. C 38.40, H 5.16, N 26.87; found C 38.18, H 5.20, N 25.45. ^1H NMR (399.89 MHz, C_6D_6 , 23°C): $\delta = 3.73$ (t, 24 H, CH_2), 2.70 (t, 24 H, CH_2) ppm. ^1H NMR (399.89 MHz, CD_3CN , 23°C): $\delta = 3.72$ (t, 24 H, CH_2), 2.97 (t, 24 H, CH_2) ppm. $^{13}\text{C}\{^1\text{H}\}$ NMR (100.55 MHz, C_6D_6 , 23°C): $\delta = 178.35$ (CN_3), 55.74 (CH_2), 50.70 (CH_2) ppm. $^{13}\text{C}\{^1\text{H}\}$ NMR (100.55 MHz, CD_3CN , 23°C): $\delta = 178.75$ (CN_3), 55.91 (CH_2), 51.23 (CH_2) ppm. IR (KBr): $\tilde{\nu} = 2952$ (m), 2916 (m), 2835 (m), 1644 (vs), 1490 (m), 1471 (w), 1433 (s), 1347 (w), 1292 (w), 1271 (m), 1237 (w), 1196 (m), 1113 (w), 1088 (s), 1012 (w), 941 (w), 923 (w), 816 (w), 797 (m), 741 (m), 664 (w), 639 (m), 485 (m), 464 (w) cm^{-1} . MS (EI⁺): $m/z = 938.5$ [M]⁺, 828.3 [$\text{M} - \text{tbo}$]⁺, 542.3 [$\text{M} - \text{Zn}_3(\text{tbo})_3$]⁺. HRMS (EI⁺): calcd. for $\text{C}_{30}\text{H}_{48}\text{N}_{18}\text{OZn}_4$ [M]⁺ 938.1355; found 938.1271. Crystal data for $\text{C}_{36}\text{H}_{58}\text{N}_{21.4}\text{OZn}_4$: $M_r = 1077.98$, $0.50 \times 0.40 \times 0.40 \text{ mm}^3$, hexagonal, space group $R\bar{3}$, $a = 12.5860(18) \text{ \AA}$, $b = 12.5860(18) \text{ \AA}$, $c = 51.406(10) \text{ \AA}$, $\alpha = 90^\circ$, $\beta = 90^\circ$, $\gamma = 120^\circ$, $V = 7052(2) \text{ \AA}^3$, $Z = 6$, $d_{\text{calcd.}} = 1.523 \text{ Mg m}^{-3}$, $T = 100 \text{ K}$, $\theta_{\text{range}} 2.38$ to 32.92° . Reflections measured 58385, independent 5892, $R_{\text{int}} = 0.1133$. Final R indices [$I > 2\sigma(I)$]: $R_1 = 0.0389$, $wR_2 = 0.1037$.

L2H₂: *N,N'*-Diisopropylcarbodiimide (0.62 mL, 4.0 mmol) was added to a solution of 2-aminoquinoline (0.58 g, 4.0 mmol) in toluene (30 mL). Subsequently 5 mol-% of AlClMe_2 was added (0.24 mL of a 0.9 M solution in heptane), and the resulting reaction mixture was stirred at r.t. for 18 h. Removal of the solvent under vacuo afforded the crude product, which was purified by sublimation (10^2 mbar , 100°C) to obtain colourless crystals (0.81 g, 3.0 mmol, 75% yield). $\text{C}_{16}\text{H}_{22}\text{N}_4$ (270.38): calcd. C 71.08, H 8.20, N 20.72; found C 71.14, H 8.17, N 20.79. ^1H NMR (399.89 MHz, C_6D_6): $\delta = 1.04$ (d, $^3J = 6.48 \text{ Hz}$, 12 H, Me_2CH), 3.81 (br., 2 H,

Me_2CH), 7.10 (t, $^3J = 7.40$ Hz, 1 H, CH_{qu}), 7.31 (d, $^3J = 8.82$ Hz, 1 H, CH_{qu}), 7.36–7.44 (m, 2 H, CH_{qu}), 7.51 (d, $^3J = 8.83$ Hz, 1 H, CH_{qu}), 7.83 (d, $^3J = 8.29$ Hz, 1 H, CH_{qu}) ppm. ^{13}C NMR (100.55 MHz, C_6D_6): $\delta = 23.32$ (Me_2CH), 42.62 (Me_2CH), 122.62 (CH_{qu}), 123.80 (CH_{qu}), 124.64 (C_{qu}), 126.34 (CH_{qu}), 127.63 (CH_{qu}), 128.31 (CH_{qu}), 128.75 (CH_{qu}), 136.11 (CH_{qu}), 147.19 (C_{qu}), 155.21 (N=CNN), 163.86 (C_{qu}) ppm. IR (CsI): $\tilde{\nu} = 3441$, 2978, 1627, 1585, 1551, 1500, 1467, 1420, 1405, 1325, 1174, 1140, 838, 764 cm^{-1} . Crystal data for $\text{C}_{16}\text{H}_{22}\text{N}_4$: $M_r = 270.38$, $0.35 \times 0.30 \times 0.30\text{ mm}^3$, monoclinic, space group $\text{P}2(1)$, $a = 9.5140(19)\text{ \AA}$, $b = 8.8840(18)\text{ \AA}$, $c = 10.069(2)\text{ \AA}$, $\beta = 115.83(3)^\circ$, $V = 766.0(3)\text{ \AA}^3$, $Z = 2$, $d_{\text{calcd.}} = 1.172\text{ Mg m}^{-3}$, $T = 100\text{ K}$, $\theta_{\text{range}} 2.25$ to 30.07° . Reflections measured 7801, independent 4386, $R_{\text{int}} = 0.0334$. Final R indices [$I > 2\sigma(I)$]: $R_1 = 0.0415$, $wR_2 = 0.0976$.

[(L2H)ZnMe]₂: Dimethylzinc (0.37 mL, 0.44 mmol) in toluene was added dropwise to a toluene (5 mL) solution of **L2H₂** (60 mg, 0.22 mmol). The solution was stirred at r.t. for 18 h. Removal of the volatile components in vacuo afforded a white solid, which was crystallized from toluene at -20°C to give colourless cubic crystals (33.1 mg, 0.05 mmol, 43%). $\text{C}_{34}\text{H}_{48}\text{N}_8\text{Zn}_2$ (699.54): calcd. C 58.37, H 6.92, N 16.02; found C 57.32, H 6.78, N 16.08. ^1H NMR (399.89 MHz, C_6D_6): $\delta = 0.32$ (s, 3 H, MeZn), 0.89 (d, $^3J = 6.42$ Hz, 6 H, Me_2CHNH), 1.15 (d, $^3J = 6.32$ Hz, 6 H, Me_2CHNZn), 3.16 (sept, $^3J = 6.28$ Hz, 1 H, Me_2CHNZn), 3.33 (d, $^3J = 8.03$ Hz, 1 H, NH), 4.66 (m, 1 H, Me_2CHNH), 6.88–7.13 (m, 4 H, CH_{qu}), 7.34 (m, 1 H, CH_{qu}), 8.46 (d, $^3J = 6.45$ Hz, 1 H, CH_{qu}) ppm. ^{13}C NMR (100.55 MHz, C_6D_6): $\delta = -6.74$ (MeZn), 23.50 (Me_2CHNH), 24.97 (Me_2CHNZn), 44.65 (Me_2CHNH), 47.93 (Me_2CHNZn), 122.94 (CH_{qu}), 124.32 (C_{qu}), 124.56 (CH_{qu}), 124.93 (CH_{qu}), 127.21 (CH_{qu}), 129.24 (CH_{qu}), 136.57 (CH_{qu}), 146.50 (C_{qu}), 159.40 (N=CNN), 163.00 (C_{qu}) ppm. IR (KBr): $\tilde{\nu} = 3440$, 3058, 2963, 2928, 2870, 2825, 1616, 1570, 1504, 1466, 1404, 1312, 1165, 1142, 1122, 1061, 903, 837, 756, 652, 625, 505 cm^{-1} . Crystal data for $\text{C}_{34}\text{H}_{48}\text{N}_8\text{Zn}_2$: $M_r = 699.54$, $0.45 \times 0.40 \times 0.40\text{ mm}^3$, triclinic, space group $\text{P}\bar{1}$, $a = 12.489(3)\text{ \AA}$, $b = 12.882(3)\text{ \AA}$, $c = 14.882(3)\text{ \AA}$, $\alpha = 73.31(3)^\circ$, $\beta = 69.22(3)^\circ$, $\gamma = 65.10(3)^\circ$, $V = 2003.3(7)\text{ \AA}^3$, $Z = 2$, $d_{\text{calcd.}} = 1.160\text{ Mg m}^{-3}$, $T = 100\text{ K}$, $\theta_{\text{range}} 1.87$ to 29.50° . Reflections measured 20031, independent 11052, $R_{\text{int}} = 0.0302$. Final R indices [$I > 2\sigma(I)$]: $R_1 = 0.0476$, $wR_2 = 0.1275$.

[L1(ZnMe)₂]₂: Dimethylzinc in toluene (1 mL, 1.2 mmol) was heated to 75°C . Subsequently a toluene (5 mL) solution of **L1H₂** (66 mg, 0.3 mmol) was added dropwise. The solution was stirred for 2 h at 75°C . Conversion (estimated from NMR Data): 85%. Crystals of the extremely water and moisture sensitive **[L1-(ZnMe)₂]₂** were grown from a toluene solution at -20°C (37.1 mg, 0.05 mmol, 33%). $\text{C}_{28}\text{H}_{48}\text{N}_8\text{Zn}_4$ (758.30): calcd. C 44.34, H 6.38, N 14.78; found C 43.59, H 6.42, N 14.53. ^1H NMR (600.13 MHz, C_6D_6): $\delta = -0.32$ (s, 3 H, MeZn), -0.15 (s, 3 H, MeZn), 1.30 (br., 6 H, Me_2CHN), 1.36 (br., 6 H, Me_2CHN), 4.04 (m, 1 H, Me_2CHN), 4.39 (m, 1 H, Me_2CHN), 5.81 (t, $^3J = 6.25$ Hz, 1 H, CH_{py}), 6.64 (d, $^3J = 8.62$ Hz, 1 H, CH_{py}), 6.74 (m, 1 H, CH_{py}), 7.04 (d, $^3J = 4.40$ Hz, 1 H, CH_{py}) ppm. ^{13}C NMR (100.55 MHz, C_6D_6): $\delta = -17.41$ (MeZn), -13.25 (MeZn), 25.89 (Me_2CHN), 26.34 (Me_2CHN), 48.55 (Me_2CHN), 49.43 (Me_2CHN), 111.79 (CH_{py}), 120.64 (CH_{py}), 137.96 (CH_{py}), 143.96 (CH_{py}), 157.86 (N=CNN), 167.45 (C_{py}) ppm. Crystal data for $\text{C}_{28}\text{H}_{48}\text{N}_8\text{Zn}_4$: $M_r = 758.30$, $0.15 \times 0.10 \times 0.10\text{ mm}^3$, monoclinic, space group $\text{C}2/c$, $a = 20.746(4)\text{ \AA}$, $b = 10.780(2)\text{ \AA}$, $c = 15.331(3)\text{ \AA}$, $\beta = 99.89(3)^\circ$, $V = 3377.7(12)\text{ \AA}^3$, $Z = 4$, $d_{\text{calcd.}} = 1.491\text{ Mg m}^{-3}$, $T = 100\text{ K}$, $\theta_{\text{range}} 2.14$ to 30.11° . Reflections measured 18259, independent 4959, $R_{\text{int}} = 0.0732$. Final R indices [$I > 2\sigma(I)$]: $R_1 = 0.0385$, $wR_2 = 0.0764$.

X-ray Crystallographic Study: Suitable crystals were taken directly out of the mother liquor, immersed in perfluorinated polyether oil,

and fixed on top of a glass capillary. Measurements were made with a Nonius-Kappa CCD diffractometer with a low-temperature unit using graphite-monochromated $\text{Mo-K}\alpha$ radiation ($\lambda = 0.71073\text{ \AA}$) at 100 K. The data were processed using standard Nonius software.^[43] All calculations were performed using the SHELXT-PLUS software package. Structures were solved by direct methods with the SHELXS-97 program and refined with the SHELXL-97 program.^[44,45] Graphical handling of the structural data during solution and refinement was performed with XPMA.^[46] Atomic coordinates and anisotropic thermal parameters of non-hydrogen atoms were refined by full-matrix least-squares calculations.

CCDC-679110 (for $[\text{ZnCl}_2(\text{hppH})_2]$), -851365 (for $[\text{ZnCl}_2(\text{Htbn})_2]$), -851364 (for $[\text{ZnCl}_2(\text{Htbo})_2]$), -679112 (for $[\text{hppH}_2][(\text{hppH})\text{ZnCl}_3]$), -679113 (for $[\text{hppH}_2][(\text{THF})\text{ZnCl}_3]$), -851369 (for $[(\text{MeAl})_2(\mu\text{-tbo})_3][\text{Zn}_2\text{Cl}_6]$), -851367 (for $[\text{ZnCl}_2(\text{tboC}(\text{CH}_3)\text{-NH})]$), -851363 (for $[\text{Zn}_3\text{Cl}_2(\text{tbo})_4]$), -851366 (for $[\text{Zn}_3\text{Cl}_2(\text{tbn})_4]$), -851368 (for $[\text{OZn}_4(\text{tbo})_6]$), -840837 (for **L2H₂**), -840838 (for **[(L2H)ZnMe]₂**), and 840839 (for **[L1(ZnMe)₂]₂**) contain the supplementary crystallographic data for this paper. These data can be obtained free of charge from The Cambridge Crystallographic Data Centre via www.ccdc.cam.ac.uk/data_request/cif.

Supporting Information (see footnote on the first page of this article): Variable-temperature ^1H NMR spectra of $[\text{ZnCl}_2(\text{Htbn})_2]$ in CDCl_3 .

Acknowledgments

Continued financial support from the Deutsche Forschungsgemeinschaft (DFG) is gratefully acknowledged.

- a) F. T. Edelmann, *Adv. Organomet. Chem.* **2008**, *57*, 183–352; b) F. T. Edelmann, *Coord. Chem. Rev.* **1994**, *137*, 403–481.
- a) J. Barker, M. Kilner, *Coord. Chem. Rev.* **1994**, *133*, 219–300; b) P. J. Bailey, S. Price, *Coord. Chem. Rev.* **2001**, *214*, 91–141.
- S. Herres-Pawlis, *Nachr. Chem.* **2009**, *57*, 20–23.
- a) M. P. Coles, *Dalton Trans.* **2006**, 985–1001; b) M. P. Coles, *Chem. Commun.* **2009**, 3659–3676.
- H.-J. Himmel, in: *Modeling of Molecular Properties* (Ed.: P. Comba), Wiley-VCH, Weinheim, Germany, **2011**.
- C. Jones, *Coord. Chem. Rev.* **2010**, *254*, 1273–1289.
- J. Börner, U. Flörke, T. Glöger, T. Bannenberg, M. Tamm, M. D. Jones, A. Döring, D. Kuckling, S. Herres-Pawlis, *J. Mol. Catal. A* **2010**, *316*, 139–145.
- M. P. Coles, P. B. Hitchcock, *Eur. J. Inorg. Chem.* **2004**, 2662–2672.
- J. Börner, S. Herres-Pawlis, U. Flörke, K. Huber, *Eur. J. Inorg. Chem.* **2007**, *36*, 5645–5651.
- J. Börner, U. Flörke, K. Huber, A. Döring, D. Kuckling, S. Herres-Pawlis, *Chem. Eur. J.* **2009**, *15*, 2362–2376.
- J. Börner, U. Flörke, A. Döring, D. Kuckling, S. Herres-Pawlis, *Macromol. Symp.* **2010**, *296*, 354–365.
- J. Börner, I. d. S. Vieira, A. Pawlis, A. Döring, D. Kuckling, S. Herres-Pawlis, *Chem. Eur. J.* **2011**, *17*, 4507–4512.
- L. Bourget-Merle, M. F. Lappert, J. R. Severn, *Chem. Rev.* **2002**, *102*, 3031–3066.
- R. Wortmann, U. Flörke, B. Sarkar, V. Umamaheshwari, G. Gescheidt, S. Herres-Pawlis, G. Henkel, *Eur. J. Inorg. Chem.* **2011**, 121–130.
- F. A. Cotton, J. H. Matonic, C. A. Murillo, *J. Am. Chem. Soc.* **1997**, *119*, 7889–7890.
- J. L. Bear, Y. Li, B. Han, K. M. Kadish, *Inorg. Chem.* **1996**, *35*, 1395–1398.
- a) R. Clérac, F. A. Cotton, L. M. Daniels, J. P. Donahue, C. A. Murillo, D. J. Timmons, *Inorg. Chem.* **2000**, *39*, 2581–2584; b)

- F. A. Cotton, C. A. Murillo, X. Wang, C. C. Wilkinson, *Inorg. Chim. Acta* **2003**, 351, 191–200.
- [18] O. Ciobanu, P. Roquette, S. Leingang, H. Wadepohl, J. Mautz, H.-J. Himmel, *Eur. J. Inorg. Chem.* **2007**, 4530–4534.
- [19] O. Ciobanu, F. Allouti, P. Roquette, S. Leingang, M. Enders, H. Wadepohl, H.-J. Himmel, *Eur. J. Inorg. Chem.* **2008**, 5482–5493.
- [20] O. Ciobanu, E. Kaifer, H.-J. Himmel, *Angew. Chem.* **2009**, 121, 5646–5649; *Angew. Chem. Int. Ed.* **2009**, 48, 5538–5541.
- [21] R. Dinda, O. Ciobanu, H. Wadepohl, O. Hübner, R. Acharaya, H.-J. Himmel, *Angew. Chem.* **2007**, 119, 9270–9273; *Angew. Chem. Int. Ed.* **2007**, 46, 9110–9113.
- [22] O. Ciobanu, A. Fuchs, M. Reinmuth, A. Lebkücher, E. Kaifer, H.-J. Himmel, *Z. Anorg. Allg. Chem.* **2010**, 636, 543–550.
- [23] O. Ciobanu, D. Emeljanenko, E. Kaifer, H.-J. Himmel, *Inorg. Chem.* **2008**, 47, 4774–4778.
- [24] N. Schulenberg, M. Jäkel, E. Kaifer, H.-J. Himmel, *Eur. J. Inorg. Chem.* **2009**, 4809–4819.
- [25] N. Schulenberg, H. Wadepohl, H.-J. Himmel, *Angew. Chem.* **2011**, 123, 10628–10631; *Angew. Chem. Int. Ed.* **2011**, 50, 10444–10447.
- [26] S. J. Birch, S. R. Boss, S. C. Cole, M. P. Coles, R. Haigh, *Dalton Trans.* **2004**, 3568–3574.
- [27] M. S. Khalaf, M. P. Coles, P. B. Hitchcock, *Dalton Trans.* **2008**, 4288–4295.
- [28] M. Reinmuth, C. Neuhäuser, P. Walter, M. Enders, E. Kaifer, H.-J. Himmel, *Eur. J. Inorg. Chem.* **2011**, 83–90.
- [29] a) N. J. Bremer, A. B. Cutcliffe, M. F. Faron, W. G. Kofron, *J. Chem. Soc. A* **1971**, 3264–3266; b) N. J. Bremer, A. B. Cutcliffe, M. F. Faron, *J. Chem. Soc. C* **1970**, 932–933.
- [30] M. K. T. Tin, G. P. A. Yap, D. S. Richeson, *Inorg. Chem.* **1998**, 37, 6728–6730.
- [31] N. Thirupathi, G. P. A. Yap, D. S. Richeson, *Chem. Commun.* **1999**, 2483–2484.
- [32] S. P. Green, C. Jones, A. Stasch, *Science* **2007**, 318, 1754–1757.
- [33] I. Resa, E. Carmona, E. Gutierrez-Puebla, A. Monge, *Science* **2004**, 305, 1136–1138.
- [34] a) S. Schulz, D. Schuchmann, U. Westphal, M. Bolte, *Organometallics* **2009**, 28, 1590–1592; b) Y. Wang, B. Quillian, P. Wie, H. Wang, X.-J. Yang, Y. Xie, R. B. King, P. v. R. Schleyer, H. F. Schaefer III, G. H. Robinson, *J. Am. Chem. Soc.* **2005**, 127, 11944–11945.
- [35] a) C. Jones, L. Furness, S. Nembenna, R. P. Rose, S. Aldridge, A. Stasch, *Dalton Trans.* **2010**, 39, 8788–8795; b) C. Jones, R. P. Rose, A. Stasch, *Dalton Trans.* **2007**, 2997–2999.
- [36] Hydrogen bonding was also found in $[\text{ZnBr}_2(\text{hppH})_2]$, see: S. H. Oakley, D. B. Soria, M. P. Coles, P. B. Hitchcock, *Polyhedron* **2006**, 25, 1247–1255.
- [37] For another example of ligand transfer to Al that involves the hpp ligand, see: M. P. Coles, P. B. Hitchcock, *J. Chem. Soc., Dalton Trans.* **2001**, 1169–1171.
- [38] See, for example: a) A. Bellfoorte, F. Calderazzo, U. Englert, J. Strähle, *Inorg. Chem.* **1991**, 30, 3778–3781; b) C. S. McCowan, T. L. Groy, M. T. Caudle, *Inorg. Chem.* **2002**, 41, 1120–1127; c) D. B. Dell'Amico, F. Calderazzo, S. Farnocchi, L. Labella, F. Marchetti, *Inorg. Chem. Commun.* **2002**, 5, 848–852; d) D. B. Dell'Amico, F. Calderazzo, L. Labella, F. Marchetti, *Inorg. Chim. Acta* **2003**, 350, 661–664; e) C. S. McCowan, M. T. Caudle, *Dalton Trans.* **2005**, 238–246; f) D. B. Dell'Amico, F. Calderazzo, L. Labella, F. Marchetti, I. Mazzoncin, *Inorg. Chim. Acta* **2006**, 359, 3371–3374; g) D. Domide, E. Kaifer, J. Mautz, O. Walter, H.-J. Himmel, *Eur. J. Inorg. Chem.* **2008**, 3177–3185.
- [39] H. Kunkely, A. Vogler, *J. Chem. Soc., Chem. Commun.* **1990**, 1204–1205.
- [40] C. N. Rowley, T.-G. Ong, J. Priem, T. K. Woo, D. S. Richeson, *Inorg. Chem.* **2008**, 47, 9660–9668.
- [41] W.-X. Zhang, M. Nishiura, Z. Hou, *Chem. Eur. J.* **2007**, 13, 4037–4051.
- [42] M. Biyikal, K. Löhnwitz, P. W. Roesky, S. Blechert, *Synlett* **2008**, 20, 3106–3110.
- [43] DENZO-SMN, Data processing software, Nonius **1998**; <http://www.nonus.com>.
- [44] a) G. M. Sheldrick, *SHELXS-97, Program for Crystal Structure Solution*, University of Göttingen, **1997**; <http://shelx.uni-ac.gwdg.de/SHELX/index.html>; b) G. M. Sheldrick, *SHELXL-97, Program for Crystal Structure Refinement*, University of Göttingen, **1997**; <http://shelx.uni-ac.gwdg.de/SHELX/index.html>.
- [45] *International Tables for X-ray Crystallography*, vol. 4, Kynoch Press, Birmingham, U.K., **1974**.
- [46] L. Zsolnai, G. Huttner, *XPMA*, University of Heidelberg, Germany, **1994**; <http://www.uni-heidelberg.de/institute/fak12/AC/huttner/software/software.html>.

Received: November 3, 2011

Published Online: February 3, 2012

Two Environmentally Friendly Energetic Compounds, $[\text{Mn}(\text{AZT})_4(\text{H}_2\text{O})_2](\text{PA})_2 \cdot 4\text{H}_2\text{O}$ and $[\text{Co}(\text{AZT})_2(\text{H}_2\text{O})_4](\text{PA})_2$, Based on 3-Azido-1,2,4-triazole (AZT) and Picrate (PA)

Bi-Dong Wu,^[a] Jian-Guo Zhang,^[a] Tong-Lai Zhang,^{*,[a]} Li Yang,^[a] and Zun-Ning Zhou^[a]

Keywords: N ligands / Picrate / Manganese / Cobalt / Decomposition / Sensitivity

Two multiligand coordination compounds, $[\text{Mn}(\text{AZT})_4(\text{H}_2\text{O})_2](\text{PA})_2 \cdot 4\text{H}_2\text{O}$ (**1**) and $[\text{Co}(\text{AZT})_2(\text{H}_2\text{O})_4](\text{PA})_2$ (**2**), were synthesized with 3-azido-1,2,4-triazole (AZT) as a ligand and picrate (PA) as a counteranion and characterized by elemental analysis and FTIR spectroscopy. The crystal structures were determined by single-crystal X-ray diffraction. The results show that the crystals of **1** and **2** have a triclinic space group ($P\bar{1}$) and orthorhombic space group ($Pbca$), respectively. Moreover, **1** and **2** have distorted octahedral structures. Their thermal decomposition mechanisms were investigated by

differential scanning calorimetry and thermogravimetric analysis. The experimental data showed that the energies of combustion were approximately equal to the energies of combustion of 1,3,5-trinitro-1,3,5-triazacyclohexane (RDX) and 1,3,5,7-tetranitro-1,3,5,7-tetraazocane (HMX). The non-isothermal kinetic parameters were studied by applying the methods of Kissinger and Ozawa. The sensitivity properties showed that **1** and **2** had a higher flame sensitivity than 2,4,6-trinitrotoluene, RDX, and HMX.

Introduction

Environmentally friendly energetic materials as new high-energy-density materials (HEDMs) have attracted significant attention due to their excellent thermal stability, mechanical insensitivity, good performance, and economical and environmentally friendly synthesis.^[1] These modern HEDMs derive most of their energy either from oxidation of the carbon backbone or their very high positive heats of formation. Examples of the first class of materials are traditional energetic materials, such as 2,4,6-trinitrotoluene (TNT), 1,3,5-trinitro-1,3,5-triazacyclohexane (RDX), and 1,3,5,7-tetranitro-1,3,5,7-tetraazocane (HMX). Examples of the second class of energetic materials are modern nitro compounds, such as hexanitroisowurtzitan, which is due to the increased number of inherently energetic C–N, N–N, and N–O bonds.

Recently, pentacyclic nitrogen-rich heterocyclic compounds have been studied because of their relatively small volume, which may reduce steric hindrance and increase their density. Generally, heterocyclic compounds have been used in energetic roles owing to their higher heats of formation, density, and oxygen balance compared to those of their carbocyclic analogues. Moreover, the role of the azole ring, which has a potential N-coordination site to extend

the structure, acts as a ligand towards transition metals in a variety of coordination compounds. In addition, their compounds have high heats of formation, which depend on an enormous energy release of the average bond energies of N–N (160 kJ mol^{-1}), N=N (418 kJ mol^{-1}), and N \equiv N (954 kJ mol^{-1}).^[2,3] Klapötke, Shreeve, and others have performed many studies on nitrogen-rich energetic compounds based on imidazole, triazole, tetrazole, and tetrazine and their derivatives^[4–46] such as 1,2,4-triazol-5-one,^[26,27] 3-nitro-1,2,4-triazol-5-one,^[28–31] 4-amino-1,2,4-triazol-5-one,^[32] 4,4'-azo-1,2,4-triazole,^[33] 1,5-diaminotetrazole,^[34–41] 5-azidotetrazole,^[42] 5-nitraminotetrazole,^[43] 5,5'-azobis(tetrazolate),^[44] 1,1'-azobis(1,2,3-triazole), which contains eight directly linked nitrogen atoms (N_8 structure),^[45] and 1,1'-azobis(tetrazole), which is a highly energetic nitrogen-rich compound with a N_{10} chain.^[46]

Recently, much research has been carried out on energetic azido coordination compounds, because they are highly energetic and have a high nitrogen content.^[47–56] The sophisticated and intriguing structures of azido compounds can range from discrete structures to 3D arrays. In particular, the azido compound was studied mainly due to its explosive nature, ability to form pure- and mixed-ligand complexes, ambidentate nature, and bridging capacity. Consequently, we have also studied the synthesis, thermal decomposition, and explosive properties of energetic azido compounds such as $[\text{Cd}_2(\text{N}_2\text{H}_4)_2(\text{N}_3)_4]_n$,^[57] $[\text{Zn}(\text{N}_2\text{H}_4)_2(\text{N}_3)_2]_n$,^[58] $\text{Mn}(\text{CHZ})_2(\text{N}_3)_2$ (CHZ = carbohydrazide),^[59] $[\text{Cd}(\text{en})(\text{N}_3)_2]_n$ (en = ethylenediamine),^[60] $\text{Cu}(\text{IMI})_4(\text{N}_3)_2$ (IMI = imidazole),^[61] and $\text{Ni}(\text{IMI})_4(\text{N}_3)_2$,^[61] which have potential application as energetic materials.

[a] State Key Laboratory of Explosion Science and Technology, Beijing Institute of Technology, Beijing 100081, China
Fax: +86-10-68911202
E-mail: ztlbit@bit.edu.cn

Supporting information for this article is available on the WWW under <http://dx.doi.org/10.1002/ejic.201100806>.

New 3-azido-1,2,4-triazole (AZT)^[62] energetic compounds have also become increasingly important. Their advantages over 3-amino-1,2,4-triazole complexes are, for example, their higher nitrogen content (76.36 wt.-%), higher heat of formation ($\Delta H_f^\circ = +458 \text{ kJ mol}^{-1}$), excellent stability, highly efficient gas production, and environmental compatibility of the explosive and the decomposition products. Recently, attention has been paid to AZT energetic salts, whereas complexes that use AZT as ligands have seldom been studied. Although there are only few coordination compounds that use AZT as ligands,^[63–65] it is worthwhile to learn more about such compounds.

In the search for clean, metal-containing energetic materials, manganese and cobalt have been selected as transition metals as they have a wide range of possibilities for coordination^[66–74] and, from environmental concerns, because they are less toxic than Ba^{II} , Pb^{II} , and Hg^{II} . In order to deepen the studies on AZT energetic compounds, we have synthesized and characterized two multiligand coordination complexes, $[\text{Mn}(\text{AZT})_4(\text{H}_2\text{O})_2](\text{PA})_2 \cdot 4\text{H}_2\text{O}$ (**1**) and $[\text{Co}(\text{AZT})_2(\text{H}_2\text{O})_4](\text{PA})_2$ (**2**), with AZT and picrate (PA). Their syntheses, crystal structures, thermal decomposition mechanisms, and sensitivity properties are presented.

Results and Discussion

Molecular Structures

To obtain a better understanding of AZT, molecular orbital analyses were carried out by using B3LYP functional analyses with the 6-311++g(d,p) basis set. The optimized structure was characterized to be true local energy minima on the potential energy surface without imaginary frequency. Figure 1 shows the highest occupied molecular orbital (HOMO) and lowest unoccupied molecular orbital (LUMO) of the AZT group. In the HOMO, the $\text{C1}=\text{N1}$ double bond can form a large π -orbital. In other words, the electronic density of the HOMO at the third atom (N) is relatively high compared to that of the LUMO. The delocalized bonding orbitals show that the AZT group has strong conjugation.

The molecular structures of **1** and **2** are shown in Figure 2. In **1**, there is one manganese(II) cation, four AZT molecules, two coordinated water molecules, four crystal

water molecules, and two PA molecules. In **2**, there is one cobalt(II) cation, two AZT molecules, four coordinated water molecules, and two PA molecules. The metal(II) cations contribute six empty orbitals ($3d + 4s$) to accommodate the lone pairs of electrons from the ligands to coordinate with the N atoms from AZT and O atoms from coordinated water. From Figure 1, it is easy to understand the coordination bond formation between the N atom (the third atom) and the metal ion, because the latter still has unoccupied $3d$ orbitals. In the AZT molecules, the μ -1-azido groups are nearly linear and asymmetric with $\angle \text{N4-N5-N6}$ $172.6(3)^\circ$, N4-N5 $1.245(3) \text{ \AA}$, and N5-N6 $1.115(4) \text{ \AA}$ for **1** and $\angle \text{N4-N5-N6}$ $171.7(3)^\circ$, N4-N5 $1.244(3) \text{ \AA}$, and N5-N6 $1.109(4) \text{ \AA}$ for **2**.

In **1**, the angles between the N atoms from two opposite AZT ligands and the Mn^{II} cation are all 180.00° [$\angle \text{N1\#1-Mn1-N1}$ $180.00(9)^\circ$, $\angle \text{N7-Mn1-N7\#1}$ $180.00(3)^\circ$]. The bond angles of the N atoms from two adjacent AZT ligands and the Mn^{II} ion deviate from 90° [$\angle \text{N7-Mn1-N1}$ $93.59(6)^\circ$, $\angle \text{N7\#1-Mn1-N1}$ $86.41(6)^\circ$]. So the four nitrogen atoms and the Mn^{II} cation exhibit a slightly distorted quadrilateral configuration. Furthermore, the distances between the Mn^{II} cation and the O atoms of the H_2O ligands are approximately equal (Mn-O 2.215 \AA). Consequently, the Mn^{II} cation exhibits a slightly distorted octahedral configuration (Supporting Information). The six coordination atoms and the central Mn^{II} cation can form two planes, and the plane equations are as follows (Supporting Information): Mn1-N1-N2-N3 (plane A): $3.585x + 9.565y - 0.304z = 9.2481$; Mn1-N7-N8-N9 (plane B): $6.547x + 3.343y + 10.418z = 13.7337$. The angle between the planes is 69.9° .

There are five types of intramolecular hydrogen bonds in **1** (Supporting Information). The first occurs between the N atom of AZT and the O atom of the crystal water molecules ($\text{N2-H2}\cdots\text{O10}$, $\text{N3-H10B}\cdots\text{O10}$, and $\text{N9-H9A}\cdots\text{O9}$). The second occurs between the O atom of the coordinated water molecules and the N atom of AZT ($\text{O1-H1B}\cdots\text{N10}$). The third occurs between the N atom of AZT and the O atom of PA ($\text{N8-H8}\cdots\text{O6}$ and $\text{N8-H8}\cdots\text{O7}$). The fourth occurs between the O atom of the crystal water molecules and the O atom of PA ($\text{O9-H9B}\cdots\text{O5}$, $\text{O9-H9B}\cdots\text{O6}$, and $\text{O10-H10A}\cdots\text{O4}$). The fifth occurs between the O atom of the coordinated water molecules and the O atom of the crystal water molecules ($\text{O1-H1}\cdots\text{O9}$). The molecules are connected by different types of intermolecular hydrogen bonds

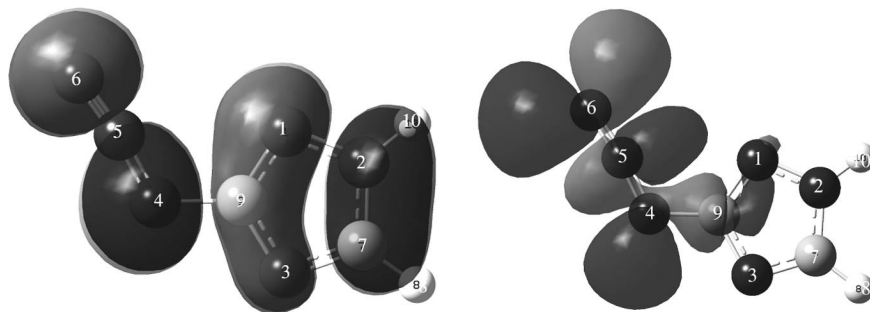


Figure 1. HOMO (left) and LUMO (right) of AZT.

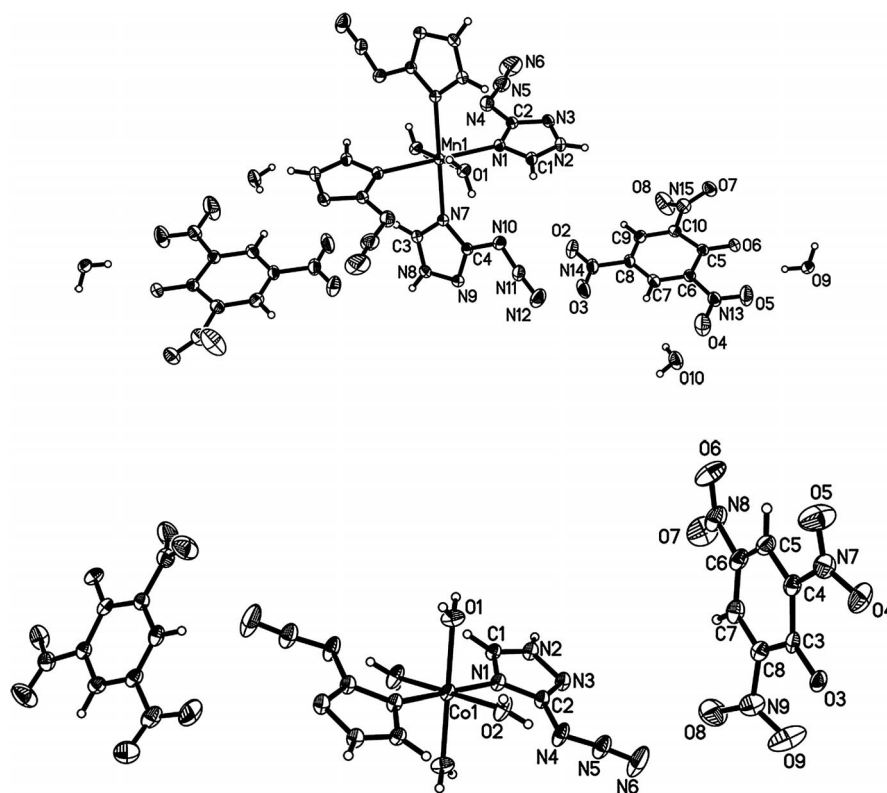


Figure 2. Molecular structures of **1** (top) and **2** (bottom), thermal ellipsoids drawn at 30% probability level.

that extend the structure into a 3D supermolecular structure and make an important contribution to enhance the thermal stability of **1**.

In **2**, the axial Co–N bonds are about 0.06–0.09 Å longer than the four basically equivalent equatorial Co–O bonds. The bond angle between the N atoms from two opposite AZT ligands and the Co cation is 180° ($\angle \text{N1\#1-Co1-N1}$ 180°). The bond angles between the O atoms from coordinated water molecules and the Co cation deviate from 90° [$\angle \text{O1-Co1-O2}$ 90.38(9)°, $\angle \text{O2-Co1-O1\#1}$ 89.62(9)°]. The distances between the Co^{II} cation and the N atoms of AZT are approximately equal (Co–N 2.164 Å). The Co^{II} ion exhibits a slightly distorted octahedral configuration (Supporting Information). The plane equations are as follows (Supporting Information): Co1–N1–N2–N3 (plane C): $-1.679x + 7.185y + 8.522z = 3.382$; Co1–O1–O2–O1A (plane D): $14.046x + 1.025y - 4.944z = 4.5511$. The angle between the planes is 92.4°.

Three types of intramolecular hydrogen bonds are observed in **2** (Supporting Information). The first is formed between the N atom of a triazole ring and the O atom of PA (N2–H2⋯O3 and N2–H2⋯O4). The second is formed between the coordinated water molecules and the O atom of PA (O1–H1B⋯O4, O2–H2A⋯O3, and O2–H2B⋯O7). The third is formed between the O atom of the coordinated water molecules and the N atom of AZT (O1–H1A⋯N3 and O2–H2B⋯N4). The molecules are also connected by different types of intermolecular hydrogen bonds that extend the structure into a 3D supermolecular structure and

make an important contribution to enhance the thermal stability of **2**.

Thermal Decomposition

Figure 3 shows the differential scanning calorimetry (DSC) and thermogravimetric/differential thermogravimetric (TG–DTG) curves of **1** and **2** with a linear heating rate of 10 °C min^{−1} under N₂.

The DSC curve of **1** shows two endothermic peaks in the ranges of 102.5–156.7 °C and 156.7–157.1 °C. There are mass losses of 6.8 and 3.4% in the TG–DTG curves that correspond to these temperature ranges, which are coincident with the loss of all four lattice and two coordinated H₂O molecules. The AZT and PA molecule structures are destroyed through three decomposition steps after the loss of all the H₂O molecules. The first decomposition step occurs between 157.1 and 217.5 °C with a peak temperature at 202.3 °C, and there is a mass loss of 38.6% that corresponds to this temperature range. In addition, there are two consecutive exothermic peaks in the range of 217.5–600 °C with peak temperatures at 346.6 and 465.0 °C in the second and third decomposition steps, respectively. There are mass losses of 27.3 and 16.1% that correspond to this temperature range. The mass of the final residue is 7.9% of the initial mass, coincident with the calculated value of a mixture of MnO (6.7%) and MnO₂ (8.2%). The absorption bands in the FTIR spectrum of the residue at 600.0 °C also

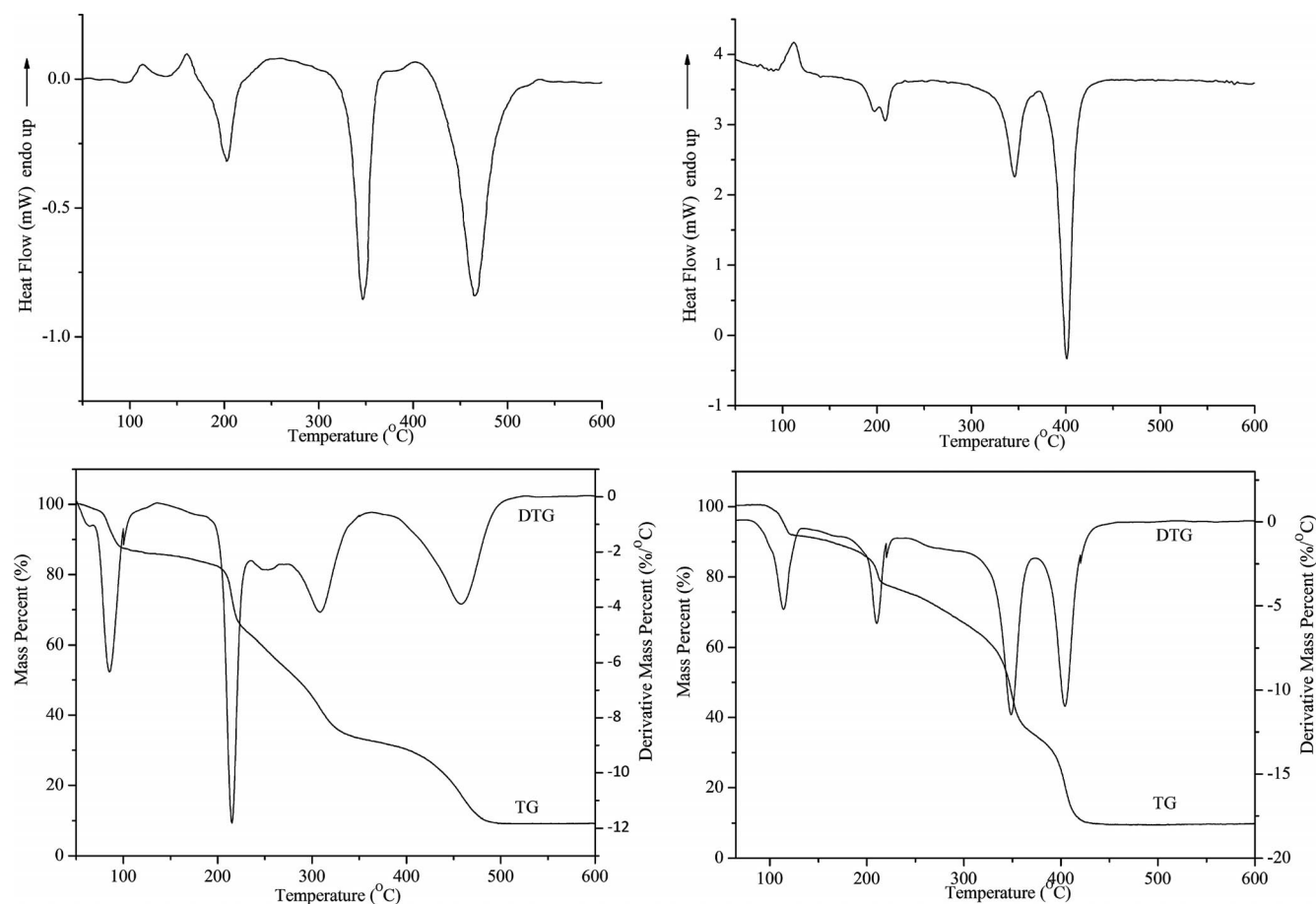


Figure 3. DSC (top) and TG–DTG curves (bottom) of **1** (left) and **2** (right) under N₂ with a heating rate of 10 °C min^{−1}.

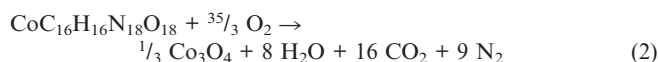
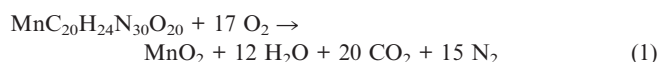
prove that the final residue is a mixture of MnO and MnO₂ (main product). The decomposition pathway of **1** can be described as follows: [Mn(AZT)₄(H₂O)₂](PA)₂·4H₂O → [Mn(AZT)₄](PA)₂ → Mn(RCOO)₂ + other polymer + gas products → Mn(NCOO) + gas products → MnO + MnO₂ (main product) + gas products.

The DSC curve of **2** shows an endothermic process in the range of 97.6–145.3 °C with a peak temperature at 112.0 °C. Corresponding to this endothermic process, there is a mass loss of 9.0% of the initial mass in the TG–DTG curves, which is coincident with the calculated loss of all four coordinated H₂O molecules (calcd. 8.9%). The nitro and azido groups are cleaved, and the benzene and triazole rings are destroyed, which is confirmed by the FTIR spectrum after the loss of all the H₂O molecules, so **2** becomes unstable and begins to decompose. It can be seen from the DSC curve that the decomposition occurs in the range of 140.0–600.0 °C in three exothermic steps. The decomposition occurs at 145.3–262.5, 262.5–372.8, and 372.8–450.6 °C, and the peak temperatures are 208.5, 345.8, and 401.2 °C, respectively. Furthermore, corresponding to these temperature ranges, there are mass losses of 18.0, 38.0, and 25.5%, respectively. The mass of the final residue is 9.6% of the initial mass, coincident with the calculated value for Co₃O₄ (9.9%). The absorption bands in the FTIR spectrum of the residue at 600 °C prove that the final residue is Co₃O₄. The

decomposition pathway of **2** can be described as follows: [Co(AZT)₂(H₂O)₄](PA)₂ → [Co(AZT)₂](PA)₂ → Co(RCOO)₂ + other polymer + gas products → Co(NCOO) + gas products → Co₃O₄ + gas products.

Energies of Combustion and Enthalpies of Formation

In order to study the energies of combustion and the enthalpies of formation of **1** and **2**, their constant-volume energies of combustion (Q_v) were measured by oxygen bomb calorimetry under O₂ (450 psi), which yielded different products to those seen in the DSC studies. The Q_v values are 10.39 and 8.77 MJ kg^{−1} for **1** and **2**, respectively. Consequently, the bomb equations are as follows [Equations (1) and (2)]:



The energies of combustion are as follows [Equations (3) and (4)] (Q_p : constant-pressure energy of combustion):

$$\Delta H_1 = Q_p = Q_v + \Delta nRT = 11054.17 \text{ kJ mol}^{-1} = 10.43 \text{ MJ kg}^{-1} \quad (3)$$

$$\Delta H_2 = Q_p = Q_v + \Delta nRT = 7132.13 \text{ kJ mol}^{-1} = 8.83 \text{ MJ kg}^{-1} \quad (4)$$

The energies of combustion of RDX, HMX, and TNT are 9.60, 9.44–9.88, and 15.22 MJ kg⁻¹, respectively.^[75] Consequently, the energies of combustion of **1** and **2** are approximately equal to the energies of combustion of RDX and HMX but lower than that of TNT.

Complexes **1** and **2** should have relatively thermodynamically stable structures. The standard enthalpies of formation of **1** and **2** were calculated from the energies of combustion from Equations (1) and (2) and Hess's law [Equations (5) and (6)]. With the known enthalpies of formation of manganese dioxide ($\Delta_f H^\circ_{298}[\text{MnO}_{2(s)}] = -519.7 \text{ kJ mol}^{-1}$), cobalt(II,III) oxide ($\Delta_f H^\circ_{298}[\text{Co}_3\text{O}_{4(s)}] = -891.0 \text{ kJ mol}^{-1}$), carbon dioxide ($\Delta_f H^\circ_{298}[\text{CO}_{2(g)}] = 393.5 \text{ kJ mol}^{-1}$), and water ($\Delta_f H^\circ_{298}[\text{H}_2\text{O}_{(l)}] = -285.8 \text{ kJ mol}^{-1}$), the enthalpies of formation of **1** and **2** were calculated as:

$$\Delta_f H^\circ_{298(1,s)} = \Delta_f H^\circ[\text{MnO}_{2(s)}] + 12\Delta_f H^\circ[\text{H}_2\text{O}_{(l)}] + 20\Delta_f H^\circ[\text{CO}_{2(g)}] + \Delta_c H^\circ_{(1,s)} = +14974.87 \text{ kJ mol}^{-1} \quad (5)$$

$$\Delta_f H^\circ_{298(2,s)} = \frac{1}{3}\Delta_f H^\circ[\text{Co}_3\text{O}_{4(s)}] + 8\Delta_f H^\circ[\text{H}_2\text{O}_{(l)}] + 16\Delta_f H^\circ[\text{CO}_{2(g)}] + \Delta_c H^\circ_{(2,s)} = +10844.73 \text{ kJ mol}^{-1} \quad (6)$$

Nonisothermal Kinetic Analysis

In this work, the methods of Kissinger^[76] and Ozawa^[77] were used to determine the Arrhenius equation. The Kissinger and Ozawa Equations (7) and (8), respectively, are as follows:

$$\ln \beta / T_p^2 = \ln [RA/E_a] - E_a/(RT_p) \quad (7)$$

$$\lg \beta = \lg [AE_a/RG(a)] - 2.315 - 0.4567E_a/RT_p \quad (8)$$

where T_p is the peak temperature [K], A is the pre-exponential factor [s⁻¹], E_a is the apparent activation energy [kJ mol⁻¹], R is the gas constant (8.314 J K⁻¹ mol⁻¹), β is the linear heating rate [K min⁻¹], and $G(a)$ is the reaction mechanism function.

Based on the first exothermic peak temperatures measured at five different heating rates (2, 5, 10, 15, and 20 K min⁻¹), the methods of Kissinger and Ozawa were applied to study the kinetics parameters of **1** and **2**. From the original data, the apparent activation energy, E_k and E_o , pre-exponential factor, A_k , linear correlation coefficient, R_k and R_o , and standard deviation, S_k and S_o , were determined and are shown in Table 1. Accordingly, the Arrhenius Equations (9) and (10) for **1** and **2**, respectively, can be expressed as follows (E is the average of E_k and E_o):

$$\ln k = 22.82 - 223.9 \times 10^3/(RT) \quad (9)$$

$$\ln k = 15.23 - 153.3 \times 10^3/(RT) \quad (10)$$

Table 1. Peak temperatures of the first main exothermal peaks at different heating rates and the chemical kinetics parameters of **1** and **2**.

β [K min ⁻¹]	T_p of 1 [K]	T_p of 2 [K]
2	464.25	451.95
5	470.95	459.45
10	477.05	470.55
15	480.95	473.25
20	481.95	476.15
Kissinger's method:		
E_k [kJ mol ⁻¹], $\ln A_k$, R_k	223.9, 22.82, -0.9974	153.3, 15.23, -0.9914
Ozawa's method:		
E_o [kJ mol ⁻¹], R_o	220.4, -0.9976	153.1, -0.9922

Sensitivity Tests

The impact, friction, and flame sensitivities were determined based on Chinese Standards^[78] (Supporting Information). The results of the sensitivity tests on **1** and **2** are listed in Table 2.

Table 2. Results of sensitivity tests on **1** and **2**.

	1	2
Flame sensitivity, h_{50} [cm]	21.44	35.93
Friction sensitivity [%]	0	60
Impact sensitivity [%]	0	0

Physicochemical Properties

The physicochemical properties of **1** and **2** are listed in Table 3. The nitrogen content of these compounds is more than 30% by weight, and they have a better oxygen balance than TNT ($\Omega = -74.0\%$).

Table 3. Physicochemical properties of **1** and **2**.

	1	2
T_m [°C] ^[a]	113.6, 160.4	112.0
T_d [°C] ^[b]	202.3, 346.6, 465.0	208.5, 345.8, 401.2
N [%] ^[c]	39.66	31.32
Ω [%] ^[d]	-49.83	-45.58
E [kJ mol ⁻¹] ^[e]	223.9	153.3
ΔH° [kJ mol ⁻¹] ^[f]	11054.17	7132.13
$\Delta_f H^\circ_{298}$ [kJ mol ⁻¹] ^[g]	+14974.87	+10844.73

[a] Melting point/DSC endothermic peak. [b] Thermal degradation/DSC main exothermic peak. [c] Nitrogen content. [d] Oxygen balance. [e] Activation energy. [f] Experimental energy of combustion. [g] Molar enthalpy of formation.

Conclusions

Two environmentally friendly energetic complexes, [Mn(AZT)₄(H₂O)₂](PA)₂·4H₂O (**1**) and [Co(AZT)₂(H₂O)₄](PA)₂ (**2**), were synthesized and characterized. Their crystal structures show that the Mn^{II} and Co^{II} ions are six-coordinate in a slightly distorted octahedral geometry. Thermal analysis indicated that there were one or two main endo-

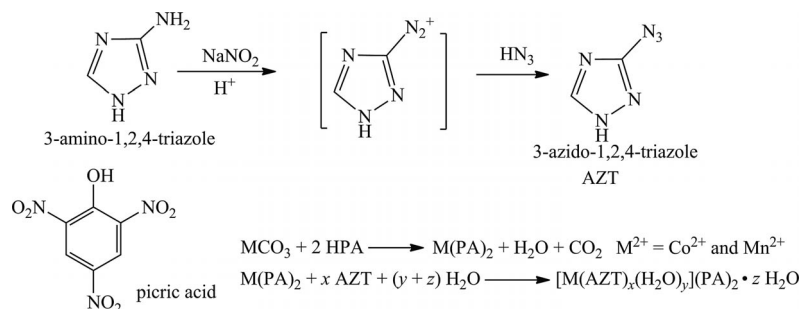
thermic processes and three main exothermic processes, and the final residues of **1** and **2** at 600 °C were a mixture of MnO/MnO₂ and Co₃O₄, respectively. The energies of combustion and the enthalpies of formation of **1** and **2** are 10.43 and 8.83 MJ kg⁻¹ and -7133.47 and -3419.53 kJ mol⁻¹, respectively. Nonisothermal kinetic analysis indicated that the Arrhenius equations of **1** and **2** can be expressed as follows: $\ln k = 22.82 - 223.9 \times 10^3/(RT)$ (for **1**) and $\ln k = 15.23 - 153.3 \times 10^3/(RT)$ (for **2**). The firing sensitivity measurements showed that the 50% firing heights were 21.44 and 35.93 cm for **1** and **2**, respectively, which imply good combustion performance. The results of these studies showed that **1** and **2** may have possible application as energetic materials in the near future.

Experimental Section

General Caution: AZT and its coordination compounds are energetic materials and tend to explode under certain conditions. Appropriate safety precautions (safety glasses, face shields, leather coat, and ear plugs) should be used, especially when these compounds are prepared on a large scale in dry states.

Materials and Physical Techniques: All reagents and solvents were all analytically pure commercial products. AZT was prepared according to a literature method in two steps (Scheme 1).^[62] The starting material, sodium azide, is a commercial product and was recrystallized before use. Elemental analyses were performed with a Flash EA 1112 full-automatic trace element analyzer. The FTIR spectra were recorded with a Bruker Equinox 55 IR spectrometer (KBr pellets) at 4000–400 cm⁻¹ with a resolution of 4 cm⁻¹. DSC and TG-DTG measurements were carried out with a Pyris-1 differential scanning calorimeter and a Pyris-1 thermogravimetric analyzer (Perkin-Elmer, USA) under dry nitrogen with a flow rate of 20 mL min⁻¹. The conditions for the thermal analyses were as follows: the crystalline samples were powdered and put into aluminum pans and open platinum pans for DSC and TGA, respectively, with a linear heating rate of 10 °C min⁻¹ from 50 to 600 °C. The energies of combustion were measured by oxygen bomb calorimetry (Parr 6200, USA).

Synthesis of [Mn(AZT)₄(H₂O)₂](PA)₂·4H₂O (1**) and [Co(AZT)₂(H₂O)₄](PA)₂ (**2**):** The preparation of **1** and **2** is given in Scheme 1. Manganese carbonate (or cobalt carbonate) (22 mmol) was added to a solution of picric acid (40 mmol) in deionized water (20 mL), and the mixture was stirred at 60–65 °C for 15 min. The reaction mixture was filtered, and the filtrate was kept for later use. A solution containing AZT (40 mmol for **1** and 80 mmol for **2**) in deion-



Scheme 1. Synthesis of AZT and **1** and **2**.

Table 4. Crystal data and structure refinement for **1** and **2**.

	1	2
Empirical formula	C ₂₀ H ₂₄ MnN ₃₀ O ₂₀	C ₁₆ H ₁₆ CoN ₁₈ O ₁₈
Formula mass	1059.63	807.4
Color	yellow	red
Crystal system	triclinic	orthorhombic
Space group	<i>P</i> $\bar{1}$	<i>Pbca</i>
Crystal dimensions [mm]	0.22 × 0.20 × 0.18	0.22 × 0.18 × 0.16
Z	1	4
<i>a</i> , <i>b</i> , <i>c</i> [Å]	8.2464(12), 9.7462(14), 13.979(2)	14.4116(18), 7.6092(10), 27.668(3)
<i>a</i> , <i>β</i> , <i>γ</i> [°]	84.352(2), 78.922(2), 78.922(2)	90, 90, 90
<i>h</i> , <i>k</i> , <i>l</i>	−9 to 4, −11 to 10, −16 to 16	−18 to 14, −8 to 9, −32 to 34
<i>V</i> [Å ³]	1044.1(3)	3034.1(7)
<i>D</i> _{calcd.} [g cm ⁻³]	1.685	1.768
μ(Mo- <i>K</i> _α) [mm ⁻¹]	0.431	0.678
<i>F</i> (000)	539	1636
θ range [°]	1.49–25.00	1.47–26.40
Measured reflections	5403	16287
Unique data	3644 [<i>R</i> _{int} = 0.0159]	3103 [<i>R</i> _{int} = 0.0595]
<i>R</i> ₁ , <i>wR</i> ₂ [<i>I</i> > 2σ(<i>I</i>)]	<i>R</i> ₁ = 0.0378, <i>wR</i> ₂ ^[a] = 0.0930	<i>R</i> ₁ = 0.0384, <i>wR</i> ₂ ^[b] = 0.0897
<i>R</i> ₁ , <i>wR</i> ₂ (all data)	<i>R</i> ₁ = 0.0464, <i>wR</i> ₂ ^[a] = 0.0996	<i>R</i> ₁ = 0.0674, <i>wR</i> ₂ ^[b] = 0.1029
Goodness of fit	1.026	1.022
Δρ _{max} , Δρ _{min} [e Å ⁻³]	0.448, −0.403	0.426, −0.261

[a] $w = 1/[\sigma^2(F_o^2) + (0.0443p)^2 + 0.7463p]$. [b] $w = 1/[\sigma^2(F_o^2) + (0.0463p)^2 + 1.4579p]$, $wR_2 = [\Sigma w(F_o^2 - F_c^2)^2 / \Sigma w(F_o^2)]^{1/2}$, $P = (F_o^2 + 2F_c^2)/3$.

ized water (40 mL) was stirred with a mechanical agitator at 60–65 °C. The metal picrate solution was added dropwise with continuous stirring over 30 min. Then the solution was cooled to room temperature with stirring and allowed to stand for 1 h until a precipitate had formed. The precipitate was collected by filtration, washed with ethanol, and dried under vacuum in an explosion-proof water-bath dryer. Single crystals suitable for X-ray measurements were obtained by recrystallization of the products from deionized water at room temperature over one month.

[Mn(AZT)₄(H₂O)₂](PA)₂·4H₂O (1): Yield: 72.0% (based on AZT). C₂₀H₂₄MnN₃₀O₂₀ (1059.63): calcd. C 22.65, H 2.26, N 39.64; found C 22.56, H 2.27, N 39.93. IR (KBr): $\tilde{\nu}$ = 2145 ($\nu_{\text{N}=\text{N}=\text{N}}$), 1333 (ν_{SNO_2}), 1532 (ν_{asNO_2}), 1165 ($\nu_{\text{C-O}}$) cm⁻¹.

[Co(AZT)₂(H₂O)₄](PA)₂ (2): Yield: 69.0% (based on AZT). C₁₆H₁₆CoN₁₈O₁₈ (807.4): calcd. C 23.78, H 1.98, N 31.21; found C 21.62, H 2.02, N 31.55. IR (KBr): $\tilde{\nu}$ = 2147 ($\nu_{\text{N}=\text{N}=\text{N}}$), 1337 (ν_{SNO_2}), 1550 (ν_{asNO_2}), 1166 ($\nu_{\text{C-O}}$) cm⁻¹.

X-ray Data Collection and Structure Refinement: Suitable crystals were chosen for X-ray determination. The X-ray diffraction data collection were collected with a Bruker SMART 1000 CCD detector diffractometer with graphite-monochromated Mo- K_{α} radiation (λ = 0.71073 Å) with ϕ and ω modes at 293(2) K. The structures were solved by direct methods using SHELXS-97^[79] and refined by full-matrix least-squares methods on F^2 with SHELXL-97.^[80] All non-hydrogen atoms were obtained from the difference Fourier map and subjected to anisotropic refinement by full-matrix least squares on F^2 . Details of the crystallographic data collection and structure refinement are summarized in Table 4. CCDC -815496 (for **1**) and -815495 (for **2**) contain the supplementary crystallographic data for this paper. These data can be obtained free of charge from The Cambridge Crystallographic Data Centre via www.ccdc.cam.ac.uk/data_request/cif.

Supporting Information (see footnote on the first page of this article): China National Military standard sensitivity testing conditions; selected bond lengths and angles for **1** and **2**; hydrogen bond lengths and angles for **1** and **2**; crystal packing of **1** and **2**; octahedral coordination around the metal atom in **1** and **2**; packing and coplanar structures of **1** and **2**.

Acknowledgments

The projects were supported by the Science and Technology on Applied Physical Chemistry Laboratory (9140C3703051105), the State Key Laboratory of Explosion Science and Technology (No.YBKT10-05 and ZDKT10-01b), and the Program for New Century Excellent Talents in University (NCET-10-0051 and CNET-09-0051).

- [1] J. Giles, *Nature* **2004**, 427, 580–581.
- [2] D. E. Chavez, M. A. Hiskey, *J. Energ. Mater.* **1999**, 17, 357–377.
- [3] M. B. Talawar, R. Sivabalan, T. Mukundan, H. Muthurajan, A. K. Sikder, B. R. Gandhe, A. S. Rao, *J. Hazard. Mater.* **2009**, 161, 589–607.
- [4] K. León, A. M. Riverón, O. Arencibia, L. López-Cánovas, *Anal. Biochem.* **2010**, 402, 96–98.
- [5] W. H. Liu, A. B. Greytak, J. M. Lee, C. Wong, J. Park, L. F. Marshall, W. Jiang, P. N. Curtin, A. Y. Ting, D. G. Nocera, D. Fukumura, R. K. Jain, M. G. Bawendi, *J. Am. Chem. Soc.* **2010**, 132, 472–483.
- [6] C. J. Hu, C. D. Sulok, F. Paulat, N. Lehnert, A. I. Twigg, M. P. Hendrich, C. E. Schulz, W. R. Scheidt, *J. Am. Chem. Soc.* **2010**, 132, 3737–3750.

- [7] M. J. Wójcik, J. Kwiendacz, M. Boczar, Ł. Boda, Y. Ozaki, *Chem. Phys.* **2010**, 372, 72–81.
- [8] K. Kawamura, M. Naganawa, F. Konno, J. Yui, H. Wakizaka, T. Yamasaki, K. Yanamoto, A. Hatori, M. Takei, Y. Yoshida, K. Sakaguchi, T. Fukumura, Y. Kimura, M. R. Zhang, *Nucl. Med. Biol.* **2010**, 37, 625–635.
- [9] L. Han, P. P. Zhang, H. S. Liu, H. J. Pang, Y. Chen, J. Peng, *J. Cluster Sci.* **2010**, 21, 81–91.
- [10] A. Pramanik, A. Basu, G. Das, *Polyhedron* **2010**, 29, 1980–1989.
- [11] H. Y. Bai, J. F. Ma, J. Yang, Y. Y. Liu, H. Wu, J. C. Ma, *Cryst. Growth Des.* **2010**, 10, 995–1016.
- [12] M. Fantini, V. Zuliani, M. A. Spotti, M. Rivara, *J. Comb. Chem.* **2010**, 12, 181–185.
- [13] L. Wang, W. Gu, J. X. Deng, M. L. Liu, N. Xu, X. Liu, Z. Anorg. Allg. Chem. **2009**, 636, 1124–1128.
- [14] Y. B. Joo, J. M. Shreeve, *Angew. Chem.* **2009**, 121, 572; *Angew. Chem. Int. Ed.* **2009**, 48, 564–567.
- [15] K. W. Paul, M. M. Hurley, K. K. Irikura, *J. Phys. Chem. A* **2009**, 113, 2483–2490.
- [16] T. M. Klapötke, C. M. Sabate, M. Rasp, *Dalton Trans.* **2009**, 10, 1825–1834.
- [17] T. M. Klapötke, C. M. Sabate, A. Penger, M. Rusan, J. M. Welch, *Eur. J. Inorg. Chem.* **2009**, 7, 880–896.
- [18] G. H. Tao, Y. Guo, Y. H. Joo, B. Twamley, J. M. Shreeve, *J. Mater. Chem.* **2008**, 18, 5524–5530.
- [19] T. M. Klapötke, P. Mayer, C. M. Sabate, J. M. Welch, N. Wiegand, *Inorg. Chem.* **2008**, 47, 6014–6027.
- [20] T. M. Klapötke, C. M. Sabate, J. M. Welch, *Z. Anorg. Allg. Chem.* **2008**, 634, 857–866.
- [21] T. M. Klapötke, C. M. Sabate, J. M. Welch, *Dalton Trans.* **2008**, 45, 6372–6380.
- [22] Y. H. Joo, B. Twamley, S. Garg, J. M. Shreeve, *Angew. Chem.* **2008**, 120, 6332; *Angew. Chem. Int. Ed.* **2008**, 47, 6236–6239.
- [23] M. H. V. Huynh, M. D. Coburn, T. J. Meyer, M. Wetzler, *Proc. Natl. Acad. Sci. USA* **2006**, 103, 10322–10327.
- [24] H. Xue, J. M. Shreeve, *Adv. Mater.* **2005**, 17, 2142–2146.
- [25] M. B. Talawar, A. P. Agrawal, S. N. Asthana, *J. Hazard. Mater.* **2005**, 120, 25–35.
- [26] J. G. Zhang, T. L. Zhang, K. B. Yu, *Acta Chim. Sin. (Engl. Ed.)* **1999**, 57, 1233–1238.
- [27] J. G. Zhang, T. L. Zhang, L. Yang, L. Q. Mao, K. B. Yu, *Chin. J. Inorg. Chem.* **2002**, 3, 284–288.
- [28] T. L. Zhang, C. H. Lv, J. G. Zhang, Z. G. Zhang, K. B. Yu, *J. Inorg. Chem.* **2002**, 2, 138–143.
- [29] G. Singh, I. P. S. Kapoor, S. P. Felix, *Propellants Explos. Pyrotech.* **2002**, 27, 16–22.
- [30] S. S. Yun, J. K. Kim, Ch. H. Kim, *J. Alloys Compd.* **2006**, 408, 945–951.
- [31] J. R. Song, H. X. Ma, J. Huang, R. Z. Hu, *Thermochim. Acta* **2004**, 416, 43–46.
- [32] J. G. Zhang, T. L. Zhang, *Acta Chim. Sin. (Engl. Ed.)* **2000**, 12, 1563–1566.
- [33] S. H. Li, S. P. Pang, X. T. Li, Y. Z. Yu, X. Q. Zhao, *Chin. Chem. Lett.* **2007**, 18, 1176–1178.
- [34] Y. Cui, T. L. Zhang, J. G. Zhang, L. Yang, X. C. Hu, J. Zhang, *J. Mol. Struct.* **2008**, 889, 177–185.
- [35] Y. Cui, J. G. Zhang, T. L. Zhang, L. Yang, J. Zhang, X. C. Hu, *J. Hazard. Mater.* **2008**, 160, 45–50.
- [36] Y. Cui, J. G. Zhang, T. L. Zhang, L. Yang, Y. Zang, Y. J. Shu, *Chin. J. Chem.* **2008**, 26, 2029–2034.
- [37] Y. Cui, J. G. Zhang, T. L. Zhang, L. Yang, J. Zhang, X. C. Hu, *Propellants Explos. Pyrotech.* **2008**, 33, 437–442.
- [38] J. Shang, J. G. Zhang, Y. Cui, T. L. Zhang, Y. J. Shu, L. Yang, *Acta Chim. Sin. (Engl. Ed.)* **2010**, 68, 233–238.
- [39] J. G. Zhang, Z. M. Li, Y. Zang, T. L. Zhang, Y. J. Shu, L. Yang, P. P. Powerd, *J. Hazard. Mater.* **2010**, 178, 1094–1099.
- [40] Z. M. Li, J. G. Zhang, Y. Cui, T. L. Zhang, Y. J. Shu, V. P. Sinditskii, V. V. Serushkin, V. Yu. Egorshin, *J. Chem. Eng. Data* **2010**, 55, 3109–3116.

- [41] S. Y. Qi, Z. M. Li, Z. N. Zhou, Y. Cui, G. T. Zhang, T. L. Zhang, J. G. Zhang, L. Yang, *Chin. J. Chem.* **2011**, *29*, 59–64.
- [42] J. Stierstorfer, T. M. Klapötke, A. Hammerl, R. Chapman, Z. Anorg. Allg. Chem. **2008**, *634*, 1051–1057.
- [43] T. M. Klapötke, J. Stierstorfer, B. Weber, *Inorg. Chim. Acta* **2009**, *362*, 2311–2320.
- [44] G. H. Tao, B. Twamly, J. M. Shreeve, *Inorg. Chem.* **2009**, *48*, 9918–9923.
- [45] Y. C. Li, C. Qi, S. H. Li, H. J. Zhang, C. H. Sun, Y. Z. Yu, S. P. Pang, *J. Am. Chem. Soc.* **2010**, *132*, 12172–12173.
- [46] T. M. Klapötke, D. G. Piercey, *Inorg. Chem.* **2011**, *50*, 2732–2734.
- [47] T. M. Klapötke, B. Krumm, M. Scherr, *J. Am. Chem. Soc.* **2009**, *131*, 72–74.
- [48] E. Q. Gao, S. Q. Bai, Y. F. Yue, Z. M. Wang, C. H. Yan, *Inorg. Chem.* **2003**, *42*, 3642–3649.
- [49] F. C. Liu, Y. F. Zeng, J. R. Li, X. H. Bu, H. J. Zhang, J. Ribas, *Inorg. Chem.* **2005**, *44*, 7298–7300.
- [50] H. H. Ko, J. H. Lim, H. C. Kim, C. S. Hong, *Inorg. Chem.* **2006**, *45*, 8847–8849.
- [51] M. A. S. Goher, B. Bitschnau, B. Sodin, C. Gspan, F. A. Mautner, *J. Mol. Struct.* **2008**, *886*, 32–38.
- [52] K. C. Patil, C. Nesamani, V. R. P. Verneker, *Synth. React. Inorg. Met.-Org. Chem.* **1982**, *12*, 383–395.
- [53] K. K. Narang, M. K. Singh, K. B. Singh, R. A. Lal, *Synth. React. Inorg. Met.-Org. Chem.* **1996**, *26*, 573–589.
- [54] D. Bose, S. H. Rahaman, G. Mostafa, R. D. B. Walsh, M. J. Zaworotko, B. K. Ghosh, *Polyhedron* **2004**, *23*, 545–552.
- [55] D. Das, B. G. Chand, K. K. Sarker, J. Dinda, C. Sinha, *Polyhedron* **2006**, *25*, 2333–2340.
- [56] S. G. Zhu, D. W. Xu, S. J. Cao, J. Y. Mou, L. G. Chen, *Explos. Mater.* **2005**, *34*, 17–18.
- [57] Z. H. Liu, T. L. Zhang, J. G. Zhang, S. Z. Wang, *J. Hazard. Mater.* **2008**, *154*, 832–838.
- [58] B. D. Wu, L. Yang, S. W. Wang, T. L. Zhang, J. G. Zhang, Z. N. Zhou, K. B. Yu, Z. Anorg. Allg. Chem. **2011**, *637*, 450–455.
- [59] Z. H. Liu, T. L. Zhang, J. G. Zhang, L. Yang, J. Zhang, Y. Zang, *Chin. J. Energy Mater.* **2008**, *6*, 663–668.
- [60] L. Yang, B. D. Wu, T. L. Zhang, Z. H. Liu, J. G. Zhang, *Propellants Explos. Pyrotech.* **2010**, *35*, 521–528.
- [61] B. D. Wu, S. W. Wang, L. Yang, T. L. Zhang, J. G. Zhang, Z. N. Zhou, K. B. Yu, *Eur. J. Inorg. Chem.* **2011**, *16*, 2616–2623.
- [62] T. P. Kofman, K. N. Krasnov, *Russ. J. Org. Chem.* **2004**, *40*, 1651–1656.
- [63] J. L. Feng, J. G. Zhang, Z. M. Li, T. L. Zhang, Y. Cui, L. Yang, *Acta Chim. Sin. (Engl. Ed.)* **2010**, *68*, 2493–2499.
- [64] J. L. Feng, J. G. Zhang, T. L. Zhang, Y. Cui, *Acta Phys.-Chim. Sin.* **2010**, *26*, 2410–2416.
- [65] Y. Cui, T. L. Zhang, J. G. Zhang, L. Yang, J. Zhang, X. C. Hu, *Struct. Chem.* **2008**, *19*, 269–278.
- [66] L. M. Zhao, H. H. Li, Y. Wu, S. Y. Zhang, Z. J. Zhang, W. Shi, P. Cheng, D. Z. Liao, S. P. Yan, *Eur. J. Inorg. Chem.* **2010**, *13*, 1983–1990.
- [67] S. Sarkar, M. Nayak, M. Fleck, S. Dutta, U. Flörke, R. Koner, S. Mohanta, *Eur. J. Inorg. Chem.* **2010**, *5*, 735–743.
- [68] V. Chandrasekhar, R. Azhakar, B. M. Pandian, J. F. Bickley, A. Steiner, *Eur. J. Inorg. Chem.* **2008**, *7*, 1116–1124.
- [69] A. Ahmed, N. S. Gajbhiye, *J. Solid State Chem.* **2010**, *183*, 3100–3104.
- [70] P. D. Battle, S. E. Dutton, P. A. V. Daesdonk, *J. Solid State Chem.* **2010**, *183*, 1620–1624.
- [71] Z. V. Dobrohotova, A. A. Sidorov, M. A. Kiskin, G. G. Aleksandrov, K. S. Gavrichiev, A. V. Tyurin, A. L. Emelina, M. A. Bykov, A. S. Bogomyakov, I. P. Malkerova, A. S. Alihanian, V. M. Novotortsev, I. L. Eremenko, *J. Solid State Chem.* **2010**, *183*, 2475–2482.
- [72] J. Z. Gu, D. Y. Lv, Z. Q. Gao, J. Z. Liu, W. Dou, Y. Tang, *J. Solid State Chem.* **2011**, *184*, 675–683.
- [73] V. G. Makhankova, O. V. Khavryuchenko, V. V. Lisnyak, V. N. Kokozay, V. V. Dyakonenko, O. V. Shishkin, B. W. Skelton, J. Jezierska, *J. Solid State Chem.* **2010**, *183*, 2695–2702.
- [74] S. Vasala, M. Lehtimäki, Y. H. Huang, H. Yamauchi, J. B. Goodenough, M. Karppinen, *J. Solid State Chem.* **2010**, *183*, 1007–1012.
- [75] Y. X. Ou, *Explosives*, Beijing Institute of Technology, China, **2006**.
- [76] H. E. Kissinger, *Anal. Chem.* **1957**, *29*, 1702–1706.
- [77] T. Ozawa, *Bull. Chem. Soc. Jpn.* **1965**, *38*, 1881–1886.
- [78] Z. T. Liu, Y. L. Lao, *Initiating Explosive Experimental*, Beijing Institute of Technology, China, **1995**.
- [79] G. M. Sheldrick, *SHELXS 97, Program for the Solution of Crystal Structure*, University of Göttingen, Germany, **1990**.
- [80] G. M. Sheldrick, *SHELXL 97, Program for Crystal Structure Refinement from Diffraction Data*, University of Göttingen, Germany, **1997**.

Received: August 1, 2011

Published Online: February 3, 2012

Application of Nickel Complexes Modified by Tridentate *O,N,O'*-Ligands as Precatalysts in Nickel-Catalyzed C(sp²)-C(sp³) Bond Formations

Chika I. Someya,^[a] Shigeyoshi Inoue,^[b] Sebastian Krackl,^[a] Elisabeth Irran,^[b] and Stephan Enthaler*^[a]

Keywords: Nickel / Tridentate ligands / Homogeneous catalysis / Cross-coupling

1-Acetyl- [**1a**; 3,5-CF₃, 1-C(=O)CH₃] and 1-benzoyl-5-hydroxypyrazolines [**1b**; 3,5-CF₃, 1-C(=O)C₆H₅] have been synthesized and treated with Ni(OAc)₂·4H₂O in the presence of an excess of base [NH₃ or 4-(dimethylamino)pyridine (DMAP)] to form the nickel complexes **4a–c**. These complexes have been characterized by various techniques, which indicate a tridentate coordination mode of the ligands. X-ray crystallography determined an *O,N,O'*-coordination of the ligands, in which the ligand is planar, the oxygen donors are *trans* to each other, and the nitrogen donor is in a *cis* position. The other coordination sites on the nickel centre are occu-

pied by the added base molecules (NH₃ or DMAP). The number of NH₃ or DMAP ligands depends on the nature of the base; in the case of ammonia, one molecule is coordinated to the nickel centre to form a diamagnetic square-planar complex, whereas with DMAP, an octahedral paramagnetic complex with three additional DMAP ligands was observed. Initial catalytic experiments have been performed by applying the complexes in the nickel-catalyzed C(sp²)-C(sp³) cross-coupling of aryl halides with benzylzinc bromides or dialkylzinc reagents; excellent yields and selectivities have been achieved.

Introduction

A huge number of methodologies for the formation of carbon–carbon bonds have been established.^[1] Based on the landmark coupling reactions of the groups of Heck, Suzuki and Negishi in the 1960s and 1970s, transition-metal-catalyzed reactions have been proven to be a powerful technique in organic synthesis, which is outlined by countless applications.^[2] Aside from palladium, nickel-based catalysts play an important role in these transformations.^[3] In the last few decades, various protocols have been established mainly for the coupling of sp²-carbon electrophiles with sp²-carbon nucleophiles. In contrast, the coupling of alkyl electrophiles and nucleophiles is underdeveloped because of various difficulties, e.g. β-hydride elimination, slow reductive elimination steps and high catalyst loadings, which significantly reduce the impact of the method.^[4] Therefore, the design of more active and selective catalysts and the search for suitable reaction conditions is highly desired. Recently, different protocols have been developed for the coupling of sp³-carbon atoms to sp-, sp²- and sp³-carbon atoms.^[5] The addition of suitable ligands is an important factor to influence the reaction outcome.^[6] Furthermore, low cost, availability,

easy synthesis, high tunability, flexibility and stability of the ligands have to be considered.^[7] We have recently investigated the potential of 1-acetyl- and 1-benzoyl-5-hydroxypyrazoline ligands in coordination chemistry (Figure 1).^[8] Depending on the metal precursor and the reaction conditions, different coordination modes were feasible. In the case of nickel, 5-hydroxypyrazoline ligands were coordinated in a tridentate *O,N,O'*-coordination mode as reported by Joshi and co-workers (Figure 1; **4**).^[9,11] Due to their high stability and the possibility for the ligand to stabilize charges by conjugation, the complexes could be suitable for catalysis.

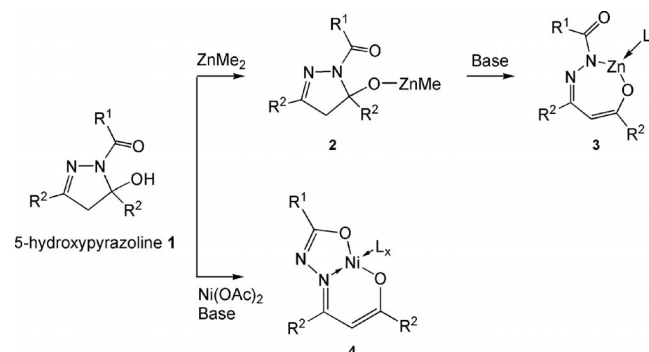


Figure 1. Coordination modes of 5-hydroxypyrazolines **1**.

On this basis, we report the synthesis and characterization of easily accessible nickel complexes modified by tridentate *O,N,O'*-ligands and their application in coupling

[a] Technische Universität Berlin, Department of Chemistry, Cluster of Excellence “Unifying Concepts in Catalysis”, Straße des 17. Juni 135/C2, 10623 Berlin, Germany
Fax: +49-30-314-29732
E-mail: stephan.enthaler@tu-berlin.de

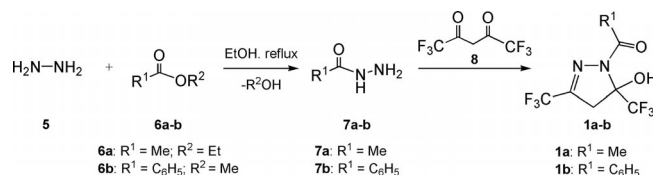
[b] Technische Universität Berlin, Department of Chemistry: Metalorganics and Inorganic Materials, Straße des 17. Juni 135/C2, 10623 Berlin, Germany

chemistry, i.e. the selective nickel-catalyzed C(sp²)-C(sp³) cross-coupling of aryl halides with benzylzinc bromides or dialkylzinc reagents.

Results and Discussion

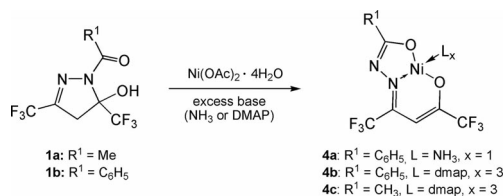
Complex Synthesis and Characterization

The ligands were synthesized according to literature methods (Scheme 1).^[10] Acetohydrazide (**7a**) and benzo-hydrazide (**7b**) were obtained from the reaction of equimolar amounts of hydrazine monohydrate with ethyl acetate (**6a**) or methyl benzoate (**6b**), respectively, in ethanol under reflux conditions. The hydrazides **7a** and **7b** were obtained in good yields as colourless solids and subsequently heated to reflux with hexafluoroacetylacetone (**8**) in ethanol. 1-Acetyl- and 1-benzoyl-5-hydroxypyrazoline **1** were obtained as crystalline compounds in good yields (69–87%) after recrystallization from *n*-hexane.



Scheme 1. Synthesis of **1**.

Having synthesized 1-acetyl- and 1-benzoyl-5-hydroxypyrazoline, the coordination of these ligands to nickel salts was investigated (Scheme 2).^[9,11] A methanol solution of the ligand and an excess of base [NH₃ (17% aqueous solution) or 4-(dimethylamino)pyridine (DMAP)] was added to a solution of Ni(OAc)₂·4H₂O in methanol at room temperature. After stirring overnight, the volatiles were removed in vacuo to obtain brown powders, which were extracted with ethanol and purified by crystallization to obtain red-brown crystals. Crystals suitable for X-ray measurements were grown from ethanol by slow evaporation of the solvent.



Scheme 2. Synthesis of **4a–c**.

The solid-state structures of **4a–c** were characterized by single-crystal X-ray diffraction. Thermal-ellipsoid plots are displayed in Figure 2, and selected bond lengths and angles are listed in Table 1. In agreement with the work of Joshi and co-workers, a square-planar arrangement was observed for **4a** with similar bond lengths and angles.^[9] The tridentate ligand is coordinated in an *O,N,O'*-mode to create a five- and six-membered ring system, which blocks one side of the metal atom. The ammonia ligand is positioned *cis* to the oxygen donors, and the nitrogen atom of the 5-hydroxy-

pyrazoline ligand connected to the nickel centre is *trans* to the ammonia ligand. Conversely, **4b** and **4c** have octahedral structures with three DMAP molecules connected to the nickel atom. The tridentate ligand is coordinated in the same fashion as seen in **4a**. However, the bond lengths to the nickel atom are slightly elongated. A similar effect was observed for the DMAP ligands in comparison to the ammonia ligand.

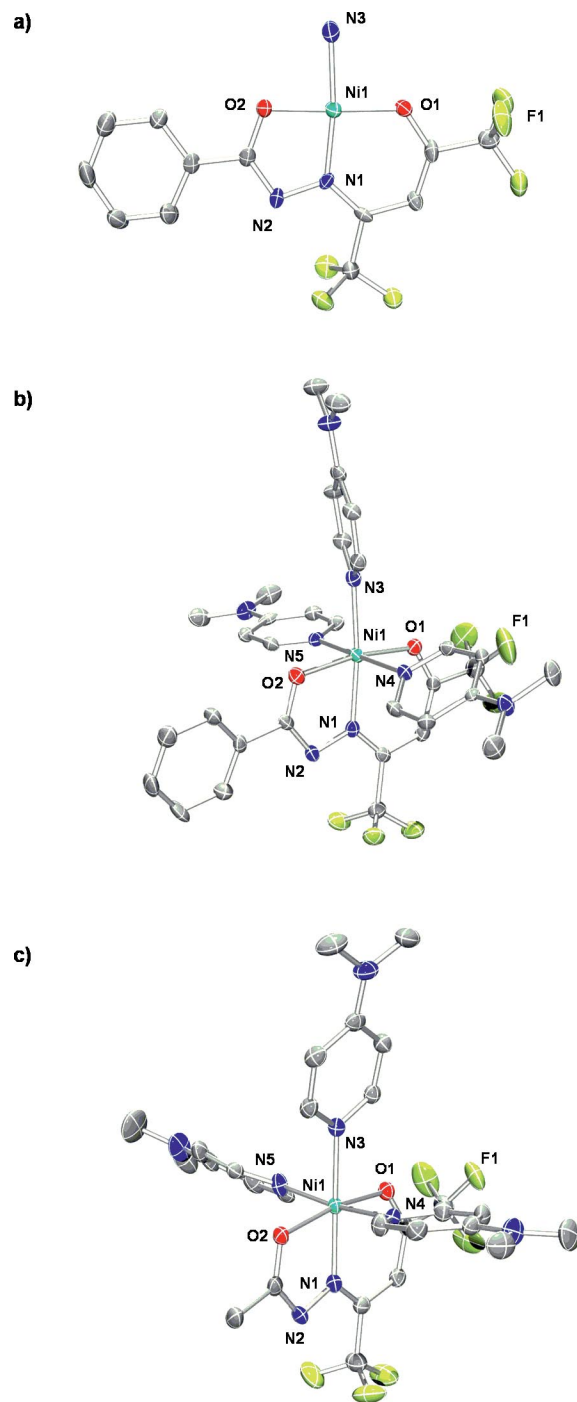


Figure 2. Molecular structures of **4a** (a), **4b** (b) and **4c** (c). Thermal ellipsoids are drawn at the 50% probability level. Hydrogen atoms are omitted for clarity.

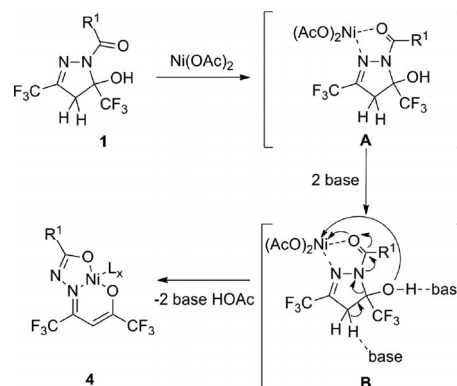
Table 1. Selected bond lengths [Å] and angles [°] for **4a**, **4b** and **4c**.

	4a	4b	4c
Ni–N1	1.816(3)	2.055(3)	2.0440(1)
Ni–O1	1.819(3)	2.021(3)	2.0260(1)
Ni–O2	1.829(4)	2.041(3)	2.0451(2)
Ni–N3	1.919(3)	2.118(3)	2.0950(2)
Ni–N4	–	2.132(3)	2.1648(2)
Ni–N5	–	2.164(3)	2.1383(2)
O(1)–Ni–O(2)	177.36(15)	170.16(1)	169.23(6)
N(1)–Ni–N(3)	171.87(17)	172.16(1)	175.43(8)

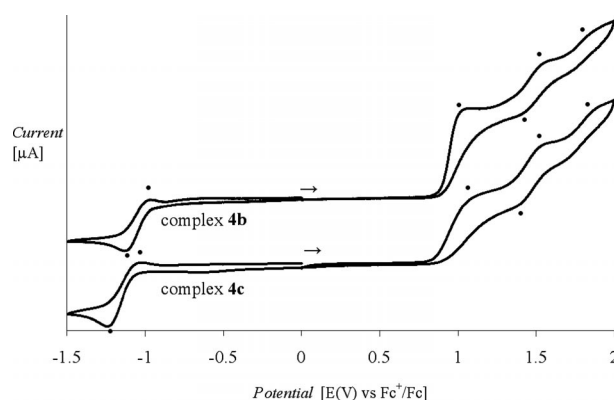
Complexes **4a–c** were also investigated by ^1H NMR spectroscopy (Table 2). Paramagnetic **4b** and **4c** gave broad signals, which could not be assigned. In contrast, for diamagnetic **4a**, a signal was found at $\delta = 5.93$ ppm, which was assigned to the C–H proton in the six-membered ring. This was further proven by the absence of any signal from the former CH_2 group in the ligand. In addition, a broad signal at $\delta = 1.50$ ppm was attributed to the N–H protons of the ammonia ligand. The coordination of the acetyl and benzoyl functionalities was investigated by IR spectroscopy (Table 2). The absence of signals in the $1610\text{--}1725\text{ cm}^{-1}$ region excludes the possibility of a free or coordinated C=O functionality in the chelated ligand. In addition, strong bands were observed in the $1515\text{--}1615\text{ cm}^{-1}$ region, which are attributed to the C=N functionality. Electron paramagnetic resonance (EPR) spectroscopy was applied to characterize paramagnetic **4b** and **4c**. Difficulties are known to arise with paramagnetic Ni^{II} complexes with an integer spin ($S = 1$).^[3b,12] Indeed, the EPR spectra of **4b** and **4c** are silent. Theoretically, in a pure octahedral complex, two unpaired electrons are expected. However, due to the sizeable zero-field splitting for the $3d^8$ configuration usually found for paramagnetic Ni^{II} complexes with an integer spin ($S = 1$), octahedral **4b** and **4c** are silent. Nevertheless, SQUID measurements confirmed the $S = 1$ state for **4b** and **4c**. These compounds both have a constant magnetic moment (μ_{eff}) of ca. $3\ \mu_{\text{B}}$ in the temperature range of $20\text{--}300\text{ K}$.

Although the reaction mechanism for the formation of **4a–c** is unknown, a reasonable mechanism is described in Scheme 3. Firstly, the nickel acetate coordinates to the basic nitrogen atom of the pyrazoline and to the acetyl functionality to form the chelating intermediate **A**. Deprotonation of the hydroxy group then occurs in the presence of the base. The ring opening of the cyclic pyrazoline is initiated by the deprotonation of the acidic CH_2 functionality by

ammonia or DMAP (**B**), which has been proven by labelling studies of the ligand in $[\text{D}_4]\text{methanol}$.^[8] The deprotonation process initiates the formation of **4a–c**.

Scheme 3. Potential reaction pathway for the synthesis of **4**.

The electrochemistry of **4b** and **4c** was investigated by cyclic voltammetry, and the results are summarized in Figure 3 and Table 3. The first oxidation process is an irrevers-

Figure 3. Cyclic voltammograms of **4b** and **4c**.Table 3. Cyclic voltammetric data for **4b** and **4c**.^[a]

	E^{Ia} [V] (q.r.) ^[b]	E^{Ic} [V] (ir.) ^[b]	E^{IIc} [V] (r.) ^[b]	E^{IIIc} [V] (ir.) ^[b]
4b	−1.05	+1.06	+1.49	+1.88
4c	−1.11	+1.11	+1.47	+1.87

[a] Electrochemical data for **4b** and **4c** at room temp., $[\text{Bu}_4\text{N}][\text{PF}_6]$ as the supporting electrolyte, scan rate = 10 mV/s , platinum disc and glassy carbon working electrode; the potentials are referenced vs. Fc^+/Fc . Reference electrode: Ag/Ag^+ in CH_3CN . [b] r. = reversible, ir. = irreversible, q.r. = quasireversible.

Table 2. Analytical properties of **1a**, **1b**, **4a**, **4b**, and **4c**.

	1a	1b	4a	4b	4c
^1H NMR [ppm] ^[a] : 4-CH(H)	3.30–3.80	3.00–3.66	5.93	–	–
^{19}F NMR [ppm] ^[a]	−67.7 −81.4	−67.4 −80.5	−65.3 −71.8	–	–
IR:					
$\nu(\text{C}=\text{O})$ [cm^{-1}] ^[b]	1699 (s)	1678 (s)	–	–	–
$\nu(\text{C}=\text{N})$ [cm^{-1}] ^[b]	1645 (s)	1639 (s)	1615 (s) 1533 (s)	1615 (s) 1533 (s)	1617 (s) 1532 (s)

[a] Chemical shifts were measured in $[\text{D}_4]\text{chloroform}$ at $25\text{ }^\circ\text{C}$. [b] Measured in KBr at $25\text{ }^\circ\text{C}$.

ible wave with a peak potential at +1.06 V for **4b** and +1.11 V for **4c**. The second oxidation process is observed as a reversible wave with half-wave potentials at +1.49 V ($\delta E = 0.13$ V) for **4b** and +1.47 V ($\delta E = 0.15$ V) for **4c**. The third oxidation process is a low-intensity irreversible wave with a peak potential at +1.88 V for **4b** and +1.87 V for **4c**. Only one reduction process was observed with a peak potential at –1.05 V for **4b** and –1.11 V for **4c**, which is best described as quasireversible.

DFT calculations have been proven to give reliable predictions of the electronic structure of **4b** [B3LYP/6-31G(d) for N, C, O, F, and H; LANL2DZ for Ni].^[13] The energy-minimized structure calculated by DFT is in good agreement with that obtained by X-ray diffraction. The molecular orbitals of **4b** are presented in Figure 4. The singly occupied molecular orbitals (SOMOs, –0.157 and –0.186 eV) are nearly degenerate. SOMO1 mainly originates from the tridentate *O,N,O'*-ligand, whereas SOMO2 comprises d-orbitals of the nickel atom with some contribution from the ligand (Figure 4a).

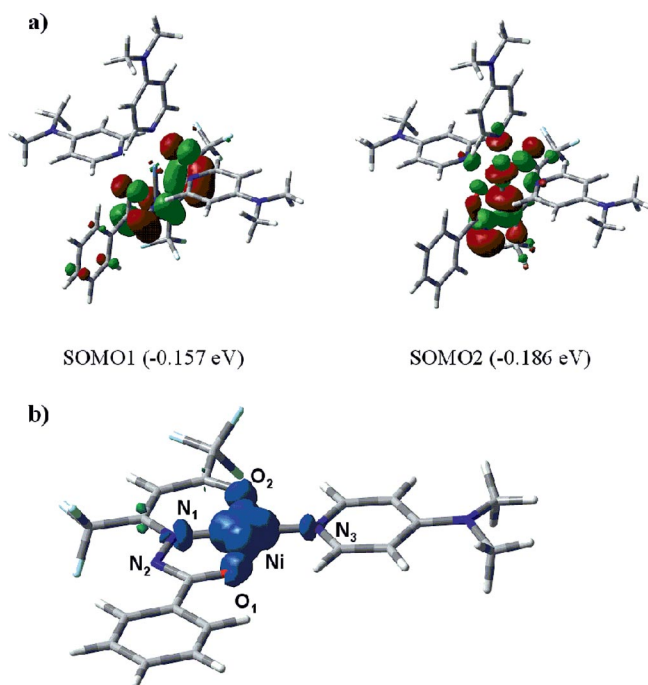


Figure 4. (a) Molecular orbitals of **4b**. B3LYP level 6-31G(d): basis set for N, C, O, F, and H atoms and LANL2DZ for the Ni atom. (b) Optimized model structure of **4b'** with an overlay of the computed spin density; UB3LYP level 6-31G(d) basis set for N, C, O, F, and H atoms and LANL2DZ for the Ni atom.

The one-electron reduction of **4b** was confirmed by chemical reduction using 1 equiv. of cobaltocene. Complex **4b** and cobaltocene (1:1) were dissolved in tetrahydrofuran (THF) at room temperature, transferred to an EPR tube, and the spectrum was immediately recorded at 77 K (Figure 5). The spectrum shows characteristic signals for a one-electron reduction at the nickel atom, which resulted in the formation of an Ni^{I} species **4b'** ($g_x = 2.041$, $g_y = 2.115$, $g_z = 2.271$). The electronic nature of **4b'** suggested by CV and

EPR measurements was confirmed by DFT calculations [UB3LYP level 6-31G(d) basis set for N, C, O, F, and H atoms and LANL2DZ for the Ni atom]. The calculations revealed that the highest occupied molecular orbital of **4b'** is localized on the Ni atom, whereas the lowest unoccupied molecular orbital comprises the π^* -orbital of the ligand. The spin density at the nickel centre (0.9264) may be regarded as the result of a large contribution from the Ni^{I} species (Figure 4b).

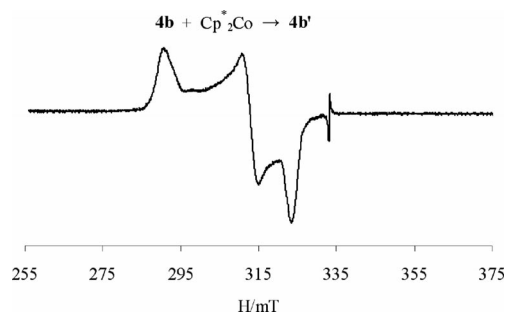


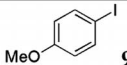
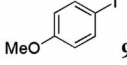
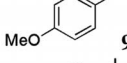
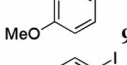
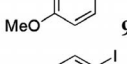
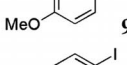
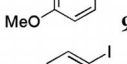
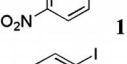
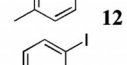
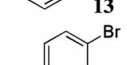
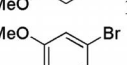
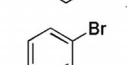
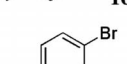
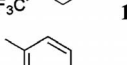
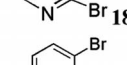
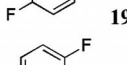
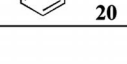
Figure 5. EPR spectrum of the mixture of **4b** (3.0×10^{-2} mmol) and cobaltocene (3.0×10^{-2} mmol) in THF at 77 K.

Nickel-Catalyzed $\text{C}(\text{sp}^2)\text{--C}(\text{sp}^3)$ Bond Formations

The catalytic abilities of **4a–c** were investigated in the coupling of aryl halides and benzylzinc bromides or dialkylzinc reagents (Table 4). Initial experiments were performed to find suitable reaction conditions. As a model reaction, the coupling of 1-iodo-4-methoxybenzene (**9**) with benzylzinc bromide (**10**) was performed in the presence of **4b** (Table 4, Entries 1–4). The reaction outcome was examined at different temperatures. Only at an elevated temperature (70 °C) was the desired coupling product observed in good yields (Table 4, Entry 4). The nickel complexes operated as precatalysts, and no reaction took place in their absence (Table 4, Entry 3). After initial optimization, we established that 2.0 mol-% of **4b** in THF performed the $\text{C}(\text{sp}^2)\text{--C}(\text{sp}^3)$ bond formation at 70 °C in excellent yield (> 99%, Table 4, Entry 4). A similar result (yield > 99%) was achieved with **4c** (Table 4, Entry 5). The coupling reaction was also examined by using diethylzinc to produce *p*-ethylanisole in a yield of 87% (Table 4, Entry 6). To study the effect of β -hydride elimination, the coupling reaction was investigated with α -methylbenzylzinc bromide (Table 4, Entry 7). The desired coupling product was obtained in a yield of 27%. However, nonnegligible amounts of the homocoupled products were detected by GC–MS [18% (2-methylbutane-1,3-diyl)dibenzene and 29% 4,4'-dimethoxybiphenyl]. Furthermore, styrene (4%) was observed as the β -hydride elimination product.

With these conditions in hand, different aryl iodides were treated with benzylzinc bromide in the presence of **4b**. Excellent yields (> 99%) were observed for 4-iodotoluene (**12**) and iodobenzene (**13**, Table 4, Entries 9 and 10). In the case of the challenging electron-withdrawing nitro group, no

Table 4. Nickel-catalyzed C–C bond formation of benzylzinc bromide with aryl halides.^[a]

9, 11–20		10		9a, 11a–20a	
Entry	Complex	Substrate	<i>T</i> [°C]	Yield ^[b] [%]	
1	4b		–78	<1	
2	4b		r.t.	<1	
3	–		70	<1	
4	4b		70	>99	
5	4c		70	>99	
6 ^c	4b		70	87 ^[d]	
7 ^e	4b		70	27 ^[f]	
8	4b		70	<1	
9	4b		70	>99	
10	4b		70	>99	
11	4b		70	84	
12	4b		70	93	
13	4b		70	51	
14	4b		70	94	
15	4b		70	>99	
16	4b		70	39	
17	4b		70	<1	

[a] Reaction conditions: substrate (0.67 mmol), benzylzinc bromide (1.00 mmol, 0.5 M in THF), catalyst (2.0 mol-%), THF (2.0 mL), 70 °C, 24 h. [b] Yield of desired product determined by GC–MS and ¹H NMR spectroscopy. [c] Et₂Zn (1.00 mmol) in THF/*n*-hexane solution. [d] 4-Ethylanisole was observed as the product. [e] (*α*-Methylbenzyl)zinc bromide (1.00 mmol) in THF. [f] 1-Methoxy-4-(1-phenylethyl)benzene was observed as the product. (2-Methylbutane-1,3-diyl)dibenzene (18%) and 4,4'-dimethoxybiphenyl (29%) were observed as homocoupled products.

product formation was observed (Table 4, Entry 8). Moreover, some examples of aryl bromides were tested. It was found that the aryl bromides gave lower yields of the coupling products than aryl iodides (Table 4, Entries 11–13). However, 1-bromo-4-(trifluoromethyl)benzene (**17**), which has a strong electron-withdrawing group, was converted in excellent yield (Table 4, Entry 14). The reaction of the heteroarene **18** with benzylzinc bromide resulted in the quantitative formation of the desired coupling product (Table 4, Entry 15). On the other hand, the coupling of 1-bromo-4-fluorobenzene (**19**) afforded 1-benzyl-4-fluorobenzene (**19a**) as the product in 39% yield. No activation of the C–F bond was observed. To verify the inactivity of the C–F bonds we tested the coupling reaction of fluorobenzene (**20**), and no coupling product was formed (Table 4, Entry 17).

In addition, we investigated the influence of the halide on the reaction outcome (Figure 6). The coupling reaction of benzylzinc bromide with substituted anisoles **9**, **14** and **21** in the presence of 2 mol-% of **4c** was evaluated by using GC–MS (Scheme 4). Complex **4c** was highly active for the conversion of the 4-iodoanisole (**9**), and full conversion was reached within 15 min (turnover frequency = 375 h^{–1}). As expected for bromo- (**14**) and chloroanisole (**21**), the catalyst activity decreased compared to that with **9**, e.g. *t*(50% yield) = 5.5 min for **9** and *t*(50% yield) = 160 min for **14**. In particular, the reaction with chloroanisole yielded only 12% of the coupling product after 24 h.

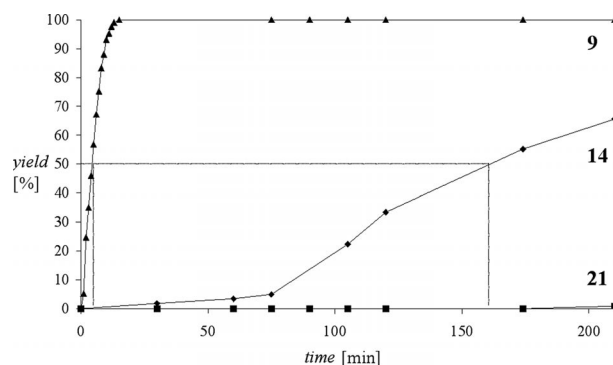
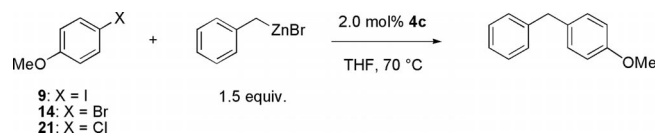


Figure 6. Comparison of different aromatic halides. Reaction conditions: substrate (0.67 mmol), benzylzinc bromide (1.00 mmol, 0.5 M in THF), catalyst **4c** (2.0 mol-%), THF (2.0 mL), 70 °C.



Scheme 4. Coupling reaction with different haloanisoles.

Conclusions

We have synthesized and characterized new nickel complexes with the highly flexible ligands 1-acetyl- [**1a**; 3,5-CF₃, 1-C(=O)CH₃] and 1-benzoyl-5-hydroxypyrazoline [**1b**; 3,5-CF₃, 1-C(=O)C₆H₅]. The added base is coordinated to the

nickel centre as a coligand. Depending on the nature of the ligand, different numbers of coligands occupy the vacancies on the nickel atom. Finally, the properties of the complexes were investigated in cross-coupling reactions. An excellent performance of the precatalysts was found for $C(sp^2)-C(sp^3)$ bond formations.

Experimental Section

General: All manipulations with oxygen- and moisture-sensitive compounds were performed under dinitrogen by using standard Schlenk techniques. Methanol was used without further purification. 1H , ^{19}F and ^{13}C NMR spectra were recorded with a Bruker AFM 200 spectrometer (1H : 200.13 MHz; ^{13}C : 50.32 MHz; ^{19}F : 188.31 MHz) and a Bruker AFM 400 spectrometer (1H : 400.13 MHz; ^{13}C : 100.61 MHz; ^{19}F : 376.07 MHz) by using the proton signals of the deuterated solvents for reference. Single-crystal X-ray diffraction measurements were recorded with an Oxford Diffraction Xcalibur S Sapphire spectrometer. IR spectra were recorded either with an Nicolet Series II Magna-IR-System 750 FTIR or a Perkin-Elmer Spectrum 100 FTIR instrument. UV spectra were recorded with a SPECORD® S600 instrument (Analytik Jena, Germany). Cyclic voltammetry was measured with a reference 600 system (GAMRY instruments, USA). EPR spectra were recorded at X-band with an ERS 300 spectrometer (ZWG/Magnetech Berlin/Adlershof, Germany) equipped with a fused quartz Dewar for measurements at 77 K. The g factors were calculated with respect to a Cr^{3+}/MgO reference ($g = 1.9796$). Magnetic-susceptibility data were measured from powder samples of solid material in the temperature range 2–300 K with a SQUID susceptometer with a field of 1.0 T (MPMS-7, Quantum Design, calibrated with a standard palladium reference sample, error < 2%). Multiple-field variable-temperature magnetization measurements were performed at 1, 4 and 7 T in the range 2–300 K with the magnetization equidistantly sampled on a $1/T$ temperature scale. The experimental data were corrected for underlying diamagnetism by use of tabulated Pascal's constants^[14] as well as for temperature-independent paramagnetism. The susceptibility and magnetization data were simulated with julX for exchange-coupled systems.^[15] The simulations are based on the usual spin-Hamilton operator for mononuclear complexes with spin $S = 5/2$:

$$\hat{H} = g\hat{S}\hat{B} + D[\hat{S}_z^2 - 1/3 S(S+1)] + E/D(\hat{S}_x^2 - \hat{S}_y^2)$$

where g is the average electronic g value and D and E/D are the axial zero-field splitting and rhombicity parameters, respectively. Diagonalization of the Hamiltonian was performed with the routine ZHEEV from the LAPACK Library,^[16] and the magnetic moments were obtained from a first-order numerical derivative dE/dB of the eigen values. The powder summations were performed by using a 16-point Lebedev grid.^[17] Intermolecular interactions were considered by using a Weiss temperature, Θ_w , as perturbation of the temperature scale, $kT' = k(T - \Theta_w)$ for the calculation.

Synthesis of 1-Acetyl-5-hydroxy-3,5-bis(trifluoromethyl)pyrazoline (1a): To a solution of 1,1,1,5,5,5-hexafluoropentane-2,4-dione (**8**, 55.8 mmol) in ethanol (60 mL) was added a solution of acetohydrazide (55.8 mmol) in ethanol (60 mL). After heating the mixture to reflux for 5 h, the solvent was removed in vacuo. The colourless residue was purified by recrystallization from *n*-hexane or by sublimation under high vacuum. Yield: 12.2 g (83%, colourless crystals). 1H NMR (200 MHz, $CDCl_3$, 25 °C): $\delta = 5.98$ (br. s, 1 H, OH),

3.30–3.80 (m, 2 H, CH_2), 2.29 [s, 3 H, $C(=O)CH_3$] ppm. ^{13}C NMR (50 MHz, $CDCl_3$, 25 °C): $\delta = 173.3$, 143.6 (m), 120.6 (m), 92.5 (m), 41.4 (CH_2), 22.4 ($H_3CC=O$) ppm. ^{19}F NMR (188 MHz, $CDCl_3$, 25 °C): $\delta = -67.7$, -81.4 ppm. IR (KBr): $\tilde{\nu} = 3393$ (br.), 1699 (s), 1645 (s), 1456 (s), 1427 (m), 1378 (m), 1338 (s), 1276 (s), 1198 (s), 1156 (s), 1116 (m), 1099 (m), 1068 (w), 1041 (w), 1026 (w), 996 (w), 924 (m), 875 (m), 760 (m), 734 (s), 658 (w), 621 (w), 581 (m), 521 (w), 501 (w), 474 (w) cm^{-1} . HRMS: calcd. for $C_7H_7F_6N_2O_2$ [$M + H$]⁺ 265.04117; found 265.04031.

1-Benzoyl-5-hydroxy-3,5-bis(trifluoromethyl)pyrazoline (1b): To a solution of **8** (55.8 mmol) in ethanol (60 mL) was added a solution of benzohydrazide (55.8 mmol) in ethanol (60 mL). After heating the mixture to reflux for 5 h, the solvent was removed in vacuo. The colourless residue was purified by recrystallization from ethanol/*n*-hexane (9:1). Yield: 15.9 g (87%, colourless crystals). 1H NMR (200 MHz, $CDCl_3$, 25 °C): $\delta = 7.84$ –7.92 (m, 2 H, Ar), 7.40–7.65 (m, 3 H, Ar), 6.40 (br. s, 1 H, OH), 3.00–3.66 (m 2 H, CH_2) ppm. ^{13}C NMR (50 MHz, $CDCl_3$, 25 °C): $\delta = 171.6$, 144.1, 143.7, 133.3, 131.6, 130.5, 128.3, 94.2, 93.8, 41.4 (CH_2) ppm. ^{19}F NMR (188 MHz, $CDCl_3$, 25 °C): $\delta = -67.4$, -80.5 ppm. IR (KBr): $\tilde{\nu} = 3391$ (br.), 1678 (s), 1639 (m), 1456 (m), 1439 (m), 1336 (s), 1308 (s), 1279 (s), 1175 (s), 1135 (s), 1116 (s), 1077 (s), 1027 (m), 1009 (m), 907 (w), 872 (w), 834 (w), 792 (w), 758 (w), 717 (s), 694 (m), 674 (w), 618 (w), 499 (w) cm^{-1} . HRMS: calcd. for $C_{12}H_9F_6N_2O_2$ [$M + H$]⁺ 327.05627; found 327.05569.

Synthesis of 4a: To a methanol (5.0 mL) solution of $Ni(OAc)_2$ (1.20 mmol) was added **1b** (0.92 mmol) in methanol (5.0 mL) and NH_3 (17% in water, 5.0 mL). The solution was heated to 60 °C and stirred overnight. After removal of the volatiles in vacuo, a brown solid was obtained. The residue was crystallized from ethanol. Crystals suitable for X-ray diffraction were obtained from an ethanol solution at room temperature. Yield: 0.25 g (51%, brown crystals). M.p. 192–193 °C. 1H NMR (200 MHz, $CDCl_3$, 25 °C): $\delta = 7.83$ (m, 2 H, Ar), 7.31 (m, 3 H, Ar), 5.93 (s, 1 H, CH), 1.50 (s, 3 H, NH_3) ppm. ^{13}C NMR (100.61 MHz, $CDCl_3$, 25 °C): $\delta = 171.9$, 157.2, 156.9, 143.4, 131.1, 128.8, 128.4, 91.5 ppm. ^{19}F NMR (188 MHz, C_6D_6 , 25 °C): $\delta = -65.3$, -71.8 ppm. IR (KBr): $\tilde{\nu} = 3430$ (br.), 2914 (br.), 1615 (s), 1533 (s), 1444 (m), 1363 (m), 1328 (w), 1266 (s), 1228 (s), 1195 (s), 1159 (s), 1068 (m), 1007 (m), 950 (w), 880 (w), 806 (m), 758 (w), 715 (m), 701 (w), 686 (w), 614 (w), 531 (w) cm^{-1} . HRMS: calcd. for $C_{12}H_{10}F_6N_3NiO_2$ [$M + H$]⁺ 400.00307; found 400.00305. $C_{12}H_9F_6N_3NiO_2 \cdot H_2O$ (417.9): calcd. C 34.49, H 2.65, N 10.05; found C 34.70, H 2.55, N 9.71. UV/Vis: $\lambda(\epsilon) = 367.5$ (11800), 405.0 (11600 $M^{-1}cm^{-1}$) nm.

Synthesis of 4b: To a mixture of **1b** (0.92 mmol) and DMAP (9.2 mmol) in methanol (10 mL) was added a solution of $Ni(OAc)_2$ (1.20 mmol) at room temperature. The solution was stirred overnight. After removal of the volatiles in vacuo, a brown solid was obtained. The residue was crystallized from ethanol. Crystals suitable for X-ray diffraction were obtained from ethanol solution at room temperature. Yield: 0.39 g (57%, first harvest, brown crystals). M.p. 191–192 °C. 1H , ^{13}C and ^{19}F NMR were not measured because of paramagnetism. IR (KBr): $\tilde{\nu} = 3433$ (br.), 2921 (br.), 1615 (s), 1533 (s), 1444 (m), 1363 (m), 1328 (w), 1266 (s), 1228 (s), 1196 (s), 1159 (s), 1068 (m), 1007 (m), 950 (w), 880 (w), 806 (m), 759 (w), 715 (m), 701 (w), 685 (w), 646 (w), 613 (w), 585 (w), 531 (w) cm^{-1} . HRMS: calcd. for $C_{33}H_{36}F_6N_8NiO_2$ [$M + H - 2 dmap$]⁺ 505.06092; found 505.05975. $C_{33}H_{36}F_6N_8NiO_2$ (749.40): calcd. C 52.89, H 4.84, N 14.95; found C 53.66, H 4.94, N 15.11. UV/Vis: $\lambda(\epsilon) = 360.5$ (2200), 405.5 (1800 $M^{-1}cm^{-1}$) nm.

Synthesis of 4c: To a mixture of **1a** (0.37 mmol) and DMAP (3.70 mmol) in methanol (5 mL) was added a solution of Ni -

(OAc)₂ (0.48 mmol) at room temperature. The solution was stirred overnight. After removing the volatiles in vacuo, a brown solid was obtained. Crystals suitable for X-ray diffraction were obtained from ethanol solution at room temperature. Yield: 0.14 g (55%, brown crystals from ethanol). M.p. 205–206 °C. ¹H, ¹³C and ¹⁹F NMR were not measured because of paramagnetism. IR (KBr): $\tilde{\nu}$ = 3438 (br.), 2921 (br.), 1617 (s), 1532 (s), 1446 (m), 1428 (w), 1388 (s), 1324 (m), 1265 (s), 1227 (s), 1182 (s), 1169 (s), 1159 (s), 1138 (s), 1108 (s), 1069 (w), 1054 (m), 1014 (m), 1006 (s), 982 (w), 951 (w), 906 (w), 828 (w), 807 (s), 768 (m), 759 (m), 742 (w), 683 (m), 641 (w), 607 (w), 581 (w), 531 (m), 483 (w) cm⁻¹. HRMS: calcd. for C₂₈H₃₅F₆N₈NiO₂ [M + H – 2 dmap]⁺ 443.04527; found 443.04435. C₂₈H₃₄F₆N₈NiO₂ (687.33): calcd. C 48.93, H 4.99, N 16.30; found C 49.47, H 5.01, N 16.36. UV/Vis: λ (ε) = 334.5 (5900), 368.0 (5900 m⁻¹ cm⁻¹) nm.

General Procedure for the Catalytic C–C Coupling Reaction: A Schlenk flask was charged with an appropriate amount of **4** (0.014 mmol, 2.0 mol-%) and the corresponding bromo- or iodo-arene (0.67 mmol). The flask was repeatedly flushed with nitrogen and evacuated. THF (2.0 mL) was added followed by benzylzinc bromide (1.00 mmol, 0.5 M in THF). The flask was sealed and heated at 70 °C for 24 h. The mixture was cooled in an ice bath, and dichloromethane and water were added. The aqueous layer was extracted with dichloromethane, and the collected organic layers were washed with water, brine and dried with Na₂SO₄. After filtration and removal of the solvent, the residue was dissolved in diethyl ether and purified by filtration through a short plug of silica gel. The analytical properties of the products are in agreement with literature data.

1-Benzyl-4-methoxybenzene (9a): ¹H NMR (200 MHz, CDCl₃): δ = 6.85–7.49 (m, 9 H), 4.06 (s, 2 H, CH₂), 3.86 (s, 3 H, CH₃) ppm.

¹³C NMR (50 MHz, CDCl₃): δ = 159.7, 143.1, 141.5, 129.9, 129.6, 129.0, 126.4, 121.9, 115.4, 112.0, 55.3, 42.0 ppm. MS (ESI): *m/z* (%) = 198 (100) [M]⁺, 183 (16), 167 (36), 153 (13), 121 (28), 91 (12).

1-Benzyl-4-methylbenzene (12a):^[18] ¹H NMR (200 MHz, CDCl₃): δ = 7.06–7.31 (m, 9 H), 3.98 (s, 2 H, CH₂), 2.36 (s, 3 H, CH₃) ppm. ¹³C NMR (50 MHz, CDCl₃): δ = 141.5, 138.2, 135.6, 129.3, 129.0, 128.9, 128.8, 128.5, 128.4, 126.1, 41.6, 21.1 ppm. MS (ESI): *m/z* (%) = 182 (75) [M]⁺, 167 (100), 152 (14), 89 (14).

Diphenylmethane (13a):^[19] ¹H NMR (200 MHz, CDCl₃): δ = 7.10–7.37 (m, 10 H), 3.95 (s, 2 H, CH₂) ppm. ¹³C NMR (50 MHz, CDCl₃): δ = 141.1, 128.9, 128.5, 126.1, 41.6 ppm. MS (ESI): *m/z* (%) = 168 (100) [M]⁺, 153 (25), 91 (22), 83 (13), 65 (14).

1-Benzyl-3-methoxybenzene (15a):^[20] ¹H NMR (200 MHz, CDCl₃): δ = 6.85–7.49 (m, 9 H), 4.06 (s, 2 H, CH₂), 3.86 (s, 3 H, CH₃) ppm. ¹³C NMR (50 MHz, CDCl₃): δ = 159.7, 143.1, 141.5, 129.9, 129.6, 129.0, 126.4, 121.9, 115.4, 112.0, 55.3, 42.0 ppm. MS (ESI): *m/z* (%) = 198 (100) [M]⁺, 183 (20), 167 (40), 152 (15), 121 (12), 91 (19).

1-Benzyl-4-(trifluoromethyl)benzene (17a):^[21] ¹H NMR (400 MHz, CDCl₃): δ = 7.58 (d, *J* = 8.1 Hz, 2 H), 7.04–7.29 (m, 7 H), 4.07 (s, 2 H) ppm. ¹³C NMR (100 MHz, CDCl₃): δ = 145.3, 140.0, 129.2, 128.9, 128.7, 127.0, 126.5, 125.4, 41.7 ppm. ¹⁹F NMR (377 MHz, CDCl₃): δ = –62.7 ppm. MS (ESI): *m/z* (%) = 236 (55) [M]⁺, 217 (7), 215 (10), 168 (11), 167 (100), 166 (18), 165 (40), 152 (12).

2-Benzyl-5-methylpyridine (18a): ¹H NMR (200 MHz, CDCl₃): δ = 8.88 (s, 1 H), 7.04–7.29 (m, 7 H), 4.49 (s, 2 H), 2.33 (s, 3 H) ppm. ¹³C NMR (50 MHz, CDCl₃): δ = 157.3, 147.7, 141.5, 137.2, 132.9, 129.4, 128.8, 128.4, 128.3, 42.2, 18.1 ppm. MS (ESI): *m/z* (%) = 182 (100) [M]⁺, 167 (15), 40 (42).

Table 5. Data collection and refinement parameters for **4a**, **4b** and **4c**.

	4a	4b	4c
Empirical formula	C ₁₂ H ₉ F ₆ N ₃ NiO ₂	C ₃₄ H ₃₇ Cl ₃ F ₆ N ₈ NiO ₂	C ₂₈ H ₃₄ F ₆ N ₈ NiO ₂
Formula mass [g/mol]	399.93	868.78	687.34
Temperature [K]	150(2)	150(2)	150(2)
Space group	C2/c	P2 ₁ /c	P3 ₂ 21
Unit-cell dimensions:			
<i>a</i> [Å]	20.259(3)	17.6376(11)	18.3746(4)
<i>b</i> [Å]	8.6098(10)	12.1712(8)	18.3746(4)
<i>c</i> [Å]	16.506(2)	19.2313(11)	15.8986(4)
α [°]	90	90	90
β [°]	97.916(13)	110.364(7)	90
γ [°]	90	90	120
Volume [Å ³]	2851.6(6)	3870.4(4)	4648.63(18)
<i>Z</i>	8	4	6
<i>D</i> _{calcd.} [g/cm ³]	1.863	1.491	1.473
<i>F</i> (000)	1600	1784	2136
Crystal size [mm]	0.34 × 0.17 × 0.04	0.41 × 0.18 × 0.17	0.68 × 0.26 × 0.20
θ range [°]	3.42–25.00	3.37–25.00	3.39–25.00
Index ranges	–24 ≤ <i>h</i> ≤ 23 –9 ≤ <i>k</i> ≤ 10 –19 ≤ <i>l</i> ≤ 18	–20 ≤ <i>h</i> ≤ 20 –14 ≤ <i>k</i> ≤ 13 –22 ≤ <i>l</i> ≤ 22	–20 ≤ <i>h</i> ≤ 21 –21 ≤ <i>k</i> ≤ 19 –18 ≤ <i>l</i> ≤ 16
Reflections collected	5643	16500	32336
Independent reflections	2509 [<i>R</i> (int) = 0.0808]	6805 [<i>R</i> (int) = 0.0601]	5436 [<i>R</i> (int) = 0.0391]
Completeness to θ = 25.00°	99.8%	99.8%	99.7%
Relative transmission factors	0.9445, 0.6395	0.8788, 0.7403	0.8722, 0.6465
Parameters	218	530	468
GOF	0.708	0.920	0.987
Final <i>R</i> indices [<i>I</i> > 2σ(<i>I</i>)] ^[a,b]	<i>R</i> ₁ = 0.0468, <i>wR</i> ₂ = 0.0492	<i>R</i> ₁ = 0.0520, <i>wR</i> ₂ = 0.0915	<i>R</i> ₁ = 0.0280, <i>wR</i> ₂ = 0.0529
<i>R</i> indices (all data) ^[a,b]	<i>R</i> ₁ = 0.1201, <i>wR</i> ₂ = 0.0597	<i>R</i> ₁ = 0.0999, <i>wR</i> ₂ = 0.0992	<i>R</i> ₁ = 0.0343, <i>wR</i> ₂ = 0.0540

[a] *R*₁ = Σ||*F*_o| – |*F*_c||/Σ|*F*_o|, [b] *wR*₂ = {Σ[(*F*_o² – *F*_c²)²]/Σ[*w*(*F*_o²)]}^{1/2}.

1-Benzyl-4-fluorobenzene (19a):^[22] ¹H NMR (400 MHz, CDCl₃): δ = 7.12–7.30 (m, 9 H), 4.69 (s, 2 H) ppm. ¹³C NMR (100 MHz, CDCl₃): δ = 161.4, 140.9, 136.7, 130.3, 128.8, 128.5, 126.2, 115.2 ppm. ¹⁹F NMR (377 MHz, CDCl₃): δ = –117.3 ppm. MS (ESI): *m/z* (%) = 186 (100) [M]⁺, 171 (9), 165 (28), 109 (18), 91 (14).

Single-Crystal X-ray Structure Determination:^[23] Crystals were mounted on a glass capillary in perfluorinated oil and measured in a cold N₂ flow. The data were collected by using an Oxford Diffraction Xcalibur S Sapphire at 150(2) K (Mo-*K*_α radiation, λ = 0.71073 Å). The structures were solved by direct methods and refined on *F*² with the SHELX-97 software package. The positions of the hydrogen atoms were calculated and considered isotropically according to a riding model (Table 5). CCDC-843194 (for **4a**), -843195 (for **4b**) and -843196 (for **4c**) contain the supplementary crystallographic data for this paper. These data can be obtained free of charge from The Cambridge Crystallographic Data Centre via www.ccdc.cam.ac.uk/data_request/cif.

Acknowledgments

Financial support from the Cluster of Excellence “Unifying Concepts in Catalysis” (EXC 314/1; www.unicat.tu-berlin.de; funded by the Deutsche Forschungsgemeinschaft and administered by the Technische Universität Berlin) is gratefully acknowledged. The authors thank Dr. Eckhard Bill (Max Planck Institute for Bioinorganic Chemistry, Mülheim an der Ruhr, Germany) for SQUID measurements and discussions and Dr. Kallol Ray and Subrata Kundu (Humboldt University, Berlin, Germany) for the EPR measurements. C. I. S. thanks the Berlin International Graduate School of Natural Sciences and Engineering (BIG-NSE) for ideational support. S. I. thanks the Japan Society for the Promotion of Science (JSPS) and the Alexander von Humboldt Stiftung for financial support.

- [1] E. J. Corey, X. M. Cheng, *The Logic of Chemical Synthesis*, John Wiley & Sons, New York, **1989**, pp. 1–91.
- [2] a) A. Suzuki, *Angew. Chem.* **2011**, *123*, 6854–6869; *Angew. Chem. Int. Ed.* **2011**, *50*, 6722–6737; b) E. Negishi, *Angew. Chem.* **2011**, *123*, 6870–6897; *Angew. Chem. Int. Ed.* **2011**, *50*, 6738–6764; c) A. de Meijere, F. Diederich (Eds.), *Metal-Catalyzed Cross-Coupling Reactions*, 2nd completely revised and enlarged ed., Wiley-VCH, Weinheim, Germany, **2004**; d) E. Negishi (Ed.), *Handbook of Organopalladium Chemistry for Organic Synthesis*, Wiley-Interscience New York, **2002**; e) F. Diederich, P. J. Stang (Eds.), *Metal-Catalyzed Cross-Coupling Reactions*, Wiley-VCH, Weinheim, Germany, **1998**.
- [3] a) R. Jana, T. P. Pathak, M. S. Sigman, *Chem. Rev.* **2011**, *111*, 1417–1492; b) X. Hu, *Chem. Sci.* **2011**, *2*, 1867–1886.
- [4] I. Rilatt, R. F. W. Jackson, *J. Org. Chem.* **2008**, *73*, 8694–8704.
- [5] A selection: a) D. J. Cárdenas, *Angew. Chem.* **1999**, *111*, 3201–3203; *Angew. Chem. Int. Ed.* **1999**, *38*, 3018–3020; b) M. R. Netherton, G. C. Fu, *Adv. Synth. Catal.* **2004**, *346*, 1525–1532; c) A. C. Frisch, M. Beller, *Angew. Chem.* **2005**, *117*, 680–695; *Angew. Chem. Int. Ed.* **2005**, *44*, 674–688; d) A. Rudolph, M. Lautens, *Angew. Chem.* **2009**, *121*, 2694–2708; *Angew. Chem. Int. Ed.* **2009**, *48*, 2656–2670; e) B. D. Sherry, A. Fürstner, *Acc. Chem. Res.* **2008**, *41*, 1500–1511; f) D. J. Cárdenas, *Angew. Chem.* **2003**, *115*, 398; *Angew. Chem. Int. Ed.* **2003**, *42*, 384–387; g) F. Glorius, *Angew. Chem.* **2008**, *120*, 8474–8476; *Angew. Chem. Int. Ed.* **2008**, *47*, 8347–8349; h) V. B. Phapale, D. J. Cárdenas, *Chem. Soc. Rev.* **2009**, *38*, 1598–1607.
- [6] See, for instance: a) J. S. Zhou, G. C. Fu, *J. Am. Chem. Soc.* **2003**, *125*, 14726–14727; b) V. B. Phapale, E. Buñuel, M. García-Iglesias, D. J. Cárdenas, *Angew. Chem.* **2007**, *119*, 8946–8951; *Angew. Chem. Int. Ed.* **2007**, *46*, 8790–8795; c) S. W. Smith, G. C. Fu, *Angew. Chem.* **2008**, *120*, 9474–9476; *Angew. Chem. Int. Ed.* **2008**, *47*, 9334–9336; d) G. D. Jones, J. L. Martin, C. McFarland, O. R. Allen, R. E. Hall, A. D. Haley, R. J. Brandon, T. Konovalova, P. J. Desrochers, P. Pulay, D. A. Vicić, *J. Am. Chem. Soc.* **2006**, *128*, 13175–13183.
- [7] See, for instance: a) A. L. Gavrilova, B. Bosnich, *Chem. Rev.* **2004**, *104*, 349–384; b) P. J. Steel, *Acc. Chem. Res.* **2005**, *38*, 243–250; c) R. D. Hancock, A. E. Martell, *Chem. Rev.* **1989**, *89*, 1875–1914; d) M. Miura, *Angew. Chem.* **2004**, *116*, 2251–2253; *Angew. Chem. Int. Ed.* **2004**, *43*, 2201–2203; e) A. S. Borovik, *Acc. Chem. Res.* **2005**, *38*, 54–61.
- [8] C. I. Someya, S. Inoue, E. Irran, S. Krackl, S. Enthaler, *Eur. J. Inorg. Chem.* **2011**, 2691–2697.
- [9] K. C. Joshi, R. Bohra, B. S. Joshi, *Inorg. Chem.* **1992**, *31*, 598–603.
- [10] a) L. Sacconi, *Z. Anorg. Allg. Chem.* **1954**, *275*, 249–256; b) K. N. Zelenin, M. Y. Malov, I. V. Zerova, P. B. Terent'ev, A. G. Kalandarishvili, *Khim. Geterotsikl. Soedin.* **1987**, *1210*–1218; c) K. N. Zelenin, M. Y. Malov, I. P. Bezhan, V. A. Khrustalev, S. I. Yakimovich, *Khim. Geterotsikl. Soedin.* **1985**, 1000–1001; d) M. Y. Malov, K. N. Zelenin, S. I. Yakimovich, *Khim. Geterotsikl. Soedin.* **1988**, 1358–1361; e) A. Y. Ershov, *Zh. Org. Khim.* **1995**, *31*, 1057–1059; f) S. I. Yakimovich, I. V. Zerova, *Zh. Org. Khim.* **1987**, *23*, 1433–1440; g) V. G. Yusupov, S. I. Yakimovich, S. D. Nasirdinov, N. A. Parpiev, *Zh. Org. Khim.* **1980**, *16*, 415–420.
- [11] a) L. Sacconi, P. Paoletti, F. Maggio, *J. Am. Chem. Soc.* **1957**, *79*, 4067–4069; b) A. Mukhopadhyay, S. Pal, *Polyhedron* **2004**, *23*, 1997–2004; c) P. Sathyadevi, P. Krishnamoorthy, R. R. Buttorac, A. H. Cowley, N. S. P. Bhuvanesh, N. Dharmaraj, *Dalton Trans.* **2011**, *40*, 9690–9702.
- [12] R. J. Pilbrow, *Transition Ion Electron Paramagnetic Resonance*, Clarendon Press, Oxford, **1990**.
- [13] a) M. J. Frisch, G. W. Trucks, H. B. Schlegel, G. E. Scuseria, M. A. Robb, J. R. Cheeseman, J. A. Montgomery Jr., T. Vreven, K. N. Kudin, J. C. Burant, J. M. Millam, S. S. Iyengar, J. Tomasi, V. Barone, B. Mennucci, M. Cossi, G. Scalmani, N. Rega, G. A. Petersson, H. Nakatsuji, M. Hada, M. Ehara, K. Toyota, R. Fukuda, J. Hasegawa, M. Ishida, T. Nakajima, Y. Honda, O. Kitao, H. Nakai, M. Klene, X. Li, J. E. Knox, H. P. Hratchian, J. B. Cross, V. Bakken, C. Adamo, J. Jaramillo, R. Gomperts, R. E. Stratmann, O. Yazyev, A. J. Austin, R. Cammi, C. Pomelli, J. W. Ochterski, P. Y. Ayala, K. Morokuma, G. A. Voth, P. Salvador, J. J. Dannenberg, V. G. Zakrzewski, S. Dapprich, A. D. Daniels, M. C. Strain, O. Farkas, D. K. Malick, A. D. Rabuck, K. Raghavachari, J. B. Foresman, J. V. Ortiz, Q. Cui, A. G. Baboul, S. Clifford, J. Cioslowski, B. B. Stefanov, G. Liu, A. Liashenko, P. Piskorz, I. Komaromi, R. L. Martin, D. J. Fox, T. Keith, M. A. Al-Laham, C. Y. Peng, A. Nanayakkara, M. Challacombe, P. M. W. Gill, B. Johnson, W. Chen, M. W. Wong, C. Gonzalez, J. A. Pople, *Gaussian 03*, Revision E.01, Gaussian, Inc., Wallingford, CT, **2004**; b) A. D. Becke, *J. Chem. Phys.* **1993**, *98*, 5648–5652; c) C. Lee, W. Yang, R. G. Parr, *Phys. Rev. B* **1988**, *37*, 785–789; d) B. Miehlich, A. Savin, H. Stoll, H. Preuss, *Chem. Phys. Lett.* **1989**, *157*, 200–206.
- [14] a) C. J. O'Connor, *Prog. Inorg. Chem.* **1982**, *29*, 203–283; b) R. C. Weast, M. J. Astle, *CRC Handbook of Chemistry and Physics*, CRC Press Inc., Boca Raton, **1979**.
- [15] E. Bill, http://ewww.mpi-muelheim.mpg.de/bac/logins/bill/julX_en.php.
- [16] The LAPACK Linear Algebra Package is written in Fortran77 and provides routines for solving systems of simultaneous linear equations, least-squares solutions of linear systems of equations, eigenvalue problems and singular value problems. The routines are available at <http://www.netlib.org/lapack/>.

- [17] a) V. I. Lebedev, D. N. Laikov, *Dokl. Math.* **1999**, 59, 477; b) a Fortran code to generate Lebedev grids up to the order $L = 131$ is available at <http://server.ccl.net/cca/software/SOURCES/>.
- [18] G. Sun, Z. Wang, *Tetrahedron Lett.* **2008**, 49, 4929–4932.
- [19] E. Alacid, C. Nájera, *Org. Lett.* **2008**, 10, 5011–5014.
- [20] N. Henry, C. Enguehard-Gueiffier, I. Thery, A. Gueiffier, *Eur. J. Org. Chem.* **2008**, 4824–4827.
- [21] M. Amatore, C. Gosmini, *Chem. Commun.* **2008**, 5019–5021.
- [22] M. J. Burns, I. J. S. Fairlamb, A. R. Kapdi, P. Schnal, R. J. K. Taylor, *Org. Lett.* **2007**, 9, 5397–5400.
- [23] G. M. Sheldrick, *SHELXL93, Program for the Refinement of Crystal Structures*, University of Göttingen, Göttingen, Germany, **1997**.

Received: November 9, 2011

Published Online: February 7, 2012

Isolation of a New C_s -Symmetrized $Mo_3(\mu_3-S)(\mu-S)(\mu-S_2)_2$ Structural Type Through Complementary Association with a Cubane-Type Mo_3NiS_4 Cluster

Rita Hernandez-Molina,^{*[a]} Javier Gonzalez-Platas,^[b] and Cristian Vicent^[c]

Keywords: Cluster compounds / Nickel / Molybdenum / Chalcogens

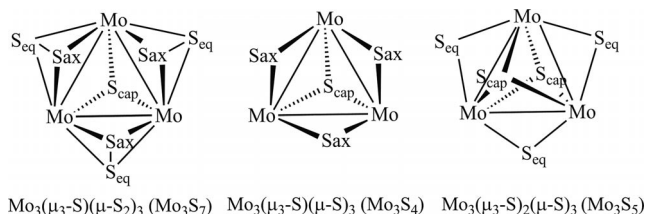
A new cluster of formula $\{[Mo_3(\mu_3-S)(\mu-S)(\mu-S_2)_2(dtp)_3(\mu-OAc)][Mo_3NiS_4(dtp)_3(\mu-OAc)(CH_3CN)]\}$ (**1**; dtp = diethyl dithiophosphate; OAc = acetate) comprising the novel C_s -symmetrized $Mo_3(\mu_3-S)(\mu-S)(\mu-S_2)_2$ structural type covalently attached to a cubane-type Mo_3NiS_4 core has been isolated and fully characterized. The reaction of a 2 M HCl solution of $[Mo_3S_4(H_2O)_9]^{4+}$ with an excess of potassium diethyl dithiophosphate and acetic acid in the presence of the $[Mo_3(NiCl)_4S_4(H_2O)_9]^{3+}$ cluster afforded a mixture of products encompassing different Mo_3S_x ($x = 4-7$) cluster cores from which the $Mo_3(\mu_3-S)(\mu-S)(\mu-S_2)_2$ structural type has been iso-

lated in analytically pure form as a Mo_3NiS_4 adduct. The robustness of the aggregate **1** was also retained in solution as judged by ESI-MS and ^{31}P NMR techniques. Single-crystal X-ray analysis revealed in detail the complementary association of the newly formed $Mo_3(\mu_3-S)(\mu-S)(\mu-S_2)_2$ entity and the Mo_3NiS_4 cluster in which $\mu-S$ sulfide ligands and $\mu-S_2$ disulfide ligands act as nucleophilic and electrophilic functional groups, respectively, towards the Mo_3NiS_4 cube through directional Ni-S covalent bonds and short S...S contacts (below 3.3 Å).

Introduction

Trinuclear molybdenum sulfides, in which the metal atoms adopt a triangular disposition, represent a family of inorganic compounds with applications in multidisciplinary fields, for example, as precursors of cubane-type industrial and biological catalysts,^[1,2] building blocks of cluster-based polymers,^[3] molecular conductors,^[4] and nonlinear optical materials.^[5] This class of Mo_3 clusters can be classified according to the number of capping and bridging ligands and in all cases they are C_3 -symmetrized. The structural types that dominate this chemistry are those formulated as $Mo_3(\mu_3-S)(\mu-S_2)_3$ (or hereafter Mo_3S_7) and $Mo_3(\mu_3-S)(\mu-S)_3$ (or hereafter Mo_3S_4), as depicted in Scheme 1.

For Mo_3S_7 , in addition to the S_{cap} sulfur atom connecting the Mo_3 triangle, each side of the triangle is bridged by a $\mu-S_2$ group with three sulfur atoms occupying an equatorial position (S_{eq}) essentially in the Mo_3 plane along with axial sulfur atoms (S_{ax}) located out of the trimetallic plane and pointing away from the S_{cap} . In Mo_3S_4 compounds, metal atoms are bridged by $\mu-S$ ligands located in axial positions. This geometric difference is not only structural, but



Scheme 1.

also electronic because sulfur atoms in axial positions in Mo_3S_7 complexes are electrophilic and display a strong tendency to bind anions^[6] whereas $\mu-S_{ax}$ ligands in Mo_3S_4 complexes are considered versatile nucleophiles and bind with transition and noble metals by sulfur-bridging coordination to yield cubane-type complexes.^[2,7] A few examples of a third structural type, namely $Mo_3(\mu_3-S)_2(\mu-S)_3$, have been found for molybdenum trinuclear sulfides (see Scheme 1, right) and feature two capping sulfide ligands and three $\mu-S$ ligands in the equatorial plane.^[8,9]

Interconversion between these three structural types depicted in Scheme 1 is well documented. For example, Mo_3S_4 clusters bearing diphosphane ligands can be transformed into Mo_3S_5 by reaction with an excess of $PhSnA$,^[9] Mo_3S_7 clusters produce Mo_3S_4 in solution by equatorial sulfur abstraction using cyanide,^[10] H_3PO_2 ,^[11] or PPh_3 ,^[12] and Mo_3S_4 can be reversibly transformed into Mo_3S_7 by reaction with sulfurizing reagents such as elemental sulfur.^[13] However, trinuclear Mo_3 species with sulfur contents different to those depicted in Scheme 1 remain unknown even though their putative formation has been proposed, for ex-

[a] Dpto de Química Inorgánica, Facultad de Química, Universidad de La Laguna, 38200 La Laguna, Tenerife, Spain
Fax: +34-922315461
E-mail: rrhernan@ull.es

[b] Dpto Física Fundamental II, Servicio Integrado de Difracción de Rayos X, Universidad de La Laguna, 38200 La Laguna, Tenerife, Spain

[c] Serveis Centrals d'Instrumentació Científica, Universitat Jaume I, Avda. Sos Baynat s/n, 12071 Castelló, Spain

Supporting information for this article is available on the WWW under <http://dx.doi.org/10.1002/ejic.201101326>.

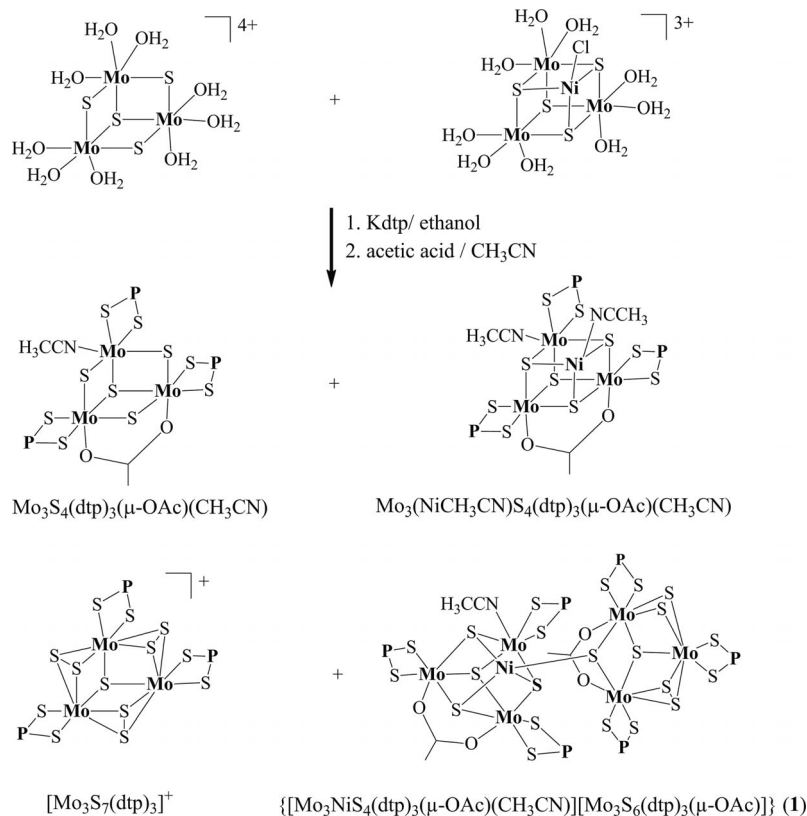
ample, during the sulfurization or desulfurization reactions of Mo_3S_4 and Mo_3S_7 cluster cores, respectively. Gas-phase mass spectrometric methods have recently revealed the existence of intermediate sulfur-rich Mo_3 species with unusual $\text{Mo}_3(\mu_3\text{-S})(\mu\text{-S})_2(\mu\text{-S}_2)$ cores.^[14] A number of Mo_3S_9 isomeric clusters with different sulfur-bridged ligands have been invoked in relation to catalytic MoS_x -based hydrodesulfurization reactions, this Mo_3S_9 unit being a widely accepted model that reproduces the periodicity of the bulk MoS_x catalyst.^[15]

In this paper we report the isolation and complete characterization of an unprecedented structural type, namely $\text{Mo}_3(\mu_3\text{-S})(\mu\text{-S})(\mu\text{-S}_2)_2$ (Mo_3S_6), a missing link between the Mo_3S_7 and Mo_3S_4 cluster types. The Mo_3S_6 cluster features the trinuclear Mo_3 cluster core, one capping sulfur atom, two disulfur bridging ligands, and one sulfur bridging ligand in a C_s -symmetrized environment. The key step in the isolation of this structural type is the complementary association with a Mo_3NiS_4 cuboidal cluster leading to the complex formulated as $\{[\text{Mo}_3\text{S}_6(\text{dtp})_3(\mu\text{-OAc})][\text{Mo}_3\text{NiS}_4(\text{dtp})_3(\mu\text{-OAc})(\text{CH}_3\text{CN})]\}$ (**1**), stable both in solution and in the solid state. Examples of incomplete cuboidal Mo_3S_4 cluster complementarity have recently been reported based on hydrogen-bonding interactions. For example, the C_3 symmetry of $[\text{Mo}_3\text{S}_4(\text{Hnta})_9]^{2-}$ (nta = nitrilotriacetate) has been exploited to act as a structuring agent or template for the self-condensation of the $[\text{Mo}_2\text{O}_2\text{S}_2(\text{H}_2\text{O})_4]^{2+}$ dication leading to Mo_{18} (Mo_2 -based) metallamacrocycles.^[16] The $[\text{Mo}_3\text{S}_4\text{-(H}_2\text{O)}_9]^{4+}$

cation is also a suitable species to form complementary hydrogen bonding with the highly symmetrical family of cucurbit[*n*]urils or to be incorporated into the trivacant $[\text{AsW}_9\text{O}_{33}]^{9-}$ ion.^[17] The association between Mo_3S_6 and Mo_3NiS_4 observed in **1** represents the first example of Mo_3 -based complementarity sustained by directional metal–sulfur and sulfur–sulfur interactions.

Results and Discussion

The trinuclear aqua $[\text{Mo}_3\text{S}_4(\text{H}_2\text{O})_9]^{4+}$ cation is one of the derivatives most widely investigated for accessing Mo_3S_4 chemistry mainly because it serves as a precursor to a wide variety of heterobimetallic aqua $[\text{Mo}_3(\text{M}'\text{H}_2\text{O})\text{S}_4(\text{H}_2\text{O})_9]^{4+}$ cations. However, the stability of the aqua $[\text{Mo}_3\text{S}_4\text{-(H}_2\text{O)}_9]^{4+}$ cation (and their heterobimetallic homologues) is restricted to acidic media, which makes their isolation and characterization difficult. Several protocols, including the judicious choice of counterions such as *p*-toluenesulfonate,^[18,19] for the derivatization by substitution of water molecules with a variety of ligands such as acetylacetonate,^[20] cyano,^[10] thiocyanate,^[21,22] or alkyl dithiophosphates,^[22] or for the formation of supramolecular compounds with cucurbit[*n*]urils,^[23] have allowed the crystallization and further characterization of this class of compounds. During our studies on ligand substitution reactions at the Mo sites in the aqua $[\text{Mo}_3\text{S}_4(\text{H}_2\text{O})_9]^{4+}$ cation we used



Scheme 2. Schematic representation of the products formed by addition of potassium diethyl dithiophosphate (dtp) to $[\text{Mo}_3\text{S}_4(\text{H}_2\text{O})_9]^{4+}$ in the presence of the cubane-type $[\text{Mo}_3\text{NiS}_4(\text{H}_2\text{O})_{10}]^{3+}$ cation. The ethoxy groups of the dtp ligands have been omitted for clarity.

a general protocol that comprises the derivatization of the $[\text{Mo}_3\text{S}_4(\text{H}_2\text{O})_9]^{4+}$ aqua ion by substitution of water molecules by diethyl dithiophosphate/acetate to facilitate the isolation and characterization of the resulting compounds.^[24] Unexpectedly, the reaction of an excess of potassium diethyl dithiophosphate with $[\text{Mo}_3\text{S}_4(\text{H}_2\text{O})_9]^{4+}$ in the presence of the cubane-type $[\text{Mo}_3\text{NiS}_4(\text{H}_2\text{O})_{10}]^{4+}$ cation yielded a brown solid that was redissolved in acetonitrile/acetic acid mixtures and from which, after slow evaporation of the solvent at room temperature, a first brown crop of crystals was obtained. A number of products (see Scheme 2), some of them previously reported, were obtained, as judged by both ^{31}P NMR and electrospray ionization mass spectrometry.

The products $[\text{Mo}_3\text{S}_4(\text{dtp})_3(\mu\text{-OAc})(\text{CH}_3\text{CN})]$ and $[\text{Mo}_3(\text{NiCH}_3\text{CN})\text{S}_4(\text{dtp})_3(\mu\text{-OAc})(\text{CH}_3\text{CN})]$ (see Scheme 2) result essentially from the substitution of water by dtp/carboxylate starting from $[\text{Mo}_3\text{S}_4(\text{H}_2\text{O})_9]^{4+}$ and $[\text{Mo}_3(\text{NiCl})\text{S}_4(\text{H}_2\text{O})_9]^{3+}$, respectively. The original synthetic protocol can be found elsewhere.^[24] $[\text{Mo}_3\text{S}_7(\text{dtp})_3]^+$ (see Scheme 2) was also present in the reaction mixture and its formation can be explained by the ability of the dtp ligand to act as a sulfurizing reagent to promote the transformation of Mo_3S_4 to Mo_3S_7 .^[25] A new compound, namely **1**, featuring fused Mo_3NiS_4 and Mo_3S_6 cluster types was initially detected by ESI mass spectrometry as a prominent single-charged peak centered at $m/z = 2126.0$ in the $m/z = 2000\text{--}2200$ range. This compound was isolated in analytically pure form by slow evaporation of an acetonitrile solution containing species depicted in Scheme 2, most likely facilitated by their distinctive solubility, which causes the preferential crystallization of **1**. Its crystal structure was determined by X-ray diffraction. An ORTEP representation is presented in Figure 1.

Compound **1** is a rare example in which two structural cluster motifs, namely Mo_3NiS_4 and the unprecedented Mo_3S_6 , are covalently linked to each other. Its geometric characteristics are described separately for the two cluster types and the main geometric data are shown in Table 1.

The arrangement of metal atoms in the Mo_3NiS_4 cube is identical to the arrangements in heterobimetallic Mo/S/Ni cubane-type structures featuring cyclopentadienyl,^[26,27] diphosphane,^[28] aqua,^[29,30] or diethyl dithiophosphate/carboxylate ligands.^[24] The Mo–Mo (unbridged) bond distances

Table 1. Selected bond lengths [Å] for compound **1**.

Mo1–Mo2	2.7404(9)	Mo3–S13	2.595(2)
Mo1–Mo3	2.8433(8)	Mo3–S4	2.4085(17)
Mo2–Mo3	2.7352(8)	Mo3–S6	2.407(2)
Mo4–Mo5	2.8014(8)	Mo3–S7	2.478(2)
Mo4–Mo6	2.6988(8)	Mo4–S14	2.3246(19)
Mo5–Mo6	2.7816(8)	Mo4–S15	2.3352(19)
Mo4–Ni1	2.7011(12)	Mo4–S17	2.3489(19)
Mo5–Ni1	2.6007(12)	Mo4–S18	2.569(2)
Mo6–Ni1	2.7586(12)	Mo4–S19	2.536(2)
Mo1–S1	2.3679(19)	Mo5–S14	2.3337(18)
Mo1–S2	2.4085(19)	Mo5–S15	2.3294(17)
Mo1–S3	2.493(2)	Mo5–S16	2.3241(18)
Mo1–S4	2.4017(17)	Mo5–S20	2.593(2)
Mo1–S8	2.549(2)	Mo5–S21	2.589(2)
Mo1–S9	2.599(2)	Mo6–S15	2.3417(18)
Mo2–S1	2.381(2)	Mo6–S16	2.3134(18)
Mo2–S10	2.546(3)	Mo6–S17	2.3539(19)
Mo2–S11	2.507(2)	Mo6–S22	2.547(2)
Mo2–S2	2.4001(18)	Mo6–S23	2.567(2)
Mo2–S3	2.460(2)	Ni1–S4	2.2397(19)
Mo2–S6	2.399(2)	Ni1–S14	2.177(2)
Mo2–S7	2.461(2)	Ni1–S16	2.218(2)
Mo3–S1	2.3733(19)	Ni1–S17	2.208(2)
Mo3–S12	2.553(2)		

are also typical of the $\text{Mo}_3\text{S}_4^{4+}$ clusters^[19,27,29,31] bearing diethyl dithiophosphate/carboxylate ligands in which the incorporation of Ni somewhat lengthens the Mo–Mo bonds with respect to its trinuclear homologue $[\text{Mo}_3\text{S}_4(\text{dtp})(\mu\text{-OAc})(\text{CH}_3\text{CN})]$, but the strong overall asymmetry of the Mo_3 face persists (see Table S1) due to the carboxylate bridge. Two of the Mo atoms [Mo(4) and Mo(6)] of the cube are coordinated by one diethyl dithiophosphate ligand and the other coordination position is occupied by an oxygen of the acetate, which acts as a bridge between these two molybdenum atoms (Mo–O 2.20 Å). The other Mo [Mo(5)] is coordinated by one diethyl dithiophosphate and by one molecule of acetonitrile (Mo–N 2.22 Å). Three bridging sulfur atoms and a sulfur ligand from the Mo_3S_6 moiety define the tetrahedral environment of the nickel.

As far as the geometric characteristics of the Mo_3S_6 subunit are concerned, the cluster anion contains a Mo_3 triangle capped by a $\mu_3\text{-S}$ atom that lies above the Mo_3 plane.

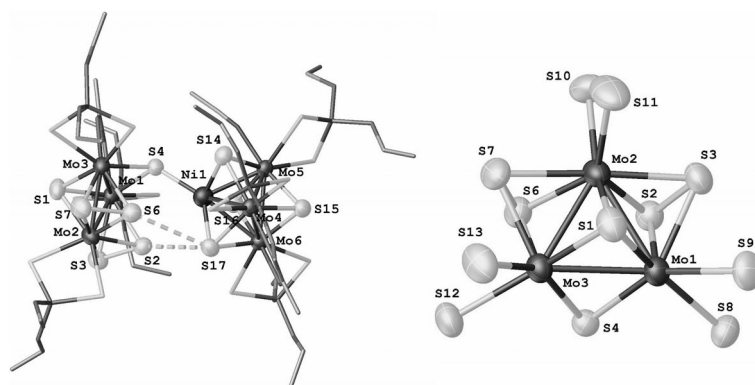


Figure 1. Structure of $\{[\text{Mo}_3\text{S}_6(\text{dtp})_3(\mu\text{-OAc})][\text{Mo}_3\text{NiS}_4(\text{dtp})_3(\mu\text{-OAc})(\text{CH}_3\text{CN})]\}$ (stick model for the terminal ligands have been used for clarity; left). Partial representation of the C_s -symmetrized Mo_3S_6 cluster core (right).

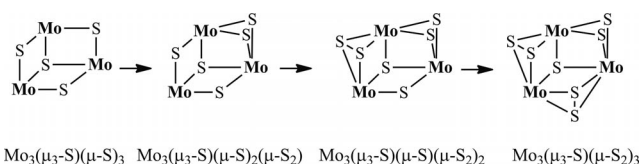
In addition, two sides of the triangle [defined by Mo(1)–Mo(2) and Mo(2)–Mo(3)] are bridged by $\mu\text{-S}_2$ groups with two sulfur atoms [S(3) and S(7)] occupying an equatorial position (S_{eq}) essentially in the Mo_3 plane with another two axial sulfur atoms (S_{ax}) located out of the trimetallic plane [S(2) and S(6)]. The remaining side, defined by Mo(1)–Mo(3), is bridged by a $\mu\text{-S}$ ligand [S(4)] occupying an axial position and by a carboxylate ligand (Mo–O 2.15 Å). Three diethyl dithiophosphate ligands fill the coordination environment of each Mo site and are oriented almost perpendicular to the Mo_3 plane. The C_s symmetry of the Mo_3S_6 cluster core is manifested in the Mo–Mo bond lengths, which present two markedly distinct values. The Mo(1)–Mo(2) and Mo(2)–Mo(3) bond lengths are 2.740 and 2.735 Å, respectively, whereas the Mo(1)–Mo(3) bond length is 2.843 Å. A schematic view highlighting the overall C_s symmetry is shown in Figure 1 (right). The two cluster entities are covalently linked through a Ni(1)–S(4) bond with a length of 2.240 Å. Additional S··S [S(2)–S(17), S(6)–S(17)] contacts of 3.390 and 3.349 Å, respectively, further stabilize the aggregate **1**.

An intriguing characteristic of the Mo_3S_6 clusters lies in the coexistence of disulfide and sulfide bridging ligands. Trinuclear Mo_3 sulfide clusters display dual nucleophilic/electrophilic character depending on whether sulfide S^{2-} (displaying a prominent nucleophilic character binding metals) or disulfide S_2^{2-} ligands (displaying a prominent electrophilic character binding anions) are coordinated. This duality is also proposed for the $\mu_3(\mu_3\text{-S})(\mu\text{-S})(\mu\text{-S}_2)_2$ subunit in compound **1** because the $\mu\text{-S}$ sulfide-bridged ligand binds to the neighboring Ni site whereas the $\mu\text{-S}_2$ disulfide-bridged ligands bind (S··S contacts shorter than the sum of the van der Waals radii) to the $\mu_3\text{-S}$ sulfide-bridged ligand of the neighboring Mo_3NiS_4 cluster. Figure 2 shows (only cluster core atoms are drawn for clarity) the complementarity between the cubane-type Mo_3NiS_4 cluster and the C_s -symmetrized Mo_3S_6 entity. Incidentally, the fused cluster **1** is reminiscent of a well-known class of cubane-type complexes, namely corner-shared double-cuboidal clusters. Figure 2 shows drawings of these two cluster types on approximately the same scale for comparison. In particular, compound **1** shares a similar cluster orientation to that found in corner-shared structural types except that two

Ni–S bonds are not present. Corner-shared compounds are known for Mo, Sn, Hg, Zn, Sb, Cd, and Ge, but no examples based on nickel are known.

Related to this work, the binding of the nickel heteroatom to a sulfur atom of another cluster unit has also been described for the edge-linked quadruple-cubane-type cluster $[(\text{Cp}^*\text{Mo})_2\text{Ni}_2(\mu_3\text{-S})_2(\mu_4\text{-S})_2]_4[\text{PF}_6]_4$ with four $\text{Mo}_2\text{Ni}_2\text{S}_4$ cores.^[31b] The four $\text{Mo}_2\text{Ni}_2\text{S}_4$ cubane-type cores are each linked by two Ni–S bonds and one Ni–Ni bond, which is similar to edge-linked double-cubane-type clusters such as $[\text{Mo}_3\text{M}'\text{S}_4(\text{H}_2\text{O})_9](\text{pts})_8$ ($\text{M}' = \text{Co}, \text{Pd}$ and Cu) or $[\text{W}_3\text{NiS}_4(\text{H}_2\text{O})_9]_2(\text{pts})_8$ ($\text{pts} = p\text{-toluenesulfonate}$).^[19]

With regard to the detailed mechanism of the formation of **1**, we reasonably hypothesize that the diethyl dithiophosphate ligand plays a crucial role acting both as a monoanionic ligand as well as a sulfurizing reagent, triggering the stepwise sulfurization reaction of the initial $[\text{Mo}_3\text{S}_4(\text{OH})_9]^{4+}$ aqua complex according to Scheme 3. Once the mixture of Mo_3S_4 , Mo_3S_5 , Mo_3S_6 , and Mo_3S_7 clusters is formed in the reaction mixture, only Mo_3S_6 has the correct geometry to be fleetingly intercepted by complementary association with the Mo_3NiS_4 cluster as depicted above in Figure 2.



Scheme 3.

The robustness of aggregate **1** is also preserved in solution. It is soluble and stable for hours in organic solvents such as CH_3OH , CH_3CN , CH_2Cl_2 , and CHCl_3 . Electrospray ionization mass spectrometry and ^{31}P NMR spectroscopy were employed to prove the structural integrity of **1** in solution. Despite the neutral nature of compound **1**, positive ESI mass spectrometry proved to be a very useful technique for characterization purposes. Figure 3 displays the positive ESI mass spectrum of $\text{CH}_2\text{Cl}_2/\text{CH}_3\text{OH}$ solutions of **1**.

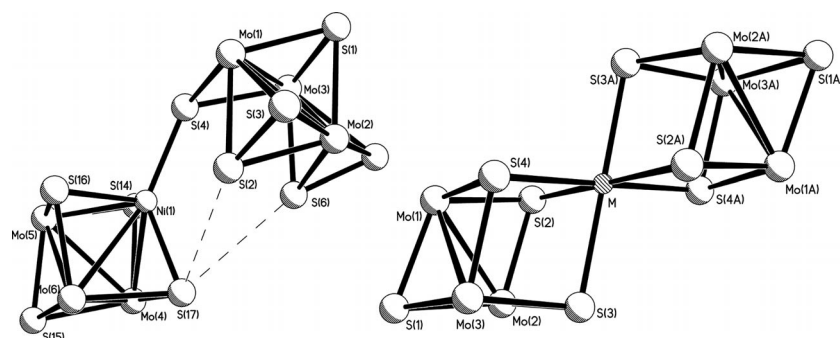


Figure 2. Schematic drawings of the complementarity between the cubane-type Mo_3NiS_4 cluster and the C_s -symmetrized Mo_3S_6 entity mediated by Ni–S and S–S interactions (left). Schematic representation of corner-shared cubane-type structures (right).

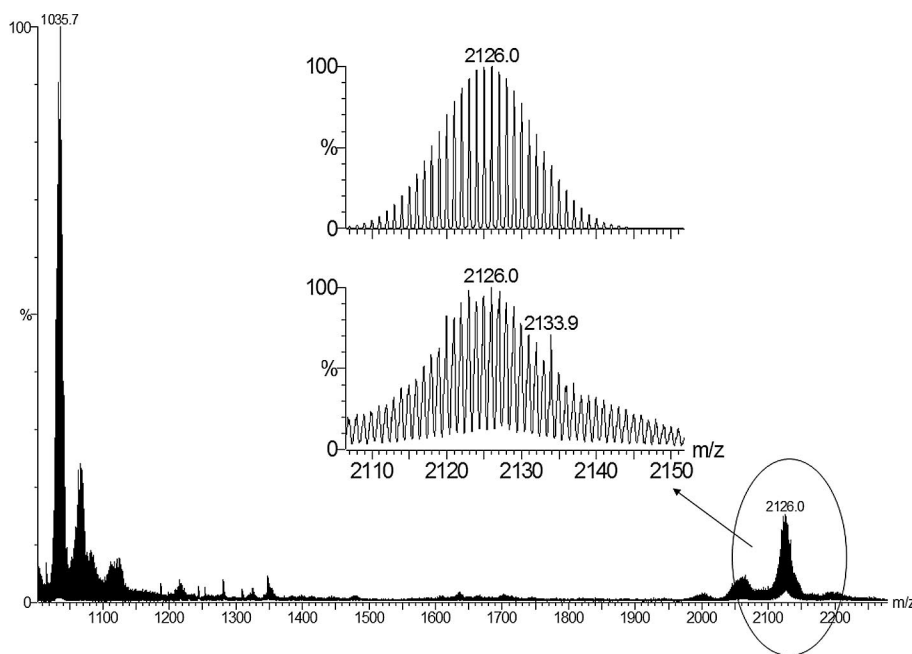


Figure 3. Positive ESI mass spectrum of $\text{CH}_2\text{Cl}_2/\text{CH}_3\text{OH}$ solutions of compound **1**. The inset shows the experimental (bottom) and simulated (top) peaks for the $[\mathbf{1} - \text{CH}_3\text{CN} - \text{CH}_3\text{CO}_2]^+$ species.

In the $m/z = 2000\text{--}2200$ range, a prominent single-charged peak centered at $m/z = 2126.0$ is observed, which corresponds to the $[\mathbf{1} - \text{CH}_3\text{CN} - \text{CH}_3\text{CO}_2]^+$ species on the basis of the m/z value as well as its characteristic isotopic pattern (see inset in Figure 3). Identical ESI mass spectra are typically observed for closely related single-cubane Mo_3NiS_4 clusters of general formula $[\text{Mo}_3(\text{NiL})(\text{dtp})_3(\mu\text{-carboxylate})(\text{L})]^+$ (L is a N-donor ligand) in which ionization upon electrospray occurs by the loss of carboxylate accompanied by the loss of the N-donor ligand.^[24] As inferred from Figure 3, two dominant peaks at $m/z = 1035.7$ and 1071.5 are observed that correspond to the $[\text{Mo}_3\text{S}_6(\text{dtp})_3]^+$ and $[\text{Mo}_3\text{NiS}_4(\text{dtp})_3(\text{CH}_3\text{CN})]^+$ cations. $^{31}\text{P}\{^1\text{H}\}$ and ^1H NMR spectra of **1** were recorded in CDCl_3 (see Figures S1 and S2). For the Mo_3NiS_4 subunit, two resonances are observed close together at room temperature ($\delta = 105.7$ and 105.5 ppm). This two-signal pattern is characteristic of closely related Mo_3S_4 and Mo_3NiS_4 clusters featuring diethyl dithiophosphates and carboxylate-bridging ligands for which a number of fluxional processes have been observed.^[24,32] For example, for compounds $[\text{Mo}_3\text{S}_4(\text{dtp})_3(\mu\text{-OAc})(\text{py})]^{[32]}$ and $[\text{Mo}_3(\text{Nipy})\text{S}_4(\text{dtp})_3(\mu\text{-OAc})(\text{py})]^{[24]}$ two resonances are observed at room temperature, however, three phosphorus resonances are detected at low temperature, as expected on the basis of X-ray structure determination. The proposed fluxional behavior is based on the hemilability of the dtp ligand coordinated to the molybdenum attached to the N-donor ligand^[24] or the lability of the N-donor ligand.^[32] Consequently, two resonances (at $\delta = 99.47$ and 98.36 ppm) are also expected for the Mo_3S_6 cluster unit because its inherent C_s symmetry is preserved in solution. A salient trend regarding ^{31}P chemical shifts is observed upon extensive inspection of a number of Mo_3

clusters bearing diethyl dithiophosphate ligands. For sulfur-bridged (or mixed sulfur/oxygen) Mo_3 clusters, dtp ligands attached to six-coordinate Mo sites typically fall in the $\delta = 107\text{--}111$ ppm range,^[24,32] whereas dtp ligands attached to seven-coordinate Mo sites (as typically found in Mo_3S_7 clusters) are observed below $\delta = 100$ ppm.^[32b] On the basis of these results, we tentatively assign P resonances at $\delta = 99.47$ and 98.36 ppm to the Mo_3S_6 subunit and those at $\delta = 105.7$ and 105.5 ppm to the Mo_3NiS_4 subunit. The ^1H NMR spectrum of compound **1** provides limited information due to signal broadening and extensive overlapping. Nevertheless, two distinct regions at $\delta = 1.2\text{--}1.9$ ppm for the CH_3 groups of the carboxylate, acetonitrile, and ethoxy groups of the dtp ligands and at $\delta = 4.1\text{--}4.7$ ppm for the CH_2 groups of the dtp ligand are evident.

It has previously been reported that the Ni heterometal in the Mo_3NiS_4 cluster presents a unique and exceptional reactivity and is able to coordinate different ligands. It shows a great tendency to coordinate soft ligands^[19,30,33,34] containing S, P, and As donors and π acceptor ligands such as alkenes, alkynes, and CO as well as sulfur ligands from neighboring clusters. The isolation and full characterization of compound **1** is the first example in which a trinuclear Mo_3 cluster acts as a ligand for the Mo_3NiS_4 cluster and it provides a unique opportunity to isolate the first Mo_3S_6 cluster.

Conclusion

An unprecedented cluster association of formula $\{\text{Mo}_3(\mu_3\text{-S})(\mu\text{-S})(\mu\text{-S})_2(\text{dtp})_3(\mu\text{-OAc})\}[\text{Mo}_3\text{NiS}_4(\text{dtp})_3(\mu\text{-S})_2(\mu\text{-OAc})(\text{CH}_3\text{CN})]$ comprising the novel C_s -symmetrized

$\text{Mo}_3(\mu_3\text{-S})(\mu\text{-S})(\mu\text{-S}_2)_2(\text{dtp})_3(\mu\text{-OAc})$ structural type covalently attached to a cubane-type Mo_3NiS_4 core has been isolated and fully characterized.

Experimental Section

General Procedures and Materials: All the experiments were performed in air. Stock solutions of the aqua complexes $[\text{Mo}_3\text{S}_4(\text{H}_2\text{O})_9]^{4+}$ and $[\text{Mo}_3(\text{NiCl})\text{S}_4(\text{H}_2\text{O})_9]^{3+}$ in 2 M HCl were prepared according to the published procedures. Potassium diethyl dithiophosphate (Kdtp) was prepared by dissolving P_4S_{10} in an excess of hot ethanol followed by neutralization with 4 equiv. of KOH, evaporation of the reaction solution, and recrystallization of the solid from acetone/diethyl ether mixtures to give a snow-white crystalline product. Other reagents (P_4S_{10} , acetic acid) were commercial quality reagents (Aldrich) and were used as purchased. A Q-TOF I (quadrupole/hexapole time-of-flight) mass spectrometer with an orthogonal Z-spray/electrospray interface (Waters, Manchester, UK) was used. Nitrogen was used as the drying and nebulizing gases at flow rates of 800 and 20 L/h, respectively. Sample solutions (approx. 5×10^{-5} M) in dichloromethane/methanol were infused directly to the interface through a syringe pump at a flow rate of 10 $\mu\text{L}/\text{min}$. The temperature of the source block was set to 120 °C and the interface to 150 °C. A capillary voltage of 3.5 kV was used in the positive scan mode and the cone voltage was set at low values ($U_c = 10$ V) to control the extent of fragmentation. The chemical composition of each peak was assigned by comparison of the isotope experimental pattern with that theoretical using the MassLynx 4.0 program. $^{31}\text{P}\{^1\text{H}\}$ and ^1H NMR spectra were recorded with a Varian Mercury 300 MHz spectrometer equipped with a four nucleus probe operating at 121.48 MHz for ^{31}P . ^{31}P and ^1H NMR chemical shifts were referenced externally to H_3PO_4 (85% in D_2O ; $\delta = 0.0$ ppm) in a capillary and to the residual solvent (referenced to tetramethylsilane), respectively.

$\{[\text{Mo}_3(\mu_3\text{-S})(\mu\text{-S})(\mu\text{-S}_2)_2(\text{dtp})_3(\mu\text{-OAc})][\text{Mo}_3\text{NiS}_4(\text{dtp})_3(\mu\text{-OAc})(\text{CH}_3\text{-CN})]\}$ (**1**): Solid Kdtp (583 mg, 2.60 mmol) was added to approx. 4 mm $[\text{Mo}_3\text{S}_4(\text{H}_2\text{O})_9]^{4+}$ (20 mL, 80 μmol) in 2 M HCl in the presence of equimolar amounts of $[\text{Mo}_3(\text{NiCl})\text{S}_4(\text{H}_2\text{O})_9]^{3+}$. A brown precipitate separated immediately, which was filtered and dried in air. The dry product was dissolved in CH_3CN (50 mL) and a few drops of acetic acid were added to the resulting brown solution and taken to dryness. This solid contains a mixture of Mo_3NiS_4 and Mo_3S_x clusters ($x = 4\text{--}7$) together with compound **1**. The solution was allowed to evaporate slowly in an open beaker. After 2 d, black crystals of **1** were collected. Yield: 275 mg (40%, based on $[\text{Mo}_3\text{S}_4(\text{H}_2\text{O})_9]^{4+}$). $^{31}\text{P}\{^1\text{H}\}$ NMR (CDCl_3 , 30 °C, 121.48 MHz): $\delta = 105.7$ (Mo_3NiS_4), 105.5 (Mo_3NiS_4), 99.5 (Mo_3S_6), 98.3 (Mo_3S_6) ppm. MS (ESI, + mode, $\text{CH}_2\text{Cl}_2/\text{CH}_3\text{OH}$): $m/z = 2126.0$ [**1** – CH_3CN – CH_3CO_2] $^+$, 1035.7 [$\text{Mo}_3\text{S}_6(\text{dtp})_3$] $^+$, 1071.5 [$\text{Mo}_3\text{-NiS}_4(\text{dtp})_3(\text{CH}_3\text{CN})$] $^+$. $\text{C}_{30}\text{H}_{67}\text{Mo}_6\text{NNiO}_{16}\text{P}_6\text{S}_{22}$ (2223.37): calcd. C 16.21, H 3.04, N 0.63, S 31.72; found C 16.52, H 3.12, N 0.71, S 31.85.

X-ray Crystallographic Study: The diffraction data were collected with a Bruker–Nonius KappaCCD diffractometer by using graphite-monochromated Mo-K_α radiation ($\lambda = 0.71073$ Å) with ϕ and ω scans chosen to give a complete asymmetric unit using the COLLECT program up to θ_{max} of 28.82° with only 91.8% for completeness of data.^[35] The Denzo SMN and HKL2000 programs were used for indexed and scaled data.^[36] The absorption correction was applied by using a semi-empirical method based on multiple scanned reflections on the PLATON program^[37] and the structure solution was performed by direct methods using the

SIR2004 program^[38] and refined by using the SHELXL-97 program.^[39] All non-hydrogen atoms were refined with anisotropic thermal parameters by using full-matrix least-squares procedures on F^2 . The dtp molecules present slight thermal disorder increases on terminal carbons. The methyl H atoms were refined as rigid groups, which were allowed to rotate but not to tip, with $U_{\text{iso}}(\text{H}) = 1.5U_{\text{eq}}(\text{C})$. All other hydrogen atoms were allowed to ride on their parent atoms with $U_{\text{iso}}(\text{H}) = 1.2U_{\text{eq}}(\text{C})$. Crystal data for **1**: $\text{C}_{30}\text{H}_{67}\text{Mo}_6\text{NNiO}_{16}\text{P}_6\text{S}_{22}$, $M_r = 2223.34$, triclinic, space group $P\bar{1}$, $a = 13.8610(10)$, $b = 14.9860(10)$, $c = 19.3630(10)$ Å, $\alpha = 77.89(1)^\circ$, $\beta = 84.17(1)^\circ$, $\gamma = 79.59(1)^\circ$, $V = 3859.3(4)$ Å³, $T = 293(2)$ K, $Z = 2$, $\mu(\text{Mo-K}_\alpha) = 1.952$ mm^{−1}. Reflections collected/unique = 103160/18539 ($R_{\text{int}} = 0.0593$). Final refinement converged with $R1 = 0.0709$ for reflections with $F_o > 4\sigma(F_o)$ and $wR2 = 0.1679$ for all reflections, max./min. residual electron density 1.043 and -2.106 e Å^{−3}.

CCDC-831580 contains the supplementary crystallographic data for this paper. These data can be obtained free of charge from The Cambridge Crystallographic Data Centre via www.ccdc.cam.ac.uk/data_request/cif.

Supporting Information (see footnote on the first page of this article): $^{31}\text{P}\{^1\text{H}\}$ and ^1H NMR spectra of CDCl_3 solutions of **1**.

Acknowledgments

R. H. M. is grateful to the Spanish Ministerio de Ciencia e Innovación (MICINN) for funding through project CTQ2009-14443-C02-02. J. G. P. also thanks the MICINN for funding through project MAT2010-21270-C04-02 and MALTA Consolider (grant number CSD2007-0045). The authors also thank the Servicios Generales de la Universidad de La Laguna for providing X-ray facilities and the Servei Central D'Instrumentació Científica (SCIC) of the Universitat Jaume I for providing mass spectrometry and NMR facilities.

- [1] G. Sakane, T. Shibahara, in: *Transition Metal Sulfur Chemistry: Biological and Industrial Significance* (Eds.: E. I. Stiefel, K. Matsumoto), ACS Symposium Series, Honolulu, HI, **1995**; H. Seino, M. Hidai, *Chem. Sci.* **2011**, 2, 847–857.
- [2] R. Llusar, S. Uriel, *Eur. J. Inorg. Chem.* **2003**, 1271–1290.
- [3] A. L. Gushchin, K. A. Kovalenko, M. N. Sokolov, D. Y. Naumov, E. V. Peresypkina, A. V. Virovets, V. P. Fedin, *Russ. Chem. Bull.* **2007**, 56, 1707–1711; M. N. Sokolov, A. L. Gushchin, K. A. Kovalenko, E. V. Peresypkina, A. V. Virovets, J. Sanchiz, V. P. Fedin, *Inorg. Chem.* **2007**, 46, 2115–2117.
- [4] R. Llusar, S. Triguero, S. Uriel, C. Vicent, E. Coronado, C. J. Gomez-Garcia, *Inorg. Chem.* **2005**, 44, 1563–1570; R. Llusar, S. Triguero, V. Polo, C. Vicent, C. Gomez-Garcia, O. Jeannin, M. Fourmigue, *Inorg. Chem.* **2008**, 47, 9400–9409; R. Llusar, S. Uriel, C. Vicent, J. M. Clemente-Juan, E. Coronado, C. J. Gómez-Garcia, B. Braidia, E. Canadell, *J. Am. Chem. Soc.* **2004**, 126, 12076–12083; A. Alberola, M. Fourmigue, C. Gómez-Garcia, R. Llusar, S. Triguero, *New J. Chem.* **2008**, 32, 1103–1109; A. Alberola, R. Llusar, S. Triguero, C. Vicent, M. N. Sokolov, C. Gómez-Garcia, *J. Mater. Chem.* **2007**, 17, 3440–3450.
- [5] J. M. Garriga, R. Llusar, S. Uriel, C. Vicent, A. J. Usher, N. T. Lucas, M. G. Humphrey, M. Samoc, *Dalton Trans.* **2003**, 4546–4551; M. Feliz, R. Llusar, S. Uriel, C. Vicent, M. G. Humphrey, N. T. Lucas, M. Samoc, B. Luther-Davies, *Inorg. Chim. Acta* **2003**, 349, 69–76.
- [6] A. V. Virovets, N. V. Podberezhskaya, *J. Struct. Chem.* **1993**, 34, 306–322; R. Llusar, C. Vicent, *Coord. Chem. Rev.* **2010**, 254, 1534–1548.
- [7] M. Hidai, S. Kuwata, Y. Mizobe, *Acc. Chem. Res.* **2000**, 33, 46–52; R. Hernandez-Molina, M. N. Sokolov, A. G. Sykes,

- Acc. Chem. Res.* **2001**, *34*, 223–230; R. Hernandez-Molina, A. G. Sykes, *Coord. Chem. Rev.* **1999**, *187*, 291–302.
- [8] K. Tsuge, S. Yajima, H. Imoto, T. Saito, *J. Am. Chem. Soc.* **1992**, *114*, 7910–7912; K. Tsuge, H. Imoto, T. Saito, *Inorg. Chem.* **1995**, *34*, 3404–3409; A. Majumdar, J. Mitra, K. Pal, S. Sarkar, *Inorg. Chem.* **2008**, *47*, 5360–5364.
- [9] P. A. Petrov, A. V. Virovets, A. Alberola, R. Llusar, S. N. Konchenko, *Dalton Trans.* **2010**, *39*, 8875–8877.
- [10] R. Hernandez-Molina, A. G. Sykes, *J. Chem. Soc., Dalton Trans.* **1999**, 3137–3148.
- [11] V. P. Fedin, A. G. Sykes, *Inorg. Synth.* **2002**, *33*, 162–170.
- [12] V. P. Fedin, M. N. Sokolov, Y. V. Mironov, B. A. Kolesov, S. V. Tkachev, V. Y. Fedorov, *Inorg. Chim. Acta* **1990**, *167*, 39–45.
- [13] T. R. Halbert, K. McGauley, W. H. Pan, R. S. Czernuszewicz, E. I. Stiefel, *J. Am. Chem. Soc.* **1984**, *106*, 1849–1851.
- [14] R. Llusar, V. Polo, E. Velez, C. Vicent, *Inorg. Chem.* **2010**, *49*, 8045–8055.
- [15] H. Jiao, Y.-W. Li, B. Delmon, J.-F. Halet, *J. Am. Chem. Soc.* **2001**, *123*, 7334–7339; X.-Q. Yao, Y.-W. Li, H. Jiao, *J. Mol. Struct.* **2005**, *726*, 67–80; X.-Q. Yao, Y.-W. Li, H. Jiao, *J. Mol. Struct.* **2005**, *726*, 81–92; T. Zeng, X.-D. Wen, Y.-W. Li, H. Jiao, *J. Phys. Chem. B* **2005**, *109*, 13704–13710; P. Murugan, V. Kumar, Y. Kawazoe, N. Ota, *J. Phys. Chem. A* **2007**, *111*, 2778–2782.
- [16] S. Duval, S. Floquet, C. Simonnet-Jegat, J. Marrot, R. N. Biboum, B. Keita, L. Nadj, M. Haouas, F. Taulelleand, E. Cadot, *J. Am. Chem. Soc.* **2010**, *132*, 2069–2077.
- [17] a) S. Duval, M. A. Pilette, J. Marrot, C. Simonnet-Jegat, M. Sokolov, E. Cadot, *Chem. Eur. J.* **2008**, *14*, 3457–3466; b) I. V. Kalinina, M. N. Sokolov, E. V. Chubarova, E. V. Peresypkina, V. P. Fedin, *J. Struct. Chem.* **2010**, *51*, 303–307.
- [18] T. Shibahara, T. Yamamoto, G. Sakane, *Chem. Lett.* **1994**, 1231–1234.
- [19] T. Shibahara, G. Sakane, M. Maeyama, H. Kobashi, T. Yamamoto, T. Watase, *Inorg. Chim. Acta* **1996**, *251*, 207–225.
- [20] R. Hernandez-Molina, M. N. Sokolov, W. Clegg, P. Esparza, A. Mederos, *Inorg. Chim. Acta* **2002**, *331*, 52–58; P. A. Abramov, M. N. Sokolov, R. Hernandez-Molina, C. Vicent, A. V. Virovets, D. Y. Naumov, P. Gili, J. Gonzalez-Platas, V. P. Fedin, *Inorg. Chim. Acta* **2010**, *363*, 3330–3337; A. L. Gushchin, B.-L. Ooi, P. Harris, C. Vicent, M. N. Sokolov, *Inorg. Chem.* **2009**, *48*, 3832–3839.
- [21] M. N. Sokolov, D. N. Dybtsev, A. V. Virovets, V. P. Fedin, P. Esparza, R. Hernandez-Molina, D. Fenske, A. G. Sykes, *Inorg. Chem.* **2001**, *40*, 1136–1139.
- [22] M. Sokolov, P. Esparza, R. Hernandez-Molina, J. G. Platas, A. Mederos, J. A. Gavin, R. Llusar, C. Vicent, *Inorg. Chem.* **2005**, *44*, 1132–1141.
- [23] M. N. Sokolov, A. V. Virovets, D. N. Dybtsev, O. Gerasko, V. P. Fedin, R. Hernandez-Molina, W. Clegg, A. G. Sykes, *Angew. Chem.* **2000**, *112*, 1725; *Angew. Chem. Int. Ed.* **2000**, *39*, 1659–1661; V. P. Fedin, V. Gramlich, M. Worle, T. Weber, *Inorg. Chem.* **2001**, *40*, 1074–1077; R. Hernandez-Molina, M. Sokolov, P. Esparza, C. Vicent, R. Llusar, *Dalton Trans.* **2004**, 847–851.
- [24] R. Hernandez-Molina, J. Gonzalez-Platas, K. A. Kovalenko, M. N. Sokolov, A. V. Virovets, R. Llusar, C. Vicent, *Eur. J. Inorg. Chem.* **2011**, 683–693.
- [25] R. Hernandez-Molina, M. Sokolov, P. Nuñez, A. Mederos, *J. Chem. Soc., Dalton Trans.* **2002**, 1072–1077.
- [26] I. Takei, Y. Wakebe, K. Suzuki, Y. Enta, T. Suzuki, Y. Mizobe, M. Hidai, *Organometallics* **2003**, *22*, 4639–4641; K. Herbst, P. Zanello, M. Corsini, N. D'Amelio, L. Dahlenburg, M. Brorson, *Inorg. Chem.* **2003**, *42*, 974–981.
- [27] K. Herbst, M. Monari, M. Brorson, *Inorg. Chem.* **2002**, *41*, 1336–1338.
- [28] M. Feliz, R. Llusar, S. Uriel, C. Vicent, M. Brorson, K. Herbst, *Polyhedron* **2005**, *24*, 1212–1220.
- [29] T. Shibahara, M. Yamasaki, H. Akashi, T. Katayama, *Inorg. Chem.* **1991**, *30*, 2693–2699.
- [30] M. N. Sokolov, E. V. Chubarova, R. Hernandez-Molina, M. Clausen, D. Y. Naumov, C. Vicent, R. Llusar, V. P. Fedin, *Eur. J. Inorg. Chem.* **2005**, *11*, 2139–2146.
- [31] a) K. Herbst, L. Dahlenburg, M. Brorson, *Inorg. Chem.* **2004**, *43*, 3327–3328; b) I. Takei, K. T. Suzuki, Y. Enta, K. Dohki, T. Susuki, Y. Mizobe, M. Hidai, *Organometallics* **2003**, *22*, 1790–1792.
- [32] a) Y. Yao, H. Akashi, G. Sakane, T. Shibahara, H. Ohtaki, *Inorg. Chem.* **1995**, *34*, 42–48; Y. Tang, Y. Qin, L. Wu, Z. Li, Y. Kang, Y. Yao, *Polyhedron* **2001**, *20*, 2911–2918; Z. J. Li, Y. Y. Qin, Y. H. Tang, Y. Kang, J. B. Xia, Z. Chen, L. Wu, Y. G. Yao, *Chin. J. Chem.* **2003**, *21*, 1174–1177; b) J. Chen, S. F. Lu, Z. X. Huang, R. M. Yu, Q. F. Wu, *Chem. Eur. J.* **2001**, *7*, 2002–2005.
- [33] T. Shibahara, S. Mochida, G. Sakane, *Chem. Lett.* **1993**, 89–92.
- [34] M. N. Sokolov, R. Hernández-Molina, D. N. Dybtsev, E. V. Chubarova, S. F. Solodovnikov, N. V. Pervukhina, C. Vicent, R. Llusar, V. P. Fedin, *Z. Anorg. Allg. Chem.* **2002**, *628*, 2335–2339.
- [35] C. P. S. Bruker–Nonius, The Netherlands, **1997–2000**.
- [36] Z. M. Otwinowski, in: *Methods in Enzymology* (Ed.: C. W. S. Carter), Academic Press, New York, **1997**, vol. 276, pp. 307–326.
- [37] A. L. Spek, *Acta Crystallogr., Sect. A* **1990**, *46*, C34.
- [38] *Sir2004, An improved tool for crystal structure determination and refinement*, see: M. C. Burla, R. Caliandro, M. Camalli, B. Carrozzini, G. L. Casciaro, L. De Caro, C. Giacovazzo, G. Polidori, R. Spagna, *J. Appl. Cryst.* **2005**, *38*, 381–388.
- [39] G. M. Sheldrick, *SHELXL-97*, University of Göttingen, Germany.

Received: November 25, 2011

Published Online: February 6, 2012

Ca₂NiSn₂ – A Polymorphic Intermetallic Phase: Atomic and Electronic Structure as well as a Topological Description of the Phase Transition by a Sigmatropic-Type Rearrangement of Ni and Sn Atoms

Lisa Siggelkow,^[a] Viktor Hlukhyy,^[a] and Thomas F. Fässler^{*[a]}

Keywords: Tin / Intermetallic phases / ELF (Electron Localization Function) / Chemical bonding / Phase transitions

The two sentences starting in line 6 from the bottom of the first column and the caption of Figure 3 on page 989 as well as the corresponding reference [8] on page 996 of the original article^[1] are erroneous, they should read as follows.

For example, the distorted square $1_{\infty}[\text{Ni}_2\text{Sn}_2]$ ladder is observed in the Ni–Sn substructure of NP-CeNiSn^[8] (TiNiSi structure type,^[9] Figure 3, a). In NP-CeNiSn the ladders are directly connected to form a three-dimensional network with Ce atoms situated in the cavities.

Figure 3. Crystal structures of a) NP-CeNiSn,^[8] b) Ca₆Cu₂Sn₇,^[10] c) SrNiSn₂,^[12] d) Sm₂NiSn₄,^[13] and e) Yb₃CoSn₆.^[31] The alkaline earth and rare earth metal atoms are drawn as black spheres, the tetrel and transition-metal atoms as white and grey spheres, respectively.

[8] a) R. V. Skolozdra, O. E. Koretskaya, Y. K. Gorelenko, *Inorg. Mater.* **1984**, 20, 520; b) G. Nakamoto, T. Takabatake, H. Fujii, A. Minami, K. Maezawa, I. Oguro, A. A. Menovsky *J. Phys. Soc. Jpn.* **1995**, 64, 4834; c) J. F. Riecken, G. Heymann, W. Hermes, U. C. Rodewald, R. D. Hoffmann, H. Huppertz, R. Pöttgen, *Z. Naturforsch., B* **2008**, 63, 695.

The Authors

[1] L. Siggelkow, V. Hlukhyy, T. F. Fässler, *Eur. J. Inorg. Chem.* **2012**, 987–997.

Received: February 10, 2012
Published Online: February 21, 2012

[a] Department Chemie, Technische Universität München, Lichtenbergstr. 4, 85747 Garching, Germany